J. Chem. Theory Comput. **2009,** *5,* 2925–2929 **2925**

JCTC Journal of Chemical Theory and Computation

Efficient Approach to Reactive Molecular Dynamics with Accurate Forces

Masahiro Higashi and Donald G. Truhlar*

Department of Chemistry and Supercomputing Institute,
University of Minnesota, 207 Pleasant Street SE,
Minneapolis, Minnesota 55455-0431

Received June 11, 2009

Abstract: Density functional theory is a powerful and efficient method for calculating potential energy surfaces for chemical reactions, but its application to complex systems, such as reactions in enzymes, is often prohibitively expensive, even when high-level theory is applied only to a primary subsystem, such as an active site, and when the remaining system is treated by molecular mechanics. Here we show how the combination of multiconfiguration molecular mechanics with charge response kernels can speed up such calculations by three or more orders of magnitude. The resulting method, called electrostatically embedded multiconfiguration molecular mechanics, is illustrated by calculating the free energy of activation profile for the dehalogenation of 1,2-dichloroethane by haloalkane dehalogenase. This shows how hybrid density functionals or other high-level electronic structure methods can now be used efficiently in simulations that require extensive sampling, such as for calculating free energy profiles along a high-barrier reaction coordinate.

"The accuracy of a simulation is largely determined by two factors: conformation sampling and model accuracy."[1] The Car−Parrinello scheme[2] created a paradigm shift in molecular dynamics simulations by suggesting an efficient way to replace empirical interatomic potential models (molecular mechanics) with density functional direct dynamics, where direct dynamics implies that "instead of using a pre-defined PEF (potential energy function), all required energies and forces for each geometry that is important for evaluating dynamical properties are obtained directly from electronic structure calculations."[3] Now density functional direct dynamics, using either the Car−Parrinello algorithm or later-generation ones, is a standard tool in materials science,[4,5] especially with density functionals that do not involve nonlocal operators because local functionals allow for less expensive plane wave calculations on extended systems. In some cases, density functional theory (DFT) is replaced by another quantum mechanical (QM) method, or QM is applied to an active site subsystem and combined with molecular mechanics (MM) for a much larger secondary subsystem. For many problems, though, such as free energy simulations of enzyme-catalyzed reactions, even combined QM/MM calculations are very expensive because of the required QM system size or the large amount of sampling required, and there is considerable research on how to make the calculations most affordable.[6−15]

The most accurate QM levels for chemistry require inclusion of dynamical correlation and nonlocal Hartree−Fock exchange, as in hybrid density functionals that represent a marriage of Kohn−Sham and Hartree−Fock theories,[16] but Hartree−Fock exchange makes calculations on large or complex systems very expensive. In the present article, we report well-converged free energy simulation of an enzymatic reaction employing a hybrid density function that includes 42.8% Hartree−Fock exchange. This calculation is made efficient by applying the new electrostatically embedded multiconfiguration molecular mechanics (EE-MCMM) algorithm,[17] which is actually a powerful but semiautomatic fitting algorithm that is adapted to be efficient in the combined QM/MM context.

Consider first the MCMM algorithm for a gas-phase reaction[18,19] with N atoms with coordinates $\mathbf{R}_\alpha \equiv (X_\alpha, Y_\alpha, Z_\alpha)$, $\alpha = 1, 2, ..., N$, and let $\mathbf{R}$ denote the set of $\mathbf{R}_\alpha$. MCMM involves approximating the PEF as the lowest eigenvalue V of a 2×2 valence bond configuration interaction matrix:[20]

$$\mathbf{H} \equiv \begin{pmatrix} H_{11} & H_{12} \\ H_{12} & H_{22} \end{pmatrix} \tag{1}$$

H_{11} is set equal to the MM PEF of reactants, and the H_{22} is set equal to the MM PEF of products.[21] At a set of K geometries called electronic structure Shepard points, $\mathbf{R}^{(k)}$, with $k = 1, 2, ..., K$, one uses electronic structure theory to calculate a Taylor expansion of V valid through second order in $\mathbf{Q}^{(k)} \equiv \mathbf{R} - \mathbf{R}^{(k)}$. One then re-expresses this as a second-order Taylor expansion $H_{12}^{(k)}$ of $H_{12}(\mathbf{Q})$.[22] A global approximation to H_{12} is then obtained by joining these expansions (possibly augmented by K^{MM} additional points where $H_{12}^{(k)}$ is assumed to be zero) by Shepard interpolation.[18,19,23]

In combined QM/MM treatments of chemical reactions, the reactive QM subsystem interacts with a (usually much larger) nonreactive subsystem described by MM.[24,25] The interaction of the subsystems is described by stretching, bending, torsion,

---

* Corresponding author. Telephone: 612-624-7555. Fax: 612-624-9390. E-mail: truhlar@umn.edu.

10.1021/ct900301d CCC: $40.75

noncovalent (repulsion and dispersion), and electrostatic terms. The electrostatic terms are the only ones that affect the QM wave function, and they correspond to including the partial atomic charges of the MM subsystem in the Hamiltonian of the electronic orbitals of the QM subsystem. As in the method of charge response kernels,[26−28] we replace these QM orbital−MM partial charge interactions by QM partial charge−MM partial charge interactions. Then the electrostatic terms depend on the MM system only through the N values Φ_α of the electrostatic potential of the MM subsystem at the nuclei of the QM subsystem. Thus, the QM energy depends on $4N$ variables: X_α, Y_α, Z_α, Φ_α, $\alpha = 1, 2, ..., N$. By using $4N$-dimensional Taylor series (rather than the $3N$-dimensional ones used for gas-phase calculations) in the Shepard interpolation, the MCMM method can treat the electrostatically embedded (EE) QM subsystem of the combined QM/MM calculation very efficiently; this is called EE-MCMM.[17] The new kinds of derivatives that appear in the Taylor series are $\partial V/\partial\Phi_\alpha$, which is a partial charge Q_α on QM atom α, and $\partial^2 V/\partial\Phi_\alpha\partial\Phi_\beta$ and $\partial^2 V/\partial\Phi_\alpha\partial\mathbf{R}_\alpha$, which are charge response kernels that, respectively, describe the QM charge fluctuations due to the MM electrostatic potential and the displacements of the QM atoms. The truncation of the Taylor series in $\phi_\alpha = \Phi_\alpha - \Phi_\alpha^{(k)}$ at second order is adequate because the linear response relation between Q_α and Φ_α generally holds quite well even when ϕ_α is large,[29] and because the trust regions around each $\mathbf{R}^{(k)}$, $\mathbf{\Phi}^{(k)}$ point are merged by Shepard interpolation.

As explained in previous papers,[18,30,31] MCMM[18] is based on a combination of several elements: (i) semiempirical valence bond theory for the potential energy surface V of a chemical reaction,[32] (ii) the combination of semiempirical valence bond theory with MM for spectator degrees of freedom,[31,33] (iii) the empirical valence bond method in which MM force fields are used for the diagonal elements of a valence bond Hamiltonian matrix, and their parameters or parameters in off-diagonal elements (H_{12} in the case of a two-configuration treatment, as used here) can be adjusted to produce either potential energy surfaces or features that agree with electronic structure calculations or features inferred from experiments,[21,34] (iv) the reversion of a Taylor series for V at a particular geometry to provide a Taylor series for H_{12},[22] (v) the multidimensional Shepard interpolation method,[23] and (vi) the efficient and orientation-independent representation of low-order expansions of potential energy surfaces in internal coordinates.[35] MCMM combines these elements in a new way. For example, whereas the Shepard interpolation was originally applied to interpolate V,[23] it is used in MCMM to interpolate H_{12}, which is a key difference because H_{12} is generally more slowly varying and less rugged. MCMM also uses a new weighting function for the Shepard interpolation. EE-MCMM[17] extends MCMM to electronically embedded QM/MM calculations[24,25] by combining MCMM with charge response kernels[26−29] for electrostatic embedding. MCMM is designed to provide a particularly efficient method for fitting global potential energy surfaces of complex systems, and EE-MCMM extends the approach to electronically embedded QM subsystems in combined QM/MM calculations.

We emphasize that, although our method involves MM, its goal is to fit a high-level potential energy surface for a specific multidimensional reaction conveniently and efficiently, not to generate a semiempirical approximation to a surface. Similarly, although the method uses charge response kernels, it is not an alternative to semiempirical fluctuating charge or electronegativity equalization models, but rather it uses these kernels to efficiently represent the response[26−29] calculated for a particular system by a high-level method. If the method is continued to convergence, then the results become independent of the MM force field employed and approach the results that would be obtained with the high-level fitted. However, it is not necessary to converge the calculations to that limit, and we accept a dependence on the assumed MM force field in the reactant and product regions if MM is reasonably accurate there, and we accept an MM dependence in the regions of the surface that are less important for the particular dynamical event under consideration, just as combined QM/MM calculations accept MM for the degrees of freedom of the system that are less strongly coupled to the reaction.

Here we demonstrate the applicability of EE-MCMM to enzyme kinetics by applying it to the reaction $\mathrm{RCH_2C(O)O^-} + \mathrm{CH_2ClCH_2Cl} \rightarrow \mathrm{RCH_2C(O)OCH_2CH_2Cl} + \mathrm{Cl^-}$, where R is haloalkane dehalogenase, and the carboxylate nucleophile participating in the reaction is the side chain of Asp124.[36] Because our objective in this letter is to provide a methodological demonstration of capability and reduction to practice, we do not review work whose objective is to understand the particular enzyme reaction used for the example.

Results

Our simulation has 15 QM atoms (substrate plus $\mathrm{CH_2C(O)O^-}$ of Asp124) and 5 812 MM atoms (the rest of the protein and water), and we used the hybrid density functional MPW1K,[37] where the fraction of Hartree−Fock exchange was optimized[37] to reproduce barrier heights and reaction energies. As a result, MPW1K includes 42.8% Hartree−Fock exchange, and the error is much smaller than the errors of local density functionals.[38]

The reaction coordinate is defined in terms of the breaking C−Cl bond distance r_1 and the forming C−Cl bond distance r_2 by

$$z = r_1 - r_2 \tag{2}$$

First, we performed constrained optimizations with $z = -0.9$, $+0.2$, and $+1.8$ Å. This yielded three sets ($k = 1, 2, 3$) of $\mathbf{R}^{(k)}$, $\mathbf{\Phi}^{(k)}$ that were used for a preliminary EE-MCMM fit. A minimum-energy path for this fit differed from a full MPW1K/MM calculation by the greatest amount at $z = 0.9$ Å, so that point was chosen as the fourth Shepard point. Four more Shepard points were then added at locations where preliminary MCMM fits differed from full calculations. The final simulations have $K = 8$ and $K^{\mathrm{MM}} = 0$.

Figure 1 shows three snapshots from the simulation. These pictures show that two tryptophans make hydrogen bonds with the substrate at the transition state.

We carried out umbrella sampling by the weighted histogram analysis method[39] (WHAM) with 33 equally spaced windows centered at values z_0 of the reaction coordinate from -1.2 to $+2.0$ Å. The resulting potential of mean force (PMF) is shown in Figure 2. The PMF is very smooth and physically reasonable. The barrier in the PMF is 15.3 kcal/mol. Correcting for the vibrational free energy along the reaction coordinate at the reactant[40] lowers this to 14.8 kcal/mol. Since z is nearly linear

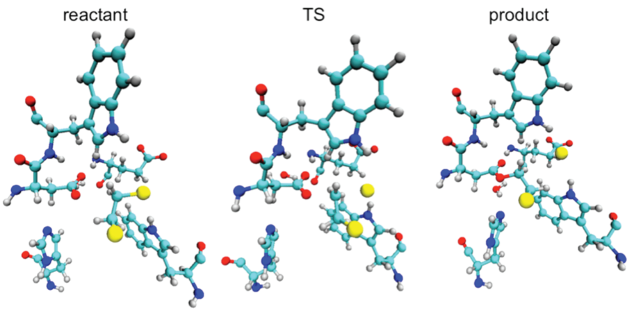

Figure 1. Hydrogen bonding in the active site. Snapshots of the QM subsystem plus key nearby MM atoms at the reactant, the transition state, and the product configurations.

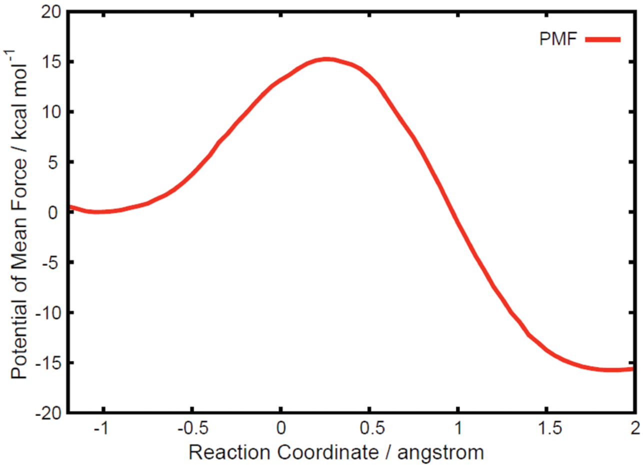

Figure 2. Free energy profile. Free energy as a function of reaction coordinate *z*.

Table 1. Errors (kcal/mol) during MD Simulations

z_0	mean signed error	mean unsigned error
−0.8	−0.3	1.1
−0.4	−0.3	0.6
0.0	−0.5	0.8
+0.4	−0.2	0.5
+0.8	0.5	0.8
+1.2	0.3	0.9
+1.6	0.7	0.9
all[a]	0.1	0.9

[a] 3 300 configurations from all windows with $-1.2 \leq z_0 \leq 2.0$ Å.

in Cartesian coordinates at the transition state, this may be considered to be a good approximation to the free energy of activation.[40] For comparison, the experimental value is 15.3 kcal/mol (obtained from the experimental rate constant[41] using transition-state theory).

During the umbrella sampling run, we saved a configuration every 0.5 ps during the data collection phase for each window, for a total of 3 300 configurations in the entire umbrella sampling calculations. We then compared the EE-MCMM/MM energies at these points to full QM/MM calculations; the error statistics are given in Table 1. This table shows that the mean signed and unsigned errors in the PEF are reasonably small all along the reaction path.

Discussion

Combined QM/MM methods are a powerful means for studying chemical reactions in solution, enzymes, and solids. Two central difficulties are using a reliable level for the QM subsystem and sampling configurations of the entire system adequately. It is difficult to carry out direct high-level ab initio or density functional calculations because both types of calculations require a high computational cost. Here we have shown that the EE-MCMM method has great promise for describing QM/MM potential energy surfaces for free energy calculations in enzyme kinetics with electronically embedded QM subsystems with reliable accuracy and low computational cost.

Table 2 compares the computational cost for the calculations presented here to the estimated computer time for straight direct dynamics without EE-MCMM. The EE-MCMM algorithm speeds up the calculation for a total simulation time of 3.3 ns by an estimated factor of 950. The ratio would become even more favorable if longer sampling times were required because in EE-MCMM the extra cost above using analytic potential energy surfaces is all up front. Therefore, EE-MCMM makes QM/MM with hybrid density functionals affordable for large and complex systems requiring extensive sampling, such as high-barrier enzymatic reactions.

Although the errors in Table 1 are small, using more than eight Hessians could reduce them further. We chose instead to show how well we can do with a very small number of Hessians. In most cases, there is a law of diminishing returns where the precision of the fit is reduced below the level of intrinsic accuracy of the underlying electronic structure method. A recent study[38] showed a mean unsigned error of 1.6 kcal/mol for MPW1K with a comparable basis to that used here, where the error was assessed with a representative database of S_N2 barrier heights (as compared to 8.7 kcal/mol for the popular[11,15] local functional BLYP with the largest basis set tested — larger than the one used here), so the mean errors in Table 1 are already less than the errors due to the inexactness of the underlying density functional. The MM force fields were not optimized for the present work, and the success of the method with standard force fields is one of the attractive features of the method. Nevertheless, although the errors are already acceptably small, we expect that they could be further reduced, if desired, by using optimized or specific reaction parameters in the MM.[42]

A potential speedup is to use analytic Hessians, which are available in many computer codes. Here we used numerical Hessians. We estimate that using analytic Hessians for $\partial^2 V/\partial \mathbf{R}_\alpha \partial \mathbf{R}_\beta$ would have decreased the cost for the Hessian step from 96 to 55 CPU hours. Analytic Hessians for $\partial^2 V/\partial \Phi_\alpha \partial \Phi_\beta$ and $\partial^2 V/\partial \Phi_\alpha \partial \mathbf{R}_\alpha$ are also available,[27] and using these would further reduce the computational time. Further efficiency could be also achieved by using partial electronic structure Hessians[43] or by using the new non-Hermitian formulation of MCMM.[44]

Methods

As the starting geometry, we used the X-ray crystal structure of the enzyme−substrate complex (Protein Data Bank code 2DHC).[36] The basis set for the quantal calculations was 6-31(+)G(d,p).[16] The MM force fields were modified MM3 (where the modifications were described previously[16]) for the substrate, AMBER ff03[1] for the protein, and TIP3P[45] for water. Partial charges were obtained by Charge Model 4 (CM4)[16,46] for the QM region and by RESP[1,47] for the MM subsystem.

Table 2. Computational Costs[a]

task	CPU hours
QM/MM geometry optimizations for a reaction path to guide Shepard point placement[b]	68
eight four-dimensional (X_α, Y_α, Z_α, Φ_α) Hessians at Shepard points[b]	96
EE-MCMM/MM MD simulations (31 windows, each with 50 ps of equilibration and 50 ps of data collection[c]	528
total	692
direct QM/MM simulations (estimated)	~6.6 × 10^5

[a] CPU hours = CPUs × hours on an SGI Altix XE 1300 Linux cluster with 2.66 GHz Intel Xeon processors. [b] Four CPUs, GAMESSPLUS. [c] Two CPUs, AMBER with MC-TINKER. One processor calculates H_{11}, and the other calculates H_{22}.

The interface between the QM and MM subsystems was treated by the link atom method[48] with the balanced[49,50] RC[51] scheme.

The umbrella sampling was carried out at $T = 300$ K to calculate the PMF. The equations of motion were integrated by the velocity Verlet method with a time step of 0.5 fs. For each umbrella sampling window, we began with a 50 ps MD trajectory calculation for equilibration, followed by 50 ps calculation for statistical sampling. The negative contribution of the reaction-coordinate motion of the reactant to the free energy of activation[40,52] was included by subtracting the vibrational free energy along the reaction coordinate at the reactant:

$$G_{\mathrm{R},z} = -k_{\mathrm{B}}T \ln \frac{k_{\mathrm{B}}T}{\hbar\omega_{\mathrm{R},z}} \tag{3}$$

from the PMF where k_{B}, T, and $\hbar$ are the Boltzmann constant, temperature, and Planck's constant divided by 2π. The effective vibrational frequency $\omega_{\mathrm{R},z}$ of the reaction coordinate at the reactant was calculated from a force constant obtained from the PMF around the reactant and an averaged reduced mass calculated in the reactant window using eq 38 in ref 40.

In applying MCMM or EE-MCMM, the quadratic Taylor series are expressed in internal coordinates for the interpolation step. For a shallow potential along a torsion coordinate, Θ_m (where m is a label distinguishing the various torsions), the second-order truncation is sometimes problematic. Therefore we replace $\theta_m = \Theta_m - \Theta_m^{(k)}$ by $\sin(n_{\Theta_m}(\Theta_m - \Theta_m^{(k)}))/n_{\Theta_m}$, where n_{Θ_m} is 1 for an X−C−O−Y torsion and 3 for an X−C−C−Y torsion. Furthermore, we set some of the quadratic coefficients involving torsions equal to zero.

The electronic structure calculations were carried out by GAMESSPLUS[53,54] in which we implemented the QM/MM optimization program. The dynamics calculations were carried out by a locally modified version of AMBER[55] with MC-TINKER.[56,57] The WHAM calculations were carried out with a program written by Grossfield.[58]

Acknowledgment. This work was supported in part by the National Science Foundation (grant CHE07-04974, supporting quantum mechanical methods for complex chemical systems) and by the Office of Naval Research (award N00014-05-0538, supporting integrated software tools for dynamics).

References

(1) Duan, Y.; Wu, C.; Chowdhury, S.; Lee, M. C.; Xiong, G.; Zhang, W.; Yang, R.; Cieplak, P.; Luo, R.; Lee, T.; Caldwell, J.; Wang, J.; Kollman, P. *J. Comput. Chem.* **2003**, *24*, 1999.

(2) Car, R.; Parrinello, M. *Phys. Rev. Lett.* **1985**, *55*, 2471.

(3) Liu, Y.-P.; Lu, D.-H.; Gonzalez-Lafont, A.; Truhlar, D. G.; Garrett, B. C. *J. Am. Chem. Soc.* **1993**, *115*, 7806.

(4) Tse, J. S. *Annu. Rev. Phys. Chem.* **2002**, *53*, 249.

(5) Huang, P.; Carter, E. A. *Annu. Rev. Phys. Chem.* **2008**, *59*, 261.

(6) Gao, J.; Truhlar, D. G. *Annu. Rev. Phys. Chem.* **2002**, *53*, 467.

(7) Claeyssens, F.; Harvey, J. N.; Manby, F. R.; Mata, R. A.; Mulholland, A. J.; Ranaghan, K. E.; Schütz, M.; Thiel, S.; Thiel, W.; Werner, H.-J. *Angew. Chem., Int. Ed.* **2006**, *45*, 6856.

(8) Senn, M.; Thiel, W. *Curr. Opinion Chem. Biol.* **2007**, *11*, 182.

(9) Lin, H.; Truhlar, D. G. *Theor. Chem. Acc.* **2007**, *117*, 185.

(10) Hu, H.; Yang, W. *Annu. Rev. Phys. Chem.* **2008**, *59*, 573.

(11) DeVivo, M.; Dal Peraro, M.; Klein, M. L. *J. Am. Chem. Soc.* **2008**, *130*, 10955.

(12) Wu, X.; Car, R.; Selloni, A. *Phys. Rev. B: Solid State* **2008**, *79*, 085102.

(13) Hu, P.; Wang, S.; Zhang, Y. *J. Am. Chem. Soc.* **2008**, *130*, 16721.

(14) Neese, F.; Wennohs, F.; Hansen, A.; Becker, U. *Chem. Phys.* **2009**, *356*, 98.

(15) Masson, F.; Laino, T.; Rothlisberger, U.; Hutter, J. *ChemPhysChem* **2009**, *10*, 400.

(16) Kohn, W.; Becke, A. D.; Parr, R. G. *J. Phys. Chem.* **1996**, *106*, 12974.

(17) Higashi, M.; Truhlar, D. G. *J. Chem. Theory Comput.* **2008**, *4*, 790.

(18) Kim, Y.; Corchado, J. C.; Villa, J.; Xing, J.; Truhlar, D. G. *J. Chem. Phys.* **2000**, *112*, 2718.

(19) Tishchenko, O.; Truhlar, D. G. *J. Chem. Phys.* **2009**, *130*, 024105.

(20) Eyring, H.; Walter, J.; Kimball, G. *Quantum Chemistry*; Wiley: New York, 1944.

(21) Warshel, A.; Weiss, R. M. *J. Am. Chem. Soc.* **1980**, *102*, 6218.

(22) Chang, Y.-T.; Miller, W. H. *J. Phys. Chem.* **1990**, *94*, 5884.

(23) (a) Ischtwan, J.; Collins, M. A. *J. Chem. Phys.* **1994**, *100*, 8080. (b) Nguyen, K. A.; Rossi, I.; Truhlar, D. G. *J. Chem. Phys.* **1995**, *102*, 5522. (c) Thompson, K. C.; Jordan, M. J. T.; Collins, M. A. *J. Chem. Phys.* **1998**, *108*, 8302.

(24) Gao, J. *Rev. Comp. Chem.* **1995**, *7*, 119.

(25) For recent reviews, see refs 9 and 10 and (a) Friesner, R. A.; Guallar, V. *Annu. Rev. Phys. Chem.* **2005**, *56*, 389. (b) Senn, H.-M.; Thiel, W. *Top. Curr. Chem.* **2007**, *268*, 173. (c) Lodola, A.; Woods, C. J.; Mulholland, A. J. *Annu. Rep. Comp. Chem.* **2008**, *4*, 155.

(26) Morita, A.; Kato, S. *J. Am. Chem. Soc.* **1997**, *119*, 4021.

(27) Ishida, T.; Morita, A. *J. Chem. Phys.* **2006**, *125*, 074112.

(28) Lu, Z.; Yang, W. *J. Chem. Phys.* **2004**, *121*, 89.

(29) Morita, A.; Kato, S. *J. Chem. Phys.* **1998**, *108*, 6809.

(30) Albu, T. V.; Corchado, J. C.; Truhlar, D. G. *J. Phys. Chem. A* **2001**, *105*, 8465.

(31) Albu, T. V.; Corchado, J. C.; Truhlar, D. G. *Chem. Rev.* **2007**, *107*, 5101.

(32) For reviews, see: (a) Eyring, H. *Trans. Faraday Soc.* **1938**, *34*, 3. (b) Parr, C. A.; Truhlar, D. G. *J. Phys. Chem.* **1971**, *75*, 1844.

(33) Raff, L. M. *J. Chem. Phys.* **1974**, *60*, 2222.

(34) (a) Hwang, J.-K.; King, G.; Creighton, S.; Warshel, A. *J. Am. Chem. Soc.* **1988**, *110*, 5297. (b) Bentzien, J.; Muller, R. P.; Florián, J.; Warshel, A. *J. Phys. Chem. B* **1998**, *102*, 2293.

(35) (a) Fogarasi; Pulay, P. In *Vibrational Spectra and Structure*; Durig, J. R., Ed.; Elsevier: Amsterdam, 1985; Vol. 14, p. 125. (b) Jackels, C. F.; Gu, Z.; Truhlar, D. G. *J. Chem. Phys.* **1995**, *102*, 3188. (c) Chuang, Y.-Y.; Truhlar, D. G. *J. Phys. Chem. A* **1998**, *102*, 242.

(36) Verschueren, K. H.; Seljée, F.; Rozeboom, H. J.; Kalk, K. H.; Dijkstra, B. W. *Nature* **1993**, *363*, 693.

(37) Lynch, B. J.; Fast, P. L.; Harris, M.; Truhlar, D. G. *J. Phys. Chem. A* **2000**, *104*, 4811.

(38) Zheng, J.; Truhlar, D. G. *J. Chem. Theory Comput.* **2009**, *5*, 808.

(39) Kumar, S.; Rosenberg, J. M.; Bouzida, D.; Swendsen, R. H.; Kollman, P. A. *J. Comput. Chem.* **2004**, *13*, 1011.

(40) Schenter, G. K.; Garrett, B. C.; Truhlar, D. G. *J. Chem. Phys.* **2003**, *119*, 5828.

(41) Schanstra, J. P.; Kingma, J.; Janssen, D. B. *J. Biol. Chem.* **1996**, *271*, 14747.

(42) Tishchenko, O.; Truhlar, D. G. *J. Phys. Chem. A* **2006**, *110*, 13530.

(43) Lin, H.; Pu, J.; Albu, T. V.; Truhlar, D. G. *J. Phys. Chem. A* **2004**, *108*, 4112.

(44) Tishchenko, O.; Truhlar, D. G. *J. Chem. Theory Comput.* **2009**, *5*, 1454.

(45) Jorgensen, W. L.; Chandrasekhar, J.; Madura, J. D.; Impey, R. W.; Klein, M. L. *J. Chem. Phys.* **1983**, *79*, 926.

(46) Kelly, C. P.; Cramer, C. J.; Truhlar, D. G. *J. Chem. Theory Comput.* **2005**, *1*, 1133.

(47) Bayly, C. I.; Cieplak, P.; Cornell, W. D.; Kollman, P. A. *J. Phys. Chem.* **1993**, *97*, 10269.

(48) Singh, U. C.; Kollman, P. A. *J. Comput. Chem.* **1986**, *7*, 718.

(49) Walker, R. C.; Crowley, M. F.; Case, D. A. *J. Comput. Chem.* **2008**, *29*, 1013.

(50) Wang, B.; Truhlar, D. G. J. Chem. Theory Comput., in press.

(51) Lin, H.; Truhlar, D. G. *J. Phys. Chem. A* **2005**, *109*, 3991–2005.

(52) Alhambra, C.; Corchado, J.; Sánchez, M. L.; Garcia-Viloca, M.; Gao, J.; Truhlar, D. G. *J. Phys. Chem. B* **2001**, *105*, 11326.

(53) Higashi, M.; Marenich, A. V.; Olson, R. M.; Chamberlin, A. C.; Pu, J.; Kelly, C. P.; Thompson, J. D.; Xidos, J. D.; Li, J.; Zhu, T.; Hawkins, G. D.; Chuang, Y.-Y.; Fast, P. L.; Lynch, B. J.; Liotard, D. A.; Rinaldi, D.; Gao, J.; Cramer, C. J.; Truhlar, D. G. *GAMESSPLUS, version 2008−2*; University of Minnesota: Minneapolis, MN, 2008.

(54) Schmidt, M. W.; Baldridge, K. K.; Boatz, J. A.; Elbert, S. T.; Gordon, M. S.; Jensen, J. H.; Koseki, S; Matsunaga, N.; Nguyen, K. A.; Su, S. J.; Windus, T. L.; Dupuis, M.; Montgomery, J. A. *J. Comput. Chem.* **1993**, *14*, 1347.

(55) Case, D. A.; Darden, T. A.; Cheatham, III; T. E.; Simmerling, C. L.; Wang, J.; Duke, R. E.; Luo, R.; Crowley, M.; Walker, R. C.; Zhang, W.; Merz, K. M.; Wang, B.; Hayik, S.; Roitberg, A.; Seabra, G.; Kolossváry, Wong, K. F.; Paesani, F.; Vanicek, J, Wu, X.; Brozell, S. R.; Steinbrecher, T.; Gohlke, H.; Yang, L.; Tan, C.; Mongan, J.; Hornak, V.; Cui, G.; Mathews, D. H.; Seetin, M. G.; Sagui, S.; Babin; V. Kollman, P. A. *AMBER, version 10*; University of California: San Francisco, CA, 2008.

(56) Tishchenko, O.; Higashi, M.; Albu, T. V.; Corchado, J. C.; Kim, Y.; Villà, J.; Xing, J.; Lin, H.; Truhlar, D. G. *MC-TINKER, version 2008−2*; University of Minnesota: Minneapolis, MN, 2008.

(57) Ponder, J. W. *TINKER, version 3.5*; Washington University: St. Louis, MO, 1997.

(58) Grossfield, A. *WHAM, version 2.0.2*; University of Rochester: Rochester, NY, 2008.

CT900301D

JCTC Journal of Chemical Theory and Computation

Dispersion Corrected Atom-Centered Potentials for Phosphorus

Michele Cascella,[†] I-Chun Lin,[‡] Ivano Tavernelli,[§] and Ursula Rothlisberger*,[§]

Departement für Chemie und Biochemie, Universität Bern, Freiestrasse 3, CH-3012 Bern, Switzerland, Department of Chemistry, New York University, 100 Washington Square East, Room 1001, New York, New York 10003-6688, and Laboratory of Computational Chemistry and Biochemistry, Institute of Chemical Sciences and Engineering, BCH 4109 Ecole Polytechnique Fédérale de Lausanne EPFL, CH-1015 Lausanne, Switzerland

Received July 20, 2009

Abstract: Dispersion-corrected atom-centered potentials (DCACPs) for the element phosphorus were generated and tested for the BLYP, BP, and PBE generalized gradient approximations of the exchange−correlation functional. The accuracy and transferability of the DCACPs were tested by evaluating the interaction energy of different weakly bound molecular systems (P_2, PH_3, and PN dimers). These results were compared to reference CCSD(T) calculations and standard density functional theory (DFT). The DCACP were also tested in the case of condensed phase systems. Specifically, the density and cohesive energies of β-white and black phosphorus were estimated and compared to available experimental data. Our results show an overall strong improvement both at the qualitative and quantitative level, with respect to uncorrected generalized gradient approximation DFT results for all three functionals. In particular, BLYP-corrected results show the maximal transferability, reporting for all systems a deviation from CCSD(T) results of less than 1% in the predicted binding energies.

Dispersion forces are a crucial type of interaction that influence many chemical and physical phenomena. At the same time, these forces are very difficult to capture by first principles calculations, due to the fact that they originate from dynamical correlation of the electronic degrees of freedom. In particular, density functional theory (DFT) with standard approximations of the exchange−correlation (xc) functional is quite weak in describing dispersion interactions.[1−4] Recently, different possible corrections to DFT that include dispersion interactions have been proposed. Different schemes presented in the literature make use of electron density partitioning,[5] solution of the adiabatic connection formula for the long-range part of the interaction energy,[6] symmetry adapted perturbation theory,[7,8] sophisticated approximation of the xc-potential,[9,10] or add an explicit "dispersion interaction" term with a C_6 coefficient either determined empirically[3,11,12] or generated by the instantaneous dipole moment of the exchange hole.[13−15] Very good results have also been achieved by Truhlar and co-workers with hybrid meta-generalized gradient approximations (GGA) of the xc functional.[4,16,17] It has been shown that dispersion interactions can also be empirically included as correction to the total Kohn−Sham potential, expressed in the form of a multicenter density functional.[18−23] In our scheme, the atom-centered corrections are determined via a penalty function that minimizes the DFT data with respect to a reference calculation at high-level (typically, CCSD(T)). These dispersion-corrected atom-centered potentials (DCACP) have been shown to be highly transferable and to provide good results in reproducing binding energies in different systems, like inert gases,[24] aliphatic and aromatic hydrocarbons,[25] stacked base pairs,[26] and hydrogen-bonded complexes.[27,28] DCACPs have been developed for local forms of the approximate xc functionals (typically, GGAs), which ensure the broadest applicability in both Gaussian and plain-wave based codes. Currently, DCACPs are available for inert gases and for hydrogen, carbon, oxygen, nitrogen, and sulfur elements.[24,29] In this letter, we present the results for phosphorus, thus, completing the library of the main elementary constituents of biological matter.

The theory and methodology to develop DCACPs have been widely discussed elsewhere.[18,24] Briefly, the electronic problem is solved in the presence of an atom-centered correction potential:

$$H = H_0 + \sum_i V_{ik}(R_i - r) \qquad (1)$$

where H_0 is the standard Kohn−Sham Hamiltonian, and V_{ik} is the correction potential, centered on each atom i, specific for each element k. Each V_{ik} has the form of a Gaussian and is tuned through a penalty function to reproduce dispersion

---

[*] Corresponding author. Telephone: +41-(0)21-6930321. Fax: +41-(0)21-6930320. Email: ursula.roethlisberger@epfl.ch.

[†] Universität Bern.

[‡] New York University.

[§] Ecole Polytechnique Fédérale de Lausanne EPFL.

10.1021/ct9003756 CCC: $40.75

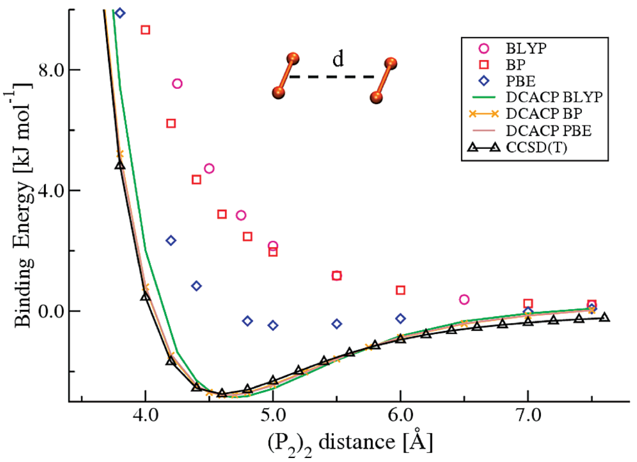

Figure 1. Calibration of DCACP for the phosphorus element based on P_2 dimer interactions. Results for BLYP, BP, and PBE xc functionals are shown with respect to the CCSD(T) reference plot.

dominated reference interaction energies, calculated for a simple system by a high-level methodology (CCSD(T)). DCACPs are, by design, effective corrections to a given approximate form of the xc functional.[30] Therefore, different DCACPs have to be generated and used for calculations using different xc functionals.

In our case, reference dispersion interactions in phosphorus were evaluated for the $(P_2)_2$ system. First, we optimized the geometry of the P_2 molecule at MP2/aug-cc-pVTZ level, finding a P−P distance of 1.927 Å. Then, we calculated the interaction energy for the $(P_2)_2$ moiety as a function of the distance of the two relative centers of mass, constraining the two P_2 molecules in a parallel D_{2h} conformation (Figure 1). The electronic problem was solved at the CCSD(T)/aug-cc-pVTZ level of theory, taking into account standard counterpoise corrections. Geometry optimization and interaction energy calculations were performed using the GAUSSIAN03 package.[31] DFT calculations were performed using the CPMD code,[32] simulating the system in an isolated box of 23 × 15 × 15 Å^3, using plane-waves with a cutoff of 200 Ry as basis functions and employing the pseudopotential of Goedecker et al.[33] Details on the calibration procedure can be found in refs 18 and 24. The parameter sets for the obtained DCACPs can be downloaded at http://lcbcpc21.epfl.ch (see also Supporting Information).

The interaction energy plot obtained by CCSD(T) calculations shows a minimum energy of about 2.65 kJ mol^{-1} for an intermolecular distance of 4.6 Å (Figure 1). As expected, DFT based on GGAs of the xc functional poorly describe this interaction. In particular, Becke−Lee−Yang−Parr (BLYP)[34,35] or Becke Perdew (BP)[36] xc functionals show a completely repulsive profile.

Perdew−Burke−Ernzerhof (PBE)[37] GGA results in a very shallow minimum at an intermolecular distance of about 5 Å. On the other hand, including DCACPs leads to good agreement of the DFT energy plots with the CCSD(T) reference curve for all three xc functionals taken under consideration (Figure 1). The largest deviations are found for the results with the corrected BLYP functional, which show an equilibrium distance of about 4.75 Å, approximately 0.15 Å longer than the CCSD(T) result. The faster decay of the long-range tail in the DCACP plots is related to the fact that DCACPs are represented with a single (nonlocal) angular momentum channel (f) that leads to minimal errors in the energy of the minimum, but it is not sufficient to completely ensure a formally correct long-range behavior.[30] The use of a single channel constitutes the best compromise between accuracy and computational cost for the DCACP method.

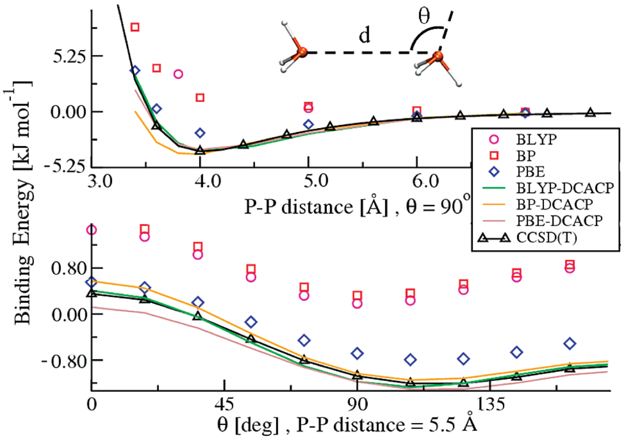

Figure 2. Top panel: interaction potential of two phosphine molecules as a function of the P−P distance. Bottom panel: interaction potential at fixed distance (d = 5.5 Å) as a function of the relative orientation.

The transferability of the newly obtained DCACPs was tested on a set of systems where dispersion interactions contribute substantially to the energetics. The first system we used is the phosphine dimer $(PH_3)_2$. The geometry of a single phosphine molecule was first optimized at the MP2/aug-cc-pVTZ level. Then, two phosphine molecules were oriented at a relative angle $\theta = 90°$ (where θ is the angle between the two principal symmetry axes of the PH_3 molecules, see Figure 2) to nullify the dipolar interactions. In this case, as in all heterogeneous compounds, DCACPs calculations were performed using DCACP-corrected potentials for both phosphorus and hydrogen elements. Additivity, transferability, and comparability of DCACPs for heterogeneous systems have been broadly discussed and successfully tested in previous papers[24−30] (see also Supporting Information). The binding energy as a function of the phosphorus−phosphorus distance was then evaluated. Figure 2 (top panel) reports the results obtained for GGA and DCACP calculations. DCACPs substantially improve the DFT/GGA results, leading, in the case of BLYP and PBE, to binding energies and equilibrium distances equal to those obtained by CCSD(T) calculations. The BP corrected functional, on the contrary, shows a slightly softer curve.

The bottom panel of Figure 2 shows the interaction potential of the two phosphines at a P−P distance of 5.5 Å when rotating the angle θ. Also in this case, the overall quantitative agreement of the DCACP results, with respect to the CCSD(T) reference, is very good. In particular, the location of the minimum at ∼115° and the relative energies of the local and global maxima at 180° and 0°, respectively, are all features that are quantitatively not well reproduced at the uncorrected DFT level. The DCACPs for phosphorus account for more than 95% of the correction to the binding energy.

A second test for the transferability of P-DCACPs was performed on the unusual PN molecule. Due to the peculiar electronic nature of this molecule, this system can be considered as a challenging test for the transferability properties of

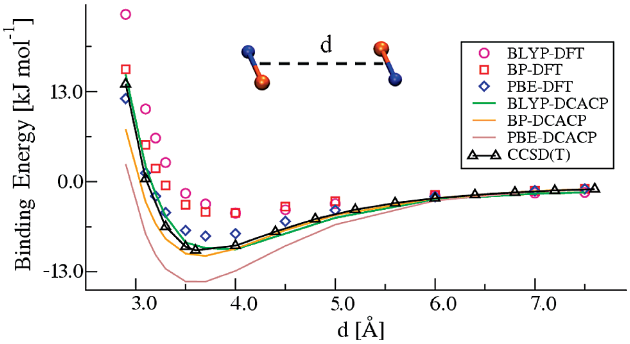

Figure 3. Interaction potential of two PN molecules placed in planar C_{2h} configuration (molecules perpendicular to *d* axis).

DCACPs. Figure 3 reports the results for this system in C_{2h} symmetry (molecules oriented perpendicular to the axis passing through their respective geometrical centers). In this case, the xc functionals based on the Becke exchange report a shallow minimum at about 3.8 (BP) and 4.0 Å (BLYP). This points to the fact that the $(PN)_2$ moiety is not bound by pure dispersion forces, but there is an additional stronger interaction present between the two PN molecules (e.g., attractive dipole−dipole interactions due to bond polarity).

However, also in this case both BP and BLYP underestimate the binding energy, with respect to CCSD(T) results (4.47 kJ mol^{-1} instead of 9.71 kJ mol^{-1}). CCSD(T) calculations also predict a shorter equilibrium binding distance of 3.64 Å.

Dispersion-corrected BLYP and BP are again able to well reproduce the CCSD(T) data. PBE GGA is already fairly close to the CCSD(T) results, providing a binding energy of 7.88 kJ mol^{-1} and a bond length of 3.72 Å. In this case, the DCACP correction to PBE xc improves the binding distance to match the CCSD(T) result but leads to an overestimation of the $(PN)_2$ binding energy (~15 kJ mol^{-1}). DCACP data were obtained combining the corrected potential for P with the one of N.[24] Also in this case, the use of DCACPs on P only accounts for most of the binding energy correction. In Table 1, binding energies and distances of the three molecular systems are compared with the corresponding data obtained with the M06−2X xc functional.[4] DCACP binding energies are closer to the CCSD(T) data than those predicted by M06−2X, while DCACPs and M06−2X perform comparably in predicting binding distances with respect to the CCSD(T) reference calculations.

A final transferability test was done by estimating the density of crystalline *β*-white phosphorus. Its primitive cell contains six P_4 molecules, placed in symmetric pairs with respect to the center of the unit cell (Figure 4a, left panel).[38] This allotropic form of phosphorus is formally a molecular crystal, and therefore, the cohesive forces are expected to have strong dispersion contributions. However, the minimal distance among P atoms of different P_4 units can be as short as 3.1 Å, well below the typical van der Waals (vdW) distance of phosphorus; therefore, covalent terms also contribute to the cohesive energy.

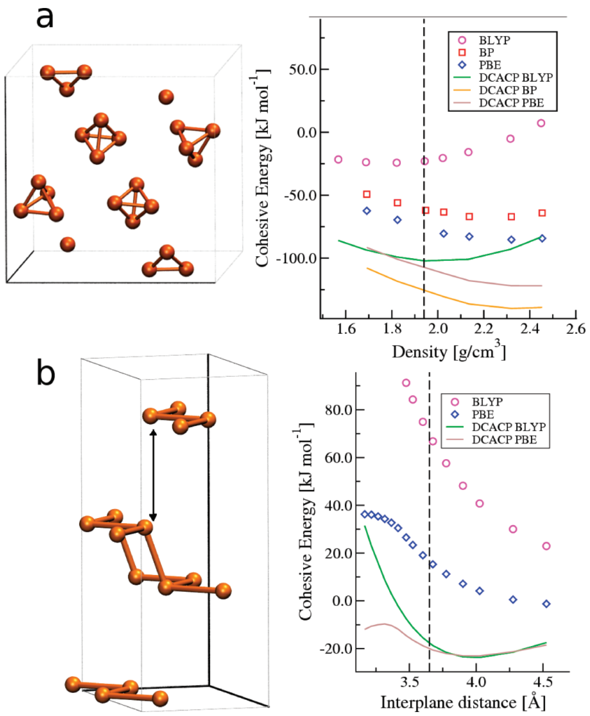

Figure 4. (a) Left panel: primitive cell of *β*-white phosphorus. Right panel: cohesive energy as a function of its density for different GGA and DCACP-corrected functionals. (b) Left panel: primitive cell of black phosphorus. Right panel: cohesive energy as a function of the P−P interplane distance (black arrow, left panel). The dashed lines in the two graphs indicate the corresponding experimental values.

In our calculations, we performed isotropic variations of the periodic cell. This means that the angles α, *β*, *γ*, and the relative ratio between the edges of the cell (*a*, *b*, *c*) were left unchanged with respect to the experimental values. Figure 4 reports the cohesive energy per P_4 molecule (calculated as: $E_c = E(\text{crystal})/6 - E(P_4)_{(\text{in vacuo})}$), as a function of the density of the crystal. Standard BLYP calculations predict the crystal to be only marginally stable at densities that are too low, with respect to

Table 1. Binding Energies and Equilibrium Distances for P_2, PH_3, and PN dimers from Both Uncorrected and DCACP-Corrected DFT/GGA Results[a]

molecule	BP	PBE	BLYP	DCACP BP	DCACP PBE	DCACP BLYP	M06-X2	CCSD(T)
$(P_2)_2$								
binding energy[b]	>0	−0.56	>0	−2.65	−2.65	−2.65	−1.83	−2.65
equilibrium distance[c]	–	5.00	–	4.60	4.60	4.75	4.50	4.60
$(PH_3)_2$								
binding energy[b]	>0	−1.64	>0	−3.19	−3.16	−3.17	−3.51	−3.17
equilibrium distance[c]	–	4.20	–	3.85	4.0	4.0	3.9	4.0
$(PN)_2$								
binding energy[b]	−4.47	−7.88	−4.47	−9.94	−14.81	−9.70	−14.01	−9.71
equilibrium distance[c]	3.85	3.70	4.0	3.68	3.63	3.74	3.50	3.64

[a] The table presents a direct comparison with other xc approximation (M06-2X)[4] and high-level CCSD(T) results. [b] Binding energies (kJ mol^{-1}). [c] Equilibrium distances (Å).

the experimental one (1.92 g/cm^3).[38] In fact, the BLYP xc predicts a density of ∼1.82 g/cm^3, which is, incidentally, the experimental density of the more expanded α-white phosphorus. On the contrary, BLYP-DCACP is again in excellent agreement with experiment, predicting a density of 1.92 g/cm^3, identical to the experimental value. Both uncorrected BP and PBE functionals overbind the P_4 molecules, predicting a density of more than 2.0 g/cm^3. Addition of the DCACP correction does not lead to an improvement of the results but only yields a constant energy shift. In fact, DCACPs cannot correct intrinsic DFT errors to binding energies for systems where the uncorrected xc functionals produce spurious covalent features. In order to confirm the differences in the intrinsic performance of the different xc functionals for covalent interactions, we have performed a final test on the structure of black phosphorus, a more compact allotropic form, where atoms bind covalently in layers displayed parallel to the x-y-plane, which then pack along the z-direction (Figure 4b). We have progressively varied the distance among layers (that is, varying the length of the edge along z of the periodic cell), forcing the single layer to remain in the same geometry along the x-y-directions and calculating the cohesive energy for every step. In this case, both BLYP and PBE functionals predict a repulsive behavior in the vdW distance region. DCACP-corrected functionals report the same energetics in the vdW region, with a minimum at around 3.8 Å (Figure 4b). At closer distances, on the contrary, the PBE functional predicts a maximum around a distance of 3.2 Å, followed by a reactive profile, which leads to covalent binding of the layers. As in the previous case, the behavior at covalent distances cannot be corrected by DCACP.

In summary, we present DCACPs for the phosphorus element in combination with BLYP, BP, and PBE xc functionals. Our benchmark calculations show that these potentials have a good transferability in systems dominated by dispersion interactions, as previously found for rare gases and second-row elements, already discussed in the literature. Tests performed on the unusual molecule PN, as well as on different allotropic forms of solid P, show that DCACP correction for BLYP keeps its good transferability in systems where the binding energy has dispersion and covalent components, while results from corrections to PBE may not be as accurate in such cases. Overall, the DCACP correction coupled to the BLYP functional performs best, as already reported for other elements (see refs 24−29). This work completes the DCACP library for "biological" elements, after the DCACP development for H, C, N, O,[24] and S[29] and, therefore, is of particular interest for studies of biochemical events involving phosphorus chemistry. Due to the sizable dispersion contributions of the phosphorus atoms, the DCACPs presented here are expected to be crucial for studies of nucleic acids, protein cofactors (FMN, FAD, NAD, etc...), enzyme-phosphorylated substrate complexes (e.g., in active sites of kinases), or in studies of protein transition-state analogue-based inhibitors.[39]

Acknowledgment. The presented work was funded by the Swiss National Science Foundation (grant N. 200020-116294). The authors thank Dr. Mauricio D. Coutinho-Neto for useful discussion.

Supporting Information Available: DCACP potentials for the phosphorus element in Goedecker−Teter−Hutter format and comparison of DCACP parameters for different elements. This material is available free of charge via the Internet at http://pubs.acs.org.

References

(1) Kristyán, S.; Pulay, P. *Chem. Phys. Lett.* **1994**, *229*, 175.

(2) Pérez-Jordá, J. M.; Becke, A. D. *Chem. Phys. Lett.* **1995**, *233*, 134.

(3) Meijer, E. J.; Sprik, M. *J. Chem. Phys.* **1996**, *105*, 8684.

(4) Zhao, Y.; Truhlar, D. G. *J. Chem. Theory Comput.* **2005**, *1*, 415.

(5) Wesolowski, T. A.; Tran, F. *J. Chem. Phys.* **2003**, *118*, 2072.

(6) Kohn, W.; Meir, Y.; Makarov, D. E. *Phys. Rev. Lett.* **1998**, *80*, 4153.

(7) Patkowski, K.; Jeziorski, B.; Szalewicz, K. *J. Chem. Phys.* **2004**, *120*, 6849.

(8) Misquitta, A.; Podeszwa, R.; Jeziorski, B.; Szalewicz, K. *J. Chem. Phys.* **2005**, *123*, 214103.

(9) Tao, J.; Perdew, J. P. *J. Chem. Phys.* **2005**, *122*, 114102.

(10) Langreth, D,; Dion, M.; Rydberg, H.; Schroder, E.; Hyldgaard, P.; Lundqvist, B. *Int. J. Quantum Chem.* **2005**, *101*, 599.

(11) Grimme, S. *J. Comput. Chem.* **2004**, *25*, 1463.

(12) Williams, R.; Malhotra, D. *Chem. Phys.* **2006**, *327*, 54.

(13) Becke, A. D.; Johnson, E. R. *J. Chem. Phys.* **2005**, *122*, 154104.

(14) Becke, A. D.; Johnson, E. R. *J. Chem. Phys.* **2005**, *123*, 154101.

(15) Johnson, E. R.; Becke, A. D. *J. Chem. Phys.* **2006**, *124*, 174104.

(16) Zhao, Y.; Truhlar, D. G. *J. Phys. Chem. A* **2004**, *108*, 6908.

(17) Zhao, Y.; Schultz, N. E.; Truhlar, D. G. J. *Chem. Theory Comput.* **2006**, *2*, 364.

(18) von Lilienfeld, O. A.; Tavernelli, I.; Rothlisberger, U.; Sebastiani, D. *Phys. Rev. Lett.* **2004**, *93*, 153004.

(19) von Lilienfeld, O. A.; Tavernelli, I.; Rothlisberger, U.; Sebastiani, D. *Phys. Rev. B: Condens. Matter* **2005**, *71*, 195119.

(20) DiLabio, G. A. *Chem. Phys. Lett.* **2008**, *455*, 348.

(21) Mackie, I. D.; DiLabio, G. A. *J. Phys. Chem. A* **2008**, *112*, 10968.

(22) Wodrich, M. D.; Jana, D. F.; Schleyer, P. V.; Corminboef, C. *J. Phys. Chem. A.* **2008**, *112*, 11495.

(23) Sun, Y. Y.; Kim, Y. H.; Lee, K.; Zhang, S. B. *J. Chem. Phys.* **2008**, *129*, 154102.

(24) Lin, I.-C.; Coutinho-Neto, M. D.; Felsenheimer, C.; von Lilienfeld, O. A.; Tavernelli, I.; Rothlisberger, U. *Phys. Rev. B: Condens. Matter* **2007**, *75*, 205131.

(25) Tapavicza, E.; Lin, I.-C.; von Lilienfeld, O. A.; Tavernelli, I.; Coutinho-Neto, M. D.; Rothlisberger, U. *J. Chem. Theory Comput.* **2007**, *3*, 1673.

(26) Lin, I.-C.; von Lilienfeld, O. A.; Coutinho-Neto, M. D.; Tavernelli, I.; Rothlisberger, U. *J. Phys. Chem. B* **2007**, *111*, 14346.

(27) Lin, I.-C.; Seitsonen, A. P.; Coutinho-Neto, M. D.; Tavernelli, I.; Rothlisberger, U. *J. Phys. Chem. B* **2009**, *113*, 1127.

(28) Arey, J. S.; Aeberhard, P. C.; Lin, I.-C.; Rothlisberger, U. *J. Phys. Chem. B* **2009**, *113*, 4726.

(29) Aeberhard, P.; Arey, J. S.; Lin, I.-C.; Tavernelli, I.; Rothlisberger, U. *J. Chem. Theory Comput.* **2009**, *5*, 23.

(30) Lin, I.-C.; Tavernelli, I.; Rothlisberger, U. *Phys. Rev. B: Condens. Matter* **2009**, *79*, 045106.

(31) Frisch, M. J.; Trucks, G. W.; Schlegel, H. B.; Scuseria, G. E.; Robb, M. A.; Cheeseman, J. R.; Montgomery, J. A., Jr.; Vreven,

T.; Kudin, K. N.; Burant, J. C.; Millam, J. M.; Iynegar, S. S.; Tomasi, J.; Barone, V.; Mennucci, B.; Cossi, M.; Scalmani, G.; Rega, N.; Petersson, G. A.; Nakatsuji, H.; Hada, M.; Ehara, M.; Toyota, K.; Fukuda, R.; Hasegawa, J.; Ishida, M.; Nakajima, T.; Honda, Y.; Kitao, O.; Nakai, H.; Klene, M.; Li, X.; Knox, J.; Hratchian, H. P.; Cross, J. B.; Adamo, C.; Jaramillo, J.; Gomperst, R.; Stratmann, R. E.; Yazyev, O.; Austin, A. J.; Cammi, R.; Pomelli, C.; Ochterski, J. W.; Ayala, P. Y.; Morokuma, K.; Voth, G. A.; Salvador, P.; Dannenberg, J. J.; Zakrzewski, V. G.; Foresman, J. B.; Ortiz, J. V.; Cui, Q.; Baboul, A. G.; Clifford, S.; Cioslowski, J.; Stefanov, B. B.; Liu, G.; Liashenko, A.; Piskorz, P.; Komaromi, I.; Martin, R. L.; Fox, D. J.; Keith, T.; Al-Laham, M. A.; Peng, C. Y.; Nanayakkara, A.; Challacombe, M.; Gill, P. M. W.; Johnson, B.; Chen, W.; Wong, M. W.; Gonzalez, C.; Pople, J. A. *GAUSSIAN03*, Revision A.1; Gaussian, Inc.: Pittsburgh, PA, 2003.

(32) CPMD, V3.13, Copyright IBM Corp. 1990−2008, Copyright MPI für Festkörperforschung Stuttgart 1997−2001 (http://www.cpmd.org).

(33) Goedecker, S.; Teter, M.; Hutter, J. *Phys. Rev. B: Condens. Matter* **1996**, *54*, 1703.

(34) Becke, A. D. *Phys. Rev. A: At., Mol., Opt. Phys.* **1988**, *38*, 3098.

(35) Lee, C.; Yang, W.; Parr, R. G. *Phys. Rev. B: Condens. Matter* **1988**, *37*, 785.

(36) Perdew, J. P. *Phys. Rev. B: Condens. Matter* **1986**, *33*, 8822.

(37) Perdew, J. P.; Burke, K.; Ernzerhof, M. *Phys. Rev. Lett.* **1996**, *77*, 3865.

(38) Simon, A.; Borrmann, H.; Craubner, H. *Phosphorus Sulfur* **1987**, *30*, 507.

(39) Vidossich, P.; Carloni, P. *J. Phys. Chem. B* **2006**, *110*, 1437.

CT9003756

J. Chem. Theory Comput. **2009,** *5,* 2935–2943

JCTC Journal of Chemical Theory and Computation

Polarizable Simulations with Second-Order Interaction Model—Force Field and Software for Fast Polarizable Calculations: Parameters for Small Model Systems and Free Energy Calculations

George A. Kaminski,*[†] Sergei Y. Ponomarev,[†] and Aibing B. Liu[†,‡]

Department of Chemistry and Biochemistry, Worcester Polytechnic Institute, Worcester, Massachusetts 01609 and Department of Chemistry, Central Michigan University, Mt. Pleasant, Michigan 48859

Received August 6, 2009

Abstract: We are presenting POSSIM (POlarizable Simulations with Second-order Interaction Model)—a software package and a set of parameters designed for molecular simulations. The key feature of POSSIM is that the electrostatic polarization is taken into account using a previously introduced fast formalism. This permits cutting the computational cost of using the explicit polarization by about an order of magnitude. In this article, parameters for water, methane, ethane, propane, butane, methanol, and N-methylacetamide (NMA) are introduced. These molecules are viewed as model systems for protein simulations. We have achieved our goal of ca. 0.5 kcal/mol accuracy for gas-phase dimerization energies and no more than 2% deviations in liquid state heats of vaporization and densities. Moreover, free energies of hydration of the polarizable methane, ethane, and methanol have been calculated using the statistical perturbation theory. These calculations serve as a model for calculating protein pK_a shifts and ligand binding affinities. The free energies of hydration were found to be 2.12, 1.80, and −4.95 kcal/mol for methane, ethane, and methanol, respectively. The experimentally determined literature values are 1.91, 1.83, and −5.11 kcal/mol. The POSSIM average error in these absolute free energies of hydration is only about 0.13 kcal/mol. Use of the statistical perturbation theory with polarizable force fields is not widespread, and we believe that this work opens the road to further development of the POSSIM force field and its applications for obtaining accurate energies in protein-related computer modeling.

I. Introduction

Computer simulations have become an integral part of chemical and biochemical research, delivering answers to a variety of questions ranging from assessing reaction kinetic data to providing microscopic insight into systems involving proteins and DNA. The key issue in any such modeling is the way the energy of the system is evaluated. Quantum mechanics provides a robust tool for this task, but there are two general problems. First, quantum mechanical calculations are resource-demanding; therefore, the size of a system which can be treated this way is limited. Second, there is no one single recipe for obtaining uniformly accurate quantum mechanical data, and the level of theory required for different problems varies.

Empirical force fields offer an alternative which is much cheaper computationally. However, it has been shown that, in many cases, accurate assessment of energy with empirical force fields necessitates explicit treatment of many-body interactions, mainly the electrostatic polarization.[1] Dimerization energies and acidity constants of small molecules, energies of protein−ligand interactions, protein pK_a values, or even the very thermodynamic stability of complexes in

---

* Corresponding author e-mail: gkaminski@wpi.edu.

[†] Worcester Polytechnic Institute.

[‡] Central Michigan University.

10.1021/ct900409p CCC: $40.75

solutions often depend on including the electrostatic polarization into the empirical Hamiltonian. For example, it has been demonstrated in earlier works that pK_a values for acidic and basic residues of the OMTKY3 can be reproduced within 0.6 and 0.7 pH units of the experimental data if explicit treatment of polarization is included. The errors with the nonpolarizable OPLS are 3.3 pH units for the acidic residues and 2.2 for the basic ones.[2] Another interesting example was a study of Sialyl LewisX in complex with SelectinE. This sugar−protein complex is known to exist experimentally but dissociated in molecular dynamics simulations with fixed charges.[3] Overall, many-body interactions play a crucial role in many applications, although they are sometimes included in surrogate forms, for example, as conformation-specific protein charges.[4]

There are two major issues pertaining to polarizable calculations which are still not uniformly resolved. On one hand, the optimal source of fitting data seems to vary from application to application. While it is attractive to rely almost solely on high-level quantum mechanical results,[5] experimental data often present more robustness. Moreover, while quantum mechanical calculations permit a great level of microscopic insight, the very values of quantum mechanical energies are often uncertain, as they may significantly change depending on the level of theory. We adopt a middle-path approach in this work, in which we rely on experimental data whenever possible and make heavy use of quantum mechanical calculations, while trying not to treat them as panacea.

The second issue with polarizable force fields is the functional form of polarization itself. There are several viable techniques present, including fluctuating charges or inducible point dipoles. It is possible to implement these quite efficiently for uniform systems known in advance (such as pure water[6]). But software for simulating arbitrary polarizable systems (including proteins and protein−ligand complexes) is usually significantly slower than its fixed-charges counterparts. Calculating induced dipoles or fluctuating charges requires solving a system of self-consistent equations. This is usually done iteratively, and the process may lead to unlimited growth of the induced dipoles (the so-called polarization catastrophe). In order to reduce the computational cost of polarizable calculations, we introduced an approximation that we termed second-order polarization. It permitted a reduction of the time needed for assessing the polarization energy by about an order of magnitude, removed any possibility of polarization catastrophe, and was done without any sacrifice of the computational accuracy.[7]

This article reports the next stage of the systematic development of the second-order polarization technique. A software suite called POSSIM (POlarizable Simulations with Second-order Interaction Model) has been created for the second-order polarizable calculations. Parameters for several model systems have been developed. The list of these systems includes N-methylacetamide (NMA), which will be further used as the main building block in protein backbones. Moreover, free energy perturbations were performed with the POSSIM force field and software to obtain relative and absolute Gibbs free energies of hydration for methane, ethane, and methanol. While being widely used with fixed-charges force fields, such calculations are still rather rare with polarizable techniques. The toolset presented in this paper will be further utilized in developing POSSIM parameters for proteins and other systems and studying biophysical and organic processes, including protein−ligand binding.

In this work, we benchmark the POSSIM results (marked PFF, for Polarizable Force Field) against the fixed-charges OPLS-AA[8] as well as the previous version of the polarizable force field (non-second-order, thus a slower one) termed PFF0.[9]

The rest of the paper is organized as follows: Given in section II is a description of the methodology involved. Section III contains results and discussion. Finally, conclusions are presented in section IV.

II. Methods

A. Force Field. The total energy E_{tot} is calculated as follows:

$$E_{\text{tot}} = E_{\text{electrostatic}} + E_{\text{vdW}} + E_{\text{stretch}} + E_{\text{bend}} + E_{\text{torsion}} \tag{1}$$

$E_{\text{electrostatic}}$ stands for the electrostatic interactions, including the dipole−dipole, dipole−charge, and charge−charge contributions. E_{vdW} is the nonelectrostatic part of the nonbonded inter- and intramolecular energy; E_{stretch} and E_{bend} are the harmonic bond stretching and angle bending, respectively. Finally, E_{torsion} is the Fourier expansion for the torsional energy.

Electrostatic Energy. The electrostatic polarization energy with inducible point dipoles is

$$E_{\text{pol}} = -\frac{1}{2}\sum_i \mu_i E_i^0 \tag{2}$$

E^0 denotes the electrostatic field in the absence of the dipoles, and μ represents the induced dipole moments, which are calculated as follows:

$$\mu_i = \alpha_i E_i^{\text{tot}} \tag{3}$$

where α represents scalar polarizabilities and E_i^{tot} is the total field, including the dipole−dipole component:

$$E_i^{\text{tot}} = E_i^0 + \sum_{j\neq i} T_{ij}\mu_j \tag{4}$$

$$T_{ij} = \frac{1}{R_{ij}^3}\left(\frac{3R_{ij}R_{ij}}{R_{ij}^2} - \mathbf{I}\right) \tag{5}$$

with R_{ij} being the distances between atomic sites i and j. $\mathbf{I}$ is the unit tensor. Then,

$$\mu_i = \alpha_i E_i^0 + \alpha_i \sum_{j\neq i} T_{ij}\mu_j \tag{6a}$$

or

$$\mathbf{A}\mu = E^0 \tag{6b}$$

The self-consistent eq 6 is usually solved iteratively. If we explicitly write down the first three iterations, we can produce "first-order", "second-order", and "third-order" approximations for the induced dipoles:

$$\mu_i^0 = \alpha_i E_i^0 \tag{7a}$$

$$\mu_i^{\mathrm{I}} = \alpha_i E_i^0 + \alpha_i \sum_{j \neq i} T_{ij}\mu_j^0 = \alpha_i E_i^0 + \alpha_i \sum_{j \neq i} T_{ij}\alpha_j E_j^0 \tag{7b}$$

$$\mu_i^{\mathrm{II}} = \alpha_i E_i^0 + \alpha_i \sum_{j \neq i} T_{ij}\mu_j^{I} = \alpha_i E_i^0 + \alpha_i \sum_{j \neq i} T_{ij}\alpha_j E_j^0 + \alpha_i \sum_{j \neq i} T_{ij}\alpha_j \sum_{k \neq j} T_{jk}\alpha_k E_k^0 \tag{7c}$$

The first-order expression requires considerably less resources than the exact expression in eq 6, as the matrix **A** does not come into play, but dipole−dipole interactions are totally ignored. It has been shown that, although more accurate than the fixed-charges description, this technique is not accurate enough in describing molecular systems.[10] We are utilizing the second-order expression in eq 7b instead. It has been previously shown to yield about an order of magnitude increase of the computational speed with no loss of accuracy.[7]

The overall electrostatic energy

$$E_{\mathrm{electrostatic}} = E_{\mathrm{pol}} + E_{\mathrm{additive}} \tag{8}$$

where

$$E_{\mathrm{additive}} = \sum_{i \neq j} \frac{q_i q_j}{R_{ij}} f_{ij} \tag{9}$$

represents the pairwise-additive Coulomb charge−charge interaction energies between charges on atoms i and j. The term f_{ij} equals zero for 1,2 and 1,3 pairs (atoms which belong to the same valence bond or angle), 0.5 for 1,4 interactions (atoms in the same dihedral angle), and 1.0 for all of the other pairs.

To avoid a nonphysical increase of the electrostatic interactions at close distances, each atom is assigned a cutoff parameter, R_{cut}. When the overall distance R_{ij} is smaller than the sum of these parameters $R_{\mathrm{min}}{}^{ij} = R_{\mathrm{cut}}{}^{i} + R_{\mathrm{cut}}{}^{j}$ for the atoms i and j, R_{ij} is replaced by an effective smooth function

$$R_{ij}^{\mathrm{eff}} = \left[1 - \left(\frac{R_{ij}}{R_{\mathrm{min}}^{ij}}\right)^2 + \left(\frac{R_{ij}}{R_{\mathrm{min}}^{ij}}\right)^3\right] \times R_{\mathrm{min}}^{ij} \tag{10}$$

The Rest of the Force Field. The van der Waals energy is evaluated with the standard Lennard-Jones formalism:

$$E_{\mathrm{vdW}} = \sum_{i \neq j} 4\varepsilon_{ij}\left[\left(\frac{\sigma_{ij}}{R_{ij}}\right)^{12} - \left(\frac{\sigma_{ij}}{R_{ij}}\right)^{6}\right] f_{ij} \tag{11}$$

Geometric combining rules are used:

$$\varepsilon_{ij} = (\varepsilon_i \cdot \varepsilon_j)^{1/2}, \sigma_{ij} = (\sigma_i \cdot \sigma_j)^{1/2} \tag{12}$$

and the coefficient f_{ij} is calculated the same way as for the electrostatic term.

The bond-stretching and angle-bending energies were obtained in accordance with eqs 13 and 14.

$$E_{\mathrm{stretch}} = \sum_{\mathrm{bonds}} K_r (r - r_{\mathrm{eq}})^2 \tag{13}$$

$$E_{\mathrm{bend}} = \sum_{\mathrm{angles}} K_{\Theta} (\Theta - \Theta_{\mathrm{eq}})^2 \tag{14}$$

Here, the subscripts eq are used to denote the equilibrium values of the bond length r and angle Θ.

Finally, the torsional term was computed as follows:

$$E_{\mathrm{torsion}} = \sum_i \frac{V_1^i}{2}[1 + \cos(\phi_i)] + \frac{V_2^i}{2}[1 - \cos(2\phi_i)] + \frac{V_3^i}{2}[1 + \cos(3\phi_i)] \tag{15}$$

with the summation performed over all of the dihedral angles i.

When a comparison is done with results obtained with the nonpolarizable OPLS-AA force field,[8] the latter lacks the first (polarizable) term in the electrostatic energy expression in eq 8. The previous generation polarizable force field[9] (denoted as PFF0) employs the full iterative solvation of eq 6, has permanent dipole moments in addition to the inducible ones, and uses the exp-6 van der Waals energy term instead of the Lennard-Jones 12−6 formalism of this work.

B. Parameterization of the Force Field. The procedure for determining values of the potential energy parameters consisted of the following stages: (i) fitting the electrostatic polarizabilities, (ii) fitting the permanent electrostatic charges, (iii) determining Lennard-Jones parameters, (iv) obtaining values of the torsional parameters, and (v) fine-tuning of the force field. All of the calculations for the newly developed PFF (both for the parametrization and free energy perturbations) were performed with the POSSIM software suite.

Electrostatic Polarizabilities. A series of electrostatic perturbations was applied to the target molecules, in the form of dipolar probes consisting of two opposite charges of magnitude 0.78e, 0.58 Å apart (for a dipole moment of 2.17 D—similar to that of nonpolarizable models for liquid water such as SPC/E[11]), placed at locations where hydrogen bonds to the molecule were formed. The perturbations were the same as used for the previous generation of the polarizable force field (PFF0).[5,12] For each perturbation, the change in the electrostatic potential at a set of gridpoints outside the van der Waals surface of the molecule, as well as the energy of the perturbed system, was computed using density-functional theory (DFT) with the B3LYP method[13] and cc-pVTZ(-f) basis set. All calculations were performed with the Jaguar electronic structure code.[14] The polarizablities α_i are assumed to be isotropic and are chosen to minimize the deviation of the three-body energy obtained with the PFF and the DFT calculations. The three-body energies were calculated in accordance with eq 16 and Figure 1.

$$E_{\mathrm{3body}} = E(1 + 2 + 3) - E(1 + 2) - E(1 + 3) - E(2 + 3) + E(1) + E(2) + E(3) \tag{16}$$

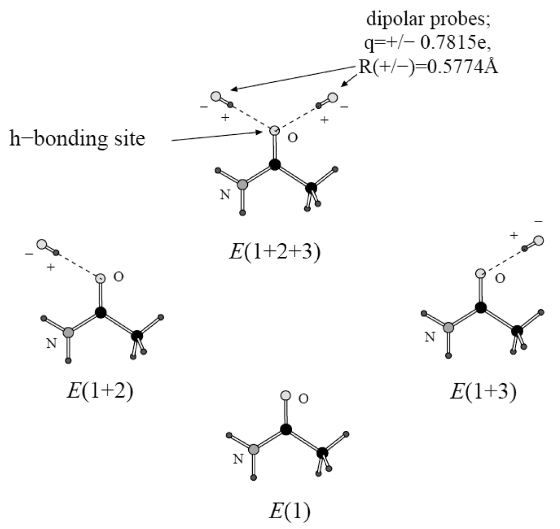

Figure 1. Calculating two- and three-body energies of a molecule with dipolar probes.

Here, the molecule for which parameters are produced is denoted as 1, and the two dipolar probes are marked as 2 and 3. This three-body energy is automatically equal to zero in a nonpolarized fixed-charges force field, in which no many-body interactions are explicitly present. It has been shown that the three-body energy is independent of the permanent charges and depends only on the values of the polarizabilities.[7] Therefore, it is justified that the polarizabilities in our force field were parametrized first.

The choice of electronic structure method (DFT/B3LYP functional, cc-pVTZ(-f) basis set) yields quite accurate permanent charge distributions but underestimates the gas-phase polarizability as compared to experimental results. Closer agreement with gas-phase experiments could be obtained by including diffuse functions in the DFT calculations. However, our previous computational experiments with liquid-state simulations strongly suggest that these diffuse function contributions are considerably damped in the condensed phase, and that ignoring them is in fact a much better approximation than fully including them.[5] Briefly, in the condensed phase, Pauli repulsion from neighboring molecules raises the energies of diffuse functions and so diminishes their contribution to the polarization. Empirically, when diffuse functions are used to develop polarization responses for small molecules, liquid-state simulations of these molecules manifest overpolarization of the solvent.

Permanent Electrostatic Charges. We have used the same quantum mechanical systems as above, except that two-body energies were employed as the fitting target:

$$E_{2\text{body}} = E(1+2) - E(1) - E(2) \tag{17}$$

The polarizabilities were not changed from their values obtained at the previous step. The charges were adjusted to minimize the two-body rms deviations.

In all of the cases (except for the dipolar probes), the R_{cut} for both dipoles and charges on the molecule involved were set to 0.8 Å.

Lennard-Jones Parameters. Fitting the Lennard-Jones part of the force field was done with high-accuracy ab initio results for intermolecular hydrogen-bonding interaction energies and distances as a target. Gas-phase energy minimizations were carried out. The quantum mechanical data were obtained as described in ref 15, and many actual target energies were adopted from the refs 9 and 12 (as noted in the tables in the Results and Discussion section). The methods employed to calculate binding energies are based on an MP2 extrapolation procedure that was previously developed using the pseudospectral local MP2 (LMP2) approach.

The goal was to reproduce the gas-phase intermolecular binding affinities and geometries as accurately as possible. We normally set a target of 0.25−0.5 kcal/mol or better for the precision of the binding affinity. For hydrogen bonds, this can be achieved via MP2 calculations extrapolated to the basis set limit, where the contribution of higher-level excitations (e.g., CCSD(T)) has been shown to be negligible (although, in some cases, such as π stacking of aromatic rings, the MP2 level is not adequate to achieve the target accuracy).

Briefly, dimer geometries were obtained by LMP2 optimizations with a cc-pVTZ(-f) basis set.[16] The empirical dimer binding energy consists of the LMP2 binding energy for a smaller cc-pVTZ(-f) basis set (E_{ccpvtz}) and the LMP2 binding energy with a larger cc-pVQZ(-g) basis set (E_{ccpvq}). The model binding energy E_{bind} takes the simple form[15]

$$E_{\text{bind}} = C_1{\bullet}E_{\text{ccpvtz}} + C_2{\bullet}E_{\text{ccpvqz}} \tag{18a}$$

$$C_1 = a_1/(a_1 - a_2); C_2 = -a_2/(a_1 - a_2) \tag{18b}$$

$$a_1 = \exp(-2.7); a_2 = \exp(-1.8) \tag{18c}$$

In calculating binding energies, the Hartree−Fock energies are corrected for basis set superposition error using the counterpoise method.

The target hydrogen-bonded distances were taken directly from the LMP2/cc-pVTZ(-f) energy minimizations.

Bond Stretching and Angle Bending. The bond-stretching and angle-bending energies were obtained according to eqs 13 and 14. The values of the parameters were taken directly from the OPLS-AA.[8] The reason is that both OPLS-AA and our PFF disregard 1,2 (covalent bond) and 1,3 (covalent angle) interactions; therefore, the energetics related to these arrangements are the same with both techniques.

Torsional Parameters. Finally, the torsional term was computed as shown in eq 15. We performed constrained geometry optimizations with dihedral angles fixed at their key positions and optimized the parameters V to minimize deviations of the relative energies from the LMP2/cc-pVTZ(-f) quantum mechanical results. For instance, for the ethane molecule, constraining the H−C−C−H dihedral to 60° and to 0° yielded relative quantum mechanical energies of 0 and 2.7762 kcal/mol, respectively. We have optimized the V_3 term of this torsion to achieve a close agreement with these numbers (0 and 2.7751 kcal/mol). The V_1 and V_2 terms in this case were set to zero.

Liquid Simulations. The final tuning of the force field parameters was achieved by reproducing experimental values of heats of vaporization and molecular volumes of the pure

$$\begin{tikzcd}
\text{A(gas)} \arrow[r, "\Delta G_{hyd}(\text{B})"] \arrow[d, swap, "\Delta G(\text{A}\rightarrow\text{B, gas})"] & \text{A(hydrated)} \arrow[d, "\Delta G(\text{A}\rightarrow\text{B, liq})"] \\
\text{B(gas)} \arrow[r, swap, "\Delta G_{hyd}(\text{B})"] & \text{B(hydrated)}
\end{tikzcd}$$

Figure 2. Thermodynamic cycle used to assess relative hydration energies.

molecular liquids involved. Each simulation was run with the POSSIM software and included 216 molecules in a cubic cell with periodic boundary conditions. The NPT ensemble (constant temperature, pressure, and the number of molecules) was employed. Methanol and water were simulated at 25 °C. The NMA liquid had a temperature of 100 °C. The hydrocarbons were modeled at their boiling temperatures: −161.49 °C for methane, −88.63 °C for ethane, −42.1 °C for propane, and −0.5 °C for butane. The calculations were carried out with the Monte Carlo technique, and the heats of vaporization were calculated according to eq 19:

$$\Delta H_{\text{vap}} = E(\text{gas}) - E(\text{liq}) + RT \qquad (19)$$

The difference between the energy for one molecule in the gas-phase and in the condensed state was augmented by the RT term to account for the $\Delta(PV)$ part of the enthalpy, in the assumption that the vapor obeys the ideal gas law, and the molecular volume of the liquid can be neglected compared to that of the gas. In all of the calculations, at least 1×10^6 Monte Carlo configurations of averaging were followed by no less than 5×10^6 configurations of averaging for the thermodynamic properties. Elements of the dipole−dipole interaction tensor in eq 5 were set to zero for distances beyond 7.0 Å. The other intermolecular interactions were cut off at 8.0 Å for water; 10.0 Å for methane and methanol; and 11.0 Å for ethane, propane, butane, and NMA. The charge−charge interactions were switched off smoothly over the last 0.5 Å. The standard correction for the neglected Lennard-Jones energies beyond the cutoff distances was applied.

C. Calculating Relative and Absolute Free Energies of Hydration. Calculating the free energies of hydration was not in any way a part of the parameter fitting procedure, but rather a test of the parameters produced as discussed above. Therefore, we believe that the high quality of the results reflects the genuinely adequate underlying physical model.

The thermodynamic cycle used to calculate relative hydration energies between species A and B is shown in Figure 2.

From this cycle, the relative free energy of hydration is

$$\Delta\Delta G_{\text{hyd}} = \Delta G_{\text{hyd}}(\text{B}) - \Delta G_{\text{hyd}}(\text{A}) = \Delta G(\text{A} \rightarrow \text{B,liq}) - \Delta G(\text{A} \rightarrow \text{B,gas}) \qquad (20)$$

The statistical perturbation theory was used to calculate the differences of free energies between solvated and gas-phase species A and B (ΔG(A→B, liq) and ΔG(A→B, gas), respectively). When B was set to nothing, the absolute free energy of hydration of species A was obtained. This was done to methane to anchor the other hydration free energies and to obtain their absolute values.

Table 1. Three-Body Energy Deviations from Quantum Mechanical Data, kcal/mol

	deviation, kcal/mol		
molecule	rms	maximum	maximum energy
H_2O	0.2682	0.3688	−0.5620
CH_3OH	0.2080	0.3588	−0.3700
NMA	0.3651	0.5902	−0.6293

Table 2. Two-Body Energy Deviations from Quantum Mechanical Data, kcal/mol

	deviation, kcal/mol		
molecule	rms	maximum	maximum energy
H_2O	1.1482	1.4819	−12.4741
CH_3OH	1.1627	1.3804	−12.1679
NMA	1.7319	2.6399	−14.9697

To calculate the ΔG(A→B, liq) and ΔG(A→B, gas), the standard statistical perturbation theory procedure was used. Differences between atoms of molecules A and B were switched on according to a parameter, $0 < \lambda < 1$, with $\lambda = 0$ corresponding to A, and $\lambda = 1$ to B. Then the interval from 0 to 1 was divided into a number of subintervals, and for each point between two intervals, a corresponding mixture of molecules A and B was created. The difference in free energies between systems corresponding to such points i and j was calculated according to eq 21:[17]

$$\Delta G(i \rightarrow j) = -RT\ln(\langle\exp[(-E_j - E_i)/RT]\rangle_i) \qquad (21)$$

Here, the brackets, $\langle ... \rangle_i$, signify averaging of the value inside the brackets over the configurational space of the mixed system at point i, and E_i and E_j are energies of the mixed systems i and j. In other words, the free energy difference between the molecular systems A and B is the thermodynamic average of their energy differences, and the whole change from A to B is broken into a number of steps in order to speed up the convergence.

The averaging was performed with Monte Carlo calculations for a single solute molecule in a water box, thus, corresponding to infinitely dilute solutions. The simulations proceeded as described in the previous subsection, except that a number of water molecules equal to the number of non-hydrogen atoms in the solute were removed (for example, for the methanol to ethane perturbation, the number of water molecules was equal to 214 instead of the pure water box of 216).

III. Results and Discussion

A. Fitting Electrostatic Part of the Force Field. As described above, fitting polarizabilities to the three-body energies and charges to the interaction energies with dipolar probes were the first two steps of the POSSIM force field production. While the further fine-tuning did lead to some adjustments, we still view reproducing the quantum mechanical three- and two-body energies as an important part of the force field validation. Listed in Tables 1 and 2 are three-body and two-body energies resulting from the final

Table 3. Dipole Moments, in Debye

molecule	dipole moment, experimental[a]	dipole moment, calculated
H_2O	1.85	1.98
CH_3OH	1.69	2.00
NMA	3.7	3.81

[a] Ref 18.

parameter sets. The following conclusions can be drawn from these data. The rms deviations of the three-body energies are within ca. 0.37 kcal/mol, with the largest deviation corresponding to the case of N-methylacetamide. This result is not surprising, given that parameter fitting for amides is by no means a straightforward business. For example, we had to build three separate parameter sets for the formamide, acetamide, and N-methylacetamide while producing the previous version of the polarizable force field (PFF0).[9,12] The acetamide parameters were ultimately used for the protein backbone.[9] Likewise, the two-body energies display a similar trend, with the maximum rms deviation (for NMA) being ca. 1.73 kcal/mol. While the absolute value of this error seems to be large, it constitutes only about 11.5% of the two-body energy itself. It is very likely that this error is, in fact, not much greater than that resulting from the imperfections of the quantum mechanical calculations as such.

As an added test, we have compared the POSSIM dipole moments with their experimental values in Table 3. It can be seen that the results are rather close and do not suffer from the overpolarization which is characteristic for the nonpolarizable fixed-charges force field. For example, the TIP4P monomer dipole moment is 2.18 D. This overpolarization is necessary to account for the increased dipole moment in polar media (such as bulk water), but it creates a nonphysical situation in the gas phase. This problem is resolved by applying the polarization formalism.

B. Alkane Parameters. It can be noticed that results for methane, ethane, propane, and butane are not present in Tables 1−3. The nonbonded parameters (including the electrostatics) for these systems were produced in a different fashion. Following the approach employed in creating the previous generation of the polarizable force field,[12] we set the electrostatic charges on alkane atoms to be the same as in the OPLS-AA. That is, each aliphatic hydrogen had a charge of 0.06 electrons, and the sp^3 carbons were charged by −0.24, −0.18, or −0.12 electron units, depending on the number of hydrogens attached to the carbon. Since the $-CH_n-$ groups are essentially spherically symmetric, the magnitudes of the charges do not make a significant difference. This has been shown previously by simulating pure liquid and hydrated saturated hydrocarbons.[19] Furthermore, the σ and ε Lennard-Jones parameters were also set to their OPLS-AA values, 3.5 Å and 0.066 kcal/mol for carbons and 2.5 Å and 0.030 kcal/mol for hydrogens, respectively. Finally, the isotropic polarizabilities for the carbon atoms in the POSSIM PFF are the same as had been previously found to perform well in the PFF0.[12] For these atoms, the inverse polarizability $\alpha^{-1} = 0.5069$ Å^{-3}. No polarizabilities were assigned to the aliphatic hydrogen atoms.

Table 4. Torsional Energy, in kcal/mol

molecule	dihedral	angle values	energy, QM[a]	energy, PFF
C_2H_6	H−C−C−H	0°	2.7762	2.7751
		60°	0.0000	0.0000
C_3H_8	H−C−C−C	0°	3.1298	3.1294
		60°	0.0000	0.0000
C_4H_{10}	C−C−C−C	0°	5.5337	5.5371
		60°	0.5751	0.5752
		120°	3.2104	3.2069
		180°	0.0000	0.0000
CH_3OH	H−C−O−H	0°	1.0643	1.0647
		60°	0.0000	0.0000
NMA	C−C−N−C	0°	2.0170	2.0185
		180°	0.0000	0.0000
	H−C−N−C	0°	0.0000	0.0000
		45°	0.0878	0.0328
		60°	0.0049	0.0480
	H−C−C−N	0°	0.0000	0.0000
		45°	0.2093	0.2154
		60°	0.2509	0.2551

[a] LMP2/cc-pVTZ(-f), this work.

Therefore, the nonbonded parameters for the alkanes were not refitted. However, the torsional coefficients for ethane, propane, and butane, H−C−C−H, H−C−C−C, and C−C−C−C, torsions were refitted to reproduce quantum mechanical energy profiles.

C. Torsional Coefficients. Torsional energy coefficients have been fitted to reproduce LMP2/cc-pVTZ(-f) energy profiles as described in the Methods section. The results of performing this task are shown in Table 4. Our original goal was to achieve a ca. 0.1 kcal/mol agreement with the quantum mechanical results, but the final accuracy was much better than that. The reason is that the molecules which we considered contained no coupled torsions (such as, for example, protein backbone ϕ and Ψ). This was true even for the NMA molecule. Therefore, we were dealing with one-dimensional torsional profiles, and adjusting the three Fourier coefficients for each torsion was enough for achieving the high level of accuracy.

D. Gas-Phase Dimerization Energies and Interatomic Distances. The next step in our force field development, and perhaps the first truly significant test of the new force field, was reproducing gas-phase binding energies and geometries of the complexes. Given in Tables 5 and 6 are the results of comparing our polarizable force field application with quantum mechanical and experimental data. As described in the previous section, the quantum mechanical results, unless otherwise noted, are taken from applying our previously developed extrapolation technique utilizing calculations with LMP2/cc-pVTZ(-f) and LMP2/cc-pVQZ basis sets.

Table 5 contains results for the aliphatic hydrocarbons (as represented by methane), water, and methanol. Unlike in generating the previous version of the polarizable force field (PFF0[12]), we have calculated energies for both the homodimer of methanol and its heterodimer with water. Moreover, both methanol dimers with water in which the latter serves as an electron donor and acceptor have been considered. This was also our routine when dealing with the NMA. We plan to follow this pattern in the future development of the POSSIM force field. Methane−water dimers were not considered, as no true hydrogen bond is formed in this case.

Table 5. Gas-Phase Dimerization Energies (kcal/mol) and Distances (Å) for H_2O, CH_4, and CH_3OH

	energy				distance			
system	QM[a]	OPLS[a]	PFF0[b]	PFF[c]	QM[a]	OPLS[a]	PFF0[b]	PFF[c]
H_2O−H_2O O···O	−5.02	−6.78	−5.54	−4.52	2.91	2.68	2.88	2.91
CH_4−CH_4 C···C	−0.5[d]	−0.48	−0.44	−0.48	3.7[d]	3.77	3.86	3.76
MeOH−MeOH O···O	−5.59	−6.41	−5.63	−5.59	2.80	2.78	2.81	2.81
MeOH−OH_2 O···O	−4.90[e]			−5.12	2.86[e]			2.80
MeHO−HOH O···O	−4.77[f]			−4.93	2.91[f]			2.90

[a] Refs 7 and 12. Results for water are from ref 20. [b] Ref 12. PFF0 data for water are from ref 21. [c] This work. [d] Ref 23. [e] Ref 22. [f] Methanol−water results: from this work, LMP2 with cc-pVTZ(-f) to cc-pVQZ extrapolation, as in ref 15.

Table 6. Gas-Phase Dimerization Energies (kcal/mol) and Distances (Å) for NMA (cis and trans conformations)

	energy				distance			
system	QM[a]	OPLS[a]	PFF0[a]	PFF[b]	QM[a]	OPLS[a]	PFF0[a]	PFF[b]
NMA(t)−NMA(t) N···O	−8.53 −7.2[c] *d*	−7.96	−5.24	−7.89	2.97	2.81	2.84	2.92
NMA(c)−NMA(c) N···O	−14.4	−11.3	−14.1	−9.48	2.92	2.83	2.90	2.92
NMA(t)−OH_2 HN···O	−5.82 −4.8[c]			−4.86	3.03			3.02
NMA(t)−HOH CO···O	−7.91 −7.0[c]			−7.10	2.91			2.79

[a] Ref 12 for NMA(c) and this work for NMA(t). [b] This work. [c] Ref 24. [d] Ref 25.

As demonstrated by the results in Table 5, the dimerization energies for all of the systems were within 0.5 kcal/mol of their quantum mechanical counterparts. For the methanol−methanol dimer, the agreement is much better than that. A water−water interaction energy lower than −5 kcal/mol has been suggested previously; therefore, the relatively high error in this case is probably not a reason for concern. The distances between the heavy atoms are within ca. 0.1 Å of the quantum mechanical results. Overall, the developed PFF performs well in reproducing these gas-phase dimerization properties.

It can also be seen that the POSSIM PFF is showing a slight improvement over the PFF0. And the improvement with comparison to the fixed-charges OPLS-AA is quite dramatic. For example, as shown in Table 5, the water−water dimerization energy is overestimated by almost 2 kcal/mol if the OPLS-AA model is used. This is natural, as fixed-charges models need to overpolarize individual molecules in order to capture the overall polarization increase in the bulk polar media (such as, for example, bulk water). Therefore, our fast second-order polarization technique does not require any sacrifice of computational accuracy as compared to the full-scale polarizable model (PFF0) and outperforms the fixed-charges one.

Given in Table 6 are results of simulating NMA dimers in the gas phase. Fitting parameters for the NMA molecule is generally a more complex task. One reason for that is that quantum mechanical data for such dimerization energies are often less reliable. Shown in the table are just two values of the *trans*-NMA dimerization energy. And the full range of this piece of data which can be found in the literature is actually considerably wider. Perhaps this is why some authors choose to simply ignore the NMA gas-phase dimerization energy when producing or reparameterizing a force field.[25] We took a middle-road approach in regard to this matter. While we did use the quantum mechanical value for the NMA(t)−NMA(t) dimer, we did not pose as strong restrictions on the PFF results as we did for the other systems. We considered an error of 0.64 kcal/mol to be acceptable, given the uncertainty of the quantum mechanical results themselves. At the same time, we adhered to the stronger criteria when reproducing geometries of the complexes, with the error being within ca. 0.1−0.15 Å range.

The new POSSIM PFF performs better in reproducing the NMA(t) and NMA− water dimers than both force fields used for comparison, the fixed-charges OPLS-AA and the previously generated PFF0. While the OPLS-AA NMA(t) dimer has an energy which is slightly closer to the QM value than the POSSIM PFF, this is achieved at the cost of underestimating the N···O distance by about 0.16 Å versus the 0.05 Å error in the new PFF. As far as the PFF0 is concerned, it provides much better values for both the energy and the distance for the NMA(c) dimer but significantly underestimates both the distance and the magnitude of the energy for the dimer of the NMA in its trans form. The reason is that we considered only the *cis*-NMA dimer when the PFF0 was developed, since its dimerization energy is stronger than for the NMA(t). At the same time, the *trans*-NMA is much less abundant than the cis form, and it is the NMA(t) which forms the building block of protein and peptide backbones. This is why we choose to use the NMA(t) dimer as the fitting target in this work, and our results definitely show an improvement over the PFF0 in this respect.

E. Simulations of Pure Liquids. Calculated heats of vaporization and molecular density are shown in Table 7. It follows from the values of the average errors that the overall performance of the POSSIM PFF is superior to both that of the OPLS-AA and PFF0. The average PFF deviation of the heats of vaporization is 0.083 kcal/mol versus the 0.0.129 kcal/mol for the OPLS-AA and 0.240 kcal/mol for the PFF0. The average error in the molecular volume is 1.485 Å^3, which is a noticeable improvement, as compared to the PFF0, and is slightly better than that for the OPLS-AA. Moreover, the worst (although still

Table 7. Liquid State Heats of Vaporization (kcal/mol) and Molecular Volumes (Å^3), at 25°C, Except for CH_4 (−161.49 °C), C_2H_6 (−88.63 °C), C_3H_8 (−42.1 °C), C_4H_{10} (−0.5 °C), and NMA (100 °C)

	ΔH_{vap}				V			
system	exptl[a]	OPLS[a]	PFF0[b]	PFF[c]	exptl[a]	OPLS[a]	PFF0[b]	PFF[c]
H_2O	10.51	10.46	10.54	10.577 ± 0.055	30.0	30.0	30.15	29.891 ± 0.226
CH_4	1.96	2.19	1.89	2.209 ± 0.026	62.8	57.2	62.2	56.863 ±0.381
C_2H_6	3.62	3.44	3.32	3.456 ± 0.063	91.5	92.5	94.4	92.140 ± 0.571
C_3H_8	4.49	4.55	4.79	4.499 ± 0.129	126.0	125.2	123.9	126.096 ± 0.903
C_4H_{10}	5.35	5.43	5.62	5.335 ± 0.164	160.3	161.3	157.2	163.433 ± 1.416
NMA	13.3	13.6	13.9	13.319 ± 0.372	135.9	133.9	128.3	135.670 ± 0.566
CH_3OH	8.95	8.95	8.84	9.005 ± 0.140	67.7	68.3	67.0	67.447 ± 0.535
average error		0.129	0.240	0.083		1.574	2.450	1.485

[a] Refs 7 and 12. [b] Refs 12 and 21. [c] This work.

Table 8. Free Energies of Hydration, kcal/mol

process	ΔG_{hyd}, experiment	ΔG_{hyd}, PFF (this work)
nothing → CH_4	2.00[a]	2.115 ± 0.057
CH_4 → C_2H_6	−0.17[a]	−0.317 ± 0.040
C_2H_6 → CH_3OH	−6.94[b]	−6.748 ± 0.053
	absolute ΔG_{hyd} (from above data)	
CH_4	2.00[a]	2.115 ± 0.057
C_2H_6	1.83[a]	1.798 ± 0.070
CH_3OH	−5.11[b]	−4.950 ± 0.088

[a] Ref 19. [b] Ref 26.

acceptable) results for the new PFF are obtained for methane and ethane, which are probably not the most relevant pure liquids considered, given their very low boiling temperatures of −161.49 and −88.63 °C, respectively. At the same time, the density of the NMA was improved very significantly as compared to the PFF0, and the NMA molecule is extremely important as the building block for protein backbones. Overall, all three models perform well in simulating the pure liquids involved. Therefore, we have clearly shown that our second-order approximation for calculating induced electrostatic dipoles is completely adequate, as is it capable of reproducing both gas-phase and liquid properties at a good level of accuracy.

F. Free Energy Perturbations. Presented in this subsection are the results of calculating relative and absolute free energies of hydration for methane, ethane, and methanol. In contrast with the work described above, this part of the project was carried out as a test and not a parametrization; thus, we did not refit any parameters to obtain good results. Therefore, these calculations can serve as a test of the physical robustness of the model. The successful results presented here have a double value of validating both the force field parameters and the overall methodological and POSSIM software robustness in calculating free energy changes with the statistical perturbation theory.

The calculated values of the free energies are shown in Table 8. We carried out three sets of these calculations: transforming methanol into ethane (by converting the −OH group into a methyl), shrinking the methyl group into an aliphatic hydrogen to mutate ethane into methane, and finally, making the methane molecule disappear altogether by converting all of the atoms into dummy ones. This last step permits us to anchor all of the results into the energy of solvation of a dummy atom (i.e. zero); thus, we can obtain the absolute hydration energies for all of the species involved.

According to the data in Table 8, the agreement of our results with those of the experiment is excellent. The hydration energy of methane is correct within 0.115 kcal/mol. The nonobvious trend of the slight hydration energy drop between methane and ethane is reproduced correctly, even though it is exaggerated by about 0.15 kcal/mol (which actually leads to the absolute hydration energy of ethane being in a better agreement with the experiment). The difference in hydration energies between methanol and ethane are correct within ca. 0.21 kcal/mol. Overall, the absolute values of these energies are within 0.13 kcal/mol of their experimental counterparts. It is important that this agreement was achieved without any specific fitting. These results represent a test of the parameters produced as described above; therefore, they attest to the robustness of the physical model and the POSSIM software.

IV. Conclusions

We have utilized a previously suggested fast polarization formalism to create a software package named POSSIM and produced polarizable force field parameters for several molecular systems relevant in organic and biological simulations. The agreement with gas-phase and liquid experimental data has been found to be very good. Moreover, we tested POSSIM by calculating absolute free energies of hydration of methane, ethane, and methanol and determined them to be within 0.13 kcal/mol of their experimental counterparts. We believe that this verifies the robustness of the parameters and the software. We view this work as the first step in creating an extensive set of force field parameters to be used in organic and biophysical simulations, including modeling of proteins and protein−ligand complexes. Furthermore, we have been able to successfully use a procedure for utilizing both quantum mechanical and experimental data as fitting targets. We hope our results will further prove the importance of treating the electrostatic polarization explicitly, when building empirical force fields, and will contribute to making polarizable calculations more affordable computationally.

Acknowledgment. The project described was supported by Grant Number R01GM074624 from the National Institute of General Medical Sciences. The content is solely the responsibility of the authors and does not necessarily represent the official views of the National Institute of

General Medical Sciences or the national Institutes of Health. The authors express gratitude to Schrödinger, LLC for the Jaguar and PFF software.

Supporting Information Available: POSSIM force field parameters. This material is available free of charge via the Internet at http://pubs.acs.org.

References

(1) See, for example: (a) Caldwell, J. W.; Kollman, P. A. *J. Am. Chem. Soc.* **1995**, *117*, 4177–4178. (b) Jiao, D.; Zhang, J. J.; Duke, R. E.; Li, G. H.; Schneiders, M. J.; Ren, P. Y. *J. Comput. Chem.* **2009**, *30*, 1701–1711.

(2) (a) MacDermaid, C. M.; Kaminski, G. A. *J. Phys. Chem. B* **2007**, *111*, 9036–9044. (b) Click, T. H.; Kaminski, G. A. *J. Phys. Chem. B* **2009**, *113*, 7844–7850.

(3) Veluraja, K.; Margulis, C. J. *J. Biomol. Struct. Dyn.* **2005**, *23*, 101–111.

(4) Ji, C.; Mei, Y.; Zhang, J. Z. H. *Biophys. J.* **2008**, *95*, 1080–1088.

(5) Kaminski, G. A.; Stern, H. A.; Berne, B. J.; Friesner, R. A.; Cao, Y. X.; Murphy, R. B.; Zhou, R.; Halgren, T. *J. Comput. Chem.* **2002**, *23*, 1515–1531.

(6) Rick, S. W.; Stuart, S. J.; Berne, B. J. *J. Chem. Phys.* **1994**, *101*, 6141–6156.

(7) Kaminski, G. A.; Zhou, R.; Friesner, R. A. *J. Comput. Chem.* **2003**, *24*, 267–276.

(8) Jorgensen, W. L.; Maxwell, D. S.; Tirado-Rives, J. *J. Am. Chem. Soc.* **1996**, *118*, 11225–11236.

(9) Maple, J. R.; Cao, Y. X.; Damm, W.; Halgren, T. A.; Kaminski, G. A.; Zhang, L. Y.; Friesner, R. A. *J. Chem. Theory Comput.* **2005**, *1*, 694–715.

(10) (a) Straatsma, T. P.; McCammon, J. A. *Chem. Phys. Lett.* **1990**, *167*, 252–254. (b) Straatsma, T. P.; McCammon, J. A. *Chem. Phys. Lett.* **1991**, *177*, 433–440. (c) Roux, B. *Chem. Phys. Lett.* **1993**, *212*, 231–240.

(11) Berendsen, H. J. C.; Grigera, J. R.; Straatsma, T. P. *J. Phys. Chem.* **1987**, *91*, 6269–6271.

(12) Kaminski, G. A.; Stern, H. A.; Berne, B. J.; Friesner, R. A. *J. Phys. Chem. A* **2004**, *108*, 621–627.

(13) (a) Becke, A. D. *Phys. Rev. A* **1988**, *38*, 3098–3100. (b) Lee, C.; Yang, W.; Parr, R. G. *Phys. Rev. B* **1988**, *37*, 785–789.

(14) (a) *Jaguar*, v3.5; Schrödinger, Inc.: Portland, OR, 1998. (b) *Jaguar*, v4.2; Schrödinger, Inc.: Portland, OR, 2000.

(15) Kaminski, G. A.; Maple, J. R.; Murphy, R. B.; Braden, D; Friesner, R. A. *J. Chem. Theory Comput.* **2005**, *1*, 248–254.

(16) Dunning, T. H. *J. Chem. Phys.* **1989**, *90*, 1007–1023.

(17) Zwanzig, R. W. *J. Chem. Phys.* **1954**, *22*, 1420–1426.

(18) Caldwell, J. W.; Kollman, P. A. *J. Phys. Chem.* **1995**, *99*, 6208–6219.

(19) Kaminski, G. A.; Duffy, E. M.; Matsui, T.; Jergensen, W. L. *J. Phys. Chem.* **1994**, *98*, 13077–13082.

(20) Mattsson, A. E.; Mattsson, T. R. *J. Chem Theory Comput.* **2009**, *5*, 887–894.

(21) Kaminski, G. A. *J. Phys. Chem. B* **2005**, *109*, 5884–5890.

(22) Tsuzuki, S.; Uchimaru, T.; Matsumura, K.; Mikami, M.; Tanabe, K. *J. Chem. Phys.* **1999**, *110*, 11906–11910.

(23) Takatani, T.; Sherrill, C. D. *Phys. Chem. Chem. Phys.* **2007**, *9*, 6106–6114.

(24) Dixon, D. A.; Dobbs, K. D.; Valentini, J. J. *J. Phys. Chem.* **1994**, *98*, 13435–13439.

(25) Xie, W.; Pu, J.; MacKerell, A. D.; Gao, J. *J. Chem. Theory Comput.* **2007**, *3*, 1878–1889.

(26) Gallicchio, E.; Zhang, L. Y.; Levy, R. M. *J. Comput. Chem.* **2002**, *23*, 517–529.

CT900409P

JCTC Journal of Chemical Theory and Computation

On the Gas-Phase Electronic Chemical Potential of Anions

Claudio Pérez-Méndez,*,† P. Fuentealba,‡ and Renato Contreras†

Departamento de Química and Departamento de Física, Facultad de Ciencias, Universidad de Chile, Casilla 653-Santiago, Chile

Received April 6, 2009

Abstract: In the process of evaluating intrinsic electronic chemical potentials and related properties of anions in the gas phase, positive values for this quantity often arise. We herein examine in detail this result in terms of computational grounds. At a low level of theory, this result is often obtained, but its origin is mainly traced to the fact that the LUMO energy level is not really converged. Therefore, this outcome may be an artifact of the calculation. We establish the minimum basis set analysis that is to be performed before the electronic chemical potential of charged electron donors, in the absence of medium (solvent) effects, may be safely calculated to yield physically meaningful results. The implications that this result may have on the phenomenological chemical reactivity theory are discussed in detail, mainly those related to the definition of the electron-donating (nucleophilicity) ability of anions in the gas phase. The arguments given are illustrated for a large number of atomic and molecular systems at different levels of theory.

Introduction

The concepts introduced from the density functional theory of chemical reactivity by Parr and Yang[1] have had an enormous impact in the fields of general physical chemistry and physical organic chemistry. A set of recent review works illustrates well this point.[2−10] However, one of the most relevant achievements of the research work done in this field is that useful concepts like electronic chemical potential, global and local electrophilicity indexes, and electrophilic and nucleophilic Fukui functions have started to be introduced in modern texts of organic chemistry,[11] and therefore they are expected to be incorporated in the current language of the physical organic chemist community. Of central importance is the electronic chemical potential μ introduced by Parr and co-workers.[12−16] This quantity is defined as

$$\mu = \left[\frac{\partial E}{\partial N}\right]_{v(\mathbf{r})} \tag{1}$$

where E is the ground state energy of an N electron atomic or molecular system under the influence of an external potential $v(\mathbf{r})$ due to the compensating nuclear charges in the system. In eq 1, the derivative is taken at fixed $v(\mathbf{r})$. The finite difference approximated expression for μ is given as follows:[2]

$$\mu \cong -\left[\frac{I + A}{2}\right] \approx \left[\frac{\varepsilon_H + \varepsilon_L}{2}\right] \tag{2}$$

in terms of the first vertical ionization potential I and electron affinity A, or in terms of the one-electron energies of the frontier molecular orbitals HOMO and LUMO, if the frozen orbital approximation together with Janak's theorem is used.[2] Extensions to incorporate solvent effects on these properties have been reported for cations and neutrals.[17,18] It is pertinent for the discussion that follows to remind ourselves that the recommended definitions for I and A for atoms and molecules[19] are

$$S \rightarrow S^+ + e^-; \qquad \Delta E = E(S^+) - E(S) = I \tag{3}$$

and

$$S^- \rightarrow S + e^-; \qquad \Delta E = E(S) - E(S^-) = A \tag{4}$$

---

* Corresponding author phone: +562 978 7272; fax: +562 271 3888; e-mail: claudioperez@icaro.dic.uchile.cl.

† Departamento de Química.

‡ Departamento de Física.

10.1021/ct900164a CCC: $40.75

Table 1. HOMO and LUMO Energy Levels (ϵ_H and ϵ_L, respectively)[a]

	compound	ϵ_H	ϵ_L	μ	η	method	reference
1	$(NO_2)C_6H_4O^-$	−3.27	5.80	1.27	9.06	HF/3-21G(d)	22
2	$(COCH_3)C_6H_4O^-$	−2.48	7.40	2.46	9.88	HF/3-21G(d)	22
3	$HC_6H_4O^-$	−1.58	9.25	3.84	10.83	HF/3-21G(d)	22
4	$(CH_3)C_6H_4O^-$	−1.52	9.14	3.81	10.67	HF/3-21G(d)	22
5	$(Br)C_6H_4O^-$	−2.12	8.63	3.25	10.75	HF/3-21G(d)	22
6	$(CH_3O)C_6H_4O^-$	−1.66	8.93	3.63	10.59	HF/3-21G(d)	22
7	CH_3O^-	−1.921	12.785	5.432	7.353	HF/6-31G(d)	23
8	$CH_3CH_2O^-$	−2.161	11.954	4.896	7.057	HF/6-31G(d)	23
9	$(CH_3)_2CHO^-$	−2.376	11.398	4.511	6.887	HF/6-31G(d)	23
10	$(CH_3)_3CO^-$	−2.595	10.819	4.112	6.707	HF/6-31G(d)	23
11	$(CH_3)_3CCH_2O^-$	−2.643	10.236	3.797	6.439	HF/6-31G(d)	23

[a] Corresponding values of electronic chemical potential (μ) and chemical hardness (η) for a series of anions. All values are in eV.

respectively. Experimental evidence shows that, for positively charged species and neutrals, the quantities I and A are in general positive numbers (with some exceptions for A), with $I \gg A$, because the energy required to remove one electron from negative species is less than that needed to take out an electron from a neutral.[20,21] Therefore, by inspection of the first equality in eq 2, it follows immediately that, for cations and neutrals, the condition $\mu < 0$ is always fulfilled. Unfortunately, experimental data regarding A values for anions are in general not available, and the second approximate expression for the electronic chemical potential given in eq 2 is used instead. In this work, the focus is put on the theoretical estimates of ionization potentials and electron affinities of anions from ab initio methods and their effect on the computed values of the electronic chemical potential in the gas phase.

If Janak's theorem is used, under the general constraint that $\epsilon_L > \epsilon_H$, the following computational cases may arise:

(a) $\epsilon_L > 0 > \epsilon_H$ (normal case: bound HOMO and unbound LUMO states)

(b) $0 > \epsilon_L > \epsilon_H$ (current computational case: bound HOMO and LUMO states)

(c) $\epsilon_L > \epsilon_H > 0$ (less current computational case: unbound HOMO and LUMO states).

We shall now examine them in the following.

Case a: $\epsilon_L > 0 > \epsilon_H$. This case leads to the following possible situations: (i) $\mu > 0$ or (ii) $\mu < 0$. For the former, we have

$$\mu \cong -\frac{(I + A)}{2} \approx \frac{(\varepsilon_H + \varepsilon_L)}{2} > 0 \qquad (5)$$

which entails that $\epsilon_L > -\epsilon_H$. This condition satisfies the constraint $\epsilon_L > \epsilon_H$, for $|\epsilon_L| > |\epsilon_H|$.

For $\mu < 0$, on the other hand, we have

$$\mu \cong -\frac{(I + A)}{2} \approx \frac{(\varepsilon_H + \varepsilon_L)}{2} < 0 \qquad (6)$$

that leads to $\epsilon_L < -\epsilon_H$, a result also consistent with the condition $\epsilon_L > \epsilon_H$, for $|\epsilon_L| < |\epsilon_H|$. Therefore, for the normal case of bound HOMO and unbound LUMO states, the occurrence of positive values of the electronic chemical potential is a possible outcome. We will come back to this problem, and we will show that this statement has only a physical meaning if the LUMO state is conveniently converged, and that this convergence requires a thorough analysis of the basis set used.

Case b: $0 > \epsilon_L > \epsilon_H$. For $\mu > 0$, we have

$$\mu \cong -\frac{(I + A)}{2} \approx \frac{(\varepsilon_H + \varepsilon_L)}{2} > 0 \qquad (7)$$

which contradicts the hypothesis $0 > \epsilon_L > \epsilon_H$ because it entails that $\epsilon_H > -\epsilon_L$, which is a positive number.

For $\mu < 0$, we have

$$\mu \cong -\frac{(I + A)}{2} \approx \frac{(\varepsilon_H + \varepsilon_L)}{2} < 0 \qquad (8)$$

which entails that $\epsilon_H < -\epsilon_L$, a result consistent with the hypothesis, and is therefore possible. Thus, for the case where both HOMO and LUMO levels are bound states, the only meaningful representation of the electronic chemical potential is the one associated with a negative value.

Case c: $\epsilon_L > \epsilon_H > 0$. This case can never occur, because it leads to a situation where $A < I < 0$, which contradicts the experimental results.

Table 1 summarizes the electronic chemical potential and chemical hardness for a series of anions evaluated in the literature. It may be seen that, independent of the basis set used, Hartree−Fock theory describes the electronic structures of anions within the normal case a discussed above, that is, with bound HOMO and unbound LUMO states. Compounds labeled 1−6 in Table 1 were reported by Mendez et al.[22] as part of a theoretical study on the basicity of p-substituted phenolates and the elimination to substitution ratio in the reaction with the reference electrophile p-nitrophenyl bromide. These reactions were analyzed in terms of the empirical HSAB rule so that the focus was put on the hardness (softness) values rather than on the positive values of the electronic chemical potential that result after using the gas-phase one-electron energies of the HOMO and LUMO levels reported therein.[22] In order to further analyze the effect of intrinsic positive electronic chemical potentials, and therefore free from solvent complications, we take another benchmark model of acid−base equilibrium of alcohols in the gas phase.[23] Therein, a relationship between relative proton affinities and relative electronic chemical potentials was proposed, using the methoxide anion as a reference for both scales. This model was assumed to correctly describe the gas-phase acidity pattern within the family of alkyl-substituted alcohols in the gas phase, using a thermodynamic

Table 2. HOMO and LUMO Energy Levels (ϵ_H and ϵ_L, respectively)[a]

	compound	ϵ_H	ϵ_L	μ	η
1	$CH_3CO_2^-$	−5.10	5.38	0.14	10.48
2	$CH_3CH_2O^-$	−2.99	4.38	0.70	7.36
3	CN^-	−5.23	6.66	0.72	11.89
4	NO_3^-	−6.04	7.56	0.76	13.60
5	SH^-	−2.55	5.22	1.33	7.77
6	Br^-	−3.79	6.94	1.57	10.74
7	OH^-	−2.86	6.04	1.59	8.89
8	CH_3S^-	−2.21	5.52	1.65	7.73
9	CH_3O^-	−2.74	6.07	1.66	8.82
10	Cl^-	−4.08	8.15	2.04	12.24
11	NH_2^-	−1.26	5.58	2.16	6.84
12	N_3^-	−2.82	7.97	2.57	10.79
13	F^-	−4.83	14.65	4.91	19.47
14	I^-	−2.67	21.57	9.45	24.24
15	H^-	−0.10	20.11	10.00	20.21

[a] Corresponding values of electronic chemical potential (μ) and chemical hardness (η) for a series of anions. All values are in eV.

cycle by combining the proton affinity (PA) of neutrals and anions. In this way, the acid−base equilibria are described in a more balanced way by including the contributions of the neutral and charged species. The variations in proton affinity given by $\Delta PA = PA(RO^-) - PA(CH_3O^-)$ were related to the variations in total electronic chemical potential given by $\Delta\mu_t = \Delta\mu^- - \Delta\mu^N$, where

$$\Delta\mu^- = [\mu(RO^-) - \mu(CH_3O^-)] \tag{9}$$

and

$$\Delta\mu^N = [\mu(CH_3OH) - \mu(ROH)] \tag{10}$$

are the contributions of the change in electronic chemical potential of anions and neutrals, respectively.[23] The values reported in ref 23 show that the contribution of the anions largely outweighs the contribution from the changes in electronic chemical potential of the neutrals, and therefore, it is the contribution of the alkoxides that drives the proton transfer involved in the gas-phase acid−base equilibria. The alkoxides involved in that study are quoted in Table 1 and labeled as compounds 7−11. This ordering is in agreement with the gas-phase acidity scale of alcohols.[24] The inversion of this ordering in the solution phase is well-known,[24] and it has been attributed to a differential solvent effect which follows an inverse trend with the anion size.[25]

Table 2 shows the values of gas-phase electronic chemical potentials for a series of anions involved in gas-phase nucleophilic substitution reactions. The electronic quantities were evaluated in this work at the HF/6-311++G(d,p) level of theory, using the Gaussian 03 program package.[26] The addition of diffuse functions is a usual prescription when dealing with anions in the gas phase. This result is useful to show that, even in the case where diffuse functions are incorporated in the calculations, the occurrence of positive values of μ for anions in the gas phase may be a current outcome.

In the process of review of the present material, two reviewers grabbed our attention by suggesting that the numerical data presented in Tables 1 and 2 were insufficient to discuss the sign of the electronic chemical potential of anions in the gas phase, and that the occurrence of calculated positive values for this quantity could be an artifact of the basis set used. One of the reviewers pointed out that the problem should be related to a “definition of electron affinity for system(s) that do not bind another electron”. The definition of the intrinsic electronic chemical potential proposed by Parr et al.[12] entails the energy difference between the neutral and a “metastable” anion. The metastable anion model has been recently addressed in the literature.[27,28] A second choice is to just put $A = 0$ for anions in the gas phase. The reviewers went on to propose that, within Hartree−Fock theory, the LUMO energy and the electron

Table 3. HOMO and LUMO Energy Levels from Reference HF/6-311++G(d,p) and HF/AUG-cc-pVDZ, HF/AUG-cc-pVTZ, and HF/AUG-cc-pVQZ Levels of Theory

Compound	$\varepsilon_H^{(1)}$	$\varepsilon_H^{(2)}$	$\varepsilon_H^{(3)}$	$\varepsilon_H^{(4)}$	$\varepsilon_L^{(1)}$	$\varepsilon_L^{(2)}$	$\varepsilon_L^{(3)}$	$\varepsilon_L^{(4)}$
NO_2PhO^-	−3.270	−3.661	−3.890	−4.052	5.800	3.566	2.192	1.348
CH_3COPhO^-	−2.480	−3.103	−3.098	−3.366	7.400	3.204	2.872	1.585
$(CH_3)_3CCH_2O^-$	−2.643	−3.296	−3.305	−3.586	10.236	3.522	3.136	1.481
NO_3^-	−6.040	−5.979	−5.984	−5.975	7.560	6.859	6.045	5.520
$CH_3CO_2^-$	−5.100	−5.094	−5.121	−5.124	5.380	3.982	3.627	3.412
PHO^-	−1.580	−2.319	−0.085	−2.305	9.250	3.538	0.117	2.965
CH_3PhO^-	−1.520	−2.210	−2.199	−2.197	9.140	3.293	2.927	2.738
$BrPhO^-$	−2.120	−2.791	−2.770	−2.766	8.630	3.626	3.252	2.990
CH_3OPhO^-	−1.660	−2.322	−2.303	−2.588	8.930	3.160	2.849	1.377
$(CH_3)_2CHO^-$	−2.376	−3.177	−3.183	−3.185	11.398	3.934	3.549	3.324
$(CH_3)_3CO^-$	−2.595	−3.387	−3.391	−3.392	10.819	3.833	3.472	3.259
CH_3O^-	−2.740	−2.801	−2.805	−2.810	6.070	4.345	3.951	3.720
CH_3S^-	−2.210	−2.257	−2.250	−2.249	5.520	4.165	3.782	3.559
$CH_3CH_2OH^-$	−2.161	−3.013	−3.016	−3.019	4.380	4.032	3.629	3.406
OH^-	−2.860	−2.935	−2.951	−2.959	6.040	5.390	4.861	4.639
N_3^-	−2.820	−2.853	−2.835	−2.834	7.970	6.460	5.852	5.354
H^-	−0.100	−1.223	−1.244	−1.248	20.110	7.666	6.587	6.078
F^-	−4.830	−4.931	−4.924	−4.925	14.650	13.850	12.042	10.785
Br^-	−3.790	−3.800	−3.792	−3.791	6.940	8.151	6.846	5.913
Cl^-	−4.080	−4.096	−4.091	−4.090	8.150	8.850	7.864	7.036
CN^-	−5.230	−5.206	−5.207	−5.205	6.660	6.378	5.699	5.209
SH^-	−2.550	−2.577	−2.582	−2.581	5.220	4.823	4.285	3.957
NH_2^-	−1.260	−1.291	−1.312	−1.323	5.580	5.016	4.500	4.235

Table 4. Electronic Chemical Potential and Chemical Hardness from Reference HF/6-311++G(d,p) and HF/AUG-cc-pVDZ, HF/AUG-cc-pVTZ, and HF/AUG-cc-pVQZ Levels of Theory in eV Units

compound	$\mu^{(1)}$	$\mu^{(2)}$	$\mu^{(3)}$	$\mu^{(4)}$	$\eta^{(1)}$	$\eta^{(2)}$	$\eta^{(3)}$	$\eta^{(4)}$
NO_2PhO^-	1.265	−0.048	−0.849	−1.352	9.070	7.227	6.082	5.400
CH_3COPhO^-	2.460	0.050	−0.113	−0.891	9.880	6.307	5.969	4.951
$(CH_3)_3CCH_2O^-$	3.797	0.113	−0.085	−1.052	12.879	6.818	6.441	5.067
NO_3^-	0.760	0.440	0.031	−0.227	13.600	12.838	12.029	11.495
$CH_3CO_2^-$	0.140	−0.556	−0.747	−0.856	10.480	9.076	8.748	8.537
PHO^-	3.835	0.610	0.016	0.330	10.830	5.858	0.202	5.270
CH_3PhO^-	3.810	0.542	0.364	0.271	10.660	5.502	5.126	4.935
$BrPhO^-$	3.255	0.417	0.241	0.112	10.750	6.416	6.022	5.756
CH_3OPhO^-	3.635	0.419	0.273	−0.606	10.590	5.482	5.152	3.965
$(CH_3)_2CHO^-$	4.511	0.378	0.183	0.070	13.774	7.112	6.732	6.509
$(CH_3)_3CO^-$	4.112	0.223	0.041	−0.066	13.414	7.220	6.864	6.652
CH_3O^-	1.665	0.772	0.573	0.455	8.810	7.145	6.756	6.530
CH_3S^-	1.655	0.954	0.766	0.655	7.730	6.422	6.032	5.807
$CH_3CH_2OH^-$	0.695	0.510	0.307	0.193	7.370	7.045	6.646	6.425
OH^-	1.590	1.227	0.955	0.840	8.900	8.325	7.812	7.597
N_3^-	2.575	1.803	1.508	1.260	10.790	9.313	8.687	8.188
H^-	10.005	3.221	2.671	2.415	20.210	8.890	7.830	7.326
F^-	4.910	4.459	3.559	2.930	19.480	18.781	16.966	15.709
Br^-	1.575	2.175	1.527	1.061	10.730	11.951	10.637	9.704
Cl^-	2.035	2.377	1.887	1.473	12.230	12.946	11.955	11.127
CN^-	0.715	0.586	0.246	0.002	11.890	11.584	10.906	10.415
SH^-	1.335	1.123	0.852	0.688	7.770	7.400	6.867	6.538
NH_2^-	2.160	1.863	1.594	1.456	6.840	6.308	5.812	5.558

Table 5. Even-Tempered Calculations of HOMO and LUMO Energy Levels Using HF/AUG-cc-pVQZ Level of Theory As Reference in eV Units

compound	$\varepsilon_H^{(a)}$	$\varepsilon_L^{(a)}$	$\varepsilon_L^{(b)}$	$\varepsilon_L^{(c)}$	$\varepsilon_L^{(d)}$	$\varepsilon_L^{(e)}$	$\varepsilon_L^{(f)}$	$\varepsilon_L^{(g)}$	$\varepsilon_L^{(h)}$
CH_3O^-	−2.810	3.720	2.414	1.622	1.044	0.652	0.596	0.438	0.322
CH_3S^-	−2.249	3.559	2.382	1.632	1.089	0.995	0.770	0.595	0.460
$CH_3CH_2OH^-$	−3.019	3.406	2.150	1.483	0.992	0.938	0.731	0.570	0.444
OH^-	−2.959	4.639	2.646	2.045	1.498	1.077	0.768	0.545	0.386
N_3^-	−2.834	5.354	3.161	2.132	1.605	1.069	0.916	0.684	0.510
H^-	−1.248	6.078	3.216	2.537	1.963	1.490	1.107	0.807	0.581
F^-	−4.925	10.785	5.870	4.283	3.019	2.092	1.441	0.995	0.690
Br^-	−3.791	5.913	3.467	2.623	1.911	1.356	0.950	0.663	0.463
Cl^-	−4.090	7.036	4.008	2.999	2.164	1.525	1.063	0.740	0.516
CN^-	−5.205	5.209	3.180	2.120	1.442	0.973	0.669	0.466	0.357
SH^-	−2.581	3.957	2.682	1.837	1.344	0.966	0.689	0.488	0.345
NH_2^-	−1.323	4.235	2.627	1.793	1.186	0.819	0.557	0.381	0.267

affinity should go to zero if a sufficiently large basis set is used. Both reviewers suggested a more complete discussion about the electron affinities and electronic chemical potential of anions in the gas phase by performing a thorough computational analysis in the infinite basis set limit, by adding diffuse functions until the LUMO energy level is converged. In order to perform such an analysis, we have chosen a modification of the even-tempered basis set approach, which consists of adding, in a systematic way, more and more diffuse functions of each symmetry to a well-established extended basis set like the family of aug-cc-pvNZ (with $N = 2, 3, 4, 5...$) bases.[29]

The procedure used to converge the HOMO and LUMO energy levels was as follows: First of all, we considered the series depicted in Table 3 and used the calculation with the reference HF/6-311++G(d,p) wave function quoted in Table 3 as $\epsilon_H^{(1)}$ and $\epsilon_L^{(1)}$. Then, the structures of anions were reoptimized using the Dunning−Huzinaga basis set (aug-cc-pVDZ, aug-cc-pVTZ, and aug-cc-pVQZ). The HOMO and LUMO energy levels obtained from these calculations are quoted in Table 3 as $\epsilon_H^{(2)}$, $\epsilon_L^{(2)}$, $\epsilon_H^{(3)}$, $\epsilon_L^{(3)}$, $\epsilon_H^{(4)}$, and $\epsilon_L^{(4)}$, respectively.

Note that the HOMO level is converged more rapidly than the LUMO level by increasing the basis set. Table 4 summarizes the calculated electronic chemical potential and chemical hardness using the numerical data of Table 3, using eq 2. It may be seen that increasing the basis set results in the inversion of the sign of the electronic chemical potential for 6 out of 23 anions within the series.

Some of the nonconverged anions quoted in Table 4 were selected for further analysis. They are displayed in Table 5. Note that this series included the harder anions that are expected to be more difficult to converge. This series was subjected to even-tempered basis set calculations. Specifically, the procedure consists of taking the geometry obtained at the HF/AUG-cc-pVQZ level of theory, and the exponents of the basis set were reduced following a geometric progression $[(1)/(2)]^n$ for $n = 1-7$. The results are quoted in Table 6 as $\varepsilon_H^{(b)}$, $\varepsilon_L^{(b)}$, $\varepsilon_H^{(c)}$, $\varepsilon_L^{(c)}$, $\varepsilon_H^{(d)}$, $\varepsilon_L^{(d)}$, $\varepsilon_H^{(e)}$, $\varepsilon_L^{(e)}$, $\varepsilon_H^{(f)}$, $\varepsilon_L^{(f)}$, $\varepsilon_H^{(g)}$, $\varepsilon_L^{(g)}$, $\varepsilon_H^{(h)}$, and $\varepsilon_L^{(h)}$, respectively.

Note that, following the even-tempered procedure, the LUMO energy level dramatically diminishes, yet the complete convergence limit has not been yet attained. However,

Table 6. Even-Tempered Calculations of the Electronic Chemical Potential Using a HF/AUG-cc-pVQZ Levels of Theory As Reference[a]

compound	$\mu^{(a)}$	$\mu^{(b)}$	$\mu^{(c)}$	$\mu^{(d)}$	$\mu^{(e)}$	$\mu^{(f)}$	$\mu^{(g)}$	$\mu^{(h)}$
CH_3O^-	0.455	−0.212	−0.608	−0.897	−1.093	−1.121	−1.200	−1.258
CH_3S^-	0.655	0.057	−0.318	−0.590	−0.636	−0.749	−0.837	−0.904
$CH_3CH_2OH^-$	0.193	−0.435	−0.769	−1.021	−1.048	−1.151	−1.232	−1.295
OH^-	0.840	−0.161	−0.462	−0.735	−0.945	−1.098	−1.208	−1.287
N_3^-	1.260	0.163	−0.351	−0.615	−0.883	−0.959	−1.076	−1.162
H^-	2.415	0.980	0.639	0.353	0.118	−0.072	−0.221	−0.334
F^-	2.930	0.472	−0.322	−0.953	−1.417	−1.742	−1.965	−2.117
Br^-	1.061	−0.162	−0.584	−0.940	−1.217	−1.421	−1.564	−1.664
Cl^-	1.473	−0.041	−0.546	−0.963	−1.282	−1.514	−1.675	−1.787
CN^-	0.002	−1.013	−1.543	−1.882	−2.116	−2.268	−2.370	−2.424
SH^-	0.688	0.049	−0.373	−0.620	−0.809	−0.947	−1.047	−1.118
NH_2^-	1.456	0.643	0.225	−0.078	−0.262	−0.391	−0.476	−0.533

[a] Units are eV.

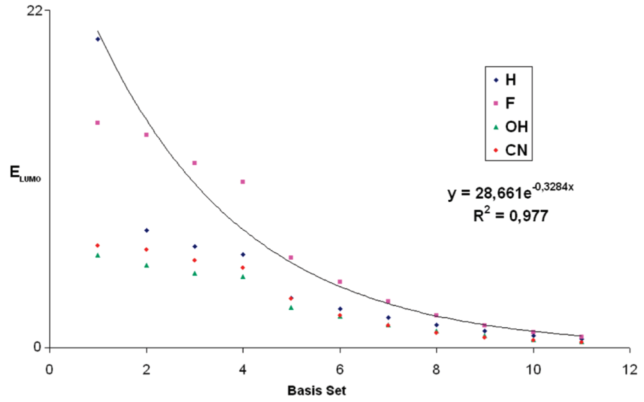

Figure 1. LUMO energy versus basis set size for hydride ion.

at this limit, the electronic chemical potential has begun to reach negative values, see Table 6.

In order to get an estimate of the convergence limit for the LUMO levels of anions quoted in Table 6, a fit of the LUMO levels against the order of the progression was performed. The results are summarized in Figure 1. It may be seen that, for $n = 12$ in the even-tempered curve, one can safely consider that the LUMO level of anions will go to zero in the infinite basis set limit, as suggested by the reviewers. This result is also consistent with a choice of $A = 0$ for the electron affinity of negatively charged systems that do not bind an extra electron.

In summary, the calculation of the electronic chemical potential and related properties of anions in the gas phase absolutely demands a thorough computational analysis in the infinite basis set limit. Any calculation using the Pople basis set even including polarization function may lead to the spurious result that the electronic chemical potential of anions may become a positive number. Our results suggest that the minimum level of theory must at least include the aug-cc-PVQZ basis set together with an even tempered calculation as the one described here for $n = 3$.

The present results strongly suggest that, for anions, the value $A = 0$ is a reasonable approach for the electron affinity of anions. With this result at hand, the electronic chemical potential of anions in the gas phase would approach the limit $\mu = - I/2 \approx \varepsilon_H/2$. This result is reasonable if we consider that anions in the gas phase are more likely expected to behave as electron donors (nucleophiles), and in this sense, the intrinsic nucleophilicity of charged electron donors appears related to the ionization potential, as suggested by one of us.[30,31]

Concluding Remarks

We have demonstrated herein that the occurrence of positive values of the electronic chemical potential for anions in the gas phase is a possible outcome in ab initio calculations that use the Pople basis set, even including polarization functions. A thorough computational analysis shows that this result may be spurious if the convergence of the LUMO level is not completed. The results obtained here strongly suggest that a reasonable approach for the electron affinity of singly charged electron donors is $A = 0$. This choice is consistent with a model of nucleophilicity in the gas phase which may be simply related to the first ionization potential.

Acknowledgment. The authors thank Fondecyt, grants 1070715 and 1080184, for financial support. Claudio Pérez-Mendez thanks Mecesup No. 0601 for a fellowship awarded to him.

References

(1) Parr, R. G.; Yang, W. *Density Functional Theory of Atoms and Molecules*; Oxford University Press: Oxford, U. K., 1989; Chapter 4, p 42.

(2) Chattaraj, P. K.; Sarkar, U.; Roy, D. R. *Chem. Rev.* **2006**, *106*, 2065–2091.

(3) Pérez, P.; Domingo, L. R.; Contreras, R. The Electrophilicity Index in Organic Chemistry. In *Theoretical Aspects of Chemical Reactivity*; Toro-Labbé, A., Ed.; Book Series Elsevier: New York, 2007; Vol. 19, pp 139−201.

(4) Chermette, H. *J. Comput. Chem.* **1999**, *20*, 129–154.

(5) Geerlings, P.; De Proft, F.; Langenaeker, W. *Chem. Rev.* **2003**, *103*, 1793–1874.

(6) Fuentealba, P.; Contreras, R. The Fukui Function in Chemistry. In *Reviews in Modern Quantum Chemistry: A Celebration of the Contributions of Robert Parr*; Sen, K. D., Ed.; World Scientific: Singapore, 2002; pp 1013−1052.

(7) Vessecchi, R.; Crotti, A. E. M.; Guaratani, T.; Colepicolo, X.; Galembeck, S. E.; López, N. P. *Mini-Rev. Org. Chem.* **2007**, *4*, 75–87.

(8) Gazquez, J. L. *J. Mex. Chem. Soc.* **2008**, *52*, 3–10.

(9) Ayers, P. W.; Anderson, J. S. M.; Bartolotti, L. J. *Int. J. Quantum Chem.* **2005**, *101*, 520–534.

(10) Liu, S. B. *Acta Phys. Chim. Sin.* **2009**, *25*, 590–600.

(11) Carey, F. A.; Sundberg, R. J. *Advanced Organic Chemistry*, 5th ed.; Springer: Berlin, 2007; Part A, Chapter 10, pp 946−951.

(12) Parr, R. G.; Donnelly, R. A.; Levy, M.; Palke, W. E. *J. Chem. Phys.* **1978**, *68*, 3801–3807.

(13) Parr, R. G.; Bartolotti, L. J. *J. Am. Chem. Soc.* **1982**, *104*, 3801–3803.

(14) Parr, R. G.; Bartolotti, L. J. *J. Phys. Chem.* **1983**, *87*, 2810–2815.

(15) Parr, R. G.; Yang, W. *J. Am. Chem. Soc.* **1984**, *106*, 4049–4050.

(16) Berkowitz, M.; Parr, R. G. *J. Chem. Phys.* **1988**, *88*, 2554–2557.

(17) Pearson, R. G. *J. Am. Chem. Soc.* **1986**, *108*, 6109–6114.

(18) Pérez, P.; Toro-Labbé, A.; Contreras, R. *J. Am. Chem. Soc.* **2001**, *123*, 5527–5531.

(19) De Proft, F.; Sablon, N.; Tozer, D. J.; Geerlings, P. *Faraday Discuss.* **2007**, *135*, 151–159.

(20) Lieb, E. H. *Phys. Rev. Lett.* **1984**, *52*, 315–317.

(21) Hati, S.; Datta, D. *J. Phys. Chem.* **1996**, *100*, 4828–4830.

(22) Méndez, F.; Romero, M. L.; De Proft, F.; Geerlings, P. *J. Org. Chem.* **1998**, *63*, 5774–5778.

(23) Pérez, P.; Toro-Labbé, A.; Contreras, R. *J. Phys. Chem. A* **1999**, *103*, 11246–11249.

(24) Olmstead, W. N. *J. Org. Chem.* **1980**, *45*, 3295–3299.

(25) Contreras, R.; Aizman, A.; Parra, J. *Chem. Phys. Lett.* **1986**, *127*, 169–171.

(26) Frisch, M. J.; Trucks, G. W.; Schlegel, H. B.; Scuseria, G. E.; Robb, M. A.; Cheeseman, J. R.; Montgomery, J. A., Jr.; Vreven, T.; Kudin, K. N.; Burant, J. C.; Millam, J. M.; Iyengar, S. S.; Tomasi, J.; Barone, V.; Mennucci, B.; Cossi, M.; Scalmani, G.; Rega, N.; Petersson, G. A.; Nakatsuji, H.; Hada, M.; Ehara, M.; Toyota, K.; Fukuda, R.; Hasegawa, J.; Ishida, M.; Nakajima, T.; Honda, Y.; Kitao, O.; Nakai, H.; Klene, M.; Li, X.; Knox, J. E.; Hratchian, H. P.; Cross, J. B.; Bakken, V.; Adamo, C.; Jaramillo, J.; Gomperts, R.; Stratmann, R. E.; Yazyev, O.; Austin, A. J.; Cammi, R.; Pomelli, C. ; Ochterski, J. W.; Ayala, P. Y.; Morokuma, K.; Voth, G. A.; Salvador, P.; Dannenberg, J. J.; Zakrzewski, V. G.; Dapprich, S.; Daniels, A. D.; Strain, M. C.; Farkas, O.; Malick, D. K.; Rabuck, A. D.; Raghavachari, K.; Foresman, J. B.; Ortiz, J. V.; Cui, Q.; Baboul, A. G.; Clifford, S.; Cioslowski, J.; Stefanov, B. B.; Liu, G.; Liashenko, A.; Piskorz, P.; Komaromi, I.; Martin, R. L.; Fox, D. J.; Keith, T.; Al-Laham, M. A.; Peng, C. Y.; Nanayakkara, A.; Challacombe, M.; Gill, P. M. W.; Johnson, B.; Chen, W.; Wong, M. W.; Gonzalez, C.; Pople, J. A. *Gaussian 03*, Revision E.01; Gaussian, Inc.: Wallingford, CT, 2004.

(27) Tozer, D. J.; De Proft, F. *J. Phys. Chem. A* **2005**, *109*, 8923–8929.

(28) Tozer, D. J.; De Proft, F. *J. Chem. Phys.* **2007**, *127*, 34108–34114.

(29) Balavanov, N. B.; Peterson, K. A. *J. Chem. Phys.* **2005**, *123*, 064107−064121.

(30) Contreras, R.; Andrés, J.; Safont, V. S.; Campodónico, P.; Santos, J. G. *J. Phys. Chem. A* **2003**, *107*, 5588–5593.

(31) Campodónico, P. R.; Andrés, J.; Aizman, A.; Contreras, R. *Chem. Phys. Lett.* **2008**, *464*, 271–275.

CT900164A

JCTC Journal of Chemical Theory and Computation

Unified Inter- and Intramolecular Dispersion Correction Formula for Generalized Gradient Approximation Density Functional Theory

Stephan N. Steinmann,[†] Gábor Csonka,*[,‡] and Clémence Corminboeuf*[,†]

Laboratory for Computational Molecular Design, Institut des Sciences et Ingénierie Chimiques, Ecole Polytechnique Fédérale de Lausanne, CH-1015 Lausanne, Switzerland, and Department of Inorganic and Analytical Chemistry, University of Technology and Economics, 1521 Budapest, Hungary

Received May 18, 2009

Abstract: Density functionals fail to provide a consistent description of weak intra- (i.e., short-range) and inter- (i.e., long-range) molecular interactions arising from nonoverlapping electron densities. An efficient way to correct the long-range errors is to add an empirical atom pair wise interaction-correction, inspired by the Lennard-Jones potential (R^{-6} dependence). We show that the universal damping function of Tang and Toennies (TT) that includes higher-order correction terms (R^{-8} and R^{-10} dependent) reduces the intramolecular errors more efficiently, without altering the long-range correction. For general applicability, the TT damping function is augmented by a Fermi damping to prevent corrections at covalent distances. The performance of the new dD10 correction was tested in combination with three nonempirical GGAs (PBE, PBEsol, RGE2) on 64 illustrative reaction energies featuring both intra- and intermolecular interactions. With only two empirical parameters, PBE-dD10 outperforms the computationally more demanding and most recent functionals such as M06-2X or B2PLYP-D (MAD = 3.78 and 1.95 kcal mol^{-1}, respectively). At the cc-pVTZ level, PBE-dD10 (MAD = 1.24 kcal mol^{-1}) considerably reduces common DFT errors successfully balancing intra- (short-range) and inter- (long-range) molecular interactions. While REG2-dD10 performs closely to PBE-dD10 (MAD = 1.48 kcal mol^{-1}), the overall MAD of PBEsol-dD10 is again slightly higher (MAD = 1.76 kcal mol^{-1}).

Introduction

This work proposes a simple and efficient, a posteriori, double-damped attractive weak interaction energy correction formula for the nonempirical generalized gradient approximations[1−6] (GGAs) of the Kohn−Sham density functional theory (DFT).[7] GGA functionals might provide a reasonable description of the weak interactions arising from nonbonded density overlap but cannot describe the long-range part of the van der Waals (vdW) interaction that acts between nonoverlapped densities. As proposed earlier,[8−14] a properly constructed damped attractive correction summed over all atom pairs in the system efficiently remedies this deficiency of GGA[12−14] (and also the hybrid GGA and meta-GGA) functionals at a negligible computational cost. Such a correction must be convergent with respect to the internuclear separation, R_{ij} and must properly follow the $\sim R^{-6}$ decay of the dispersion interaction at large R_{ij}. At shorter internuclear separations the $\sim R^{-8}$ and $\sim R^{-10}$ terms might also have non-negligible contribution to the interaction energy. In this paper, we further develop the idea of a general interatomic-corrected GGA functional as suggested by Grimme[13,14] and show the benefits of using a double-damping as well as higher order dispersion terms for such corrections. In our formulation, the inter- and intramolecular dispersion corrections are treated jointly in a single formula as opposed to two separate parametrizations (i.e., PBE-inter or PBE-intra)[15,16] containing only $\sim R^{-6}$ terms.

---

* Corresponding author e-mail: clemence.corminboeuf@epfl.ch (C.C.), csonka@mail.bme.hu (G.C.).

[†] Ecole Polytechnique Fédérale de Lausanne.

[‡] University of Technology and Economics.

10.1021/ct9002509 CCC: $40.75

Inter- and intramolecular van der Waals interactions are responsible for many energetic and structural phenomena such as the heats of sublimation of hydrocarbons, the crystal packing of organic molecules, host−guest chemistry, the orientation of molecules on surfaces, the stacking of nucleic acids in DNA,[17] and protein folding[18] as well as the properties of polar and apolar solvents.

It is known that the Hartree−Fock (HF) method cannot describe these weak interactions, arising from a pure electron correlation effect. High level, expensive treatment of electron correlation coupled with large basis sets (typically CCSD(T)/aug-cc-pVQZ) are required to evaluate such interactions accurately.[19−22] Alternatively, less expensive and somewhat less accurate estimation of weak interactions can be obtained from MP2 complete basis set extrapolated results.[23] These methods are computationally very expensive and are applicable only to benchmark studies of small systems.

GGA, hybrid GGA, and meta-GGA are much less expensive than CCSD(T) and MP2 methods. Such functionals can at best provide an estimate of the bonding between weakly overlapped densities but fail to reproduce the long-range part of the vdW interaction, which tends to $-C_6/R^6$ as $R \rightarrow \infty$. The calculated GGA or meta-GGA interaction energies arising from overlapping electron densities decays exponentially,[24] which results in a serious underestimation of the long-range part of the interaction.[25−29] A typical example is the sandwich and T-shaped configurations of the benzene dimer, which is dispersion-bound at the CCSD(T) level[22] but essentially unbound in a PBE GGA computation.[24] For shorter-range weak interactions characteristic in rare-gas dimers[24,30−35] and other noncovalently bound diatomics,[36−40] the performance of GGA,[24,30,33,35−40] hybrid GGA,[31,34] and TPSS or TPSSh meta-GGA[24,32] functionals varies. While the B88 GGA[41] exchange functional tends to underbind (or not bind at all),[24,42,43] LSDA seriously overbinds.[24,32] In contrast, PBE and TPSS often give reasonable binding energies.[24,30−32,35] The partial success of PBE and TPSS was attributed predominantly to the large gradient behavior (satisfaction of the Lieb-Oxford bound lower bound on the exchange-correlation energy for all possible electron densities).[24] In some rare-gas diatomics, however, the PBE, TPSS, and TPSSh density functionals overcorrect the serious overbinding tendency of LSD[24,32] resulting in too-long bond lengths and reduced binding energies. This deficiency suggests the need for some attractive shorter-range correction. In other words, a consistent description of the weak attractive interactions by a GGA or meta-GGA requires a full treatment of the long-range behavior[25,44,45] along with an improved treatment of the shorter-range part. These results also show that including rare gas diatomics (short-range interactions) into the DFT training sets for empirically fitted density functionals does not guarantee an improvement for larger stacking complexes (long-range interactions) of chemical or biological interest.

Fully nonlocal functionals[25,44,45] or generalizations of the random phase approximation[29] that capture the long-range correlation effects are more promising and also computationally more demanding for the description of the dispersion effects. Further possibilities are the following: the optimized potential method within KS perturbation theory,[46,47] empirically calibrating dispersion corrected atom centered potentials,[48,49] or fitting the exchange correlation enhancement function (using large number of empirical parameters) to a data set that contains weakly bonded compounds.[50] Although the resulting M06-2X hybrid meta-GGA functional shows good overall performance for treating weak interactions, its highly fitted nature does not guarantee the correct asymptotic behavior and leads to failures.[51] Similarly, the so-called double hybrid functionals[52] (which scale roughly as MP2) not only are partially successful but also need a long-range attractive correction for a more general description of weak interactions.[53]

Computational Methods

An efficient solution to improve the performance of density functionals for weak interactions is to add a damped attractive long-range dispersion energy correction[12−14] to the GGA, hybrid GGA, or meta-GGA energy

$$E_{disp} = -\sum_{i=2}^{N}\sum_{j=1}^{i-1} d(R_{ij}) \qquad (1)$$

The summation is over all atom pairs (ij) in the N atomic system, and the $d(R_{ij})$ attractive function is properly damped at short internuclear separations R_{ij}. We suggest the following double-damped formula for $d(R_{ij})$

$$d(R_{ij}) = Fd(a, R_{ij})\sum_{n=3}^{5} f_{2n}(bR_{ij})\frac{C_{2n}^{ij}}{R_{ij}^{2n}} \qquad (2)$$

where

$$Fd(a, R_{ij}) = \frac{1}{1 + \exp\left(-46\left(\frac{R_{ij}}{aR_{ij}^{vdW}} - 1\right)\right)} \qquad (3)$$

In eq 2, $Fd(a,R_{ij})$ is a Fermi damping function[12] given in eq 3, that is used to switch off the first damping (i.e., $f_{2n}(bR_{ij})$) at short internuclear separation. $f_{2n}(bR_{ij})$ are damping functions specific to a given dispersion coefficient (vide infra), a and b are empirical damping parameters, and the C_{2n}^{ij} are the dispersion coefficients.

The steepness factor in eq 3 (i.e., 46) was chosen such as to minimize the effect of the Fermi function on the damping function $f_{2n}(bR_{ij})$ at larger internuclear separations by imposing $Fd(a, 1.1 \cdot a \cdot R_{vdw}) \geq 0.99$ (for details see the Supporting Information). R_{ij}^{vdW} is the vdW distance of the atom pair, and a is the parameter that scales the vdW radii to improve the flexibility in the parametrization scheme.[54] The summation in eq 2 goes up to 5 to include damped C_6, C_8, and C_{10} terms leading to the resulting dD6, dD8, and dD10 formulas (the latter contains all terms up to C_{10}). The f_{2n} damping functions are used in the following form

$$f_{2n}(x) = 1 - \exp(-x)\sum_{k=0}^{2n}\frac{x^k}{k!} \qquad (4)$$

where $x = bR_{ij}$, with b being the damping (due to overlapping densities) parameter.[55] These general damping function terms were proposed by Tang and Toennies[55] (TT), and it was successfully used for dispersion interaction of several noble-gas and metal atom pairs.[55−57] In the original TT model, the long-range attractive potential, which is calculated from the damped dispersion series, is added to a short-range purely repulsive Born−Mayer potential with b being the range parameter. The importance of the C_8 and C_{10} terms is emphasized in ref 58. As DFT is able to treat short-range correlation accurately, regions of strongly overlapping densities do not need to be corrected, which justifies the use of the second damping (Fermi) function. The hybridization state dependent[12] C_6 dispersion coefficients are averaged and combined according to the rule proposed by Grimme:[13] $C_6^{ij} = 2(C_6^i C_6^j)/(C_6^i + C_6^j)$. Other atomic coefficients[14] or combination rules[14,59] give similar but slightly less consistent results after refitting. C_8 and C_{10} coefficients were estimated based on the average C_6 dispersion coefficients and empirical rules as established in refs 60 and 61: i.e. $C_8/C_6 = 45.9$ and $C_6C_{10}/C_8^2 = 1.21$ (in atomic units). An alternative that is going to be investigated in a subsequent study would be to use Becke-Johnson exchange-dipole model.[62−65]

Bondi's[66] vdW radii were used and combined according to a "cubic mean" combination rule put forward by Halgren:[59] $R_{ij}^{vdW} = (R^3_{i,vdW} + R^3_{j,vdW})/(R^2_{i,vdW} + R^2_{j,vdW})$.

The motivation for the use of a damped dispersion series along with a Fermi formula such as in eq 2 is the removal of the systematic errors for the treatments of short-range weak interactions, while preserving good performance for more typical long-range vdW interactions. Recently, several studies pointed to large errors in the description of the nonbonded intramolecular interaction in alkanes.[67−71] Corminboeuf et al.[16] showed that the atom pairwise correction containing only $\sim R^{-6}$ terms and optimized for reproducing intermolecular energies (PBE-inter, vide infra)[15] only slightly improve the description of intramolecular interactions. In contrast, the reparametrized PBE-intra (i.e., parametrized for intramolecular interactions) performs considerably better for isodesmic (i.e., the number of formal bond types is conserved) bond separation equation (BSE) reaction energies[72,73] of hydrocarbons but seriously overbinds the T-shaped benzene dimer. While the PBE-inter T-shaped dimer dissociation curve is considerably better than that of the PBE-intra, it has a much higher curvature than the corresponding CCSD(T) curve (vide infra). The correction formula suggested in eq 2 should preserve the description of both interactions.

The two empirical parameters, a and b, contained in eq 2 are obtained from two prototypes of reaction energies that are the Pople's isodesmic bond energy separation reaction of propane (eq 5 with $m = 1$) and the hydrogenation reaction of [2.2]paracyclophane to p-xylene (6)

$$CH_3(CH_2)_mCH_3 + mCH_4 \rightarrow (m + 1)C_2H_6 \qquad (5)$$

Correcting (5) accounts for the intramolecular (short-range) error. Note that the bond lengths do not change considerably along reaction (5). The reaction is therefore not suited for determining the value of the parameter a that describes the distance where to switch off the correction. On the other hand, obtaining an accurate energy for the challenging hydrogenation reaction of [2.2]paracyclophane to *p*-xylene (6)[53,74] necessitates a correct description of the long-range interactions between the two benzene rings of paracyclophane as well as the reaction energy for converting a H−H and two C−C bonds into two C−H bonds

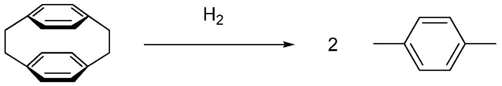

(6)

The first-principle GGA functionals are very efficient computationally and provide reasonable results for a wide range of problems (molecular geometry, vibration, reaction energies, lattice constants, bulk moduli, cohesive energies, surface energies). Several nonempirical functionals that use the PBE form were selected for this study. PBE itself is generally used in chemistry and physics. Its failure to improve the solid lattice constants, bulk moduli, and surface energies upon LSDA motivated the development of the recent PBEsol first-principles GGA functional that is based on the exact second-order gradient expansion of the exchange energy (the PBE functional is also a first principles GGA functional that satisfies other exact constraints as second-order gradient expansion for correlation and LSD-like linear density response of a uniform electron gas). PBEsol gives not only excellent lattice constants and surface energies but also poorer atomization energies than PBE. An attempt to develop a simple GGA that unites the good properties of PBE and PBEsol led to the second regularized gradient expansion (RGE2). For further details the interested readers turn to refs 3, 4, and 6.

Because of the different energy range of the two prototype reactions (2.8 kcal mol^{-1} for the propane BSE and −58.5 kcal mol^{-1} for the hydrogenation of [2.2]paracyclophane), a straightforward least-squares minimization of the combined error is not suited. The error criterion for the hydrogenation reaction was therefore chosen to be 2 kcal mol^{-1} ("chemical accuracy"). From all combinations fulfilling this requirement, the one with the lowest error for the propane BSE was selected. Parameter a is 1.45 for all functionals. b is 0.88, 1.03, and 1.00 for PBEsol, PBE, and RGE2, respectively.

Figure 1 shows the R_{ij} dependence of the dD10 formula of eq 2 using the a and b parameters obtained for PBE vs C...C internuclear separation. The dD10 correction balances between the inter- (i.e., long-range) and intra- (short-range) molecular corrections. Figure 1 also demonstrates that obtaining good BSE energies requires a correction up to relatively short 4.5 au internuclear separations. At short distances the correction coming from PBE-inter vanishes and is absolutely ineffective. On the other hand, PBE-intra is steeper and larger in magnitude as compared to PBE-dD10 resulting in inaccurate energies for intermolecular interactions. The double-damped dispersion series with up to C10 terms (i.e dD10) easily resolves this dilemma. For comparison, D10, which is a correction free of the Fermi damping function (that "turns off" the correction at covalent bond distance), is given as well.

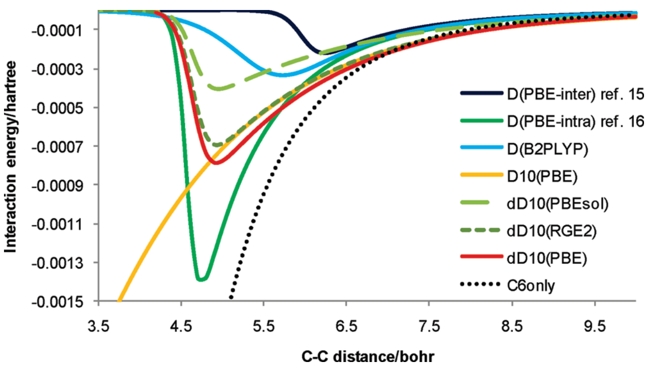

Figure 1. Dispersion energy correction curve for C...C dispersion interaction vs the C...C distance. Parameters of eq 2 are *a* = 1.45 PBE-dD10: *b* = 1.03; PBEsol-dD10: *b* = 0.88; RGE2-dD10: *b* = 1.00. For PBE-D10 without Fermi damping *b* = 1.0001.

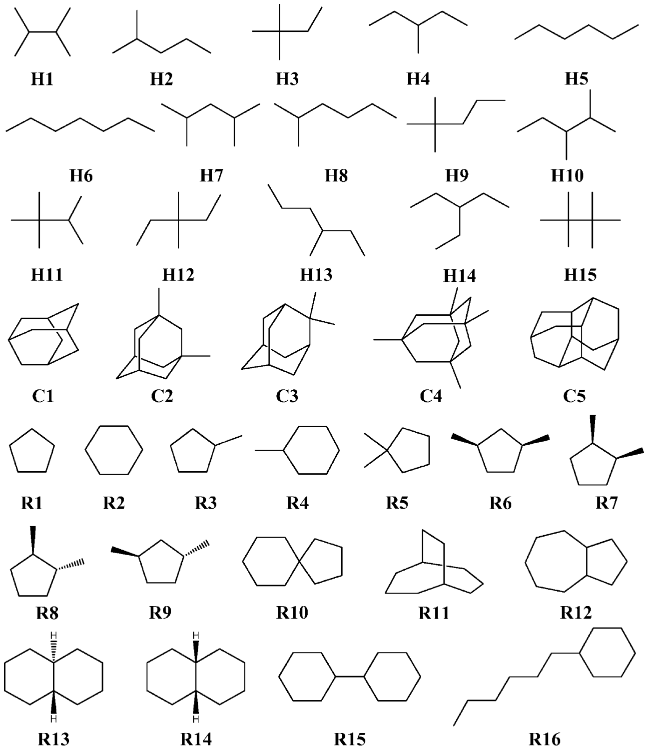

Figure 2. Schematic representation of the 36 saturated hydrocarbons in the H, C, and R sets.

The performance of the dD10 attractive correction is tested on five test sets. Three of the sets assess Pople's isodesmic bond energy separation reaction (BSE, eq 5) of saturated hydrocarbons (chains, rings, and cages in H, R, and C sets, respectively, Figure 2).[16] The fourth set that reflects "intramolecular dispersion interactions in hydrocarbons" (IDHC)[53] contains two isomerization reactions, two folding reactions of large hydrocarbon chains, the dimerization of anthracene, and the hydrogenation reaction of [2.2]paracyclophane (for details on the test sets see Table S6-S10 in the Supporting Information). The fifth set corresponds to the common benchmark for noncovalent complexes (S22)[75] and includes the benzene dimers.

Geometries of the H, R, and C sets were optimized at the B3LYP/6-311+G** level using Gaussian 03.[76] Zero points and thermal corrections to the enthalpy are taken from these calculations. Experimental heats of formation (NIST)[77] at 298 K are used as reference. Geometries and reference values for the IDHC-set were taken from ref 53. Our results are compared to LSDA (SWVN5),[78,79] TPSS,[80] M06-2X,[81] B3LYP,[82,83] B97-D,[14] B2PLYP,[52] and B2PLYP-D.[53] Benzene dimers were derived from the equilibrium structures of ref 22 and the monomers[84] kept frozen. The geometries and reference values (CCSD(T)/CBS) for the S22 set were obtained from the BEGDB database.[85]

Given the size of the molecules in our test sets, the cc-pVTZ basis set was chosen for the single point energy computations. This basis set contains small exponent functions and gives only a small artificial binding error for weakly bond complexes.[54] The energy differences between the cc-pVTZ and the aug-cc-pVTZ basis set computed with the PBE GGA are 0.006 kcal mol^{-1} (0.4%) for the propane BSE (eq 5), 2 kcal mol^{-1} (2.8%) for the hydrogenation reaction energy of [2.2]paracyclophane to *p*-xylene (eq 6), and 0.25 kcal mol^{-1} for the *n*-octane isomerization problem (vide infra). This latter difference is negligible compared to the 7.6 kcal mol^{-1} error with respect to the experimental energy for octane isomerization. The cc-pVTZ basis set performs considerably better than the diffuse 6-311+G(2*d*,2*p*) basis set used earlier[86] for the octane isomerization. The 0.26 kcal mol^{-1} difference between the PBE/cc-pVTZ and PBE/aug-cc-pVTZ energies for the anthracene dimer dissociation energy is also negligible compared to the 23.6 kcal mol^{-1} error of the PBE (the reaction energy is 14.6 kcal mol^{-1} with the cc-pVTZ basis set) against the best experimental estimate (−9 kcal mol^{-1} in ref 87). Note that the S22 test set contains several hydrogen bonded complexes for which a larger basis set is required to reach convergence.[88] For this set, computations at the aug-cc-pVTZ level are also provided and discussed.

A modified version of deMon-2K 2.3[89] was used for all computations with the new correction. B2PLYP computations were performed with Turbomole 5.1.[90,91] M06-2X calculations were performed with NWChem 5.1[92,93] using the 'xfine' grid.

Results and Discussion

Figure 3 and Table 1 summarize the mean absolute deviation (MAD) for the functionals tested. Detailed performance, including PBEsol-dD10 and RGE2-dD10, can be found in the Supporting Information. The proposed dD10 attractive correction reduces the errors of PBE drastically (MAD for chains/cages of 8.0/22.5 and 1.0/1.7 kcal mol^{-1} for PBE and PBE-dD10, respectively). Only the dD10 correction reduces the systematic increase in MAD going from chains to rings to cages. Similar improvements are obtained while correcting PBEsol and RGE2.

Remarkably, for the subtle intramolecular interactions, Perdew's "Jacobs-ladder"[94] is reversed! Ascending toward more sophisticated (and expectedly more robust[95]) functionals corresponds to a significant increase in error (e.g., MAD over alkane chains increases from 0.8, to 8.0 and 10.3 kcal mol^{-1} for LSDA, PBE, and TPSS, respectively). PBEsol (constructed to recover the exact second order gradient expansion for the exchange energy at the sacrifice of accuracy for atoms[96]) shows the best uncorrected performance. This

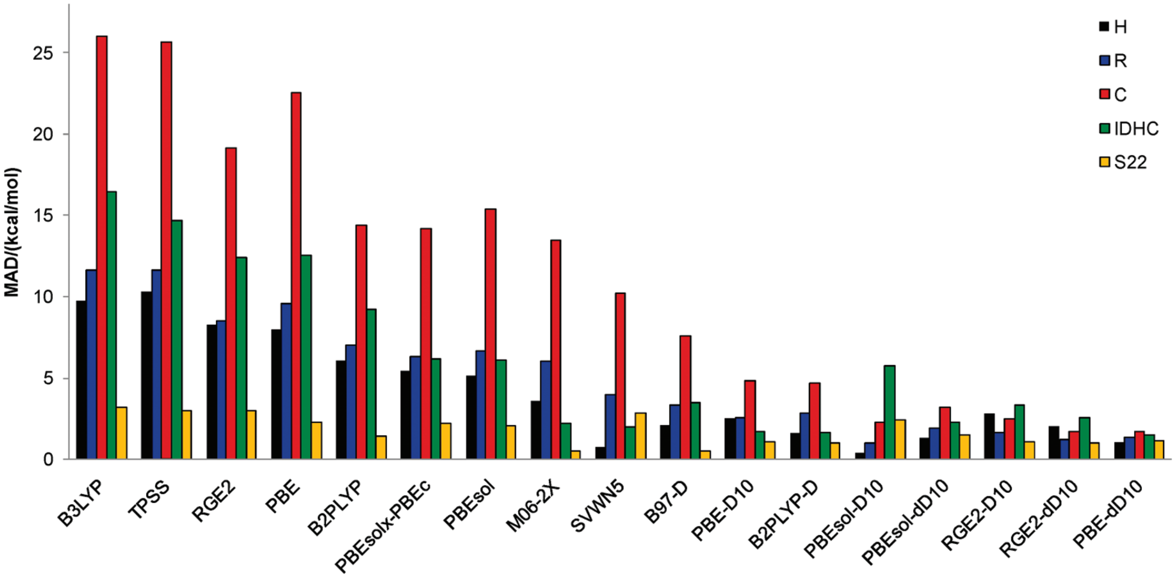

Figure 3. Mean absolute deviations for bond separation energies over hydrocarbon chains (H set), rings (R set), and cages (C set); for reaction energies of the test set "intramolecular dispersion in hydrocarbons" (IDHC) and the common benchmark for noncovalent complexes (S22) using the cc-pVTZ basis set.

Table 1. MAD (in kcal mol^{-1}) Comparison for All Functionals Tested[b]

	H	R	C	IDHC	S22	weighted average
B3LYP	9.73	11.60	25.99	16.45	3.20	**9.85**
TPSS	10.33	11.64	25.67	14.66	3.01	**9.75**
PBE	7.99	9.59	22.52	12.52	2.24 *(2.55)*	**7.97 *(8.08)***
RGE2	8.27	8.52	19.14	12.41	2.97 *(3.51)*	**7.75 *(7.93)***
B2PLYP	6.05	7.02	14.41	9.19	1.41 *(1.20)*[a]	**5.64 (5.57)**
PBEsol	5.16	6.68	15.41	6.10	2.09 *(1.89)*	**5.37 (5.31)**
PBEsol-PBE	5.40	6.31	14.20	6.19	2.21	**5.29**
PBEsol-D6	2.48	3.06	9.06	9.09	3.24 *(2.56)*	**4.02 *(3.79)***
M06-2X	3.60	6.02	13.45	2.23	0.51	**3.78**
SVWN5	0.78	3.97	10.21	2.01	2.85	**3.14**
B97-D	2.06	3.37	7.59	3.48	0.52 *(0.36)*	**2.42 *(2.37)***
PBE-D10	2.50	2.59	4.84	1.69	1.06 *(0.48)*	**2.14 *(1.94)***
B2PLYP-D	1.60	2.82	4.66	1.60	1.02 *(0.44)*[a]	**1.95*(1.75)***
RGE2-D10	2.78	1.60	2.49	3.30	1.06 *(0.90)*	**1.92 *(1.86)***
PBEsol-D10	0.42	0.98	2.29	5.76	2.40 *(1.72)*	**1.89 *(1.65)***
PBEsol-dD10	1.32	1.92	3.21	2.27	1.48 *(0.92)*	**1.76 *(1.57)***
PBE-dD6	1.16	1.76	2.67	2.34	1.43 *(0.95)*	**1.63 *(1.47)***
RGE2-dD10	2.02	1.21	1.70	2.53	0.97 *(0.89)*	**1.48 *(1.45)***
PBE-D6	0.31	1.05	2.19	2.94	1.90 *(1.17)*	**1.44 *(1.18)***
PBE-dD10	1.01	1.33	1.69	1.50	1.16 *(0.45)*	**1.24 *(1.00)***
PBE-dD6	0.82	1.17	1.58	2.01	0.95 *(0.55)*	**1.12 *(0.99)***

[a] The B2PLYP(-D) number in parentheses refer to non-counterpoise corrected energies taken from ref 53 for an optimized value of $s = 0.35$. [b] Values in parentheses refers to aug-cc-pVTZ computations for the S22 test set.

is best understood recalling that PBEsol exchange enhancement function $F_x(s)$ does not correct LSDA as much as the PBE functional for wide range of the reduced gradient, s, and that LSDA performs well for these reactions. Note also that the combination of the PBEsol exchange with PBE correlation gives lower MAD than the PBE functional (Figure 3). This result demonstrates that the origin of the improvement arises from the modified PBEsol exchange.[4] RGE2 is also designed to recover the second-order gradient expansion for exchange over a wide range of s (typically important for correct description of solids), but it is more similar to PBE in the large density gradient region (important for free atoms) than to PBEsol. While RGE2 is built to be more satisfying from the point of view of general applicability, it performs only slightly better than PBE for the reactions tested. However, PBE-dD10 slightly outperforms RGE2-dD10 and gives the best overall results. Interestingly, the overall performance of the double hybrid B2PLYP is less satisfactorily unless an attractive correction is added. Similarly, the empirical M06-2X meta GGA results are better than those of all the noncorrected GGA but still far from the PBE-dD10 for the test sets investigated herein. The relevance of the double-damping, that is the necessity of switching off the D10 correction at short internuclear separations (<4.5 au for carbon), is illustrated by the significantly larger total MAD (2.14 kcal mol^{-1} vs 1.24 kcal mol^{-1}) obtained with the singly damped D10 correction to PBE (i.e., PBE-D10 in Figure 3). The correction discussed in this paper works well also in the D6 form as shown by the results obtained with the damped dispersion series including the C6 terms only (Table 1). PBE-D6 performs better than PBE-D10 for the alkanes series but has a significantly larger MAD for both the IDHC and S22 sets (mean error larger by 1.25 and 0.69 kcal mol^{-1}, respectively). While PBE-dD10 is best overall, excellent results are obtained with the simpler PBE-dD6 correction. For the H, R, C and S22 test sets, the performance of PBE-dD6 is marginally better (by ~0.1 kcal mol^{-1} on average) than that of PBE-dD10, but the latter is better by 0.5 kcal mol^{-1} for the IDHC test set. Since the dD6 curve mimics the position and the depth of the minima of the dD10 correction curve, these results demonstrate that the small difference between the two correction functions in the longer distances does not influence the results considerably (see Figure S1 in the Supporting Information).

Another illustrative example of common DFT errors is the relative stability of isomers. As shown in Table 2, the errors in the alkane isomerization energies also suffer dramatically from the systematic GGA error. Apart from LDA and M06-2X, none of the (uncorrected) density functional gives an acceptable correlation with respect to the experimental heat of formations.[77] In contrast, the three empirically corrected functionals, B97-D, PBE-dD10, and

Table 2. Computed Relative Enthalpies (ZPE and Thermal Corrected to 298 K, in kcal mol^{-1}) for Selected Alkanes Isomerization Reactions in the H and R Sets[97]

	H3→H5	H11→H6	H12→H6	R5→R6	MAD
Exp[a]	4.39	4.07	3.28	1.12	
B3LYP	−0.26	−2.56	−2.62	−1.07	4.84
PBE	0.28	−1.48	−1.74	−0.93	4.18
PBEsol	1.34	−0.04	−0.65	−0.34	3.14
B2PLYP	1.67	0.75	0.09	−0.33	2.67
M06-2X	3.03	2.64	1.58	0.69	1.23
B97-D	3.19	3.23	2.22	0.63	0.90
PBE-dD10	3.26	3.34	2.14	0.54	0.90
B2PLYP-D	3.51	3.52	2.29	0.73	0.70
SVWN5	3.69	3.88	2.63	0.43	0.56

[a] Reference 77.

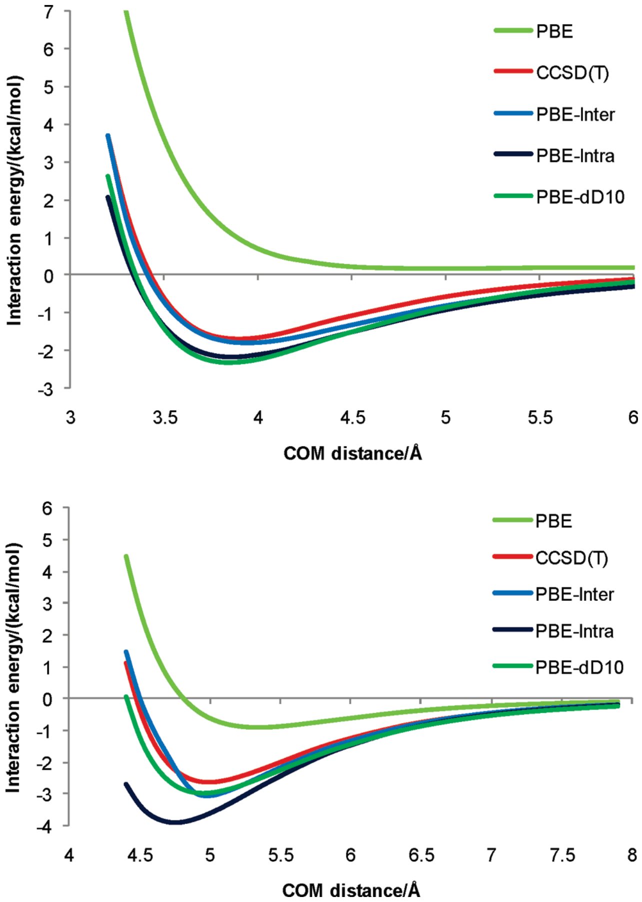

Figure 4. Stacked (upper) and T-shaped (lower) benzene dimer interaction energies against the center of mass distance (COM). CCSD(T) reference curve taken from ref 22, PBE-inter and PBE-intra from ref 16.

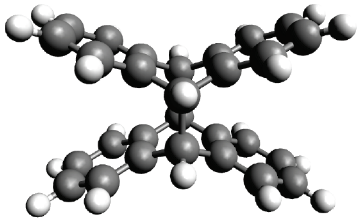

Figure 5. The anthracene dimer.

in particular B2PLYP-D, lead to a considerable improvement and describe the more compact structures (e.g., H3, H11, H12) as reasonably more stable (>2 kcal mol^{-1}) than their linear counterparts (e.g., H5, H6).

The benzene dimers serve as prototypical examples for evaluating the detailed performance of the dD10 correction on typical intermolecular interactions (Figure 4). For the stacked dimer, the equilibrium distance at the PBE-dD10 level is the same as with the CCSD(T) reference curve, but the dissociation energy is overestimated (by 0.59 kcal mol^{-1}, 35%). A more detailed analysis (Figure S2 in the Supporting Information) shows that the PBEsol-dD10 potential energy curve agrees better (−0.06 kcal mol^{-1} difference at the minimum) with the CCSD(T) curve above the equilibrium distances (3.9 Å), but it is, like the PBE-dD10 curve, somewhat too attractive below that distance. For the T-shaped dimer, the dD10 correction leads to a considerable improvement as compared to the intramolecular alternative (i.e., PBE-intra). Both PBE-dD10 and PBEsol-dD10 give slightly larger dissociation energies than CCSD(T) (by 0.35 kcal mol^{-1}, 13% and 0.27 kcal mol^{-1}, 10% respectively) but match the curvature of the reference potential better than that of the correction parametrized for intermolecular interactions (PBE-inter).[15,16] The PBE-inter curve indeed exhibits a sudden repulsive change below 5 Å (Figure 4 lower curve). The RGE2-dD10 potential curve is too repulsive at short distances and too attractive above 4.5 and 5.9 Å for both the stacked and T-shaped dimers, respectively. For the benzene dimers as well as the full S22 set, the agreement between PBE-dD10 and CCSD(T)/CBS can be considerably improved by using the larger aug-cc-pVTZ basis set (vide infra).

The results on the full S22 set confirm the good overall performance of dD10 on common weakly bound complexes. Unlike the DFT-D methods, which use the S22 test set to obtain parameters for the dispersion correction,[14,53] the S22 test set was not used in the parametrization of PBE-dD10.With a MAD of 0.45 kcal mol^{-1} using the aug-cc-pVTZ basis set (Table 1), PBE-d10 gives binding energies comparable to those obtained with B2PLYP-D/aug-cc-pVTZ (0.44 kcal mol^{-1}) given in ref 53 and B97-D/aug-cc-pVTZ (0.36 kcal mol^{-1}). Note that counterpoise corrected results for B2PLYP-D can be better (MAD = 0.25 kcal mol^{-1}).[53] However, such counterpoise corrections are not straightforward for intramolecular situations and can be expensive. They have not been applied here.

The general applicability of the PBE-dD10 correction is further illustrated by the assessment of two challenging reaction energies: the dimerization reaction of anthracene (Figure 5) and the isomerization reaction of *n*-octane into tetramethylbutane. The anthracene dimer is connected by two covalent C−C bonds resulting from a [4 + 4] cycloaddition reaction. The conversion of C−C π double bonds into two C−C σ bonds upon dimerization results in considerable change in the energetic properties. Similar large energy difference can be observed between protobranched *n*-octane and the highly branched tetrametylbutane.

PBE-dD10 performs once again nearly perfectly for both these difficult cases (Figure 6), while none of the other functionals are fully satisfactory. PBE-dD10 also leads to very accurate results for the IDHC set in general (MAD 1.5 kcal mol^{-1}, Figure 3, Tables S6-S10 in the Supporting Information) outperforming the other methods tested. For

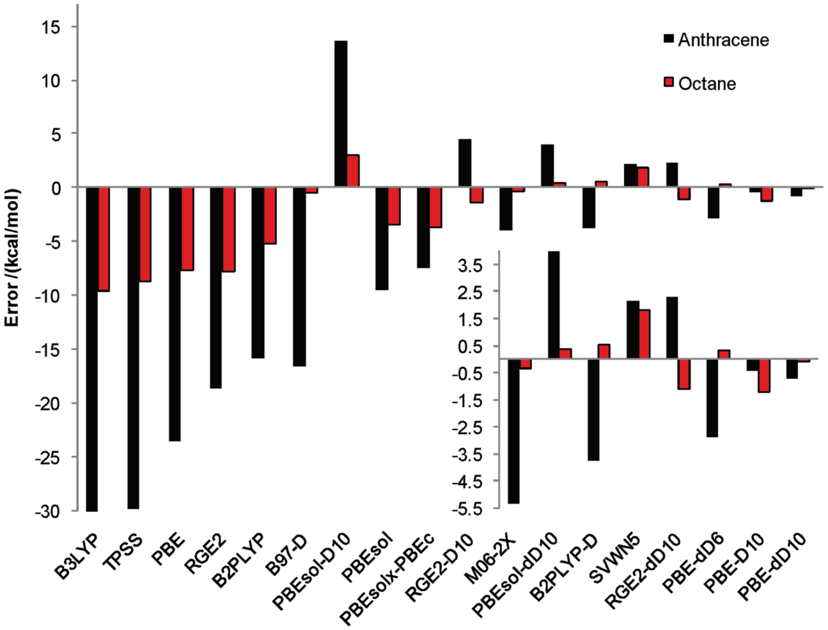

Figure 6. Errors associated with the two examples of reaction energies (E(exp)-E(calc)) the IDHC set: the anthracene dimerization and the octane isomerization. Details of the right-hand side are given as an inset.

these two reactions and the IDHC set in general, the singly damped PBE-D10 performs almost as well as PBE-dD10.

Overall, PBE-dD10 gives the most robust results and the lowest MAD for a series of prototypical and challenging reaction and binding energies. With a total MAD of only 1.00 kcal mol^{-1} for the five sets of Figure 3, PBE-dD10 outperforms both uncorrected and corrected functionals. For the S22 test set, the aug-cc-pVTZ basis set is necessary to obtain converged results. The smaller cc-pVTZ basis set gives converged energies for the other test sets. The success of the correction is attributed to the inclusion of an adequate damping function. In addition, the necessity of switching off the correction at short internuclear separations (<4.5 au for carbon), is illustrated by a 1 kcal mol^{-1} higher total MAD (1.94 kcal mol^{-1}) obtained with the singly damped D10 correction to PBE (Figure 3). Note that our preliminary benchmarks on additional properties such as molecular thermochemistry, reaction barriers, and equilibrium geometries show that the —dD corrections do not worsen the results of the parent GGAs (Tables S23-S26 in the Supporting Information). GGAs show poor performance for reaction barriers and atomization energies.[98] B2LYP(-D) and M06-2X obviously perform much better for these. However, poor atomization energy does not lead to poor thermochemistry as exemplified by the good performance of PBE for thermochemistry[99,100] (Table S26). Equilibrium geometries obtained for a test set of covalent bond lengths and angles (Table S25) also show that the dD10 correction barely affects the geometrical parameters.

Conclusions

We have presented a unified empirical correction formula for first principle GGA functionals. The Lennard-Jones potential R^{-6} dependence is augmented with higher-order correction terms (R^{-8} and R^{-10} dependent) through the use of the universal damping function of Tang and Toennies.[55] For general applicability, a second damping function is employed to turn off the correction at short distances. Among the three first-principal GGA tested (PBE, PBEsol, and RGE2), PBE-dD10 give the most robust results, closely followed by PBE-dD6 and RGE2-dD10. With only two empirical parameters and one prefactor, PBE-dD10 outperforms the computationally more demanding B2PLYP-(D) and the most recent functionals such as M06-2X, which contain more empirical parameters. PBE-dD10 considerably reduces common DFT errors for a set of 64 illustrative reaction energies, successfully balancing intra- (short-range) and inter- (long-range) molecular interactions. The corrections introduced here do not deteriorate the performance for equilibrium geometries, atomization energies, and reaction barriers.

Acknowledgment. C.C. acknowledges the Sandoz family foundation, the Swiss NSF Grant 200021_121577/1, and EPFL for financial support. Matthew D. Wodrich is acknowledged for helpful suggestions.

Supporting Information Available: Computed absolute and reaction energies of relevant compounds for Figures 3 and 5 and the benzene dimer interaction energies for PBEsol-dD10 and RGE2-dD10 as well as details on the barrier heights, atomization energies, and geometry test set. This material is provided free of charge via the Internet at http://pubs.acs.org.

References

(1) Perdew, J. P. *Phys. Rev. Lett.* **1985**, *55*, 1665–1668.

(2) Perdew, J. P.; Yue, W. *Phys. Rev. B* **1986**, *33*, 8800–8802.

(3) Perdew, J. P.; Burke, K.; Ernzerhof, M. *Phys. Rev. Lett.* **1996**, *77*, 3865–3868.

(4) Perdew, J. P.; Ruzsinszky, A.; Csonka, G. I.; Vydrov, O. A.; Scuseria, G. E.; Constantin, L. A.; Zhou, X.; Burke, K. *Phys. Rev. Lett.* **2008**, *100*, 136406.

(5) Perdew, J. P.; Ruzsinszky, A.; Csonka, G. I.; Vydrov, O. A.; Scuseria, G. E.; Constantin, L. A.; Zhou, X.; Burke, K. *Phys. Rev. Lett.* **2009**, *102*, 039902.

(6) Ruzsinszky, A.; Csonka, G. I.; Scuseria, G. E. *J. Chem. Theory Comput.* **2009**, *5*, 763–769.

(7) Kohn, W.; Sham, L. J. *Phys. Rev.* **1965**, *140*, A1133–A1138.

(8) Conway, A.; Murrell, J. N. *Mol. Phys.* **1974**, *27*, 873–878.

(9) Wagner, A. F.; Das, G.; Wahl, A. C. *J. Chem. Phys.* **1974**, *60*, 1885–1891.

(10) Hepburn, J.; Scoles, G.; Penco, R. *Chem. Phys. Lett.* **1975**, *36*, 451–456.

(11) Ahlrichs, R.; Penco, R.; Scoles, G. *Chem. Phys.* **1977**, *19*, 119–130.

(12) Wu, Q.; Yang, W. *J. Chem. Phys.* **2002**, *116*, 515–524.

(13) Grimme, S. *J. Comput. Chem.* **2004**, *25*, 1463–1473.

(14) Grimme, S. *J. Comput. Chem.* **2006**, *27*, 1787–1799.

(15) Ducere, J.-M.; Cavallo, L. *J. Phys. Chem. B* **2007**, *111*, 13124–13134.

(16) Wodrich, M. D.; Jana, D. F.; Schleyer, P. v. R.; Corminboeuf, C. *J. Phys. Chem. A* **2008**, *112*, 11495–11500.

(17) Dabkowska, I.; Gonzalez, H. V.; Jurecka, P.; Hobza, P. *J. Phys. Chem. A* **2005**, *109*, 1131–1136.

(18) Bashford, D.; Chothia, C.; Lesk, A. M. *J. Mol. Biol.* **1987**, *196*, 199–216.

(19) Chalasinski, G.; Szczesniak, M. M. *Chem. Rev.* **1994**, *94*, 1723–1765.

(20) Hobza, P.; Selzle, H. L.; Schlag, E. W. *J. Phys. Chem.* **1996**, *100*, 18790–18794.

(21) Mourik, T. V.; Wilson, A. K.; Dunning, T. H. *Mol. Phys.* **1999**, *96*, 529–547.

(22) Sinnokrot, M. O.; Sherrill, C. D. *J. Phys. Chem. A* **2004**, *108*, 10200–10207.

(23) Csonka, G. I.; French, A. D.; Johnson, G. P.; Stortz, C. A. *J. Chem. Theory Comput.* **2009**, *5*, 679–692.

(24) Ruzsinszky, A.; Perdew, J. P.; Csonka, G. I. *J. Phys. Chem. A* **2005**, *109*, 11015–11021.

(25) Langreth, D. C.; Dion, M.; Rydberg, H.; Schröder, E.; Hyldgaard, P.; Lundqvist, B. I. *Int. J. Quantum Chem.* **2005**, *101*, 599–610.

(26) Sponer, J.; Jurecka, P.; Hobza, P. *J. Am. Chem. Soc.* **2004**, *126*, 10142–10151.

(27) Zhao, Y.; Truhlar, D. G. *J. Chem. Theory Comput.* **2005**, *1*, 415–432.

(28) Zhao, Y.; Truhlar, D. G. *J. Phys. Chem. A* **2005**, *109*, 4209–4212.

(29) Dobson, J. F.; Wang, J.; Dinte, B. P.; McLennan, K.; Le, H. M. *Int. J. Quantum Chem.* **2005**, *101*, 579–598.

(30) Patton, D. C.; Pederson, M. R. *Phys. Rev. A* **1997**, *56*, R2495–R2498.

(31) Adamo, C.; Barone, V. *J. Chem. Phys.* **1999**, *110*, 6158–6170.

(32) Tao, J.; Perdew, J. P. *J. Chem. Phys.* **2005**, *122*, 114102.

(33) Tsuzuki, S.; Luthi, H. P. *J. Chem. Phys.* **2001**, *114*, 3949–3957.

(34) Xu, X.; Goddard, W. A. *J. Phys. Chem. A* **2004**, *108*, 8495–8504.

(35) Zhang, Y.; Pan, W.; Yang, W. *J. Chem. Phys.* **1997**, *107*, 7921–7925.

(36) Furche, F.; Perdew, J. P. *J. Chem. Phys.* **2006**, *124*, 044103.

(37) Jellinek, J.; Acioli, P. H. *J. Phys. Chem. A* **2002**, *106*, 10919–10925.

(38) Kohn, A.; Weigend, F.; Ahlrichs, R. *Phys. Chem. Chem. Phys.* **2001**, *3*, 711–719.

(39) Murray, C. W.; Handy, N. C.; Amos, R. D. *J. Chem. Phys.* **1993**, *98*, 7145–7151.

(40) Ruzsinszky, A.; Perdew, J. P.; Csonka, G. I. *J. Phys. Chem. A* **2005**, *109*, 11006–11014.

(41) Becke, A. D. *Phys. Rev. A* **1988**, *38*, 3098.

(42) Kristyán, S.; Pulay, P. *Chem. Phys. Lett.* **1994**, *229*, 175–180.

(43) Pérez-Jordá, J.; Becke, A. D. *Chem. Phys. Lett.* **1995**, *233*, 134–137.

(44) Andersson, Y.; Langreth, D. C.; Lundqvist, B. I. *Phys. Rev. Lett.* **1996**, *76*, 102.

(45) Dion, M.; Rydberg, H.; Schröder, E.; Langreth, D. C.; Lundqvist, B. I. *Phys. Rev. Lett.* **2004**, *92*, 246401.

(46) Engel, E.; Höck, A.; Dreizler, R. M. *Phys. Rev. A* **2000**, *61*, 032502.

(47) Kummel, S.; Kronik, L. *Rev. Mod. Phys.* **2008**, *80*, 3.

(48) Lin, I.-C.; Coutinho-Neto, M. D.; Felsenheimer, C.; Lilienfeld, O. A. v.; Tavernelli, I.; Rothlisberger, U. *Phys. Rev. B* **2007**, *75*, 205131.

(49) von Lilienfeld, O. A.; Tavernelli, I.; Rothlisberger, U.; Sebastiani, D. *Phys. Rev. Lett.* **2004**, *93*, 153004.

(50) Zhao, Y.; Truhlar, D. G. *Acc. Chem. Res.* **2008**, *41*, 157–167.

(51) Valdes, H.; Spiwok, V.; Rezac, J.; Reha, D.; Abo-Riziq, Ali, G.; de Vries, Mattanjah, S.; Hobza, P. *Chem.—Eur. J.* **2008**, *14*, 4886–4898.

(52) Grimme, S. *J. Chem. Phys.* **2006**, *124*, 034108.

(53) Schwabe, T.; Grimme, S. *Phys. Chem. Chem. Phys.* **2007**, *9*, 3397–3406.

(54) Jurecka, P.; Cerný, J.; Hobza, P.; Salahub, D. R. *J. Comput. Chem.* **2007**, *28*, 555–569.

(55) Tang, K. T.; Toennies, J. P. *J. Chem. Phys.* **1984**, *80*, 3726–3741.

(56) Tang, K. T.; Toennies, J. P. *J. Chem. Phys.* **2003**, *118*, 4976–4983.

(57) Sheng, X. W.; Li, P.; Tang, K. T. *J. Chem. Phys.* **2009**, *130*, 174310.

(58) Johnson, E. R.; Becke, A. D. *J. Chem. Phys.* **2006**, *124*, 174104.

(59) Halgren, T. A. *J. Am. Chem. Soc.* **1992**, *114*, 7827–7843.

(60) Thakkar, A. J.; Hettema, H.; Wormer, P. E. S. *J. Chem. Phys.* **1992**, *97*, 3252–3257.

(61) Wu, X.; Vargas, M. C.; Nayak, S.; Lotrich, V.; Scoles, G. *J. Chem. Phys.* **2001**, *115*, 8748–8757.

(62) Becke, A. D.; Johnson, E. R. *J. Chem. Phys.* **2005**, *122*, 154104.

(63) Becke, A. D.; Johnson, E. R. *J. Chem. Phys.* **2005**, *123*, 154101.

(64) Becke, A. D.; Johnson, E. R. *J. Chem. Phys.* **2006**, *124*, 014104.

(65) Becke, A. D.; Johnson, E. R. *J. Chem. Phys.* **2007**, *127*, 154108.

(66) Bondi, A. *J. Phys. Chem.* **1964**, *68*, 441–451.

(67) Wodrich, M. D.; Corminboeuf, C.; Schleyer, P. v. R. *Org. Lett.* **2006**, *8*, 3631–3634.

(68) Grimme, S. *Angew. Chem., Int. Ed.* **2006**, *45*, 4460–4464.

(69) Schreiner, P. R. *Angew. Chem., Int. Ed.* **2007**, *46*, 4217–4219.

(70) Wodrich, M. D.; Corminboeuf, C.; Schreiner, P. R.; Fokin, A. A.; Schleyer, P. v. R. *Org. Lett.* **2007**, *9*, 1851–1854.

(71) Wodrich, M. D.; Wannere, C. S.; Mo, Y.; Jarowski, P. D.; Houk, K. N.; Schleyer, P. v. R. *Chem.—Eur. J.* **2007**, *13*, 7731–7744.

(72) Hehre, W. J.; Ditchfield, R.; Radom, L.; Pople, J. A. *J. Am. Chem. Soc.* **1970**, *92*, 4796–4801.

(73) Pople, J. A.; Radom, L.; Hehre, W. J. *J. Am. Chem. Soc.* **1971**, *93*, 289–300.

(74) Grimme, S. *Chem.—Eur. J.* **2004**, *10*, 3423–3429.

(75) Jurecka, P.; Sponer, J.; Cerny, J.; Hobza, P. *Phys. Chem. Chem. Phys.* **2006**, *8*, 1985–1993.

(76) Frisch, M. J.; Trucks, G. W.; Schlegel, H. B.; Scuseria, G. E.; Robb, M. A.; Cheeseman, J. R.; Montgomery, J. A.; Vreven, T.; Kudin, K. N.; Burant, J. C.; Millam, J. M.; Iyengar, S. S.; Tomasi, J.; Barone, V.; Mennucci, B.; Cossi, M.; Scalmani, G.; Rega, N.; Petersson, G. A.; Nakatsuji, H.; Hada, M.; Ehara, M.; Toyota, K.; Fukuda, R.; Hasegawa, J.; Ishida, M.; Nakajima, T.; Honda, Y.; Kitao, O.; Nakai, H.; Klene, M.; Li, X.; Knox, J. E.; Hratchian, H. P.; Cross, J. B.; Bakken, V.; Adamo, C.; Jaramillo, J.; Gomperts, R.; Stratmann, R. E.; Yazyev, O.; Austin, A. J.; Cammi, R.; Pomelli, C.; Ochterski, J. W.; Ayala, P. Y.; Morokuma, K.; Voth, G. A.; Salvador, P.; Dannenberg, J. J.; Zakrzewski, V. G.; Dapprich, S.; Daniels, A. D.; Strain, M. C.; Farkas, O.; Malick, D. K.; Rabuck, A. D.; Raghavachari, K.; Foresman, J. B.; Ortiz, J. V.; Cui, Q.; Baboul, A. G.; Clifford, S.; Cioslowski, J.; Stefanov, B. B.; Liu, G.; Liashenko, A.; Piskorz, P.; Komaromi, I.; Martin, R. L.; Fox, D. J.; Keith, T.; Laham, A. M. A.; Peng, C. Y.; Nanayakkara, A.; Challacombe, M.; Gill, P. M. W.; Johnson, B.; Chen, W.; Wong, M. W.; Gonzalez, C.; Pople, J. A. *Revision E.01 ed.*; Gaussian Inc.: Wallingford, CT, 2004.

(77) Afeefy, H. Y.; Liebman, J. F.; Stein, S. E. In *NIST Chemistry WebBook, NIST Standard Reference Database Number 69*; National Institute of Standards and Technology: Gaithersburg, MD, 20899.

(78) Slater, J. C. *Phys. Rev.* **1951**, *81*, 385.

(79) Vosko, S. H.; Wilk, L.; Nusair, M. *Can. J. Phys.* **1980**, *58*, 1200–1211.

(80) Tao, J.; Perdew, J. P.; Staroverov, V. N.; Scuseria, G. E. *Phys. Rev. Lett.* **2003**, *91*, 146401.

(81) Zhao, Y.; Truhlar, D. *Theo. Comput. Mod.* **2008**, *120*, 215–241.

(82) Becke, A. D. *J. Chem. Phys.* **1993**, *98*, 5648–5652.

(83) Stephens, P. J.; Devlin, F. J.; Chabalowski, C. F.; Frisch, M. J. *J. Phys. Chem.* **1994**, *98*, 11623–11627.

(84) Gauss, J.; Stanton, J. F. *J. Phys. Chem. A* **2000**, *104*, 2865–2868.

(85) Řezáč, J.; Jurečka, P.; Riley, K. E.; Černý, J.; Valdes, H.; Pluháčková, K.; Berka, K.; Řezáč, T.; Pitoňák, M.; Vondrášek, J.; Hobza, P. *Collect. Czech. Chem. Commun.* **2008**, *73*, 1261–1270.

(86) Csonka, G. I.; Ruzsinszky, A.; Perdew, J. P.; Grimme, S. *J. Chem. Theory Comput.* **2008**, *4*, 888–891.

(87) Grimme, S.; Diedrich, C.; Korth, M. *Angew. Chem., Int. Ed.* **2006**, *45*, 625–629.

(88) Csonka, G. I.; Ruzsinszky, A.; Perdew, J. P. *J. Phys. Chem. B* **2005**, *109*, 21471–21475.

(89) Köster, A. M.; Calaminici, P.; Casida, M. E.; Flores-Moreno, R.; Geudtner, G.; Goursot, A.; Heine, T.; Ipatov, A.; Janetzko, F.; Campo, J. M. d.; Patchkovskii, S.; Reveles, J. U.; Salahub, D. R.; Vela, A. *deMon2k*; 2006.

(90) Ahlrichs, R.; Bär, M.; Häser, M.; Horn, H.; Kölmel, C. *Chem. Phys. Lett.* **1989**, *162*, 165–169.

(91) Ahlrichs, R. et al. *TURBOMOLE V5.10*; University of Karlsruhe: Karlsruhe, 2008.

(92) Bylaska, E. J. Govind, W. A. d. J. N. Kowalski, K. Straatsma, T. P. Valiev, M. Wang, D. Apra, E. Windus, T. L. Hammond, J. Nichols, P. Hirata, S. Hackler, M. T. Zhao, Y. Fan, P.-D. Harrison, R. J. Dupuis, M. Smith, D. M. A. Nieplocha, J. Tipparaju, V. Krishnan, M. Wu, Q. Van Voorhis, T. Auer, A. A. Nooijen, M. Brown, E. Cisneros, G. Fann, G. I. Fruchtl, H. Garza, J. Hirao, K. Kendall, R. Nichols, J. A. Tsemekhman, K. Wolinski, K. Anchell, J. Bernholdt, D. Borowski, P. Clark, T. Clerc, D. Dachsel, H. Deegan, M. Dyall, K. Elwood, D. Glendening, E. Gutowski, M. Hess, A. Jaffe, J. Johnson, B. Ju, J. Kobayashi, R. Kutteh, R. Lin, Z. Littlefield, R. Long, X. Meng, B. Nakajima, T. Niu, S. Pollack, L. Rosing, M. Sandrone, G. Stave, M. Taylor, H. Thomas, G. van Lenthe, J. Wong, A. Zhang; Z. 5.1 ed.; Pacific Northwest National Laboratory: Richland, Washington 99352−0999, 2007.

(93) Kendall, R. A.; Aprà, E.; Bernholdt, D. E.; Bylaska, E. J.; Dupuis, M.; Fann, G. I.; Harrison, R. J.; Ju, J.; Nichols, J. A.; Nieplocha, J.; Straatsma, T. P.; Windus, T. L.; Wong, A. T. *Comput. Phys. Commun.* **2000**, *128*, 260–283.

(94) Perdew, J. P.; Schmidt, K. *Density Functional Theory and Its Application to Materials*; 2001; Vol. *577*, pp 120−207.

(95) Korth, M.; Grimme, S. *J. Chem. Theory Comput.* **2009**, *5*, 993–1003.

(96) Weintraub, E.; Henderson, T. M.; Scuseria, G. E. *J. Chem. Theory Comput.* **2009**, *5*, 754–762.

(97) Note that the computed energies are based on single most stable conformers and not on the Boltzmann distribution of conformers. For those small selected alkanes, it is reasonable to assume that other conformers have a negligible contribution to the experimental result.

(98) Zhao, Y.; Gonzalez-Garcia, N.; Truhlar, D. G. *J. Phys. Chem. A* **2005**, *109*, 2012–2018.

(99) Csonka, G. I.; Ruzsinszky, A.; Tao, J.; Perdew, J. P. *Int. J. Quantum Chem.* **2005**, *101*, 506–511.

(100) Brothers, E. N.; Scuseria, G. E. *J. Phys. Chem. A* **2008**, *112*, 13706–13711.

CT9002509

JCTC Journal of Chemical Theory and Computation

Activation of Carbon−Hydrogen and Hydrogen−Hydrogen Bonds by Copper−Nitrenes: A Comparison of Density Functional Theory with Single- and Multireference Correlation Consistent Composite Approaches

Sammer M. Tekarli, T. Gavin Williams, and Thomas R. Cundari*

Department of Chemistry, Center for Advanced Scientific Computing and Modeling (CASCaM), University of North Texas, Box 305070, Denton, Texas 76203-5070

Received May 29, 2009

Abstract: The kinetics and thermodynamics of copper-mediated nitrene insertion into C−H and H−H bonds (the former of methane) have been studied using several levels of theory: B3LYP/6-311++G(d,p), B97-1/cc-pVTZ, PBE1KCIS/cc-pVTZ, and ccCA (correlation consistent Composite Approach). The results show no significant difference among the DFT methods. All three DFT methods predict the ground state of the copper−nitrene model complex, L′Cu(NH), to be a triplet, while single reference ccCA predicts the singlet to be the ground state. The contributions to the total ccCA energy indicate that the singlet state is favored at the MP2/CBS level of theory, while electron correlation beyond this level (CCSD(T)) favors a triplet state, resulting in a close energetic balance between the two states. A multireference ccCA method is applied to the nitrene active species and supports the assignment of a singlet ground state. In general, the largest difference in the model reaction cycles between DFT and ccCA methods is for processes involving radicals and bond dissociation.

Introduction

Carbon−hydrogen bond activation and functionalization are among the most heavily researched endeavors in catalysis, given their importance in the production of useful products from natural gas and petroleum. Development of catalysts for functionalization of carbon−hydrogen bonds (particularly for unactivated aliphatics and aromatics) has been actively pursued by experimentalists and theorists attempting to identify better catalysts.[1−6] Catalysis of such reactions by late transition metal (TM) complexes has received much recent attention due to their lower electrophilicity and thus greater heteroatom tolerance (versus comparable early TM complexes).[7] Moreover, such metals are relatively inexpensive in relation to the noble metals.

Phosphines (PR_3) have long been the ligand of choice for many middle−late TM catalysts.[8−14] Notable experimental work on late 3d TM multiply bonded complexes supported by bis-phosphine ligation has been done by the Hillhouse group, who have demonstrated group transfer to a variety of substrates (e.g., olefins and CO) using nickel−nitrene, −carbene, and −phosphinidene complexes.[8−14] Ligands in the β-diketiminate family have started to augment phosphines in the study of late TM catalysis.[15] Attention has also focused on β-diketiminate and related ligands because of their ability to enforce low metal coordination numbers. Also, varying the substituents on the ligating nitrogens, the backbone carbons, linking the β-diketiminate ring with other moieties to form fused rings, and so forth gives these ligands tunable electronic and steric features.[15] For example, varying β-diketiminate substituents has been shown by Shimokawa et al. to produce different coordination geometries (i.e., tetrahedral, distorted tetrahedral, and square planar), different electronic spectra, and electrochemical responses for a series of copper complexes.[16] In a review on β-diketiminates,[15] these ligands are seen to bind strongly to a diverse assortment

---

* Corresponding author e-mail: t@unt.edu.

10.1021/ct900277m CCC: $40.75

of metals in a wide range of bonding modes and stabilize lower than typical metal oxidation states (e.g., Fe(I), Co(I) or Ni(I)).

These features have led to many notable examples of transition metal β-diketiminate complexes of the late 3d metals: Fe, Co, Ni, and Cu. For example, a recent report by Holland et al.[17] investigated the metastable iron(III)−imido complexes that effect hydrogen atom abstraction (HAA) of 1,4-cyclohexadiene. The imido complex becomes active only after the addition of a fourth ligand, 4-*tert*-butyl-pyridine. Coordination of the fourth ligand to iron is postulated—via a combination of experimental Mossbauer spectroscopy and DFT calculations—to induce a “flip” from a lower to a high spin state.[17] The synthesis and X-ray crystal structure characterization of a β-diketiminato Co(I) arene adduct and its reactivity with dioxygen and organoazides has been reported by Warren et al.[18] A terminal imido Ni(III) complex, also reported by Warren and co-workers, has been shown to effect C−H bond activation.[19]

Among late TMs, the coinage metals Cu, Ag, and Au have been extensively studied for catalytic nitrene transfer.[20−26] For example, Dias et al. have reported Cu(I) and Ag(I) scorpionate complexes as carbene and nitrene transfer catalysts.[24] A silver-catalyzed amination of saturated C−H bonds (including relatively inert C_{sp3}−H bonds of cycloalkanes) has also been reported by He et al.[22] A disilver structure has been identified by the He group as critical in silver-based nitrene transfer.[22] He and co-workers also reported C−H bond activation at room temperature using gold-catalyzed nitrene insertion.[23] They found that, for C−H bond activation, a nearby aromatic C−H bond is needed, presumably to “direct” the activation/insertion event. Copper−scorpionate catalysts (i.e., $Tp^{Br3}Cu(NCMe)$) have been reported by Perez and co-workers to aminate C−H bonds.[21] The complex $Tp^{Br3}Cu(NCMe)$ catalyzes the amination of C−H bonds of cyclohexane and benzene and the primary C−H bond of toluene and mesitylene methyl groups using iodonium imide (PhI=NT) as a nitrene transfer reagent.[21]

Warren and Badiei[27] synthesized and structurally characterized Cu−β-diketiminate−carbene complexes and concluded from density functional theory (DFT) calculations that there is significant π bonding between Cu and the C of the CPh_2 (i.e., carbene). The foregoing suggests the potential for (meta)stable nitrene complexes of Cu. Warren et al. reported that the reaction of N_3Ar with $\{[Me_3NN]Cu\}_2$-(toluene) produces a dicopper nitrene $\{[Me_3NN]Cu\}_2(\mu$-NAr). Evidence has been obtained that the latter gives rise to a terminal Cu−nitrene through slow dissociation.[28] Cundari et al. studied complexes of the form (β-diketiminate)Cu(NPh) using DFT, complete active space self-consistent-field (CASSCF), and hybrid quantum mechanical/molecular mechanical (QM/MM) methods. CASSCF and QM/MM calculations (the QM portion of the latter is of the CASSCF variety) indicate an “open shell” singlet ground state, contrary to prior DFT predictions.[29] A singlet is synthetically preferable, as this implies (and experimental studies support this contention)[30] that the copper nitrene will thus undergo amination reactions via concerted C−H insertion bonds rather than less selective radical reactions one might expect from a triplet active species.[29] Recent work thus suggests that such complexes can provide a rational basis for engineering novel C−H functionalization catalysts capable of activating even the strongest C−H bonds.[29,30]

Many computational studies of C−H activation, most notably early research by Hoffmann and more recently by Goddard et al., Cundari and co-workers, and Hall et al.[31−38] have modeled the mechanisms of C−H activation. In this work, first-principles modeling of nitrene insertion into C−H and H−H bonds has been performed. Reactions of a β-diketiminate−Cu−nitrene (i.e., L′Cu(NH); L′ is the parent β-diketiminate anion, $C_3N_2H_5^-$) with H_2 and CH_4 have been performed in order to understand strong ($BDE_{Me-H} \sim 104$ kcal mol^{-1}) bond activation. Also, we seek to probe the impact of changes to the level of theory beyond approaches (i.e., B3LYP and Pople-style basis sets) now commonplace in the literature. Hence, the kinetics and thermodynamics of B3LYP/6-311++G(d,p), B97-1/cc-pVTZ, PBE1KCIS/cc-pVTZ, and the correlation consistent Composite Approach (ccCA)[39−43] are compared. The aforementioned methods have also been used to delineate the singlet ($S = 0$) and triplet ($S = 1$) surfaces for these model catalytic reactions. A multireference ccCA, reported by Wilson and co-workers, is also used to study the nitrene active species.

Computational Methods

Geometry optimizations of all minima and transition states were performed using the Gaussian 03 suite of programs.[44] Unless otherwise specified, calculations were performed using the B3LYP hybrid functional in conjunction with the 6-311++G(d,p) where (d,p) signifies addition of d- and p-polarization functions to main group elements and hydrogen atoms, respectively.[45] This basis set adds diffuse spd and f polarization functions to copper. PBE1KCIS was used in conjunction with the cc-pVTZ basis set.[46−54] The PBE1KCIS functional was found by Wilson and co-workers to best predict enthalpies of formation for TM complexes and therefore is utilized in this study to provide a base of comparison with the more popular B3LYP functional.[45,55−57] The B97-1 functional has the lowest mean absolute deviation for calculated versus experimental enthalpies of formation of 3d TM-containing molecules in a study by Wilson and co-workers.[57] Therefore, the B97-1 has also been used in this research. Vibrational frequencies are calculated at all DFT optimized stationary points to confirm them as minima or transition states. Modeling of triplet species with density functional theory employs unrestricted Kohn−Sham methods.

Previous work has shown that the mean absolute deviation for energetics using ccCA is 0.89 kcal mol^{-1}, which is within “chemical accuracy” (i.e., ±1 kcal mol^{-1}).[39−43] Hence, the ccCA approach was employed in this study to compare with results obtained from DFT methods. Classical activation barriers as predicted by ccCA[42] were in much better agreement than G3B as compared to very high accuracy computed values obtained from the Truhlar et al. databases.[58]

The ccCA composite method uses the correlation consistent basis sets originally developed by Dunning et al.[46] The ccCA method has also been shown to achieve “transition

Scheme 1

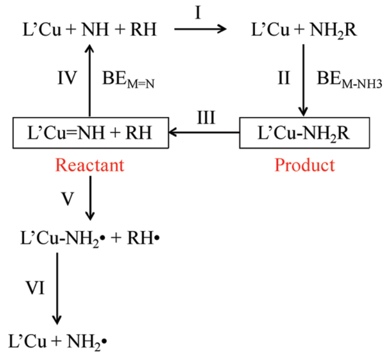

metal accuracy" for the enthalpies of formation of a data set of 17 3d TM complexes. It was suggested by DeYonker and co-workers that "transition metal accuracy" for ΔH_f° is ca. ±3 kcal mol^{-1} due to the larger experimental uncertainty inherent in the study of such species.[41] The ccCA methodology employed in this study is outlined by DeYonker et al.[41] Briefly, the equilibrium geometry, frequency analysis, and zero-point energy (scaled by 0.9890) were obtained at the B3LYP/cc-pVTZ level of theory using the Gaussian 03 software package. Separate extrapolation of the HF and correlation energy to the complete basis set (CBS) limit was performed, because, as shown in prior work, the HF energy converges more rapidly to the CBS limit than the correlation energy.[41] The HF/CBS energy and MP2/CBS correlation energy were then combined to form the "reference energy." A series of contributions were then added to the reference energy, E(MP2/CBS), to account for correlation energy beyond the MP2 level of theory {estimated at the CCSD(T)/cc-pVTZ level of theory, [ΔE(CC)]}, core−valence effects at the MP2 level of theory [ΔE(CV)], and scalar relativistic effects at the MP2 level of theory [ΔE(SR)]. The zero-point energy (ZPE) corrections were used to account for anharmonicity and were taken from the B3LYP/cc-pVTZ calculations. The ccCA energy is calculated as

$$E_{\mathrm{ccCA}} = E(\mathrm{MP2/CBS}) + \Delta \mathrm{E(CC)} + \Delta E(\mathrm{CV}) + \Delta E(\mathrm{SR}) + \mathrm{ZPE} \quad (1)$$

The energies for methane functionalization reactions by L′Cu(NMe), outlined in Scheme 1 (H_2 activation and functionalization by L′Cu(NH) are analogous) have been calculated using DFT and ccCA methods. In an effort to improve and quantify our understanding of the response of TM reaction mechanisms—thermodynamics and kinetics—to differing levels of theory (in particular, composite ab initio methods), models of important reactions involved in strong bond activation have been studied. Points of particular interest in this research are to compare and contrast (a) the popular B3LYP functional with newer PBE1KCIS and B97-1 functionals and (b) DFT versus ccCA techniques.

For the L′Cu(NH) active species, a singlet ground state has been predicted by CASSCF; this is an open-shell singlet that single reference methodologies such as DFT and ccCA cannot fully characterize (note that pure functionals such a BLYP and BP86 also predict a triplet ground state for the nitrene complex). Therefore, it is of interest to also investigate this important entity with a multireference (MR) equivalent of the ccCA. To create a MR-ccCA methodology, Wilson and co-workers replaced the MP2 calculations within the ccCA method with CASPT2 calculations and the CCSD(T) calculation of the E(CC) term with an average quadratic coupled cluster (AQCC) calculation. All multireference calculations were performed in the MOLPRO 2006.1 program package.[59] This formalism has been utilized recently by Mintz et al. to study the potential energy surfaces of C_2 and N_2 and resulted in good agreement for their reaction coordinates, which are particularly multireference in the vicinity of the dissociation asymptote.[60] Due to the size of the copper nitrene system and the computational demand of the AQCC calculation, the active space chosen for all MR calculations was four electrons in five orbitals. Previous calculations by Dinescu et al. on copper−nitrene complexes indicated that CASSCF active spaces of this size were suitable for modeling the different low-energy electronic states.[29]

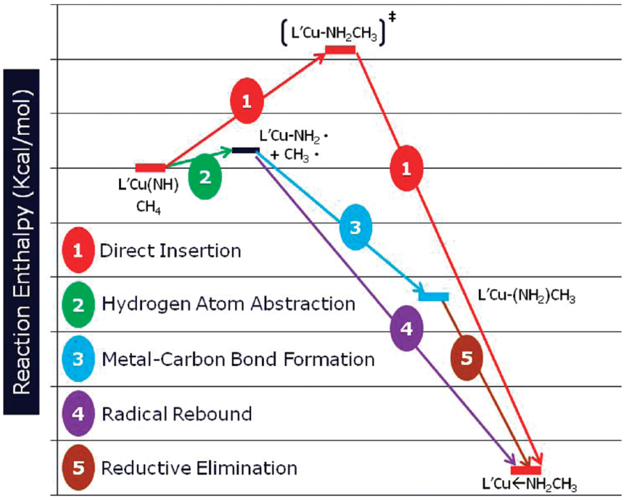

Figure 1. Reaction pathways of C−H bond activation of CH_4 by L′Cu(NH). Pathways for H_2 activation are analogous. Enthalpy scale is arbitrary.

Results and Discussion

The copper model catalyst, L′Cu, is a closed-shell system with a singlet ground state as supported by DFT calculations by Cundari et al.[29] The substrates chosen were H_2 and CH_4 as models for the H−H and C−H bond activation, respectively. The copper−nitrene active species, L′Cu(NH) or L′Cu(NMe), were evaluated in both singlet and triplet spin states. It is worth reiterating that CASSCF calculations of copper−nitrene complexes indicated an "open-shell" singlet ground state, contrary to prior DFT predictions.[29]

1. DFT Calculations. *1.1. Comparison of Different Levels of Theory.* Calculated reaction pathways for H−H and C−H bond activation of methane by L′Cu(NH) are depicted in Figure 1. The nitrene L′Cu(NH) can undergo [1 + 2] insertion to lead directly to a metal-bound amine product (i.e., L′Cu←NH_2CH_3), shown in Figure 2. Previous experimental and computational research implicate a direct insertion pathway.[27,28] We also dissected the direct [1 + 2] path into HAA of the substrate to produce an amide intermediate

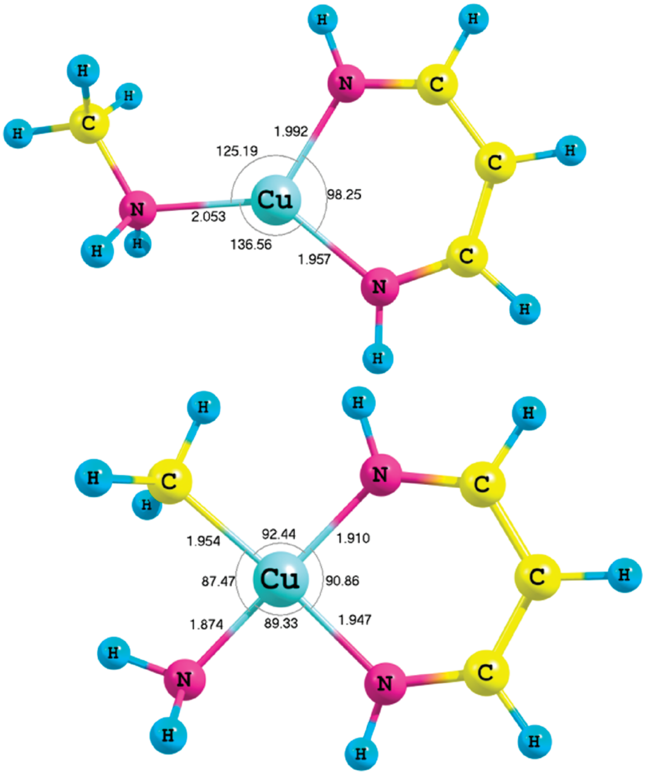

Figure 2. Optimized geometries of L′Cu←NH_2CH_3 (top) and L′CuNH_2(CH_3) (bottom) using the B3LYP/6-311++G(d,p) method. The pertinent bond lengths (Å) and bond angles (deg) are shown.

L′Cu−$NH_2^{\bullet}$ and a radical $CH_3^{\bullet}$ (or $H^{\bullet}$), which may undergo either (i) metal−carbon bond formation to form (pathway 3, Figure 2) the four-coordinate complex L′Cu(NH_2)CH_3 (Figure 2) or (ii) radical rebound to form L′Cu←NH_2CH_3 (Figure 2). The methyl(amide) intermediate L′Cu(NH_2)CH_3 can undergo reductive elimination to produce amine product L′Cu←NH_2CH_3. Calculations show pathways similar to those depicted in Figure 1.

There is no significant difference in optimized bond lengths and bond angles for the species investigated (see Scheme 1 and Figure 2) among all three DFT methods evaluated. Therefore, the optimized geometries for all stationary points given in the figures are those determined at the B3LYP/6-311++G(d,p) level. Figures 3 and 4 show the nitrene active species and [1 + 2] insertion transition states (for the latter, methane is the substrate) for singlet and triplet multiplicities.

As can be deduced from Table 1, calculated differences among the energetics for the three DFT methods are minimal for hybrid (B3LYP and B97-1) and hybrid meta-GGA (PBE1KCIS) functionals, Pople and correlation consistent basis sets. For H_2 reactions, the largest calculated deviation among DFT energetics is 5.9 kcal mol^{-1}, the difference between B3LYP/6-311++G(d,p) and PBE1KCIS/cc-pVTZ enthalpies for reaction III in Scheme 1 on both the singlet and triplet state surfaces. Reaction III is the microscopic reverse of H−H bond activation by L′Cu(NH) to create L′Cu←NH_3.

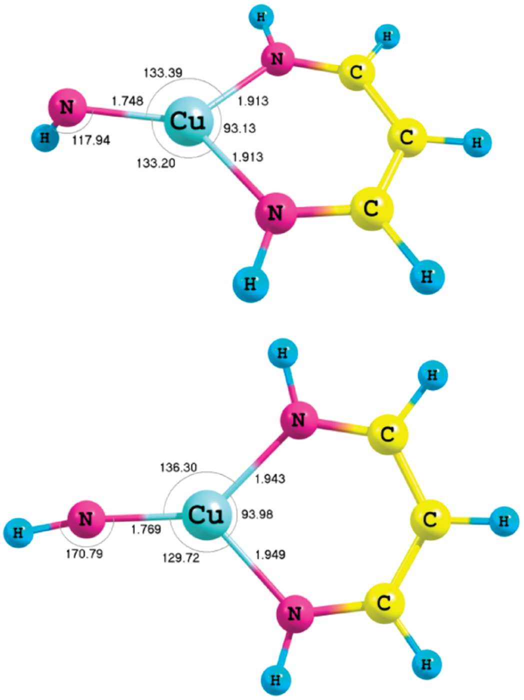

Figure 3. Optimized geometries of the singlet (top) and triplet (bottom), L′Cu(NH) using the B3LYP/6-311++G(d,p) method. The pertinent bond lengths (Å) and bond angles (deg) are shown.

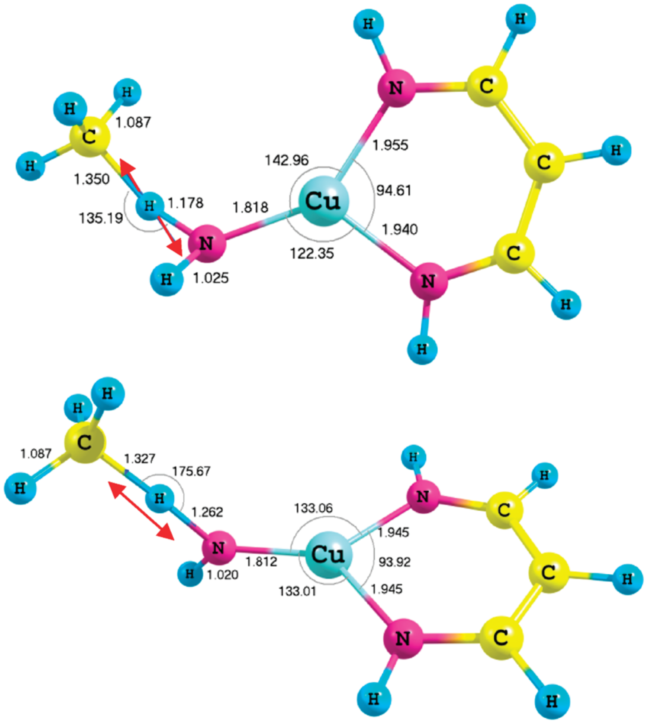

Figure 4. Transition state for direct C−H insertion at the B3LYP/6-311++G(d,p) level of theory. The top geometry is the singlet ($\nu i = 861i\ cm^{-1}$), while the bottom geometry is the triplet ($\nu i = 1643i\ cm^{-1}$). The pertinent bond lengths (Å) and bond angles (deg) are shown.

For methane reactions, Scheme 1, the most significant difference is 10.5 kcal mol^{-1} between PBE1KCIS/cc-pVTZ and B97−1/cc-pVTZ for the calculation of the reaction barrier height (i.e., R → TS) on the triplet surface. While sensitivity of transition states and hence reaction barriers to the level of theory is perhaps expected, what is more surprising are the differences in the ground state energetics.

Table 1. ΔH in kcal mol^{-1} for All Reactions Shown in Scheme 1[a]

	H−H Activation Results							
	singlet state (S = 0) calculation results				triplet state (S = 1) calculation results			
method	B3LYP	PBE1KCIS	B97-1		B3LYP	PBE1KCIS	B97-1	
basis set	6-311++G(d,p)	cc-pVTZ	cc-pVTZ	ccCA	6-311++G(d,p)	cc-pVTZ	cc-pVTZ	ccCA
R → P	−83.9	−89.7	−84.9	−72.5	−70.5	−76.4	−72.1	−76.1
R → TS	3.4	0.7	2.4	5.9	8.9	6.0	7.7	27.3
TS → P	−87.3	−90.4	−87.3	−78.4	−79.3	−82.4	−79.8	−103.5
I	−92.9	−99.9	−96.3	−96.9	−92.9	−99.9	−96.3	−96.9
II	−16.5	−17.4	−17.3	−18.1	−16.5	−17.4	−17.3	−18.1
III	83.9	89.7	84.9	72.5	70.5	76.4	72.1	76.1
IV	25.5	27.6	28.7	42.6	38.9	40.9	41.5	38.9
V	−9.6	−14.7	−13.6	19.0	3.8	−1.4	−0.8	15.3
VI	47.0	49.4	50.0	34.5	47.0	49.4	50.0	34.5

	C−H Activation Results							
	singlet state (S = 0) calculation results				triplet state (S = 1) calculation results			
method	B3LYP	PBE1KCIS	B97-1		B3LYP	PBE1KCIS	B97-1	
basis set	6-311++G(d,p)	cc-pVTZ	cc-pVTZ	ccCA	6-311++G(d,p)	cc-pVTZ	cc-pVTZ	ccCA
R → P	−60.5	−65.0	−62.1	−51.0	−46.5	−51.6	−49.2	−54.7
R → TS	7.3	4.8	5.9	12.7	13.1	10.2	18.8	29.7
TS → P	−67.8	−69.8	−68.0	−63.7	−59.6	−61.8	−59.3	−84.4
I	10.9	9.7	11.0	11.5	10.9	9.7	11.0	11.5
II	−96.9	−102.2	−101.8	105.2	−96.9	−102.2	−101.8	105.2
III	60.5	65.0	62.1	51.0	46.5	51.6	49.2	54.7
IV	25.5	27.6	28.7	42.6	39.5	40.9	41.5	38.9
V	−11.0	−11.8	−9.6	19.5	3.0	1.5	3.2	15.8
VI	47.0	49.4	50.0	34.5	47.0	49.4	50.0	34.5

[a] R, TS, and P denote the reactant, transition state, and product, respectively.

More specifically, there are cases where the absolute value of the deviation among the three DFT methods is 10.4 (B3LYP/6-311++G(d,p) versus PBE1KCIS/cc-pVTZ) and 10.1 (B3LYP/6-311++G(d,p) vs B97−1/cc-pVTZ) kcal mol^{-1} in the C−H bond activation reaction coordinates. Both of these results are for reaction II in Scheme 1, which is the binding enthalpy of methyl amine to the β-diketiminate−Cu complex. The sensitivity of reaction II is noteworthy given that it entails the coordination of a closed-shell Lewis base (ammonia) to a closed-shell Lewis acid (L′Cu). *The average difference as quantified by the mean absolute deviation (MAD) among the three DFT methods is generally small (1.6−5.4 kcal mol*$^{-1}$*) with the exception of the reactions mentioned above.* In section 2, we will compare ccCA predicted energetics to those obtained with density functional theory.

1.2. The Ground State of Copper Nitrene [L′Cu(NH)]. DFT calculations on L′Cu(NH), Figure 3, predict that the triplet state is lower than the singlet state for all three levels of theory evaluated here: B3LYP/6-311+G(d,p), PBE1KCIS/cc-pVTZ, and B97-1/cc-pVTZ. The difference between the triplet and singlet states is nearly identical for each functional, 13.4, 13.3, and 12.9 kcal mol^{-1}, respectively, similar to DFT values reported previously by Cundari et al.[29] However, previous multireference calculations indicated the ground state of copper(β-diketiminate)(nitrene) complexes to be a singlet.[29] The singlet state of L′Cu(NH) is thus best described with methods that can incorporate the multireference character of this open-shell singlet. DFT is, of course, a single determinant modeling technique.[61] We will revisit the singlet−triplet splitting of L′Cu(NH) with ab initio techniques in the following section.

2. ccCA Calculations. In light of the prediction of the singlet−triplet splitting of L′Cu(NH) by different DFT methods, in comparison to previous CASSCF calculations,[29] it is of interest to evaluate the predictions of wave function-based approaches such as ccCA. These calculations were performed at the B3LYP/cc-pVTZ optimized geometries given the similarity in geometry among the different functional/basis set combinations. *The ccCA method predicts that the singlet state of L′Cu(NH) is lower than the triplet state by 3.7 kcal mol*$^{-1}$*, which is comparable in magnitude and direction with the predictions made via CASSCF calculations (5.6 kcal mol*$^{-1}$*).*[29] Since there is similarity among the DFT methods vis-à-vis the difference in energy between ^{1,3}L′Cu(NH), the deviation between ccCA and all three DFT predictions of the singlet−triplet splitting is very similar, that is, a difference of ∼17 kcal mol^{-1} and with a reversal of ordering of the two multiplicities.

2.1. ccCA Prediction of Copper Nitrene Ground State. A breakdown of the ccCA energy into its components is very interesting in terms of how each constituent "prefers" either the singlet or triplet state of L′Cu(NH) as the ground state. Table 2 shows ccCA reference energy [E(MP2/CBS) in eq 1] and the breakdown of each contributing term to the total ccCA energy. Note that similar comments can be made for the singlet−triplet ordering of the transition states for C−H and H−H insertion, Table 2. *The ccCA reference energy predicts that the singlet state is lower than the triplet state for the L′Cu(NH) active species by 14.9 kcal mol*$^{-1}$*.* When

Table 2. Correlation Consistent Composite Approach (ccCA) Total Energy at 298 K and the Constituent Terms in au for Complexes at the Singlet and Triplet States

complex	electronic state	ccCA reference energy[a]	correlation effects term	core valence term	relativistic effects term	zero-point correction	ccCA total energy at 298 K
L′Cu−NH	singlet	−1921.315616	−0.019974	−0.807883	−14.309706	0.104388	−1936.348792
L′Cu−NH	triplet	−1921.291884	−0.040519	−0.806430	−14.307726	0.103626	−1936.342932
L′Cu−NH_3(TS)[b]	singlet	−1922.461932	−0.038028	−0.809139	−14.310405	0.118110	−1937.501394
L′Cu−NH_3(TS)	triplet	−1922.391377	−0.094062	−0.785643	−14.305786	0.115420	−1937.461448
L′Cu−NH_2CH_3(TS)	singlet	−1961.714306	−0.062155	−0.856912	−14.321781	0.150333	−1976.804821
L′Cu−NH_2CH_3(TS)	triplet	−1961.652950	−0.112235	−0.834112	−14.320529	0.148067	−1976.771758

[a] Reference energy is computed from the Schwartz two-point extrapolation equation of the MP2 energies at the aug-cc-pVTZ and aug-cc-pVQZ basis sets. [b] TS refers to the energy of complex at the transition state.

Table 3. Multireference Correlation Consistent Composite Approach (MR-ccCA) Total Energy and the Constituent Terms in au for Complexes at the Singlet and Triplet State

complex	electronic state	MR-ccCA reference energy[a]	correlation effects term	core valence term	relativistic effects term	zero-point correction	MR-ccCA total energy at 298 K
L′Cu−NH	singlet	−1921.176380	0.043125	−0.760333	−14.308796	0.104388	−1936.097995
L′Cu−NH	triplet	−1921.152392	0.031002	−0.760049	−14.305705	0.103626	−1936.083518

[a] Reference energy is computed from the Schwartz two-point extrapolation equation of the CASPT2 energies with the aug-cc-pVDZ and aug-cc-pVTZ basis sets for L′Cu−NH.

electron correlation [ΔE(CC)] is added beyond the MP2 level, the singlet and triplet state of L′Cu(NH) now display a difference of 2.0 kcal mol^{-1}, with the singlet still lower in energy. The coupled cluster calculation thus counteracts, but does not reverse, the MP2-based reference energy, leaving L′Cu(NH) in a close energetic balance among the two spin states. The other additive terms (core−valence, relativistic, and zero-point energy) have negligible difference, although the difference in core−valence contributions is more significant for the transition states than the ground state L′Cu(NH), Table 2. The core−valence correction favors the singlet state and may be a reflection of the change in formal oxidation state at copper.

2.2. Multireference ccCA (MR-ccCA) Prediction of Copper Nitrene Ground State. As shown in Table 3, MR-ccCA supports previous CASSCF and single-reference ccCA calculations, that is, that a singlet is the electronic ground state of the copper nitrene, L′Cu(NH). In the case of MR-ccCA, the singlet state is predicted to be 9.1 kcal mol^{-1} lower in energy than the triplet state. Interestingly, this value is approximately halfway between DFT and single reference ccCA predictions. Furthermore, we note that all of the MR component calculations in MR-ccCA predict that the singlet state is the lower energy than the triplet state, Table 3; although, similar to single reference ccCA, adding in electron correlation beyond second-order perturbation theory acts to reduce the singlet−triplet splitting of L′Cu(NH). As a final justification for the use of MR-ccCA, the leading reference coefficients predicted with the AQCC method for both the singlet and triplet system are 0.722 and 0.814, respectively, indicating significant multireference character.

2.3. Reaction Coordinates: Comparison of ccCA versus DFT. Since the reaction energy differences among the three DFT methods are similar for the majority of the component reactions, Scheme 1 and Figure 2, we focus on B3LYP/6-311++G(d,p) and ccCA results for the remaining discussion. Comparing the H−H bond activation reaction coordinates (singlet state), we find that the largest B3LYP-ccCA difference is 28.6 kcal mol^{-1} for reaction V, which involves the multireference molecule, L′Cu(NH): the HAA reaction of L′Cu(NH) with H_2 to yield L′Cu(NH_2) and H atom. The lowest difference is 0 kcal mol^{-1} for reaction IV, the dissociation of imidogen (^{3}NH) from the triplet copper−nitrene complex to yield the copper catalyst model, L′Cu (i.e., there was essentially no difference between ccCA and B3LYP for reaction IV). Comparing the triplet potential energy surface for H−H bond activation, we found that the largest DFT-ccCA calculated difference is 12.5 kcal mol^{-1} for reaction VI, which described the bond dissociation energy of the copper−nitrogen bond of L′Cu(NH_2). *Thus, in general, it appears that the biggest divergence between the DFT and ccCA methods is for those processes that involve radical species and homolytic bond dissociation.*

There are two plausible reaction mechanisms for C−H and H−H bond activation by a copper−nitrene complex: a concerted [1 + 2] direct insertion and nonconcerted pathways initiated by HAA reaction. Previous DFT calculations in concert with experimental studies support a mechanism involving direct [1 + 2] insertion.[30] On the singlet surface for H_2 functionalization, the [1 + 2] insertion reaction is calculated to be exothermic by −72.5 kcal mol^{-1} versus −83.9 kcal mol^{-1} determined at the B3LYP/6-311++G(d,p) level of theory, Table 1. The singlet insertion barrier is small using both density functional and wave function based techniques (3.4 kcal mol^{-1} for B3LYP/6-311++G(d,p) and 5.9 kcal mol^{-1} for ccCA). The kinetic barrier to H_2 insertion is more divergent on the triplet surface: 8.9 kcal mol^{-1} for B3LYP/6-311++G(d,p) and 27.3 kcal mol^{-1} for ccCA. For the methane functionalization pathway, Table 1, there is more congruity between DFT- and ccCA-calculated energetics, although as for the H_2 reactions, discrepancies are more apparent on the triplet than the singlet surface.

Summary and Conclusions

The kinetics and thermodynamics of nitrene insertion into C−H and H−H have been studied using several levels of theory: B3LYP/6-311++G(d,p), B97-1/cc-pVTZ, PBE1KCIS/

cc-pVTZ, and ccCA. Each DFT method shows no significant difference from the other two DFT methods despite the use of both hybrid and meta-GGA functionals, as well as both Pople-style and correlation consistent basis sets. Hence, the deviations of ccCA results with respect to the different DFT methods studied here are very similar. All three DFT methods predict the ground state of L′Cu(NH) to be the triplet; however, ccCA results show the singlet state to be the ground state. The contributions to the total ccCA energy indicate that ccCA prediction of the singlet state is due to ccCA reference energy. The ccCA reference energy (which mimics the complete basis set limit of MP2) predicts that the singlet state is lower than the triplet state for the L′Cu(NH) active species by 14.9 kcal mol^{-1}. When electron correlation [ΔE(CC)] is added beyond the MP2 level, the singlet and triplet state of L′Cu(NH) display a difference of 2.0 kcal mol^{-1}, with the singlet still lower in energy. The coupled cluster calculation thus counteracts, but does not reverse, the MP2-based reference energy, leaving L′Cu(NH) in a close energetic balance among the two spin states. MR-ccCA calculations are in agreement with CASSCF and single reference ccCA and yield a singlet−triplet splitting of 8.3 kcal mol^{-1}, which is halfway between the DFT and single-reference ccCA predictions. In general, the largest difference between DFT and ccCA methods is for those processes that involve radical species and homoloytic bond dissociation. Other research in our group indicates that spin contamination can be problematic in open-shell organic[62] and inorganic compounds,[63] making the use of restricted open-shell methodologies a prudent choice. However, no evidence for spin contamination was seen in the present research.

Acknowledgment. This research was supported in part by a grant from the National Science Foundation (CHE-0701247) to T.R.C. Calculations employed the UNT computational chemistry resource, for which T.R.C. acknowledges the NSF for support through CRIF grant CHE-0741936.

Supporting Information Available: Tables of total energies and enthalpies of all complexes in au. Animated graphics files for the calculated TSs are also available. This material is available free of charge via the Internet at http://pubs.acs.org.

References

(1) Fairlamb, I. J. S. *Annu. Rep. Prog. Chem. B* **2006**, *102*, 50.

(2) Fekl, U.; Goldberg, K. I. *Adv. Inorg. Chem.* **2003**, *54*, 259.

(3) Goj, L. A.; Gunnoe, B. T. *Curr. Org. Chem.* **2005**, *9*, 671.

(4) Labinger, J. A.; Bercaw, J. E. *Nature* **2002**, *417*, 507.

(5) Lersch, M.; Tilset, M. *Chem. Rev.* **2005**, *105*, 247.

(6) Cenini, S.; Gallo, E.; Caselli, A.; Ragaini, F.; Fantauzzi, S.; Piangiolino, C. *Coord. Chem. Rev.* **2006**, *250*, 1234.

(7) Ittel, S. D.; Johnson, J. K.; Brookhart, M. *Chem. Rev.* **2000**, *100*, 1169.

(8) Kitiachvili, K. D.; Mindiola, D. J.; Hillhouse, G. L. *J. Am. Chem. Soc.* **2004**, *126*, 10554.

(9) Melenkivitz, R.; Mindiola, D. J.; Hillhouse, G. L. *J. Am. Chem. Soc.* **2002**, *124*, 3846.

(10) Mindiola, D. J.; Hillhouse, G. L. *Chem. Comm.* **2002**, *17*, 1840.

(11) Mindiola, D. J.; Hillhouse, G. L. *J. Am. Chem. Soc.* **2002**, *124*, 9976.

(12) Miniola, D. J.; Hillhouse, G. L. *J. Am. Chem. Soc.* **2001**, *123*, 4623.

(13) Waterman, R.; Hillhouse, G. L. *Organometallics* **2002**, *23*, 5182.

(14) Waterman, R.; Hillhouse, G. L. *J. Am. Chem. Soc.* **2003**, *125*, 13350.

(15) Bourget-Merle, L.; Lappert, M. F.; Severn, J. R. *Chem. Rev.* **2002**, *102*, 3031.

(16) Shimokawa, C.; Yokota, S.; Tachi, Y.; Nishiwaki, N.; Ariga, M.; Itoh, S. *Inorg. Chem.* **2003**, *42*, 8395. See also: Hong, S.; Hill, L. M. R.; Gupta, A. K.; Naab, B. D.; Gilroy, J. B.; Hicks, R. G.; Cramer, C. J.; Tolman, W. B. *Inorg. Chem.* **2009**, *48*, 4514.

(17) Eckert, N. A.; Vaddadi, S.; Stoian, S.; Lachicotte, R. J.; Cundari, T. R.; Holland, P. L. *Angew. Chem., Int. Ed.* **2006**, *45*, 6868.

(18) Dai, X.; Kapoor, P.; Warren, T. H. *J. Am. Chem. Soc.* **2003**, *126*, 4798.

(19) Kogut, E.; Wiencko, H. L.; Zhang, L.; Cordeau, D. E.; Warren, T. H. *J. Am. Chem. Soc.* **2005**, *127*, 11248. Baik and coworkers have studied structural transformations in three-coordinate b-diketiminate complexes of chromium:Fan, H.; Adhikari, D.; Saleh, A. A.; Clark, R. L.; Zuno-Cruz, F. J.; Cabrera, G. S.; Huffman, J. C.; Pink, M.; Mindiola, D. J.; Baik, M. *J. Am. Chem. Soc.* **2008**, *130*, 17351.

(20) Gillespie, K. M.; Crust, E. J.; Deeth, R. J.; Scott, P. *Chem. Commun.* **2001**, 785.

(21) Diaz-Requejo, M. M.; Belderrain, T. R.; Nicasio, M. C.; Trofimenko, S.; Perez, P. J. *J. Am. Chem. Soc.* **2003**, *125*, 12079.

(22) Li, Z.; Capretto, D. A.; Rahaman, R.; He, C. *Angew. Chem., Int. Ed.* **2007**, *46*, 5184.

(23) Li, Z.; Capretto, D. A.; Rahaman, R. O.; He, C. *J. Am. Chem. Soc.* **2007**, *129*, 12058.

(24) Lovely, C. J.; Browning, R. G.; Polach, S. A.; Dias, H. V. R. *Carbene and Nitrene Transfer Reactions Catalyzed by Fluorinated Tris(Pyrazolyl)Borato Copper(I) and Silver(I) Complexes*; Abstracts of Papers, 225th ACS National Meeting, New Orleans, LA, March 23−27, 2003, ORGN-032.

(25) Perez, J.; Morales, D.; Garcia-Escudero, L. A.; Martinez-García, H.; Miguelb, D.; Bernada, P. *Dalton Trans.* **2009**, 375.

(26) Cano, I.; Nicasio, M. C.; Perez, P. J. *Dalton Trans.* **2009**, 730.

(27) Badiei, Y. M.; Warren, T. H. *J. Organomet. Chem.* **2005**, *690*, 5989.

(28) Badiei, Y. M.; Krishnaswamy, A.; Melzer, M. M.; Warren, T. H. *J. Am. Chem. Soc.* **2006**, *128*, 15056.

(29) Cundari, T. R.; Dinescu, A.; Kazi, A. B. *Inorg. Chem.* **2008**, *47*, 10067.

(30) Badiei, Y. M.; Dinescu, A.; Dai, X.; Palomino, R. M.; Heinemann, F. W.; Cundari, T. R.; Warren, T. H. *Angew. Chem., Int. Ed.* **2008**, *47*, 9961.

(31) Periana, R. A.; Taube, D. J.; Gamble, S.; Taube, H.; Satoh, T.; Fuji, H. *Science* **1998**, *280*, 560 .

(32) Periana, R. A.; Taube, D. J.; Evitt, E. R.; Loffler, D. G.; Wentrcek, P. R.; Voss, G.; Masuda, T. *Science* **1993**, *253*, 340.

(33) Jones, C. J.; Taube, D. J.; Ziatdinov, V. R.; Periana, R. A.; Nielsen, R. J.; Oxgaard, J.; Goddard, W. A., III. *Angew. Chem., Int. Ed.* **2004**, *43*, 4626.

(34) Xu, X.; Fu, G.; Goddard, W. A., III.; Periana, R. A. *Stud. Surf. Sci. Catal.* **2004**, *147*, 499.

(35) Periana, R. A.; Ortmann, D. A.; Mironov, O. A. *Mechanistic Aspects of the High-Yield, Methane to Methanol Catalytic System*; Abstracts of Papers, 224th ACS National Meeting, Boston, MA, August 18−22, 2002, INOR-465.

(36) Kua, J.; Xu, X.; Periana, R. A.; Goddard, W. A., III. *Organometallics* **2002**, *21*, 511.

(37) Periana, R. A.; Ortmann, D. A. *Experimental and Theoretical Study of a High-Yield, Methane Hydroxylation Catalyst*; Abstracts of Papers, 223rd ACS National Meeting, Orlando, FL, April 7−11, 2002, INOR-157.

(38) Webster, C. E.; Fan, Y.; Hall, M. B.; Kunz, D.; Hartwig, J. F. *J. Am. Chem. Soc.* **2003**, *125*, 858.

(39) Ho, D. S.; DeYonker, N. J.; Wilson, A. K.; Cundari, T. R. *J. Phys. Chem. A* **2006**, *110*, 9767.

(40) DeYonker, N. J.; Mintz, B.; Cundari, T. R.; Wilson, A. K. *J. Chem. Theory Comput.* **2008**, *4*, 328.

(41) DeYonker, N. J.; Peterson, K. A.; Steyl, G.; Wilson, A. K.; Cundari, T. R. *J. Phys. Chem.* **2007**, *111*, 11269.

(42) Grimes, T. V.; Wilson, A. K.; DeYonker, N. J.; Cundari, T. R. *J. Chem. Phys.* **2007**, *127*, 154117.

(43) DeYonker, N. J.; Grimes, T.; Yockel, S.; Dinescu, A.; Mintz, B.; Cundari, T. R.; Wilson, A. K. *J. Chem. Phys.* **2006**, *125*, 104111/1.

(44) Frisch, M. J.; Trucks, G. W.; Schlegel, H. B.; Scuseria, G. E.; Robb, M. A.; Cheeseman, J. R.; Montgomery, J. A., Jr.; Vreven, T.; Kudin, K. N.; Burant, J. C.; Millam, J. M.; Iyengar, S. S.; Tomasi, J.; Barone, V.; Mennucci, B.; Cossi, M.; Scalmani, G.; Rega, N.; Petersson, G. A.; Nakatsuji, H.; Hada, M.; Ehara, M.; Toyota, K.; Fukuda, R.; Hasegawa, J.; Ishida, M.; Nakajima, T.; Honda, Y.; Kitao, O.; Nakai, H.; Klene, M.; Li, X.; Knox, J. E.; Hratchian, H. P.; Cross, J. B.; Bakken, V.; Adamo, C.; Jaramillo, J.; Gomperts, R.; Stratmann, R. E.; Yazyev, O.; Austin, A. J.; Cammi, R.; Pomelli, C.; Ochterski, J. W.; Ayala, P. Y.; Morokuma, K.; Voth, G. A.; Salvador, P.; Dannenberg, J. J.; Zakrzewski, V. G.; Dapprich, S.; Daniels, A. D.; Strain, M. C.; Farkas, O.; Malick, D. K.; Rabuck, A. D.; Raghavachari, K.; Foresman, J. B.; Ortiz, J. V.; Cui, Q.; Baboul, A. G.; Clifford, S.; Cioslowski, J.; Stefanov, B. B.; Liu, G.; Liashenko, A.; Piskorz, P.; Komaromi, I.; Martin, R. L.; Fox, D. J.; Keith, T.; Al-Laham, M. A.; Peng, C. Y.; Nanayakkara, A.; Challacombe, M.; Gill, P. M. W.; Johnson, B.; Chen, W.; Wong, M. W.; Gonzalez, C.; Pople, J. A. *Gaussian03*, revision D.02; Gaussian, Inc.: Wallingford, CT, 2004.

(45) Stephens, P. J.; Devlin, F. J.; Chabalowski, C. F.; Frisch, M. J. *J. Phys. Chem.* **1994**, *98*, 11623.

(46) Dunning, T. H., Jr.; Peterson, K. A.; Wilson, A. K. *J. Chem. Phys.* **2001**, *114*, 9244.

(47) Kendall, R. A.; Dunning, T. H., Jr.; Harrison, R. J. *J. Chem. Phys.* **1992**, *96*, 6796.

(48) Peterson, K. A.; Dunning, T. H., Jr. *J. Chem. Phys.* **2002**, *117*, 10548.

(49) Dunning, T. H., Jr. *J. Chem. Phys.* **1989**, *90*, 1007.

(50) Van Mourik, T.; Dunning, T. H., Jr. *Int. J. Quantum Chem.* **2000**, *76*, 205.

(51) Wilson, A. K.; Van Mourik, T.; Dunning, T. H., Jr. *THEOCHEM* **1996**, *388*, 339.

(52) Wilson, A. K.; Woon, D. E.; Peterson, K. A.; Dunning, T. H., Jr. *J. Chem. Phys.* **1999**, *110*, 7667.

(53) Woon, D. E.; Dunning, T. H., Jr. *J. Chem. Phys.* **1993**, *98*, 1358.

(54) Woon, D. E.; Dunning, T. H., Jr. *J. Chem. Phys.* **1995**, *103*, 4572.

(55) Becke, A. D. *Phys. Rev. A* **1988**, *38*, 3098.

(56) Lee, C.; Yang, W.; Parr, R. G. *Phys. Rev. B* **1988**, *37*, 785.

(57) Tekarli, S. M.; Drummond, M. L.; Williams, T. G.; Cundari, T. R.; Wilson, A. K. *J. Phys. Chem. A* **2009**, *113*, 8607.

(58) Zhao, Y.; González-García, N.; Truhlar, D. G. *J. Phys. Chem. A* **2005**, *109*, 2012.

(59) Werner, H. J.; Knowles, P. J.; Lindh, R.; Manby, F. R.; Schütz, M.; Celani, P.; Korona, T.; Rauhut, G.; Amos, R. D.; Bernhardsson, A.; Berning, A.; Cooper, D. L.; Deegan, J. O.; Dobbyn, A. J.; Eckert, F.; Hampel, C.; Hetzer, G.; Lloyd, A. W.; McNicholas, S. J.; Meyer, W.; Mura, M. E.; Nicklass, A.; Palmieri, P.; Pitzer, R.; Schumann, U.; Stoll, H.; Stone, A. J.; Tarroni, R.; Thorsteinsson, T. *MOLPRO*, version 2006.1; University College Cardiff Consultants Limited: Cardiff, South Glamorgan, U. K., 2006.

(60) Mintz, B.; Williams, T. G.; Howard, L.; Wilson, A. K. *J. Chem. Phys.* **2009**, *130*, 234104/1.

(61) Schultz, N. E.; Zhao, Y.; Truhlar, D. G. *J. Phys. Chem. A.* **2005**, *109*, 11127.

(62) Gao, Y.; DeYonker, N. J.; Garrett, E. C.; Wilson, A. K.; Cundari, T. R.; Marshall, P. *J Phys. Chem. A* **2009**, *113*, 6955.

(63) DeYonker, N. J.; Williams, T. G.; Imel, A. E.; Cundari, T. R.; Wilson, A. K. *J. Chem. Phys.* **2009**, *131*, 024106/1.

CT900277M

J. Chem. Theory Comput. **2009,** *5,* 2967–2976 **2967**

JCTC Journal of Chemical Theory and Computation

What Active Space Adequately Describes Oxygen Activation by a Late Transition Metal? CASPT2 and RASPT2 Applied to Intermediates from the Reaction of O_2 with a Cu(I)-α-Ketocarboxylate

Stefan M. Huber,[†] Abdul Rehaman Moughal Shahi,[†] Francesco Aquilante,[†]
Christopher J. Cramer,*[,‡] and Laura Gagliardi*[,†,‡]

Department of Physical Chemistry, University of Geneva, 30, Quai Ernest Ansermet, 1211 Genève, Switzerland and Department of Chemistry and Supercomputing Institute, University of Minnesota, 207 Pleasant Street SE, Minneapolis, Minnesota 55455-0431

Received June 3, 2009

Abstract: Multiconfigurational second-order perturbation theory calculations based on a complete active space reference wave function (CASPT2), employing active spaces of increasing size, are well converged at the level of 12 electrons in 12 orbitals for the singlet−triplet state−energy splittings of three supported copper−dioxygen and two supported copper−oxo complexes. Corresponding calculations using the restricted active space approach (RASPT2) offer similar accuracy with a significantly reduced computational overhead provided an inner (2,2) complete active space is included in the overall RAS space in order to account for strong biradical character in most of the compounds. The effects of the different active space choices and the outer RAS space excitations are examined, and conclusions are drawn with respect to the general applicability of the RASPT2 protocol.

Introduction

In order to better understand the mechanistic details of substrate oxidations catalyzed by copper-containing metalloenzymes, considerable effort has been devoted to the synthesis and the characterization of smaller copper coordination complexes capable of activating molecular oxygen.[1−9] In a recent example, Hong et al.[10] reported the preparation, structural characterization, and reactivities of related Cu(I)-α-ketocarboxylate complexes supported by iminopyridine ligands appended with arene substituents positioned so as to be susceptible to intramolecular attack by an activated oxygen species (Scheme 1). Using density functional theory (DFT) and multiconfigurational second-order perturbation theory based on a complete active space reference wave function (CASSCF/CASPT2), the microscopic details of the multistep mechanism for the observed oxidation reaction have been elucidated,[10] as has the sensitivity of the reaction path energetics to different ligand sets.[11]

Scheme 1

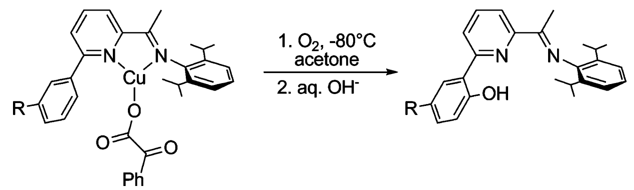

As indicated in Scheme 2 (in which only the N atoms of the supporting ligand are shown), the reaction proceeds by an initial coordination of molecular oxygen to the supported copper complex. Three isomeric structures were predicted at the DFT level, two of which were characterized by end-on coordination of the O_2 moiety, while the other exhibited side-on coordination. Following decarboxylation and subsequent cleavage of the O−O bond in an intermediate peroxybenzoate complex, two isomeric Cu(II)−oxyl species could be accessed, differing in the coordination geometry about the Cu center (square-planar (SP) vs trigonal-bipyra-

---

* Corresponding authors: E-mail: cramer@umn.edu and laura.gagliardi@unige.ch.

[†] University of Geneva.

[‡] University of Minnesota.

10.1021/ct900282m CCC: $40.75

Scheme 2

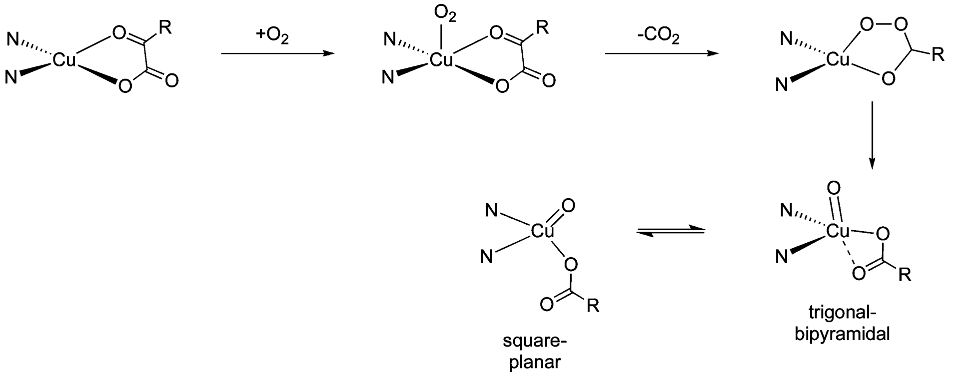

midal (TBP); the literature alternatively sometimes refers to such species as formal Cu(III)−oxo complexes, but calculations make clear that a Cu(II)−oxyl formulation is more appropriate given the relevant electronic structures).[10,12−15] Both the peroxybenzoate and the Cu(II)-oxyl intermediates were determined to be highly reactive with respect to the oxidation of the pendant arene ring in the iminopyridine ligand. Experimental investigations designed to isolate a Cu(II)-oxyl intermediate and to extend the reactivity of such species to external substrates continue to be actively pursued.

Considering in more detail the theoretical modeling of these species, several key intermediates are well described as having biradical character. In particular, the initial oxygen adducts and the Cu(II)-oxyl intermediates. In the case of the oxygen adducts, whether viewed as complexes of molecular O_2 with Cu(I) or as Cu(II)-superoxide compounds, two electrons are effectively localized on distinct centers: the two O atoms in the former instance and the Cu(II) and one O atom in the latter.[16] The latter localization also prevails in the Cu(II)-oxyl intermediates. Such biradical character introduces challenges with respect to computing the properties of singlet electronic states based on single-determinant formalisms, like Kohn−Sham density functional theory (KS-DFT).[17] A proper spin and spatial wave function for a biradical singlet, also sometimes referred to as an open-shell singlet, formally requires a minimum of two determinants. Nevertheless, by invocation of a relationship between the eigenvalues of the Heisenberg−Slater−Dirac Hamiltonian[18−21] and the energies obtained from broken-symmetry and high-spin single-determinant calculations,[22−25] DFT models have been successfully employed to compute state−energy splittings in many open-shell coordination compounds.[9,26−28]

However, this practical approach has a number of drawbacks, particularly insofar as no spin-pure wave function (or density) can be represented by a single determinant for states other than that of the highest spin. Instead, the broken-symmetry states having S_z values below the $S_{\max}$ value for the high spin state may be said to be spin contaminated, and as such it is not clear how to evaluate properties *other* than the state energies. To be more precise, we should say that it is the Kohn−Sham determinant that is spin contaminated − the wave function for the corresponding density is not known, so we cannot rigorously assess its spin expectation value, but, in practice, properties determined from broken-symmetry DFT calculations do appear to suffer from spin contamination.

In contrast to single determinantal KS-DFT, multideterminantal states *are* properly represented in multiconfigurational self-consistent field (MCSCF) theory.[29] The complete active space (CASSCF)[30] implementation of this theory constructs a wave function as a linear combination of all possible spin and spatially adapted determinants that may be formed from the distribution of a given number of “active” electrons in a given number of orbitals. The “active space” orbitals are typically chosen based on chemical analysis of the problem at hand, e.g., all bonding and antibonding orbitals associated with one or more bond-making or -breaking processes along a reaction coordinate. When supplemented by multireference second-order perturbation theory, CASSCF/CASPT2,[31] in order to account for dynamical electron correlation effects not included at the CASSCF level, accuracies on the order of 0.2 eV have been documented for state−energy splittings in molecules containing elements throughout the periodic table.[32−41] In the particular case of the copper chemistry discussed above, Hong et al.[10] and Huber et al.[11] compared CASSCF/CASPT2 singlet−triplet splittings to those derived from broken-symmetry DFT calculations in order to assess the likely accuracy of the latter. The two models were in generally good agreement for the Cu(II)-oxyl species, but agreement was not as good for the initial oxygen adducts.

While such comparisons between broken-symmetry DFT and CASSCF/CASPT2 can be informative, the number of determinants in the CASSCF model increases factorially with an increasing number of orbitals in the active space, leading to a practical limit of roughly 16 electrons in 16 orbitals.[17,42] When larger active spaces are needed, e.g., in a trinuclear transition metal complex where a balanced active space might require three sets of valence d and s orbitals, the CASSCF/CASPT2 model cannot be applied in a practical fashion. In order to address this limitation, Malmqvist et al.[43] recently developed a second-order perturbation theory based on the restricted active space self-consistent field method, namely, RASSCF/RASPT2. By subdividing the active space orbitals into three sets, one set entirely equivalent to a CAS space, one set consisting of occupied orbitals *from which* only a limited number of electrons may be excited, and one set consisting of virtual orbitals *into which* only a limited number of electrons may be excited; the number of orbitals and electrons that may be considered is substantially increased relative to the CASSCF/CASPT2 model. While initial results

Scheme 3

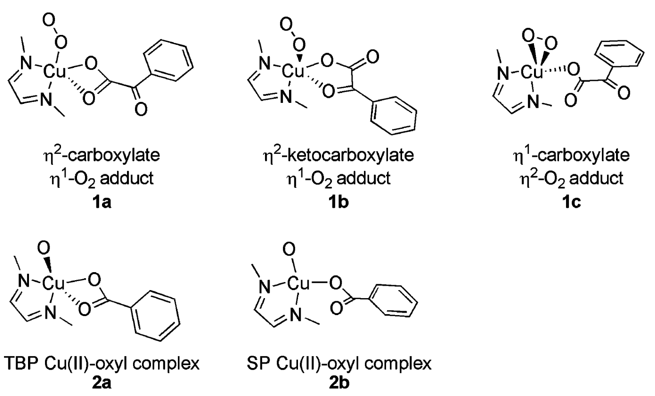

from studies of mono- and binuclear copper−oxygen adducts have been promising, much remains to be learned with respect to the question of how best to choose a RASSCF active space and excitation protocol. The aim of the present paper is to explore this question for biradical copper−oxygen adducts and Cu(II)-oxyl intermediates analogous to those already discussed above. In particular, we examine the predicted singlet−triplet splittings and the relative isomer energies for the three adducts **1a**−**c** and the two intermediates **2a** and **2b** shown in Scheme 3. In order to facilitate this benchmarking study, the sterically demanding N-donor ligand shown in Scheme 1 is replaced by a simplified diimine ligand similarly characterized by two sp^2-hybridized donor nitrogen atoms. We begin with a discussion of the computational details, then present results designed to assess convergence in predicted energies with respect to methodological choices, and conclude with some general observations likely to prove useful in future applications of the RASSCF/RASPT2 model.

Computational Details

Geometries of the structures in Scheme 3 were optimized at the M06-L[44] level of density functional theory adopting a broken-symmetry unrestricted formalism for the nominal singlet states. As we are interested here in comparing different RASSCF/RASPT2 protocols for given geometries, the choice of any particular geometry is arbitrary, but it is perhaps worth emphasizing that computed state−energy splittings in this work are vertical and not adiabatic. Geometry optimizations employed the Cu basis set and pseudopotential of Dolg et al.[45] augmented with three f functions having exponents of 5.10, 1.275, and 0.32; the 6-31G(d) basis set[46] was used for all other atoms.

Multiconfigurational calculations were accomplished according to a number of different protocols. In all cases, basis sets of atomic natural orbital (ANO) and ANO-RCC (for Cu) type[47,48] were employed using contractions of 5s3p2d1f, 3s2p1d, 3s2p1d, 3s2p, and 1s for Cu, O, N, C, and H, respectively. In prior work on the experimentally characterized system of Hong et al., (12,12) CAS spaces were adopted for CASSCF/CASPT2 calculations on the various species with the orbitals included based on a careful assessment of occupation numbers for different active space constructions.[10] These spaces inevitably contained orbitals formed from the bonding and the antibonding combinations of O 2p orbitals and Cu 3d orbitals, with the precise number of σ, π, and nonbonding orbitals being dictated by the chemical structure. The size of the active space was chosen based on consideration of 12 intermediate- and transition-state structures along the reaction coordinate for the overall reaction indicated in Scheme 1. Our goal was to find an active space size that was consistent for all structures and well converged for the predicted singlet−triplet energy splittings. The (12,12) space fulfilled these criteria. With respect to convergence issue, calculations employing expanded (14,14) active spaces predicted very similar singlet−triplet splittings, e.g., 2.33 and 2.34 kcal/mol for structure **1b** of the present study with (12,12) and (14,14) active spaces, respectively.

Those CAS(12,12) active space orbitals most relevant to the present study are illustrated in Figures 1 and 2; in particular, for each of the five structures discussed in this paper, two orbitals in the relevant active space had occupation numbers in the singlet state differing substantially from 2.0 or 0.0, which is consistent with varying degrees of biradical character and are shown in Figure 1. In addition, for the particular case of **1a**, the remaining 10 orbitals are shown in Figure 2. These orbitals are roughly representative of the analogous ones used for the various other structures, which, in the interest of brevity, are not depicted here. For **1a**−**c**, the orbitals in Figure 1 involve π bonding and antibonding combinations of a Cu 3d orbital and an O_2 π^* orbital, and the CAS(12,12) occupation numbers were 1.30, 0.70 (**1a**), 1.05, 0.95 (**1b**), and 1.78, 0.25 (**1c**). In the cases of **2a** and **b**, it was hybrid π orbitals from the Cu 3d and the O 2p orbitals that had occupation numbers of 1.16, 0.85 (**2a**) and 1.11, 0.89 (**2b**). All of these orbitals had occupation numbers of 1.0 in the corresponding triplet states. The other orbitals of the (12,12) active space included all remaining Cu 3d orbitals and a second shell of Cu d orbitals for correlation. When forming smaller (10,10) and (8,8) active spaces, as described below, hybrid orbitals having substantial Cu d character were sequentially removed based on the degree to which their occupation numbers were very near 2.0 or 0.0 for occupied and virtual orbitals, respectively.

In the RASSCF model, the active subspace is divided into three distinct regions: RAS1, RAS2, and RAS3. The RAS2 region is identical to the active region in a CASSCF calculation, i.e., all possible spin- and symmetry-adapted configuration state functions (CSFs) that can be constructed from the orbitals in RAS2 are included in the multiconfigurational wave function. The RAS1 and RAS3 spaces, on the other hand, permit the generation of additional CSFs subject to the restriction that a maximum number of excitations may occur from RAS1, which otherwise contains only doubly occupied orbitals, and a maximum number of excitations may occur into RAS3, which otherwise contains only external orbitals. There are various ways in which one can select the orbitals. In the present case, the maximum size of the full active space was kept at 12 orbitals, in analogy with the CASSCF calculations. Only the two orbitals with an occupation number significantly different from two and zero (see above) were placed in RAS2, with the remaining occupied 3d orbitals (mostly) being in RAS1 orbitals) and the unoccupied 4d orbitals (mostly) being in RAS3. Several levels of maximum excitation

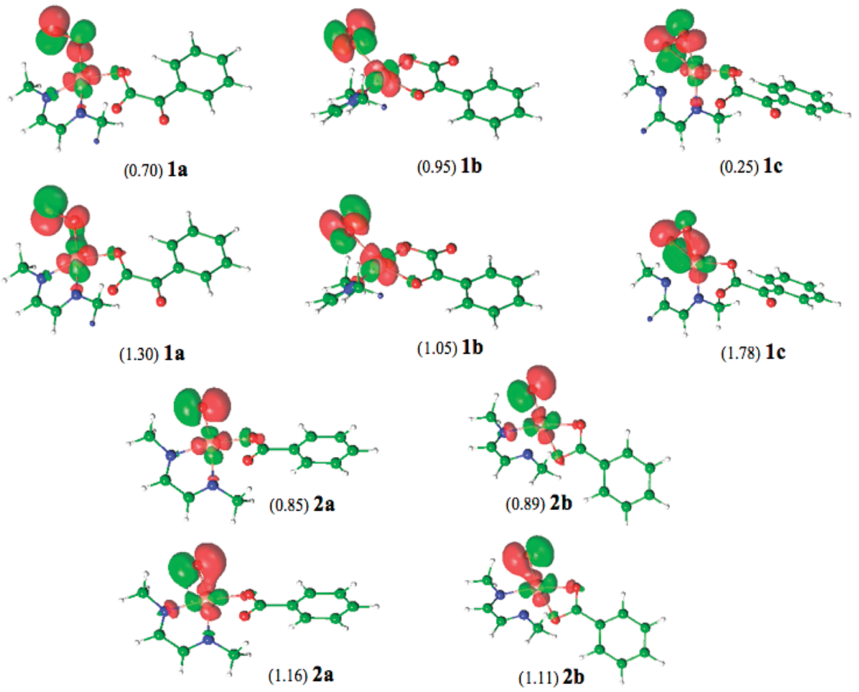

Figure 1. Isodensity surfaces (0.04 au) and occupation numbers for the two active space orbitals with occupation numbers closest to 1.0 from CAS(12,12) calculations for **1a**−**c** and **2a** and **b**. Pairs of orbitals are ordered above and below one another (see also Scheme 3 for isomer ordering). Atomic colors are white (H), green (C), blue (N), red (O), and bronze (Cu).

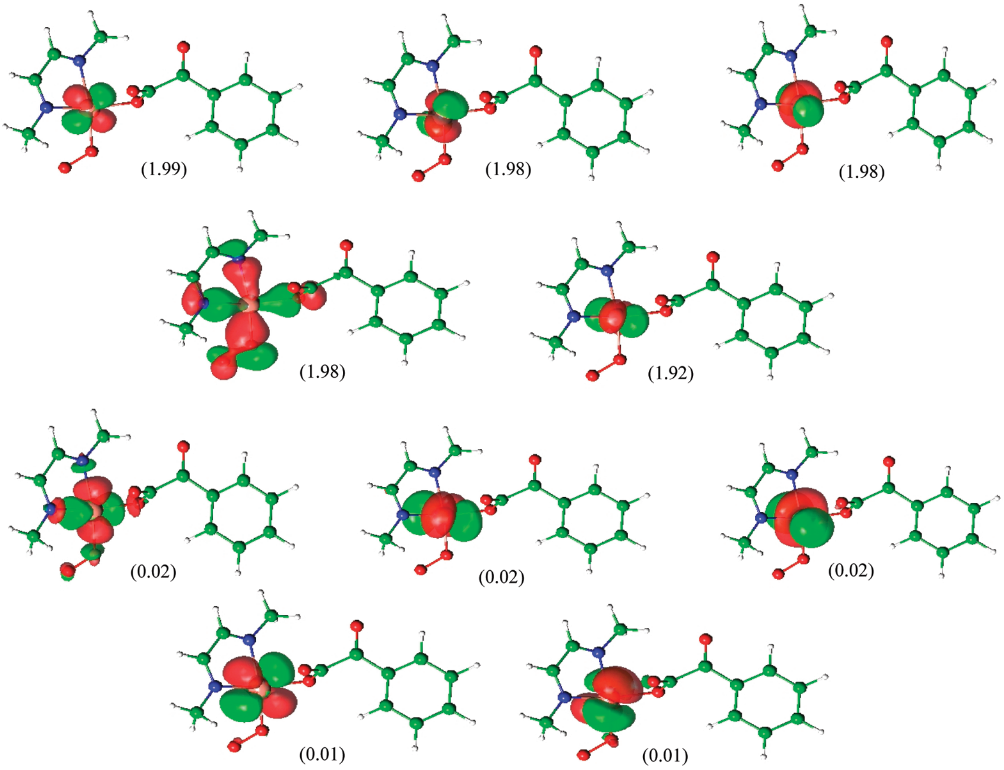

Figure 2. Isodensity surfaces (0.04 au) and occupation numbers for the remaining 10 active space orbitals that are not shown in Figure 1 from a CAS(12,12) calculation for **1a**. Atomic colors are white (H), green (C), blue (N), red (O), and bronze (Cu).

from RAS1 or into RAS3 were considered, namely up to double (SD), triple (SDT), and quadruple excitations (SDTQ). The general notation for a RASPT2 calculation is RASPT2(j,k)/(l,m)/n, where j is the number of electrons in RAS1 and RAS2, k is the number of orbitals in all RAS spaces, l is the number of electrons in RAS2, m is the number of orbitals in RAS2, and n is the maximum level of excitation permitted out of RAS1 and into RAS3. Thus, for instance, a RASPT2(12,12)/(2,2)/3 calculation would have 10 electrons and five orbitals in RAS1, two electrons and two orbitals in RAS2, five orbitals in RAS3, and would permit up to triple excitations out of RAS1 or into RAS3.

Table 1. Singlet-Triplet State−Energy Splittings (Kcal/Mol) Predicted at the CASSCF and CASPT2 Levels for Various Active Space Choices

	structure				
active space	**1a**	**1b**	**1c**	**2a**	**2b**
			CASSCF		
(2,2)	0.4	0.4	−4.5	1.8	2.1
(8,8)	−11.7	−13.1	−23.0	−10.7	−10.1
(10,10)	1.8	0.9	−8.8	3.2	3.6
(12,12)	0.8	1.1	−9.4	4.0	4.4
			CASPT2		
(2,2)	−0.1	0.4	−11.7	2.8	3.6
(8,8)	8.1	7.8	−3.9	9.7	10.7
(10,10)	2.5	1.8	−5.4	4.7	5.3
(12,12)	1.2	2.3	−3.1	5.2	6.0

Table 2. Number of Configuration State Functions and Dominant Weights for Various CASSCF Active Space Choices

		dominant CSF weights				
active space	no. CSFs	**1a**	**1b**	**1c**	**2a**	**2b**
(2,2)	3[a]	55/45[b]	51/49	79/21	56/44	54/46
	1	100	100	100	100	100
(8,8)	1 764	59/39	51/48	83/15	61/37	58/40
	2 352	99	99	98	98	98
(10,10)	19 404	59/39	51/47	85/12	57/41	55/43
	29 700	98	98	97	97	97
(12,12)	226 512	63/34	51/46	85/10	56/41	54/43
	382 239	97	97	97	96	96

[a] Singlet above triplet. [b] Singlet above triplet; the weights of the two dominant CSFs are reported in the former case, and the weight of the one dominant CSF in the latter case.

In all calculations, Cholesky decomposition[49,50] of the two electron integrals was accomplished with a threshold of 10^{-5} au. Reduced scaling evaluation of the Fock exchange matrices in the CASSCF and RASSCF calculations was accomplished by means of the local-K (LK) screening approach[51] employing localized Cholesky orbitals.[52]

M06-L calculations were done with MN-GFM,[53] a locally modified version of the Gaussian03 electronic structure program suite.[54] All CASSCF/CASPT2 and RASSCF/RASPT2 calculations were done with the MOLCAS 7.2 package.[42]

Results and Discussion

Singlet−Triplet State−Energy Splittings. We begin with an examination of the predicted singlet−triplet splittings at the CASSCF and RASSCF and the CASPT2 and RASPT2 levels, as a function of active space choice. Results from CASSCF and CASPT2 calculations are presented in Table 1.

A few trends merit discussion in the CASSCF/CASPT2 singlet−triplet splittings. First, at the CASSCF level, expanding the active space from (10,10) to (12,12) causes changes in the predicted splittings of 1 kcal/mol or less. At the CASPT2 level, the same change in active space size has an effect of roughly similar magnitude, with the exception of **1c** where it is a somewhat larger 2.3 kcal/mol. In addition, the change in the splitting going from the CASSCF level to the CASPT2 level is 0.4, 1.2, 6.3, 1.2, and 1.6 kcal/mol, respectively, for **1a**−**c** and **2a** and **b**. Dynamical correlation at the CASPT2 level favors the triplet state in every instance, but the change is small with the exception of **1c**, which continues to be somewhat of an outlier. All of these observations suggest that the CASPT2(12,12) values may be considered to be reasonably well converged (and, as noted in the Computational Details Section, expanding to (14,14) in select instances led to negligible changes in the predicted splittings). Thus, for future discussion purposes, we will consider the CASPT2(12,12) values to be reliable, with the possible exception of **1c**, where a larger uncertainty exists.

With respect to smaller active spaces, it is noteworthy that the very simple (2,2) space offers a reasonable accuracy in most instances, consistent with a fairly simple biradical description for the species under consideration. The exception is again **1c**, but, as can be judged by the occupation numbers of the frontier orbitals for this structure in Figure 1, it is the least biradicaloid of the five compounds considered here, so one would not expect the (2,2) active space to capture as much nondynamical correlation as in the other instances. The (8,8) space leads to very poor predictions at the CASSCF level because it is difficult to find any clear distinction between different (8,8) spaces based on occupation numbers (cf. Figure 2 for the case of **1a**, suggesting that either more or fewer orbitals leads to a better balance). Including additional correlation effects at the CASPT2 level moderates the poor balance of the (8,8) spaces to some extent, but results remain poor compared to CASPT2(12,12).

To put into a better perspective the efficiencies of different active spaces and the biradical characters of the singlet wave functions, we list in Table 2 the numbers of CSFs and the dominant CSF weights for different active space choices. As the numbers of CSFs in the (2,2) spaces are about 5 orders of magnitude fewer than in the (12,12) spaces, the reasonable accuracy of the (2,2) predictions is certainly noteworthy from an efficiency standpoint. Inspection of the CSF weights makes clear that all triplets are essentially single determinantal, while most singlets have very high biradical character (defined as having roughly equal weights of the two dominant configurations), with **1c** being the least biradical.

Turning next to the RASSCF and RASPT2 calculations, Table 3 lists the computed state−energy splittings for various RAS protocols, and Table 4 provides information on the numbers of CSFs and the weights of the dominant configurations associated with different active space choices. For convenience, in Table 3 the results from CASPT2(2,2) and CASPT2(12,12) calculations are recapitulated, and the same is true for CAS(12,12) in Table 4.

The first point to address is the very good performance of the RASPT2(12,12)/(2,2)/2 protocol. Compared to CASPT2-(12,12), all state−energy splittings are predicted to within a mean unsigned error of 0.8 kcal/mol and a maximum unsigned error of 1.1 kcal/mol. Note in particular, that this is a better accuracy than that of CASPT2(2,2), suggesting that the additional excitations considered in the RAS protocol are important. With respect to dynamical correlation energy, the difference between the RASPT2(12,12)/(2,2)/2 and RASSCF(12,12)/(2,2)/2 state−energy splittings is usually small (except for **1c**, it does not exceed 1.2 kcal/mol), but

Table 3. Singlet-Triplet State−Energy Splittings (kcal/mol) Predicted at the RASSCF and RASPT2 levels for Various Active Space Choices

	structure				
active space	**1a**	**1b**	**1c**	**2a**	**2b**
		RASSCF			
(12,12)/(2,2)/2	0.7	0.9	−7.7	3.4	3.8
(12,12)/(2,2)/3	0.8	1.0	−8.5	3.8	4.2
(12,12)/(2,2)/4	0.8	1.1	−9.2	3.9	4.4
(12,12)//2[a]	24.4	20.4	5.5	32.1	32.6
(12,12)//3[a]	11.7	12.2	−4.7	17.8	14.7
		RASPT2			
(12,12)/(2,2)/2	0.8	1.5	−2.6	4.1	5.0
(12,12)/(2,2)/3	0.8	1.9	−2.1	4.8	5.8
(12,12)/(2,2)/4	1.6	2.3	2.0	5.3	6.0
(12,12)//2[a]	22.9	25.6	5.3	25.8	25.4
(12,12)//3[a]	2.3	3.0	−5.9	17.5	9.4
		CASPT2			
(2,2)	−0.1	0.4	−11.7	2.8	3.6
(12,12)	1.2	2.3	−3.1	5.2	6.0

[a] The excitation level for the triplet state is formally one higher, since the generation of a triplet state from the starting set of six occupied RAS1 and six virtual RAS3 orbitals requires an initial single excitation.

Table 4. Number of Configuration State Functions and Dominant Weights for Various Rasscf Active Space Choices and Excitation Levels

			dominant	CSF	weights	
active space	no. CSFs	**1a**	**1b**	**1c**	**2a**	**2b**
(12,12)/(2,2)/2	2 028[a]	60/37[b]	51/46	84/13	56/41	54/43
	2 891	97	97	97	97	96
(12,12)/(2,2)/3	14 428	57/31	47/41	77/10	51/37	49/39
	22 991	88	88	87	87	87
(12,12)/(2,2)/4	54 678	62/33	51/44	84/9	55/40	53/42
	91 091	95	95	95	94	94
(12,12)//2[c]	703	90/−[d]	90/−[d]	89/6	82/15	84/13
	8 991	97	97	97	97	97
(12,12)//3[c]	6 003	66/15	67/13	65/31	59/22	56/24
	45 441	90	88	88	82	88
CAS(12,12)	226 512	63/34	51/46	85/10	56/41	54/43
	382 239	97	97	97	96	96

[a] Singlet above triplet. [b] Singlet above triplet; the weights of the two dominant CSFs are reported in the former case, and the weight of the one dominant CSF in the latter case. [c] The excitation level for the triplet state is formally one higher, since the generation of a triplet state from the starting set of six occupied RAS1 and six virtual RAS3 orbitals requires an initial single excitation. [d] No second singlet CSF has a weight of 5% or higher.

the RASPT2 model is in better agreement with CASPT2(12,12) in every instance, indicating the utility of the post-RASSCF PT2 calculation. Considering, as indicated in Table 4, that the number of CSFs is reduced by about 2 orders of magnitude on going from CASPT2(12,12) to RASPT2(12,12)/(2,2)/2, this is a particularly impressive level of accuracy.

As an additional measure of the importance of the orbital relaxation associated with RASSCF excitations outside the central (2,2) CAS space, we examined using the orbitals from a CASSCF(2,2) calculation as *frozen* orbitals for a subsequent RASPT2(12,12)/(2,2)/2 calculation. That is, we did *not* reoptimize any molecular orbital coefficients after the CAS(2,2) step but instead only optimized the configuration interaction coefficients in the RAS(12,12)/(2,2)/2 wave function that was used as the multiconfigurational reference for the PT2. Such a calculation is computationally very inexpensive. However, the results were essentially the same as those obtained at the CASPT2(2,2) level, indicating that orbital relaxations associated with the RAS outer space excitations do improve the agreement with CASPT2 calculations using larger active spaces.

Turning to the consideration of triple and quadruple excitations in the outer RAS spaces, changes in predicted state−energy splittings tend to be small but offer quantitative improvement in the agreement with CASPT2(12,12) values. At the RASPT2(12,12)/(2,2)/4 level, for which the number of CSFs is reduced by a factor somewhat larger than 4 compared to the CASPT2(12,12) level, the agreement averages within 0.1 kcal/mol for all structures other than **1c**. For this latter structure, higher RAS excitations lead to progressively worse agreement with CASPT2(12,12). As already noted above, this structure is the one case where the (12,12) active space may not represent a sufficiently large space to be considered converged, and thus, it may not be as meaningful to make a comparison for this least biradicaloid dioxo species. As a technical note, the current implementation of the RASPT2 model in MOLCAS is such that RASSCF convergence tends to be rapid when only double excitations are considered and slows down considerably when higher levels of excitations are allowed. While future development efforts will be targeted to improve the convergence in the latter instance, the excellent accuracy of the RASPT2(12,12)/(2,2)/2 model for the present test set bodes well for future applications to other analogous biradicaloid transition-metal oxo species.

A curious feature of the outer-space RAS excitations that merits further study is the degree to which dominant configuration weights are reduced when excitations are limited to no more than triples. As seen in Table 4, in every instance the dominant configuration weights drop by 3−10% at the RASSCF(12,12)/(2,2)/3 level compared to that of the RASSCF(12,12)/(2,2)/2 level. Of course, one might argue that as the number of possible CSFs increases to the full CI limit, one might naturally expect the weights of the individual configurations to drop somewhat, but on going to the RASSCF(12,12)/(2,2)/4 level, i.e., including quadruples, the weights return to very near the RASSCF(12,12)/(2,2)/2 values and are moreover almost identical to the CASSCF(12,12) values. Such oscillating behavior among the even and the odd levels of excitations is reminiscent of the convergence behavior of the correlation energy in the Møller−Plesset perturbation theory explored in detail by Olsen et al.[55,56] and also by Luna et al.[57] This last reference[57] deserves special attention since it focuses on the problem of poor convergence with second-order perturbation theory for ground-state Cu(I) complexes.

In order to study this point further, one would have to monitor CSF weights for still higher levels of excitation. For the present molecules, however, such calculations are prohibitively expensive. We will investigate this behavior for smaller test systems in the future.

We now consider an alternative protocol, which one might adapt in the absence of any knowledge of biradical character in the subject molecules. In particular, we examine RASPT2 protocols with a total of 12 electrons in 12 orbitals without any inner CAS(2,2) space, permitting up to double the excitations from the occupied to the virtual space. To be precise, it is the singlet state for which excitations up to double are allowed. For the triplet state, generation of a triplet wave function already requires a single excitation (with spin flip), so that the triplet-state calculations actually permit up to triple excitations in order to correspond properly with the singlet analogs. In any case, as shown in Table 3, the accuracy of the RASPT2(12,12)//2 approach is extremely poor, with errors as high as 23 kcal/mol. The direction of the errors indicates that the correlation energies predicted for the singlet states are considerably smaller than those for the triplet states. Inspection of the CSF weights (Table 4) indicates that the problem appears to be with the failure of the RAS(12,12)//2 protocol to adequately relax the orbitals such that the weight of a formally doubly excited configuration becomes fairly close to that of the reference configuration for the biradicaloid singlet states.

In addition to noting that this problem is least severe for **1c**, which is the least biradicaloid of all of the singlets, inspection of the absolute electronic energies further illustrates the importance of this point. Triplet **1a**, for example, has a predicted electronic energy at the CAS(2,2) level of −2 598.57346. At the RAS(12,12)/(2,2)/2 level, the corresponding energy is −2 598.73770, and at the RAS(12,12)//2, it is −2 598.73794; thus, the two are very close, as might be expected. For the singlet state, on the other hand, the CAS(2,2) electronic energy is −2 598.57290, and the RAS(12,12)/(2,2)/2 energy is −2 598.73662, but the RAS-(12,12)//2 energy is −2 598.69905, the final value being 37 mE_h more positive than the RAS(12,12)/(2,2)/2 reference. This failure to adequately rotate the most important occupied and virtual orbital(s) in the SCF procedure of the RAS(12,12)//2 calculations will merit further attention but suggests that strong nondynamical correlation effects should still be addressed with inner CASSCF spaces when possible.

The situation improves somewhat when the RASSCF excitation level is increased. Examining the state−energy splittings and the CSF weights for the RASPT2(12,12)//3 level, the former are in reasonable agreement with the CASPT2(12,12) results (except for **2a**) but are not as good as the state−energy splittings predicted at the RASPT2(12,12)/(2,2)/2 level, where fewer CSFs are required. Interestingly, the CSF weights are again depressed upon the inclusion of triple excitations; the amount of that depression for the most dominant CSF in the singlet is coincidentally about equal to the degree to which a single configurational character is overemphasized by the failure to include an interior CASSCF(2,2) space, but consideration of the minor singlet CSF or the dominant triplet CSF clearly illustrates the phenomenon. The trend on going from the RASPT2(12,12)//2 to the RASPT2(12,12)//3 level suggests that good results might be expected from the RASPT2(12,12)//4 level. However, the final level requires formal quintuple excitations to generate quadruply excited triplet states, and we were not successful in converging such calculations, which in any case require a number of CSFs so large that there is little point in not simply carrying out a full CASPT2 calculation.

Table 5. Triplet Energies (kcal/mol) of **1b** and **1c** Relative to **1a** and **2b** Relative to **2a** Computed at Various Levels of Theory

	structure		
theory	**1b**	**1c**	**2b**
	RASPT2		
(12,12)/(2,2)/2	3.9	−12.9	−0.1
(12,12)/(2,2)/3	4.3	−14.0	0.4
(12,12)/(2,2)/4	4.4	−13.3	0.1
(12,12)//2[a]	3.8	−13.4	0.0
(12,12)//3[a]	3.2	−15.1	−2.4
	CASPT2		
(2,2)	2.3	−12.6	1.3
(8,8)	4.2	−12.8	1.2
(10,10)	4.6	−13.6	1.1
(12,12)	4.7	−13.8	1.3
	DFT		
M06-L	1.9	4.4	−0.7

[a] The excitation level for the triplet state is formally one higher, since the generation of a triplet state from the starting set of six occupied RAS1 and six virtual RAS3 orbitals requires an initial single excitation.

Table 6. Singlet Energies (kcal/mol) of **1b** and **1c** relative to **1a** and **2b** relative to **2a** Computed at Various Levels of Theory

	structure		
theory	**1b**	**1c**	**2b**
	RASPT2		
(12,12)/(2,2)/2	4.7	−16.3	−0.9
(12,12)/(2,2)/3	5.4	−16.9	−0.6
(12,12)/(2,2)/4	5.0	−13.0	−0.6
(12,12)//2	6.6	−31.0	0.4
(12,12)//3	3.8	−23.3	5.8
	CASPT2		
(2,2)	2.9	−24.2	0.5
(8,8)	3.9	−24.8	0.1
(10,10)	3.8	−21.5	0.5
(12,12)	5.9	−18.0	0.4

Relative Energies of Different Isomers. In addition to state−energy splittings, we examined the differences in specific spin-state energies for the three dioxygen adducts and the two copper−oxo isomers. These results are presented in Table 5 for the triplet states and Table 6 for the singlet states. As we consider here only a single geometry for each species (see Computational Details Section) and as we have already noted the relative performances of the various models for singlet−triplet energy differences, in principle, the data in Table 6 should be evident from the consideration of Table 5 and the foregoing data, but it is helpful to see where errors cancel or reinforce the isomer energies.

For the triplet states, there is good convergence in the CASPT2 relative energies as the active space is increased from (2,2) to (12,12) in size. Moreover, all of the RASPT2 protocols are in fairly good agreement with the CASPT2(12,12) predictions, with the best agreement given by the RASPT2(12,12)/(2,2)/3 model (the results are very nearly as good at the RASPT2(12,12)/(2,2)/4 level). While this agreement suggests that the RASPT2 approaches are doing as good a job as CASPT2, the latter model itself may not be particularly accurate for the isomer energies. For comparison, we computed the M06-L relative energies for the same geometries, and these are also listed in Table 5. For the copper−oxo isomerization, the multireference models and M06-L are in fair agreement, while M06-L predicts the **1b**−**a** energy difference to be smaller by about 3 kcal/mol than computed at the multireference levels. Finally, there is a very large discrepancy between the two types of theory for the **1c**−**a** energy difference, with the multireference models predicting the side-on geometry to be much more stable than either end-on copper−oxygen complex and M06-L predicting the opposite.

As for which, if either, level of theory is more likely to be correct, various considerations suggest that the M06-L predictions are likely to be the more trustworthy, at least for the **1c**−**a** energy difference, where the discrepancy is largest. First, the triplets are all well described by single determinants in which instance DFT is generally quite robust for conformational analysis.[17] Second, consideration of a wide range of supported Cu(I)−dioxygen complexes suggests that the particular ligand set employed here would be more likely to favor an end-on coordination geometry to a side-on one.[6,7,16,58] Third, and perhaps most importantly, were **1c** to be as stable as it is predicted to be at the RASPT2 and CASPT2 levels, the activation energy associated with the subsequent decarboxylation step (Scheme 2) would be inconsistent with the experimental kinetics, where the M06-L prediction *is* consistent.[10] (A precise quantification of this point would require more attention to the optimization of the geometries for all relevant states, but the CASPT2/DFT discrepancy of 18.2 kcal/mol listed for **1c** in Table 5 seems well outside the range of energies that might be associated with minor geometric relaxations in the triplet states).

Thus, while we have established that the (12,12) active space is in all cases, with the possible exception of **1c**, adequate to compute converged state−energy splittings, it would appear that it is *not* adequate to compute isomer energies when the active space is not perfectly converged for all structures considered, with **1c** again being the most problematic case. The geometric differences between **2a** and **b** are small enough that even the (12,12) space seems adequate. It would be interesting to examine whether a full valence active space, using a RAS protocol, would give better results, but such calculations remain outside our present capabilities.

With respect to the relative singlet energies, most trends identified for the triplet states remain the same: RASPT2(12,12)/(2,2)/3 shows the best agreement with CASPT2(12,12) with the double and quadruple excitation levels being nearly as good. However, the RASPT2(12,12)//2 and //3 models are less consistent. They are surprisingly good for both **1b** and **2b**, considering that these levels do very poorly for state−energy splittings, suggesting that the failure to capture singlet correlation energy is quite consistent across geometric isomers. The exception is **1c**, where there is a greater sensitivity to the excitation level. In this case, we do not compare to M06-L, as the computation of biradical singlet energies with DFT presents its own set of complications that go beyond our interests in the present work.

Significance. We have compared the CASPT2 and RASPT2 models for the determination of the singlet−triplet state−energy splittings of five intermediates associated with the formation and the reaction of copper−oxo species derived from oxygenation of Cu(I)-α-ketocarboxylate complexes. Based on consideration of several active spaces, we determined that the CASPT2 model was well converged with a (12,12) active space, but that semiquantitative results could be obtained with a minimal (2,2) space in most instances. Certain intermediate active spaces failed to be balanced, e.g., no good (8,8) active space could be identified. At the RASPT2 level, results were quantitatively very accurate (compared to CASPT2(12,12)) when an inner (2,2) CAS space was included in a total (12,12) space. Including up to double excitations in the outer RAS spaces generated 2 orders of magnitude fewer configuration state functions than the full CASPT2(12,12) calculations but provided essentially equivalent accuracy. Adding additional excitations in the outer RAS spaces led to small but systematic improvements in accuracy.

RASPT2 calculations with a (12,12) space that did *not* include an inner (2,2) CAS space were less accurate in their predictions; such calculations suffer from the requirement that triplet states begin as single excitations (with spin flip) from the (12,12) starting configuration, so the number of triplet configuration state functions is artificially inflated when additional excitations are desired to be consistent with singlet state wave functions. While it was not possible to include a sufficient number of excitations with this approach to demonstrate convergence, the trend in going from singles and doubles to singles, doubles, and triples suggests that it *could* be an effective strategy if efficient SCF convergence schemes are developed.

Neither CASPT2 nor similar RASPT2 isomer energies were judged to be especially accurate with (12,12) active spaces. This may reflect a greater demand on active space size for the computation of geometric energy differences in transition-metal complexes, or it may be specific to the systems under consideration here. This issue deserves further study in systems where full-valence active spaces may be accessible.

Overall, the RASPT2 model, when applied with careful attention to the most critical features associated with possible nondynamical correlation, offers an efficient alternative to more demanding CASPT2 calculations with no loss in accuracy. These results seem particularly encouraging for the study of chemical systems having minimal balanced active spaces that are still so large that they are inaccessible to the conventional CASPT2 method.

Acknowledgment. This work was supported by the Swiss and the U.S. National Science Foundation (grants 200020-120007 and CHE-0610183, respectively). S.M.H. thanks the DAAD for a postdoctoral fellowship.

Supporting Information Available: Geometries of all structures together with electronic state energies from various levels of theory. This material is available free of charge via the Internet at http://pubs.acs.org.

References

(1) Solomon, E. I.; Baldwin, M. J.; Lowery, M. D. *Chem. Rev.* **1992**, *92*, 521–542.

(2) Mirica, L. M.; Ottenwaelder, X.; Stack, T. D. P. *Chem. Rev.* **2004**, *104* (2), 1013–1045.

(3) Lewis, E. A.; Tolman, W. B. *Chem. Rev.* **2004**, *104* (2), 1047–1076.

(4) Klinman, J. P. *J. Biol. Chem.* **2006**, *281*, 3013–3016.

(5) Hatcher, L. Q.; Karlin, K. D. *Adv. Inorg. Chem.* **2006**, *58*, 131–184.

(6) Itoh, S. *Curr. Opin. Chem. Biol.* **2006**, *10* (2), 115–122.

(7) Cramer, C. J.; Tolman, W. B. *Acc. Chem. Res.* **2007**, *40* (7), 601–608.

(8) Rolff, M.; Tuczek, F. *Angew. Chem., Int. Ed.* **2008**, *47* (13), 2344–2347.

(9) Gherman, B. F.; Cramer, C. J. *Coord. Chem. Rev.* **2009**, *253*, 723–753.

(10) Hong, S.; Huber, S. M.; Gagliardi, L.; Cramer, C. J.; Tolman, W. B. *J. Am. Chem. Soc.* **2007**, *129* (46), 14190–14192.

(11) Huber, S. M.; Ertem, M. Z.; Aquilante, F.; Gagliardi, L.; Tolman, W. B.; Cramer, C. J. *Chem. Eur. J.* **2009**, *15*, 4886–4895.

(12) Yamaguchi, K.; Takahara, Y.; Fueno, T. In *Applied Quantum Chemistry*; Smith, V. H., Schaefer, H. F., Morokuma, K., Eds. Kluwer: Dordrecht, The Netherlands, 1986; pp 155−184.

(13) Schroder, D.; Holthausen, M. C.; Schwarz, H. *J. Phys. Chem. B* **2004**, *108* (38), 14407–14416.

(14) Decker, A.; Solomon, E. I. *Curr. Opin. Chem. Biol.* **2005**, *9*, 152–163.

(15) Gherman, B. F.; Tolman, W. B.; Cramer, C. J. *J. Comput. Chem.* **2006**, *27* (16), 1950–1961.

(16) Cramer, C. J.; Gour, J. R.; Kinal, A.; Włoch, M.; Piecuch, P.; Moughal Shahi, A. R.; Gagliardi, L. *J. Phys. Chem. A* **2008**, *112* (16), 3754–3767.

(17) Cramer, C. J. *Essentials of Computational Chemistry: Theories and Models*, 2nd ed.; John Wiley & Sons: Chichester, U.K., 2004; pp 385−427.

(18) Heisenberg, W. *Z. Phys.* **1928**, *49*, 619.

(19) Dirac, P. A. M. *Proc. R. Soc. London, Ser. A* **1929**, *123*, 714.

(20) Van Vleck, J. H. *Rev. Mod. Phys.* **1945**, *17*, 27.

(21) Slater, J. C. *Rev. Mod. Phys.* **1953**, *25*, 199.

(22) Ziegler, T.; Rauk, A.; Baerends, E. J. *Theor. Chim. Acta* **1977**, *43*, 261–271.

(23) Noodleman, L. *J. Chem. Phys.* **1981**, *74* (10), 5737–5743.

(24) Yamaguchi, K.; Jensen, F.; Dorigo, A.; Houk, K. N. *Chem. Phys. Lett.* **1988**, *149*, 537–542.

(25) Soda, T.; Kitagawa, Y.; Onishi, T.; Takano, Y.; Shigeta, Y.; Nagao, H.; Yoshioka, Y.; Yamaguchi, K. *Chem. Phys. Lett.* **2000**, *319* (3−4), 223–230.

(26) Ciofini, I.; Daul, C. A. *Coord. Chem. Rev.* **2003**, *238*, 187–209.

(27) Neese, F. *Coord. Chem. Rev.* **2009**, *253*, 526–563.

(28) Harvey, J. N. *Struct. Bonding (Berlin)* **2004**, *112*, 151–183.

(29) Schmidt, M. W.; Gordon, M. S. *Annu. Rev. Phys. Chem.* **1998**, *49*, 233–266.

(30) Roos, B. O.; Taylor, P. R.; Siegbahn, P. E. M. *Chem. Phys.* **1980**, *48*, 157–173.

(31) Andersson, K.; Malmqvist, P.-Å.; Roos, B. O. *J. Chem. Phys.* **1992**, *96* (2), 1218–1226.

(32) Roos, B. O.; Malmqvist, P-Å. *Phys. Chem. Chem. Phys.* **2004**, *6*, 2919–2927.

(33) Azizi, Z.; Roos, B. O.; Veryazov, V. *Phys. Chem. Chem. Phys.* **2006**, *8* (23), 2727–2732.

(34) Gagliardi, L. *J. Am. Chem. Soc.* **2003**, *125*, 7504–7505.

(35) Gagliardi, L.; La Manna, G.; Roos, B. *Faraday Discuss.* **2003**, *124*, 63–68.

(36) Gagliardi, L.; Pyykkö, P. *Angew. Chem., Int. Ed.* **2004**, *43* (12), 1573–1576.

(37) Gagliardi, L.; Pyykkö, P.; Roos, B. O. *Phys. Chem. Chem. Phys.* **2005**, *7*, 2415–2417.

(38) Gagliardi, L.; Cramer, C. J. *Inorg. Chem.* **2006**, *45* (23), 9442–9447.

(39) Roos, B. O.; Gagliardi, L. *Inorg. Chem.* **2006**, *45*, 803–807.

(40) Roos, B. O.; Borin, A. C.; Gagliardi, L. *Angew. Chem., Int. Ed.* **2007**, *46* (9), 1469–1472.

(41) Gagliardi, L.; Roos, B. O. *Chem. Soc. Rev.* **2007**, *36*, 893–903.

(42) Karlström, G.; Lindh, R.; Malmqvist, P.-Å.; Roos, B. O.; Ryde, U.; Veryazov, V.; Widmark, P. O.; Cossi, M.; Schimmelpfennig, B.; Neogrady, P.; Seijo, L. *Comput. Matl. Sci.* **2003**, *28* (2), 222–239.

(43) Malmqvist, P. Å.; Pierloot, K.; Moughal; Shahi, A. R.; Cramer, C. J.; Gagliardi, L. *J. Chem. Phys.* **2008**, *128*, 204109.

(44) Zhao, Y.; Truhlar, D. G. *J. Chem. Phys.* **2006**, *125* (19), 194101.

(45) Dolg, M.; Wedig, U.; Stoll, H.; Preuss, H. *J. Chem. Phys.* **1987**, *86*, 866–872.

(46) Hehre, W. J.; Radom, L.; Schleyer, P. v. R.; Pople, J. A. *Ab Initio Molecular Orbital Theory*; John Wiley & Sons: New York, 1986.

(47) Pierloot, K.; Dumez, B.; Widmark, P.-O.; Roos, B. O. *Theor. Chim. Acta* **1995**, *90*, 87.

(48) Roos, B. O.; Lindh, R.; Malmqvist, P.-Å.; Veryazov, V.; Widmark, P.-O. *J. Phys. Chem. A* **2005**, *109*, 6575–6579.

(49) Aquilante, F.; Malmqvist, P.-A.; Pedersen, T. B.; Ghosh, A.; Roos, B. O. *J. Chem. Theor. Comput.* **2008**, *4*, 694–702.

(50) Aquilante, F.; Pedersen, T. B.; Lindh, R.; Roos, B. O.; de Meras, A. S.; Koch, H. *J. Chem. Phys.* **2008**, *129* (2), 024113−8.

(51) Aquilante, F.; Pedersen, T. B.; Lindh, R. *J. Chem. Phys.* **2007**, *126* (19), 194106–11.

(52) Aquilante, F.; Pedersen, T. B.; de Meras, A. S.; Koch, H. *J. Chem. Phys.* **2006**, *125* (17), 174101–7.

(53) Zhao, Y.; Truhlar, D. G. *MN-GFM*, Version 4.1; University of Minnesota: Minneapolis, MN, 2008.

(54) Frisch, M. J.; Trucks, G. W.; Schlegel, H. B.; Scuseria, G. E.; Robb, M. A.; Cheeseman, J. R.; Montgomery, J. A.; Vreven, T.; Kudin, K. N.; Burant, J. C.; Millam, J. M.; Iyengar, S. S.; Tomasi, J.; Barone, V.; Mennucci, B.; Cossi, M.; Scalmani, G.; Rega, N.; Petersson, G. A.; Nakatsuji, H.; Hada, M.; Ehara, M.; Toyota, K.; Fukuda, R.; Hasegawa, J.; Ishida, M.; Nakajima, T.; Honda, Y.; Kitao, O.; Nakai, H.; Klene, M.;

Li, X.; Knox, J. E.; Hratchian, H. P.; Cross, J. B.; Adamo, C.; Jaramillo, J.; Gomperts, R.; Stratmann, R. E.; Yazyev, O.; Austin, A. J.; Cammi, R.; Pomelli, C.; Ochterski, J. W.; Ayala, P. Y.; Morokuma, K.; Voth, G. A.; Salvador, P.; Dannenberg, J. J.; Zakrzewski, V. G.; Dapprich, S.; Daniels, A. D.; Strain, M. C.; Farkas, O.; Malick, D. K.; Rabuck, A. D.; Raghavachari, K.; Foresman, J. B.; Ortiz, J. V.; Cui, Q.; Baboul, A. G.; Clifford, S.; Cioslowski, J.; Stefanov, B. B.; Liu, G.; Liashenko, A.; Piskorz, P.; Komaromi, I.; Martin, R. L.; Fox, D. J.; Keith, T.; Al-Laham, M. A.; Peng, C. Y.; Nanayakkara, A.; Challacombe, M.; Gill, P. M. W.; Johnson, B.; Chen, W.; Wong, M. W.; Gonzalez, C.; Pople, J. A. *Gaussian 03, Revision D.01*. Gaussian, Inc.: Wallingford, CT, 2004.

(55) Olsen, J.; Christiansen, O.; Koch, H.; Jorgensen, P. *J. Chem. Phys.* **1996**, *105* (12), 5082–5090.

(56) Christiansen, O.; Olsen, J.; Jörgensen, P.; Koch, H.; Malmqvist, P-Å. *Chem. Phys. Lett.* **1996**, *261* (3), 369–378.

(57) Luna, A.; Alcamí, M.; Mó, O.; Yáñez, M. *Chem. Phys. Lett.* **2000**, *320* (1−2), 129–138.

(58) Maiti, D.; Fry, H. C.; Woertink, J. S.; Vance, M. A.; Solomon, E. I.; Karlin, K. D. *J. Am. Chem. Soc.* **2007**, *129* (2), 264–265.

CT900282M

J. Chem. Theory Comput. **2009,** *5,* 2977–2984

Journal of Chemical Theory and Computation

Universal Theoretical Approach to Extract Anisotropic Spin Hamiltonians

Rémi Maurice,*[,†,§] Roland Bastardis,[‡] Coen de Graaf,[§,⊥] Nicolas Suaud,[†]
Talal Mallah,[||] and Nathalie Guihéry*[,†]

Laboratoire de Chimie et Physique Quantiques, IRSAMC/UMR5626, Université de Toulouse III, 118 route de Narbonne, F-31062 Toulouse Cédex 4, France, Laboratoire de Mathématiques, Physiques et Systemes, Université de Perpignan Via Domitia, 52 Avenue Paul Alduy, 66860 Perpignan, France, Departament de Química Física i Inorganica, Universitat Rovira i Virgili, Marcel lí Domingo s/n, 43007 Tarragona, Spain, Institut de Chimie Moléculaire et des Matériaux d'Orsay, Université Paris sud 11, 91405 Orsay, France, and Institució Catalana de Recerca i Estudis Avançats (ICREA), Passeig Lluis Companys 23, 08010, Barcelona, Spain

Received June 27, 2009

Abstract: Monometallic Ni(II) and Co(II) complexes with large magnetic anisotropy are studied using correlated wave function based ab initio calculations. Based on the effective Hamiltonian theory, we propose a scheme to extract both the parameters of the zero-field splitting (ZFS) tensor and the magnetic anisotropy axes. Contrarily to the usual theoretical procedure of extraction, the method presented here determines the sign and the magnitude of the ZFS parameters in any circumstances. While the energy levels provide enough information to extract the ZFS parameters in Ni(II) complexes, additional information contained in the wave functions must be used to extract the ZFS parameters of Co(II) complexes. The effective Hamiltonian procedure also enables us to confirm the validity of the standard model Hamiltonian to produce the magnetic anisotropy of monometallic complexes. The calculated ZFS parameters are in good agreement with high-field, high-frequency electron paramagnetic resonance spectroscopy and frequency domain magnetic resonance spectroscopy data. A methodological analysis of the results shows that the ligand-to-metal charge transfer configurations must be introduced in the reference space to obtain quantitative agreement with the experimental estimates of the ZFS parameters.

1. Introduction

The recent interest for information storage at the molecular scale motivates both experimental and theoretical studies of molecules presenting a bistability. Among the different bistable chemical systems, single molecule magnets (SMMs)[1−5] are the smallest species that have been conceived. Their remarkable properties come from their intrinsic feature to present two high spin states of different magnetization $+M_S$ and $-M_S$ separated by an energy barrier. From a fundamental point of view, works on these systems have opened new perspectives in the study of quantum mechanics effects such as tunnelling, coherence, and interference. Magnetic anisotropy is responsible for both the existence of the energy barrier and the dominant factor of the tunnelling, and hence, it determines the magnetic behavior of these systems. A crucial landmark for chemistry, for technological devices as well as for fundamental investigations, would be the control and tuning of the magnetic anisotropy.

From a theoretical point of view, the understanding of the electronic and the structural factors governing the anisotropy

---

* Corresponding author. Telephone: +33561556488. E-mail: rmaurice@irsamc.ups-tlse.fr.

[†] Université de Toulouse III.

[§] Universitat Rovira i Virgili.

[‡] Université de Perpignan Via Domitia.

[⊥] Institució Catalana de Recerca i Estudis Avançats (ICREA).

[||] Université Paris.

10.1021/ct900326e CCC: $40.75

is of primary importance. The first attempts to calculate anisotropy parameters from first principles are less than 10 years old. Most of the studies concern one component density functional theory (DFT) based calculations with a perturbative inclusion of spin−orbit (SO) coupling (see the ORCA[6−11] and NRLMOL[12−16] code). Very recently, a two-component DFT method[17] has been implemented in the ReSpect code[18] and used to study the zero field splittings (ZFS) of several mononuclear complexes. For polynuclear systems, good agreement with experimental values was obtained using the NRLMOL method for the calculated D and E ZFS parameters of the Fe_4, Mn_{12}, and Mn_6-based SMMs.[19,20] Nevertheless, only the global ZFS parameters of the SMMs in its ground spin states (i.e., the parameters of the giant spin Hamiltonian) were accessible within the DFT scheme. The understanding and control of the property requires studying the local anisotropies of each metal ion and the anisotropies of their interactions. To extract such quantities, the multideterminantal descriptions are mandatory, and the excited spin states should be calculated. Wave function based calculations can provide this accurate description of the multideterminantal character of SMMs wave functions, but only few works dealt with the extraction of ZFS parameters using wave function based computational schemes. One can mention the pioneering work of Michl[21] involving a perturbative treatment of spin dependent terms and the work done by Ågren et al.[22] based on the linear response theory. Among the most popular methods, we quote the ones implemented in the ORCA[6] and MOLCAS[23] codes. Both codes provide accurate results on the mono- and polynuclear nuclear complexes.[7−11,24−28]

In the present paper, spin-orbit restricted active space state interaction (SO-RASSI) calculations on mononuclear species are performed in order to determine the energies and wave functions of the lowest electronic states. These solutions are then used to build and to calculate the matrix elements of the effective Hamiltonian that best fits the ab initio results. Since this Hamiltonian matrix can be compared to the commonly used model Hamiltonian matrix, the procedure provides a rational way to check (and eventually to improve) the ability of the phenomenological Hamiltonian to describe accurately the magnetic anisotropy. The same philosophy has been applied to many magnetic systems in order to measure the different contributions to the magnetic exchange integral[29,30] and to rationally parametrize t-J models,[31,32] double exchange models,[33−39] and spin Hamiltonians.[40] In all cases, the procedure has shown the validity and the application limits of the phenomenological Hamiltonians that are commonly used to interpret the experimental data or to understand the physics of the system under study. The comparison has led to different improvements of the model Hamiltonians, such as the inclusion of a priori neglected exchange interactions,[31] and the three- or four-body operators[41,42] that are crucial for the reproduction of the magnetic properties of the systems. Concerning the study of magnetic anisotropy, the effective Hamiltonian theory is particularly promising for polynuclear species given the uncertainties in the proper definition of the model Hamiltonian for these systems.[43−45] In this work, we use the effective Hamiltonian theory to extract the anisotropic spin Hamiltonian from the first principles for mononuclear species, laying in this way, the foundation for the study of the more complicated polynuclear systems. We show how the magnetic anisotropy axes can be determined, and that the rigorous computational extraction of the anisotropy parameters for the high spin d^7 configuration requires the construction of an effective Hamiltonian.

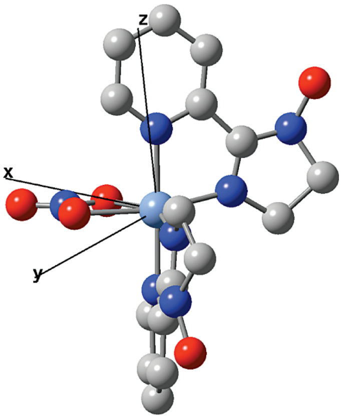

Figure 1. The $[Ni(HIM2-Py)_2NO_3]^+]$ complex (**1**) and its proper magnetic axes. The magnetic *z*-axis has an angle of 12.7° with the normal of the plane formed by Ni and by the NO_3^- ligand.

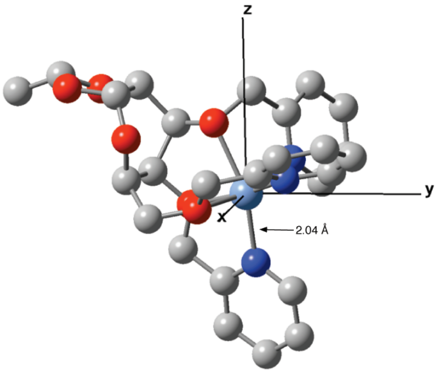

Figure 2. The $[Ni(glycoligand)]^{2+}]$ complex (**2**) and its proper magnetic axes. The magnetic *z*-axis has an angle of 9.5° with the 2.04 Å Ni−N bond.

2. Methodological Study

2.1. Description of the Compounds and Computational Information. Three Ni(II) complexes and one Co(II) complex were studied. $[Ni(HIM2-Py)_2 NO_3]^+$ (**1**, see Figure 1) and $[Ni(glycoligand)]^{2+}$ (**2**, see Figure 2) show a quasi-octahedral coordination of Ni(II), while $[Ni(i\text{Prtacn})Cl_2]$ (**3**, see Figure 3) has a pentacoordinated Ni(II) ion in an arrangement of the ligands that is intermediate between a trigonal bipyramid and a square pyramid. The geometries have been taken from crystallographic data and experimental information about the structure, high-field, high-frequency electron paramagnetic resonance (HF-HFEPR) and frequency domain magnetic resonance spectroscopy (FDMRS) data can be found in refs 46−48 for each compound, respectively. In order to reduce the computational cost for **1**, the CH_3 groups, which are geometrically distant from the metal ion, have been modeled

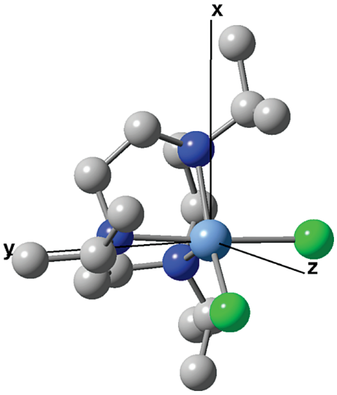

Figure 3. The [Ni(*i*Prtacn)Cl$_2$] complex (**3**) and its proper magnetic axes. The magnetic *z*-axis has an angle of 26.0° with the Cl−N−Cl plane.

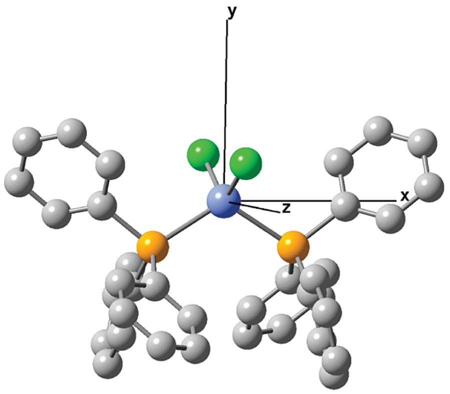

Figure 4. The [Co(PPh$_3$)$_2$Cl$_2$] (Ph = phenyl) complex (**4**) and its proper magnetic axes.

by H atoms. Owing to the local character of the ZFS property, this simplification should not affect the results. The local geometry of Co(II) in [Co(PPh$_3$)$_2$Cl$_2$][49,50] (**4**, see Figure 4), is a distorted tetrahedron.

The electronic structure of the complexes have been studied using the SO-RASSI method[51,52] implemented in MOLCAS 7. The scalar relativistic effects are included through the use of the Douglas−Kroll−Hess Hamiltonian,[53,54] and the SO effects are treated within the one-component formalism through the so-called spin-orbit state interaction (SO-SI) technique using the atomic mean-field approximation (AMFI). The method is a two-step procedure based on the idea that electron−correlation and SO effects are largely decoupled. The first step involves a complete active space self-consistent field (CASSCF) calculation to treat nondynamic correlations followed by the introduction of dynamic correlation effects through the evaluation of the single and double excitation contributions in a second-order perturbative manner (CASPT2). The second step calculates the SO interactions between the CASSCF states. The CASSCF diagonal elements of the so-obtained SO-SI matrix are substituted by the CASPT2 energies in order to take into account the main dynamic correlation effects.[55,56] In this method, the dipole-spin coupling is neglected. Contrarily to what was assumed for several decades, it has recently been shown that for Mn(III) complexes, the spin−spin part is not negligible for a quantitative description of the anisotropy.[22,10] In the considered Ni(II) and Co(II) complexes, the contribution of the SO interaction to the anisotropy is relatively important, and the number of unpaired electrons is small. Hence, the spin−spin part is expected to bring a minor contribution to the overall anisotropy.

Two different active spaces have been considered in the CASSCF calculations. The minimal active space has five TM-3d (TM = Ni,Co) orbitals and an extra set of five TM-d′ orbitals to accurately describe the radial electron correlation. This gives a CAS(8,10) and CAS(7,10) for the Ni- and Co-based compounds, respectively. The second, extended active space also includes some doubly occupied *σ* ligand−metal bonding orbitals. These orbitals essentially represent the nonbonding pairs of the atoms coordinated to the metal ion. Adding the orbitals with the strongest TM−ligand interaction leads to CAS(12,12) and CAS(13,13) for Ni- and Co-based compounds, respectively. Molecular orbitals have been optimized in an average way for all states belonging to a given spin multiplicity. The following all-electron ANO-RCC basis sets[57] are used: Ni and Co (6s 5p 4d 2f), Cl and P (5s 4p 1d), coordinated N (4s 3p 1d), other N (3s 2p 1d), O (4s 3p 1d), C (3s 2p), and H (2s).

The IP-EA shift has been set to zero for the nickel complexes since the states which are strongly coupled through the SO interaction are the lowest triplets, which have the same number of unpaired electrons, and to 0.25 for the cobalt one for which the excited doublets were suspected to play an important role. The minimal imaginary shift necessary in order to remove intruder states has been introduced in all cases (0.05 for **1** and **2**, 0.10 for **3,** and 0.20 au for **4**).

2.2. Dependence of the Zero-Field Splitting on the Computational Degrees of Freedom of the SO-RASSI Method. In addition to the usual computational degrees of freedom, such as the number of basis functions and the size of the active space, the outcomes of the SO-RASSI calculations also depend on the number of states included in the state interaction and the choice of the diagonal elements in the SO matrix: CASSCF or CASPT2 energies. To establish the precision of the SO-RASSI method, we explored these computational degrees of freedom in **1** and **4**. We concentrated on three aspects: (i) the number of excited states, which are included in the SO-SI space. Here a balance should be found between the computational cost of calculating many excited states and the influence of the matrix elements on the final result; (ii) The size of the active space, i.e. the effect of the inclusion of the ligand-to-metal charge transfer excitations in the CASSCF wave function affect the low-energy spectrum; and (iii) the comparison of the results using CASSCF or CASPT2 energies on the diagonal of the SO-SI matrix.

The dependence of the results to the number of states considered in the SO-SI calculations is studied for compounds **1** and **4**. The number of states has progressively been reduced starting from the complete TM-3d^n manifold to finally four states only. The selection of the states is based on an energy criterion, and states which are close in energy are removed from the SO-SI space simultaneously. In both cases, the smallest calculations (four states) couples the ground state with the first three excited states. These three states correspond to the three degenerate spatial components

Table 1. Energy Differences (in cm^{-1}) of the Spin−Orbit Splitted States Arising from the Fundamental Triplet State of **1** as Function of the Number of Spin−Orbit Coupled States[a]

		ΔE_1		ΔE_2	
number of states in SI	active space	CASSCF	CASPT2	CASSCF	CASPT2
10T, 14S	(8,10)	15.1	11.6	13.2	10.1
10T, 9S	(8,10)	17.1	14.2	14.5	11.7
7T, 2S	(8,10)	14.1	10.7	12.4	9.3
4T	(8,10)	14.8	13.0	13.0	11.3
4T	(12,12)	12.9	11.4	11.3	9.8
FDMRS[46]		10.3 ± 0.1		9.7 ± 0.1	

[a] $\Delta E_1 = E(|1,0\rangle) - E(|1,1\rangle - |1,-1\rangle)$ and $\Delta E_2 = E(|1,0\rangle) - E(|1,1\rangle + |1,-1\rangle)$. The number and spin multiplicity of the coupled states are indicated as *n*T(triplets) and *m*S(singlets).

Table 2. Energy Differences (in cm^{-1}) of the Spin−Orbit Splitted States Arising from the Fundamental Quartet State of **4** as Function of the Number of Spin−Orbit Coupled States[a]

		ΔE	
number of states in SI	active space	CASSCF	CASPT2
10Q, 40D	(7,10)	36.0	42.6
7Q	(7,10)	29.0	35.8
7Q	(13,13)	22.7	29.7
4Q	(7,10)	17.9	26.0
4Q	(13,13)	14.4	21.6
HF-HFEPR[49,50]		29.8	

[a] ΔE is the absolute value of $E(|3/2,\pm 3/2\rangle) - E(|3/2,\pm 1/2\rangle)$. The number and spin multiplicity of the coupled states are indicated as *n*Q (quartets) and *m*D (doublets).

of the first excited state in an ideal octahedral (Ni) or tetrahedral (Co) coordination. A further reduction of the SO-SI space is physically not grounded and has not been performed.

The d^8 configuration of the Ni(II) ion contains 25 spin free states, 10 triplets, and 15 singlets. Due to an intruder state problem, the CASPT2 energy of the highest singlet state could not be obtained with a high enough precision, hence 14 singlets have been considered in the SO calculation. Since this last singlet is very high in energy, its neglect is not expected to have any significant influence on the ZFS parameters. The Co(II)-d^7 configuration contains 10 quadruplets and 40 doublets. In this case, the energetic decomposition is not trivial since, except for the seven first quadruplet states which are well separated in energy from the others, all the other excited states are close in energy. We have, therefore, only compared the results obtained for the four and seven quadruplets and the complete collection of the 50 states of the configuration.

Table 1 compares the computed relative energies of the M_S components (or their combinations) of the ground state of **1** to the experimental ones for different SO-SI spaces. Table 2 lists the energy difference of the lowest two Kramers doublets for **4**. In all cases, the states are labelled using the main M_S components (or their combinations) appearing in the SO wave functions computed in the proper magnetic axes frame (the determination of this frame is discussed in Section 3). FDMRS transition energies are available for compound **1**, while the transition energy has been calculated from the ZFS parameters derived from the EPR data for **4**.

From the results reported in Tables 1 and 2, several conclusions can be inferred:

(i) In the Ni compounds, the lowest excited states of the same spin multiplicity as the ground state, i.e., the three lowest excited triplets, make the main contribution to ZFS. The analysis of the physical content of the wave functions of these SO excited states rationalizes their predominant role. They all result from a single electron replacement in the TM-3d orbitals with respect to the fundamental state. These excited states are, therefore, not only low in energy but also strongly coupled through SO coupling with the ground state. For the quasi-tetrahedrally coordinated Co complex, the SO-SI space cannot be restricted to the lowest four quartet states, which arise from the $^4A_2$ and $^4T_2$ states of the perfect tetrahedron. The three excited states arising from the $^4T_1$ state are so low in energy that they have a non-negligible interaction via the SO operator with the ground state, notwithstanding the marked contribution of the doubly excited configurations in the wave functions of these states.

(ii) At first sight, it may be surprising that the best agreement with experiment is obtained for the smaller SO-SI spaces (4T for **1** and 7Q for **4**), and that the inclusion of more states does not improve the result or even worsen it. However, the use of the state-average CASSCF orbitals to obtain the higher excited states affects the description of the lowest states. Indeed, in these averaged orbital sets, these states are less precisely described than in a set of orbitals optimized for the lowest states only. Hence, the precision that is gained by enlarging the SO-SI space is lost by the more approximate description of the lowest excited states. This is a limitation of the CASPT2/SO-SI methodology, enlarging the SI space does not guarantee a convergence of the results. Hence, we would recommend to optimize the orbitals in an average way for only those states that strongly interact through the SO coupling with the ground state.

(iii) Reasonable results can be obtained with a relatively small computational effort. Qualitative agreement with experiment is observed for the CASSCF wave functions and the energies calculated with the smaller active space, averaging for the lowest electronic states only. The incorporation of dynamic correlation effects (CASPT2) moderately modifies the obtained results. For a quantitative agreement with experiment, it is necessary to extend the active space to those ligand orbitals that have sizable tails on the metal center. This shows that the ligand-to-metal charge transfer (LMCT) configurations can play an important role in the magnetic anisotropy and should be variationally described. The active space should be chosen in such a way that it does not only include the radial electron correlation (smaller active space) but also the nondynamical correlation effects associated to the LMCT configurations.

3. Theory and Results

3.1. General Approach. The model spin Hamiltonian of a mononuclear anisotropic complex in the absence of a magnetic field is given by the following expression:

$$\hat{H}^{\mathrm{mod}} = \hat{S} \cdot \bar{\bar{D}} \cdot \hat{S} \tag{1}$$

where $\hat{S}$ is the spin operator, and $\bar{\bar{D}}$ is the second-order anisotropy tensor. For more than three unpaired electrons, even higher-order terms can be considered in the model Hamiltonian.[43] These higher-order terms will not be considered here since the complexes studied are limited to two or three unpaired electrons only. The projections of the lowest SO states onto the $|S,M_S\rangle$ states constitute the basis functions of the model space S_0 on which this model Hamiltonian is spanned. The SO coupling results in a mixing of the M_S components and, therefore, in a removal of their degeneracy. The procedure to extract the ZFS tensor, which is proposed here, uses the effective Hamiltonian theory.[58,59] This theory is based on the existence of a biunivocal relation between a model space S_0 and a target space S constituted of those eigenstates Ψ_i of the all-electron Hamiltonian that should be accurately reproduced by the model Hamiltonian. The effective Hamiltonian (which will be later compared to the model Hamiltonian) may be written as

$$\hat{H}^{\mathrm{eff}} = \sum_i |\tilde{\Psi}_i\rangle E_i \langle \tilde{\Psi}_i| \tag{2}$$

where $|\tilde{\Psi}_i\rangle$ are the orthogonalized projections of the $|\Psi_i\rangle$ states onto S_0, and E_i are their ab initio energies. The projections were orthogonalized by an $S^{-1/2}$ orthonormalization (where S is the overlap matrix) as proposed by des Cloizeaux.[59] This formalism guarantees that the eigenvalues of the model Hamiltonian are the eigenvalues of the all-electron Hamiltonian, and that its eigenfunctions are the orthogonalized projections $|\tilde{\Psi}_i\rangle$ of the eigenfunctions of the all-electron Hamiltonian onto the model space, such that:

$$\hat{H}^{\mathrm{eff}} |\tilde{\Psi}_i\rangle = E_i |\tilde{\Psi}_i\rangle \tag{3}$$

The norm of these projections provides a rational way to check the relevance of the model Hamiltonian to be extracted. If the norm of the projection is small, then important physics are missing in the model space, and one should reconsider the definition of the model Hamiltonian. Therefore, the method provides a rigorous and controlled way to extract the model Hamiltonian. Another advantage of the use of the effective Hamiltonian theory resides in the possibility to determine the principal axes of the ZFS tensor. Indeed, the expressions of both the eigenfunctions of the all-electron Hamiltonian and the matrix elements of the effective Hamiltonian defined in eq 2 depend on the axes frame. An identification of these terms with those of the analytical matrix of the model Hamiltonian expressed in the general case of a nondiagonal tensor leads to a complete determination of the $\bar{\bar{D}}$ components in an arbitrary frame. The proper magnetic axes are then determined from the diagonalization of the ZFS tensor. In comparison to the perturbative approach of calculating the ZFS tensor components, the effective Hamiltonian theory enables one to identify as high-order terms as required, since the interactions of the model Hamiltonian (and therefore its operators) are not guessed a priori. To recover the results of the effective Hamiltonian theory, one should expand the perturbation until an infinite order.

3.2. Extraction of the ZFS Parameters from the Effective Hamiltonian Theory.

The ZFS tensor is only diagonal in the magnetic anisotropy axes frame. In the following development, its matrix representation in an arbitrary frame will be denoted as

$$\mathbf{D} = \begin{pmatrix} D_{11} & D_{12} & D_{13} \\ D_{12} & D_{22} & D_{23} \\ D_{13} & D_{23} & D_{33} \end{pmatrix} \tag{4}$$

The elements of the analytical matrix of $\hat{H}^{\mathrm{mod}}$ (eq 1) are functions of the different components D_{ij}, including the extradiagonal elements of the ZFS tensor. Using $|1,-1\rangle$, $|1,0\rangle$, and $|1,1\rangle$ as basis functions, the matrix elements $\langle S,M_S|\hat{H}^{\mathrm{mod}}|S,M'_S\rangle$ for the high spin d^8 configuration are

$$\begin{array}{cccc} \hat{H}_{\mathrm{mod}} & |1,-1\rangle & |1,0\rangle & |1,1\rangle \\ \langle 1,-1| & \frac{1}{2}(D_{11}+D_{22})+D_{33} & -\frac{\sqrt{2}}{2}(D_{13}+iD_{23}) & \frac{1}{2}(D_{11}-D_{22}+2iD_{12}) \\ \langle 1,0| & -\frac{\sqrt{2}}{2}(D_{13}-iD_{23}) & D_{11}+D_{22} & \frac{\sqrt{2}}{2}(D_{13}+iD_{23}) \\ \langle 1,1| & \frac{1}{2}(D_{11}-D_{22}-2iD_{12}) & \frac{\sqrt{2}}{2}(D_{13}-iD_{23}) & \frac{1}{2}(D_{11}+D_{22})+D_{33} \end{array} \tag{5}$$

The next step is the construction of the effective Hamiltonian based on the ab initio calculations. We take here, as an example, the CAS(12,12)PT2 results of **1** with the 4T SO-SI space (one but last row in Table 1). The projections of the eigenfunctions all electron Hamiltonian on the model space at this level of calculation are

$$\begin{aligned} |\tilde{\Psi}_1\rangle &= (0.045 + 0.092i)|1,-1\rangle + (-0.668 + 0.724i)|1,0\rangle + \\ &\qquad (0.096 + 0.037i)|1,1\rangle \\ |\tilde{\Psi}_2\rangle &= (-0.395 + 0.578i)|1,-1\rangle + (0.062 + 0.088i)|1,0\rangle + \\ &\qquad (-0.678 + 0.173i)|1,1\rangle \\ |\tilde{\Psi}_3\rangle &= (0.701 + 0.026i)|1,-1\rangle + (-0.090 - 0.037i)|1,0\rangle + \\ &\qquad (-0.519 - 0.472i)|1,1\rangle \end{aligned}$$

Using these projections and the corresponding energy eigenvalues ($E_1 = 0.000$, $E_2 = 1.529$, $E_3 = 11.369\ \mathrm{cm}^{-1}$), the application of eq 2 leads to the following numerical effective Hamiltonian:

$$\begin{array}{cccc} & |1,-1\rangle & |1,0\rangle & |1,1\rangle \\ \langle 1,-1| & 6.386 & -0.690 + 0.376i & -3.734 + 3.134i \\ \langle 1,0| & -0.690 - 0.376i & 0.125 & 0.690 - 0.376i \\ \langle 1,1| & -3.734 - 3.134i & 0.690 + 0.376i & 6.386 \end{array} \tag{6}$$

Before calculating the ZFS tensor **D**, we observe that there is a perfect one-to-one correspondence of the matrix elements of the effective Hamiltonian derived from the ab initio calculations and those of the model Hamiltonian of eq 5. The effective Hamiltonian does not present extra interaction to those expected from the model Hamiltonian. Combined with the large norm of the projections, we conclude that the model Hamiltonian (eq 1) perfectly describes the ZFS in this case. The same behavior is found for the other Ni(II) compounds. The comparison of eqs 5 and 6 leads to six linear independent equations in terms of the D_{ij}, which determine uniquely the ZFS tensor. The full expression of the numerical effective Hamiltonians for **2** and **3** can be found in the

Supporting Information. From eqs 5 and 6 we derive the values of the **D** tensor of **1** in the original coordinates frame.

$$\mathbf{D} = \begin{pmatrix} -3.671 & 3.134 & 0.976 \\ 3.134 & 3.797 & -0.532 \\ 0.976 & -0.532 & 6.323 \end{pmatrix} \tag{7}$$

The **D** tensors for **2** and **3** are given in the Supporting Information. The diagonalization of **D** gives us the transformation matrix to rotate the coordinates frame such that the axes coincide with the magnetic one. These axes are indicated in the Figures 1−3 for the complexes studied here. Note that the orientation of the magnetic axes is almost independent of the computational degrees of freedom, unlike the energy differences between the lowest spin−orbit states, as shown in the previous section. Furthermore, it allows us to determine the commonly used ZFS parameters for the axial ($D = (3/2)D_{zz}$) and the rhombic ($E = (1/2)(D_{xx} - D_{yy}) > 0$) anisotropy. In the general case presented here, (Tr $\mathbf{D} \neq 0$), D and E can be derived from

$$\begin{aligned} D &= D_{33} - \frac{1}{2}(D_{11} + D_{22}) \\ E &= \frac{1}{2}(D_{11} - D_{22}) > 0 \end{aligned} \tag{8}$$

In practice, D_{33} is chosen as the diagonal element that maximizes the spacing with respect to the other two diagonal elements. D_{11} and D_{22} are identified by the convention that E is always positive. The resulting anisotropy parameters for **1**−**3** are listed in Table 3 and will be discussed in the next section.

For the Ni(II) complexes, the ZFS parameters can, of course, also be extracted from the spectrum only without going through the construction of the effective Hamiltonian. One should notice, however, that the magnetic anisotropy axes could not be determined, and that no information about the character of the wave functions can be used.

3.3. Extraction of ZFS Parameters for the d^7 Configuration. Spin−orbit interaction splits the quartet ground state of the high spin d^7 configuration into two Kramers doublets. Hence, the information from the spectrum is obviously not enough to determine the ZFS parameters D and E. It is not even possible to determine the sign of the axial anisotropy, except for the case when the magnetic axes are known and the wave function is available. This is, however, generally not the case, and the construction of an effective Hamiltonian is the preferred route toward a full description of the ZFS. Following the previously outlined procedure, we first calculate the matrix elements of the model Hamiltonian in the $|S,M_S\rangle$ basis for the d^7 configuration:

$$\begin{array}{ccccc} \hat{H}_{\text{mod}} & \left|\frac{3}{2},-\frac{3}{2}\right\rangle & \left|\frac{3}{2}-\frac{1}{2}\right\rangle & \left|\frac{3}{2},\frac{1}{2}\right\rangle & \left|\frac{3}{2},\frac{3}{2}\right\rangle \\ \left\langle\frac{3}{2},-\frac{3}{2}\right| & \frac{3}{4}(D_{11}+D_{22})+\frac{9}{4}D_{33} & -\sqrt{3}(D_{13}+iD_{23}) & \frac{\sqrt{3}}{2}(D_{11}-D_{22}+2iD_{12}) & 0 \\ \left\langle\frac{3}{2},-\frac{1}{2}\right| & -\sqrt{3}(D_{13}-iD_{23}) & \frac{7}{4}(D_{11}+D_{22})+\frac{1}{4}D_{33} & 0 & \frac{\sqrt{3}}{2}(D_{11}-D_{22}+2iD_{12}) \\ \left\langle\frac{3}{2},\frac{1}{2}\right| & \frac{\sqrt{3}}{2}(D_{11}-D_{22}-2iD_{12}) & 0 & \frac{7}{4}(D_{11}+D_{22})+\frac{1}{4}D_{33} & \sqrt{3}(D_{13}+iD_{23}) \\ \left\langle\frac{3}{2},\frac{3}{2}\right| & 0 & \frac{\sqrt{3}}{2}(D_{11}-D_{22}-2iD_{12}) & \sqrt{3}(D_{13}-iD_{23}) & \frac{3}{4}(D_{11}+D_{22})+\frac{9}{4}D_{33} \end{array} \tag{9}$$

Subsequently, the effective Hamiltonian is constructed from the ab initio energies and wave functions. The numerical expression of this Hamiltonian can be found in the Supporting Information. We note again that the model Hamiltonian perfectly fits the effective Hamiltonian, and hence, the full **D** tensor can be extracted. The magnetic axes are shown in Figure 4, and the ZFS parameters are listed in Table 3. The appearance of off-diagonal terms in the effective Hamiltonian suggests that the eigenfunctions can have contributions from determinants with different M_S values. This implies that M_S is not a good quantum number anymore. Nevertheless, the off-diagonal terms that cause the interaction between the determinants with different M_S values are strictly zero in the proper magnetic frame under the condition of no rhombic distortion. In the case of **4**, the rhombic distortions are small ($E/|D| = 0.08$), and the wave functions that describe the four lowest states have almost pure $M_S = \pm 1/2$ or $M_S = \pm 3/2$ character.

3.4. Magneto-Structural Relations for *D* and *E*. Table 3 compares the calculated anisotropy parameters with the experimental values of these parameters extracted from HF-HFEPR data.[46−49] While the agreement with experiment is excellent for **1**, **3**, and **4**, the calculated D-value for **2** deviates by approximately 4 cm^{-1}. The smallness of the anisotropy of this complex may be the origin of the difference between theory and experiment. The SO-SI methodology may have reached its numerical precision for this complex. This is subject to further study on other complexes with small anisotropy.

A less equally important question is whether it can be established why **1** has a large negative D, **2** a very small D, and **3** a large positive D. For this purpose, we study the effect of different distortions on the anisotropy in the three Ni(II) complexes using CASSCF energies and the 4T SO-SI space. The starting point for the decomposition is the isotropic, perfect octahedron of the model compound [Ni(NCH)$_6$]$^{2+}$. The first coordination sphere of complex **1** shows two major distortions in the *xy*-plane. The first distortion is a cis elongation, and the second is an angular distortion in which one N−Ni−N angle increases to

Table 3. SO-SI Axial and Rhombic Anisotropy Parameters *D* and *E* (in cm^{-1}) for Three Ni(II) Complexes (**1**−**3**) and One Co(II) Complex (**4**)[a]

complex	SO-SI *D*	SO-SI *E*	exptl *D*	exptl *E*
1	−10.60	0.76	−10.15	0.10
2	8.10	0.58	4.40	0.75
3	16.45	3.82	15.70	3.40
4	−14.86	0.54	−14.76	1.14

[a] Calculations were performed with the extended CAS and the 4T or 7Q SO-SI space for **1**−**3** and **4**, respectively. The energies of the spin-free states are calculated with CASPT2.

100° and the opposite angle reduces to 60°. Other smaller distortions complete the route from perfect octahedron to real geometry. The subsequent application of these three distortions gives $D = +0.2\ \text{cm}^{-1}$ (*xy*-plane elongation), $D = -4.9\ \text{cm}^{-1}$ (after adding the angular distortion), and $D = -9.6\ \text{cm}^{-1}$ for the complete distortion. Hence, the largest effect on the anisotropy is found to be the *xy*-plane angular distortion, while the combination of the smaller angular distortions significantly enhances the *D* parameter.

The geometry of **2** is close to octahedral, showing an elongation along the positive *z*-axis and an angular distortion of both axial ligands in cis mode. Applying these distortions on the model complex gives $D = +3.0\ \text{cm}^{-1}$ for the elongation and $D = -4.5\ \text{cm}^{-1}$ for the axial distortion. The application of both distortions simultaneously gives $D = +6.1\ \text{cm}^{-1}$, close to the value calculated for the real complex.

Complex **3** is pentacoordinated. Hence, the first obvious distortion is the removal of one of the ligands from the model complex. The resulting square pyramid leads to a large positive *D* of $+16.3\ \text{cm}^{-1}$, while the trigonal bypiramid leads to a first-order angular momentum in the ground state, and the model Hamiltonian, which only contains spin operators, no longer applies. On the way to the real geometry, we apply an elongation of two equatorial cis ligands on the square pyramid, reducing the *D*-value to $+11.2\ \text{cm}^{-1}$. The next distortion that should be applied is an angular out-of-plane distortion of 60° from one the equatorial ligands. This causes, again, a near degeneracy and an appearance of a first-order angular momentum. Alternatively, we constructed a $[\text{Ni(NCH)}_5]^{2+}$ model with the same geometry as the first coordination sphere as the real complex **3**. This resulted in a *D*-value of $+24.4\ \text{cm}^{-1}$. After replacing two NCH groups by Cl ligands, as in the real complex, *D* further increases to $+27.7\ \text{cm}^{-1}$. The only remaining difference with the real complex is the replacement of the three NCH ligands with *i*Prtacn, which reduces the anisotropy to $D = +20\ \text{cm}^{-1}$. This demonstrates the important interplay between the geometry and the σ-donating character of the ligands in the anisotropy of the complex, whose character is mainly determined by its resemblance to the square pyramid.

4. Conclusions

From the wave functions and the energies of the all-electron Hamiltonian, effective Hamiltonian theory rigorously determines the anisotropic spin Hamiltonian of anisotropic monometallic compounds. The method gives access to all the components of the ZFS tensor and, therefore, leads to the extraction of both the axial *D* and the rhombic *E* anisotropy parameters and to the proper magnetic axes frame.

The advantages of the proposed method of extraction are most obvious for the high spin Co(II) compound for which the anisotropy parameters cannot be extracted from the relative energies of the lowest spin−orbit states.

The extracted *D* and *E* parameters are in good agreement with the HF-HFEPR data for large magnetic parameters, establishing the precision of the SO-SI method to describe single-ion anisotropy. The main conclusions of the methodological study are that the best results are obtained with wave functions and energies obtained from an enlarged active space that includes ligand orbitals.

Finally, the effective Hamiltonian theory permits the accuracy of the model Hamiltonian to reproduce the physics of the studied systems to be checked. In the present case, the validity of the usual Hamiltonian is confirmed for the d^7 and the d^8 configurations of monometallic complexes. The procedure is now being applied to other d^n configurations and to polymetallic systems in order to extract the interactions of both multispin and giant spin Hamiltonians.

Acknowledgment. We thank Carmen J. Calzado for providing us the basis for the effective Hamiltonian program. Financial support has been provided by the Spanish Ministry of Science and Innovation (Project CTQ2008-06644-C02-01) and the Generalitat de Catalunya (Project 2009SGR462 and Xarxa d'R+D+I en Química Teorica i Computacional, XRQTC). This work was supported by the French Centre National de la Recherche Scientifique (CNRS), Université de Toulouse.

Supporting Information Available: Numerical expression of the effective Hamiltonians for **1**, **2**, and **4**, **D**-tensors for **2**, **3**, and **4**, and orthogonalized projections of the ab initio wave function of **1** on the model space. This material is available free of charge via the Internet at http://pubs.acs.org.

References

(1) Caneschi, A.; Gatteschi, D.; Sessoli, R.; Barra, A. L.; Brunel, L. C.; Guillot, M. *J. Am. Chem. Soc.* **1991**, *113*, 5873.

(2) Friedman, J. R.; Sarachik, M. P.; Tejada, J.; Ziolo, R. *Phys. Rev. Lett.* **1996**, *76*, 3830.

(3) Thomas, C.; Lionti, F.; Ballou, R.; Gatteschi, D.; Sessoli, R.; Barbara, B. *Nature* **1996**, *383*, 145.

(4) Gatteschi, D.; Sessoli, R. *Angew. Chem., Int. Ed.* **2003**, *42*, 246.

(5) Gatteschi, D.; Sessoli R.; Villain J. *Molecular Nanomagnets*; Oxford University Press: Oxford, U.K., 2006.

(6) Neese, F. *ORCA*, Version 2.6; an ab initio, density functional and semiempirical program package; University of Bonn: Bonn, Germany, 2008.

(7) Sinnecker, S.; Neese, F.; Noodleman, L.; Lubitz, W. *J. Am. Chem. Soc.* **2004**, *126*, 2613.

(8) Neese, F.; Solomon, E. I. *Inorg. Chem.* **1998**, *37*, 6568.

(9) Ganyushin, D.; Neese, F. *J. Chem. Phys.* **2006**, *125*, 024103.

(10) Neese, F. *J. Am. Chem. Soc.* **2006**, *128*, 10213.

(11) Neese, F. *J. Chem. Phys.* **2007**, *127*, 164112.

(12) Pederson, M. R.; Khanna, S. N. *Phys. Rev. B: Condens. Matter* **1999**, *60*, 9566.

(13) Kortus, J.; Pederson, M. R.; Baruah, T.; Bernstein, N.; Hellberg, C. S. *Polyhedron* **2003**, *22*, 1871.

(14) Postnikov, A. V.; Kortus, J.; Pederson, M. R. *Phys. Status Solidi B* **2006**, *128*, 9497.

(15) Jackson, K. A.; Pederson, M. R. *Phys. Rev. B: Condens. Matter* **1990**, *42*, 3276.

(16) Pederson, M. R.; Jackson, K. A. *Phys. Rev. B: Condens. Matter* **1990**, *41*, 7453 (see also: http://cst-www.nrl.navy.mil/users/nrlmol).

(17) Reviakine, R.; Arbuznikov, A.; Tremblay, J. C.; Remenyi, C.; Malkina, O.; Malkin, V. G.; Kaupp, M. *J. Phys. Chem.* **2006**, *125*, 054110.

(18) Malkin, V. G.; Malkina, O. L.; Reviakine, R. *RESPECT Program*, Version 2.1, 2005. The property part of the code (MAG-ReSpect) is freely available as binary for LINUX PCs from the authors (vladimir.malkin@savba.sk).

(19) Ruiz, E.; Cirera, J.; Cano, J.; Alvarez, S.; Loose, C.; Kortus, J. *Chem. Commun.* **2008**, *1*, 52.

(20) Loose, C.; Ruiz, E.; Kersting, B.; Kortus, J. *Chem. Phys. Lett.* **2008**, *452*, 38.

(21) Havlas, Z.; Downing, J. W.; Michl, J. *J. Phys. Chem. A* **1998**, *102*, 5681.

(22) Engström, M.; Vahtras, O.; Ågren, H. *Chem. Phys. Lett.* **2000**, *328*, 483.

(23) Karlström, G.; Lindh, R.; Malmqvist, P.-Å.; Roos, B. O.; Ryde, U.; Veryazov, V.; Widmark, P.-O.; Cossi, M.; Schimmelpfennig, B.; Neogrady, P.; Seijo, L. *Comput. Mater. Sci.* **2003**, *28*, 222.

(24) Chibotaru, L.; Ungur, L.; Soncini, A. *Angew. Chem., Int. Ed.* **2008**, *120*, 4194.

(25) Petit, S.; Pilet, G.; Luneau, D.; Chibotaru, L. F.; Ungur, L. *Dalton Trans.* **2007**, 4582.

(26) Soncini, A.; Chibotaru, L. F. *Phys. Rev. B: Condens. Matter* **2008**, *77*, 220406.

(27) Chibotaru, L. F.; Ungur, L.; Aronica, C.; Elmoll, H.; Pilet, G.; Luneau, D. *J. Am. Chem. Soc.* **2008**, *130*, 12445.

(28) Sousa, C.; de Graaf, C. *Int. J. Quantum Chem.* **2006**, *106*, 2470.

(29) Calzado, C. J.; Cabrero, J.; Malrieu, J. P.; Caballol, R. *J. Chem. Phys.* **2002**, *116*, 2728.

(30) Calzado, C. J.; Cabrero, J.; Malrieu, J. P.; Caballol, R. *J. Chem. Phys.* **2002**, *116*, 3985.

(31) Calzado, C. J.; Malrieu, J. P. *Phys. Rev. B: Condens. Matter* **2001**, *63*, 214520.

(32) Bordas, E.; de Graaf, C.; Caballol, R.; Calzado, C. J. *Phys. Rev. B: Condens. Matter* **2005**, *71*, 045108.

(33) Guihéry, N.; Malrieu, J. P. *J. Chem. Phys.* **2003**, *119*, 8956.

(34) Taratiel, D.; Guihéry, N. *J. Chem. Phys.* **2004**, *121*, 7127.

(35) Bastardis, R.; Guihéry, N.; de Graaf, C. *Phys. Rev. B: Condens. Matter* **2006**, *74*, 014432.

(36) Guihéry, N. *Theor. Chem. Acc.* **2006**, *116*, 576.

(37) Bastardis, R.; Guihéry, N.; Suaud, N.; de Graaf, C. *J. Chem. Phys.* **2006**, *125*, 194708.

(38) Bastardis, R.; Guihéry, N.; Suaud, N. *Phys. Rev. B: Condens. Matter* **2007**, *75*, 132403.

(39) Bastardis, R.; Guihéry, N.; de Graaf, C. *Phys. Rev. B: Condens. Matter* **2008**, *77*, 054426.

(40) de P. R. Moreira, I.; Suaud, N.; Guihéry, N.; Malrieu, J. P.; Caballol, R.; Bofill, J. M.; Illas, F. *Phys. Rev. B: Condens. Matter* **2002**, *66*, 134430.

(41) Bastardis, R.; Guihéry, N.; de Graaf, C. *Phys. Rev. B: Condens. Matter* **2007**, *76*, 132412.

(42) Calzado, C. J.; de Graaf, C.; Bordas, E.; Caballol, R.; Malrieu, J. P. *Phys. Rev. B: Condens. Matter* **2003**, *67*, 132409.

(43) Boča, R. *Theoretical Foundations of Molecular Magnetism*; Elsevier: Amsterdam, The Netherlands, 1999, 642−680.

(44) Boča, R. *Coord. Chem. Rev.* **2004**, *248*, 757.

(45) Park, K. N.; Pederson, M. R.; Richardson, S. L.; Aliaga-Alcalde, N.; Christou, G. *Phys. Rev. B: Condens. Matter* **2003**, *68*, 020405.

(46) Rogez, G.; Rebilly, J. N.; Barra, A. L.; Sorace, L.; Blondin, G.; Kirchner, N.; Duran, M.; Van Slageren, J.; Parsons, S.; Ricard, L.; Marvilliers, A.; Mallah, T. *Angew. Chem., Int. Ed.* **2005**, *44*, 1876.

(47) Charron, G.; Bellot, F.; Cisnetti, F.; Pelosi, G.; Rebilly, J. N.; Riviere, E.; Barra, A. L.; Mallah, T.; Policar, C. *Chem. Eur. J.* **2007**, *13*, 2774.

(48) Rebilly, J. N.; Charron, G.; Riviere, E.; Guillot, R.; Barra, A. L.; Serrano, M. D.; Van Slageren, J.; Mallah, T. *Chem. Eur. J.* **2008**, *14*, 1169.

(49) Krzystek, J.; Zvyagin, S. A.; Ozarowski, A.; Fiedler, A. T.; Brunold, T. C.; Tesler, J. *J. Am. Chem. Soc.* **2004**, *126*, 2148.

(50) Carlin, R. L.; Chirico, R. D.; Sinn, E.; Mennenga, G.; de Jongh, L. J. *Inorg. Chem.* **1982**, *21*, 2218.

(51) Malmqvist, P.-Å.; Roos, B. O. *Chem. Phys. Lett.* **1989**, *155*, 189.

(52) Malmqvist, P.-Å.; Roos, B. O.; Schimmelpfennig, B. *Chem. Phys. Lett.* **2002**, *357*, 230.

(53) Douglas, N.; Kroll, N. M. *Ann. Phys.* **1974**, *82*, 89.

(54) Hess, B. *Phys. Rev. A: At., Mol., Opt. Phys.* **1986**, *33*, 3742.

(55) Llusar, R.; Casarrubios, M.; Barandiarán, Z.; Seijo, L. *J. Chem. Phys.* **1996**, *105*, 5321.

(56) Baradiarán, Z.; Seijo, L. *J. Chem. Phys.* **2003**, *118*, 7439.

(57) Roos, B. O.; Lindh, R.; -Å.; Malmqvist, P.; Veryazov, V.; Widmark, P. O. *J. Phys. Chem. A* **2005**, *109*, 6575.

(58) Bloch, C. *Nucl. Phys.* **1958**, *6*, 329.

(59) des Cloizeaux, J. *Nucl. Phys.* **1960**, *20*, 321.

CT900326E

JCTC Journal of Chemical Theory and Computation

Coupled-Perturbed Scheme for the Calculation of Electronic g-Tensors with Local Hybrid Functionals

Alexei V. Arbuznikov* and Martin Kaupp*

Institut für Anorganische Chemie, Universität Würzburg,
Am Hubland, D-97074 Würzburg, Germany

Received July 28, 2009

Abstract: A coupled-perturbed Kohn−Sham (CPKS) scheme for calculating second-order magnetic properties has been developed for the case of general occupied-orbital-dependent (OOD) exchange-correlation functionals involving the exact-exchange energy density. The origin of the coupling terms in the functional derivatives of OOD functionals with respect to the orbitals has been thoroughly analyzed, and general expressions for the resulting coupling terms have been obtained. The generalized CPKS scheme thus obtained has been implemented within the MAG-ReSpect code and tested in calculations of electronic g-tensors with local hybrid functionals. Compared to previously tested global hybrids, like B3LYP, thermochemically optimized local hybrids provide only little to moderate improvement for test sets of main-group radicals and paramagnetic transition-metal complexes. Closer analyses point to possible areas in which the fundamentally more flexible local hybrids may be improved for the property at hand.

1. Introduction

Accurate prediction of magnetic resonance (MR) parameters is an important field of modern quantum chemistry. Examples include electronic g-tensors, hyperfine coupling tensors or zero-field splittings in electron paramagnetic resonance (EPR), and chemical shifts or spin-spin coupling constants in nuclear magnetic resonance (NMR). The past 20 years have seen tremendous success of new computational methods based on both post-Hartree−Fock methods (multiconfiguration SCF, many-body perturbation theory, coupled cluster, etc.) and Kohn−Sham (KS) density functional theory (DFT).[1] The advantage of DFT is its often an excellent compromise between the accuracy and the computational efficiency for larger systems. The underlying exchange-correlation (xc) functional is known to be the principal factor determining the accuracy of a DFT calculation. A particular place is occupied by the so-called hybrid xc functionals first introduced by Becke,[2,3] which include a constant, fractional admixture of the exact-exchange (EXX) energy:

$$E_{\mathrm{xc}}^{\mathrm{hybr}} = a_0 E_{\mathrm{x}}^{\mathrm{exact}}[\{\varphi_k\}_k^{\mathrm{occ}}] + \tilde{E}_{\mathrm{xc}}^{\mathrm{DFT}}[\rho, \nabla\rho, ...], 0 \le a_0 \le 1 \tag{1}$$

where

$$E_{\mathrm{x}}^{\mathrm{exact}} = -\frac{1}{2}\sum_{\sigma=\alpha,\beta}\sum_{j_\sigma,k_\sigma}^{\mathrm{occ}}\int\int\frac{\varphi_{j_\sigma}^*(\mathbf{r})\varphi_{k_\sigma}^*(\mathbf{r}')\varphi_{j_\sigma}(\mathbf{r}')\varphi_{k_\sigma}(\mathbf{r})}{|\mathbf{r}-\mathbf{r}'|}\mathrm{d}\mathbf{r}\mathrm{d}\mathbf{r}' \tag{2}$$

and $\tilde{E}_{\mathrm{xc}}^{\mathrm{DFT}}[\rho,\nabla\rho, ...]$ is some "conventional" density functional contribution based, for instance, on the local (spin) density approximation (LDA, LSDA),[4−7] the generalized gradient approximation (GGA),[8−12] or the meta-GGA:[13,14]

$$\tilde{E}_{\mathrm{xc}}^{\mathrm{DFT}} = \int \tilde{\varepsilon}_{\mathrm{xc}}^{\mathrm{DFT}}[\rho(\mathbf{r}), \nabla\rho(\mathbf{r}), ...]\mathrm{d}\mathbf{r} \tag{3}$$

These *global* hybrid functionals have been very successful for various properties (in particular also for MR parameters[1,15]). However, a number of limitations associated with global hybrids are known. In particular, it is usually not possible to find a unique constant a_0 for the EXX admixture to obtain optimum accuracy for different properties as well as for different systems. For example, accurate prediction of the atomization energies requires relatively modest EXX admixtures of about 0.16−0.30. Larger values are required,

---

* Corresponding authors. Fax: +49-931-31-8-7135. E-mail: arbouznikov@mail.uni-wuerzburg.de and kaupp@mail.uni-wuerzburg.de.

10.1021/ct900392e CCC: $40.75

e.g., for reaction barriers.[16] Similar divergences are known for many properties.[15,17−20] For example, GGA functionals without EXX admixture provide accurate main group g-tensors,[21] whereas relatively large EXX admixtures are required for accurate g-tensors of transition-metal complexes.[17,18] There is, thus, clearly a need for improved exchange-correlation functionals not exclusively but also for MR parameters. A new class of functionals that has shown promise for thermochemistry and for reaction barriers (and for nuclear shieldings within an approximate optimized effective potential (OEP) scheme)[22] are so-called local hybrid functionals.[23−32] In contrast to the constant EXX admixture of global hybrids, eq 1, local hybrids include EXX in a position-dependent way, governed by a "local mixing function" (LMF), γ:

$$E_{\mathrm{xc}}^{\text{loc-hybr}} = \sum_{\sigma=\alpha,\beta} \int \{\gamma_{\sigma}(\mathbf{r})\varepsilon_{\mathrm{x},\sigma}^{\mathrm{exact}}(\mathbf{r}) + [1 - \gamma_{\sigma}(\mathbf{r})]\varepsilon_{\mathrm{x},\sigma}^{\mathrm{DFT}}(\mathbf{r})\}\mathrm{d}\mathbf{r} + E_{\mathrm{c}}^{\mathrm{DFT}} \qquad (4)$$

where $\varepsilon_{\mathrm{x},\sigma}^{\mathrm{exact}}$ is the exact-exchange energy density:

$$\varepsilon_{\mathrm{x},\sigma}^{\mathrm{exact}}(\mathbf{r}) = -\frac{1}{2}\sum_{j_{\sigma},k_{\sigma}}^{\mathrm{occ}} \varphi_{j_{\sigma}}^{*}(\mathbf{r})\varphi_{k_{\sigma}}(\mathbf{r}) \int \frac{\varphi_{k_{\sigma}}^{*}(\mathbf{r}')\varphi_{j_{\sigma}}(\mathbf{r}')}{|\mathbf{r} - \mathbf{r}'|}\mathrm{d}\mathbf{r}' \qquad (5)$$

whose integral over the entire real space is the alpha- or beta-spin $E_{\mathrm{x}}^{\mathrm{exact}}$ (cf. eq 2). Note that in this paper we use the symbol "γ" rather than "g" for the LMF (see refs 22, 26−28, 32) to avoid any confusion with the "g-tensor". The performance of local hybrids is determined by the LMF as well as by the choice of density functional exchange and correlation contributions. We have been able to construct simple local hybrids, so far with only one or two semiempirical parameters and mixing only local and exact exchange, which are successful simultaneously for thermochemistry and barriers.[22,26−28,32]

A first self-consistent application to MR parameters employed the localized Hartree−Fock (LHF) approximation[33] to the OEP[34,35] to transform the nonlocal and nonmultiplicative potential of local hybrids into a local and multiplicative potential (localized-local hybrid potentials).[36] This allowed the use of an uncoupled KS perturbation scheme to obtain nuclear shieldings.[22] While the first results were encouraging, comparisons of a similar LHF-based scheme[37] with a basis-set expansion OEP method[38] for global hybrids indicated discrepancies between the results of the two approaches. This is possibly due to inaccuracies of the virtual orbitals obtained with the LHF approximation. Yet, currently, there are still problems with the numerical stability of basis-set OEP expansions and use of the, possibly necessary, very large basis sets limits the efficiency.[39,40]

While the OEP is the correct way to obtain local and multiplicative potentials from orbital-dependent functionals, most self-consistent implementations of global hybrid functionals omit the OEP transformation step and use directly the nonlocal Hartree−Fock-type potential obtained by taking straightforward functional derivatives with respect to the orbitals (FDOs) followed by the substitution:

$$\hat{\mathrm{v}}_{\mathrm{xc}}(\mathbf{r})\varphi_{k}(\mathbf{r}) \leftarrow \frac{1}{2}\frac{\delta E_{\mathrm{xc}}}{\delta \varphi_{k}(\mathbf{r})} \qquad (6)$$

in the corresponding one-electron Kohn−Sham equations. This is sometimes termed "generalized KS approach".[41,42] In calculations of second-order magnetic properties (as are most MR parameters), the nonlocal exchange potential leads to coupling terms, and coupled-perturbed Kohn−Sham (CPKS) equations have to be solved iteratively.[43−45]

This is well-established for global hybrids but has, so far, not been reported for local hybrids or for other comparably complex occupied-orbital-dependent (OOD) functionals[46,47] (also often termed "hyper-GGA functionals"[24,48,49]). We fill this gap here by reporting a CPKS scheme for a generalized OOD functional. The scheme has been implemented with local hybrid functionals and is tested for electronic g-tensors of main-group radicals and transition-metal complexes.

2. Local Hybrids, Generalized OOD Functionals and Their Potentials

Local hybrids are sometimes considered to be "hyper-GGA" functionals. From an implementation point of view, we prefer to assign them to the general class of OOD functionals (see Introduction):

$$E_{\mathrm{xc}}^{\mathrm{OOD}} = \int \varepsilon_{\mathrm{xc}}^{\mathrm{OOD}}(\mathbf{r})\mathrm{d}\mathbf{r}$$

$$\varepsilon_{\mathrm{xc}}^{\mathrm{OOD}} = \varepsilon_{\mathrm{xc}}^{\mathrm{OOD}}[\rho_{\alpha}, |\nabla\rho_{\alpha}|, \nabla^{2}\rho_{\alpha}, \tau_{\alpha}, \varepsilon_{\mathrm{x},\alpha}^{\mathrm{exact}}; \rho_{\beta}, |\nabla\rho_{\beta}|, \nabla^{2}\rho_{\beta}, \tau_{\beta}, \varepsilon_{\mathrm{x},\beta}^{\mathrm{exact}}; \nabla\rho_{\alpha}\cdot\nabla\rho_{\beta}] \qquad (7)$$

where

$$\tau_{\sigma}(\mathbf{r}) = \frac{1}{2}\sum_{k_{\sigma}}^{\mathrm{occ}} |\nabla\varphi_{k_{\sigma}}(\mathbf{r})|^{2}, \qquad \sigma = \alpha, \beta \qquad (8)$$

is the noninteracting local kinetic energy density. The extra variable τ_{σ} leads to additional nonmultiplicative terms in the corresponding FDOs $(-(1/2)\{[\nabla(\partial\varepsilon_{\mathrm{xc}}/\partial\tau_{\sigma})]\cdot\nabla + (\partial\varepsilon_{\mathrm{xc}}/\partial\tau_{\sigma})\nabla^{2}\}\ \varphi_{k_{\sigma}})$. However, in contrast to the exact-exchange operator, which is defined by its action on an arbitrary one-particle function $\psi(\mathbf{r})$ as

$$[\hat{\mathrm{v}}_{\mathrm{x}}^{\mathrm{exact}}\psi](\mathbf{r}) = -\sum_{k}^{\mathrm{occ}} \varphi_{k}(\mathbf{r}) \int \frac{\varphi_{k}^{*}(\mathbf{r}')\psi(\mathbf{r}')}{|\mathbf{r} - \mathbf{r}'|}\mathrm{d}\mathbf{r}' \qquad (9)$$

neither the permutation of spatial variables ($\mathbf{r}$,$\mathbf{r}'$) nor the integration over $\mathbf{r}'$ are involved, and therefore, no additional complications arise for magnetic linear-response properties (see below). In some OOD functionals (eq 7), the exact-exchange energy density appears in a more complicated nonlinear form, for example, as an ingredient of the local mixing function γ (cf. eq 4) in a recent local hybrid.[31] These types of subtle differences between various OOD functionals regarding their ingredients affect not only their FDOs but also potentially the evaluation of the linear response to a magnetic perturbation (see below). This will be taken into account in the following discussion.

3. Electronic g-Tensors and Generalized CPKS Scheme

The CPKS scheme will now be developed for the particular case of electronic g-tensors when treated with a second-order perturbation theory on top of a nonrelativistic one-component SCF calculation. We will report the g-shift tensor, $\mathbf{\Delta g}$, which is the correction to the isotropic free-electron g-tensor,

$$\mathbf{g} = g_e\mathbf{1} + \mathbf{\Delta g} \tag{10}$$

where $g_e = 2.002319...$ Cartesian components ($u, v = x, y, z$) of $\mathbf{\Delta g}$ are defined as

$$\Delta g_{uv} = \frac{1}{\mu_B}\frac{\partial^2 E}{\partial B_u \partial S_v}\bigg|_{\mathbf{B}=\mathbf{S}=0} = 2\frac{\partial^2 E}{\partial B_u \partial S_v}\bigg|_{\mathbf{B}=\mathbf{S}=0} \tag{11}$$

(we employ atomic units based on the SI system with the Bohr magneton $\mu_B = 1/2$), where E is the energy of the molecular system in the magnetic field $\mathbf{B}$, and $\mathbf{S}$ is its effective spin. Therefore, one has to look for terms bilinear in $\mathbf{B}$ and $\mathbf{S}$. Perturbational treatment of spin-orbit coupling with a Breit−Pauli-type Hamiltonian (or related quasirelativistic Hamiltonians) leads to a second-order perturbation scheme to compute $\mathbf{\Delta g}$. Its detailed description can be found elsewhere[21,45,50] (see also refs 43, 44, 51). Here, we restrict ourselves only to the points relevant to derive the CPKS scheme for OOD functionals. At Breit−Pauli level, the g-shift $\mathbf{\Delta g}$ consists of three terms:

$$\mathbf{\Delta g} = \mathbf{\Delta g}_{\mathrm{SO/OZ}} + \mathbf{\Delta g}_{\mathrm{RMC}} + \mathbf{\Delta g}_{\mathrm{GC}} \tag{12}$$

of which the "paramagnetic" second-order spin-orbit/orbital Zeeman cross term, $\mathbf{\Delta g}_{\mathrm{SO/OZ}}$, usually dominates. The remaining terms are due to the relativistic mass correction, $\mathbf{\Delta g}_{\mathrm{RMC}}$, and the one-electron part of the gauge correction. These are calculated as "first-order properties" (expectation values, see eqs 7 and 9 in ref 21 for details). We will, in the following, be concerned exclusively with the Cartesian components u, v of the second-order $\mathbf{\Delta g}_{\mathrm{SO/OZ}}$. These are evaluated as

$$\Delta g_{\mathrm{SO/OZ},uv} = \frac{\alpha^2}{2}g_e\left[\sum_{k_\alpha}^{\mathrm{occ}}\sum_{a_\alpha}^{\mathrm{vac}}\frac{\langle\varphi_{k_\alpha}|\hat{H}_{\mathrm{SO},v}|\varphi_{a_\alpha}\rangle\langle\varphi_{a_\alpha}|\hat{f}_{\mathrm{O},u}|\varphi_{k_\alpha}\rangle}{\varepsilon_{k_\alpha} - \varepsilon_{a_\alpha}} - \sum_{k_\beta}^{\mathrm{occ}}\sum_{a_\beta}^{\mathrm{vac}}\frac{\langle\varphi_{k_\beta}|\hat{H}_{\mathrm{SO},v}|\varphi_{a_\beta}\rangle\langle\varphi_{a_\beta}|\hat{f}_{\mathrm{O},u}|\varphi_{k_\beta}\rangle}{\varepsilon_{k_\beta} - \varepsilon_{a_\beta}}\right] \tag{13}$$

where α is the fine structure constant (α = 1/137.035999...), and $\hat{H}_{\mathrm{SO},v}$ denotes the v component of the spatial part of the spin-free spin-orbit (SO) Hamiltonian (cf. eqs 3 and 5 of ref 21).

Next,

$$\hat{f}_{\mathrm{O},u} = \hat{l}_{\mathrm{O},u} + i\hat{\omega}_u^1 \tag{14}$$

where $\hat{l}_{\mathrm{O},u}$ is a spatial component of the orbital Zeeman operator

$$\hat{\mathbf{l}}_O = -i(\mathbf{r} - \mathbf{R}_O) \times \nabla \tag{15}$$

(subscript "O" denotes a common gauge origin at point $\mathbf{R}_O$, see Computational Details below), and $\hat{\omega}_u^1$ is a "response" operator, which may vanish or persist depending on the exchange-correlation functional employed (see below). As is seen from eq 13, $\mathbf{\Delta g}_{\mathrm{SO/OZ}}$ arises from the interplay between two perturbations: spin-orbit coupling and orbital Zeeman operator (both operators are purely imaginary). According to the interchange theorem of double-perturbation theory,[52] one may evaluate a perturbed wave function (a KS determinant in the present case) up to first order in one of the perturbations, followed by computation of matrix elements of the second perturbation with the first-order perturbed and unperturbed wave functions and subtraction of zero-order terms. Translating this into one-electron language in the context of a KS determinant and using conveniently the orbital Zeeman operator (external magnetic field) as the initial perturbation, we rewrite eq 13 as

$$\Delta g_{\mathrm{SO/OZ},uv} = \frac{i\alpha^2}{2}g_e\left[\sum_{k_\alpha}^{\mathrm{occ}}\langle\varphi_{k_\alpha}|\hat{H}_{\mathrm{SO},v}|\varphi_{k_\alpha}^{1,u}\rangle - \sum_{k_\beta}^{\mathrm{occ}}\langle\varphi_{k_\beta}|\hat{H}_{\mathrm{SO},v}|\varphi_{k_\beta}^{1,u}\rangle\right] \tag{16}$$

where $\varphi_{k_\sigma}^{1,u}$ ($\sigma = \alpha, \beta$) is the first-order correction (linear response) to the occupied orbital φ_{k_σ} (below we omit subscript σ for notational simplicity where it is not crucial; a tilde will always indicate the perturbed quantities):

$$\varphi_k \xrightarrow{OZ,u} \tilde{\varphi}_k^u; \quad \tilde{\varphi}_k^u = \varphi_k + iB_u\varphi_k^{1,u} + ..., \quad u = x, y, z \tag{17}$$

$$\varphi_k^{1,u} = -i\sum_a^{\mathrm{vac}}\frac{\langle\varphi_a|\hat{f}_{\mathrm{O},u}|\varphi_k\rangle}{\varepsilon_k - \varepsilon_a}\varphi_a \equiv \sum_a^{\mathrm{vac}}\beta_{ak}^u\varphi_a \tag{18}$$

In case of an unperturbed orbital φ_k and a semilocal exchange-correlation potential $\hat{v}_{xc}$ of LSDA, GGA, or meta-GGA type (the latter may be viewed as an OOD functional (eq 7) without dependence on $\varepsilon_x^{\mathrm{exact}}$), operator $\hat{\omega}_u^1$ vanishes in eq 14, and $\hat{f}_{\mathrm{O},u} = \hat{l}_{\mathrm{O},u}$. Then, the linear response coefficients β_{ak}^u of eq 18 (cf. eqs 14 and 15) are found straightforwardly in one step as

$$\beta_{ak}^u = \frac{\langle\varphi_a|-[(\mathbf{r} - \mathbf{R}_O) \times \nabla]_u|\varphi_k\rangle}{\varepsilon_k - \varepsilon_a} \tag{19}$$

If a global hybrid nonlocal operator is employed, then

$$\beta_{ak}^u = \frac{\langle\varphi_a|-[(\mathbf{r} - \mathbf{R}_O) \times \nabla]_u + \hat{\omega}_u^1|\varphi_k\rangle}{\varepsilon_k - \varepsilon_a} \tag{20}$$

where $\hat{\omega}_u^1 \equiv a_0\,\hat{v}_{x,u}^{\mathrm{exact},1}$, and $\hat{v}_{x,u}^{\mathrm{exact},1}$ is the linear response from the exact-exchange operator (eq 9):

$$[\hat{v}_{x,u}^{\mathrm{exact},1}\psi](\mathbf{r}) = -\sum_k^{\mathrm{occ}}\int\frac{\{\varphi_k^*(\mathbf{r}')\varphi_k^{1,u}(\mathbf{r}) - [\varphi_k^{1,u}(\mathbf{r}')]^*\varphi_k(\mathbf{r})\}\psi(\mathbf{r}')}{|\mathbf{r} - \mathbf{r}'|}d\mathbf{r}' \tag{21}$$

When an external magnetic field is switched on, the exact-exchange operator (eq 9) is modified, as it depends on the occupied orbitals. Thus, substituting the complex perturbed orbitals $\tilde{\varphi}_k^u$, eq 17 into eq 9, one obtains

$$[\hat{\tilde{\mathrm{v}}}_{\mathrm{x},u}^{\mathrm{exact}}\psi](\mathbf{r}) = [\hat{\mathrm{v}}_{\mathrm{x}}^{\mathrm{exact}}\psi](\mathbf{r}) + iB_u[\hat{\mathrm{v}}_{\mathrm{x},u}^{\mathrm{exact},1}\psi](\mathbf{r}) + O(\mathbf{B}^2) \tag{22}$$

(as in eq 9, in eqs 21, 22 $\psi(\mathbf{r})$ is an arbitrary one-particle function). Equation 20 has to be solved iteratively, since its right-hand side depends on the complete set of linear-response coefficients $\{\beta_{bj}^{u}\}$ ($j = 1, ..., N_{\mathrm{occ}}$; $b = 1, ..., N_{\mathrm{vac}}$) (cf. eqs 18 and 21).

How is the CPKS scheme modified when passing from a global hybrid (eq 1) to a general OOD (or hyper-GGA) functional (eq 7)? Let us consider the FDOs (eq 6) of such a functional. We assemble them using the partial derivatives of the exchange-correlation energy density, $\varepsilon_{\mathrm{xc}}$, with respect to its "ingredients" ρ_σ, $|\nabla\rho_\sigma|$, $\nabla^2\rho_\sigma$, τ_σ, $\varepsilon_{\mathrm{x},\sigma}^{\mathrm{exact}}$ ($\sigma = \alpha, \beta$), and $\nabla\rho_\alpha \cdot \nabla\rho_\beta$ (for brevity, we will employ the general designation $\partial\varepsilon_{\mathrm{xc}}/\partial\kappa$ for these quantities, where $\kappa = \rho_\alpha, |\nabla\rho_\alpha|, ..., \varepsilon_{\mathrm{x},\beta}^{\mathrm{exact}}, \nabla\rho_\alpha \cdot \nabla\rho_\beta$). We will refrain from providing all the lengthy explicit expressions of $\partial\varepsilon_{\mathrm{xc}}/\partial\kappa$ (see, e.g., refs 22 and 47 for details) but focus only on their structural features. Some of the ingredients are more critical than others. Obviously, this holds in particular for the exact-exchange energy density, $\varepsilon_{\mathrm{x}}^{\mathrm{exact}}$. For global hybrids (eq 1), the situation is particularly simple as none of the derivatives $\partial\varepsilon_{\mathrm{xc}}/\partial\kappa$ depend further on $\varepsilon_{\mathrm{x}}^{\mathrm{exact}}$ itself. Moreover,

$$\frac{\partial\varepsilon_{\mathrm{xc}}^{\mathrm{hybr}}}{\partial\varepsilon_{\mathrm{x}}^{\mathrm{exact}}} = a_0 = \mathrm{const} \tag{23}$$

and only the term $a_0\mathrm{v}_{\mathrm{x}}^{\mathrm{exact}}\varphi_i$ survives for the corresponding contribution to the FDOs. The CPKS treatment, in this case, is well elaborated (see above).

At first sight, matters appear much more complicated for general OOD functionals (eq 7). The local mixing function γ may depend on any of the ingredients listed above, and $\partial\varepsilon_{\mathrm{xc}}/\partial\kappa$ may depend on $\varepsilon_{\mathrm{x}}^{\mathrm{exact}}$. Some nonzero contributions from those quantities to the linear response $\hat{\omega}_u^1$, thus, might be expected. It turns out, however, that this is fortunately not the case, since, at the nonrelativistic one-component level, $\varepsilon_{\mathrm{x}}^{\mathrm{exact}}$ itself yields no response. To show this, we recall that the exact-exchange operator $\hat{\mathrm{v}}_{\mathrm{x}}^{\mathrm{exact}}$ is defined by eq 9 and rewrite eq 5 as

$$\varepsilon_{\mathrm{x}}^{\mathrm{exact}}(\mathbf{r}) = \frac{1}{2}\sum_{k}^{\mathrm{occ}}\varphi_k^*(\mathbf{r})[\hat{\mathrm{v}}_{\mathrm{x}}^{\mathrm{exact}}\varphi_k](\mathbf{r}) \tag{24}$$

Then, substituting the perturbed orbitals $\tilde{\varphi}_k^{u}$ (eq 17), as well as $\hat{\mathrm{v}}_{\mathrm{x},u}^{\mathrm{exact}}$ 22, into eq 24, we have

$$\begin{aligned}\tilde{\varepsilon}_{\mathrm{x}}^{\mathrm{exact}}(\mathbf{r}) &= \frac{1}{2}\sum_{k}^{\mathrm{occ}}\tilde{\varphi}_k^*(\mathbf{r})[\hat{\tilde{\mathrm{v}}}_{\mathrm{x}}^{\mathrm{exact}}\tilde{\varphi}_k](\mathbf{r}) = \\ &\frac{1}{2}\sum_{k}^{\mathrm{occ}}\varphi_k^*(\mathbf{r})[\hat{\mathrm{v}}_{\mathrm{x}}^{\mathrm{exact}}\varphi_k](\mathbf{r}) + \frac{i}{2}B\sum_{k}^{\mathrm{occ}}\{\varphi_k^*(\mathbf{r})[\hat{\mathrm{v}}_{\mathrm{x},u}^{\mathrm{exact},1}\varphi_k](\mathbf{r}) + \\ &\varphi_k^*(\mathbf{r})[\hat{\mathrm{v}}_{\mathrm{x}}^{\mathrm{exact}}\varphi_k^{1,u}](\mathbf{r}) - [\varphi_k^{1,u}(\mathbf{r})]^*[\hat{\mathrm{v}}_{\mathrm{x}}^{\mathrm{exact}}\varphi_k](\mathbf{r})\} + O(\mathbf{B}^2) \equiv \\ &\varepsilon_{\mathrm{x}}^{\mathrm{exact}}(\mathbf{r}) + iB\varepsilon_{\mathrm{x},u}^{\mathrm{exact},1}(\mathbf{r}) + O(\mathbf{B}^2)\end{aligned} \tag{25}$$

where the linear response of the exact-exchange energy density, $\varepsilon_{\mathrm{x},u}^{\mathrm{exact},1}$, can be rewritten as

$$\begin{aligned}\varepsilon_{\mathrm{x},u}^{\mathrm{exact},1}(\mathbf{r}) = \frac{1}{2}\sum_{k}^{\mathrm{occ}}\sum_{j}^{\mathrm{occ}}\Bigg(&\{[\varphi_k^{1,u}(\mathbf{r})]^*\varphi_j(\mathbf{r}) - \\ &\varphi_k^*(\mathbf{r})\varphi_j^{1,u}(\mathbf{r})\}\int\frac{\varphi_j^*(\mathbf{r}')\varphi_k(\mathbf{r}')}{|\mathbf{r}-\mathbf{r}'|}\mathrm{d}\mathbf{r}' + \\ &\varphi_k^*(\mathbf{r})\varphi_j(\mathbf{r})\int\frac{\{[\varphi_j^{1,u}(\mathbf{r}')]^*\varphi_k(\mathbf{r}') - \varphi_j^*(\mathbf{r}')\varphi_k^{1,u}(\mathbf{r}')\}}{|\mathbf{r}-\mathbf{r}'|}\mathrm{d}\mathbf{r}'\Bigg)\end{aligned} \tag{26}$$

The double sum on the right-hand side of eq 26 should be invariant with respect to the permutation of indices k and j (both indices run the same set of occupied orbitals). On the other hand, one can easily see that such a permutation leads to $-(\varepsilon_{\mathrm{x},u}^{\mathrm{exact},1})^*$. Therefore,

$$\varepsilon_{\mathrm{x},u}^{\mathrm{exact},1} = -(\varepsilon_{\mathrm{x},u}^{\mathrm{exact},1})^* \tag{27}$$

i.e., $\varepsilon_{\mathrm{x},u}^{\mathrm{exact},1}$ is a purely imaginary quantity. It is well-known that within the nonrelativistic approach, the unperturbed orbitals φ_k can always be chosen real valued without a loss of generality (at least, in the case of orbitally nondegenerate states for which the employed formalism is designed). Then, because of the purely imaginary character of the magnetic (orbital Zeeman) perturbation, the $\varphi_k^{1,u}$ are also real (cf. eqs 17–19). Therefore, $\varepsilon_{\mathrm{x},u}^{\mathrm{exact},1}$ (eq 26) should be real as well since it is composed of real quantities. This in turn contradicts our above observation that the linear response of the exact-exchange energy density is purely imaginary, unless $\varepsilon_{\mathrm{x},u}^{\mathrm{exact},1}$ is zero. Therefore, up to second- and higher-order terms in B, the exact-exchange energy density itself (but not the operator $\hat{\mathrm{v}}_{\mathrm{x}}^{\mathrm{exact}}$!) and, hence, any analytical functions of $\varepsilon_{\mathrm{x}}^{\mathrm{exact}}$ are invariant with respect to the presence of the external magnetic field (note that the individual terms $\varphi_k\hat{\mathrm{v}}_{\mathrm{x},u}^{\mathrm{exact},1}\varphi_k + \varphi_k\hat{\mathrm{v}}_{\mathrm{x}}^{\mathrm{exact}}\varphi_k^{1,u} - \varphi_k^{1,u}\hat{\mathrm{v}}_{\mathrm{x}}^{\mathrm{exact}}\varphi_k$ are not necessarily zero, and only their summation over k gives an overall vanishing result). These arguments for a vanishing $\varepsilon_{\mathrm{x},u}^{\mathrm{exact},1}$ do not hold anymore when passing to two- or four-component relativistic approaches where spin-orbit effects are taken into account variationally, since the unperturbed orbitals cannot be chosen real valued in such a case.

The overall exact-exchange contribution to the FDO (eq 6) of a general OOD functional (eq 7) $(\delta E_{\mathrm{xc}}^{\mathrm{OOD}}/\delta\varphi_k)_{\varepsilon_{\mathrm{x}}^{\mathrm{exact}}}$ is[47]

$$\frac{1}{2}\left(\frac{\delta E_{\mathrm{xc}}^{\mathrm{OOD}}}{\delta\varphi_k}\right)_{\varepsilon_{\mathrm{x}}^{\mathrm{exact}}} = \frac{1}{2}\left[\left(\frac{\partial\varepsilon_{\mathrm{xc}}^{\mathrm{OOD}}}{\partial\varepsilon_{\mathrm{x}}^{\mathrm{exact}}}\right)\hat{\mathrm{v}}_{\mathrm{x}}^{\mathrm{exact}}\varphi_k + \hat{\mathrm{v}}_{\mathrm{x}}^{\mathrm{exact}}\left\{\left(\frac{\partial\varepsilon_{\mathrm{xc}}^{\mathrm{OOD}}}{\partial\varepsilon_{\mathrm{x}}^{\mathrm{exact}}}\right)\varphi_k\right\}\right] \tag{28}$$

For global hybrids, the right-hand side of eq 28 reduces simply to $a_0\hat{\mathrm{v}}_{\mathrm{x}}^{\mathrm{exact}}\varphi_k$ (cf. eq 23). For local hybrids *without* dependence of the LMF γ on $\varepsilon_{\mathrm{x}}^{\mathrm{exact}}$:

$$\frac{\partial\varepsilon_{\mathrm{xc}}^{\mathrm{Lh}}}{\partial\varepsilon_{\mathrm{x}}^{\mathrm{exact}}} = \gamma \tag{29}$$

[cf., e.g., eq 14 of ref 22]. For the more general case of local hybrid functionals *with* a dependence of γ on $\varepsilon_{\mathrm{x}}^{\mathrm{exact}}$:[31]

$$\frac{\partial\varepsilon_{\mathrm{xc}}^{\mathrm{OOD/Lh}}}{\partial\varepsilon_{\mathrm{x}}^{\mathrm{exact}}} = \gamma + \frac{\partial\gamma}{\partial\varepsilon_{\mathrm{x}}^{\mathrm{exact}}}(\varepsilon_{\mathrm{x}}^{\mathrm{exact}} - \varepsilon_{\mathrm{x}}^{\mathrm{DFT}}) \tag{30}$$

By writing "OOD/Lh", we emphasize that such a functional may still be structured in the form of eq 4, while a general OOD functional (eq 7) may take any sophisticated form, including some implicitly defined functions. An example is Becke's model for nondynamical correlation (B05).[48]

With the above-mentioned invariance of $\varepsilon_x^{\text{exact}}$ and with eq 28, the response operator in the general OOD case is obtained as

$$\hat{\omega}_u^1 = \frac{1}{2}\left[\left(\frac{\partial \varepsilon_{\text{xc}}^{\text{OOD}}}{\partial \varepsilon_{\text{x}}^{\text{exact}}}\right)\hat{v}_{\text{x},u}^{\text{exact},1} + \hat{v}_{\text{x},u}^{\text{exact},1}\left(\frac{\partial \varepsilon_{\text{xc}}^{\text{OOD}}}{\partial \varepsilon_{\text{x}}^{\text{exact}}}\right)\right] \tag{31}$$

while eq 20 itself remains unchanged. It, thus, turns out that implementation of the envisioned generalized CPKS scheme is relatively straightforward: we need to compute the relevant matrix elements of operator (eq 31) instead of $a_0\ \hat{v}_{\text{x},u}^{\text{exact},\,1}$ for global hybrids.

4. Computational Details

The generalized CPKS scheme has been implemented within the MAG-ReSpect code,[53] which uses Gaussian-type orbital basis sets. For evaluating the one- and two-electron spin-orbit integrals entering eq 13 and 16, we have employed the atomic mean-field approximation (AMFI),[54,55] which has proven to combine computational efficiency with high accuracy (see refs 17, 21 and 56 for further details).

A completeness insertion (or resolution of the identity, RI) in the orbital basis set has been employed when evaluating the exact-exchange energy density, eq 5, as described in ref 33 (see also refs 22, 26−28, 32, and 36). To minimize any errors from the RI and from the gauge dependence (see below) and to guarantee the evaluation of the true performance of different functionals, uncontracted basis sets have been used in this work. In the case of main group radicals, we started from H−Ar basis sets due to Jensen,[57−59] which are designed to provide a fast and a controlled convergence toward the basis set limit for spin-spin coupling constants (pcJ-*n* family[58]) and nuclear shielding constants (pcS-*n* family[59]). After a number of trials, we chose the aug-pcS-3 basis sets, composed of (10s6p3d2f) for H, (15s11p5d3f) for B to F (g functions omitted), (18s14p3d2f) for Mg, and (18s15p5d3f) for S (g functions omitted). After some calibration work on the TiF_3 complex, we decided to employ Fægri's (16s11p8d) basis sets[60] for the 3d transition metals, supplemented by three f functions.[61] The ligand atoms were treated by uncontracted IGLO-IV basis sets[62] (good compatibility of IGLO and Fægri basis sets has been noted[63] and could be confirmed in our studies). While we have recently constructed specific basis sets for molybdenum EPR parameter calculations[64] for consistency with the calculations on 3d systems, we chose also a Fægri basis for molybdenum (20s14p11d)[60] and augmented it by an even-tempered set of four f exponents (20.31, 5.39, 1.43, and 0.38) based partly on extrapolation from the 3f polarization set for chromium.[61]

We consider here one- and two-parameter local hybrid functionals optimized previously to yield the best atomization energies[26,27] as well as reaction barriers.[32] That is, five different local hybrids have been evaluated: (i) *Lh*-SVWN with $\gamma_\sigma = 0.48t_\sigma$ (cf. eq 4; "S" stands for Slater−Dirac LSDA exchange[4,5] employed as $\varepsilon_{\text{x},\sigma}^{\text{DFT}}$, and "VWN" stands for Vosko−Wilk−Nusair LSDA correlation model V[6] employed as $E_{\text{c}}^{\text{DFT}}$), where

$$t_\sigma = \tau_{\text{W},\sigma}/\tau_\sigma, \qquad \sigma = \alpha, \beta \tag{32}$$

$$\tau_{\text{W},\sigma} = |\nabla\rho_\sigma|^2/(8\rho_\sigma) \tag{33}$$

is the von Weizsäcker kinetic energy density, and τ_σ is given by eq 8. This has, so far, been one of the most successful local hybrids for atomization energies and for reaction barriers;[26,28] (ii) *Lh*-SVWN with $\gamma_\sigma = 0.22s_\sigma$, where

$$s_\sigma = |\nabla\rho_\sigma|/[2(3\pi^2)^{1/3}\rho_\sigma^{4/3}] \tag{34}$$

is the dimensionless density gradient; and (iii) *Lh*-SLYP with $\gamma_\sigma = 0.24s_\sigma$ (here VWN LSDA correlation has been replaced by Lee−Yang−Parr GGA correlation).[11] The last two local hybrids[27] exhibited somewhat inferior atomization energies and reaction barriers compared to the first but provided superior nuclear shielding constants[22] (in that case implemented as localized local hybrid potentials[36] followed by an uncoupled DFT perturbation treatment). Finally, we have evaluated also two local hybrids[32] that include an explicit dependence on spin polarization

$$\zeta = (\rho_\alpha - \rho_\beta)/(\rho_\alpha + \rho_\beta) \tag{35}$$

These are (iv) *Lh*-SVWN with $g_\sigma = (0.446 \pm 0.0531\ \zeta)t_\sigma$ and (v) *Lh*-SVWN with $\gamma_\sigma = \text{erf}[(0.196 \pm 0.0416\ \zeta)s_\sigma]$ (the plus sign holds for $\sigma = \alpha$, the minus sign holds for $\sigma = \beta$). These two very recent functionals are particularly accurate for atomization energies.[32] According to the order above, we will abbreviate the functionals in the following as "*Lh*-I" to "*Lh*-V" (Tables 1 and 2).

For comparison, we also include results obtained with four global hybrids (B3LYP[3,11] and B3PW91[3,10] with 20% exact exchange and BHLYP[2,11] and BHPW91[1,10] with 50% exact exchange[65]), one GGA (BP86),[8,9] and one LSDA (SVWN)[5,6] functional. These more traditional functionals have previously been evaluated for g-tensor calculations in refs 17, 21, 45, 50, 51, and 66 but with smaller (contracted) basis sets.

Due to the use of the AMFI approximation[54] for the spin-orbit integrals, we used a common gauge origin at the center of mass for the small main group radicals and at the metal nucleus for the transition-metal systems. This choice is well justified for g-tensors (see ref 17 and references therein) and seems to yield negligible gauge errors, in particular, in view of the large uncontracted basis sets used. Indeed, test calculations of the g-tensor for the Fe(CO)_5^+ complex (tetragonal pyramid) with the gauge origin shifted to axial carbon and oxygen nuclei give absolute relative deviations of the g-shift components of less than 0.3%.

The molecular structures are DFT-optimized ones employed already in refs 17−19, 50, 21, 66, and 67.

5. Results and Discussion

Table 1 shows the calculated g-shift components for a selection of light main-group radicals compared to experi-

Table 1. Comparison of Calculated and Experimental g-Shift Components for 13 Light Main-Group Radicals (ppm)

		pure DFT		global hybrids				local hybrids					
		SVWN	BP86	B3PW91	B3LYP	BHPW91	BHLYP	*Lh*-I[a,f]	*Lh*-II[b,f]	*Lh*-III[c, f]	*Lh*-IV[d, f]	*Lh*-V[e,f]	expt.[g]
H_2O^+	Δg_{11}	−184	−186	−185	−185	−183	−183	−187	−181	−178	−186	−183	200
	Δg_{22}	4607	3784	3819	3974	3724	3920	3925	3998	4095	3955	4013	4800
	Δg_{33}	16308	10621	11466	12434	11886	13260	12654	13329	14260	12742	13174	18800
CO^+	$\Delta g_{\parallel}$	−100	−102	−97	−102	−86	−95	−94	−94	−93	−94	−92	
	$\Delta g_{\perp}$	−2488	−2399	−2453	−2486	−2547	−2556	−2407	−2506	−2501	−2406	−2476	−2400
CO_2^-	Δg_{11}	430	344	758	684	1075	1004	775	744	586	760	835	880
	Δg_{22}	−5075	−4948	−5280	−5155	−5586	−5464	−5119	−5333	−5199	−5112	−5286	−5070
	Δg_{33}	−679	−690	−695	−704	−732	−729	−717	−772	−798	−710	−713	−710
O_3^-	Δg_{11}	−330	−355	−438	−434	−609	−609	−496	−444	−442	−481	−430	1300
	Δg_{22}	16154	14931	17737	17963	21200	21622	17058	18462	18263	16923	18122	16400
	Δg_{33}	8973	8543	10664	10814	13726	14045	10282	10792	10742	10163	10548	10000
HCO	Δg_{11}	2379	2226	2297	2331	2321	2381	2232	2310	2305	2238	2304	1500
	Δg_{22}	−159	−166	−174	−144	−192	−138	−209	−192	−169	−204	−189	0
	Δg_{33}	−9377	−7726	−7838	−7820	−7752	−7694	−7675	−8296	−8449	−7709	−8380	−7500
H_2CO^+	Δg_{11}	5473	5059	5326	5406	5476	5612	5339	5519	5520	5337	5500	4600
	Δg_{22}	73	92	156	143	782	937	182	184	211	185	179	200
	Δg_{33}	−1551	−966	−293	−231	282	252	−173	−288	−450	−278	−462	−800
C_3H_5	Δg_{11}	−42	−48	−44	−42	−40	−39	−46	−49	−48	−44	−44	0
	Δg_{22}	524	355	386	434	416	473	457	505	526	458	503	400
	Δg_{33}	602	513	500	505	466	475	483	529	557	490	535	800
NO_2	Δg_{11}	−540	−547	−578	−577	−669	−656	−600	−610	−627	−594	−603	−300
	Δg_{22}	3284	3223	3563	3543	3928	3930	3416	3610	3493	3398	3566	3900
	Δg_{33}	−12022	−11021	−11593	−11600	−12005	−12017	−11146	−11889	−11756	−11148	−11873	−11300
NF_2	Δg_{11}	−566	−572	−643	−621	−743	−707	−720	−712	−695	−705	−689	−100
	Δg_{22}	4370	4028	3958	4060	3616	3771	3746	3805	3805	3795	3869	2800
	Δg_{33}	7220	6438	6555	6770	6298	6633	6417	6570	6602	6470	6644	6200
CN	$\Delta g_{\parallel}$	−104	−104	−103	−106	−95	−101	−103	−103	−103	−102	−102	
	$\Delta g_{\perp}$	−1878	−1782	−1915	−1967	−2042	−2216	−1929	−2005	−2015	−1915	−1980	−2000
MgF	$\Delta g_{\parallel}$	15	14	16	9	18	9	16	17	14	16	38	−300
	$\Delta g_{\perp}$	−1804	−1728	−1625	−1606	−1477	−1484	−1550	−1616	−1622	−1567	−1766	−1300
BO	$\Delta g_{\parallel}$	−40	−42	−38	−44	−34	−42	−36	−35	−36	−36	−31	
	$\Delta g_{\perp}$	−1794	−1749	−1739	−1720	−1744	−1693	−1681	−1792	−1764	−1684	−1765	−1700
BS	$\Delta g_{\parallel}$	−57	−60	−59	−61	−59	−62	−59	−58	−58	−58	−57	
	$\Delta g_{\perp}$	−9725	−8997	−8967	−8988	−8899	−8810	−8892	−9180	−9124	−8921	−9164	−8900
MAE[h,i]		602 (537)	711 (453)	653 (422)	640 (443)	904 (697)	901 (741)	554 (361)	656 (490)	611 (476)	543 (353)	638 (466)	
MaxSE [j,i]		−2492 (−1877)	−8179 (−1655)	−7334 (−1738)	−6366 (−1734)	−6914 (4800)	−5540 (5222)	−6146 (−1796)	−5471 (2062)	−4540 (1863)	−6058 (−1781)	−5626 (−1730)	
linear regression analysis for comparison between theory and experiment[k,i]													
slope (A)		0.989 (1.037)	0.836 (0.949)	0.916 (1.048)	0.938 (1.057)	0.999 (1.162)	1.031 (1.178)	0.914 (1.017)	0.968 (1.079)	0.979 (1.073)	0.913 (1.014)	0.960 (1.070)	
intercept (B)		−263 (−212)	−304 (−184)	−170 (−30)	−124 (3)	−13 (160)	66 (221)	−145 (−35)	−164 (−46)	−154 (−54)	−150 (−43)	−178 (−61)	
RC		0.991 (0.992)	0.974 (0.994)	0.972 (0.995)	0.977 (0.995)	0.960 (0.988)	0.966 (0.988)	0.981 (0.995)	0.981 (0.995)	0.985 (0.995)	0.982 (0.995)	0.981 (0.995)	
SD		834 (705)	1235 (576)	1394 (562)	1292 (577)	1842 (968)	1728 (1005)	1135 (542)	1215 (570)	1067 (562)	1110 (533)	1204 (554)	

[a] *Lh*-SVWN, $\gamma = 0.48t$. [b] *Lh*-SVWN, $\gamma = 0.22s$. [c] *Lh*-SLYP, $\gamma = 0.24s$. [d] *Lh*-SVWN, $\gamma = (0.446 \pm 0.0531\ \zeta)t$. [e] *Lh*-SVWN, $\gamma = \mathrm{erf}[(0.196 \pm 0.0416\ \zeta)s]$. [f] For notational simplicity, the spin labels $\sigma = \alpha, \beta$ have been omitted. [g] See refs 50 and 70 for the detailed references to experimental data. [h] Mean absolute error. [i] Data in parentheses correspond to omission of Δg_{33} for H_2O^+. [j] Maximal (signed) error. [k] $\Delta g(\text{calc.}) = A\ \Delta g(\text{expt.}) + B$, with $\Delta g(\text{expt.})$ and B in ppm; the standard deviation (SD) is $[\sum_{j=1}^{n}(\Delta g_j - \Delta\bar{g})^2/(n-1)]^{1/2}$. Perfect agreement with experiment corresponds to $A = 1$, $B = 0$, SD = 0, and regression coefficient (RC) = 1.

Table 2. Comparison of Calculated and Experimental g-Shift Components for 12 Transition-Metal Compounds (ppt)

		pure DFT		global hybrids				local hybrids					
		SVWN	BP86	B3PW91	B3LYP	BHPW91	BHLYP	*Lh*-I[a]	*Lh*-II[b]	*Lh*-III[c]	*Lh*-IV[d]	*Lh*-V[e]	expt.
$Co(CO)_4$	$\Delta g_{\parallel}$	3.51	4.08	12.3	12.7	65.5	69.7	8.1	8.16	8.74	7.78	7.56	3.6[f]
	$\Delta g_{\perp}$	96.8	80.5	108.6	112.9	148.5	157.2	116.1	115.2	121.4	115.0	112.0	127.6[f]
$CrOF_4^-$	$\Delta g_{\parallel}$	−22.5	−18.5	−24.6	−24.4	−35.7	−35.3	−25.4	−25.6	−25.8	−25.1	−25.3	−43.3[g]
	$\Delta g_{\perp}$	−31.5	−25.2	−30.5	−30.0	−54.1	−54.3	−31.3	−32.5	−32.5	−31.0	−32.2	−34.3[g]
$CrOCl_4^-$	$\Delta g_{\parallel}$	21.2	18.9	14.6	16.3	−0.82	1.15	15.1	15.3	14.9	15.8	16.5	10[h]
	$\Delta g_{\perp}$	−22.5	−19.3	−27.1	−26.7	−56.5	−56.8	−27.2	−28.0	−28.0	−26.6	−27.2	−25[h]
$Cu(NO_3)_2$	Δg_{zz}	125.8	121.3	184.7	182.7	326.7	319.6	176.0	179.9	183.8	171.4	172.0	246.6[i]
	Δg_{xx}	28.2	28.6	46.5	46.3	84.5	84.1	43.1	43.1	44.3	41.7	40.8	49.9[i]
	Δg_{yy}	30.8	30.7	46.8	46.7	86.8	86.1	43.5	43.5	44.9	42.3	41.6	49.9[i]
$Cu(acac)_2$	Δg_{zz}	125.1	120.1	182.8	181.1	304.1	297.7	172.3	177.6	181.8	168.2	170.1	285.2[j]
	Δg_{xx}	30.5	30.5	47.2	46.9	77.9	76.9	43.1	43.8	45.1	42.0	41.8	48.7[j]
	Δg_{yy}	35.3	34.8	51.7	51.5	79.9	79.2	47.6	48.5	49.7	46.6	46.6	48.7[j]
$Fe(CO)_5^+$	$\Delta g_{\parallel}$	−1.03	−1.42	−3.48	−3.56	−10.1	−9.4	−2.1	−2.31	−2.51	−2.05	−2.26	−1.4[k]
	$\Delta g_{\perp}$	61.8	51.4	66.6	68.8	86.2	90.1	73.0	71.8	74.9	72.3	69.4	78.4[k]
$Mn(CO)_5$	$\Delta g_{\parallel}$	−1.05	−1.30	−2.55	−2.69	−6.78	−6.72	−1.93	−1.97	−2.14	−1.87	−1.89	−2.3[l]
	$\Delta g_{\perp}$	27.3	23.7	28.4	29.3	32.8	33.9	31.0	30.2	31.6	30.8	28.9	35.7[l]
MnO_3	$\Delta g_{\parallel}$	3.65	2.63	−1.71	−1.27	−17.9	−18.3	−0.3	−0.19	−0.71	0.025	0.19	1.3[m]
	$\Delta g_{\perp}$	−0.78	2.54	1.78	3.96	−213.7	−233.0	3.3	3.17	2.12	3.76	3.40	6.1[m]
$MoOF_4^-$	$\Delta g_{\parallel}$	−77.6	−70.5	−82.8	−85.0	−99.5	−102.4	−86.4	−84.7	−84.6	−85.7	−84.3	−107.7[n]
	$\Delta g_{\perp}$	−66.9	−58.6	−63.2	−63.7	−69.4	−69.8	−66.1	−66.9	−66.4	−66.0	−66.9	−76.9[n]
$MoOCl_4^-$	$\Delta g_{\parallel}$	7.10	5.97	−3.95	−3.46	−21.8	−21.5	−2.86	−1.48	−1.29	−2.03	−0.47	−37.3[n]
	$\Delta g_{\perp}$	−51.3	−46.5	−51.8	−52.2	−59.7	−60.1	−53.1	−53.5	−53.0	−52.8	−53.3	−56.1[n]
$Ni(CO)_3H$	$\Delta g_{\parallel}$	1.39	1.72	4.96	5.34	14.6	15.4	2.93	2.86	3.08	2.82	2.54	1.9[o]
	$\Delta g_{\perp}$	41.6	42.4	72.6	74.1	168.3	173.5	61.3	65.3	66.2	58.8	60.1	65.1[o]
TiF_3	$\Delta g_{\parallel}$	−1.26	−1.33	−1.44	−1.28	−1.43	−1.23	−1.66	−1.59	−1.51	−1.61	−1.60	−3.7[p]
	$\Delta g_{\perp}$	−53.5	−37.2	−51.1	−49.4	−76.2	−70.9	−60.9	−58.3	−57.6	−60.2	−59.1	−123.7[p]
MAE[q]		24.7	27.9	16.3	16.2	32.6	33.6	15.5	15.2	14.5	16.2	16.6	
MaxSE[q,r]		−160.1	−165.1	−102.4	−104.1	−219.8	−239.1	−112.9	−107.6	−103.4	−117.0	−115.1	
		linear regression analysis for comparison between theory and experiment[s]											
slope (A)		0.539	0.491	0.702	0.701	1.14	1.13	0.692	0.701	0.714	0.678	0.678	
intercept (B)		0.6	2.0	5.4	5.8	4.9	4.9	3.8	4.2	4.8	3.6	3.4	
RC		0.956	0.965	0.981	0.979	0.887	0.872	0.980	0.981	0.980	0.979	0.980	
SD		14.7	12.5	13.0	13.7	55.3	59.3	13.0	13.0	13.5	13.1	12.8	

[a] *Lh*-SVWN, $\gamma = 0.48t$. [b] *Lh*-SVWN, $\gamma = 0.22s$. [c] *Lh*-SLYP, $\gamma = 0.24s$. [d] *Lh*-SVWN, $\gamma = (0.446 \pm 0.0531\ \zeta)t$. [e] *Lh*-SVWN, $\gamma = \mathrm{erf}[(0.196 \pm 0.0416\ \zeta)s]$. [f] ref 71 (EPR in Kr matrix). [g] ref 72 (EPR in aqueous $KCrOF_4$−HF solutions). [h] refs 73 (EPR of Cr-surface impregnated rutile (TiO_2) subjected to the exposure of SO_2, Cl_2, and HCl), and 74 (EPR in CH_2Cl_2 solution). [i] ref 75 (EPR in Ne matrix). [j] ref 76 (EPR of radicals trapped in $CHCl_3$ glass). [k] ref 77 (EPR in $Co(CO)_6$ host crystal). [l] ref 78 (EPR in C_6D_6 matrix). [m] ref 79 (EPR in Ne matrix). [n] ref 80 (single crystal EPR). [o] ref 81 (EPR in Kr matrix). [p] ref 82 (EPR in Ar matrix). [q] See footnotes h and j in Table 1. [r] Except for BHPW91 and BHLYP, where the largest error is observed for the $\Delta g_{\perp}$ component of MnO_3 (due to strongly spin-contaminated solutions), for all other functionals, the largest outlier is the Δg_{zz} component of $Cu(acac)_2$. [s] See footnote k to Table 1 (data in ppt).

ment. It has been demonstrated previously[21] that standard GGA or global hybrid functionals tend to reproduce the spread of these main-group g-tensors well, with a slight overestimate of the absolute value in most cases. A notable exception is the Δg_{33} component of the H_2O^+ radical, which is significantly underestimated by standard functionals. This has been traced back previously to a near-degeneracy situation.[17] We do, therefore, not expect much room for improvement with local hybrid functionals, in particular, as the experimental error bars often exceed 500 ppm (0.5 ppt or 0.0005), and the agreement between theory and experiment of ca. 500−1000 ppm should be considered as satisfactory.[45]

Looking at the mean absolute errors (MAEs) and results of linear regression analyses, we do indeed confirm the previously found[17] relatively small overall sensitivity of the results to the functional. Even LSDA, which is poor for thermochemistry, kinetics, and other properties, performs well here. We, therefore, use the local hybrid data in Table 1 mainly to validate the generalized CPKS implementation. Indeed, the performance of the five local hybrids *Lh*-I to *Lh*-V is overall similar to that of standard global hybrids like B3PW91 or B3LYP. Looking more closely, we see that, upon consideration of all molecules and components, the *s*-LMF functionals provide a somewhat larger and, thus, an improved slope than those of the *t*-LMF-based local hybrids and the standard global hybrids. This changes upon exclusion of the Δg_{33} component of H_2O^+. Now all slopes (except for BP86) are larger than 1, and the *t*-LMFs give the slightly better slopes than the *s*-LMFs. The global hybrids BHLYP and BHPW91 with 50% exact exchange give even larger slopes. MAEs and standard deviations (SD) of all local hybrids are comparable to B3PW91, B3LYP, or BP86 and are lower than those of BHLYP or BHPW91 (the 50% EXX admixture of the latter two functionals leads to some spin contamination, which may be responsible for the larger scatter of the data).[17]

Looking at the special case of H_2O^+ (see above), performance of the local hybrids is also similar to that of the global hybrids. The slightly larger Δg_{33} component with *Lh*-III may reflect the use of the LYP correlation functional (see also BHLYP results). For this radical, the LSDA, in form of the SVWN functional, has been shown previously to perform particularly well, most likely due to fortuitous error cancellation regarding the near-degeneracy of the Kohn−Sham eigenvalues.[17] Apart from H_2O^+, the largest deviations from experiment (cf. maximal signed errors (MaxSEs) in Table 1) are observed almost always for either Δg_{11} (negative) or Δg_{22} (positive) components of the O_3^- radical anion (the only exception is SVWN, which shows the largest error for the Δg_{33} component of HCO).

A rather different situation than for these main-group radicals holds for the transition-metal complexes (Table 2). Here, the dependence on EXX admixture is much more pronounced. As shown previously,[17] the semilocal functionals (SVWN and BP86) exhibit reasonable correlation with experiment but with a severe systematic underestimation of the linear regression slope. Global hybrids with a moderate EXX admixture (B3PW91 and B3LYP) improve matters but still recover only ca. 70% of the slope. The “half and half” functionals BHPW91 and BHLYP finally overestimate the slope somewhat and exhibit unacceptably large scattering of the results (cf. MAEs and SDs). This is related to significant spin contamination in many cases (much more so than in the main-group radicals), as has been analyzed in detail previously.[17,19,68]

The five local hybrids tested perform essentially as good as B3PW91 and B3LYP. This holds not only for the overall statistics of the results but also for most individual systems. A very slight reduction of the slope is found when introducing spin polarization into the LMF (*Lh*-IV and *Lh*-V). This may reflect the overall somewhat reduced average EXX admixture.[32]

Looking at individual complexes, we note TiF_3 as a case with particularly large underestimate of the $\Delta g_\perp$ component (Table 2). Here, even a larger than 50% EXX admixture would still improve the agreement with experiment (spin contamination is not a problem for this molecule). For this example, all five local hybrids provide results intermediate between the hybrids with 20% and 50% exact exchange. Similar behavior pertains, e.g., to $Co(CO)_4$ and $Ni(CO)_3H$, where, however, the local hybrid results are already in favorable agreement with experiment (in the latter case, the standard global hybrids overshoot already). In contrast, for the two copper complexes, $Cu(NO_3)_2$ and $Cu(acac)_2$, the local hybrids give slightly lower g-shifts than B3LYP or B3PW91 and, thus, also slightly worse agreement with experiment.

A possible explanation for the fact that the local hybrids exhibit larger g-shifts than B3LYP or B3PW91 for the early 3d complex TiF_3 but reduced g-shifts for the later metal centers Ni and Cu (for the intermediate Co, the g-shifts are very similar) relates to a previously discussed behavior[27,36] of the *average* exact exchange admixtures of the simple one- or two-parameter local hybrids discussed here. This trend may be monitored by density-averaged LMF values:

$$\bar{\gamma}_\sigma = \int \gamma_\sigma(\mathbf{r})\rho_\sigma(\mathbf{r})d\mathbf{r} / \int \rho_\sigma(\mathbf{r})d\mathbf{r} = (1/N_\sigma)\int \gamma_\sigma(\mathbf{r})\rho_\sigma(\mathbf{r})d\mathbf{r}, \qquad \sigma = \alpha, \beta \quad (36)$$

or, in a simplified spin-averaged way, by

$$\bar{\gamma} = \frac{N_\alpha \bar{\gamma}_\alpha + N_\beta \bar{\gamma}_\beta}{N_\alpha + N_\beta} \quad (37)$$

It has been found that these average EXX admixtures tend to decrease as one moves to higher nuclear charges both for isolated atoms and for molecules made from these atoms.[27,36] For the free 3d atoms, $\bar{\gamma}$ gradually decreases from 0.229 (Ti) to 0.186 (Cu). The overall range for the complexes is less pronounced (they exhibit all values between 0.21 and 0.25) due to the contributions from the ligand spheres. However, as the g-shift is dominated by the spin-orbit contributions of the metal center and localized ligand-field-type excitations in all of these systems, the observed decrease of $\bar{\gamma}$ (which derives mainly from core and semicore regions of the atoms) is certainly most relevant and explains some of the observed trends. The future development of local hybrids will benefit from an improved understanding of the predominant density regions affecting certain properties.

The lowest atomic $\bar{\gamma}$ value (0.167) is found for the 4d element Mo. However, for the two Mo complexes in the test series, the local hybrids provide, again, g-shift results close to the B3LYP and B3PW91 data. They underestimate the absolute value of the (negative) experimental $\Delta g_\perp$ components slightly and of the $\Delta g_\parallel$ components more strongly. However, in these cases, one has to keep in mind that for 4d complexes, higher-order spin-orbit effects, which have been neglected in the present work, become already notable. In axially symmetric Mo complexes, they have been shown in our previous work to render particularly the $\Delta g_\parallel$ component more negative.[64,69] For example, at B3PW91 level, $\Delta g_\parallel$ in $MoOCl_4^-$ is lowered by about 11 ppt and $\Delta g_\perp$ by about 4 ppt when going from a perturbational treatment of spin-orbit coupling to a two-component variational Douglas−Kroll−Hess calculation of the g-shift tensors.[64] Taking into account similar corrections for higher-order spin-orbit effects in 4d systems, performance of the standard global hybrids and the local hybrids for the two Mo complexes is somewhat better than suggested by the data in Table 2, in particular for the parallel component.

The present local-hybrid results for g-tensors of transition-metal complexes suggest that for the systems and the particular property at hand, the (average or local) EXX admixture at the metal center itself is most crucial for the performance. Overall, the five local hybrids studied perform as good but not notably better than standard global hybrids B3LYP or B3PW91. Probably, the one- or two-parameter LMFs studied, which were optimized exclusively for thermochemistry and for reaction barriers, provide too low exact exchange near the transition-metal center to improve the agreement compared to global hybrids with ca. 20% exact-exchange admixture throughout the system. This provides clues toward the construction of improved LMFs, a line we intend to follow in the future.

6. Conclusions and Outlook

A generalized coupled-perturbed Kohn−Sham (CPKS) scheme for the calculation of second-order magnetic properties has been derived and implemented for occupied orbital-dependent (OOD) functionals depending on the exact-exchange energy density. Within a nonrelativistic one-component approach, the coupling terms in the CPKS scheme arise exclusively from variation of the exact-exchange energy density itself with respect to the orbitals, cf. eq 31. These terms involve the nonlocal exchange operator. Other occurrences of the exact-exchange energy density in functional derivatives of the OOD functionals, with respect to the orbitals, do not contribute to the coupling terms. This allows a relatively straightforward implementation of the CPKS equations for OOD ("hyper-GGA") functionals and for magnetic properties.

The generalized CPKS scheme has been implemented and tested for electronic g-tensors with local hybrid functionals. Overall, the five local hybrids tested exhibit similar performance for the g-shift tensors of main-group radicals and transition-metal complexes as the standard global hybrids, like B3LYP. In case of the transition-metal complexes, in particular, closer analysis of the results suggests that with the local mixing functions (LMFs) tested, the larger flexibility of local over global hybrids has not yet been exploited sufficiently. This pertains mostly to the EXX admixture around the transition-metal center. This result may not be surprising given: (i) the use of only one or two semiempirical parameters in the LMFs studied so far; and (ii) the optimization of these parameters only for main group thermochemistry and reaction barriers. Indeed, these simple local hybrids outperform standard global hybrids already notably in these areas. Improved performance for g-tensors and, of course, for various other magnetic or electric properties will depend on the construction of more flexible LMFs and on their optimization for the various critical regions within an atom, molecule, or solid.

Finally, comparison between a direct use of nonlocal exact-exchange potentials and a transformation to local and multiplicative potentials within an OEP framework will be of interest. This will require the implementation of more accurate OEP-based schemes than used in our previous evaluation of localized local hybrid potentials for nuclear shieldings.[22]

Acknowledgment. This work has been funded by Deutsche Forschungsgemeinschaft (project KA1187/10-1) within Priority Program 1145, "Modern and universal first-principles methods for many-electron systems in chemistry and physics".

References

(1) See e.g., In *Calculation of NMR and EPR Parameters. Theory and Applications*; Kaupp, M., Bühl, M., Malkin, V. G., Eds.; Wiley-VCH: Weinheim, Germany, 2004; and references therein.

(2) Becke, A. D. *J. Chem. Phys.* **1993**, *98*, 1372.

(3) Becke, A. D. *J. Chem. Phys.* **1993**, *98*, 5648.

(4) Dirac, P. A. M. *Proc. Cambridge Phil. Soc.* **1930**, *26*, 376.

(5) Slater, J. C. *Phys. Rev.* **1951**, *81*, 385.

(6) Vosko, S. J.; Wilk, L.; Nusair, M. *Can. J. Phys.* **1980**, *58*, 1200. and references therein.

(7) Perdew, J. P.; Wang, Y. *Phys. Rev. B: Condens. Matter* **1992**, *45*, 13244.

(8) Perdew, J. P. *Phys. Rev. B: Condens. Matter* **1986**, *33*, 8822.

(9) Becke, A. D. *Phys. Rev. A: At., Mol., Opt. Phys.* **1988**, *38*, 3098.

(10) Perdew, J. P.; Chevary, J. A.; Vosko, S. H.; Jackson, K. A.; Pederson, M. R.; Singh, D. J.; Fiolhais, C. *Phys. Rev. B: Condens. Matter* **1992**, *46*, 6671.

(11) (a) Lee, C.; Yang, W.; Parr, R. G. *Phys. Rev. B: Condens. Matter* **1988**, *37*, 785. (b) Miehlich, B.; Savin, A.; Stoll, H.; Preuss, H. *Chem. Phys. Lett.* **1989**, *157*, 200.

(12) Perdew, J. P.; Burke, K.; Ernzerhof, M. *Phys. Rev. Lett.* **1996**, *77*, 3865.

(13) Proynov, E. I.; Vela, A.; Salahub, D. R. *Chem. Phys. Lett.* **1994**, *230*, 419.

(14) Tao, J.; Perdew, J. P.; Staroverov, V. N.; Scuseria, G. E. *Phys. Rev. Lett.* **2003**, *91*, 146401.

(15) Bühl, M.; Kaupp, M.; Malkin, V. G.; Malkina, O. L. *J. Comput. Chem.* **1999**, *20*, 91.

(16) (a) Durant, J. L. *Chem. Phys. Lett.* **1996**, *256*, 595. (b) Chermette, H.; Razafinjanahary, H.; Carrion, L. *J. Chem. Phys.* **1997**, *107*, 10643.

(17) Kaupp, M.; Reviakine, R.; Malkina, O. L.; Arbuznikov, A. V.; Schimmelpfennig, B.; Malkin, V. G. *J. Comput. Chem.* **2002**, *23*, 794.

(18) Arbuznikov, A. V.; Kaupp, M. *Chem. Phys. Lett.* **2004**, *391*, 16.

(19) Munzarová, M.; Kaupp, M. *J. Phys. Chem. A* **1999**, *103*, 9966.

(20) Arbuznikov, A. V.; Kaupp, M. *Chem. Phys. Lett.* **2004**, *386*, 8.

(21) Malkina, O. L.; Vaara, J.; Schimmelpfennig, B.; Munzarová, M.; Malkin, V. G.; Kaupp, M. *J. Am. Chem. Soc.* **2000**, *122*, 9206.

(22) Arbuznikov, A. V.; Kaupp, M. *Chem. Phys. Lett.* **2007**, *442*, 496.

(23) Cruz, F. G.; Lam, K.-C.; Burke, K. *J. Phys. Chem. A.* **1998**, *102*, 4911.

(24) Perdew, J. P.; Schmidt K. In *Density Functional Theory and ist Application to Materials*, Proceedings of American Institute of Physics, Antwerp, Belgium, June 8−10, 2000; van

Doren, V., van Alsenoy, C., Geerlings, P., Eds.; AIP: Melville, NY, 2001; Vol. 577, pp 1−20.

(25) Jaramillo, J.; Scuseria, G. E.; Ernzerhof, M. *J. Chem. Phys.* **2003**, *118*, 1068.

(26) Bahmann, H.; Rodenberg, A.; Arbuznikov, A. V.; Kaupp, M. *J. Chem. Phys.* **2007**, *126*, 011103.

(27) Arbuznikov, A. V.; Kaupp, M. *Chem. Phys. Lett.* **2007**, *440*, 160.

(28) Kaupp, M.; Bahmann, H.; Arbuznikov, A. V. *J. Chem. Phys.* **2007**, *127*, 194102.

(29) Janesko, B. G.; Scuseria, G. E. *J. Chem. Phys.* **2007**, *127*, 164117.

(30) Janesko, B. G.; Scuseria, G. E. *J. Chem. Phys.* **2008**, *128*, 084111.

(31) Perdew, J. P.; Staroverov, V. N.; Tao, J.; Scuseria, G. E. *Phys. Rev. A: At., Mol., Opt. Phys.* **2008**, *78*, 052513.

(32) Arbuznikov, A. V.; Bahmann, H.; Kaupp, M. *J. Phys. Chem. A*; accessed online 07/15/2009; DOI: 10.1021/jp903233q.

(33) Della Sala, F.; Görling, A. *J. Chem. Phys.* **2001**, *115*, 5718.

(34) (a) Sharp, R. T.; Horton, G. K. *Phys. Rev.* **1953**, *90*, 317. (b) Talman, J. D.; Shadwick, W. F. *Phys. Rev. A: At., Mol., Opt. Phys.* **1976**, *14*, 36.

(35) Görling, A. *J. Chem. Phys.* **2005**, *123*, 062203.

(36) Arbuznikov, A. V.; Kaupp, M.; Bahmann, H. *J. Chem. Phys.* **2006**, *124*, 204102.

(37) (a) Arbuznikov, A. V.; Kaupp, M. *Int. J. Quantum Chem.* **2005**, *102*, 261. (b) Arbuznikov, A. V.; Kaupp, M. *Chem. Phys. Lett.* **2004**, *386*, 8.

(38) Wilson, P. J.; Tozer, D. J. *J. Chem. Phys.* **2002**, *116*, 10139.

(39) Hesselmann, A.; Götz, A. W.; Della Sala, F.; Görling, A. *J. Chem. Phys.* **2007**, *127*, 054102 and references therein.

(40) Staroverov, V. N.; Scuseria, G. E.; Davidson, E. R. *J. Chem. Phys.* **2006**, *124*, 141103.

(41) Seidl, A.; Görling, A.; Vogl, P.; Majewski, J. A.; Levy, M. *Phys. Rev. B: Condens. Matter* **1996**, *53*, 3764.

(42) Janesko, B. G.; Krukau, A. V.; Scuseria, G. E. *J. Chem. Phys.* **2008**, *129*, 124110.

(43) Kutzelnigg, W. *Israel J. Chem.* **1980**, *19*, 193.

(44) Schindler, M.; Kutzelnigg, W. *J. Chem. Phys.* **1982**, *76*, 1919.

(45) Neese, F. *J. Chem. Phys.* **2001**, *115*, 11080.

(46) Kümmel, S.; Kronik, L. *Rev. Mod. Phys.* **2008**, *80*, 3.

(47) Arbuznikov, A. V.; Kaupp, M. *J. Chem. Phys.* **2009**, *131*, 084103.

(48) (a) Becke, A. D. *J. Chem. Phys.* **2003**, *119*, 2972. (b) Becke, A. D. *J. Chem. Phys.* **2005**, *122*, 064101.

(49) (a) Mori-Sánchez, P.; Cohen, A. J.; Yang, W. *J. Chem. Phys.* **2006**, *124*, 091102. (b) Cohen, A. J.; Mori-Sánchez, P.; Yang, W. *J. Chem. Phys.* **2007**, *126*, 191109. (c) Mori-Sánchez, P.; Cohen, A. J.; Yang, W. *J. Chem. Phys.* **2007**, *127*, 034101.

(50) Schreckenbach, G.; Ziegler, T. *J. Phys. Chem. A: At., Mol., Opt. Phys.* **1997**, *101*, 3388.

(51) Reviakine, R. Ph.D. Thesis. Institute of Inorganic Chemistry, Slovak Academy of Sciences, Bratislava, Slovak Republic, 2002.

(52) McWeeny, R. *Methods of Molecular Quantum Mechanics*, 2nd ed.; Academic Press: London, NY, 1989.

(53) Malkin, V. G.; Malkina, O. L.; Reviakine, R.; Arbuznikov, A. V.; Kaupp, M.; Schimmelpfennig, B.; Malkin, I.; Repiský, M.; Komorovský, S.; Hrobárik, P.; Malkin, E.; Helgaker, T.; Ruud, K. *ReSpect*, Version 2.1; 2008.

(54) Hess, B. A.; Marian, C.; Wahlgren, U.; Gropen, O. *Chem. Phys. Lett.* **1996**, *251*, 365.

(55) The AMFI code used is due to: Schimmelpfennig, B. *Atomic Spin-Orbit Meanfield Integral Program*; Stockholms Unviersitet: Sweden; 1996.

(56) Malkina, O. L.; Schimmelpfennig, B.; Kaupp, M.; Hess, B. A.; Chandra, P.; Wahlgren, U.; Malkin, V. G. *Chem. Phys. Lett.* **1998**, *296*, 93.

(57) (a) Jensen, F. *J. Chem. Phys.* **2001**, *115*, 9113. **2002**, *116*, 3502 (E). (b) Jensen, F. *J. Chem. Phys.* **2002**, *116*, 7372. (c) Jensen, F. *J. Chem. Phys.* **2002**, *117*, 9234. (d) Jensen, F. *J. Chem. Phys.* **2003**, *118*, 2459. (e) Jensen, F.; Helgaker, T. *J. Chem. Phys.* **2004**, *121*, 3463.

(58) Jensen, F. *J. Chem. Theory Comput.* **2006**, *2*, 1360.

(59) Jensen, F. *J. Chem. Theory Comput.* **2008**, *4*, 719.

(60) Fægri K. http://folk.uio.no/knutf/bases/one; accessed September 2003.

(61) Bauschlicher, C. W., Jr.; Langhoff, S. R.; Barnes, L. A. *J. Chem. Phys.* **1989**, *91*, 2399.

(62) Kutzelnigg, W.; Fleischer, U.; Schindler, M. *NMR - Basic Principles and Progress*; Diehl, P., Fluck, E., Günther, H., Kosfeld, R., Eds.; Springer: Heidelberg, Germany, 1990; Vol. 23, pp 165−262.; and references therein.

(63) Arbuznikov, A. V.; Vaara, J.; Kaupp, M. *J. Chem. Phys.* **2004**, *120*, 2127.

(64) Fritscher, J.; Hrobárik, P.; Kaupp, M. *J. Phys. Chem. B* **2007**, *111*, 4616.

(65) In contrast to Becke's original "half-and-half" functional (ref 1), where 50% of the exact exchange is mixed with the same amount of the LSDA exchange, the latter is replaced by B88 GGA exchange (ref 8) in BHPW91 and BHLYP.

(66) Patchkovskii, S.; Ziegler, T. *J. Chem. Phys.* **1999**, *111*, 5730.

(67) Arbuznikov, A. V.; Kaupp, M.; Malkin, V. G.; Reviakine, R.; Malkina, O. L. *Phys. Chem. Chem. Phys.* **2002**, *4*, 5467.

(68) Munzarová, M. L.; Kubáček, P.; Kaupp, M. *J. Am. Chem. Soc.* **2000**, *112*, 11900.

(69) Hrobárik, P.; Malkina, O. L.; Malkin, V. G.; Kaupp, M. *Chem. Phys.* **2009**, *356*, 229.

(70) (a) Lushington, G. H.; Grein, F. *Theor. Chim. Acta* **1996**, *93*, 259. (b) Bruna, P.; Lushington, G. H.; Grein, F. *Chem. Phys.* **1997**, *225*, 1. (c) Lushington, G. H. PhD Thesis, University of New Brunswick, Canada, 1996.

(71) Fairhust, S. A.; Morton, J. R.; Preston, K. F. *J. Magn. Reson.* **1983**, *55*, 453.

(72) Manoharan, P. T.; Rogers, M. T. *J. Chem. Phys.* **1968**, *49*, 5510.

(73) Amorelli, A.; Amorelli, T. S.; Evans, J. C.; Rowlands, C. C. *J. Mater. Sci.* **1990**, *25*, 796.

(74) Gahan, B.; Garner, D. C.; Hill, L. H.; Mabbs, F. E.; Hargrave, K. D.; McPhail, A. T.; Gross, P. M. *J. Chem. Soc., Dalton Trans.* **1977**, 1726.

(75) Kasai, P. H.; Whipple, E. B.; Weltner, W., Jr. *J. Chem. Phys.* **1966**, *44*, 2581.

(76) Wilson, R.; Kivelson, D. *J. Chem. Phys.* **1966**, *44*, 4445.

(77) Morton, J. R.; Preston, K. F. *J. Chem. Phys.* **1982**, *76*, 234.

(78) Howard, J. A.; Morton, J. R.; Preston, K. F. *Chem. Phys. Lett.* **1981**, *83*, 226.

(79) Ferrante, R. F.; Wilkerson, J. L.; Graham, W. R. M.; Weltner, W., Jr. *J. Chem. Phys.* **1977**, *67*, 5904.

(80) Sunil, K. K.; Rogers, M. T. *Inorg. Chem.* **1981**, *20*, 3283.

(81) Morton, J. R.; Preston, K. F. *J. Chem. Phys.* **1984**, *81*, 5775.

(82) De Vore, T. C.; Weltner, W., Jr. *J. Am. Chem. Soc.* **1977**, *99*, 4700.

CT900392E

JCTC Journal of Chemical Theory and Computation

Localized Orbital Corrections for the Barrier Heights in Density Functional Theory

Michelle Lynn Hall, Dahlia A. Goldfeld, Arteum D. Bochevarov, and Richard A. Friesner*

Department of Chemistry, Columbia University,
3000 Broadway, New York, New York, 10027

Received July 30, 2009

Abstract: This work describes the extension of a previously reported empirical localized orbital correction model for density functional theory for atomization energies, ionization potentials, electron affinities, and reaction enthalpies to the correction of barrier heights. Various chemical reactions' barrier heights are corrected, including cycloadditions, cycloreversions, dipolar cycloadditions, S_N2's, carbon and hydrogen radical reactions, sigmatropic shifts, and electrocyclizations. The B3LYP localized orbital correction version of the model reduces the number of outliers and overall mean unsigned error versus experiment or ab initio values from 3.2 to 1.3 kcal/mole for barrier heights and from 5.1 to 1.1 kcal/mole for reaction enthalpies versus B3LYP. Furthermore, the new model has essentially zero additional computational cost beyond standard DFT calculations. Although the model is heuristic and is based on multiple linear regression to experimental or ab initio data, each of the parameters is justified on chemical grounds and provides insight into the fundamental limitations of DFT, most importantly the failure of current DFT methods to accurately account for nondynamical electron correlation.

I. Introduction

In a series of previous publications, we have developed an approach to improving density functional theory (DFT) methods[1] based on empirical localized orbital corrections (DFT-LOC).[2] When used in conjunction with the B3LYP functional[3] (B3LYP-LOC, which will be the focus of the present publication), these corrections provide a remarkable improvement in atomization energies,[2a] ionization potentials and electron affinities,[2b] and heats of reaction for molecules composed of atoms in the first two rows of the periodic table,[2c] as detailed in Sections II.A, II.B, and II.D, respectively. Recently we have also demonstrated improvements for thermochemistry of small transition-metal species as summarized in Section II.C.[2d]

Our aforementioned correction scheme is based upon assignment of parameters using the equilibrium geometries (i.e., reactant and product) only. A general theory must enable calculation of the energy of the molecule as a function of the atomic coordinates for an arbitrary arrangement of the atoms. This in turn requires that the corrections be formulated as a continuous function, rather than discrete parameters.

Such a function can be easily constructed and optimized, utilizing a molecular mechanics-like formulation, with the addition of empirical terms to rectify errors endemic to B3LYP. These parameters can eventually even be deployed to treat dispersion, an area in which B3LYP is known to perform poorly. Still, optimization of such a function cannot proceed without an understanding of how the parameters change as bonds are made and broken. We have developed parameters for errors manifested in reactants and products, allowing more accurate calculation of enthalpies, in previous publications as summarized in Section II.D. Note that we do not attempt to correct for errors found in energies of dissociated atoms themselves but instead correct for the errors found in differences of energies exclusively. For example, we studied reaction enthalpies[2d] where we considered the differences in energies of the well-defined reactants and products only. By considering these well-behaved species instead of attempting to tackle dissociated atoms, we focus

---

* Corresponding author. Telephone: 212-854-7606. Fax: 212-854-7454. E-mail: rich@chem.columbia.edu.

10.1021/ct9003965 CCC: $40.75

our efforts on areas where DFT has already been shown to produce reasonable results and, therefore, can produce remarkable results upon application of corrections schemes, such as those we continue to develop.[2a−d] In the intermediate region connecting reactant to product, parameterization of the model is necessary, particularly at the transition state where unusual geometries and effective hybridization states of central atoms are routinely observed. With transition-state correction parameters in place, the remainder of the potential surface can be approximated via interpolation between the key stationary points (equilibrium geometry, transition state, and separated reactants and products). Ideally the interpolating function would be modeled after accurate ab initio quantum chemical behavior in the bond-breaking region. In practice, unrestricted DFT actually performs reasonably well (although not perfectly) in this regime, and highly precise results for the bond-breaking region are not critical for the vast majority of practical chemical applications. Consequently, we focus in this paper on the task of developing accurate and robust parameters for B3LYP-LOC for correcting the barrier height at the transition state, fitting to experimental and high-quality ab initio data for more than 100 chemical reactions taken from the literature.

We have assembled a wide range of reactions[4] of various types, encompassing radical reactions, additions, cyclizations and reactions containing neutral, cationic, and anionic species. The size and diversity of the training set is, thus, larger and more varied than has been used in previous tests of DFT functionals or in efforts to optimize these functionals.[5] In our view, the use of large and diverse data sets is critical to avoid over-fitting, to overcome noise in the data set (inevitable as one moves away from the highly filtered experimental data sets employed by e.g., Pople and coworkers in testing and optimizing G3 theory),[8] and to present to the model a variety of qualitatively different transition-state motifs which may require new parameters. The present data set, while still far from completely extensive, does represent progress as compared to alternatives in the literature.[5]

In many cases, data is available for both forward and backward reactions, with the barriers related (as mandated by detailed balance) by the enthalpy of reaction. This implies that one cannot obtain good results for both directions, regardless of the parameterization of the transition-state model, unless the enthalpies of reaction are accurate. As a result, we have carefully examined the enthalpies of reaction for all of our test cases, with regard to both performance of B3LYP-LOC, and in terms of possible errors in the literature estimates (experimental or derived from high-level ab initio calculations) of these values. For example, Truhlar and coworkers have assembled a series of radical reactions, which have formed a key component of their DFT test and training sets for many years.[7] They incorporate many sophisticated terms into their estimations of experimental barrier heights (e.g., tunneling corrections), which undoubtedly have improved the precision of the data set. Nevertheless, there are cases (noted in the text) where the “experimental” enthalpies of reaction they use are in significant conflict with, for example, results obtained by the Pople group for the same quantity (as derived from the Pople results for atomization energies,[6] which can be combined to yield enthalpies of reaction). In these cases, we have had to make decisions concerning which data to employ, and the choices are described below. The main point is that the construction of true benchmark data sets for testing barrier height calculations, with well defined error bars, is still a work in progress, and this impinges upon what one can expect in any set of theory/experiment comparisons in these areas. In contrast, for small-molecule atomization energies, the ability to converge high-level CCSD(T) calculations with basis set extrapolations, relativistic corrections, etc., provides a means to resolve most disputes concerning interpretation of experimental data around equilibrium geometries. True benchmarks have been available for some time, at least for small molecules, as they predominantly populate the G2 data set.[8] For transition states and geometries far from equilibrium, more sophisticated approaches than CCSD(T) might be required, such as methods based on multireference wavefunctions.

In addition to facilitating the development of new transition-state parameters, the present set of reactions provides an opportunity to test the B3LYP-LOC performance for enthalpies of reaction on a new data set, which has not been included in the training set. A subset of the reactions we study here can be constructed from the Pople G3 data base,[6] which we did use as a training set for B3LYP-LOC. Yet, if these reactions are removed, there remains a substantial number of cases to which B3LYP-LOC has never been exposed. The results, reported below, obtained with no parameter adjustment for the equilibrium geometry parameter set, demonstrate that the performance for this test set (which contains some rather complex and unusual molecules) is comparable to that of the training set, further validating the B3LYP-LOC parameterization as robust and applicable outside the domain of its training set with no falloff in the quality of the results. The overall average error for enthalpies of reaction, 1.2 kcal/mole, is comparable to that expected for high-level ab initio methods, such as G3 theory, and is likely within the error bars of the experimental and high-level computational data.

The transition-state parameterization itself requires a total of 8 new parameters unique to transition states; hence, a total of 36 parameters, including 22 for neutral equilibrium species[2a] and an additional 6 for the charged species,[2b] were utilized in this work. While this number might seem large, it is comparable to the number of parameters exploited by modern DFT functionals, such as M06-2X.[17] Some of these parameters address new hybridization states that are created by attacks on various types of central atoms, and these parameters are generally consistent with those already optimized for enthalpies of reaction.[2a] Similarly there are a few new parameters for stretched or half bonds, which again are consistent with the equilibrium results[2a] (despite the lack of constraints used in the parameter optimization). Overall, the ratio of the number of new adjustable parameters (8) to that of training set cases (105) appears reasonable, and the parameters can all be physically rationalized in light of previous results.

Charged molecules present a special challenge for the B3LYP-LOC method in that corrections for charging and discharging must be performed via a separate set of parameters, developed in ref 2b. We have used the parameters from that reference without adjustment, achieving reasonable results for both anions and cations. Specialized parameters for unusual groups, such as azides, would in fact improve the results, but we have avoided this because we do not believe there is sufficient or diverse enough data to avoid the danger of over-fitting for such cases. Nevertheless, such a path could readily be pursued in the future, if additional data were to be generated [e.g., via converged CCSD(T) calculations].

The paper is organized as follows. In Section II, we provide a brief summary of the B3LYP-LOC approach, referring to previous papers for detailed discussion of parameterization and validation. Section III presents the development of the B3LYP-LOC model for transition states, introducing the eight new parameters required for these calculations. Section IV describes the results obtained for the 105 reactions in the training set, for both reaction enthalpies and barrier heights, and discusses the distribution of errors, including possible explanations for the small number of outliers that are observed. Finally, in Section V, the Conclusion, we summarize our results and briefly discuss future directions.

II. Overview of the B3LYP-LOC Methodology

In this section, we simply review the work on the B3LYP-LOC methodology that has already been published, as this forms the foundation for the work presented herein. Note that no additions or modifications are made to any of the methods presented in our previous publications.

II.A. Atomization Energies. The original B3LYP-LOC work[2a] utilized 22 empirically determined, but chemically justified, parameters to reduce the mean absolute deviation for atomization energies on the G3 dataset of 222 molecules from 4.8 to 0.8 kcal/mole, for uncorrected B3LYP and B3LYP-LOC, respectively. This value is comparable to that obtained using G3 theory, 1.1 kcal/mole, but G3 theory incorporates coupled cluster methods, thus, making it intractable for larger molecules. Almost all outliers were eliminated with essentially zero additional computational cost beyond standard DFT calculations, as the corrections are applied a posteriori in an additive fashion. All corrections are based upon valence bond assignments and are divisible into four major categories: corrections of atoms, individual bonds, neighboring bonds of a given bond, and radical environmental corrections. These parameters also provide valuable insight into the fundamental limitations of DFT, specifically, the difficulties exhibited by DFT methods in accurately modeling variations in nondynamical electron correlation across different types of chemical bonds, lone pairs, hybridization states, and singly vs doubly occupied orbitals. [9,10]

To better understand these limitations, first consider the simple case of diatomic hydrogen, H_2. As this molecule is stretched to increasing bond lengths, the exact [Hartree−Fock (HF)] exchange hole remains delocalized over both atoms, even though the true exchange correlation hole is localized over mostly just one atomic center. Combining this exact HF exchange with localized correlation produces a delocalized exchange−correlation hole, which is qualitatively incorrect in nature, producing large errors in DFT calculations that employ a full exact exchange model. This is substantially improved by combining the exact exchange with Becke exchange and the generalized gradient approximation, producing a more localized exchange hole. The qualitatively correct behavior of the exchange-correlation hole enabled significant progress to be made in reducing errors for gradient-corrected DFT functionals, such as BP86,[12] BLYP,[13] and PBE.[14]

Dynamical electron correlation (taken on the length scale of an atom) is well modeled by gradient corrections in the exchange and correlation components of modern functionals; on the other hand, nondynamical electron correlation (taken on the length scale of a bond) is more problematic.[10] Within each localized electron pair (in a bond or lone pair), there is a self-interaction “error” given by the difference in the self-Coulomb and exchange terms. Although this self-interaction is necessarily zero for unpaired electrons, i.e., the Coulomb and exchange terms cancel, DFT assigns a non-zero value in this case, resulting in detrimental errors, especially at increasing bond lengths, where the self-interaction becomes very large and negative. In the case of doubly occupied orbitals, we posit that the self-interaction error embodied in DFT is actually used to quantitatively model the nondynamical electron correlation present within a localized bond.[9] The addition of a component of HF exchange, as is done in B3LYP and other hybrid functionals, can then be thought of as adjusting the size of the self-interaction term in the DFT exchange functional; since the HF exchange term has no self-interaction, increasing the fraction of HF exchange lowers the remaining self-interaction in the functional. Fitting the fraction of HF exchange to experimental atomization energies then allows a more accurate matching between the self-interaction energy for an electron pair and between what is required to represent nondynamical correlation for that pair. The success of B3LYP in reducing the average error in atomization energies for the G2 data set, as compared to the great majority of gradient corrected functionals, is evidence that this approach is successful in realizing its objective.[6]

However, the addition of HF exchange is effective at treating only the “average” nondynamical correlation of an electron pair in a localized bond, whereas differences in the local environment of various bonds and in their effects on the nondynamical correlation are not modeled easily by a localized gradient expansion.[10] Notably, while so-called global hybrid functionals, such as B3LYP, employ constant fractional admixtures of exact exchange, local hybrid functionals[22] employ position-dependent exact-exchange admixtures, allowing for deviations in the nondynamical correlation to be better modeled, at least in principle. This presents a unique and interesting way to address the issue of capturing nondynamical correlation that differs from our own approach but is not explored further here. Instead, the DFT-LOC methodology rests upon the assumption that the localized nuclear framework supporting an electron pair is a principal factor controlling the deviations in value of the nondynamical correlation from the “average” value within global hybrid functionals. Therefore, empirical corrections are applied based upon these localized frameworks. Consider, for example, the corrections applied to single bonds between heavy atoms of various lengths, for example the 6-311++G (3df,3pd) basis: short (−1.36 kcal/mole), medium (−1.90 kcal/mole), and long (−2.57 kcal/mole). These values become appreciably more negative with increasing bond length. This reflects the notion that as bond length increases, nondynamical correlation becomes more negative (as the electrons have more room to avoid each other), and DFT systematically underestimates this effect with increasing severity. In the extreme case, where there is a charge transfer leading to predominantly ionic bonding (e.g., in NaCl), implying substantial localization of the electron pair of the bond near one atom, the B3LYP results are most severely underbound (by 4.5 kcal/mole for NaCl); this parameter is consistent with the others listed above and, when used to correct all bonds of this type, leads to enormous improvement in B3LYP-LOC predictions for molecules in the G3 data set containing one or more bonds with substantial charge transfer character.

A further problem that can be observed with B3LYP calculations, and other functionals, is that the average error (as judged by the mean unsigned error) increases systematically with the size of the molecule under investigation.[15] For example, the MUE for B3LYP atomization energies for the G2,[8] extended G2,[8] and G3 datasets are 2.43, 3.08, and 4.81 kcal/mole, respectively, consistent with the increasing average molecular weight of the components of each of these three data sets. This systematic increase in error with molecule size is effectively addressed by the empirical corrections in the LOC scheme. Indeed, the errors in B3LYP are not random but are attributable to the specific localized chemical bonds in each molecule as well as the local environments of those bonds. It is important to emphasize that other functionals we tested (BLYP, B3PW91, SVWN, BP86, BPW91, B3P86, and later M05-2X and M06-2X) display greater average errors than B3LYP-LOC upon application of LOC corrections and, thus, apparently have errors that are less systematic in the LOC framework than B3LYP. Notably, the LOC-corrected versions of these other methods, including other hybrid functionals, GGAs and even the LDA, displayed non-trivial improvements when coupled with LOCs but are still not comparable to the remarkable improvement displayed by B3LYP-LOC itself. For example, the average error in BLYP for the G3 set is reduced from 7.3 kcal/mole to 2.1 kcal/mole, not as good an end point as for B3LYP whose errors were reduced from 3.1 kcal/mole to 0.6 kcal/mole but still an impressive improvement nonetheless. Effectively, the LOC scheme removes the systematic errors for each bond type, thereby qualitatively diminishing the accumulation of such errors with increasing molecular size to the point where the errors for the G3 data set, which contains much larger molecules, is only a few tenths of a kcal/mole larger than that of the G2 or extended G2 sets. Furthermore, problems with properly modeling cyclic, branched, and linear molecules (for which B3LYP exhibits quite different error patterns) are ameliorated via a simple correction based on nearest-neighbors of a given bond, noting that underbinding is present when the atoms comprising the bond make additional bonds that would enable an electron from the initial bond (e.g., long single bonds) to make excursions.

The validity of this method is verified by the successful application of the LOC parameters to the G3 dataset in which the mean unsigned error is reduced from 4.8 to 0.8 kcal/mole, a value not only competitive with that of G3 theory but also demanding orders of magnitude less computational cost. Further, after the application of the LOC scheme, the number of B3LYP outliers is substantially reduced. Thus, this DFT-based method consistently achieves near-chemical accuracy. Detailed parameters and results for atomization energies and enthalpies of reaction can be found in refs 2a and 2c and the accompanying Supporting Information.

II.B. Ionization Potentials and Electron Affinities. In a subsequent publication,[2b] the B3LYP-LOC methodology was extended from atomization energies to ionization potentials (IP) and electron affinities (EA). In this manner, B3LYP-LOC can now be extended to ionic, in addition to neutral, molecules with 37 parameters developed specifically for charged species. (Be that as it may, only six of these parameters were employed here, as they cover the most common chemistries, such as those studied in this work.) Further, systems with multiple unpaired electrons are also addressed. These new features are requisite for an approach that is aimed at applicability across a wide range of chemical phenomena. The methodology is applied to the G2 dataset of 134 molecules (IPs and EAs) with a resultant decrease in MUE (vs experiment) of 0.137 to 0.039 eV. This error is more than three times smaller than the original B3LYP error and is comparable to the errors obtained with G2 theory, a high-level ab initio method. Further, the number of outliers is also substantially reduced to levels below that achieved with G2 wave-function-based theory.

As with the B3LYP-LOC application to atomization energies, the corrections are applied a posteriori in an additive fashion and, therefore, account for only a trivial increase in computational cost over uncorrected B3LYP. The 22 empirical parameters from the original work[2a] are employed in addition to parameters exclusive to ions developed in this specific work. Again, these parameters are physically justifiable and provide insight into the fundamental nature of DFT. Unsurprisingly, DFT’s failure to accurately model nondynamical electron correlation and self-interaction error contributes substantially to errors in IPs and EAs, just as with atomization energies.

Here, the neutral atoms are taken as the reference state, and corrections are applied to the atomic or molecular ions and the neutral molecules, as necessary. The B3LYP-LOC energy of a charged atom is then given by the sum of the corrections for that charged atom (as specified in ref 2a) and the B3LYP energy for the charged atom. The B3LYP-LOC energy of a charged molecule is given by the full suite of LOC molecular corrections as specified in the original LOC work,[2a] in addition to those corrections defined for the charged species.[2b]

The original B3LYP-LOC work noted the striking similarity in the atomization energy errors as a function of valence bond structures, using this as the basis for the development of the LOC methodology. An investigation of the errors in EA and IP evidences another set of striking patterns, enabling a facile extension of the previous LOC methodology to these charged species.

For a complete discussion of all the parameters available for IP and EA calculations, the reader is referred to the relevant work,[2b] while those IP and EA parameters employed in this work are discussed below. These include corrections for delocalization of positive charge and for the removal or addition of an electron from an atomic or molecular orbital. The specific implementation of these parameters is discussed in Sections II.D.1 and II.D.2 for enthalpies of ionic reactions and in Sections III.B and III.C for barrier heights of ionic reactions. For cationic reactions, corrections for delocalization of positive charge included IP_D_A_A−H and IP_D_A_A−B. These correct for the delocalization of positive charge on an atom (A) through neighboring electron density from adjacent A−H and A−B bonds, respectively. Cationic reactions also necessitated corrections for the removal of an electron from an atomic orbital. These included IP_P3p_A/M and IP_P2p_M for the removal of an electron from a paired 3p or hybrid 3p orbital in a free atom or molecule and from a paired 2p-hybridized orbital in a molecule, respectively. Lastly, anionic reactions required corrections for the addition of an electron to an unpaired 2p orbital on an atom (EA_AO_U2p) or to the molecular orbital of a first-row atom with a localized radical and no adjacent multiple bonds (EA_R1_noMB).

The parameters from the IP/EA model[2b] are used in the present work without any modification. As is noted below, there are a few special cases (such as azides) where defining new parameters would likely reduce errors. In spite of this, we do not believe that the current data set is sufficiently large or diverse to justify such development at this time. As more data becomes available (via either experiments or calculations), increases in the number of parameters can be considered.

II.C. Transition Metals. The B3LYP-LOC methodology has also been successfully extended to transition-metal containing systems[2d] in which a data set of 36 experimental atomic energies and 71 bond dissociation energies were employed. Sets of 10 and 21 parameters were built to correct for atomic energy and bond dissociation energy errors, respectively, resulting in a MUE decrease from 7.7 to 0.4 kcal/mole for atomic data and 5.3 to 1.7 kcal/mole for bond dissociation data. This initial model is based upon a wide range of excitation energies, IPs, and bond energies gathered from experimental gas-phase measurements. Coupled cluster calculations on transition-metal species can be problematic; nonetheless, we provided benchmark coupled cluster calculations that agreed reasonably well with experiment for various metal diatomic species. Further, this work shows that the dominant sources of error are qualitatively analogous to those identified in the previous B3LYP-LOC publications[2a−c] and corrects for them accordingly, employing phenomenologically similar reasoning.

While the results contained within this work on transition metals are highly encouraging, they do not represent a complete treatment of transition metals containing systems. As most gas-phase bond energy data exist primarily for metals in their neutral state or as singly charged cations and metals with low coordination numbers, the dataset was limited to these types of systems. Obviously, a more complete treatment should include transition metals with higher coordination numbers and oxidation states, these being highly common in various biological systems. However, we reserve this endeavor for a subsequent publication. The present paper does not consider any transition-metal-containing reactions, although such systems will be examined in future efforts.

II.D. Enthalpy of Reaction. The most recent B3LYP-LOC work[2c] demonstrates that this methodology is robust across different basis sets [6-31G*, 6-311++G(3df,3pd), cc-pVTZ, and aug-cc-pVTZ] and reaction types (atomization reactions and molecular reactions). This work further demonstrates a reduction in the MUE from 4.7 to 0.8 kcal/mole over B3LYP for a test set of 70 molecular reactions [at the B3LYP-LOC/6-311++G(3df,3pd) level]. Our series of works[2] show that the systematic errors native to B3LYP make it particularly well suited to the LOC scheme. Importantly, some modern functionals perform noticeably better than B3LYP. Even so, their errors, still being non-negligible, are more random and, hence, are harder to treat by such trivially defined parameterizations. Several well-known functionals (SVWN, BLYP, BPW91, etc.) were investigated in this regard. Furthermore, the modern M05-2X[16] and M06-2X[17] functionals were also combined with the LOC scheme. While uncorrected B3LYP is outperformed by M05-2X, which is, in turn, outperformed by M06-2X, neither of these new functionals integrates as favorably with the LOC methodology as B3LYP for calculation of reaction enthalpies. While non-trivial improvements in performance are seen for M05-2X-LOC and M06-2X-LOC (where the LOC parameters are optimized for each functional individually) over uncorrected M05-2X and M06-2X, they are both consistently outperformed by B3LYP-LOC, which makes it the best method of the three for computing reaction enthalpies. This is not to imply that B3LYP is an inherently better functional than M05-2X or M06-2X when all are in their uncorrected forms. Nor does it imply that other functionals we have not yet tested might not produce better results than B3LYP when combined with our LOC methodology. This is a point we intend to examine in future publications. Further, we have provided a complete prescription in this publication, and the others,[2a−d] for application of our LOC scheme such that other researchers may investigate our LOC scheme with other functionals, if they so desire.

On that note, we have not yet explored the possibility of coupling our LOC scheme with various screened hybrids such as the Heyd−Scuseria−Ernzerhof (HSC) functional[24] for the treatment of large molecules. Nonetheless, this presents a promising approach to further treating systematic errors found in DFT, as screened hybrids attenuate those errors found at relatively long length scales (>5 Å), and our

LOC approach corrects for those at shorter length scales. We reserve this endeavor for future publications.

In order for a method to be physically viable, optimal results should emerge as the basis set is converged. This convergence is observed for the B3LYP-LOC approach; the MUE is, in fact, decreased as the basis set size is increased. This represents substantive evidence for the chemical validity of the LOC methodology and interpretation.

Importantly, this most recent work is the first instance in which an automated protocol is employed to assign the LOC parameters and corrections, in contrast to the hand assignments performed in previous works. Specifically, for any reaction given in SMILES format, the total correction to its reaction enthalpy is computed automatically according to the valence bond structure given. This is an important step forward in the process of making the methodology automated and accessible to a wider audience.

II.D.1. Enthalpy of Reaction for Neutral Reactions. The LOC-corrected enthalpy of reaction can be calculated in a straightforward fashion using the standard B3LYP-LOC parameters and is done just as in ref 2c. The sum of the corrections for the reactant(s) is subtracted from the sum of corrections for the product(s), and this total correction is then added directly to the B3LYP enthalpy of reaction to yield the B3LYP-LOC enthalpy of reaction.

II.D.2. Enthalpy of Reaction for Ionic Reactions. Imagine an anionic S_N2 reaction:

$$\mathrm{Nu^-} + \mathrm{R{-}LG} \rightarrow \mathrm{LG^-} + \mathrm{R{-}Nu}$$

where Nu, R−LG, and LG represent the nucleophile, electophile, and leaving group, respectively. This may equivalently be written as a series of reactions:

$$\text{(a) } \mathrm{Nu^-} \rightarrow \mathrm{Nu^\circ} + e^-$$

$$\text{(b) } \mathrm{R{-}LG} \rightarrow \mathrm{R^\circ} + \mathrm{LG^\circ}$$

$$\text{(c) } \mathrm{R^\circ} + \mathrm{Nu^\circ} \rightarrow \mathrm{R{-}Nu}$$

$$\text{(d) } \mathrm{LG^\circ} + e^- \rightarrow \mathrm{LG^-}$$

Reaction (a) and (d) are described by the EA of Nu° and LG°, respectively. EA is defined as

$$\mathrm{EA}(X^\circ) = \mathrm{energy}(X^\circ) - \mathrm{energy}(X^-) \qquad (1)$$

for the reaction:

$$X^\circ + e^- \rightarrow X^- \qquad (2)$$

Note that this thermodynamic property is defined as energy (reactants) − energy (products), opposite from other thermodynamic properties, which are defined as energy (product) − energy (reactant).

Each of these sub-reactions will have associated with it a certain correction due to adding or removing an electron. Specifically:

$$\text{(a) } \mathrm{corr}(\mathrm{Nu^\circ}) - \mathrm{corr}(\mathrm{Nu^-}) + \mathrm{corr}(\mathrm{EA}, \mathrm{Nu^\circ})$$

$$\text{(b) } \mathrm{corr}(\mathrm{R^\circ}) + \mathrm{corr}(\mathrm{LG^\circ}) - \mathrm{corr}(\mathrm{R{-}LG})$$

$$\text{(c) } \mathrm{corr}(\mathrm{R{-}Nu}) - \mathrm{corr}(\mathrm{R^\circ}) - \mathrm{corr}(\mathrm{Nu^\circ})$$

$$\text{(d) } \mathrm{corr}(\mathrm{LG^-}) - \mathrm{corr}(\mathrm{LG^\circ}) - \mathrm{corr}(\mathrm{EA}, \mathrm{LG^\circ})$$

For reaction (a), the EA correction is added to the other terms. While reaction (a) does not match eq 2 in form, its reaction enthalpy does match that of eq 1, therefore, the EA correction should be added to the other terms. Conversely, the enthalpy for reaction (d) is defined opposite that of eq 1, and therefore, the EA term is subtracted from the others. Note that reactions (b) and (c) contain only neutral species and are, therefore, completely described by the original suite of LOC parameters.[2a]

Combining all the corrections for (a) − (d) gives a total correction:

$$\mathrm{corr}(\mathrm{anionic}, S_N2) = \mathrm{corr}(\mathrm{R{-}Nu}) + \mathrm{corr}(\mathrm{LG^-}) - \mathrm{corr}(\mathrm{Nu^-}) - \mathrm{corr}(\mathrm{R{-}LG}) + \mathrm{corr}(\mathrm{EA}, \mathrm{Nu^\circ}) - \mathrm{corr}(\mathrm{EA}, \mathrm{LG^\circ}) \qquad (3)$$

Obviously, this is not limited in application to just anionic S_N2 reactions but can be applied to all anionic reactions. Also, cationic reactions are treated by the following formula using the same logic:

$$\mathrm{corr}(\mathrm{cationic}, S_N2) = \mathrm{corr}(\mathrm{R{-}Nu^+}) + \mathrm{corr}(\mathrm{LG{:}}) - \mathrm{corr}(\mathrm{R{-}LG^+}) - \mathrm{corr}(\mathrm{Nu{:}}) + \mathrm{corr}(\mathrm{IP}, \mathrm{Nu{:}}) - \mathrm{corr}(\mathrm{IP}, \mathrm{LG{:}}) \qquad (4)$$

III. Development of a B3LYP-LOC Model for Barrier Heights

III.A. Overview. The B3LYP-LOC methodology has been well described for ground states,[2a−d] but it has yet to be applied to transition states. As a first approximation, we assume, for purposes of estimating the valence bond states needed to assign correction parameters, that all transition states lie exactly mid-way along the reaction coordinate connecting product and reactant. Specifically, if a bond has an order of 1 (single bond) in the reactant and 2 (double bond) in the product, it is assigned a bond order of 1.5 in the transition state. Similarly, an atom with hybridization sp^3 in the reactant and sp^2 in the product is assigned a hybridization of $sp^{2.5}$ in the transition state. Obviously, this assumption is crude and is likely to lead to less than optimal results in many cases. Therefore, it is desirable to develop a continuous functional form of the B3LYP-LOC correction such that the entire reaction coordinate may be mapped, better accommodating asynchronous transition states. Yet, we reserve this for a subsequent publication and use the approximation here to show the validity, applicability, and power of the model, even in its crudest form.

Where possible, the previously developed B3LYP-LOC parameters are assigned to the transition state. For example, a carbon−carbon bond that maintains its bond order in the reactant and transition state will be assigned the standard parameter, MSBC (medium single-bond correction), in both. After assigning these parameters, parameters specific to

Table 1. B3LYP-LOC Parameters for Transition States

parameter	description	value (kcal/mol)
N/P_sp$^{1.5}$	applied for every N or P atom with hybridization that can be considered partly sp and partly sp^2	4.47
N/P_sp$^{2.5}$	applied for every N or P atom with hybridization that can be considered partly sp^2 and partly sp^3	4.03
O_sp$^{2.5}$	applied for every O atom with hybridization that can be considered partly sp^2 and partly sp^3	2.02
MSBC/LSBC_0.5	applied for every bond of approximate order 0.5 between any atom pairs falling within the description of MSBC and LSBC. Specifically, C···C, C···Cl, N···N, O···O, N···O, F···F, O···Cl, Na···Na, Si···C, S···C, S···O, S···N, any pair of second-row atoms other than NaCl	−1.82
AA_1.5	applied for every bond with approximate bond order 1.5	−0.36
AA_2.5	applied for every bond with approximate bond order 2.5	−0.91
HH_0.5	applied for every H−H bond with approximate bond order 0.5	0.55
H_dival	applied for every transition state in which a hydrogen atom is partly bonded to two atoms, at least one of which is neither carbon nor hydrogen	3.79
ESBC[a]	applied for every bond A−B (of order 0.5, 1, or 1.5; where neither A nor B are fluorine or hydrogen, and the bond is not part of a three- or four-membered ring) with neighboring single bond A′−A (where neither A nor A′ is fluorine or hydrogen); likewise, 0.5 ESBC is applied for every neighboring bond A′−A (where neither A nor A′ is fluorine or hydrogen) with bond order 0.5 or 1.5, with the same restrictions on A−B stated above.	−0.50[b], −0.51[c]
OCT_EXP[a]	defined previously for Cl, P, or S atoms that have a valence shell expansion beyond the usual octet; also applied to any transition state in which an atom (other than hydrogen) experiences an increase in coordination number beyond its octet; this includes the pseudo-penta coordinate transition state of S_N2 reactions, for example.	4.92[b], 3.54[c]
RH[a]	defined previously to apply to every atom on which the localized singly occupied orbital is bonded to a hydrogen atom; extended here to also apply to any atoms of the transition state with partial radical character; applied additively for each unpaired electron and each hydrogen.	0.55[b], 0.34[c]
RA[a]	previously assigned for every atom (of the first or second row) with a localized radical and a single or double bond to another atom; extended here to include all atoms of the transition state with partial radical character; applied additively for each unpaired electron and each bonded first- or second-row atom.	1.62[b], 1.71[c]

[a] This parameter was first defined in ref 2a, and here its definition is simply extended to include transition states. [b] As defined in ref 2a for the 6-311++G(3df,3pd) basis. [c] As defined in ref 2a for the cc-pVTZ++ basis.

transition states must be assigned. These new parameters are given in Table 1.

The environmental single-bond correction (ESBC) was previously described.[2a,c] Yet, it is included in Table 1, as its definition has been modified, so that it can be applied in an automated fashion to the transition states as well. As previously defined, ESBC is applied additively for every single bond A−B (where neither A nor B is fluorine or hydrogen nor is the single bond part of a three- or four-membered ring) with a neighboring single bond, A′−A−B (A′ not fluorine or hydrogen). In this most recent implementation, for every A−B bond with approximate bond order $n + 0.5$ ($n = 0, 1$), with neighboring bond A′−A, 1 ESBC is applied if A′−A is a single bond. Likewise, only 0.5 ESBC is applied for A′−A having approximate bond order $n + 0.5$ ($n = 0, 1$). The original restriction applies in that A−B, regardless of bond order, cannot be a bond in a three- or four-membered ring. This is presumably because the bond angles in these three- or four-membered rings are too small to appreciably allow for electronic excursions that ESBC was designed to treat. Therefore, transition states which also display this same characteristic small bond angle (< 94.0°) do not receive ESBCs either. Specifically, consider four atoms connected by single bonds, A−B−C−D. If bond angle ABC is < 94.0°, neither bond AB nor bond BC may count as a base orbital for ESBCs. Yet, bond CD is still treated in the normal fashion − receiving 1 ESBC for its neighboring BC bond. Via this rational, the bonds of the bridge in the transition states for reactions 1 and 2 in addition to all bonds of the partial three- or four-membered rings in the transition states for reactions 8, 10, 101, and 102 were not assigned ESBCs.

After assigning all the corrections to the reactant and transition states, the difference in these corrections may then be applied directly to the B3LYP barrier height to obtain the B3LYP-LOC barrier height in an additive fashion. This is straightforward for neutral reactions. Anionic and cationic reactions require one additional correction each and are discussed in the following sections.

The original B3LYP-LOC scheme[2a] provides corrections for various hybridization states of atoms, including N/P_sp, N/P_sp^2, etc. The transition-state parameters unsurprisingly take on similar values to the previously defined ones. For example, N/P_sp$^{\mathbf{1.5}}$ has a value of 4.47 kcal/mole, which is similar in value to that of N/P_sp^2 at 4.31 kcal/mole (for the 6-311++G(3df,3pd) basis set, for example). N/P_sp$^{2.5}$ (4.03 kcal/mole) is intermediate in value between N/P_sp^2 and N/P_sp^3 with values of 4.31 and 3.00 kcal/mole, respectively. It is not necessarily true that the parameter N/P_sp$^{n.5}$ must be intermediate in value between that of N/P_sp^n and N/P_sp^{n+1} for it to be physically viable; the formation of a transition state is a complex change in electronic structure in which various competing factors will play a role in determining the error in the original B3LYP calculation, and the empirical corrections absorb all of these effects simultaneously. The original DFT-LOC paper emphasized the transformation of the lone pair in atomic nitrogen from the more localized 2s orbital to a significantly more extended sp-, sp^2-, or sp^3-hybridized orbital, as a qualitative rationalization of the overbinding associated with achieving the standard hybridization states for nitrogen. Yet, when a transition state is formed, the first shell of neighboring atoms and their distance distribution differs from any ground state, and the effects so introduced can modify the observed DFT error, in a direction that is not easy to infer from the structural transformation. Finally, the original B3LYP-LOC work treats nitrogen and phosphorus equally, finding no appreciable degradation in performance upon combining the two. This is easily justified by the similarity of phosphorus and nitrogen in electronic structure. Accordingly, we have chosen to combine the corresponding nitrogen and phosphorus corrections into N/P_sp$^{n.5}$. Although there are no cases of phosphorus atoms that fit into the N/P_sp$^{1.5}$ category and only one transition state with phosphorus that fits into the N/P_sp$^{2.5}$ category, we assert this is a likely categorization for any possible future occurrences based upon the precedence set in the previous work.[2a]

Like the transition-state parameters for nitrogen of intermediate hybridization, O_sp$^{2.5}$ (2.02 kcal/mole) is similar in value to the previously defined parameters, O_sp^2 and O_sp^3, which have values of 0.95 and 1.67 kcal/mole, respectively.

MSBC/LSBC_0.5 (−1.82 kcal/mole) also has a value similar to those originally defined for MSBC and LSBC, −1.92 and −2.49 kcal/mole, respectively. The original B3LYP-LOC work[2a] shows a clear correlation between the ratio of orbital size to bond length and the corresponding correction for each bond. Specifically, the corrections for heavy atom pair short single bonds (SSBC), medium single bonds (MSBC), and long single bonds (LSBC) are −1.26, −1.92, and −2.49 kcal/mole, respectively. The longer bond length relative to the orbital size bestows a greater nondynamical correlation energy onto the electron pair in the longer bond than would be if the bond were shorter, necessitating a correction of greater magnitude. We see that the value for MSBC/LSBC_0.5 is smaller than both MSBC and LSBC in magnitude, despite the fact that the bond length is clearly larger. Yet, while the bond length is larger for such “half bonds”, the orbital size also experiences a concomitant increase in size (with respect to “full” single bonds). Consider for example the reaction $H_2C{=}CH_2 + CH_3^\circ \rightarrow H_2C^\circ{-}CH_2{-}CH_3$. While the “half” bond between the ethene and methyl in the transition state is longer than the corresponding single bond, its orbital size is also larger. Whereas the corresponding C−C bond is comprised of two sp^3 orbitals, this “half” bond is comprised of two orbitals intermediate in hybridization between pure p orbitals (as in the reactants) and sp^3 orbitals (as in the products), making it comparatively larger. Accordingly, the ratio of orbital size to bond length does not vary greatly between the “full” medium and long single bonds and the medium and long single “half” bonds.

A second argument (not contradictory to the discussion above — the final parameter value reflects both chemical effects in combination) is that, as any bond is driven to infinite separation, the correction parameter for the bond must go to zero. When atom B is infinitely far from atom A, excursions of the now unpaired electrons on atom A toward atom B (and vice versa) no longer deviate from those seen in an atom; thus, the estimate of the two particle correlation function by the DFT functional cannot be presumed to have the systematic error inferred for C−C, C−Cl, etc., bonds. At what point the correction term peaks cannot be rigorously determined without performing accurate high level ab initio computations of the full bond-breaking curve and comparing the DFT results, but it seems reasonable to propose that the maximum in fact occurs close to the equilibrium bond length and prior to the length associated with the transition-state structure (at least in a typical transition state; early transition states might exhibit a systematically different trend, a subject we leave to future investigation). The fact that we are able to combine the MSBC and LSBC parameters here (no transition-state bond would be characterized as “short”) and that the value obtained is smaller than the MSBC equilibrium value provides strong evidence that this hypothesis is correct. This transition-state bond correction parameter is employed in virtually every molecule in the training set, and there is often more than one bond per test case; thus, the value of the parameter has a major effect on the average error. The successful use of a single parameter for all single bonds between heavy atoms in the transition state and the low average error and number of outliers obtained by doing so provides confidence that this parameter is not overfit, as does its chemically consistent, readily interpretable value (per the two arguments made above).

The parameter AA_1.5 is applied for all bonds of approximate bond order 1.5. Its value (−0.36 kcal/mole) is similar to the value for double bonds (−0.53 kcal/mole), reflecting the fact that correlation between multiple orbitals in a bond exerts a substantial effect on the correction term (in a fashion that is more difficult to dissect than the corresponding effects for single bonds). This value most likely corresponds to the reorganization of electrons from the localized p orbitals of the double bond to the localized sp^n bonds. The precise value obtained, while more difficult to interpret than the transition-state single bond value, is at least reasonable. More test cases will be required to investigate whether the fitted parameter obtained here is unduly influenced by the specific set of bonds with bond order 1.5 found in transition states for the current data set.

Similarly, AA_2.5, with a value of −0.91 kcal/mole, is employed for all bonds with approximate bond order 2.5. The original B3LYP-LOC work gives optimized values of −0.53, −1.31, and 1.51 kcal/mole for double bonds (DBC), nonpolar triple bonds (TBNPOL), and polar triple bonds (TBPOL), respectively. As in the case of AA_1.5, an obvious rationale for this parameter's exact value is lacking. Notably, this correction is employed many times for the dipolar cycloaddition reactions with azides. In fact, this parameter is employed exclusively for the treatment of dipolar cycloaddition transition states with the lone exception of the transition state for reaction 55 and 56, carbon radical reactions. Accordingly, this parameter may in actuality be capturing effects unique to the azides employed in the dipolar cycloadditions (which present a challenge for localized treatments due to their nonlocal nature) rather than a characteristic of bonds with an approximate order of 2.5. Further investigation will be necessary to determine just how general this parameter is and whether additional parametrization is necessary for other chemistries containing transition-state bonds intermediate between double- and triple-bond character. In contrast, we have much more confidence in the MSBC/LSBC_0.5 bond parameter, which covers many different chemistries, as discussed above.

All hydrogen−hydrogen bonds of approximate bond order 0.5 are assigned the parameter HH_0.5 (0.55 kcal/mole). The previous B3LYP-LOC work[2a] defined a special parameter for diatomic hydrogen with a value of 0.25 kcal/mole. The value for HH_0.5 is larger despite the fact that it will necessarily vanish as the bond order approaches zero. The reason for this is clear if one considers the relevant transition states, such as that of the reaction $H + H_2 \rightarrow H_2 + H$, for example.[18] These transition states are highly analogous to the well-described H_2^+ molecule.[11] In such cases, approximately one electron is shared between the two hydrogen atoms. Here the self-interaction term does not serve to model nondynamical correlation but instead engenders a clear source of systematic error.[3] Further, the magnitude of this error becomes larger as the bond is stretched. It is for this reason that the value of the HH_0.5 parameter is larger than that of the value assigned for diatomic hydrogen alone.

The importance of environmental correction terms has already been noted. For example, in a doubly occupied localized orbital, one electron might make excursions into the area of other localized orbitals in order to avoid the second electron of the same orbital. Accordingly, the availability of neighboring bonds to accommodate such excursions is included in the B3LYP-LOC scheme via introduction of the environmental single-bond correction, ESBC. While not as prevalent, such excursions are also possible in the partial bonds of transition states. Accordingly, excursions into partial bonds of approximate bond order 0.5 and 1.5 are treated with 0.5 ESBC corrections. Of course, the coefficient of 0.5 for the ESBC correction reflects the assumption that the transition state lies exactly midway along the reaction coordinate and can be fine-tuned to reflect exact transition-state location in the continuous implementation of the correction scheme, reserved for future work. Environmental bond corrections are not applied for double or triple bonds. Accordingly, partial environmental corrections for partial bond transition states are only applied for bonds of approximate order 0.5 and 1.5.

The original B3LYP-LOC work defined a parameter for any hypervalent atom, OCT_EXP, such as seen in ClF_3. The large value of this parameter compensates for a very substantial overestimation of nondynamical correlation in these highly electron dense systems. Notably, this same parameter accurately describes the pseudo-pentacoordinate transition state of the S_N2 reaction. Here a hypervalent carbon atom is coordinated to five different atoms with a concomitant increase in electron density and overestimation of nondynamical correlation analogous to that of the ClF_3 case, for example. Accordingly, all transition states with hypervalent non-hydrogen atoms (only S_N2 reactions on carbon centers in this work) are assigned this parameter.

While hypervalent heavy atoms of the transition state receive the OCT_EXP parameter, hypervalent hydrogen atoms receive the H_dival parameter. Interestingly, both OCT_EXP and H_dival are similar, taking on values of 3.54 to 4.64 kcal/mole (depending upon basis set) and 3.79 kcal/mole (independent of basis set), respectively. This similarity is not fortuitous, as these parameters arise from the same phenomenon: overestimation of nondynamical electron correlation due to localized high electron density. Accordingly, the H_dival parameter is only assigned when the hydrogen atom is flanked by at least one atom that is neither hydrogen nor carbon. This leads to a clear improvement in performance and can be justified based upon consideration of the virtual orbitals. Transition states in which the hydrogen atom is flanked by only carbon and/or hydrogen atoms, such as $CH_3\cdots H\cdots CH_3$, are well described without consideration of virtual orbitals. In molecules such as CH_4 and H_2, where the HOMO-LUMO gaps are larger [11.7 eV for methane at the B3LYP/cc-pVQZ(-G) level for example], the virtual orbitals do not contribute substantially to a complete description of the electronic state. Accordingly, B3LYP does not produce substantial errors in describing such systems. Nevertheless, transition states in which a hydrogen atom is sandwiched between at least one atom other than hydrogen or carbon, such as $HO\cdots H\cdots CH_3$, have a much larger error. Because the HOMO−LUMO gap in these heavy atoms (O, P, N, S, etc.) is smaller [8.9 and 8.0 eV for water and ammonia at the B3LYP/cc-pVQZ(-G) level, respectively], excitations of electrons in the heteroatom lone pairs into these virtual orbitals make a more significant contribution to the electronic state. The octet expansion parameter (OCT_EXP) is interpreted similarly; B3LYP does not accurately capture the effect of virtual orbitals for hypervalent atoms, leading to the large errors seen in these cases. In essence, hypervalent compounds cannot place all of their valence electrons into the standard valence shell orbitals and accessing virtual lone-pair orbitals in the first shell of atoms around the central atom (or in the central atom itself) is the most economical means of distributing electrons in structures of this type. The low-energy gaps of such states then appear to cause problems for B3LYP, leading to overbinding of the corresponding structures.

III.B. Barrier Height Corrections for Anionic Transition States. Consider the anionic S_N2 reaction:

$$\mathrm{Nu^- + R{-}LG \rightarrow LG^- + R{-}Nu}$$

where again, Nu, R−LG, and LG refer to the nucleophile, electrophile, and leaving group, respectively. Here, the corrections to the transition state are applied in the usual fashion. Yet, another parameter is added to the calculated barrier height to account for the negative charges:

$$\mathrm{corr(BH)} = 0.5[\mathrm{corr(EA, Nu^\circ)} + \mathrm{corr(EA, LG^\circ)}]$$

The coefficient of 0.5 is added to reflect the assumption that the negative charge in the transition state is equally distributed between the Nu and the LG. The above equations follow readily from equation (3). Obviously the parameter of 0.5 can be tuned to reflect the location of the transition state along the reaction coordinate; earlier transition states weighing the term corr(EA, LG°) more heavily and later transition states weighing corr(EA, Nu°) more heavily. This is reserved for subsequent publication in which a continuous functional form is developed.

III.C. Barrier Height Corrections for Cationic Transition States. Analogously, imagine a cationic S_N2 reaction:

$$\mathrm{Nu{:} + R{-}LG^+ \rightarrow R{-}Nu^+ + LG{:}}$$

where again, Nu, R−LG, and LG refer to the nucleophile, electrophile, and leaving group, respectively. Here, the barrier height also receives an additional correction derived from equation (4) where the assumption is made that half of the positive charge resides on the Nu, while the other half resides on the LG in the transition state:

$$\mathrm{corr(BH)} = 0.5[\mathrm{corr(IP, Nu{:})} + \mathrm{corr(IP, LG{:})}]$$

Just as with anionic transition states, the coefficient of 0.5 can be tuned once a continuous functional is developed.

III.D. Computational Methods. All stationary points (reactants, products, and transition states) were optimized at the UB3LYP/6-31G* level using the JAGUAR ab initio quantum chemistry code.[19] Vibrational frequencies were also calculated and scaled by 0.9806 (as suggested by Scott and Radom[20]) to obtain the zero-point energy (ZPE) and enthalpy of each species. Single-point calculations were then performed at the 6-311++G(3df,3pd) level for neutral and cationic reactions and at cc-pVTZ++ level for anionic reactions. The total enthalpy of each species *x* (H_x) was then taken as the sum of the SCF energy computed in the higher basis [6-311++(3df,3pd) or cc-pVTZ++] and the enthalpy and ZPE computed in the 6-31G* basis. The uncorrected B3LYP reaction enthalpy is then given by

$$\Delta H_{\mathrm{rxn,B3LYP}} = \Delta H_{\mathrm{product}} - \Delta H_{\mathrm{reactant}}$$

The uncorrected B3LYP barrier height is also given by

$$\Delta H^{\ddagger}_{\mathrm{B3LYP}} = \Delta H_{\mathrm{transition\ state}} - \Delta H_{\mathrm{reactant}}$$

(Note that, in many publications, barrier height is used interchangeably with Arrhenius activation energy. It is important to recognize that these two quantities differ by a factor of *nRT*. Barrier height is used exclusively here.)

From these, the B3LYP-LOC reaction enthalpy and barrier height are readily obtained by a simple correction term:

$$\Delta H_{\mathrm{rxn,B3LYP\text{-}LOC}} = [\Delta H_{\mathrm{product}} + \mathrm{corr}_{\mathrm{product}}] - [\Delta H_{\mathrm{reactant}} + \mathrm{corr}_{\mathrm{reactant}}] = \Delta H_{\mathrm{rxn,B3LYP}} + \mathrm{corr}_{\mathrm{product}} - \mathrm{corr}_{\mathrm{reactant}}$$

$$\Delta H^{\ddagger}_{\mathrm{B3LYP\text{-}LOC}} = [\Delta H_{\mathrm{transition\ state}} + \mathrm{corr}_{\mathrm{transition\ state}}] - [\Delta H_{\mathrm{reactant}} + \mathrm{corr}_{\mathrm{reactant}}] = \Delta H^{\ddagger}_{\mathrm{B3LYP}} + \mathrm{corr}_{\mathrm{transition\ state}} - \mathrm{corr}_{\mathrm{reactant}}$$

Lastly, each of the corr_x terms is obtained simply from the sum of all corrections for species *x*, as assigned from its valence bond structure and as given by the full suite of LOC parameters.[2a−d] The reader is referred to the Supporting Information for additional details and examples.

IV. Results and Discussion

The B3LYP-LOC methodology as described in Section III was applied to a large dataset of 105 unique barrier heights and 69 enthalpies of reaction for which ab initio or experimental data were available. This dataset, shown in Figure 1, is notable for the many different reaction types, including cycloadditions, electrocyclizations, dipolar cycloadditions, S_N2, carbon radical, and hydrogen radical reactions. After applying the original B3LYP-LOC parameters, as previously developed,[2a] the new parameters were assigned, and their values (shown in Table 1) were determined in a linear-least-squares fashion.

Table 3 summarizes the results of applying the B3LYP-LOC methodology to this large dataset and compares uncorrected B3LYP to B3LYP-LOC. The B3LYP-LOC method performs significantly better than the uncorrected B3LYP, with essentially zero additional computational cost. The error in the MUE of the entire dataset is reduced to near-chemical accuracy for both reaction enthalpies and barrier heights. Further, Table 3 shows that the MUE is reduced across nearly all categories for both the reaction enthalpy and barrier height, again often achieving chemical accuracy. This is also shown visually in Figures 2 and 3.

For reaction enthalpies, the MUE is reduced nearly 20-fold for cycloadditions, 6-fold for dipolar cycloadditions, and 4-fold for both carbon radical and electrocyclic reactions. The same trend holds for barrier heights in which B3LYP-LOC displays up to a 7-fold improvement in MUE over B3LYP.

A few exceptions exist in which B3LYP-LOC displays greater error than B3LYP. These include the enthalpy of S_N2 reactions and the barrier heights for electrocyclizations and sigmatropic shifts. While B3LYP-LOC performs less favorably than B3LYP for the S_N2 reactions, this degradation is relatively small in magnitude, especially when compared to the remarkable improvement displayed by the other reactions subcategories when employing B3LYP-LOC. It is also true that B3LYP outperforms B3LYP-LOC when calculating barrier heights for both electrocyclizations and sigmatropic shifts. Yet, because of the limited availability of benchmark data, both of these reaction subcategories only contain three reactions each. Further, B3LYP, perhaps fortuitously, per-

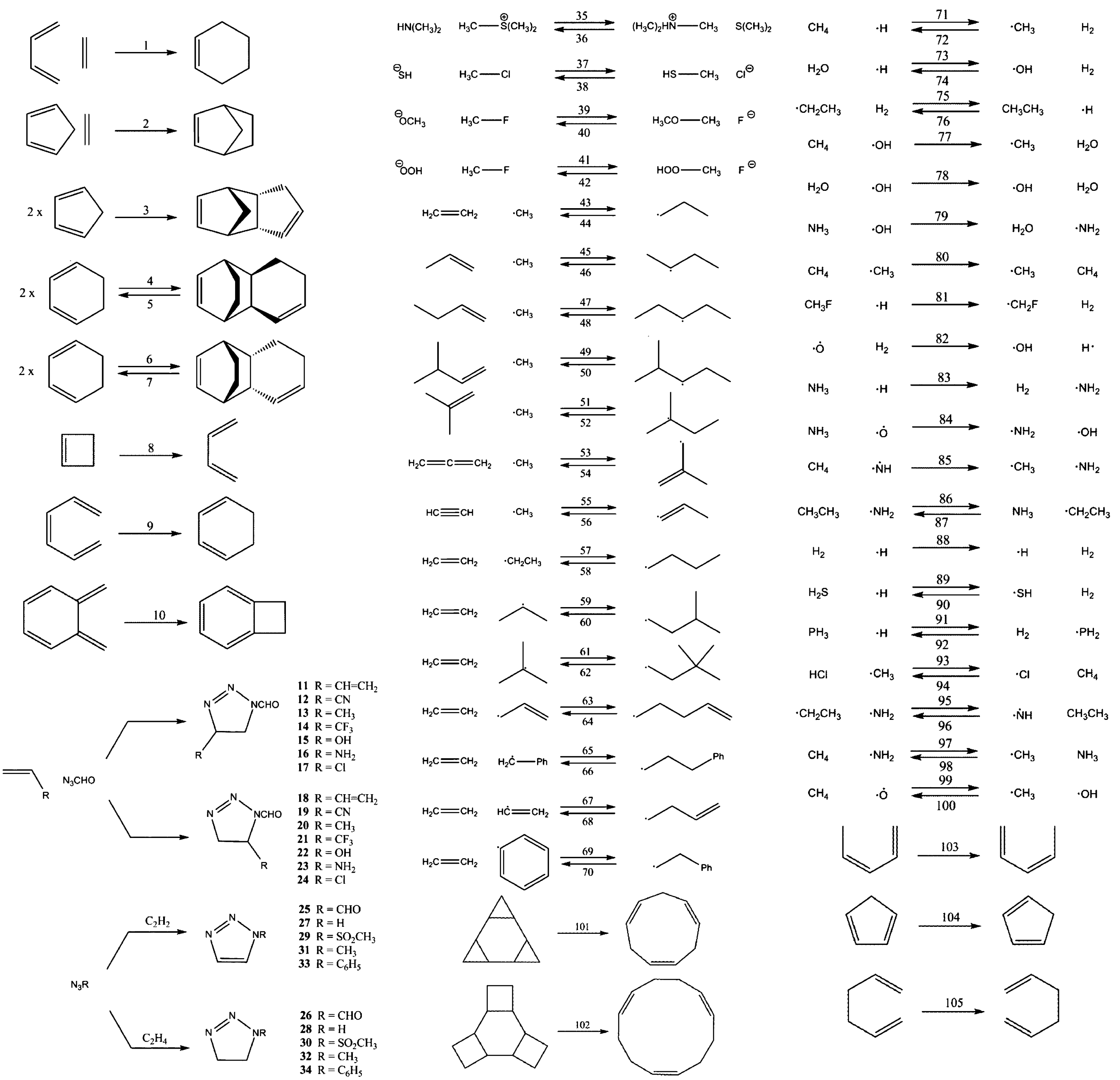

Figure 1. Reactions of the test set.

forms anomalously well for these small datasets. Therefore, additional reactions within these subcategories should be investigated once benchmark data becomes available to truly gauge B3LYP-LOC's performance for these reaction types.

One particular type of chemistry requires some explicit comments. Our dataset contains several azides: hydrazoic acid (N_3H), methylazide (N_3CH_3), formylazide (N_3CHO), phenylazide ($N_3C_6H_5$), and methane sulfonylazide ($N_3SO_2CH_3$). Each of these possesses, at least two unique resonance forms shown in Figure 4. Therefore, we must decide upon one resonance structure for each in order to successfully apply the LOC scheme.

Ab initio or experimental enthalpies of formation can be located for only hydrazoic acid and methylazide.[21] Comparing the ab initio numbers to those computed with B3LYP-LOC shows clearly superior performance when resonance structure (a), as opposed to (b), is utilized. As argued in ref 2a, B3LYP-LOC analysis can be viewed in difficult cases like this one as implying the dominance of a particular resonance structure.

With this in mind, all azides were assumed to have the resonance structure (a). Yet, other resonance structures need to be considered for some other azides. Specifically, in accordance with previous B3LYP-LOC work,[2a] methane sulfonylazide is taken as shown in Figure 5.

Lastly, formylazide requires even further analysis. We propose that it deviates from resonance structure (a) and instead adopts the form shown in Figure 6. We make this assertion given that the reaction enthalpy MUE of the formylazide-containing reactions drops from 2.6 or 3.5 kcal/mole to 1.2 kcal/mole using this structure. One can also argue that this is the best resonance structure, as the

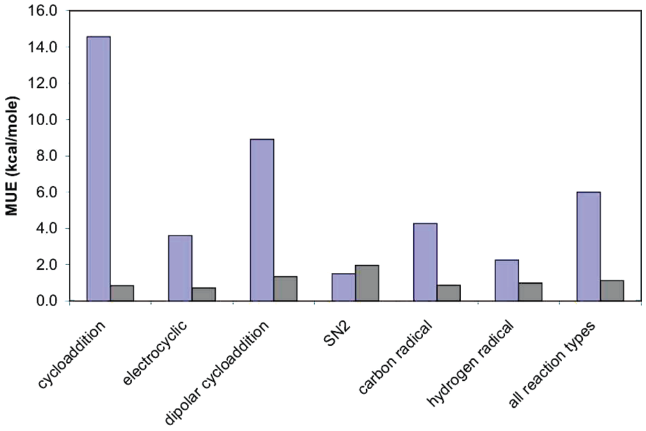

Figure 2. Mean unsigned error (MUE) for enthalpy of reaction (ΔH_{rxn}) for various reaction types. B3LYP-LOC is shown in gray, while uncorrected B3LYP is shown in blue.

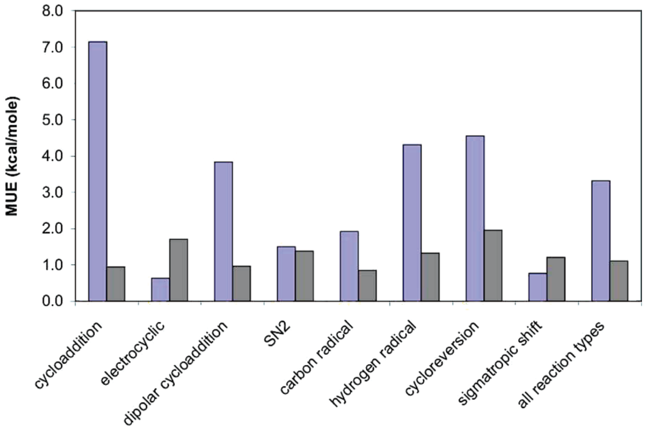

Figure 3. Mean unsigned error (MUE) for barrier heights ($\Delta H^{\ddagger}$) for various reaction types. B3LYP-LOC is shown in gray, while uncorrected B3LYP is shown in blue.

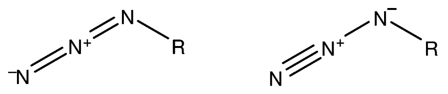

(a) (b)

Figure 4. Resonance structures for a general azide.

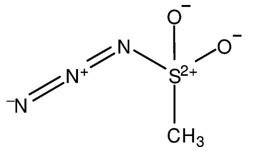

Figure 5. Methane sulfonyl azide.

negative charge is localized on the most electronegative element. It should also be noted that this molecule was assigned a charge transfer (CT) parameter.

In conclusion, we recommend that resonance structure (a) be employed for all azides N_3R unless the negative charge may be delocalized through the R group to a more electronegative element than nitrogen when employing structure (b). Note that phenylazide was treated successfully with resonance structure (a) despite the fact that (b) would allow for delocalization of charge through the phenyl ring. Arguably, such a charge delocalization is not the dominant resonance structure, and a phenyl group does not play the same role as the aldehyde.

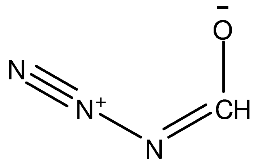

Figure 6. Formylazide.

Table 2. Experimental and Calculated Enthalpies of Formation

enthalpies of formation (kcal/mole)	hydrazoic acid	methylazide
Ab initio (G2 theory)	70.4	71.0
B3LYP	59.4	62.1
B3LYP-LOC (a)	71.2	73.1
B3LYP-LOC (b)	65.1	67.1

Unfortunately, while Mulliken charge analysis was employed to probe for dominant resonance structures for all of these azides, the results were highly inconclusive as they depended highly on basis set and did not seem to converge with higher levels of theory. This dependence is entirely consistent with the observations of other researchers.[23] Accordingly, no conclusions were drawn from this data.

In general, any successful parameterization method must guard against over-fitting. We put forward that the large data set employed (>100 barrier heights) and comparatively small number of parameters developed (8) makes the possibility of over-fitting small. Nonetheless, to confirm this hypothesis, we have divided the data set into roughly equal halves, using each half independently as a training set. The parameter values obtained from these two different sets were then applied to the other half of the data to give MUEs of 1.1 to 1.4 kcal/mole. This value should be compared to the MUE derived using the whole dataset as a training set, 1.1 kcal/mole. This provides significant evidence that overfitting is not a major problem, at least as judged by the present data set. As noted above, there may be specific cases where additional parameters will be required as new types of structures are investigated. Lack of transferability, a problem that is fundamentally different from overfitting, can be fully addressed only by using substantially larger and more diverse data sets.

The results for reaction enthalpies presented in Table 3 require the use of no additional adjustable parameters and, hence, can be regarded as a true test set for the B3LYP-LOC methodology developed previously. (All reaction enthalpies and barrier heights are given in the Supporting Information.) Some of the reactions can be derived from the atomization reactions of the G2/G3 database and, hence, cannot be used for this objective. If we consider only reactions that cannot be derived from the G2/G3 atomization reactions (52 in all), the average MUE for B3LYP and B3LYP-LOC enthalpies of reaction are 7.4 and 1.1 kcal/mole, respectively. Note that this B3LYP-LOC reaction enthalpy MUE is identical to the MUE for all reactions (1.1 kcal/mole) and also to the average error for the training set,[2a] on the order of 1.0 kcal/mole. Independent of the validity of

Table 3. Mean Unsigned Error (kcal/mole) of ΔH_{rxn} and $\Delta H^{\ddagger}$ calculated with B3LYP and B3LYP-LOC

	ΔH_{rxn}		$\Delta H^{\ddagger}$	
reaction type	B3LYP	B3LYP-LOC	B3LYP	B3LYP-LOC
cycloaddition	14.6	0.8	7.1	0.9
electrocyclic	3.6	0.7	0.6	1.7
dipolar cycloaddition	8.9	1.3	3.8	1.0
S_N2	1.5	2.0	1.5	1.4
carbon radical	4.3	0.9	1.9	0.8
hydrogen radical	2.3	1.0	4.3	1.3
cycloreversion[a]	n/a	n/a	4.6	2.0
sigmatropic shift[b]	n/a	n/a	0.8	1.2
all reaction types	6.1	1.1	3.3	1.1

[a] Enthalpy of reaction data unavailable. [b] Enthlapy of reaction is necessarily zero, as the reactant and product are identical.

the transition-state parameters we have derived here, these results suggest that, for reaction thermochemistry, B3LYP-LOC will perform at the level of near-chemical accuracy within its current domain of applicability (molecules composed of first- and second-row atoms). Furthermore, the largest absolute error in reaction energy is 3.3 kcal/mole, whereas the largest absolute B3LYP error is on the order of 19 kcal/mole (and there is a significant number of reactions with errors of this order of magnitude). The consistency of the methodology, across a wide range of chemical phenomena and without further parameter adjustment, continues to be a strong aspect of the approach.

For barrier heights, there is only one reaction with error greater than 3.5 kcal/mole. Entry 99, $CH_4 + O$ (triplet) → $CH_3\cdot + \cdot OH$, has a signed error of 6.3 kcal/mole. Interestingly, the B3LYP error for this reaction barrier is 10.6 kcal/mole, the largest such error in the entire data set and roughly 3−5 kcal/mole higher than that of comparable radical reactions in the database. This observation suggests at least the possibility that there is a problem with the reference data; if the B3LYP error were more in line with other reactions, then the B3LYP-LOC error would be much smaller. We plan to follow up on this point in future work. It is of course also possible that at least some of the residual errors are a result of inaccuracies in the reference data as well; unlike the G2/G3 set of atomization energies, it is not possible to put rigorous error bars on the reference data for many of the reactions included here. Nevertheless, the level of agreement, for an initial effort, is quite satisfactory and encourages us to continue the development of the B3LYP-LOC model along the lines discussed in the introduction.

V. Conclusions

The results discussed above confirm that the core B3LYP-LOC approach provides high-accuracy results for enthalpies of reaction and introduce, for the first time, a viable model for obtaining barrier heights with this methodology. The barrier height results are comparable in accuracy to what is obtained for enthalpies of reaction, and they display little fluctuation in performance across a diverse set of transition-state structures and reaction chemistry. The ratio of adjustable parameters (8) to new data points (105) is reasonable, and the parameters obtained from fitting are physically consistent with previously developed B3LYP-LOC parameters for ground-state thermochemistry.

As indicated above, our next objective is to construct a B3LYP-LOC methodology that is a continuous function of the coordinates. Now that we have parameters for the key stationary points, this should be straightforward. We also intend to assemble a substantially larger data set and to carry out comparisons using this data set with methods such as M06-2X and screened hybrids (in both the original and LOC-corrected forms), which have also shown great promise with regard to reducing DFT errors. Head to head comparisons on large and diverse data sets will enable the strengths and weaknesses of each approach to be examined in detail. Ultimately, adjustment of both additive empirical valence bond-type corrections, such as those used here, and intrinsic DFT functional parameters, as has been carried out quite effectively by the Truhlar group, is likely to yield the most accurate and reliable methodology. An effort of this type will require a significant amount of additional work but does appear to represent a promising path forward for the long run. Further, it should ultimately be possible to extend this methodology to excited states.

Acknowledgment. This work was supported in part by a grant from the National Institute of Health (NIH) training program in Molecular Biophysics (M. L. Hall, T32GM008281) and by a grants to R. A. Friesner from the NIH (GM40526) and from the Columbia University's Rabi Scholar program (D. A. Goldfeld).

Supporting Information Available: Images and xyz coordinates for all species considered in the study; specific assignment of all B3LYP-LOC parameters; the complete suite of all B3LYP-LOC parameters, their values and descriptions; and tables of all enthalpies of reaction and barrier heights for all 105 reactions can be found. This material is available free of charge via the Internet at http://pubs.acs.org.

References

(1) Kohn, W.; Becke, A. D.; Parr, R. G. *J. Phys. Chem.* **1996**, *100*, 12974.

(2) (a) Friesner, R. A.; Knoll, E. H.; Cao, Y. *J. Chem. Phys.* **2006**, *125*, 124107. (b) Knoll, E. H.; Friesner, R. A. *J. Phys. Chem. B* **2006**, *110*, 18787. (c) Goldfeld, D. A.; Bochevarov, A. D.; Friesner, R. A. *J. Chem. Phys.* **2008**, *129*, 214105. (d) Rinaldo, D.; Tian, L.; Harvey, J. N.; Friesner, R. A. *J. Chem. Phys.* **2008**, *129*, 164108.

(3) (a) Becke, A. D. *J. Chem. Phys.* **1993**, *98*, 1372. (b) Becke, A. D. *J. Chem. Phys.* **1993**, *98*, 5648.

(4) (a) Guner, V.; Khoung, K.; Leach, A. G.; Lee, P. S.; Bartberger, M. D.; Houk, K. N. *J. Phys. Chem. A* **2003**, *107*, 11445. (b) Ess, D. H.; Houk, K. N. *J. Phys. Chem. A* **2005**, *109*, 9542. (c) Ess, D. H.; Hayden, A. E.; Klarner, F.-G.; Houk, K. N. *J. Org. Chem.* **2008**, *73*, 7586. (d) Gunaydin, H.; Acevado, O.; Jorgenson, W. L.; Houk, K. N. *J. Chem. Theory Comput.* **2007**, *3*, 1028–1035. (e) Ren, Y.; Yamataka, H. *Chem. Eur. J.* **2007**, *13*, 677–682. (f) Zhao, Y.; Gonzalez-Garcia, N.; Truhlar, D. G. *J. Phys. Chem. A* **2005**, *109*, 2012–2018.

(5) (a) Zhao, Y.; Truhlar, D. G. *J. Phys. Chem. A* **2004**, *108*, 6908–6918. (b) Zhao, Y.; Truhlar, D. G. *J. Chem. Theory Comput.* **2005**, *1*, 415–432. (c) Zhao, Y.; Gonzalez-Garcia, N.; Truhlar, D. G. *J. Phys. Chem. A* **2005**, *109*, 2012–2018.

(6) (a) Curtiss, L. A.; Raghavachari, K.; Redfern, P. C.; Rassolov, V.; Pople, J. A. *J. Chem. Phys.* **1998**, *109*, 7764. (b) Curtiss, L. A.; Raghavachari, K.; Redfern, P. C.; Pople, J. A. *J. Chem. Phys.* **2000**, *112*, 7374. (c) Parthiban, S.; de Oliveira, G.; Martin, J. M. L. *J. Phys. Chem. A* **2001**, *105*, 895–904. (d) Zhao, Y.; Truhlar, D. G. *J. Chem. Theory Comput.* **2007**, *3*, 289–300.

(7) Zhao, Y.; Gonzalez-Garcia, N.; Truhlar, D. G. *J. Phys. Chem. A* **2005**, *109*, 2012–2018.

(8) (a) Curtiss, L. A.; Raghavachari, K.; Redfern, P. C.; Pople, J. A. *J. Chem. Phys.* **1991**, *94*, 1063. (b) Curtiss, L. A.; Raghavachari, K.; Redfern, P. C.; Pople, J. A. *J. Chem. Phys.* **1997**, *106*, 1063.

(9) (a) Vydrov, O. A.; Scuseria, G. E. *J. Chem. Phys.* **2004**, *121*, 8187. (b) Polo, V.; Kraka, E.; Cremer, D. *Mol. Phys.* **2002**, *100*, 1771. (c) Grafenstein, J.; Kraka, E.; Cremer, D. *Phys. Chem. Chem. Phys.* **2004**, *6*, 1096. (d) Grafenstein, J.; Kraka, E.; Cremer, D. *J. Chem. Phys.* **2004**, *120*, 524.

(10) (a) Cremer, D. *Mol. Phys.* **2001**, *99*, 1899–1940. (b) Polo, V.; Kraka, E.; Cremer, D. *Mol. Phys.* **2002**, *100*, 1771–1790.

(11) Zhang, Y. K.; Yang, W. T. *J. Chem. Phys.* **1998**, *109*, 2604.

(12) (a) Becke, A. D. *Phys. Rev. A: At., Mol., Opt. Phys.* **1988**, *38*, 3098. (b) Perdew, J. P. *Phys. Rev. B: Condens. Matter* **1986**, *33*, 8822.

(13) (a) Lee, C.; Yang, W.; Parr, R. G. *Phys. Rev. B: Condens. Matter* **1988**, *37*, 785. (b) Becke, A. D. *J. Chem. Phys.* **1993**, *98*, 5648.

(14) (a) Perdew, J. P.; Burke, K.; Ernzerhof, M. *Phys. Rev. Lett.* **1996**, *77*, 3865. (b) Perdew, J. P.; Burke, K.; Ernzerhof, M. *Phys. Rev. Lett.* **1997**, *78*, 1396(E).

(15) Woodrich, M. D.; Corminboeuf, C.; Schleyer, P. V. *Org. Lett.* **2006**, *8*, 3631–3635.

(16) Zhao, Y.; Shultz, N. E.; Truhlar, D. G. *J. Chem. Theory Comput.* **2006**, *2*, 364.

(17) Zhao, Y.; Truhlar, D. G. *Theor. Chem. Acc.* **2008**, *120*, 215.

(18) Johnson, B. G.; Gonzales, C. A.; Gill, P. M. W.; Pople, J. A. *Chem. Phys. Lett.* **1994**, *221*, 100.

(19) *JAGUAR 7.0*; Schrödinger, Inc.: Portland, OR, 2009.

(20) Scott, A. P.; Radom, L. *J. Phys. Chem.* **1996**, *100*, 16502.

(21) Rogers, D. W.; McLafferty, F. J. *J. Chem. Phys.* **1995**, *103*, 8302–8303.

(22) (a) Tao, J. M.; Staroverov, V. N.; Scuseria, G. E.; Perdew, J. P. *Phys. Rev. A: At., Mol., Opt. Phys.* **2008**, *77*, 012509. (b) Perdew, J. P.; Staroverov, V. N.; Tao, J. M.; Scuseria, G. E. *Phys. Rev. A: At., Mol., Opt. Phys.* **2008**, *78*, 052513. (c) Arbuznikov, A. V. *J. Struct. Chem.* **2007**, *48*, S1–S31. (d) Kaupp, M.; Bahmann, H.; Arbuznikov, A. V. *J. Chem. Phys.* **2007**, *127*, 194102. (e) Bahmann, H.; Rodenberg, A.; Arbuznikov, A. V.; Kaupp, M. *J. Chem. Phys.* **2007**, *126*, 011103. (f) Janesko, B. G.; Scuseria, G. E. *J. Chem. Phys.* **2007**, *127*, 164117.

(23) Guerra, C. F.; Handgraaf, J.-W.; Baerends, E. J.; Bickelhaupt, F. M. *J. Comp. Chem.,* **2003**, *25*, 189.

(24) Heyd, J.; Scusceria, G. E. *J. Chem. Phys.* **2004**, *121*, 1187–1192.

CT9003965

JCTC Journal of Chemical Theory and Computation

Robust Periodic Hartree−Fock Exchange for Large-Scale Simulations Using Gaussian Basis Sets

Manuel Guidon, Jürg Hutter, and Joost VandeVondele*

Physical Chemistry Institute, University of Zurich, Winterthurerstrasse 190, CH-8057 Zurich, Switzerland

Received September 17, 2009

Abstract: Hartree−Fock exchange with a truncated Coulomb operator has recently been discussed in the context of periodic plane-waves calculations [Spencer, J.; Alavi, A. *Phys. Rev. B*: *Solid State*, **2008**, *77*, 193110]. In this work, this approach is extended to Gaussian basis sets, leading to a stable and accurate procedure for evaluating Hartree−Fock exchange at the Γ-point. Furthermore, it has been found that standard hybrid functionals can be transformed into short-range functionals without loss of accuracy. The well-defined short-range nature of the truncated exchange operator can naturally be exploited in integral screening procedures and makes this approach interesting for both condensed phase and gas phase systems. The presented Hartree−Fock implementation is massively parallel and scales up to ten thousands of cores. This makes it feasible to perform highly accurate calculations on systems containing thousands of atoms or ten thousands of basis functions. The applicability of this scheme is demonstrated by calculating the cohesive energy of a LiH crystal close to the Hartree−Fock basis set limit and by performing an electronic structure calculation of a complete protein (rubredoxin) in solution with a large and flexible basis set.

1. Introduction

The construction of reliable models for the exchange and correlation energy of electrons is an active research field within the density functional theory (DFT) community. For nearly 50 years, new ideas and approximations have been proposed that increase the accuracy and are improvements compared to the local density approximation[1,2] (LDA). Nowadays, most new functionals go beyond the semilocal generalized gradient approximations[3−5] (GGAs) by incorporating a certain amount of Hartree−Fock exchange (HFX) or similar nonlocal functionals.[6−11,12] Generally, these hybrid functionals are more accurate than their local counterparts. Whereas the use of these hybrid functionals is well established in the quantum chemistry community for the study of molecules, condensed phase systems, such as liquids or solids, are usually treated at a GGA level. Not only is the cost of computing exchange interactions in large condensed phase systems significant, the technical difficulty of obtaining results that are accurate and properly converged cannot be underestimated in calculations employing periodic boundary conditions (PBC). In this work, a robust and accurate scheme, suitable for large condensed phase systems is presented.

In recent work, ref 13, we have presented a linear scaling implementation of HFX that makes it feasible to perform large-scale molecular dynamics simulations with hybrid functionals in PBC. The focus on large systems has guided several design decisions for the implementation. Atom-centered Gaussian basis functions are employed, which makes a linear scaling implementation, based on a screening with the density matrix elements, relatively straightforward.[14−16] Additionally, large systems can be described without **k**-point sampling, and the approach is, thus, Γ-point only. All algorithms are massively parallel and focus on in-core operation to allow for thousands of MD steps in a reasonable time. Our initial implementation of periodic HFX at the Γ-point has been based on an approach by Challacombe and co-workers.[17] In this scheme, the minimum image convention (MIC) is applied at the level of primitives while computing the four center integrals. This is efficient and has been shown to accurately converge to reference results as

---

* Corresponding author. E-mail: vondele@pci.uzh.ch.

10.1021/ct900494g CCC: $40.75

the system size is increased.[17] However, it has been observed that this approximation is generally unstable if extended or flexible Gaussian basis sets are used. The instability is the result of a spurious minimum in the energy functional, yielding an unphysical wave function with a total energy that can be several Hartrees beyond the physical solution. This is similar to the behavior observed in traditional HFX calculations that employ a too loose screening threshold. As will be discussed in more detail below, in the MIC, there is no screening parameter which can be adjusted to guarantee stability. The new approach presented here does not employ the MIC, only requires the Γ-point, and is stable with large and flexible basis sets. The use of the truncated Coulomb (TC) operator[18] is a key ingredient. All algorithms and methods presented are implemented within the framework of the CP2K/Quickstep[19,20] program, a freely avaliable molecular simulation package.

2. The Truncated Coulomb Operator for Calculations at the Γ-point Using Gaussian Basis Sets

2.1. Periodic Hartree−Fock calculations. For finite systems such as molecules, which employ open boundary conditions, the HFX energy is computed from its definition:

$$E_x^{\text{open}} = -\frac{1}{2}\sum_{i,j}\int\int \psi_i(r_1)\psi_j(r_1)g(|r_1 - r_2|) \times \psi_i(r_2)\psi_j(r_2)d^3r_1d^3r_2 \quad (1)$$

The potential $g(|r_1 - r_2|) = 1/(|r_1 - r_2|) = 1/r_{12}$ in conventional HFX calculations but is commonly replaced by other operators, such as $\text{erfc}(\omega r_{12})/r_{12}$, $\exp(-\omega^2 r^2)$ or $\exp(-\omega r)/r$ in modern electronic structure theory.[7,8,21,22] Computing this energy poses no special problems. In the condensed phase, the HFX energy must take the periodic nature of the system into account, and an integration over **k**-vectors, which reflects the translational invariance and the infinite nature of the system, is formally required. In practice, a finite mesh of **k**-points is employed, which usually becomes less dense as the unit cell increases in size. The HFX energy in periodic systems is, thus, defined as

$$E_x^{\text{PBC}} = -\frac{1}{2N_\text{k}}\sum_{i,j}\sum_{\mathbf{k},\mathbf{k}'}\int\int \psi_i^{\mathbf{k}}(r_1)\psi_j^{\mathbf{k}'}(r_1)g(|r_1 - r_2|) \times \psi_i^{\mathbf{k}}(r_2)\psi_j^{\mathbf{k}'}(r_2)d^3r_1d^3r_2 \quad (2)$$

Where N_k is the number of **k**-points within the Brillouin zone, and the integrals are over all space. The wave functions are assumed to be normalized over the crystal volume $N_\text{k}V$, where V is the volume of the unit cell. This expression, however, is troublesome to compute. The reason for this is the integratable singularity at $\mathbf{k} = \mathbf{k}'$, which is related to the conditionally convergent nature of the integral for that choice of **k**-vectors. Several schemes have been developed to obtain good convergence with respect to the **k**-point sum.[23−27] Of particular interest here is the method by Spencer and Alavi.[18] This method is based on the observation that the TC operator:

$$g_{\text{TC}}(r_{12}) = \begin{cases} \frac{1}{r_{12}}, & r_{12} \le R_c \\ 0, & r_{12} > R_c \end{cases} \quad (3)$$

yields an expression for the HFX energy that does not exhibit a singularity at $\mathbf{k} = \mathbf{k}'$, that converges to the exact expression as R_c goes to infinity, and that becomes increasingly easy to converge in **k**-space as R_c becomes smaller. It is intuitive that, contrary to the Hartree energy, the exchange energy converges rapidly with R_c for the TC operator. Since the convergence of the exchange energy is related to the decay of the density matrix, it will be most rapid for systems with a large gap. However, this also means that the minimum R_c, which yields a properly converged exchange energy, is a system-dependent property. As illustrated in Section 3, the exchange energy computed with g_{TC}, in open systems or with full **k**-point convergence, decreases monotonically to its limiting value for increasing R_c. Clearly, one can define truncated versions of other commonly employed operators. In ref 18, it is demonstrated that it is reasonable to take the number of **k**-points as

$$N_\text{k} \approx \frac{4\pi}{3}R_c^3\frac{1}{V} \quad (4)$$

(see that work for an in-depth discussion). Once R_c is fixed, eq 4 shows that the Γ-point alone will be sufficient for large systems, since large systems imply a large V. For a cubic unit cell with edges of length L, eq 4 suggests that having $R_c < 0.62L$ is sufficient for Γ-point only sampling. If needed, sufficiently large systems can always be obtained by replicating the unit cell in all directions. The Γ-point expression for the exchange energy is given by

$$E_x^{\Gamma} = -\frac{1}{2}\sum_{i,j}\int\int \psi_i^{\mathbf{0}}(r_1)\psi_j^{\mathbf{0}}(r_1)g_{\text{TC}}(|r_1 - r_2|) \times \psi_i^{\mathbf{0}}(r_2)\psi_j^{\mathbf{0}}(r_2)d^3r_1d^3r_2 \quad (5)$$

This expression for E_x^{Γ} looks similar to the one for E_x^{open} (eq 1). However, E_x^{Γ} will diverge for $R_c \to \infty$. It has to be emphasized that only for a finite range of R_c, i.e. sufficiently small to allow for Γ-point only sampling of the integral, E_x^{Γ}, as defined by eq 5, will be a meaningful approximation to the full **k**-space integrated HFX energy. A hand-waving argument for the fact that the Γ-point only expression implies a limit on R_c can also be made as follows: for well localized electrons (i.e., if the maximally localized Wannier functions fit the unit cell), the exchange energy between electrons in different unit cells of the system is small. However, eq 5 would nevertheless predict a large contribution to the exchange energy for an electron and its ‘periodic image’ if R_c is large enough. This spurious ‘self-exchange’ with the image electron should not be present, and R_c needs, thus, to be chosen accordingly. Based on this reasoning, a somewhat more conservative rule than eq 4 for determining the maximum R_c can be proposed: R_c should be smaller than or equal to the radius of the largest sphere that fits the unit cell. This guarantees, for localized electrons, that no interactions with image electrons are possible. For cubic unit cells this yields $R_c \le L/2$, similar to eq 4, while for orthorhombic or strongly distorted triclinic unit cells, this estimate can be significantly different from eq 4.

The expression for the Hartree−Fock energy at the Γ-point (eq 5) can be computed per unit cell and in an atom-centered basis set as

$$E_x^{\Gamma} = -\frac{1}{2}\sum_{\lambda\sigma\mu\nu} P^{\mu\sigma}P^{\nu\lambda}\sum_{\mathbf{abc}}(\mu\nu^{\mathbf{a}}|\lambda^{\mathbf{b}}\sigma^{\mathbf{b+c}})_{g_{\mathrm{TC}}} \tag{6}$$

with **a**, **b**, and **c** denoting translations of the unit cell. This exact result can be obtained easily by introducing in eq 5 the expression of the periodic wave function in an atomic orbital basis:

$$\psi_i(r) = \sum_{\mu\mathbf{a}} C^{\mu i}\varphi_{\mu}^{\mathbf{a}}(r) \tag{7}$$

Here, $C^{\mu i}$ are the wave function coefficients, which are complex in the general case but can be taken real at the Γ-point. $\phi_{\mu}^{\mathbf{a}}(r)$ is the atom-centered basis sets, translated by a multiple of the unit cell given by **a**. The density matrix elements $P^{\mu\nu}$ are obtained from $\sum_i C^{\mu i}C^{\nu i}$. The two-electron four center integrals are defined as

$$(\mu\nu^{\mathbf{a}}|\lambda^{\mathbf{b}}\sigma^{\mathbf{b+c}})_{g_{\mathrm{TC}}} = \int\int \mu(\mathbf{r}_1)\nu^{\mathbf{a}}(\mathbf{r}_1)g_{\mathrm{TC}}(r_{12})\lambda^{\mathbf{b}}(\mathbf{r}_2)\sigma^{\mathbf{b+c}}(\mathbf{r}_2)\mathrm{d}\mathbf{r}_1\mathrm{d}\mathbf{r}_2 \tag{8}$$

These integrals can be obtained analytically for the TC operator, and their numerical treatment will be discussed in detail in Section 2.3. The triple sum over the lattice vectors in eq 6 converges quickly in **a** and **c** because the overlap of the corresponding Gaussian basis functions decays quickly with distance, while the sum over **b** is finite by virtue of the short-range nature of the truncated Coulomb operator. In eq 6, all terms that are larger than a given screening threshold $\varepsilon_{\mathrm{screening}}$ should be retained. As discussed in more detail in section 4.3, screening based on the traditional Schwarz-inequality combined with a simple distance criterium based on the centers of the product densities $\mu\nu^{\mathbf{a}}$ and $\lambda^{\mathbf{b}}\sigma^{\mathbf{b+c}}$ can be used to eliminate negligible terms.

At this point, some differences and similarities between the approach summarized by eq 6, and the MIC, proposed in ref 17 shall be discussed. First, there is the difference in operator $g(r)$, which is the conventional $1/r$ in the MIC and TC operator (eq 3) here. Second, in the MIC, one retains only one term from the sum over **b**, i.e., that particular index **b′**, which guarantees that the distance between the centers of the product densities $\mu\nu^{\mathbf{a}}$ and $\lambda^{\mathbf{b}'}\sigma^{\mathbf{b}'+\mathbf{c}}$ is as small as possible. This is usually the dominant contribution to the sum but generally ignores terms larger than a given $\varepsilon_{\mathrm{screening}}$. With increasing basis set size and quality, this leads to a spurious minimum in the MIC HFX energy functional. This instability is illustrated in Table 1 and analyzed in some more detail in the Section 4.2. Note that for potentials with shorter range, such as erfc(ωr)/r, the instability is less pronounced. The new method based on the TC operator and the full sum is stable for all basis sets employed, as shown in Table 2. The total energy converges rapidly with R_c reaching, for this simple system, a plateau at $R_c \approx 4$ Å. As expected, for R_c larger than the value suggested by eq 4, 7.7 Å for this system, Γ-point sampling is not sufficient anymore, and the integral diverges. Also the more conservative choice ($R_c = L/2$ for cubic cells) gives good results. Comparing Tables 1 and 2, it can be seen that the MIC results equal the results of the truncated method with $R_c = L/2$ to micro-Hartree accuracy, in the case where the MIC procedure is stable, i.e. the SZV, DZVP, and TZVP basis sets. Even though the instability of the MIC procedure is fundamental, this approach is, by construction, able to eliminate the spurious self-exchange with image electrons, even if the conventional Coulomb operator is used. Further validation and testing of the truncated Coulomb potential method based on eq 6 is presented in Section 3.

Table 1. PBC Hartree−Fock Total Energies [Hartree] Computed with the Minimum Image Convention for Two Operators[a,b]

	total energy [au]	
basis set	$1/r$	erfc(ωr)/r
SZV	−33.531805	−32.552246
DZVP	−33.781652	−32.801068
TZVP	−33.798435	−32.817981
TZV2P	−83.287255	−33.827285
QZV2P	−219.806121	−41.438744

[a] The conventional $1/r$ Coulomb potential and the short-range potential erfc(ωr)/r with $\omega = 0.11$. [b] The system consists of two water molecules, described with pseudo potentials, in a cubic unit cell with $L = 12.42$ Å and with a geometry that appears sensitive to the instability. It can be observed that the total energy converges to an unphysical result as soon as the basis set quality reaches TZV2P.

2.2. A long-range correction to the truncated Coulomb operator. In the limit $R_c \rightarrow \infty$, the truncated and full Coulomb potential become identical. In the context of hybrid density functionals, the question arises whether the missing long-range exchange at finite R_c can be corrected by the long-range part of a local density functional. In a similar fashion, this has been done for the HSE06[7,8] hybrid functional that uses the short-range erfc(ωr)/r potential. The basic concept behind this range separation relies on the fact that the exchange energy can be written in terms of the spherically averaged exchange hole $\rho_{\mathrm{xc}}^{\mathrm{SA}}(\mathbf{r}, s)$:

$$E_{\mathrm{x}}^{\mathrm{DFT}}[\rho] = \frac{1}{2}\int \rho(\mathbf{r})\mathrm{d}\mathbf{r}\int_0^{\infty} 4\pi u\rho_{\mathrm{xc}}^{\mathrm{SA}}(\mathbf{r}, u)\mathrm{d}u \tag{9}$$

where u denotes the electron−electron interaction distance. The long-range part for a system that interacts via a truncated Coulomb potential is then simply given by

$$E_{\mathrm{x}}^{\mathrm{DFT,LRC}}[\rho] = \frac{1}{2}\int \rho(\mathbf{r})\mathrm{d}\mathbf{r}\int_{R_c}^{\infty} 4\pi u\rho_{\mathrm{x}}^{\mathrm{SA}}(\mathbf{r}, u)\mathrm{d}u \tag{10}$$

Within this range-separation ansatz, the exchange energy can be written as

$$E_{\mathrm{x}} = E_x^{\mathrm{HF,TC}} + E_{\mathrm{x}}^{\mathrm{DFT,LRC}} \tag{11}$$

For convenience, a model with an analytical expression of the spherically averaged exchange hole has been chosen. Similar to the range-separated hybrid functional of Heyd et al., the starting point for the long-range correction is the exchange hole formulation of the PBE functional by Ernzerhof and Perdew.[28]

Table 2. PBC Hartree−Fock Total Energies [Hartree] with the Scheme for the Truncated Coulomb Operator For Various Choices of R_c [Å][a]

cutoff radius, R_c	SZV	DZVP	TZVP	TZV2P	QZV2P
0.5	−30.074404	−30.273802	−30.298149	−30.309740	−30.330732
1.0	−32.693538	−33.024934	−33.052548	−33.061415	−33.064684
2.0	−33.459119	−33.722827	−33.738480	−33.747451	−33.750486
3.0	−33.527563	−33.778845	−33.794977	−33.803751	−33.807027
4.0	−33.531707	−33.781608	−33.798342	−33.807131	−33.810757
5.0	−33.531804	−33.781651	−33.798433	−33.807222	−33.810894
6.0	**−33.531805**	**−33.781652**	**−33.798435**	**−33.807224**	**−33.810898**
7.0	−33.531805	−33.781652	−33.798435	−33.807224	−33.810898
8.0	−33.531806	−33.781652	−33.798436	−33.807225	−33.810900
10.0	−33.533982	−33.783206	−33.800223	−33.809006	−33.812843
12.0	−33.912427	−34.152952	−34.170470	−34.179272	−34.183189
16.0	−33.533982	−35.851041	−35.869063	−35.877848	−35.882304

[a] The system is the same as the one described in Table 1, but the results are stable, independent of the basis set. For large values of R_c, the Γ-point sampling of the exchange energy is not sufficient. As discussed in the text, the choice of $R_c \approx L/2 \approx 6.0$ Å (shown in bold) guarantees that no spurious self-exchange parts enter the Γ-point calculation.

The PBE exchange energy is defined via an integral over the exchange energy density $\varepsilon_x^{\mathrm{PBE}}$:

$$E_x^{\mathrm{PBE}} = \int \rho(\mathbf{r})\varepsilon_x^{\mathrm{PBE}}(\rho, \nabla\rho)\mathrm{d}\mathbf{r} \qquad (12)$$

$\varepsilon_x^{\mathrm{PBE}}$ is a function of the electron density $\rho(\mathbf{r})$ and its gradient $\nabla\rho(\mathbf{r})$ and is defined as the product of the LDA exchange energy density and the enhancement factor F_x^{PBE} that additionally depends on the gradient of the electronic density:

$$\varepsilon_x^{\mathrm{PBE}}(\rho, \nabla\rho) = \varepsilon_x^{\mathrm{LDA}}(\rho) \times F_x^{\mathrm{PBE}}(\rho, \nabla\rho) \qquad (13)$$

The PBE exchange hole model J_x^{PBE} enters into the definition of the enhancement factor, defining the latter to be an integral of the following kind:

$$F_x^{\mathrm{PBE}}(s) = -\frac{8}{9}\int_0^{\infty} yJ_x^{\mathrm{PBE}}(s, y)\mathrm{d}y \qquad (14)$$

with $s = |\nabla\rho|/2\pi k_F\rho$ the reduced gradient, k_F being the local Fermi vector, and $y = \mathrm{k}_F u$ the scaled interaction coordinate. For the analytic expression of J_x^{PBE}, the following parametrized form:

$$J_x^{\mathrm{PBE}}(s, y) = \left[-\frac{A}{y^2}\frac{1}{1 + (4/9)Ay^2} + \left(\frac{A}{y^2} + B + C[1 + s^2F(s)]y^2 + E[1 + s^2G(s)]y^4\right)\exp(-Dy^2)\right] \times \exp(-s^2H(s)y^2) \qquad (15)$$

with parameters $A-E$ being constants and $F-H$ being functions of the reduced gradient, has been found by Ernzerhof et al. (see ref 28 for details). For the current purpose, the long-range enhancement factor is given by

$$F_x^{\mathrm{PBE,LRC}}(s) = -\frac{8}{9}\int_{R_c'}^{\infty} yJ_x^{\mathrm{PBE}}(s, y)\mathrm{d}y \qquad (16)$$

with $R_c' = R_c\mathrm{k}_F$. This integration can be carried out analytically (see Section A) yielding an expression for the long-range correction of the exchange energy.

The final form of the range-separated exchange energy reads now:

$$E_x = E_x^{\mathrm{HF,TC}}(R_c) + E_x^{\mathrm{PBE,LRC}}(R_c) \qquad (17)$$

both parts depending on the cutoff radius, R_c. Using these results, one can define three different hybrid functionals:

$$\mathrm{PBE0:}\ E_{\mathrm{xc}}^{\mathrm{PBE0}} = aE_x^{\mathrm{HF}} + (1 - a)E_x^{\mathrm{PBE}} + E_c^{\mathrm{PBE}} \qquad (18)$$

$$\mathrm{PBE0{-}TC:}\ E_{\mathrm{xc}}^{\mathrm{PBE0-TC}} = aE_x^{\mathrm{HF,TC}} + (1 - a)E_x^{\mathrm{PBE}} + E_c^{\mathrm{PBE}} \qquad (19)$$

$$\mathrm{PBE0{-}TC{-}LRC:}\ E_{\mathrm{xc}}^{\mathrm{PBE0-TC-LRC}} = aE_x^{\mathrm{HF,TC}} + aE_x^{\mathrm{PBE,LRC}} + (1 - a)E_x^{\mathrm{PBE}} + E_c^{\mathrm{PBE}} \qquad (20)$$

PBE0 is, for $a = 0.25$, the standard PBE hybrid functional.[29−31] PBE0-TC denotes the original functional of PBE0 in which the standard HFX energy is replaced by the TC expression with cutoff radius R_c, and PBE0-TC-LRC is the PBE0-TC functional with the long-range correction (LRC) based on the PBE exchange hole. Of course, similar variants can be defined for other hybrid functionals. It is demonstrated in Section 3.2 that the use of a LRC allows for a very small R_c ($\approx$ 2 Å) without negatively impacting the performance of the functional for typical thermochemical quantities. HFX with such a short-range can be evaluated very efficiently. Note that, in the limit of R_c going to zero, the PBE functional is recovered but based in part on the spherically averaged PBE exchange hole.

2.3. Efficient Calculation of Two-Electron Integrals for General *g*(*r*). Two-electron four center integrals are commonly calculated analytically using recurrences.[32−34] CP2K employs the LIBINT[56] library for this. These algorithms start from the lowest angular momentum interaction, i.e., $(ss|ss)_g$, for a given interaction potential $g(r_{12})$ and then recursively calculate higher order contributions from that. In order to calculate integrals with a total angular momentum n, these routines have to be provided with $n + 1$ initial values as the starting vector. With the notation used by Ahlrichs,[34] this reads as

$$G_n(\rho, T) = \left(-\frac{\partial}{\partial T}\right)^n G_0(\rho, T) \qquad (21)$$

$$G_0(\rho, T) = \frac{2\pi}{\rho^{3/2}\sqrt{T}} \int_0^\infty g\left(\frac{y}{\sqrt{\rho}}\right) y e^{-y^2-T} \sinh(2y\sqrt{T}) \mathrm{d}y \tag{22}$$

where T and ρ are parameters determined by the geometry and the involved Gaussian basis functions. For several commonly used operators, there exist efficient recursive formulas to calculate the higher order derivatives. In the case of the full range Coulomb potential, the whole procedure reduces to an evaluation of the Γ-function at various parameters T. For the TC potential one arrives at

$$G_0(\rho, T, R'_c) = \frac{\pi^{3/2}}{2\rho} \frac{2\mathrm{erf}(\sqrt{T}) + \mathrm{erf}(R'_c - \sqrt{T}) - \mathrm{erf}(R'_c + \sqrt{T})}{\sqrt{T}} \tag{23}$$

which depends on the parameter T and the cutoff radius $R'_c = R_c\sqrt{\rho}$. Unfortunately, there is no obvious recurrence to compute higher order derivatives, but (lengthy) explicit formulas are readily derived. Nevertheless, since the explicit dependence on ρ is trivial, it is sufficient to be able to evaluate the bivariate function (R'_c and T) and its derivatives, with respect to T to be able to evaluate the required four center integrals. An example of a higher order derivative is shown in Figure 1. Here, a largely automatic approach is presented that yields an accurate and efficient procedure to evaluate representations of these bivariate functions. This approach can be used with general operators $g(r)$ even if no explicit recurrences are known or if the numerical evaluation is troublesome. For example, the procedure has also been tested on the Yukawa potential for which Ten-no[22] skillfully derived a sequence of suitable expressions. Therefore, this technique might be useful for investigating density functionals that are based on a more flexible form of $g(r)$.

In a first step, computer code for the explicit calculation of the function and the required derivatives is generated by a computer algebra system. This can be either an explicit expression, as obtained for the TC operator, a symbolic Taylor series,[34] or any other convenient representation. Neither efficiency nor stability of the generated expression are a particular concern at this point. On a potentially large set of reference points, to be discussed below, this code is evaluated with arbitrary precision using a multi-precision floating point library (mpfr).[35,36] By doubling the number of digits employed in this evaluation until the result is accurate, a good numerical quality of the reference data is guaranteed. In order to evaluate accurately the higher derivatives of the TC operator, hundreds of digits are essential for the intermediate expressions. Finally, an automatic piece-wise bivariate interpolation of these reference points, using Chebyshev polynomials, is performed. This bivariate interpolation is constructed using the algorithm of Caliari et al.[37] In this scheme, the full two-dimensional parameter space has to be mapped first on the square $[-1, 1]^2$, which is the natural domain for the interpolation. The function must also be defined on the boundary of the domain. In this square, the Padua2D points of order n are a special set of optimal nodes used for the polynomial interpolation:

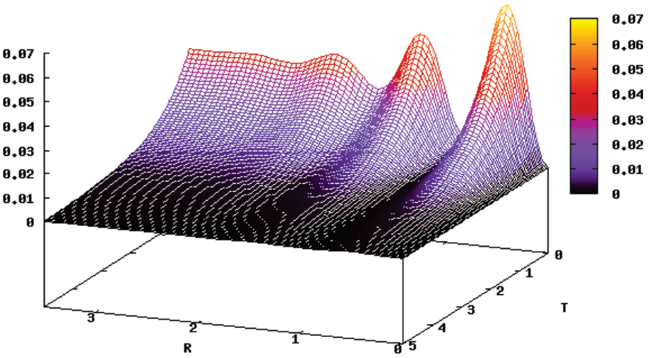

Figure 1. The figure shows $G_{14}(R'_c, T)$ as defined by eqs 21 and 23 for the TC operator.

$$\xi = (\xi_1, \xi_2) = \left\{\gamma\left(\frac{k\pi}{n(n+1)}\right), \quad k = 0, ..., n(n+1)\right\} \tag{24}$$

with the generating curve:

$$\gamma(t) = (-\cos((n+1)t), -\cos(nt)), \qquad t \in [0, \pi] \tag{25}$$

The usage of these points guarantees an almost optimal convergence with increasing degree of the Chebyshev basis functions. The polynomial interpolation of a two-dimensional function $f(x_1, x_2)$ is then given by

$$f(x_1, x_2) \approx \sum_{k=0}^{n} \sum_{j=0}^{k} c_{j,k-j} \hat{T}_j(x_1) \hat{T}_{k-j}(x_2) - \frac{c_{n,0}}{2} \hat{T}_n(x_1) \hat{T}_0(x_2) \tag{26}$$

where the coefficients:

$$c_{j,k-j} = \sum_{\xi \in [1,1]^2} f(\xi) w_\xi \hat{T}(\xi_1) \hat{T}_{k-j}(\xi_2), \qquad 0 \le j \le k \le n \tag{27}$$

with weights w_ξ and Chebyshev polynomials $\hat{T}_m$ of order m can be computed once and for all and, thus, be stored in a table. Using the multi-precision enabled code, these coefficients are computed and stored in a standard 64-bit floating point representation. Function values of a bivariate function are then evaluated based on eq 26 and, thanks to the favorable properties of the Chebyshev expansion, will be accurate to nearly machine precision, provided the expansion is of sufficient order. This also holds for the G_n functions required for the TC operator.

However, since the target function typically shows different behavior in terms of smoothness and continuity at different argument ranges, it is not beneficial to perform a global interpolation, as this requires a high order and, thus, expensive interpolation. Instead, an adaptive scheme has been devised that, given a specified low order of the expansion, automatically bisects the full domain (e.g., using alternate directions) until the accuracy of the interpolation is accurate to a given threshold (e.g., 10^{-12} or machine precision). This procedure is facilitated by the fact that the Padua2D interpolation procedure provides an automatic estimate of the accuracy.[37] As the procedure bisects the domain, computer code is generated such that the proper interpolation coefficients can be found efficiently in a table of patch-wise interpolating functions. In this way, evaluations of the interpolation can be performed orders of magnitude more efficiently than with the global interpolation. For the case of the TC operator, an interpolation order of 13 has been employed. The down-side is, of course, that the interpolation is only piece-wise contiguous but nevertheless accurate to the chosen threshold everywhere. Note, that the interpolation is constructed for all derivatives simultaneously, i.e. eq 26, is never explicitely derived. In terms of efficiency, it can be concluded that calculating the starting vector $\mathbf{G}_n$ for the truncated potential is approximately twice as expensive as computing with an optimized implementation of the Γ-function, the starting vector for the full Coulomb potential. The code for evaluating $\mathbf{G}_n$ for the truncated potential is available, as is the code for constructing the adaptive interpolation.[38]

3. Assessment and Validation of the Method

3.1. Illustration on Gas- and Condensed-Phase Systems. In this section, the convergence behavior of the truncated operator for increasing cutoff radius R_c is investigated. As model systems, chains of poly-ethylene and poly-acetylene with a length of about 38 Å (30 carbon atoms) have been chosen. For both systems, self-consistent total energies have been calculated with the Hartree−Fock/pc-2[39−41] level of theory applying the standard Coulomb operator, which serves as a reference, and with the truncated operator for different cutoff radii in the range of 0.1−15 Å. In order to illustrate the effect of the long-range correction, the same calculations have been performed again, including the correction based on the PBE exchange hole. In addition, similar data for a two-dimensional hexagonal boron−nitride mesh in periodic boundary conditions are presented. The latter system consists of 128 atoms in total, has a dimension of 20.1 × 17.4 Å and was computed with a pc-1 basis set.[39−41] The reference value has been obtained from an exponential extrapolation of the last three data points.

All findings are summarized in Figure 2. In the case of the uncorrected TC operator, one observes that the total energy of all three systems decreases monotonically to the limiting value for increasing cutoff radius R_c. Furthermore, the logarithmic plot shows that all calculations converge approximately exponentially to the correct value. The faster convergence for poly-ethylene relative to poly-acetylene can directly be attributed to its larger band gap. The computed HF band gaps are 13.67, 7.34, and 13.95 eV for poly-ethylene, poly-acetylene, and the hexagonal boron−nitride mesh, respectively. The long-range correction improves upon the uncorrected total energies in the short-range (0−2.5 Å) but overestimates the correction to the total energy in the long-range part. It is not so surprising that the LRC does not capture the tail of the exchange hole very well, since the underlying model is essentially derived to capture the short-range behavior of the exchange hole. It appears that this model does not decay sufficiently fast. Very accurate Hartree−Fock energies are, thus, obtained more easily without correction.

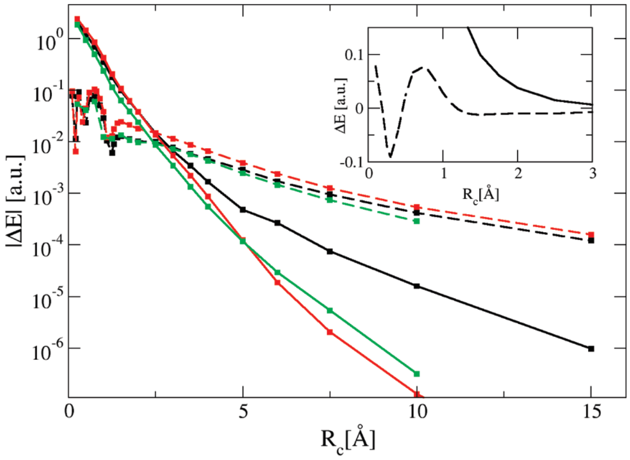

Figure 2. Shown are absolute errors in total energies with respect to the limiting case $R_c \rightarrow \infty$. Results for nonperiodic poly-ethylene and poly-acetylene are drawn in red and black, respectively, while results for periodic hexagonal boron−nitride are displayed in green. Solid and dotted lines represent data obtained without and with the long-range correction. All errors are scaled by the number of non-hydrogen atoms in each system. As shown in the inset for poly-acetylene, the correction over and under estimates the total energy at different ranges, which is the cause of the spikes in the logarithmic plot.

This analysis suggests that HFX calculations with a TC potential could serve as an interesting tool for investigating the behavior of the exchange hole at different ranges and could support the development of new density-based exchange hole models.

3.2. Barrier Heights and Reaction Energies for Gas-Phase Reactions. In order to analyze the accuracy of calculations based on the TC potential, the method has been benchmarked against a database established by Truhlar et al.[42] This database consists of 22 reactions involving 47 molecules in gas phase and provides geometries of reactants, products, and saddle points. This database has been selected because reaction energies are particularly sensitive to the precise treatment of exchange and because saddle point geometries usually involve somewhat delocalized electronic states. The dependence of the reaction energies and the barrier heights on the choice of R_c for both the PBE0-TC and PBE0-TC-LRC functionals has been investigated. In order to provide a reference, a comparison of these results to the established PBE,[5] PBE0,[29−31] HSE06,[7,8] and MCY3[21] functionals are presented. In addition, all benchmark runs have been performed twice, once with an all-electron representation and once applying pseudo-potentials. All-electron calculations employ the Gaussian and augmented plane waves (GAPW) method[43] and the MG3S basis,[44] while pseudo-potential calculations use the Gaussian and plane-waves (GPW) method,[45] PBE optimized pseudo-potentials,[46] and molecularly optimized TZV2P basis sets.[47] All results are summarized in Table 3. The first observation is that, as expected, the results of the standard PBE0 calculations are recovered as $R_c \rightarrow \infty$. Based on these results, the replacement of the standard HFX expression with its truncated counterpart seems to be possible without loss of accuracy, if $R_c > 6.0$ Å. As emphasized before, this is system dependent but appears

Table 3. The Table Shows Mean-Square Errors in kcal/mol of Classical Barrier Heights and Classical Reaction Energies with Respect to Experimental Values[a]

	GAPW				GPW			
	barriers		energies		barriers		energies	
PBE	9.9		3.3		9.1		2.3	
PBE0	4.6		1.7		4.3		2.0	
HSE06	4.6		1.7		4.4		2.1	
MCY3	2.9		1.7		3.0		1.3	
R_c [Å]	TC	TC-LRC	TC	TC-LRC	TC	TC-LRC	TC	TC-LRC
∞	4.6	4.6	1.7	1.7	4.3	4.3	2.0	2.0
8.0	4.6	4.6	1.7	1.7	4.3	4.3	2.0	2.0
6.0	4.6	4.6	1.7	1.7	4.3	4.3	2.0	2.0
4.0	4.4	4.5	1.7	1.7	4.2	4.2	2.0	2.0
3.5	4.2	4.2	1.7	1.7	4.0	4.0	2.0	2.0
3.0	3.8	3.8	1.7	1.7	3.5	3.6	2.0	2.0
2.5	3.2	3.2	1.5	1.6	3.0	3.0	1.9	1.9
2.0	**2.7**	**2.6**	**1.4**	**1.4**	**2.5**	**2.5**	**2.0**	**1.9**
1.5	3.4	3.3	1.5	1.5	3.1	3.1	2.1	2.1
1.0	5.0	5.0	3.1	2.0	4.5	4.7	2.5	2.0
0.5	7.6	8.8	2.6	2.1	7.4	8.5	2.3	2.7

[a] The data is shown for standard functionals PBE, PBE0, HSE06, and MCY3 and for the TC PBE0-TC and long-range corrected PBE0-TC-LRC functionals. For the latter two functionals, truncation radii (R_c) ranging from 0.5 to 8.0 Å have been employed. Calculations have been performed using an all-electron approach (GAPW) with a MG3S basis and using pseudo-potentials (GPW) with a molecularly optimized TZV2P basis. Relative to experiment, the best results are obtained for $R_c = 2.0$ Å, shown in bold.

to hold for the (small) molecules in this test set. Interestingly, already for $R_c = 4.0$ Å, results obtained with either PBE0-TC and PBE0-TC-LRC are basically converged. If some small influence on the final results can be tolerated, a choice of $R_c = 4.0-6.0$ Å appears appropriate, which can bring noticeable savings in computer time for large systems. PBE0-TC and PBE0-TC-LRC appear only significantly different at short-range $R_c \leq 2.5$ Å.

For the very short-range calculations ($R_c = 0.5$ Å), where only the PBE0-TC-LRC functional is meaningful, the calculations yield, as expected, approximately PBE results. It can be observed that in the intermediate range, around $R_c = 2.0$, the best estimates are obtained for the reaction barriers, similar in quality to MCY3. This suggests that the use of very short-range exchange functionals, such as PBE0-TC-LRC at $R_c = 2.0$ Å is meaningful, and that even more accurate functionals that explicitly limit the action of exact exchange to such a short distance can be developed.

3.3. Parallel Performance. Given the computational cost of simulations including exact exchange, an efficient and scalable implementation is essential if exact exchange is to be a successful ingredient for simulations of large and complex systems. The initial implementation presented in ref 13 scaled to a few hundreds of cores for a condensed phase system containing 64 water molecules, described with a TZV2P basis for both oxygen and hydrogen (2560 basis functions). Combined with an in-core compression scheme and a multiple-time step approach, this was sufficient to compute 13 ps of MD trajectory. As shown in Figure 3, the new implementation, using the PBE0-TC-LRC($R_c = 2.0$) functional, allows the same system to scale up to a few thousands of cores, effectively allowing simulations to proceed 10 times faster. Currently, 10 ps of simulation can be obtained in two days, even without a multiple-time step scheme. As will be illustrated in Section 3.4, for systems that are computationally more demanding than 64 water molecules, scalability to 10′000s of cores can be reached effectively enabling CP2K[19] to obtain good performance on the largest supercomputers currently available.

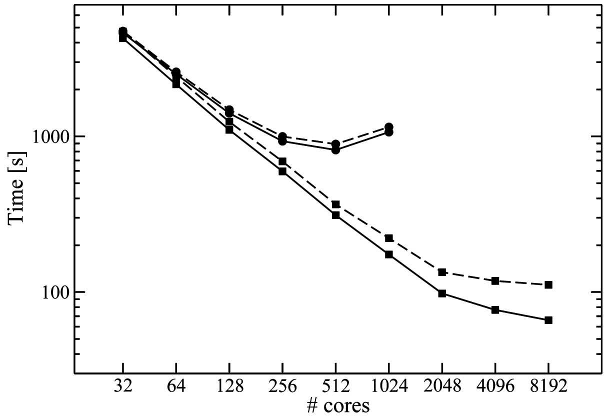

Figure 3. A comparison of the scaling of the current (squares) and previous (circles, ref 13) implementation of periodic HFX. The benchmark is 10 steps of ab initio molecular dynamics of 64 water molecules in PBC using a TZV2P basis and pseudo potentials. The solid lines represent the time spent in the HFX routines, and the dashed lines represent the total run time. Using 2 048 cores, successive Born−Oppenheimer MD steps take approximately 9 s. All timings were on a Cray XT5 with 8 cores per node.

The basic parallelization strategy has remained unchanged from the initial implementation, i.e., replicated density, and Kohn−Sham matrices are made available on all MPI processes. Based on a load-balancing step, the work of each process is decided in advance, and computation proceeds in a communication-free way until all local contributions to the Kohn−Sham matrix have been computed and until the matrix can be redistributed and summed. One key advantage of this approach is that full integral symmetry can be exploited. Furthermore, there are only communication steps in the beginning and end, and these can be performed efficiently in a ring topology. The disadvantage of this approach is that neither the communication nor the memory decreases as the number of processes increases. The memory bottleneck limits the size of the systems that can be studied, while the communication bottleneck ultimately limits scalability, provided the load balance can be maintained throughout. However, the current implementation reduces the impact of the matrix replication by employing a mixed MPI/openMP scheme, where density and Kohn−Sham matrix are shared between the threads (one per core) on a node. In this way, the communication needed for the replication is reduced, and, depending on the available RAM, much larger systems (3×10^4 basis functions and more for 16 Gb/node) can fit in memory. A further benefit of the MPI/openMP scheme is that load balancing between threads can easily be performed. Such a dynamic load balancing is helpful for inhomogeneous systems that are difficult to load balance before the calculations start. Nevertheless, the importance of a good initial

Table 4. Results Obtained with the Truncated Coulomb Operator and a Large and Flexible Basis for Unit Cells That Are a Multiple of the Basic Cubic Unit Cell (4.084 Å)[a]

	R_c [Å]	E(HF)[au]	H[au]	Li[au]	$\varepsilon_{\mathrm{HF}}^{\mathrm{coh}}$ [au]
2 × 2 × 2	4.0	−32.244609	−0.499957	−7.428493	−0.132702
3 × 3 × 3	6.0	−32.256844	−0.499974	−7.432137	−0.132100
4 × 4 × 4	8.0	−32.258022	−0.499974	−7.432582	−0.131949
5 × 5 × 5	10.0	−32.258179	N/A	N/A	N/A

[a] The columns show the size of the unit cell, the range of the TC operator (R_c), the Hartree−Fock energy per unit cell, the H atom energy, the Li atom energy, and the cohesive energy, respectively ($\varepsilon_{\mathrm{HF}}^{\mathrm{coh}}$).

distribution of work cannot be underestimated, and a carefully constructed load-balancing algorithm is essential. The full description of this part of the algorithm is beyond the scope of the current paper. The basic ingredient is a binning procedure that collects batches of four center integrals of approximately equal estimated computational cost. These bins, typically 64 per core, are the basic unit of work and are distributed such that the computational load is balanced.

3.4. The Cohesive Energy of LiH at Hartree−Fock Basis Set Limit. Recent HF and post-HF results on crystalline LiH[48−57] have received much interest in the solid-state community. The availability of accurate reference numbers has made this system a challenging benchmark to judge the accuracy of various theoretical methods applied to condensed-phase systems. This work contributes to this ongoing research by computing the HF cohesive energy of LiH near the basis set limit. These results have been published in part in ref 51, where a comparison of the total energy of the LiH crystal obtained directly using the truncated method with results by Scuseria and co-workers based on extrapolation of screened exchange has been presented. Here, these results are summarized, and more details of these calculations are presented.

In a first step, an optimized basis set for an accurate HF calculation on bulk LiH, similar in composition to the polarization consistent (pc-3) basis sets derived by Jensen,[39−41] has been constructed. The composition of this basis set is 8s3p2d1f/6s3p2d1f and 13s6p2d1f/11s5p2d1f for hydrogen and lithium (see ref 51 for details). The accuracy of the optimized basis has been estimated to be within 0.001 au of the basis set limit for the total energy, while the basis set error on the cohesive energy is likely smaller than 0.1%. All calculations, summarized in Table 4, have been performed on the experimental cubic unit cell with linear dimension $L = 4.084$ Å, which contains 4 Li and 4 H atoms, using truncated HF without the long-range correction. Total energies have been computed for systems of increasing system size by explicitely repeating this unit cell periodically in three dimensions. The largest system employed, a 5 × 5 × 5 repetition, consists of exactly 1 000 atoms and uses 37 500 Gaussian basis functions. With increasing system size, the range of the TC operator has been increased as well. The results have been found to converge exponentially with system size, and an accurate estimate for the total energy per unit cell of approximately −32.258179 au could be obtained directly from a calculation of the largest system. This number is in excellent agreement with the Padé-extrapolated SR-HFX results of ref 51 −32.258171 au. By calculating the HF energy of the H and Li atoms in periodic boundary conditions and retaining the basis functions of all other (ghost) atoms in the unit cell, a consistent number for the cohesive energy could be obtained. However, due to the fact that unrestricted calculations are needed for the atoms, these calculations are more demanding (memory-wise) than the bulk and are, therefore, only performed for the 4 × 4 × 4 repetition of the basis cell. The 4 × 4 × 4 crystal required 11 terabytes of memory for the integral storage. The best estimate of the cohesive energy obtained in this way is −131.949 mE_h. This result is derived in an extrapolation-free way and based on just three calculations (bulk LiH and the atoms Li and H). It is in very good agreement with the best estimate reported by Gillan et al.,[48] −131.95 mE_h. In order to investigate quantitatively the convergence of the energies with respect to R_c, systematic calculations of the HFX energies for the 5 × 5 × 5 unit cell, using a smaller basis set (adjusted pc-2 basis 4s2p1d/4s2p1d and 9s3p1d/9s3p1d for H and Li, respectively, 19 000 basis functions in total) have been performed. These results are presented in Table 5 and show that the cohesive energy is obtained with milli-Hartree accuracy for $R_c = 6$ Å and micro-Hartree accuracy for $R_c = 10$ Å.

Table 5. Hartree−Fock results Obtained with the Truncated Coulomb Operator for Various Values of R_c without Long-Range Correction[a]

R_c [Å]	E(HF)[au]	H[au]	Li[au]	$\varepsilon_{\mathrm{HF}}^{\mathrm{coh}}$ [au]
3	−32.231006	−0.498769	−7.405766	−0.153216
4	−32.242905	−0.499298	−7.423518	−0.137911
5	−32.246980	−0.499325	−7.429613	−0.132807
6	−32.247893	−0.499326	−7.431395	−0.131252
7	−32.248177	−0.499326	−7.431845	−0.130873
8	−32.248275	−0.499326	−7.431944	−0.130798
9	−32.248308	−0.499326	−7.431964	−0.130787
10	−32.248321	−0.499326	−7.431967	−0.130787

[a] The 5 × 5×5 repetition of the basic cubic unit cell (4.084 Å) has been employed, together with a smaller basis set. The columns show the range of the TC operator (R_c), the Hartree−Fock energy per unit cell, the H atom energy, the Li atom energy, and the cohesive energy, respectively ($\varepsilon_{\mathrm{HF}}^{\mathrm{coh}}$).

This system has also been used to measure the parallel efficiency of the implementation. Using the 3 × 3 × 3 repetition of the basic unit cell, consisting of 216 atoms and 8 100 basis functions, calculations, taking advantage of the hybrid MPI/openMP approach discussed above, have been performed. The results for this setup, summarized in Figure 4, show that this approach scales beyond 32 768 cores. The scaling is superlinear up to approximately 2 048 cores because the increasing amount of memory (2Gb/core) is used to store four center integrals, and successive SCF steps benefit from the in-core storage. The total amount of storage used for integrals exceeds 3 terabytes in this case. For the runs on more than 16 384 cores, the impact of the com-

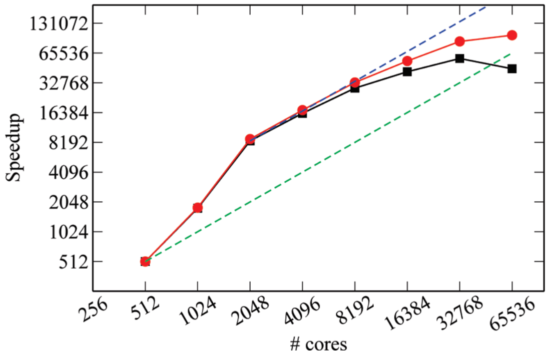

Figure 4. Shown is the speedup obtained from a computation of the 3 × 3 × 3 repetition of the basic unit cell of LiH (8 100 basis functions). Black and red curves depict the observed speedups for the full calculation and for the Hartree−Fock part, respectively. Dotted lines correspond to theoretical speedups, assuming either an infinite amount of memory per node (blue) or the actually 16 Gb/node (green). All calculations have been performed using 8 threads per MPI process on a 8 core node (CRAY XT5).

munication becomes significant and ultimately limits scalability. For this system, the load balance remains excellent and the local construction of the Fock matrix itself scales perfectly even at 65 536 cores.

3.5. The Electronic Structure of Rubredoxin. In order to demonstrate the ability of the TC method to compute large, inhomogeneous condensed phase systems with high quality basis sets, the electronic structure of a fully solvated iron−sulfur protein, rubredoxin, in periodic boundary conditions with a polarized triple-ζ valence basis set[52] for all atoms, including hydrogen, has been computed. In this setup, the system is described with 31 247 basis functions, containing 2 825 atoms, and the unit cell has edges 31.136 × 28.095 × 30.502 Å^3. Due to the iron−sulfur active site, the multiplicity of the system is 6. The same system has been employed in earlier work with semilocal functionals to demonstrate the ability to compute ab initio free energy differences[53] and total energies near the basis set limit[47] for systems containing nearly 3 000 atoms. A single-point wave function optimization takes less than two hours, with about two-thirds of the time spent in the HFX routines using 8 196 cores of a CRAY XT5. The storage needed for the integrals is approximately 2.5 terabytes, using a threshold of 10^{-8} for Schwarz screening and an in-core compression scheme described in ref 13. With this calculation, the difference in spin density distribution for the active site between a hybrid functional (B3LYP[2,4,54,55]) with the TC operator ($R_c = 6.0$ Å) and a semilocal functional (BLYP[3,4]) has been investigated. The result of the calculation is illustrated in Figure 5 where the difference in spin density between the GGA and the hybrid calculation is shown. Not unexpectedly, a more localized spin density is found with the hybrid functionals.

4. Conclusions

A new approach for Hartree−Fock calculations at the Γ-point using Gaussian basis functions has been presented. This approach is based on the TC operator and is demonstrated to be robust. With increasing truncation radius, results converge exponentially to the limiting Hartree−Fock values. Furthermore, a density functional based long-range correction to the TC operator has been derived. With this correction, a very short-range exchange ($R_c = 2.0$ Å) yields excellent results for reaction energies and for barrier heights. The finite range of the operator allows for efficient screening and can be exploited in a linear-scaling implementation of exchange. The current implementation is massively parallel and allows for calculations on systems containing thousands of atoms and ten thousands of basis functions. These developments will enable simulations based on hybrid functionals that probe the rich chemistry and the physics of large and complex condensed-phase systems.

5. Appendices

A. Long-Range Correction. In this section, analytical expressions for the long-range part of the PBE exchange hole enhancement factor are presented in closed form for any given cutoff radius R_c. Indeed, based on $J_x^{\text{PBE}}(s, y)$ as defined by eq 15 (see ref 28 for details, including definition of the quantities A−H), one finds that:

$$F_x^{\text{PBE,LRC}}(s) = -\frac{8}{9}\int_{R_c'}^{\infty} yJ_x^{\text{PBE}}(s, y)\mathrm{d}y = -\frac{8}{9}(I_1 - I_2 + I_3 + I_4) \quad (28)$$

where:

$$I_1 = -\frac{A}{2}\exp\left(\frac{9}{4}\frac{s^2H}{A}\right)\mathrm{Ei}\left(-\frac{9}{4}\frac{s^2H}{A} - s^2HR_c'^2\right) \quad (29)$$

$$I_2 = -\frac{A}{2}\mathrm{Ei}(-s^2HR_c'^2) \quad (30)$$

$$I_3 = -\frac{A}{2}\mathrm{Ei}(-(D + s^2H)R_c'^2) \quad (31)$$

$$I_4 = \alpha(\alpha_0 + \alpha_2R_c'^2 + \alpha_4R_c'^4)\exp(-R_c'^2(D + Hs^2)) \quad (32)$$

with

$$\alpha = \frac{1}{2}\frac{1}{(D + s^2H)^3} \quad (33)$$

$$\alpha_0 = 2E + DC + D^2B + s^2(HC + 2DHB + 2EG + DCF) + s^4(H^2B + HCF) \quad (34)$$

$$\alpha_2 = D^2C + 2DE + s^2(2EH + 2DEG + 2DHC + D^2CF) + s^4(2EGH + 2DHCF + CH^2) + s^6CFH^2 \quad (35)$$

$$\alpha_4 = D^2E + s^2(D^2EG + 2DHE) + s^4(2DHEG + EH^2) + s^6EGH^2 \quad (36)$$

and:

$$R_c' = R_c\mathrm{k}_F \quad (37)$$

$\mathbf{k}_F$ denoting the local Fermi vector. Ei(x) is the exponential integral and defined as

$$\mathrm{Ei}(x) = \int_{-\infty}^{x} \frac{e^t}{t}\mathrm{d}t \tag{38}$$

B. Stability Criterion. In this section, the effect of thresholding and the MIC on the stability of the SCF is analyzed. Starting from the exchange energy for a system containing N basis functions:

$$E_x^{\mathrm{HF}} = -\frac{1}{2}\sum_{\mu\nu\lambda\sigma} P^{\mu\sigma}P^{\nu\lambda}(\mu\nu|\lambda\sigma)_g \tag{39}$$

which can be rewritten in terms of matrix−vector products as the quadratic form

$$E_x^{\mathrm{HF}} = \mathbf{P}^T\mathbf{v}_{\mathrm{exact}}\mathbf{P} \tag{40}$$

where $\mathbf{v}_{\mathrm{exact}}$ is a $N^2 \times N^2$ matrix containing all four center integrals, and $\mathbf{P}$ is a vector of size N^2 with the density matrix elements. If screening is applied to the four center integrals using a given threshold ε, the above equation can be written as

$$E_x^{\mathrm{HF}} = \mathbf{P}^T\mathbf{v}_{\mathrm{screened}}\mathbf{P} + \mathbf{P}^T\mathbf{v}_{\varepsilon}\mathbf{P} \tag{41}$$

where $\mathbf{v}_{\mathrm{screened}}$ collects all integrals that pass the screening, i.e., contributions that are larger than the threshold, and $\mathbf{v}_{\varepsilon}$ is a matrix of error terms of order $\mathcal{O}(\varepsilon)$ that are ignored throughout the calculation. For a reliable and stable optimization procedure, the maximum error introduced by ignoring $\mathbf{P}^T\mathbf{v}_{\varepsilon}\mathbf{P}$ should be small.

In order to get an estimate for the maximum magnitude of the error, it is sufficient to obtain an estimate of the maximum eigenvalue of the $\mathbf{P}$ matrix because

$$\mathbf{P}^T\mathbf{v}_{\varepsilon}\mathbf{P} \le \lambda_{\max}^2(\mathbf{P})\mathcal{O}(\varepsilon) \tag{42}$$

The above formula can be derived under the assumption that the largest eigenvalue of $\mathbf{v}_{\varepsilon}$ is $\mathcal{O}(\varepsilon)$. In the worst case, this eigenvalue could be $N^2\varepsilon$ but is usually smaller ($\sim N\varepsilon$).

Since $\mathbf{C}^{\mathrm{T}}\mathbf{S}\mathbf{C} = 1$ with $\mathbf{C}$ being the matrix of the molecular orbitals, and $\mathbf{S}$ the overlap matrix of the basis functions, the following upper bound for the norm of $\mathbf{C}$ can be obtained

$$\|\mathbf{C}\| \le \frac{1}{\sqrt{\lambda_{\min}(\mathbf{S})}} \tag{43}$$

Writing the density matrix $\mathbf{P}$ in terms of molecular orbitals, $\boldsymbol{P} = \mathbf{C}\mathbf{C}^{\mathrm{T}}$, one finds that:

$$\lambda_{\max}^2(\mathbf{P}) \le \frac{1}{\lambda_{\min}^2(\mathbf{S})} \tag{44}$$

Finally, the above expression can be related to the condition number of the overlap matrix:

$$\kappa(\mathbf{S}) = \frac{\lambda_{\max}(\mathbf{S})}{\lambda_{\min}(\mathbf{S})} \approx \frac{1}{\lambda_{\min}(\mathbf{S})} \tag{45}$$

where the largest eigenvalue of $\mathbf{S}$ is assumed to be of order one. Based on these estimates, one can conclude that the SCF calculations will be stable as long as

$$\varepsilon \le \mathcal{O}\left(\frac{1}{\kappa^2(\mathbf{S})}\right) \tag{46}$$

This stability estimate is usually too conservative but it does represent a worst-case scenario. On the other hand, as long as the SCF is stable, it is usually observed that $\lambda_{\max}(\mathbf{P}) \approx \mathcal{O}(1)$, which confirms that the error due to screening is typically ε per electron.

Finally, an analysis of the instability observed with the MIC algorithm is presented. Essentially, the MIC can be interpreted as a calculation with a TC potential using $R_c = L/2$ but with two sources of error in the computed four center integrals. The first source of error is due to the fact that only one term in the sum over $\mathbf{b}$ is retained, while the second source of error is due to the fact that these integrals are computed with the $1/r$ operator. These errors add an additional term $\mathbf{v}_{\mathrm{MIC}}$ to the expression:

$$E_x^{\mathrm{HF}} = \mathbf{P}^T\mathbf{v}_{\mathrm{screening}}\mathbf{P} + \mathbf{P}^T\mathbf{v}_{\varepsilon}\mathbf{P} + \mathbf{P}^T\mathbf{v}_{\mathrm{MIC}}\mathbf{P} \tag{47}$$

which can not be controlled by the threshold ε. As before, the error related to $\mathbf{P}^T\mathbf{v}_{\mathrm{MIC}}\mathbf{P}$ might grow quickly as the condition number of the basis set becomes worse, explaining

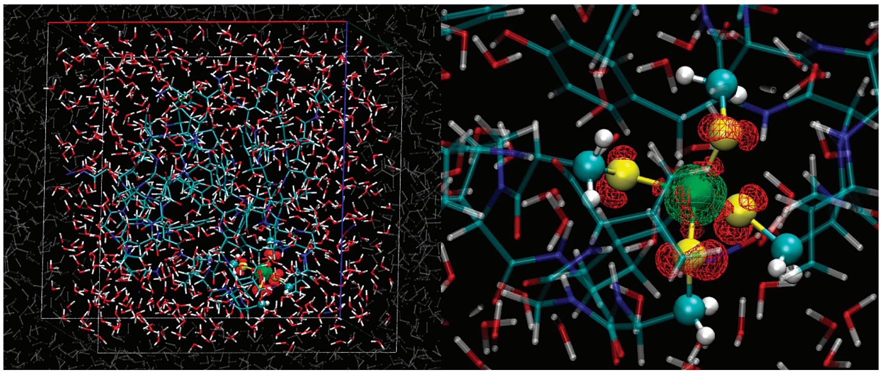

Figure 5. The left panel shows the unit cell of the solvated protein rubredoxin, while the right panel focuses on its iron−sulfur active site. The contour shows the difference in spin density distribution between calculations performed with BLYP and B3LYP with the TC operator. Red indicates an excess in spin density with the local functional, while green indicates an excess with the hybrid functional. Clearly, the use of a hybrid functional favors localization of the spin density.

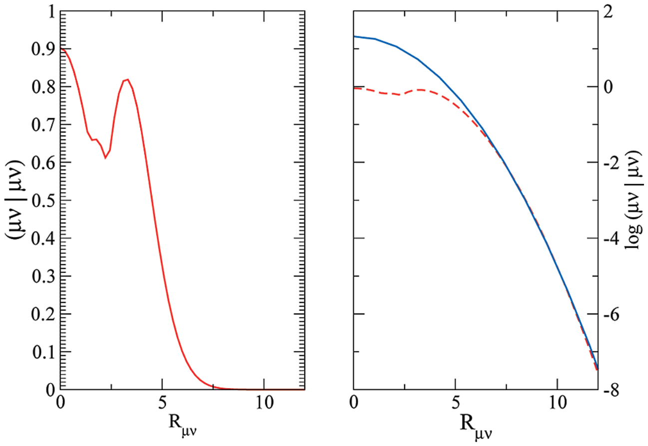

Figure 6. Shown are plots for $(\mu\nu|\mu\nu)$ as a function of the interatomic distance $R_{\mu\nu}$ for a lithium p-function and a hydrogen d-function. The left panel shows the calculated values and the right panel shows the logarithm of this data (dotted line) together with the fitting function (blue).

the stability of the algorithm with small and well-conditioned basis sets and the instability with large and flexible basis sets.

C. Efficient Near- and Far-Field Screening. Determining in advance which four center integrals are smaller than a given threshold and can, thus, be ignored in the calculation is important in an implementation of HFX that targets large systems. Indeed, screening reduces the number of integrals that need to be computed from $\mathcal{O}(N^4)$ to $\mathcal{O}(N)$. Two kinds of screening are commonly employed for the four center integrals, namely near- and far-field screening. Near-field screening[14] relies on the Schwarz-inequality and reduces the number of terms to $\mathcal{O}(N^2)$ also for calculations employing the $1/r$ operator, far-field screening only becomes really efficient[15] for operators $g(r)$ that decay faster than $1/r$ and reduces the number of required four center integrals to $\mathcal{O}(N)$. For systems with decaying density matrix (i.e., systems with an electronic gap), combining near-field screening with screening on the density matrix elements[16] also reduces the effort to $\mathcal{O}(N)$. A brute-force implementation of the screening, as implemented in CP2K,[19] is $\mathcal{O}(N^2)$. It is, therefore, important to reduce the prefactor of this term as much as possible and to have an efficient screening algorithm. An approach which is sufficiently efficient to deal with systems containing thousands of atoms without significant screening overhead is presented below.

For the near-field screening one can rely on the Cauchy–Schwarz inequality,

$$|(\mu\nu^{\mathbf{a}}|\lambda^{\mathbf{b}}\sigma^{\mathbf{b+c}})| \le |(\mu\nu^{\mathbf{a}}|(\mu\nu^{\mathbf{a}})|^{1/2} \times |(\lambda\sigma^{\mathbf{c}}|\lambda\sigma^{\mathbf{c}})|^{1/2} \qquad (48)$$

which only requires two center integrals. However, instead of storing or computing these two center integrals, it is very efficient to instead parametrize screening functions that are an upper bound to these integrals. These screening functions only depend parametrically on the interatomic distance $R_{\mu\nu}$ but are different for each type of Gaussian basis function (atom kind, shell, sets). These fits can be easily performed once one observes (see Figure 6) that the logarithm of the integral is similar to a quadratic function at larger distance:

$$\log((\mu\nu|\mu\nu)(R_{\mu\nu})) \approx a_2R_{\mu\nu}^2 + a_0 \qquad (49)$$

This choice leads to the useful properties that the estimate decays monotonically with increasing distance and that the expression only requires the square distance between the centers. The coefficients a_0 and a_2 are calculated once and for all at the beginning of a calculation, minimizing an asymmetric penalty function:

$$\sum_i k(\Delta_i)\Delta_i^2 \qquad (50)$$

over a grid of suitably chosen values $R_{\mu\nu}^i$, with $\Delta_i = \log((\mu\nu|\mu\nu)(R_{\mu\nu})) - (a_2R_{\mu\nu}^2 + a_0)$, and $k(\Delta_i) = 1$, if $\Delta_i < 0$ and $k(\Delta_i) = 1 \times 10^4$ otherwise. This choice of k guarantees that $a_2R_{\mu\nu}^2 + a_0$ will be approximately an upper bound and not merely a least-squares fit. Clearly, once the coefficients are determined, obtaining a Schwarz estimate of the integral is particularly fast.

The far-field screening is currently based on a rather crude estimate, which only flags if the integral will be smaller than a given threshold. For the TC operator this estimate can be obtained easily. It is based on the radii of the product densities of $R_{\mu\nu}^{\rho}$ for $\mu\nu^{\mathbf{a}}$ and $R_{\lambda\sigma}^{\rho}$ for $\lambda^{\mathbf{b}}\sigma^{\mathbf{b+c}}$ and cycles as soon as $R_{\mu\nu}^{\rho} + R_{\lambda\sigma}^{\rho} + R_c < |\mathbf{P} - \mathbf{Q}|$, where $\mathbf{P}$ and $\mathbf{Q}$ are the centers of the product densities. The radii $R_{\mu\nu}^{\rho}$ and $R_{\lambda\sigma}^{\rho}$ are similarly obtained from a two-parameter fit to precomputed values.

Acknowledgment. J.V. acknowledges interesting discussions with J. Spencer and A. Alavi. The authors acknowledge E. Valeev for making LIBINT available under the Gnu public license. A fruitful collaboration with John Levesque (Cray Inc.) is also acknowledged. His extensive testing on the Cray XT5 (Jaguar) at the Oak Ridge National Laboratory (ORNL) enabled the massively parallel implementation of the Hartree–Fock code in CP2K. Additional computer resources have been provided by the Swiss National Supercomputing Center (CSCS) and, as part of the PRACE project, by the Finnish IT Center for Science (CSC). The PRACE project receives funding from the EU's Seventh Framework Programme (FP7/2007-2013) under grant agreement no. RI-211528.

References

(1) Dirac, P. A. M. *Math. Proc. Cambridge Philos. Soc.* **1930**, *26*, 376–385.

(2) Vosko, S. H.; Wilk, L.; Nusair, M. *Can. J. Phys.* **1980**, *58*, 1200–1211.

(3) Becke, A. D. *Phys. Rev. A: At., Mol., Opt. Phys.* **1988**, *38*, 3098.

(4) Lee, C. T.; Yang, W. T.; Parr, R. G. *Phys. Rev. B: Condens. Matter* **1988**, *37*, 785–789.

(5) Perdew, J. P.; Burke, K.; Ernzerhof, M. *Phys. Rev. Lett.* **1996**, *77*, 3865–3868.

(6) Tao, J. M.; Perdew, J. P.; Staroverov, V. N.; Scuseria, G. E. *Phys. Rev. Lett.* **2003**, *91*, 146401.

(7) Heyd, J.; Scuseria, G. E.; Ernzerhof, M. *J. Chem. Phys.* **2003**, *118*, 8207–8215.

(8) Heyd, J.; Scuseria, G. E.; Ernzerhof, M. *J. Chem. Phys.* **2006**, *124*, 219906 Erratum.

(9) Zhao, Y.; Truhlar, D. G. *Theor. Chem. Acc.* **2008**, *120*, 215.

(10) Zhao, Y.; Truhlar, D. G. *J. Chem. Phys.* **2006**, *125*, 194101.

(11) Zhao, Y.; Truhlar, D. G. *J. Phys. Chem. A* **2006**, *110*, 13126.

(12) Zhao, Y.; Truhlar, D. G. *Acc. Chem. Res.* **2008**, *41*, 157.

(13) Guidon, M.; Schiffmann, F.; Hutter, J.; VandeVondele, J. *J. Chem. Phys.* **2008**, *128*, 214104.

(14) Strout, D. L.; Scuseria, G. E. *J. Chem. Phys.* **1995**, *102*, 8448–8452.

(15) Izmaylov, A. F.; Scuseria, G. E.; Frisch, M. J. *J. Chem. Phys.* **2006**, *125*, 104103.

(16) Ochsenfeld, C.; White, C. A.; Head-Gordon, M. *J. Chem. Phys.* **1998**, *109*, 1663–1669.

(17) Tymczak, C. J.; Weber, V. T.; Schwegler, E.; Challacombe, M. *J. Chem. Phys.* **2005**, *122*, 124105.

(18) Spencer, J.; Alavi, A. *Phys. Rev. B: Condens. Matter* **2008**, *77*, 193110.

(19) *CP2K*, the CP2K developers group, is freely available from http://cp2k.berlios.de/ (2009).

(20) VandeVondele, J.; Krack, M.; Mohamed, F.; Parrinello, M.; Chassaing, T.; Hutter, J. *Comput. Phys. Commun.* **2005**, *167*, 103.

(21) Cohen, A. J.; Mori-Sánchez, P.; Yang, W. *J. Chem. Phys.* **2007**, *126*, 191109.

(22) Ten-no, S. *J. Chem. Phys.* **2007**, *126*, 014108.

(23) Gygi, F.; Baldereschi, A. *Phys. Rev. B: Condens. Matter* **1986**, *34*, 4405.

(24) Pisani, C.; Dovesi, R. *Int. J. Quantum Chem.* **1980**, *17*, 501–516.

(25) Wenzien, B.; Cappellini, G.; Bechstedt, F. *Phys. Rev. B: Condens. Matter* **1995**, *51*, 14701.

(26) Sorouri, A.; Foulkes, W. M. C.; Hine, N. D. M. *J. Chem. Phys.* **2006**, *124*, 064105.

(27) Carrier, P.; Rohra, S.; Görling, A. *Phys. Rev. B: Condens. Matter* **2007**, *75*, 205126.

(28) Ernzerhof, M.; Perdew, J. P. *J. Chem. Phys.* **1998**, *109*, 3313–3320.

(29) Perdew, J. P.; Ernzerhof, M.; Burke, K. *J. Chem. Phys.* **1996**, *105*, 9982–9985.

(30) Perdew, J. P.; Ernzerhof, M.; Burke, K. *Int. J. Quantum Chem.* **1997**, *64*, 285–295.

(31) Ernzerhof, M.; Scuseria, G. E. *J. Chem. Phys.* **1999**, *110*, 5029–5036.

(32) Obara, S.; Saika, A. *J. Chem. Phys.* **1986**, *84*, 3963–3974.

(33) Helgaker, T.; Jørgensen, P.; Olsen, J. *Molecular Electronic Structure Theory*; John Wiley & Sons: Chichester, U.K., 2000.

(34) Ahlrichs, R. *Phys. Chem. Chem. Phys.* **2006**, *8*, 3072–3077.

(35) Fousse, L.; Hanrot, G.; Lefèvre, V.; Pélissier, P.; Zimmermann, P. *ACM Trans. Math. Softw.* **2007**, *33*, 13.

(36) *The MPFR Library*, http://www.mpfr.org (2009). For additional reference information see ref 35.

(37) Marchi, M. C. S.; Vianello, M. *ACM Trans. Math. Softw.* **2008**, *35*, 1–11.

(38) *Fun2D*, the CP2K developers group, is freely available from http://cvs.berlios.de/cgi-bin/viewvc.cgi/cp2k/cp2k/tools/Fun2D/ (2009).

(39) Jensen, F. *J. Chem. Phys.* **2001**, *115*, 9113.

(40) Jensen, F. *J. Chem. Phys.* **2002**, *116*, 7372.

(41) Jensen, F. *J. Phys. Chem. A* **2007**, *111*, 11198–11204.

(42) Lynch, B. J.; Truhlar, D. G. *J. Phys. Chem. A* **2001**, *105*, 29362936.

(43) Krack, M.; Parrinello, M. *Phys. Chem. Chem. Phys.* **2000**, *2*, 2105–2112.

(44) Lynch, B. J.; Zhao, Y.; Truhlar, D. G. *J. Phys. Chem. A* **2003**, *107*, 1384.

(45) Lippert, G.; Hutter, J.; Parrinello, M. *Theor. Chem. Acc.* **1999**, *103*, 124.

(46) Krack, M. *Theor. Chem. Acc.* **2005**, *114*, 145–152.

(47) VandeVondele, J.; Hutter, J. *J. Chem. Phys.* **2007**, *127*, 114105.

(48) Gillan, M. J.; Alfe, D.; Gironcoli, S.; Manby, F. R. *J. Comput. Chem.* **2008**, *29*, 2098.

(49) Manby, F. R.; Alfe, D.; Gillan, M. J. *Phys. Chem. Chem. Phys.* **2006**, *8*, 5178.

(50) Marsman, M.; Grüneis, A.; Paier, J.; Kresse, G. *J. Chem. Phys.* **2009**, *130*, 184103.

(51) Paier, J.; Diaconu, C. V.; Scuseria, G. E.; Guidon, M.; VandeVondele, J.; Hutter, J. submitted.

(52) Schäfer, A.; Huber, C.; Ahlrichs, R. *J. Chem. Phys.* **1994**, *100*, 5829.

(53) Sulpizi, M.; Raugei, S.; VandeVondele, J.; Carloni, P.; Sprik, M. *J. Phys. Chem. B* **2007**, *111*, 3669.

(54) Becke, A. D. *J. Chem. Phys.* **1993**, *98*, 5648.

(55) Stephens, P. J.; Devlin, F. J.; Chabalowski, C. F.; Frisch, M. J. *J. Phys. Chem.* **1994**, *98*, 11623–11627.

(56) Valeev, E., Fermann, J. T. http://www.chem.vt.edu/chem-dept/valeev/software/libint/libint.html, 2009.

(57) Nolan, S. J.; Gillan, M. J.; Alfè, D.; Allan, N. L.; Manby, F. R. *Phys. Rev. B* **2009**, *80*, 165109.

CT900494G

JCTC Journal of Chemical Theory and Computation

Polarizable Intermolecular Potentials for Water and Benzene Interacting with Halide and Metal Ions

Fabien Archambault,[†] Christophe Chipot,*[,†,‡,§] Ignacio Soteras,[¶] F. Javier Luque,[¶]
Klaus Schulten,[‡] and François Dehez*[,†]

Équipe de Dynamique des Assemblages Membranaires, UMR 7565, Nancy Université, BP 239, 54506 Vandoeuvre-lès-nancy Cedex, France, Theoretical and Computational Biophysics Group, Beckman Institute, University of Illinois at Urbana−Champaign, Urbana, Illinois 61801, and Departament de Fisicoquímica and Institut de Biomedicina (IBUB), Facultat de Farmàcia, Universitat de Barcelona, Avgda. Diagonal 643, Barcelona 08028, Spain

Received August 10, 2009

Abstract: A complete derivation of polarizable intermolecular potentials based on high-level, gas-phase quantum-mechanical calculations is proposed. The importance of appreciable accuracy together with inherent simplicity represents a significant endeavor when enhancement of existing force fields for biological systems is sought. Toward this end, symmetry-adapted perturbation theory can provide an expansion of the total interaction energy into physically meaningful, for example, electrostatic, induction and van der Waals terms. Each contribution can be readily compared with its counterpart in classical force fields. Since the complexity of the different intermolecular terms cannot be fully embraced using a minimalist description, it is necessary to resort to polyvalent expressions capable of encapsulating overlooked contributions from the quantum-mechanical expansion. This choice results in consistent force field components that reflect the underlying physical principles of the phenomena. This simplified potential energy function is detailed, and definitive guidelines are drawn. As a proof of concept, the methodology is illustrated through a series of test cases that include the interaction of water and benzene with halide and metal ions. In each case considered, the total energy is reproduced accurately over a range of biologically relevant distances.

1. Introduction

The development of increasingly scalable software and greater access to massively parallel computer architectures allow longer numerical simulations to be performed on continuously more complex molecular assemblies. This, in turn, has brought the investigation of biologically relevant systems over realistic time scales within reach, for example, atomistic simulations of a membrane for hundred of microseconds[1] or folding of small proteins.[2] In the latter examples, the use of a pairwise additive force field, for example, Amber,[3] Charmm,[4] Gromos,[5] or Opls-AA,[6] provides in general a reasonable reproduction of experimental data as long as polarization effects are not dominant.

When, on the contrary, induction effects can no longer be neglected, or vary significantly in the course of the simulation, nonpolarizable potential energy functions rapidly attain the inherent limits of their validity. Two recent studies[7,8] endeavored to describe the folding of a small protein, the human Pin1 WW domain, by means of the Charmm macromolecular force field. Whereas this potential energy function was able to preserve the β-sheet-like native structure over the 200 ns time scale, it failed to fold within 10 μs the

---

* Corresponding author e-mail: chipot@ks.uiuc.edu (C.C.); Francois.Dehez@edam.uhp-nancy.fr (F.D.).

[†] Nancy Université.

[‡] University of Illinois at Urbana−Champaign.

[¶] Universitat de Barcelona.

[§] On leave from Équipe de Dynamique des Assemblages Membranaires, UMR 7565, Nancy Université, BP 239, 54506 Vandoeuvre-lès-nancy Cedex, France.

10.1021/ct9004189 CCC: $40.75

protein chain from an extended motif into the native conformation. It was demonstrated that this failure is due to force-field accuracy rather than insufficient sampling—whether or not neglect of polarization phenomena is responsible for protein misfolding remains at this stage a matter of debate, which would require additional investigation to find a definitive answer. Metalloproteins constitute another class of biologically relevant systems where induction effects need to be accounted for. In this case, a metal ion polarizes the environment, which, in turn, alters the binding hierarchy[9] of neighboring chelating agents. In particular,[10,11] when using a standard nonpolarizable potential energy function, the stability of the active site is perturbed on account of the exaggerated interaction of the ion with water, compared to that with either the vicinal carbonyl or carboxylate groups. Ion channels also represent important biological systems, in which small ions permeate through narrow pores, strongly polarizing the walls of the latter[12] and modulate as a result the ionic selectivity.[13] The formation of crystals can also be governed by polarization effects.[14−17] When decomposing the total interaction energy into electrostatic, induction, and van der Waals contributions, the importance of the induction energy suggests that it may play a predominant role in the stability of the crystal and, hence, should not be ignored.

The need for taking into account polarization phenomena explicitly in molecular-dynamics simulations constitutes an ongoing effort that can be traced back to the 1980s.[18] One of the grand challenges for polarizable force fields is the derivation of functions that are suitable for biological simulations. Toward this end, a number of routes have been explored to include polarization effects explicitly. A first route is based on Drude oscillators,[19] which describe electronic induction by the movement of a fictitious mass bonded to polarizable atoms by means of a stiff spring. Another approach, referred to as fluctuating charges,[20−23] consists of changing the charge of the atoms along the simulation. These charges are adjusted according to the principle of partial equalization of orbital electronegativities.[24] A third path, namely, multipole expansions,[21,25−30] uses distributed polarizabilities to model induction energies following a self-consistent procedure to determine the induced dipoles. These methods have been probed in a variety of applications ranging from liquid simulations[31−34] to simulations of DNA.[35] They have been combined with molecular-dynamics simulations of increasing complexity, such as that of polarizable membranes—see for instance ref 36. In the latter reference, Drude oscillators model induction effects and allow a better agreement to be reached between simulation and experiment for the reproduction of the dipole potential that arises at the water−lipid interface.

The main thrust of the present work is to build a polarizable force field that reconciles simplicity and accuracy. The chosen approach relies on the central idea[37] of partitioning the interaction energy into physically meaningful contributions and to determine the associated parameters using quantum-mechanical (QM) methods. A logical roadmap is followed for the construction of a consistent potential energy function.[9,38−43] This consistency imposes a de novo derivation of gas-phase atomic charges. The induction contribution is then derived from ab initio calculations and modified by ad hoc damping functions. Last, van der Waals parameters are determined using an appropriate mathematical expression that guarantees the faithful description of the overall intermolecular interactions at play. Despite the precision of such a description, a number of key elements are still missing for a faithful reproduction of nonbonded interaction energies between molecules over a wide range of distances. In the reproduction of the total quantum-mechanical interaction energy, the rudimentary description needed for large-scale simulations of biological systems is bound to failure if high accuracy is sought, as several terms, like nonmultipolar contributions, are not described explicitly. Choices have, therefore, to be made to obtain a model of sufficient accuracy, while remaining concise. Appropriate functions ought to be determined to include implicitly the missing contributions. In this study, a complete set of definitive guidelines is proposed to derive compact polarizable intermolecular potentials. The approach is illustrated through a series of test cases that include the interaction of water and benzene with halide and metal ions.

2. Theoretical Underpinnings

The QM calculations reported here rely on symmetry-adapted perturbation theory[44,45] (SAPT), which provides a formal, rigorous framework for the expansion of the total interaction energy into meaningful contributions utilized as a reference. In particular, use is made in this work of the SAPT2 expansion, henceforth called SAPT for simplicity, which accounts for correlation effects at the second-order Møller−Plesset[46] (MP2) level of theory. Within SAPT, the interaction energy is decomposed into the individual contributions shown in eq 1. In the latter expression, the first four terms stand for the electrostatic (U_{ele}), induction (U_{ind}), exchange (U_{exc}), and dispersion (U_{dis}) components. In addition, the SAPT expansion embraces two terms corresponding to the coupling between exchange and induction ($U_{\text{exc-ind}}$) and between exchange and dispersion ($U_{\text{exc-dis}}$). Finally, the last term (δHF) accounts for a collection of higher-order induction and exchange−induction terms. Altogether, the contributions are written

$$\Delta \mathscr{U}_{\text{tot}}^{\text{SAPT}} = U_{\text{ele}} + U_{\text{ind}} + U_{\text{exc}} + U_{\text{dis}} + U_{\text{exc-ind}} + U_{\text{exc-dis}} + \delta\text{HF} \quad (1)$$

The stated energy components cannot, when taken separately, be studied in a straightforward fashion with a classical decomposition.[47] For a comparison on a one-to-one basis, certain individual contributions need to be summed, as has been done previously by several authors.[9,48−51] It is then possible to cast the description into three potential energy functions, namely, for electrostatic, induction, and van der Waals contributions.

The electrostatic component ($\Delta \mathscr{U}_{\text{ele}}^{\text{SAPT}}$) corresponds to the first-order contribution to the electrostatic energy. The pure induction term given by SAPT ought to be added to the exchange−induction term, as well as to higher-order induction and exchange−induction terms to encompass the full induction potential ($\Delta \mathscr{U}_{\text{ind}}^{\text{SAPT}}$). The last contribution, referred to as the van der Waals potential ($\Delta\mathcal{U}_{\text{vdW}}^{\text{SAPT}}$), consists of the sum of exchange and dispersion terms.

As was put forth previously, a molecular-mechanical expansion can mimic the above-summed QM energies. This includes an electrostatic potential that relies upon atomic charges, an induction term associated with an appropriate damping function, and an ad hoc van der Waals function.[9]

The first order contribution, of electrostatic nature, is modeled by a set of atom-centered point charges and is a rudimentary approach to describe the molecular electrostatic potential. While this description is simple, it has proven[52] to reproduce under most circumstances the target quantity with an appreciable accuracy. Determination of atomic charges is achieved[53] by means of regular grids surrounding the molecule of interest, over which the QM electrostatic potential is mapped. Penetration effects, which represent an important, short-range component of the electrostatic interaction, are evidently absent from the classical, Coulomb potential.[54] The incompleteness of the model is rooted in the computation of the molecular electrostatic potential outside the sphere of convergence.[55] To a large extent, these effects stem from the overlap of electron densities of interacting compounds, which cannot be accounted for by a localized atomic description of the electrostatic potential.[56] Ad hoc functions[57−60] have been shown to mimic the respective short-range interactions. Here, use will only be made of an ansatz inferred from the formulation of Freitag et al. by Cisneros et al.[60] It holds the advantage of being derived explicitly for atomic charges, and compared to other functions, it offers a simpler expression and parametrization. Charges are, therefore, modified as stated in eq 3 in ref 60.

As detailed above, different routes can be chosen for the description of induction phenomena in the classical simulations of biological systems. Here, polarization is modeled by means of distributed polarizabilities[61,62] over subsets of atoms. Previous articles[9,43,63] have demonstrated that the use of charge-flow polarizabilities between chemically bonded atoms supplemented by isotropic dipole polarizabilities on heavy atoms is able to recover the anisotropy of the molecular polarizability with both simplicity and effectiveness. Polarizabilities were determined by means of a fitting procedure[41] that relies on three-dimensional maps of the induction energy evaluated quantum-mechanically. As was asserted previously,[9,43,63] the classical expansion of polarization ought to be damped in order to reproduce the destabilizing effect of exchange-induction effects occurring at short intermolecular distances. In the present work, the Jensen et al.[64] and the Tang and Toennies[65,66] (TT) functions have been chosen. In the former expression, the distances in the interaction tensor are modified by a scalar parameter, *a*, that appears in eq 16 in ref 64. In the latter expression, truncation of the series is done at the sixth order, as suggested by Millot and Stone,[67] and subsequently rewritten at the third order, as proposed by Meredith and Stone.[68] The final expressions for the induction energy utilized herein are

$$\Delta\mathcal{U}_{\text{ind}}^{\text{MM/TT}} = \frac{1}{2}\sum_{A}\sum_{B\neq A}\Delta Q_t^a T_{tu}^{ab} f_3(\beta;r_{ab}) Q_u^b \tag{2}$$

$$\Delta Q_t^a = -\sum_{B\neq A}\alpha_{tt'}^{aa'} T_{t'u}^{a'b} f_3(\beta;r_{a'b})(Q_u^b + \Delta Q_u^b) \tag{3}$$

$$f_3(\beta;r_{ab}) = 1 - \exp(-\beta r_{ab})\sum_{k=0}^{3}\frac{(\beta r_{ab})^k}{k!} \tag{4}$$

where Q_t^a and ΔQ_t^a are, respectively, the permanent moment and the induced moment of rank t located at site a of molecule A, T_{tu}^{ab} is the element of the electrostatic tensor for the interaction of the multipole moments of ranks t and u, found, respectively, at sites a and b, and $f_3(\beta;\, r_{ab})$ is the truncated Tang and Toennies damping function, in which β is a scalar parameter. The term $\alpha_{tt'}^{aa'}$ is the atomic polarizability, which describes the change in the multipole moment of rank t at site a resulting from the t'th derivative of the potential created by all other moments at site a'. The above expressions are also detailed in eqs 21 and 22 in ref 50.

The last term of the classical intermolecular potential is the van der Waals contribution, which is modeled in the present work by three alternate formulations depending on the r distance. The first one is the standard 6−12 Lennard-Jones (LJ) expression,[69] namely, $\Delta\mathcal{U}_{\text{vdW}}^{\text{MM/LJ}} = \varepsilon\,[(\sigma/r)^{12} - (\sigma/r)^6]$, where the parameters ε and σ correspond respectively to the depth of the potential well and the distance at which the interparticle potential is zero. The second one, used among others in the Amoeba[70] force field, is the Halgren[71] potential, namely, $\Delta\mathcal{U}_{\text{vdW}}^{\text{MM/Halgren}} = \varepsilon\,[1.07R^*/(r + 0.07R^*)]^7 \times [1.12R^{*7}/(r^7 + 0.12R^{*7}) - 2]$, where R^* is the minimum-energy distance. The third one is the exp-6 Buckingham function,[72] namely, $\Delta\mathcal{U}_{\text{vdW}}^{\text{MM/Buckingham}} = \varepsilon\exp(-A_1 r) - (A_2/r)^6$, where A_1 and A_2 are shape parameters.

3. Computational Details

All molecular geometries were optimized using the Gaussian03 suite of programs[73] at the MP2(Full)/6-311++G(2d,2p) level of approximation. Electronic properties were computed at the MP2(Full)/Sadlej level of approximation, considering that the Sadlej[74−77] basis set provides a very good compromise between the number of Gaussian contractions and accuracy.[78] All individual contributions to the interaction energy were determined with the SAPT2008 program of Jeziorski et al.,[44] interfaced to the ATMOL integral and self-consistent-field package.[79] The QM contributions to the total interaction energy serve as a basis of comparison for the parametrization of the classical model.

The atomic charges of water and benzene were derived employing the Opep package,[42] using 2375 and 8070 grid points, respectively. As shown in Table 1, the molecular electrostatic potential of an isolated water molecule is reproduced with a mean error of about 48% when use is made of atom-centered charges only. As water is one of the most important components in computer simulations of condensed phases, in particular, in biological systems, an appreciable error in the description of its electrostatic potential is not acceptable. An improvement of the rudimentary three-point (3-p) charge model is, therefore, proposed. The simplest way to improve the reproduction of the potential consists in adding a fictitious site along the bisector of the molecule, in the spirit of the TIP4P[80,81] model.

Table 1. Models of Net Atomic Charges and Regenerated Multipole Moments for Water and Benzene at the MP2(Full)/Sadlej//MP2(Full)/6-311++G(2d,2p) Level of Approximation[a]

	point charges		molecular multipoles	regenerated	MP2(Full)/Sadlej
water (3-p)	Q_{00}^{O}	−0.672	Q_{10}	−0.749	−0.732
	Q_{00}^{H}	−0.336	Q_{20}	−0.189	−0.231
	rmsd	0.990			
	$\Delta\varepsilon$	48.573			
water (4-p)	Q_{00}^{X}	−1.237	Q_{10}	−0.730	−0.732
	Q_{00}^{O}	0.000	Q_{20}	−0.200	−0.231
	Q_{00}^{H}	−0.6185			
	rmsd	0.231			
	$\Delta\varepsilon$	6.258			
benzene (12-p)	Q_{00}^{C}	−0.124	Q_{20}	−5.553	−5.655
	Q_{00}^{H}	0.124	Q_{40}	120.200	163.700
	rmsd	0.219			
	$\Delta\varepsilon$	20.849			

[a] All multipoles are expressed in atomic units. The root-mean-square deviation (rmsd) between the electrostatic potentials determined quantum-mechanically and regenerated from the point charge models is expressed in 10^{-3} au. The corresponding mean error, $\Delta\varepsilon$, is given in percent.

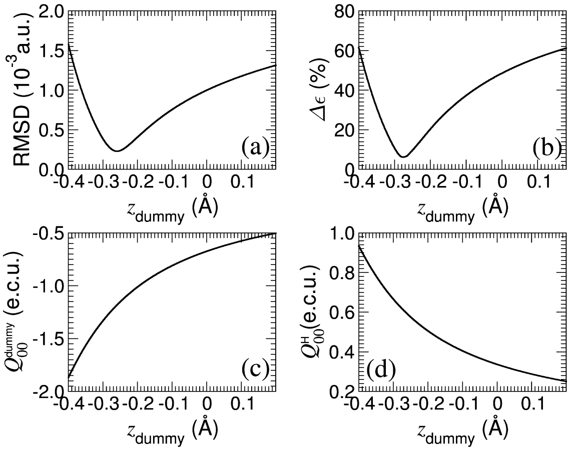

Figure 1. (a) Root-mean-square deviation (RMSD) between the electrostatic potentials determined quantum-mechanically and the point charge model expressed as a function of the position of the dummy atom for water along the C_2 axis. (b) Corresponding mean error ($\Delta\varepsilon$) expressed as a function of the position of the dummy atom for water along the C_2 axis. (c) Value of the atomic charge of the dummy atom expressed as a function of the position of the dummy atom for water along the C_2 axis. (d) Value of the atomic charge of the hydrogen atom expressed as a function of the position of the dummy atom for water along the C_2 axis.

Table 2. Models of Distributed Polarizabilities and Regenerated Molecular Polarizabilities of Water and Benzene at the MP2(Full)/Sadlej//MP2(Full)/6-311++G(2d,2p) Level of Approximation[a]

	distributed polarizabilities		molecular polarizabilities	regenerated	MP2(Full)/Sadlej
water	$\alpha_{00,00}^{OH}$	−0.808	$\alpha_{10,\,10}$	10.177	9.747
	$\alpha_{1\kappa,1\kappa}^{OO}$	8.1808	$\alpha_{11c,\,11c}$	11.483	10.058
			$\alpha_{11s,\,11s}$	8.180	9.539
	rmsd	0.127			
	$\Delta\varepsilon$	7.000			
benzene	$\alpha_{00,00}^{CC}$	−1.822	$\alpha_{10,\,10}$	47.537	45.121
	$\alpha_{00,00}^{CH}$	−0.280	$\alpha_{11c,\,11c}$	89.089	81.333
	$\alpha_{1\kappa,1\kappa}^{CC}$	7.953	$\alpha_{11s,\,11s}$	89.089	81.333
	rmsd	0.025			
	$\Delta\varepsilon$	2.737			

[a] All polarizabilities are given in atomic units. The root-mean-square deviation (rmsd) between the induction energies determined quantum-mechanically and regenerated from the models of distributed polarizabilities is expressed in 10^{-3} au. The corresponding mean error, $\Delta\varepsilon$, is given in percent.

Table 3. Dipole Polarizability of Ions Computed at the MP2(Full)/Sadlej Level of Approximation

	K^+	F^-	Cl^-	Br^-	I^-
$\alpha_{1\kappa,\,1\kappa}$ (a.u.)	5.174	10.513	30.316	39.074	60.333
$\alpha_{1\kappa,\,1\kappa}^{\text{exp}}$ (a.u.)[a]	5.736	9.313	26.588	35.226	52.704
$\alpha_{1\kappa,\,1\kappa}^{\text{exp}}$ (a.u.)[b]	5.473	10.527	29.760	39.410	60.128

[a] Ref 83. [b] Ref 84.

As can be seen in Figure 1, a minimum in the root-mean-square deviation between the QM and the point-charge derived potentials can be found when moving the fictitious site. At this minimum, the additional charge is located 0.276 Å below the oxygen atom (see “Water (4-p)” in Table 1). The resulting enhanced agreement with the target electrostatic potential can be largely explained by the position of the supplementary charge, closer to the center of the molecule. This result is consistent with the nearly isotropic molecular electrostatic potential of water.[54] In the case of benzene, as was shown in a recent article,[82] the use of atom-centered charges is sufficient to model the electrostatic potential with an acceptable accuracy. As can be seen in Table 1, a comparable agreement between the QM potential and that regenerated from point charges is also found here.

Penetration of electron clouds results in a short-range contribution, which, for completeness and for attaining the desired accuracy in the reproduction of the intermolecular interaction energy, ought to be included in the electrostatic model. Toward this end, a novel parametrization of the function of Cisneros et al. was probed, wherein the term Ω_{ij} of eq 4 in ref 60 had been modified. Though conceptually simple, the expression proposed to account for penetration effects lacks generality to be of routine practical use for the modeling of large biomolecular assemblies. For this reason, no analytical correction of penetration effects will be introduced explicitly in the intermolecular potential but will instead be incorporated in the van der Waals potential.

The induction energy was mapped employing the Opep package,[42] with grids of 3905 and 3192 points for water and benzene, respectively (see refs 9 and 43 for details). The models of distributed polarizabilities utilized herein rely on a multipole expansion of the molecular polarizability reduced to a combination of zeroth-order charge flow ($\alpha_{00,\,00}$) and first-order isotropic dipole ($\alpha_{1\kappa,\,1\kappa}$) polarizabilities. For clarity, it should be noted that charge-flow polarizabilities are not equivalent to the popular fluctuating charges,[20−23] which are based on a partial equalization of orbital electronegativities and, hence, are very different in spirit. The complete set of parameters fitted simultaneously to quantum-mechanically determined induction energy maps[53] has been shown to reproduce with appreciable accuracy the average molecular polarizability alongside its intrinsic anisotropy. The distributed polarizabilities are reported in Table 2 for water and benzene and in Table 3 for all the ions considered as polarizable in this work.

Damping parameters are determined with the objective to reproduce the induction energy supplied by SAPT. The first damping function considered is that of Jensen et al., the parameters of which can be found for a number of atom types. For the Tang and Toennies damping function, parameters are given for pair interactions. In some cases, no damping is necessary, due to the importance of the nonmultipolar contribution to the induction energy, as has been documented by Torheyden and Jansen.[49] This contribution to the induction cannot be extracted from the SAPT expansion and, hence, cannot be modeled explicitly in the model proposed here. This missing information can still be added in an appropriately chosen form of the van der Waals potential, compatible with the exponential, repulsive nature of nonmultipolar contributions.

The last contribution to the total energy is the van der Waals potential, which, in the SAPT expansion, is considered as being the sum of exchange and dispersion terms. As outlined previously, both the electrostatic and the induction models adopted here lack a number of contributions that cannot be accounted for to satisfy the stringent criteria of simplicity and tractability. Since the overall model is not sufficiently precise at short distances and when dealing with appreciable nonmultipolar effects, determination of the van der Waals parameters was not carried out on the basis of the exact contribution supplied by the SAPT expansion but using a slightly modified term, which is the total energy ($\Delta\mathscr{U}_{\text{tot}}^{\text{SAPT}}$) minus the electrostatics and induction components of the molecular-mechanical potential. This statement implies that the optimized van der Waals parameters inherently depend on the electrostatic and induction models that have been used here. In other words, modification of either the electrostatic or the polarization term necessarily imposes a requirement that the van der Waals potential be adjusted. Derivation of these parameters was achieved employing a Levenberg-Marquart algorithm.[85] The range of chemically and biologically relevant distances spans from a minimum separation, where the energy is roughly equal to $\Delta\mathscr{U}_{\text{tot, min}}^{\text{SAPT}} - 10$ kcal/mol, to a quasi-infinite one. The van der Waals contribution was determined on the basis of three alternate functions, that is, Lennard-Jones,[69] Halgren[71] and Buckingham.[72] The exponential nature of the repulsive van der Waals contribution makes the Buckingham exp-6 potential a well-suited candidate to model the van der Waals contribution and short-range interactions, such as nonmultipolar terms.

4. Results and Discussion

4.1. Interaction of Water with Metal Cations. Classical models derived to describe the interaction of cations and anions with water molecules are to a large extent suboptimal. This can be ascribed to three main reasons, recently highlighted in a study covering the interaction of water with a divalent calcium cation.[9] First, a significant error arises on account of the rudimentary representation of the molecular electrostatic potential for water by means of a three-point (3-p) charge model, which misreproduces the target quantity by up to 50%. Second, the description of the exchange-induction term of the SAPT expansion using the damping function devised by Jensen et al., while constituting a judicious choice, appears to suffer from a number of shortcomings. Last, the most questionable aspect of the proposed polarizable model lies in the use of the 6-12 LJ potential, traditionally utilized in macromolecular force fields. As was shown, however, this potential systematically fails to reproduce in a consistent fashion the exchange and dispersion contributions to the intermolecular energy computed within the SAPT framework. This shortcoming has prompted several authors to turn to more appropriate functions.[6,27,86−88] To address the above issues, the interaction of a series of metal ions with water has been investigated (see Figure 2). For conciseness, only the water−sodium

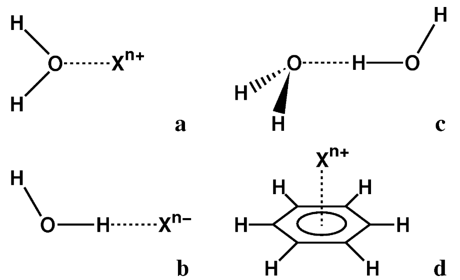

Figure 2. (a) Interaction of a water molecule with a cation along the C_2 axis. (b) Interaction of a water molecule with an anion along the O−H bond. (c) Interaction of a water molecule with another water molecule defining a hydrogen bond. (d) Interaction of the benzene molecule with a cation along the C_6 axis.

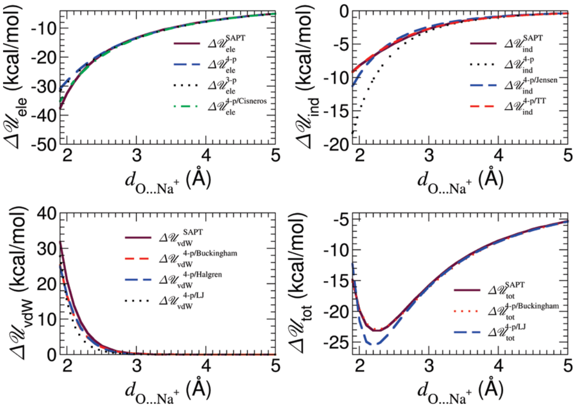

Figure 3. Interaction of a monovalent sodium ion with water. The reference (SAPT) curve is shown as a solid line. Three models for the electrostatic contribution are represented through either no penetration with a three-point (3-p) charge model (dotted line), a four-point (4-p) charge model (long-dashed line), or the function derived by Cisneros et al. (dot-dashed line). Three models for the induction contribution are represented using either no damping (dotted line), the damping function derived by Jensen et al. (long-dashed line), or the damping function derived by Tang and Toennies (TT, short-dashed line). Three models for the van der Waals contribution are fitted to $\Delta\mathscr{U}_{\text{tot}}^{\text{SAPT}} - \Delta\mathscr{U}_{\text{ele}}^{\text{4-p}} - \Delta\mathscr{U}_{\text{ind}}^{\text{4-p/TT}}$ using either a Buckingham (short-dashed line), a Halgren (long dashed line), or a Lennard-Jones (LJ, dotted line) potential. The total energy is computed as the sum of $\Delta\mathscr{U}_{\text{ele}}^{\text{4-p}}$ plus $\Delta\mathscr{U}_{\text{ind}}^{\text{4-p/TT}}$ plus either $\Delta\mathscr{U}_{\text{vdW}}^{\text{4-p/LJ}}$ (short-dashed line) or $\Delta\mathscr{U}_{\text{vdW}}^{\text{4-p/Buckingham}}$ (dotted line).

Table 4. Values of the Jensen et al. Damping Parameter (*a*) for Each Atom Type

	Li^+	Na^+	K^+	Mg^{2+}	Ca^{2+}	$O(H_2O)$	$X(H_2O)$	$H(H_2O)$
a	0.095	0.085	0.190	0.200	0.105	4.103	4.103	0.358

Table 5. Values of the Damping Parameter (β) in the Tang and Toennies Damping Function[a]

β	Li^+	Na^+	K^+	Mg^{2+}	Ca^{2+}	F^-
H_2O	2.38	2.00	2.15	2.10	2.10	4.50
benzene	2.10	1.70	1.75	1.85	1.85	

[a] Each value corresponds to a pair of interactions.

interaction will be detailed here (see Figure 3); results for all of the systems are provided in the Supporting Information.

As can be observed in Figure 3, the electrostatic contribution is equally well reproduced using a 4-p or the 3-p charge model. This result is not surprising given that the cation approaches water along the C_2 axis of the latter. Error in the reproduction of the molecular electrostatic potential in the direction of the bisector, on the order of 5% at the equilibrium intermolecular distance, is equivalent for the two models. This, unfortunately, is no longer true when the molecular electrostatic potential is measured quantum-mechanically along the O−H bond. In this event, the error reaches 15% for the 3-p charge model, but only 5% for the 4-p one. The electrostatic term modified by a penetration function is also displayed in Figure 3. This modification suggested by Cisneros et al. improves the accuracy of the model at short distances, even though, for water−cation dimers, the effect of electron-cloud penetration is nearly negligible at distances around the intermolecular equilibrium separation (around 2.2 Å). As underlined in the previous section, this correction to the electrostatic potential will not be introduced explicitly but will, instead, be embedded in the relevant representation of the van der Waals potential, thereby simplifying the model, while remaining physically consistent.

The undamped induction energy of the classical model overestimates the quantity supplied by the SAPT expansion.[9] The damping functions considered here are that of Jensen et al. and that of Tang and Toennies. The latter function is to be favored over the former, as is reflected in the better behavior of the corresponding damped potential. All of the parameters determined for these damping functions are gathered in Tables 4 and 5.

The negligible errors in the reproduction of the electrostatic and induction contributions in water−cation complexes makes the total energy ($\Delta\mathscr{U}_{\rm tot}^{\rm SAPT}$) minus $\Delta\mathscr{U}_{\rm ele}^{\text{4-p}}$ and $\Delta\mathscr{U}_{\rm ind}^{\text{4-p/TT}}$ very similar for the SAPT van der Waals contribution ($\Delta\mathscr{U}_{\rm vdW}^{\rm SAPT}$). Employing a traditional 6-12 LJ function, the repulsive component of the latter results in a systematic failure to match the target van der Waals potential—the associated error is magnified when the induction effects dominate over the Coulomb and dispersion components. Conversely, if use is made of a Halgren or a Buckingham function, reproduction of this potential proves to be extremely accurate. Although depicted in Figure 3, the Halgren function will not be used hereafter, because the exponential part of the exp-6 Buckingham function constitutes a more physically sound framework, capable of absorbing the errors due to penetration effects. Interestingly enough, nonmultipolar contributions to the induction energy appear to be negligible in water−cation interactions and can, thus, be safely omitted. All of the parameters of the aforementioned three van der Waals functions are given in Table 6. These parameters are the raw coefficients for each interaction in the absence of combination rules.

When adding the different terms of the potential energy function, the total interaction energy is reproduced accurately, hence, confirming the applicability of the model (see Tables 7 and 8 for geometrical and energetic properties of the minimum-energy complex). Not too unexpectedly, calculations based on a LJ potential lead to a severely flawed reproduction of the total interaction energy.

4.2. The Water Dimer and Interaction of Water with Anions. In this section, the first four halide ions have been considered to interact with water along one O−H bond of the latter, which corresponds to the most favorable approach of these chemical species. In addition, a water dimer has been examined in the geometry provided in ref 89 (see also Figure 2). The results obtained for these two classes of complexes show similar trends. For conciseness, only the interaction in the water dimer will be detailed here (see Figure 4); results for all of the systems are provided in the Supporting Information.

The importance of the 4-p charge model ought to be emphasized for the reproduction of the electrostatic potential. Even at distances where penetration effects are known to be negligible, the 3-p charge model fails to reproduce the electrostatic contribution, whereas the 4-p charge model describes it successfully. Inclusion of a penetration correction yields an overall agreement between the classical model and the QM reference, irrespective of the intermolecular distance explored. Penetration effects for water−anion systems, as well as for the water dimer are crucial, as they account for up to 50% of the total electrostatic contribution at very short distances. They are, nonetheless, noticeably smaller (approximately 8%) at an intermolecular distance corresponding to the minimum-energy complex. Accordingly, it is reasonable to expect that penetration effects can be transferred in an effective fashion into the van der Waals potential, as discussed previously.

When penetration effects are large, nonmultipolar contributions are anticipated to be equally substantial. In this event, the induction term is burdened by overwhelming nonmultipolar stabilizing effects, which counterbalance the destabilizing effect of the exchange-induction component. These antagonistic phenomena preclude the use of a damping function for the present complexes. As can be seen in Table 5, no damping function is used, except for fluoride, which is the smallest anion with the least nonmultipolar effects. The missing nonmultipolar contribution to the induction energy will, thus, be incorporated into the Buckingham potential.

The conclusions reached in light of the calculations based on the water−cation dimers appear to hold also for the present complexes. Furthermore, the assumption that an exp-6 Buckingham potential, unlike a 6-12 LJ potential, can compensate

Table 6. van der Waals Parameters for H_2O−X Systems[a]

		Li^+	Na^+	K^+	Mg^{2+}	Ca^{2+}	F^-	Cl^-	Br^-	I^-	H_2O
(1)	ε	19149	66526	120694	94937	94131	5837	11843	12340	17204	14946
	A_1	3.944	4.147	3.842	3.900	3.738	3.598	3.352	3.106	3.132	3.949
	A_2	0.025	0.032	1.418	3.385	2.332	0.019	1.679	2.600	0.034	2.541
(2)	ε	0.041	0.100	0.115	0.433	0.151	0.003	0.021	0.025	0.038	0.041
	R^*	3.412	3.390	3.880	2.848	3.700	5.132	4.113	4.205	4.284	2.864
(3)	ε	468.3	94.27	11.58	1308	7.547	65.52	93.85	323.2	12.20	61468
	σ	1.302	1.715	2.395	1.355	2.405	1.301	1.600	1.566	2.248	0.763

[a] The parameters are obtained using a model of point charges and an induction model of distributed polarizabilities damped by the function of Tang and Toennies. (1) ε and A_n (n = 1, 2) correspond to the parameters of the Buckingham function. (2) ε and R^* are the parameters of the Halgren function. (3) ε and σ correspond to the parameters of the Lennard-Jones function. ε is given in kilocalories per mole. All other parameters are in ångströms.

Table 7. Values of the Interaction Distance for All the Minimum-Energy Complexes[a]

$d_{A...B}$	Li^+	Na^+	K^+	Mg^{2+}	Ca^{2+}	F^-	Cl^-	Br^-	I^-	H_2O
H_2O	1.90	2.22	2.70	1.90	2.30	1.60	2.20	2.40	2.70	2.10
	1.90	**2.25**	**2.66**	**1.90**	**2.30**	**1.60**	**2.20**	**2.40**	**2.70**	**2.10**
benzene	1.90	2.41	2.85	2.02	2.40					
	1.90	**2.41**	**2.90**	**1.92**	**2.40**					

[a] The reference quantum-mechanical values are given in bold. All distances are expressed in ångströms.

Table 8. Values of the Interaction Energy for All the Minimum-Energy Complexes[a]

$\Delta\mathcal{U}_{\text{tot,min}}$	Li^+	Na^+	K^+	Mg^{2+}	Ca^{2+}	F^-	Cl^-	Br^-	I^-	H_2O
H_2O	−32.63	−22.91	−16.85	−78.80	−52.98	−22.38	−13.07	−11.14	−9.25	−3.60
	−32.69	**−23.12**	**−16.91**	**−79.85**	**−52.75**	**−22.46**	**−13.00**	**−11.08**	**−9.22**	**−3.60**
benzene	−37.45	−23.41	−17.57	−114.17	−74.25					
	−37.43	**−23.70**	**−17.60**	**−116.41**	**−74.23**					

[a] The reference quantum-mechanical values are given in bold. All energies are expressed in kilocalories per mole.

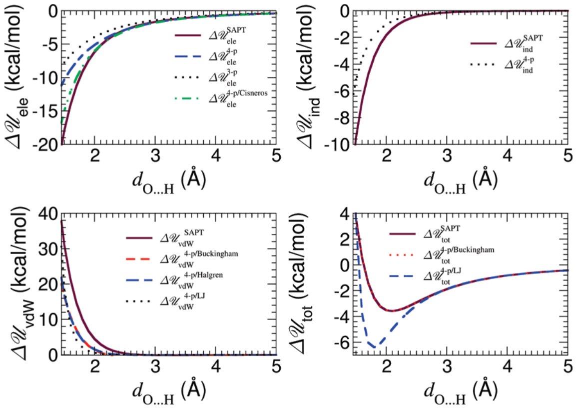

Figure 4. Interaction of two water molecules. The reference (SAPT) curve is shown as a solid line. Three models for the electrostatic contribution are represented through either a three-point (3-p) charge model with no penetration (dotted line), a four-point (4-p) charge model with no penetration (long-dashed line), or the function derived by Cisneros et al. (dot-dashed line). The induction contribution is represented without damping function (dotted line). Three models for the van der Waals contribution are fitted to $\Delta\mathcal{U}^{\text{SAPT}}_{\text{tot}} - \Delta\mathcal{U}^{\text{4-p}}_{\text{ele}} - \Delta\mathcal{U}^{\text{4-p}}_{\text{ind}}$ using either a Buckingham (short-dashed line), a Halgren (long dashed line), or a Lennard-Jones (LJ, dotted line) potential. The total energy is computed as the sum of $\Delta\mathcal{U}^{\text{4-p}}_{\text{ele}}$ plus $\Delta^{\text{4-p}}_{\text{ind}}$ plus either $\Delta\mathcal{U}^{\text{4-p/LJ}}_{\text{vdW}}$ (short-dashed line) or $\Delta\mathcal{U}^{\text{4-p/Buckingham}}_{\text{vdW}}$ (dotted line).

for the incompleteness of the classical model by embracing its overlooked, sizable contributions proves to be perfectly legitimate and reasonable (see Tables 7 and 8).

In the particular instance of negatively charged compounds, the SAPT expansion can, under certain circumstances, fail to converge.[90] For this reason, the results (not shown here) supplied by an SAPT and an RVS[91] expansion, using the Gamess[92] suite of programs, have been compared. If intramolecular correlation is ignored, the RVS and the SAPT expansions yield the same energies for all the dimers considered here, which provides a safeguard, inasmuch as convergence of the SAPT reference calculation is concerned. Moreover, the recent work of Kim et al.[93] on halide anions interacting with π systems further suggests convergence of the SAPT expansion for such dimers.

4.3. Interaction of Benzene with Metal Cations. The same series of metal cations utilized in the above study of water−cation dimers was considered for the interaction with benzene along its C_6 axis (see Figure 2). This approach corresponds to the most favorable interaction pattern[94] for a π-electron cloud interacting with a positively charged species. For conciseness, only the benzene−sodium interaction will be displayed in Figure 5; results for all systems investigated (viz., Li^+, K^+, Mg^{2+}, and Ca^{2+}) are provided in the Supporting Information.

A twelve-point (12-p) charge model derived from the molecular electrostatic potential tends to overestimate the interaction in cation-π systems, despite the appropriate reproduction of the molecular quadrupole moment of benzene and, more generally, its full molecular electrostatic potential. This overestimation is more prone to be manifested with ions bearing a highly localized charge and, on the contrary, is expected to be less perceptible for a diffuse charge, as in the case of ammonium,[43] let alone guanidinium. The results suggest that the interaction of cations with π systems is not strictly speaking an attractive quadrupole-charge one.[94] A case in point is the benzene−lithium dimer, where the electrostatic energy changes its slope at very short distances,

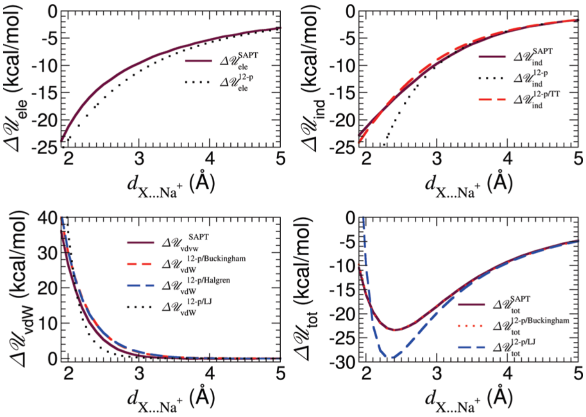

Figure 5. Interaction of a monovalent sodium ion with benzene. The reference (SAPT) curve is shown as a solid line. The electrostatic contribution obtained with a twelve-point (12-p) charge model with no penetration is represented as a dotted line. Two models for the induction contribution are represented using either no damping (dotted line) or the damping function derived by Tang and Toennies (TT, short-dashed line). Three models for the van der Waals contribution are fitted to $\Delta\mathscr{U}_{tot}^{SAPT} - \Delta\mathscr{U}_{ele}^{12\text{-}p} - \Delta\mathscr{U}_{ind}^{12\text{-}p/TT}$ using either a Buckingham (short-dashed line), a Halgren (long dashed line), or a Lennard-Jones (LJ, dotted line) potential. The total energy is computed as the sum of $\Delta\mathscr{U}_{ele}^{12\text{-}p}$ plus $\Delta\mathscr{U}_{ind}^{12\text{-}p/TT}$ plus either $\Delta\mathscr{U}_{vdW}^{12\text{-}p/LJ}$ (short-dashed line) or $\Delta\mathscr{U}_{vdW}^{12\text{-}p/Buckingham}$ (dotted line).

which, in all likelihood, is due to the positively charged lobes of the quadrupole moment interacting with the cation. The resulting destabilizing effect, which largely counterbalances the penetration contribution, is not accounted for in the electrostatic potential and is transferred to a short-distance, repulsive van der Waals term.

As noted above for the cation−water complexes, the undamped induction energy overestimates the values obtained from an SAPT analysis, but inclusion of the Tang and Toennies damping formalism reproduces the SAPT induction profile very nicely. Similarly, the 6-12 LJ potential departs markedly from the SAPT van der Waals contribution, which is always better reproduced when Halgren or Buckingham functions are used. Conclusions drawn on the basis of the water−cation complexes are shown to hold for all other π-cation interactions reported herein (van der Waals parameters are gathered in Table 9, and the geometrical and energetic properties of the minimum-energy complex are given in Tables 7 and 8).

5. Conclusion

The present study addresses the shortcomings of a simplified polarizable potential energy function and how these shortcomings can be overcome to model with an appreciable accuracy intermolecular interactions. It is desirable to have access to a simple polarizable potential energy function that satisfies the criteria of tractability and precision. This necessarily demands that important choices be made, inasmuch as the contributions to be included are concerned. In other words, it is pivotal that all of the underlying physics of the interactions be properly introduced to reflect the various contributions at play.

Table 9. van der Waals Parameters for Benzene−X^{n+} Systems^a

		Li$^+$	Na$^+$	K$^+$	Mg^{2+}	Ca^{2+}
(1)	ε	3556	8821	38649	103962	61104
	A$_1$	2.624	2.841	2.924	3.184	2.753
	A$_2$	2.419	0.067	3.502	4.583	4.661
(2)	ε	0.002	0.016	0.104	0.138	0.157
	R*	6.331	4.871	4.261	3.471	4.157
(3)	ε	8124	539.9	6.103	33.21	9.573
	σ	2.624	2.841	2.924	1.860	2.753

^{a} The parameters are obtained using a model of point charges on atoms with no penetration and an induction model of distributed polarizabilities damped by the function provided by Tang and Toennies. (1) ε and A_n (n = 1, 2) correspond to the parameters of the Buckingham function. (2) ε and R* are the parameters for the Halgren function. (3) ε and σ correspond to the parameters of the Lennard-Jones function. ε is given in kilocalories per mole. All other parameters are in ångströms.

With this objective in mind, a series of guidelines is proposed. These guidelines can be summarized as follows. The electrostatic contribution to the total energy is described by a truncation of the molecular electrostatic potential at the monopole level, which has proven in many instances to constitute a very reasonable approximation.[52] As indicated by Swart et al.,[95] this description leads to small errors for nonsymmetric systems but can fail in the case of small, symmetric molecules. Such is the case for the water molecule, where fictitious sites are needed to enhance the reproduction of the true molecular electrostatic potential. Accordingly, a TIP4P-like[80,81] potential was proposed for water. In addition to the first-order contribution to the total energy, penetration effects are present at short distances in all interacting systems. This term can be modeled with an exponential function and can be introduced through the exp-6 Buckingham potential. The total interaction energy is further decomposed into an induction component, which, at the classical level, relies on the conjunction of charge-flow polarizabilities between covalently bonded atoms and isotropic dipole polarizabilities determined from QM induction energy maps.

The resulting polarizable models are simple, yet sufficiently accurate for recovering the anisotropy of the molecular polarizability. In most circumstances, the damping function proposed by Tang and Toennies recovers the exchange-induction contribution. This particular function can be expanded up to third order only, which greatly simplifies its calculation. Furthermore, when the nonmultipolar component to the induction energy cannot be neglected, a classical multipole expansion systematically underestimates the polarization part of the interaction energy. Should this situation arise, it is necessary to remove the damping function from the model and encapsulate this stabilizing effect through another suitable function. The remaining terms of the QM expansion that are described explicitly can be incorporated in a single contribution that involves the exp-6 Buckingham potential. The latter is highly appropriate because it encompasses each and every missing term that can be expressed by way of an exponential, repulsive representation.

Extension of the present work to an all-atom description for the van der Waals potential is underway to provide a better three-dimensional description of the short-range potential. The very encouraging results reported herein suggest that the proposed methodology for deriving polarizable force fields on the basis of a small set of prototypical interacting chemical species can be readily extended to more complex molecular systems.

Acknowledgment. The authors thank János G. Ángyán, Georg Jansen, and Krzysztof Szalewicz for stimulating discussions. The authors are indebted to the Centro de Supercomputación de Catalunya, Barcelona, Spain, and to the Centre Informatique National de l'Enseignement Supérieur, Montpellier, France, for provision of generous amounts of computational time.

Supporting Information Available: Intermolecular energy profiles for water and benzene interacting with halide and metal ions. This material is available free of charge via the Internet at http://pubs.acs.org.

References

(1) Yin, Y.; Arkhipov, A.; Schulten, K. *Structure* **2009**, *17*, 882–892.

(2) Lei, H.; Duan, Y. *J. Mol. Biol.* **2007**, *370*, 196–206.

(3) Cornell, W. D.; Cieplak, P.; Bayly, C. I.; Gould, I. R.; Merz, K. M., Jr.; Ferguson, D. M.; Spellmeyer, D. C.; Fox, T.; Caldwell, J. C.; Kollman, P. A. *J. Am. Chem. Soc.* **1995**, *117*, 5179–5197.

(4) MacKerell, A. D., Jr.; et al. *J. Phys. Chem. B* **1998**, *102*, 3586–3616.

(5) Oostenbrink, C.; Villa, A.; Mark, A. E.; van Gunsteren, W. F. *J. Comput. Chem.* **2004**, *25*, 1656–1676.

(6) Kaminski, G. A.; Stern, H. A.; Berne, B. J.; Friesner, R. A. *J. Phys. Chem. A* **2003**, *108*, 621–627.

(7) Freddolino, P. L.; Liu, F.; Gruebele, M.; Schulten, K. *Biophys. J.* **2008**, *94*, 75–77.

(8) Freddolino, P. L.; Park, S.; Roux, B.; Schulten, K. *Biophys. J.* **2009**, *96*, 3772–3780.

(9) Dehez, F.; Archambault, F.; Soteras, I.; Luque, F. J.; Chipot, C. *Mol. Phys.* **2008**, *106*, 1685–1696.

(10) Shiratori, Y.; Nakagawa, S. *J. Comput. Chem.* **1991**, *12*, 717–730.

(11) Project, E.; Nachliel, E.; Gutman, M. *J. Comput. Chem.* **2008**, *29*, 1163–1169.

(12) Bucher, D.; Guidoni, L.; Maurer, P.; Rothlisberger, U. *J. Chem. Theory Comput.* **2009**, *5*, 2173−2179.

(13) Allen, T.; Andersen, O.; Roux, B. *Biophys. Chem.* **2006**, *124*, 251–267.

(14) Fowler, P. W.; Stone, A. J. *J. Phys. Chem.* **1987**, *91*, 509–511.

(15) Gavezzotti, A. *J. Phys. Chem. B* **2002**, *106*, 4145–4154.

(16) Gavezzotti, A. *J. Phys. Chem. B* **2003**, *107*, 2344–2353.

(17) Welch, G. W. A.; Karamertzanis, P. G.; Misquitta, A. J.; Stone, A. J.; Price, S. L. *J. Chem. Theory Comput.* **2008**, *4*, 522–532.

(18) Barnes, P.; Finney, J. L.; Nicholas, J. D.; Quinn, J. E. *Nature* **1979**, *282*, 459–464.

(19) Lamoureux, G.; Roux, B. *J. Chem. Phys.* **2003**, *119*, 3025–3039.

(20) Rappe, A. K.; Goddard, W. A. *J. Phys. Chem.* **1991**, *95*, 3358–3363.

(21) Stern, H. A.; Kaminski, G. A.; Banks, J. L.; Zhou, R.; Berne, B. J.; Friesner, R. A. *J. Phys. Chem. B* **1999**, *103*, 4730–4737.

(22) Patel, S.; Brooks, C. L. *J. Comput. Chem.* **2003**, *25*, 1–16.

(23) Patel, S.; Mackerell, A. D., Jr.; Brooks, C. L. *J. Comput. Chem.* **2004**, *25*, 1504–1514.

(24) Sanderson, R. T. In *Chemical Bonds and Bond Energy*; Academic Press: New York, 1976; pp 1−15.

(25) Le Sueur, C. R.; Stone, A. J. *Mol. Phys.* **1994**, *83*, 293–307.

(26) Engkvist, O.; Åstrand, P.-O.; Karlström, G. *Chem. Rev.* **2000**, *100*, 4087–4108.

(27) Ren, P.; Ponder, J. W. *J. Comput. Chem.* **2002**, *23*, 1497–1506.

(28) Hagberg, D.; Brdarski, S.; Karlström, G. *J. Phys. Chem. B* **2005**, *109*, 4111–4117.

(29) Gresh, N.; Cisneros, G. A.; Darden, T. A.; Piquemal, J.-P. *J. Chem. Theory Comput.* **2007**, *3*, 1960–1986.

(30) Darley, M. G.; Popelier, P. L. A. *J. Phys. Chem. A* **2008**, *112*, 12954–12965.

(31) Berendsen, H. J. C.; Grigera, J. R.; Straatsma, T. P. *J. Phys. Chem.* **1987**, *91*, 6269–6271.

(32) Masella, M.; Flament, J. P. *J. Chem. Phys.* **1997**, *107*, 9105–9116.

(33) Zhang, Q.; Zhang, X.; Yu, L.; Zhao, D.-X. *J. Mol. Liq.* **2009**, *145*, 58–66.

(34) Zhang, Q.; Zhang, X.; Zhao, D.-X. *J. Mol. Liq.* **2009**, *145*, 67–81.

(35) Babin, V.; Baucom, J.; Darden, T. A.; Sagui, C. *J. Phys. Chem.* **2006**, *110*, 11571–11581.

(36) Harder, E.; MacKerell, A. D., Jr.; Roux, B. *J. Am. Chem. Soc.* **2009**, *131*, 2760–2761.

(37) Claverie, P. In *Intermolecular Interactions: From Diatomics to Biopolymers*; Pullman, B., Ed.; Wiley Interscience: New York, 1978; pp 69−305.

(38) Celebi, N.; Ángyán, J. G.; Dehez, F.; Millot, C.; Chipot, C. *J. Chem. Phys.* **2000**, *112*, 2709–2717.

(39) Dehez, F.; Soetens, J.-C.; Chipot, C.; Ángyán, J. G.; Millot, C. *J. Phys. Chem. A* **2000**, *104*, 1293–1303.

(40) Chipot, C.; Dehez, F.; Ángyán, J. G.; Millot, C.; Orozco, M.; Luque, F. J. *J. Phys. Chem. A* **2001**, *105*, 11505–11514.

(41) Dehez, F.; Chipot, C.; Millot, C.; Ángyán, J. G. *Chem. Phys. Lett.* **2001**, *338*, 180–188.

(42) Ángyán, J. G.; Chipot, C.; Dehez, F.; Hättig, C.; Jansen, G.; Millot, C. *J. Comput. Chem.* **2003**, *24*, 997–1008.

(43) Dehez, F.; Ángyán, J. G.; Soteras, I.; Luque, F. J.; Schulten, K.; Chipot, C. *J. Chem. Theory Comput.* **2007**, *3*, 1914–1926.

(44) Jeziorski, B.; Moszynski, R.; Szalewicz, K. *Chem. Rev.* **1994**, *94*, 1887–1930.

(45) Bukowski, R.; Cencek, W.; Jankowski, P.; Jeziorska, M.; Jeziorski, B.; Kucharski, S. A.; Lotrich, V. F.; Misquitta, A. J.; Moszyński, R.; Patkowski, K.; Podeszwa, R.; Rybak, S.; Szalewicz, K.; Williams, H. L.; Wheatley, R. J.; Wormer, P. E. S.; Zuchowski, P. S. *SAPT2008*; Department of Physics and Astronomy, University of Delaware: Newark, DE;

Department of Chemistry, University of Warsaw: Warsaw, Poland, 2008.

(46) Møller, C.; Plesset, M. S. *Phys. Rev.* **1934**, *46*, 618–622.

(47) Burcl, R.; Chalasiński, G.; Bukowski, R. *J. Chem. Phys.* **1995**, *103*, 1498–1507.

(48) Szalewicz, K.; Patkowski, K.; Jeziorski, B. *Structure Bonding* **2005**, *116*, 43–117.

(49) Torheyden, M.; Jansen, G. *Mol. Phys.* **2006**, *104*, 2101–2138.

(50) Misquitta, A. J.; Stone, A. J. *J. Chem. Theory Comput.* **2008**, *4*, 7–18.

(51) Berka, K.; Laskowski, R.; Riley, K. E.; Hobza, P.; Vondrasek, J. *J. Chem. Theory Comput.* **2009**, *5*, 982–992.

(52) Chipot, C.; Ángyán, J. G. *New J. Chem.* **2005**, *29*, 411–420.

(53) Ángyán, J. G.; Chipot, C. *Int. J. Quantum Chem.* **1994**, *52*, 17–37.

(54) Vigné-Maeder, F.; Claverie, P. *J. Chem. Phys.* **1988**, *88*, 4934–4948.

(55) Stone, A. J. In *Theoretical Models of Chemical Bonding*; Maksić, H., Ed.; Springer-Verlag: Berlin, 1991; Vol. 4, pp 103−131.

(56) Stone, A. J. In *The Theory of Intermolecular Forces*; Clarendon Press: Oxford, U. K., 1996.

(57) Freitag, M. A.; Gordon, M. S.; Jensen, J. H.; Stevens, W. J. *J. Chem. Phys.* **2000**, *112*, 7300–7306.

(58) Gordon, M. S.; Freitag, M. A.; Bandyopadhyay, P.; Jensen, J. H.; Kairys, V.; Stevens, W. J. *J. Phys. Chem. A* **2001**, *105*, 293–307.

(59) Piquemal, J.-P.; Gresh, N.; Giessner-Prettre, C. *J. Phys. Chem. A* **2003**, *107*, 10353–10359.

(60) Cisneros, G. A.; Na-Im Tholander, S.; Parisel, O.; Darden, T. A.; Elking, D.; Perera, L.; Piquemal, J.-P. *Int. J. Quantum Chem.* **2008**, *108*, 1905–1912.

(61) Applequist, J.; Carl, J. R.; Fung, K.-K. *J. Am. Chem. Soc.* **1972**, *94*, 2952–2960.

(62) Stone, A. J.; Alderton, M. *Mol. Phys.* **1985**, *56*, 1047–1064.

(63) Soteras, I.; Curutchet, C.; Bidon-Chanal, A.; Dehez, F.; Ángyán, J. G.; Orozco, M.; Chipot, C.; Luque, F. J. *J. Chem. Theory Comput.* **2007**, *3*, 1901–1913.

(64) Jensen, L.; Åstrand, P.-O.; Osted, A.; Kongsted, J.; Mikkelsen, K. V. *J. Chem. Phys.* **2002**, *116*, 4001–4010.

(65) Tang, K. T.; Toennies, J. P. *J. Chem. Phys.* **1984**, *80*, 3726–3741.

(66) Tang, K. T.; Toennies, J. P. *J. Chem. Phys.* **1977**, *66*, 1496–1506.

(67) Millot, C.; Stone, A. J. *Mol. Phys.* **1992**, *77*, 439–462.

(68) Meredith, A. W.; Stone, A. J. *J. Phys. Chem. A* **1998**, *102*, 434–445.

(69) Jones, J. *Proc. R. Soc. London, Ser. A* **1924**, *106*, 441–462.

(70) Ren, P.; Ponder, J. W. *J. Phys. Chem. B* **2003**, *107*, 5933–5947.

(71) Halgren, T. A. *J. Am. Chem. Soc.* **1992**, *114*, 7827–7843.

(72) Buckingham, R. A.; Hamilton, J.; Massey, H. S. W. *Proc. R. Soc. London, Ser. A* **1941**, *179*, 103–122.

(73) Frisch, M. J.; Trucks, G. W.; Schlegel, H. B.; Scuseria, G. E.; Robb, M. A.; Cheeseman, J. R.; Montgomery, J. A., Jr.; Vreven, T.; Kudin, K. N.; Burant, J. C.; Millam, J. M.; Iyengar, S. S.; Tomasi, J.; Barone, V.; Mennucci, B.; Cossi, M.; Scalmani, G.; Rega, N.; Petersson, G. A.; Nakatsuji, H.; Hada, M.; Ehara, M.; Toyota, K.; Fukuda, R.; Hasegawa, J.; Ishida, M.; Nakajima, T.; Honda, Y.; Kitao, O.; Nakai, H.; Klene, M.; Li, X.; Knox, J. E.; Hratchian, H. P.; Cross, J. B.; Bakken, V.; Adamo, C.; Jaramillo, J.; Gomperts, R.; Stratmann, R. E.; Yazyev, O.; Austin, A. J.; Cammi, R.; Pomelli, C.; Ochterski, J. W.; Ayala, P. Y.; Morokuma, K.; Voth, G. A.; Salvador1, P.; Dannenberg, J. J.; Zakrzewski, V. G.; Dapprich, S.; Daniels, A. D.; Strain, M. C.; Farkas, O.; Malick, D. K.; Rabuck, A. D.; Raghavachari, K.; Foresman, J. B.; Ortiz, J. V.; Cui, Q.; Baboul, A. G.; Clifford, S.; Cioslowski, J.; Stefanov, B. B.; Liu, G.; Liashenko, A.; Piskorz, P.; Komaromi, I.; Martin, R. L.; Fox, D. J.; Keith, T.; Al-Laham, M. A.; Peng, C. Y.; Nanayakkara, A.; Challacombe, M.; Gill, P. M. W.; Johnson, B.; Chen, W.; Wong, M. W.; Gonzalez, C.; Pople, J. A. *Gaussian 03*, revision C.02; Gaussian, Inc.: Wallingford, CT, 2004.

(74) Sadlej, A. J. *Theor. Chim. Acta* **1992**, *79*, 123–140.

(75) Sadlej, A. J. *Theor. Chim. Acta* **1992**, *81*, 45–63.

(76) Sadlej, A. J. *Theor. Chim. Acta* **1992**, *81*, 339–354.

(77) Sadlej, A. J. *Collect. Czech. Chem. Commun.* **1988**, *53*, 1995–2016.

(78) Misquitta, A. J.; Stone, A. J.; Price, S. L. *J. Chem. Theory Comput.* **2008**, *4*, 19–32.

(79) Saunders, V. R.; Guest, M. F. *ATMOL*; SERC Daresbury Laboratory: Daresbury, Great Britain, 1976.

(80) Jorgensen, W. L.; Chandrasekhar, J.; Madura, J. D.; Impey, R. W.; Klein, M. L. *J. Chem. Phys.* **1983**, *79*, 926–935.

(81) Colonna, F.; Ángyán, J. G.; Tapia, O. *Chem. Phys. Lett.* **1990**, *172*, 55–61.

(82) Dzyabchenko, A. V. *Russ. J. Phys. Chem. A* **2008**, *82*, 758–766.

(83) Coker, H. *J. Phys. Chem.* **1976**, *80*, 2084–2091.

(84) Fajans, K. *J. Phys. Chem.* **1970**, *74*, 3407–3410.

(85) Marquart, D. *SIAM J. Appl. Math.* **1963**, *11*, 431–441.

(86) Gresh, N.; Garmer, D. R. *J. Comput. Chem.* **1995**, *17*, 1481–1495.

(87) Brdarski, S.; Karlström, G. *J. Phys. Chem. A* **1998**, *102*, 8182–8192.

(88) Lago, N. F.; Larranaga, F. H.; Albertí, M. *Eur. Phys. J. D* **2009**, *1*, 75−85.

(89) Mas, E. M.; Szalewicz, K. *J. Chem. Phys.* **1996**, *104*, 7606–7614.

(90) Szalewicz, K. Private communication.

(91) Chen, W.; Gordon, M. S. *J. Phys. Chem.* **1996**, *100*, 14316–14328.

(92) Schmidt, M. W.; Baldridge, K. K.; Boatz, J. A.; Elbert, S. T.; Gordon, M. S.; Jensen, J. H.; Koseki, S.; Matsunaga, N.; Nguyen, K. A.; Su, S.; Windus, T. L.; Dupuis, M.; Montgomery, J. A. *J. Comput. Chem.* **1993**, *14*, 1347–1363.

(93) Kim, D.; Tarakeshwar, P.; Kim, K. S. *J. Phys. Chem. A* **2004**, *108*, 1250–1258.

(94) Ma, J. C.; Dougherty, D. A. *Chem. Rev.* **1997**, *97*, 1303–1324.

(95) Swart, M.; van Duijnen, P. T.; Snijders, J. G. *J. Comput. Chem.* **2000**, *22*, 79–88.

CT9004189

JCTC Journal of Chemical Theory and Computation

Toward Understanding the Photochemistry of Photoactive Yellow Protein: A CASPT2/CASSCF and Quantum Theory of Atoms in Molecules Combined Study of a Model Chromophore in Vacuo

P. B. Coto,*,† D. Roca-Sanjuán,† L. Serrano-Andrés,† A. Martín-Pendás,‡ S. Martí,§
and J. Andrés*,§

Instituto de Ciencia Molecular (ICMOL), Universidad de Valencia, Apdo. 22085, ES-46071, Valencia, Spain, Departamento de Química-Física y Analítica, Facultad de Química, Universidad de Oviedo, 33006, Oviedo, Spain, Departamento de Química-Física y Analítica, Universidad Jaume I, 224, 12071, Castellón, Spain

Received June 17, 2009

Abstract: Photochemical processes that take place in biological molecules have become an increasingly important research topic for both experimentalists and theoreticians. In this work, we report the reaction mechanism of a model of the photoactive yellow protein (PYP) chromophore in vacuo. The results obtained here, using a strategy based on the simultaneous use of the minimum energy path concept and the quantum theory of atoms in molecules applied to this excited state process, suggest a possible way in which the protein could increase the efficiency of the reaction. The role played by other electronic states of the same and different spin multiplicities in the reaction process is also analyzed, with special emphasis on that played by the lowest-lying triplet state. The possibility of a more complex than expected reaction mechanism is finally discussed, with some suggestions on the possible roles of the protein.

1. Introduction

The photoactive yellow protein (PYP) is a cytosolic protein found in certain types of bacteria. It works as a sensor, being responsible for the negative phototactic response of these bacteria when exposed to blue light.[1,2] The protein uses its chromophore, the *p*-hydroxycinnamoyl anion, as a molecular motor able to transform the energy of light into chemical work. This energy is employed for the modification of the conformation of the chromophore in the protein through a fast trans-to-cis isomerization process, part of which takes place in an excited electronic state. This change in the structure of the chromophore ultimately prompts a series of conformational changes in the protein structure that lead to the generation of a response of the organism, which moves away from the blue light source.

Together with rhodopsin, PYP is perhaps one of the most exhaustively studied protein photoreceptors, both experimentally[1,2] and theoretically.[3−13] The most accepted mechanism for the early events of the photocycle, based on experimental measurements[1,2,14] and molecular dynamics simulations,[6,7] points to a conical intersection (CI) mediated process as the one responsible for the formation of the cis isomer. The role of the hydrogen bond network of amino acids close to the chromophore in controlling the maximum absorption and the isomerization process has also been discussed, with particular emphasis on the function of Cys_{69}, Glu_{46}, and Tyr_{42}[6,11,12,14] residues. The possible electrostatic control exerted by the counterion of the chromophore (Arg_{52}) has also been addressed with conflicting results.[7,15] Moreover, a clear differentiation between the intrinsic properties of the chromophore and the effects of the protein in the full reaction process has remained elusive, in part due to the difficulties of performing experiments with anionic substances in vacuo, to the problems associated

---

* Corresponding author e-mail: pedro.brana@uv.es (P.B.C.), andres@qfa.uji.es (J.A.).

† Universidad de Valencia.

‡ Universidad de Oviedo.

§ Universidad Jaume I.

10.1021/ct900401z CCC: $40.75

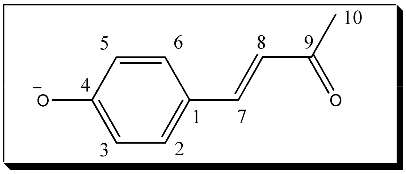

Figure 1. Model of the PYP chromophore considered in this study.

with the interpretation of the results obtained with the protein, and also to the complexities inherent in the theoretical modeling of large biological molecules and anionic systems, particularly when involved in excited state reactions. Thus, and despite all of the efforts carried out to date, this reaction remains not fully understood. Its complex nature, which combines short reaction times, different electronic states, and a complex anionic chromophore, turns this process into a challenge for both experimentalists and theoreticians. As a continuation of previous work[12] on the PYP photochemistry where the role of the protein in the control of the absorption wavelength was disentangled, we now focus on the intrinsic reactivity and structural properties of a model chromophore of the *p*-hydroxycinnamoyl anion (see Figure 1) in vacuo, as an initial step for understanding the possible role of the protein in the early events of the isomerization process. This model differs from the natural chromophore as well as other chromophore models used in previous works[3,4,8,10,11,16] dealing with different aspects of the photochemistry of PYP. The reason for selecting this model is twofold. On the one hand, the insights obtained with this reduced model, disentangled of the protein environment and linkage, will show the intrinsic behavior of the central structure and the isomerizing double bond[17] while at the same time allowing a differential comparison with the full protein. On the other hand, the results obtained can be compared with recent experimental observations where the fast dynamics of this chromophore were analyzed and proven to be similar (in the isomerization time and also in the coherence reflecting the involvement of low-frequency motions in isomerization[17]) to that of the protein. Furthermore, the nature of the lowest-lying electronic excited state is qualitatively similar (the dominant configuration is characterized by an excitation that involves the same kind of orbitals, and it also displays a significant value of the related oscillator strength) to that of the full protein model,[12] thus indicating that the model is a reliable one.

To tackle this problem, we employed a combined strategy based on the use of the minimum energy path (MEP) approach, which can be considered a zero-order static description of the reactive process that takes place in the first low-lying excited state (the bright $\pi \rightarrow \pi^*$ state, S_1), together with the application of the quantum theory of atoms in molecules (QTAIM)[18] for understanding the key changes in the molecular structure of the chromophore, an intrinsic aspect that may also help to shed light on the favorable reaction mechanism, while at the same time rendering some insight into the role of the protein. The theoretical description of reactive processes that take place in excited electronic states also needs a method that can describe in a balanced way all of the electronic states involved, which can be very different in their chemical nature.[19] The method must not only be qualitatively correct but also reasonably precise at a moderate computational cost. Moreover, it must also be able to describe situations where energetic degeneracy is present and nonadiabatic effects have a fundamental contribution. For molecules of this size, the CASPT2/CASSCF method (i.e., CASSCF optimizations followed by CASPT2 single-point computations) has proven to be a flexible as well as computationally affordable tool. It combines both the ability of describing in a balanced way electronic states of a different nature, which ultimately allows the method to characterize a full reaction path, with a reasonable accuracy, being able to account for the dynamic correlation effects. The reliability of this theoretical approach in the description of the kind of reactive process discussed here has been proven in similar[12] and related systems.[20-24]

Since rationalizing the chemical nature of excited electronic states is not always easy, we have used QTAIM[18] to avoid any methodological bias. This is a generalization of quantum mechanics to open systems that provides orbital invariant chemical bonding indicators and a topological partition of the physical space into quantum atoms which provide additive contributions to every global quantum mechanical expectation value (see Supporting Information for further details).

In this work, we will focus on the reaction path associated with the twisting of the C_7-C_8 double bond (see Figure 1) in the selected model chromophore. Even when it has been experimentally shown using blocked chromophores similar to the natural one that both single and double bond twisting can be active in the photochemical deactivation process, the C_7-C_8 double bond twisting has proven to be involved in the main reaction channel.[25] This has also been recently shown through direct observation of the fast in vacuo dynamics of the model chromophore used in this work.[17] Moreover, in the case of the chromophore embedded in the protein, single-bond twisting of the C_1-C_7 seems unlikely, as such a process will suffer the steric hindrance imposed by the protein structure. As a final result, we will also discuss the possible role that the triplet state can have in this and other photochemical processes carried out by biological photoreceptors.

2. Theoretical Methods

We have used the CASPT2/CASSCF strategy in the description of this photochemical process. The relevant critical points as well as the MEP optimized geometries in the S_1 potential energy surface (PES) have been located using a two-roots−equal-weights state average CASSCF level of theory (see Supporting Information for details). An active space that comprises 12 electrons in 11 π-like orbitals has been used. Due to the nature of the electronic states involved and its sensitivity to the quality of the basis set employed,[11] we have used a flexible and reasonably large ANO-S basis set[26] with contraction, C,O[4s3p1d]/H[2s1p]. To account for the dynamic correlation effects, at each optimized point we have carried out CASPT2 calculations using as reference wave functions those obtained at the six-roots−equal-weights state average CASSCF level with an active space of 16 electrons in 13 orbitals, where the *n* (lone pair) orbitals of both oxygen atoms were included, following the same strategy used in a previous work in the full (PYP) protein.[12]

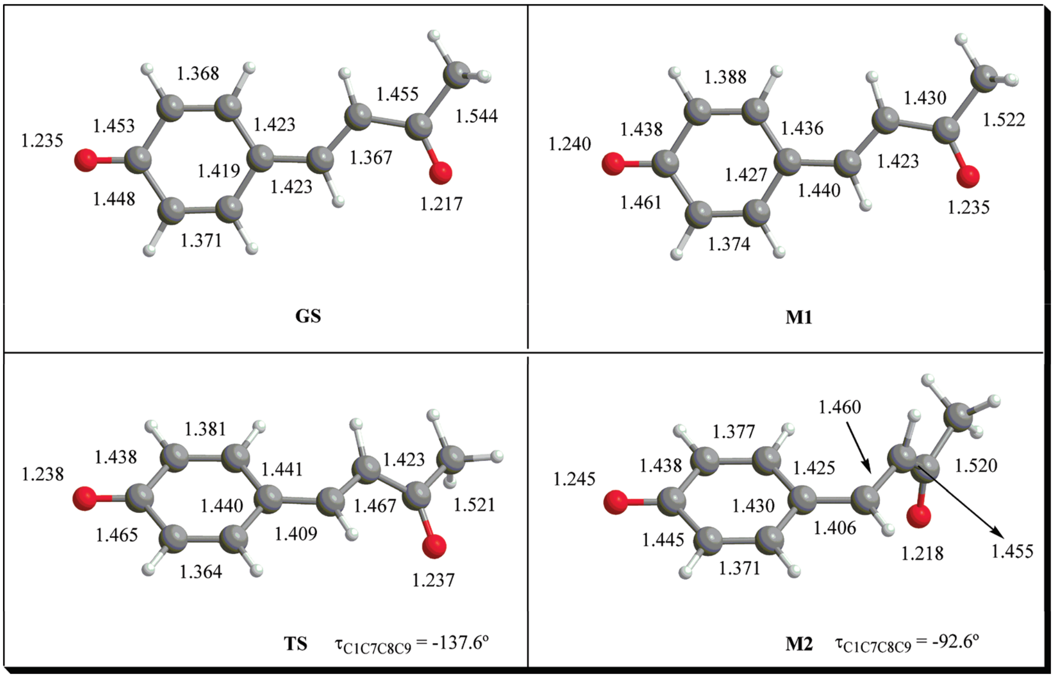

Figure 2. Most relevant geometrical parameters for the different equilibrium structures located in the S_0 and S_1 potential energy surfaces.

This protocol has also been employed to evaluate the position of the triplet and doublet (neutral) states. Throughout all of the CASPT2 computations, an imaginary level shift[27] of 0.2 au has been used to limit the effects of intruder states. All of the computations were carried out using the MOLCAS 7 program.[28] QTAIM analyses have been performed with the AIMPAC suite of programs[29] from the MOLCAS output wave functions. Care was taken that a full set of critical points (cp's) of the density was found at every stationary point, and bonding information was taken from standard scalars obtained at relevant (3,−1) cp's.

Some previous concerns about the applicability of the QTAIM to excited states[30] have now been fully rebutted,[31] and recent work[32] has shown that the theory may be used safely in these cases.

3. Results and Discussion

3.1. Geometries. In this subsection, we will describe the most relevant characteristics of the intermediates involved in the process. Figure 2 displays the optimized structures involved in the isomerization mechanism on both the S_0 and S_1 PES through the C_7-C_8 bond twisting, together with some selected geometrical parameters.

The corresponding values for both Mulliken population analysis (MPA) and Bader topological charges (BTC) are presented in Table 1. Although it is well-known that the former is both method- and basis-set-dependent, most computational chemists are used to their values. BTCs, on the other hand, are measurable quantum expectation values, routinely obtained from X-ray charge density crystallography[33] and much more stable versus changes in computational parameters. BTCs are usually larger than those of the MPA but reflect the actual distribution of electrons in real space, a particularly important point in excited states, where charge separations are much more likely to occur. Four stationary points, three minima (**GS**, **M1**, and **M2**) and a transition state (**TS**), have been characterized in the reaction path. **GS**, the trans ground state minimum structure, displays a geometry with some quinonic type character (see Figure 2), but just up to some degree; therefore, a clear characterization cannot be established. This behavior points to a delocalization of the negative charge throughout the structure, rather than to a concentration on the phenoxy moiety. Indeed, both MPA and BTC show the negative charge only partially localized on the phenoxy ring, with a significant amount of charge located in the carbon chain (see Table 1).

Table 1. Negative Charge Distribution (au) Computed Using Mulliken Population Analysis and Bader Topological Charges (between brackets) for All of the Equilibrium Structures Located along the Minimum Energy Path of the Model Chromophore[a]

	S_0		S_1	
structure	q_{ph}	q_{chain}	q_{ph}	q_{chain}
GS	−0.58 (−0.69)	−0.42 (−0.30)	−0.37 (−0.44)	−0.63 (−0.55)
M1	−0.55 (−0.67)	−0.45 (−0.32)	−0.38 (−0.47)	−0.62 (−0.53)
TS	−0.45 (−0.58)	−0.55 (−0.41)	−0.40 (−0.51)	−0.60 (−0.48)
M2	−0.10 (−0.26)	−0.90 (−0.73)	−0.64 (−0.75)	−0.36 (−0.24)

[a] q_{ph} stands for the charge located in the phenoxy ring, while q_{chain} is the charge located in the rest of the molecule.

M1, the first minimum located in the S_1 reaction path, displays again a structure that seems to lose, at least partially, the quinonic-like character. This structure is characterized by a modification of the bond lengths of the carbon chain. In particular, an increase in the length of the (isomerizing) C_7-C_8 and C_1-C_7 bonds (yet, in the case of the last one, to a minor extent) is observed. The region of the keto group changes noticeably with respect to the **GS** structure, with an increase in the bond length of the C=O group and a decrease of the C_8-C_9 and C_9-C_{10} bond lengths. MPA and

Table 2. Relative Energies (to S_0, eV) and Oscillator Strengths (in parentheses) for the Most Significant Electronic States at the Franck−Condon Geometry Computed at the CASPT2/CASSCF/ANO-S Theoretical Level

electronic state	ΔE
S_1 ($\pi \rightarrow \pi^*$)	2.54 (0.928)
S_2 ($n \rightarrow \pi^*$)	3.48 ($<10^{-3}$)
S_3 ($\pi \rightarrow \pi^*$)	3.67 (0.092)
S_4 ($n \rightarrow \pi^*$)	3.72 ($<10^{-3}$)
D_1 ($\pi \rightarrow \pi^*$)	2.79
T_1 ($\pi \rightarrow \pi^*$)	1.83

BTC values are consistent with a situation where the negative charge is mainly localized at the carbon chain (see Table 1), with values very similar to those displayed by the bright (S_1) state at the Franck−Condon (FC) structure. **TS**, the transition state for the twisting of the C_7-C_8 bond in S_1, displays similar characteristics to those of the **M1** structure, except for the twisting of the C_7-C_8 bond and the increase of its length (see Figure 2). The C_1-C_7 bond also perceptibly shortens. MPA and BTC values show a negative charge distribution similar to the one found in **M1**. Finally, **M2**, the twisted minimum optimized in S_1, displays a nearly 90° twisted structure where the keto oxygen bond length has shortened and that of the C_8-C_9 bond has lengthened, rendering values similar to those found in the **GS** structure. MPA and BTC values indicate that part of the negative charge has moved from the carbon chain to the phenoxy ring when compared with the previous structures. As a result, it can be seen that both MPA and BTC render the same qualitative trend with a gradual partial localization of the negative charge in the phenoxy ring along the MEP.

3.2. Energies of the States and Minimum Energy Path. Table 2 shows the ordering of the lowest-lying electronic states at the FC point, whereas Figure 3 shows the MEP computed for the S_1 twisting process of the C_7-C_8 bond. The first thing to note is the energetic order of the different electronic states at the FC point. The lowest-lying singlet excited state of the anion is not metastable with respect to the autoionization process at the FC point.

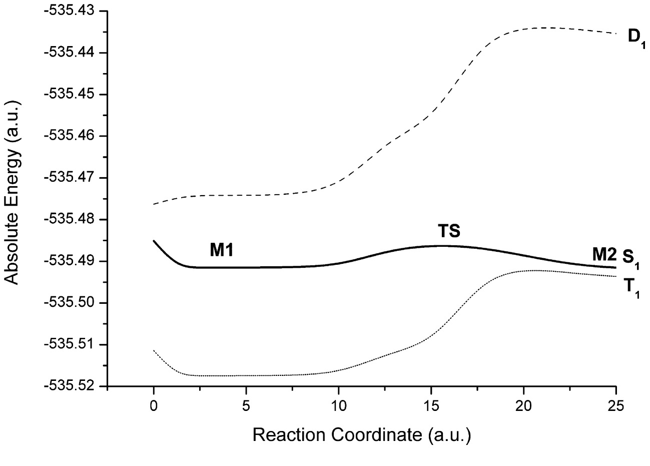

Figure 3. Graphical representation of the minimum energy path computed for the twisting of the C_7-C_8 bond in the lowest-lying singlet electronic state (S_1) at the CASPT2/CASSCF/ANO-S theoretical level (optimized structures along the path are indicated). The doublet (D_1) and triplet (T_1) states are also included.

As can be seen in Table 2, the neutral radical (D_1) is energetically less stable (2.79 eV vs 2.54 eV) than the S_1 $\pi \rightarrow \pi^*$ lowest-lying singlet state. This result is in line with the experimental results of Lee et al.,[17] where it is shown that the highest quantum yield is obtained for the reaction channel associated with the isomerization process. The results obtained are consistent with a process in which population of the neutral state would not be possible unless high excitation energies are used, with the system being excited either to a different electronic state (higher in energy than S_1, see Table 2) or to a high vibrational state; that is, the system becomes vibrationally hot in S_1. However, due to the relatively small energetic difference, we cannot rule out the possibility of regions of the potential energy surface close to the FC region where the anion becomes a metastable state. Special caution must be taken when analyzing those regions,[34,35] a problem that is out of the scope of this work and has previously been addressed using different computational methods.[10,11,16p]

Another point is that the computed S_0-S_1 vertical excitation energy is in line with previous results obtained for the full protein.[12] Despite both calculations cannot be directly compared due to the differences in the models and level of theory employed, this result is consistent with the proposal of Andersen and co-workers,[36] who suggested that the role of the protein is that of shielding the chromophore from the solvent (that would produce a large shift on the absorption maximum) and creating an environment similar to that of the chromophore in vacuo with a small difference in the absorption color due to the fine-tuning carried out by the protein. It must be stressed, however, that vertical excitation energy does not correspond in general to the absorption band maximum, yet a reasonable degree of agreement can be usually expected. More accurate comparisons would require calculation of the vibrational profile of the absorption band. It is also interesting to note that, for the carboxilate derivative of a related model of the PYP chromophore, the trans p-coumaric acid, some popular methods render significant and unexpected differences,[16q] pointing out that caution must be taken with the models and theoretical methods employed. Moreover, recent computational work has cast some doubt on the interpretation of photodestruction spectroscopy results in related systems.[37]

The following excited state, S_2, is of $n \rightarrow \pi^*$ type like S_4, whereas S_3 is again a $\pi \rightarrow \pi^*$ state. It is also interesting to note that both S_2 and S_4 show a clear multiconfigurational character, pointing out that only a method able to describe appropriately this characteristic can render a correct description of these states and their energies. In particular, the use of single-reference-based methods for the study of these kinds of states can be problematic. Moreover, the inclusion of dynamic correlation effects through CASPT2 single-point calculations alters the order and energy gap among the states (see Supporting Information), pointing out that the use of the CASSCF method for the computation of molecular dynamics must be carefully assessed.

Figure 3 shows a reaction profile in which, after an initial relaxation from the FC point and formation of the relaxed planar minimum **M1**, a small barrier (0.15 eV) must be surmounted to reach the twisted **M2** minimum, which is 0.19 eV more stable than the FC point, nearly degenerate with the lowest-lying triplet state (T_1), and 1.49 eV more stable than the neutral doublet state (D_1). Contrary to the behavior of D_1, T_1 is more stable than the lowest-lying singlet state (see also Table 2) along this reaction profile. As the reaction path proceeds, the energies of the S_1 and T_1 states approach and are almost degenerate in the region close to **M2**, the twisted minimum in S_1. Indeed, the differences in energy along the reaction path are virtually negligible soon after **TS** (see Figure 3). This fact may have important consequences for the reaction process, particularly under the experimental conditions used, characterized for the existence of an excess of energy. For the intersystem crossing (ISC)-mediated (S_1/T_1) process to be competitive with the internal conversion (CI)-mediated (S_1/S_0) one, this has to happen on a time scale on the same order as the one assigned for the S_1/S_0 nonradiative transition. The possible implications for the mechanism discussed here rely on the existence of such a competitive and fast ISC process operating simultaneously with the S_1/S_0 nonradiative relaxation. Lee et al.[17] give a time estimate for the latter of about 1 ps. This is not the usual time scale for an ISC process (with rough estimates[38] for an S_1/T_1 transition in the range 10^{-6} to 10^{-11} s) except for those systems where the spin−orbit coupling (SOC) is large (like transition metals). However, upon excitation to higher vibrational energies, the possibility of population of the T_1 state cannot be disregarded. It could be argued that the main interaction underlying the formation of the triplet state (T_1) after excitation to the first low-lying singlet excited state (S_1), the SOC, is not fast enough to compete with the nonradiative deactivation process mediated by a conical intersection. This may initially be thought to be due to the usually low values of the SOC obtained for polyenes, like the system studied here, when compared with other systems, where the SOC is a strong interaction that cannot be neglected in the study of reactive processes. Were this the case, the time needed for the transition from the S_1 to the T_1 state would be very long compared with the fast time scale proposed for the early events of the trans−cis isomerization reaction. However, when computing the rate constant for the ISC process using the Fermi golden rule approach (see eq 1), different factors contribute to the efficiency of ISC. One is, as already mentioned, the value of the SOC term.

$$k_{i\to f} = \frac{2\pi}{\hbar}\sum_{\{|f\rangle\}} |\langle i|\hat{H}'_{\mathrm{SO}}|f\rangle|^2 \delta(E_i^0 - E_f^0) \qquad (1)$$

The other one is the density of states, ρ_E. Thus, in order to determine the possible coexistence of a triplet deactivation channel, we have to analyze whether in the experimental conditions a high density of states is available (it is clear that the number of states that obey the resonance or near resonance condition will be larger provided that an excess of energy exists in the system, like the experimental conditions of Lee et al.[17]) and also determine the value of the SOC term. It is in the evaluation of this term that some care must be taken. As has been recently shown,[39] the vibronic contribution to the SOC (see eq 2) can produce an important effect (of several orders of magnitude in molecules of moderate size[39]) in the nonradiative relaxation mediated by a S/T crossing. Both aspects, the density of states available at the experimental conditions and the SOC value including the first-order vibrational term,

$$\langle i, v|\hat{H}'_{\mathrm{SO}}|f, v'\rangle = \langle i|\hat{H}'_{\mathrm{SO}}|f\rangle|_{q_0=0}\langle v|v'\rangle + \sum_k \left(\frac{\partial}{\partial_{q_k}}\langle i|\hat{H}'_{\mathrm{SO}}|f\rangle\right)_{q_0=0}\langle v|q_k|v'\rangle + O(|q|^2) \qquad (2)$$

will contribute to increase the value of $k_{i\to f}$ giving rise to a fast intersystem crossing process. It is interesting to note that, when the energetic levels lie close in energy, the overlap between the vibrational wave functions will be non-negligible, with an important contribution of the Franck−Condon factors. Moreover, in the region of the MEP where a near energetic degeneracy between S_1 and T_1 exists, the molecule is twisted, and therefore, the out-of-plane deformations will increase the SOC coupling between $\pi \to \pi^*$ states through the second term in eq 2. This competitive process could be even more important inside the protein, where a high ρ_E exists in the region of ISC. Experimental monitoring of the formation of a putative triplet species[40] would be highly desirable to test the validity and generality of this proposal, particularly in the protein environment. However, it has to be stressed that population of the triplet state would be a process leading to a decrease in the efficiency of the protein to carry out its sensory role, so the impact of this putative competitive deactivation channel in the natural photochemical reaction has to be minimized in favor of the trans-to-cis isomerization one. This can be accomplished by turning the region around **M2** into a conical intersection seam, as proposed in ref 6.

3.3. QTAIM Analysis of the Excited States. Table 3 contains the most significant structural indicators for the isomerizing double bond at all of the significant equilibrium

Table 3. Relevant Structural Information [Eigenvalues of the Hessian of the Density (λ_1, λ_2, λ_3), Ellipticity (ε), Value of the Density at the Critical Point (ρ_c), and Value of the Laplacian of the Density at the Critical Point ($\nabla^2\rho_c$)] Obtained Using QTAIM for the Isomerizing Double Bond in All of the Equilibrium Structures Located along the Reaction Path

structure	λ_1[a]	λ_2[a]	λ_3[a]	ε	ρ_c[a]	$\nabla^2\rho_c$[a]
GS	-7.51×10^{-1}	-5.97×10^{-1}	2.01×10^{-1}	2.57×10^{-1}	3.34×10^{-1}	-1.15×10^{0}
M1	-6.45×10^{-1}	-5.40×10^{-1}	2.60×10^{-1}	1.96×10^{-1}	2.99×10^{-1}	-9.24×10^{-1}
TS	-5.65×10^{-1}	-5.18×10^{-1}	2.93×10^{-1}	9.10×10^{-2}	2.75×10^{-1}	-7.91×10^{-1}
M2	-5.58×10^{-1}	-5.28×10^{-1}	2.84×10^{-1}	5.62×10^{-2}	2.78×10^{-1}	-8.03×10^{-1}

[a] Values are given in au.

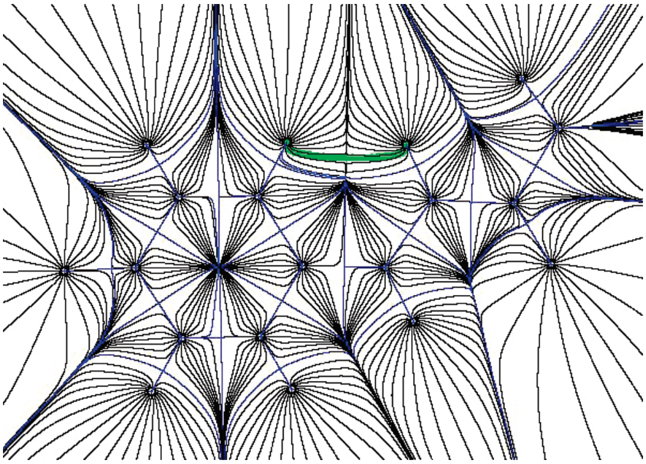

Figure 4. Plot of the gradient field lines of the electronic density (ρ) for the **M1** intermediate. The green line is the bond path of the H−H bonding interaction.

structures located for this process obtained with the QTAIM method (see the Supporting Information for a brief description of their meaning). As shown in Table 3, the decrease in the values of the ellipticity (ε) and the density (ρ_c) at the bond critical point as well as the negative values of the laplacian of the density ($\nabla^2\rho_c$) at the bond critical point are consistent with a mechanism in which the covalent C_7-C_8 bond modifies its character from double-like to single-like (see Supporting Information). The weakening of the isomerizing double bond in S_1 is expected to facilitate the trans-to-cis transformation.

A remarkable result is the appearance of a new ring critical point in **M1** as a consequence of the formation of a H−H bond. Accordingly, **M1** displays the bonding pattern depicted in Figure 4. The energetic stabilization created by the formation of this bonding interaction in this planar structure is estimated to be about 3−4 kcal/mol,[41] which is on the same order or magnitude of the energy stabilization of this minimum compared to **TS** and seems to indicate that it is associated with the existence of a small barrier for the process in vacuo. It is interesting to note that such a kind of planar structure is not found in the S_1 state of the protein as a consequence of the steric restrictions existing in the protein binding pocket, which forces the chromophore to adopt a slightly bandy structure.[12] This distortion from planarity in the protein environment will induce a chromophore structure where the hydrogen atoms involved in the H−H bond will move further away. As a result, it is expected that the stabilization generated through this bonding interaction will at least decrease or even disappear, and the S_1 minimum in the protein (equivalent to **M1**) can then become a shallow one. This may ultimately lead to a faster process due to the decrease (or even disappearance) of the barrier in the lowest-lying excited state. Such a kind of profile is also present in other proteins that perform a similar role.[23] Thus, the PYP protein not only would act as a shield avoiding the interaction of the solvent with the chromophore,[36] but it could also modulate the S_1 profile, improving the efficiency of the mechanism when the process takes place with a moderate excess of energy, which should be the case under natural conditions.

4. Conclusions

We have analyzed the excited state isomerization process of a model of the PYP chromophore in vacuo combining the energetic analysis based on the MEP approach with the QTAIM theory at the CASPT2/CASSCF multiconfigurational level. We have shown that the isomerization process through direct twisting of the C_7-C_8 double bond leads to a reaction profile with a small barrier in the excited state. This barrier could in part be originated by the formation of a prereactive planar intermediate characterized by the existence of a bonding H−H interaction that contributes to enhancing its energetic stability. This behavior is not expected to be present at the same extent in the PYP where the steric interactions existing in the protein binding pocket will prevent the chromophore of adopting a planar structure, pointing to one possible role of the protein in modulating the efficiency of this reaction. We have also analyzed the role of the triplet state in the general reactive process. The possibility of competition between the population of the triplet state and the trans/cis isomerization process has been critically discussed, and new experimental studies are suggested. A possible role of the PYP protein in the enhancement of the isomerization process efficiency has also been proposed. We hope the results outlined will be helpful not only for a better understanding of the photochemistry of PYP but also for a general understanding of photochemical processes in biological photoreceptors.

Acknowledgment. Financial support is acknowledged from MEC/MICINN/FEDER projects CTQ2007-61260 and CSD2007-0010 Consolider-Ingenio in Molecular Nanoscience, contract Juan de la Cierva (PBC), and FPU grant (DRS), from Generalitat Valenciana, project GVPRE/2008/059, and from Universitat de València, project UV-EQUIP09-5764. The authors wish to thank Prof. M. Merchán and Prof. M. Olivucci for helpful discussions.

Note Added after ASAP Publication. This article was released ASAP on September 24, 2009 with minor errors in the Results and Discussion section. The correct version was posted on September 29, 2009.

Supporting Information Available: Further details of the theoretical methods used, geometries, absolute energies, and MPA and BTA charges for all of the stationary structures located. This information is available free of charge via the Internet at http://pubs.acs.org/.

References

(1) Hellingwerf, K. J.; Hendriks, J.; Gensch, T. *J. Phys. Chem. A* **2003**, *107*, 1082, and references therein.

(2) Cusanovich, M. A.; Meyer, T. E. *Biochemistry* **2003**, *42*, 4759, and references therein.

(3) Molina, V.; Merchán, M. *Proc. Natl. Acad. Sci. U. S. A.* **2001**, *98*, 4299–4304.

(4) Thompson, M. J.; Bashford, D.; Noodleman, L.; Getzoff, E. D. *J. Am. Chem. Soc.* **2003**, *125*, 8186–8194.

(5) Yamada, A.; Ishikura, T.; Yamato, T. *Proteins* **2004**, *55*, 1063–1069.

(6) Groenhof, G.; Bouxin-Cademartory, M.; Hess, B.; de Visser, S. P.; Berendsen, H. J. C.; Olivucci, M.; Mark, A. E.; Robb, M. A. *J. Am. Chem. Soc.* **2004**, *128*, 4228–4233.

(7) Groenhof, G.; Schäfer, L. V.; Boggio-Pasqua, M.; Grubmüller, H.; Robb, M. A. *J. Am. Chem. Soc.* **2008**, *130*, 3250–3251.

(8) Heyne, K.; Mohammed, O. F.; Usman, A.; Dreyer, J.; Nibbering, E. T. J.; Cusanovich, M. A. *J. Am. Chem. Soc.* **2005**, *127*, 18100–18106.

(9) Matsuura, A.; Sato, H.; Houjou, H.; Saito, S.; Hayashi, T.; Sakurai, M. *J. Comput. Chem.* **2006**, *27*, 1623–1630.

(10) Gromov, E. V.; Burghardt, I.; Köppel, H.; Cederbaum, L. S. *J. Am. Chem. Soc.* **2007**, *129*, 6798–6806.

(11) Gromov, E. V.; Burghardt, I.; Hynes, J. T.; Köppel, H.; Cederbaum, L. S. *J. Photochem. Photobiol. A* **2007**, *190*, 241–257.

(12) Coto, P. B.; Martí, S.; Oliva, M.; Olivucci, M.; Merchán, M.; Andrés, J. *J. Phys. Chem. B* **2008**, *112*, 7153–7156.

(13) Ko, C.; Virshup, A. M.; Martínez, T. J. *Chem. Phys. Lett.* **2008**, *460*, 272–277.

(14) van Wilderen, L. J. G. W.; van der Horst, M. A.; van Stokkum, I. H. M.; Hellingwerf, K. J.; van Grondelle, R.; Groot, M. L. *Proc. Natl. Acad. Sci. U. S. A.* **2006**, *103*, 15050–15055.

(15) Changenet-Barret, P.; Plaza, P.; Martin, M. M.; Chosrowjan, H.; Taniguchi, S.; Mataga, N.; Imamoto, Y.; Kataoka, M. *Chem. Phys. Lett.* **2007**, *434*, 320–325.

(16) See, among others: (a) He, Z.; Martin, C. H.; Birge, R.; Freed, K. F. *J. Phys. Chem. A* **2000**, *104*, 2939–2952. (b) Sergi, A.; Grüning, M.; Ferrario, M.; Buda, F. *J. Phys. Chem. B* **2001**, *105*, 4386–4391. (c) Yoda, M.; Houjou, H.; Inoue, Y.; Sakurai, M. *J. Phys. Chem. B* **2001**, *105*, 9887–9895. (d) Yamada, A.; Yamamoto, S.; Yamato, T.; Kakitani, T. *THEOCHEM* **2001**, *536*, 195–201. (e) Unno, M.; Kumauchi, M.; Sasaki, J.; Tokunaga, F.; Yamauchi, S. *Biochemistry* **2002**, *41*, 5668–5674. (f) Ko, C.; Levine, B.; Toniolo, A.; Manohar, L.; Olsen, S.; Werner, H.-J.; Martínez, T. J. *J. Am. Chem. Soc.* **2003**, *125*, 12710–12711. (g) Toniolo, A.; Granucci, G.; Martínez, T. J. *J. Phys. Chem. A* **2003**, *107*, 3822–3830. (h) Unno, M.; Kumauchi, M.; Sasaki, J.; Tokunaga, F.; Yamauchi, S. *J. Phys. Chem. B* **2003**, *107*, 2837–2845. (i) Chosrowjan, H.; Taniguchi, S.; Mataga, N.; Unno, M.; Yamauchi, S.; Hamada, N.; Kumauchi, M.; Tokunaga, F. *J. Phys. Chem. B* **2004**, *108*, 2686–2698. (j) Premvardhan, L. L.; Buda, F.; van der Horst, M. A.; Lührs, D. C.; Hellingwerf, K. J.; van Grondelle, R. *J. Phys. Chem. B* **2004**, *108*, 5138–5148. (k) El-Mashtoly, S. F.; Unno, M.; Kumauchi, M.; Hamada, N.; Fujiwara, K.; Sasaki, J.; Imamoto, Y.; Kataoka, M.; Tokunaga, F.; Yamauchi, S. *Biochemistry* **2004**, *43*, 2279–2287. (l) Li, Q.-S.; Fang, W.-H. *Chem. Phys.* **2005**, *313*, 71–75. (m) Gromov, E. V.; Burghardt, I.; Köppel, H.; Cederbaum, L. S. *J. Phys. Chem. A* **2005**, *109*, 4623–4631. (n) de Groot, M.; Buma, W. J.; Gromov, E. V.; Burghardt, I.; Köppel, H.; Cederbaum, L. S. *J. Chem. Phys.* **2006**, *125*, 204303(17). (o) Unno, M.; Kumauchi, M.; Tokunaga, F.; Yamauchi, S. *J. Phys. Chem. B* **2007**, *111*, 2719–2726. (p) Muguruza González, E.; Guidoni, L.; Molteni, C. *Phys. Chem. Chem. Phys.* **2009**, *11*, 4556–4563. (q) Rocha-Rinza, T.; Christiansen, O.; Rajput, J.; Gopalan, A.; Rahbek, D. B.; Andersen, L. H.; Bochenkova, A. V.; Granovsky, A. A.; Bravaya, K. B.; Nemukhin, A. V.; Christiansen, K. L.; Brøndsted Nielsen, M. *J. Phys. Chem. A* **2009**, *113*, 9442–9449.

(17) Lee, I.-R.; Lee, W.; Zewail, A. H. *Proc. Natl. Acad. Sci. U. S. A.* **2006**, *103*, 258–262.

(18) Bader, R. F. W. *Atoms in Molecules: A Quantum Theory*; Oxford University Press: New York, 1994; pp 1−438.

(19) Roos, B. O.; Fülscher, M. P.; Malmqvist, P.-Å; Serrano-Andrés, L.; Pierloot, K.; Merchán, M. *Adv. Chem. Phys.* **1996**, *93*, 219–331.

(20) Coto, P. B.; Strambi, A.; Ferré, N.; Olivucci, M. *Proc. Natl. Acad. Sci. U. S. A.* **2006**, *103*, 17154–17159.

(21) Coto, P. B.; Sinicropi, A.; De Vico, L.; Ferré, N.; Olivucci, M. *Mol. Phys.* **2006**, *104*, 983–991.

(22) Strambi, A.; Coto, P. B.; Ferré, N.; Olivucci, M. *Theor. Chem. Acc.* **2007**, *118*, 185–191.

(23) Strambi, A.; Coto, P. B.; Frutos, L. M.; Ferré, N.; Olivucci, M. *J. Am. Chem. Soc.* **2008**, *130*, 3382–3388.

(24) Coto, P. B.; Strambi, A.; Olivucci, M. *Chem. Phys.* **2008**, *347*, 483–491.

(25) El-Gezawy, H.; Rettig, W.; Danel, A.; Jonusauskas, G. *J. Phys. Chem. B* **2005**, *109*, 18699–18705.

(26) Pierloot, K.; Dumez, B.; Widmark, P. O.; Roos, B. O. *Theor. Chim. Acta* **1995**, *90*, 87–114.

(27) Forsberg, N.; Malmqvist, P.-Å. *Chem. Phys. Lett.* **1997**, *274*, 196–204.

(28) Karlström, G.; Lindh, R.; Malmqvist, P.-Å.; Roos, B. O.; Ryde, U.; Veryazov, V.; Widmark, P.-O.; Cossi, M.; Schimmelpfennig, B.; Neogrady, P.; Seijo, L. *Comput. Mater. Sci.* **2003**, *28*, 222–239.

(29) Biegler-König, F. W.; Bader, R. F. W.; Ting-Hua, T. *J. Comput. Chem.* **1982**, *3*, 317–328.

(30) Cassam-Chenaï, P.; Jayatilaka, D. *Theor. Chem. Acc.* **2001**, *105*, 213–218.

(31) Popelier, P. L. A. *Struct. Bonding (Berlin)* **2005**, *115*, 1–56.

(32) Wang, Y.-G.; Wiberg, K. B.; Werstiuck, N. H. *J. Phys. Chem. A* **2007**, *111*, 3592–3601.

(33) Bader, R. F. W.; Matta, C. F. *J. Phys. Chem. A* **2004**, *108*, 8385–8394.

(34) Sommerfeld, T.; Riss, U. V.; Meyer, H.-D.; Cederbaum, L. S.; Engels, B.; Suter, H. U. *J. Phys. B: At., Mol. Opt. Phys.* **1998**, *31*, 4107–4122.

(35) Epifanovski, E.; Polyakov, I.; Grigorenko, B.; Nemukhin, A.; Krylov, A. I. *J. Chem. Theor. Comput.* **2009**, *5*, 1895–1906.

(36) Nielsen, I. B.; Boyé-Péronne, S.; El Ghazaly, M. O. A.; Kristensen, M. B.; Brøndsted Nielsen, S.; Andersen, L. H. *Biophys. J.* **2005**, *89*, 2597–2604.

(37) Filippi, C.; Zaccheddu, M.; Buda, F. *J. Chem. Theory Comput.* **2009**, *5*, 2074–2087.

(38) Klessinger, M.; Michl, J. *Excited States and Photochemistry of Organic Molecules*; VCH Publishers Inc.: New York, 1995; p 247.

(39) Tatchen, J.; Gilka, N.; Marian, C. M. *Phys. Chem. Chem. Phys.* **2007**, *9*, 5029–5221.

(40) It is interesting to note that data of ref 17 show the existence of a long-lived (58 ps) intermediate that could match with triplet state population.

(41) Martín-Pendás, A.; Francisco, E.; Blanco, M. A.; Gatti, C. *Chem.—Eur. J.* **2007**, *13*, 9362–9371.

CT900401Z

J. Chem. Theory Comput. **2009,** *5,* 3039–3048 **3039**

JCTC Journal of Chemical Theory and Computation

Theoretical Determination of the Dissociation Energy of Molecular Hydrogen

Konrad Piszczatowski,[†] Grzegorz Łach,[†,||] Michal Przybytek,[†,‡] Jacek Komasa,[¶]
Krzysztof Pachucki,[§] and Bogumil Jeziorski*[,†]

Faculty of Chemistry, University of Warsaw, Pasteura 1, 02-093, Warsaw, Poland,
Center for Theoretical and Computational Chemistry, University of Oslo,
P.O. Box 1033 Blindern, N-0315 Oslo, Norway, Faculty of Chemistry, A. Mickiewicz
University, Grunwaldzka 6, 60-780 Poznań, Poland, and Institute of Theoretical
Physics, University of Warsaw, Hoża 69, 00-681 Warsaw, Poland

Received July 28, 2009

Abstract: The dissociation energy of molecular hydrogen is determined theoretically with a careful estimation of error bars by including nonadiabatic, relativistic, and quantum electrodynamics (QED) corrections. The relativistic and QED corrections were obtained at the adiabatic level of theory by including all contributions of the order α^2 and α^3 as well as the major (one-loop) α^4 term, where α is the fine-structure constant. The computed α^0, α^2, α^3, and α^4 components of the dissociation energy of the H_2 isotopomer are 36 118.7978(2), −0.5319(3), −0.1948(2), and −0.0016(8) cm^{-1}, respectively, while their sum amounts to 36 118.0695(10) cm^{-1}, where the total uncertainty includes the estimated size (±0.0004 cm^{-1}) of the neglected relativistic nonadiabatic/recoil corrections. The obtained theoretical value of the dissociation energy is in excellent agreement with the most recent experimental determination 36 118.0696(4) cm^{-1} [J. Liu et al. *J. Chem. Phys.* **2009**, *130*, 174 306]. This agreement would have been impossible without inclusion of several subtle QED contributions which have not been considered, thus far, for molecules. A similarly good agreement is observed for the leading vibrational and rotational energy differences. For the D_2 molecule we observe, however, a small disagreement between our value 36 748.3633(9) cm^{-1} and the experimental result 36 748.343(10) cm^{-1} obtained in a somewhat older and less precise experiment [Y. P. Zhang et al. *Phys. Rev. Lett.* **2004**, *92*, 203003]. The reason of this discrepancy is not known.

1. Introduction

Theoretical determination of the dissociation energy D_0 of the simplest, prototypical chemical bond in the hydrogen molecule has a long history. It started in 1927, very shortly after the discovery of quantum mechanics, by the work of Heitler and London[1] who approximately solved the Schrödinger equation for two electrons in the Coulomb field of two protons and found that this system is stable against the dissociation to two hydrogen atoms. The approximate dissociation energy they obtained represented only about 60% of the observed value, but it could be argued that by virtue of the variational principle this was only a lower bound and, consequently, that the new quantum theory satisfactorily explained the hitherto puzzling stability of the chemical bond between electrically neutral atoms. A few years later, James and Coolidge[2,3] computed a much better, 13-term wave function depending explicitly on the interelectron distance and found that $D_0 = 4.454 \pm 0.013$ eV − a value within error bars of the experimental value 4.46 ± 0.04 eV available

---

* Corresponding author. E-mail: jeziorsk@chem.uw.edu.pl.

[†] Faculty of Chemistry, University of Warsaw.

[||] Current address: Institute of Physics, University of Heidelberg, Philosophenweg 12, 69120 Heidelberg, Germany.

[‡] Center for Theoretical and Computational Chemistry, University of Oslo.

[¶] Faculty of Chemistry, A. Mickiewicz University.

[§] Institute of Theoretical Physics, University of Warsaw.

10.1021/ct900391p CCC: $40.75

at that time[4] (obtained from the heat of dissociation) and within about 0.5% of the present day value of 4.478 eV. This was an amazing achievement for a computation carried out and checked by, as the authors of ref. 2 put it, "an experienced computer".

When the electronic computers became available Kolos and Wolniewicz[5] extended the work of James and Coolidge to much longer wave function expansions (up to about 100 terms) and developed methods and codes to account for the coupling of the electronic and the nuclear motion and for the effects of relativity. The theoretical dissociation energy obtained by Kolos and Wolniewicz $D_0 = 36\,117.4$ cm^{-1} [6,7] could be confronted with the most accurate experimental determination from Herzberg and Monfils amounting to $36\,113.6 \pm 0.3$ cm^{-1}.[8] Since, by virtue of the variational principle, the theoretical result can be viewed as a lower bound, both of these values can be correct only if the quantum mechanics fails to describe the dissociation of the H−H bond with quantitative accuracy. Fortunately, new experimental determinations from Herzberg[9] ($36\,116.3$ cm^{-1} $< D_0 <$ $36\,118.3$ cm^{-1}) and Stwalley[10] ($D_0 = 36\,118.6 \pm 0.5$ cm^{-1}) resolved this difficulty in favor of theory. This development demonstrated that the Schrödinger equation when solved accurately and corrected for small effects of relativity can predict the molecular energy levels with very high precision and, therefore, it laid a foundation for the current faith in the quantitative predictive power of quantum chemistry.

Further theoretical[11−13] and experimental[14−16] work has reduced the discrepancy between theory and experiment to several hundredths of a cm^{-1}. Very recently Liu et al.[17] described a hybrid, experimental−theoretical determination of D_0 based on several transition frequency measurements[17−20] and theoretical calculations of the energy levels of the H_2^+ ion.[21−24] The dissociation energy $D_0 = 36\,118.06962$ cm^{-1} determined in this way[17] has been reported with an uncertainty of ± 0.00037 cm^{-1} − almost 2 orders of magnitude smaller than that of the previous most accurate determination $D_0 = 36\,118.062 \pm 0.010$ cm^{-1} of Zhang et al.[16] The best available theoretical predictions of $36\,118.049$ cm^{-1} from Kolos and Rychlewski[12] and $36\,118.069$ cm^{-1} from Wolniewicz[13] are significantly less precise and have been reported without any error bar estimates. Both of these predictions involve an incomplete treatment of α^3 quantum electrodynamics (QED) corrections,[25] so it is not clear if the perfect agreement between the experiment and Wolniewicz's calculation is not fortuitous. In fact, Wolniewicz has concluded his paper[13] with the remark that the main uncertainty in his dissociation energy is due to the neglected QED effects. Specifically, he has neglected the α^3 contributions, resulting from two-photon exchanges between electrons—the so-called Araki−Sucher effect[26,27]—and used a simple approximation of the Bethe logarithm,[28,29] which was shown to be rather inaccurate when applied to H_2^+.[30]

In this communication, we present a complete calculation of the α^3 QED contribution to D_0 and give an approximate value of the next α^4 term in the fine-structure constant expansion of D_0. We have also recomputed the nonrelativistic and α^2 relativistic parts of D_0, paying special attention to an estimation of the error bars for all evaluated contributions. We hope that this estimation will enable a more meaningful comparison of theoretical predictions with the newest experimental result.[17]

2. Method

For molecules with light nuclei, the most convenient theoretical framework for the description of molecular properties is the expansion in powers of the fine-structure constant α (in our calculations we assumed that $\alpha = 1/137.0359997$, cf. ref 31). Specifically, the molecular or atomic energy levels needed to compute D_0 can be obtained from the expansion:

$$E = E^{(0)} + \alpha^2 E^{(2)} + \alpha^3 E^{(3)} + \alpha^4 E^{(4)} + \cdots \tag{1}$$

where $E^{(0)}$ is the nonrelativistic energy, i.e., an eigenvalue of the Schrödinger equation for the electrons and nuclei (with the center-of-mass motion separated out), $\alpha^2 E^{(2)}$ is the expectation value of the Breit−Pauli Hamiltonian[25] with the nonrelativistic wave function (assuming the molecular center of mass at rest), $\alpha^3 E^{(3)}$ is the leading QED correction,[25−27] and $\alpha^4 E^{(4)}$ collects all relativistic and QED corrections proportional to α^4 [32,33] (when expressed in atomic units).

2.1. Nonrelativistic Energy. The nonrelativistic approximation $D_0^{(0)}$ to D_0 can be obtained variationally by minimization of the expectation value of the complete four-particle Hamiltonian with an appropriate trial function.[33,34] To have better error control and to generate wave functions and potentials needed in QED calculations, we adopted, however, a stepwise approach and computed D_0 as the sum:

$$D_0^{(0)} = D_0^{\mathrm{BO}} + \delta D_0^{\mathrm{ad}} + \delta D_0^{\mathrm{na}} \tag{2}$$

where D_0^{BO} is the result of standard Born−Oppenheimer calculation, δD_0^{ad} is the adiabatic (diagonal Born−Oppenheimer) correction,[36,37] and δD_0^{na} is a (very small) nonadiabatic correction defined essentially as the difference between $D_0^{(0)}$ and the sum of D_0^{BO} and δD_0^{ad}.

The Born−Oppenheimer potential $V(R)$ needed in the computation of D_0^{BO}, δD_0^{ad}, and δD_0^{na} and of the relativistic/QED corrections was represented in the following form:

$$V(R) = e^{-\beta R^2 - \gamma R}\left(R^{-1} + \sum_{n=0}^{16} b_n R^n\right) + \left(\sum_{n=0}^{2} a_n R^n + a_3 R^{5/2}\right) e^{-2R} - \sum_{n=6}^{26} f_n(\eta R)\frac{C_n}{R^n} \tag{3}$$

where R is the internuclear distance, C_6, ..., C_{26} are van der Waals coefficients fixing the large R asymptotics of $V(R)$, and $f_n(x) = 1 - e^{-x}(1 + x + x^2/2! + \cdots + x^n/n!)$ is the Tang−Toennies damping function.[38] The asymptotic coefficients C_6, C_8, C_{10}, C_{11}, ..., C_{26} (C_7, C_9 vanish) were taken from the work of Mitroy and Ovsiannikov[39] with the full 13 digit accuracy (we recomputed the five leading coefficients C_6, C_8, C_{10}, C_{11}, and C_{12} obtaining the same results as the ones reported in ref 39). Accurate values of the asymptotic C_n coefficients are available also for $n > 26$,[38,39] but we found that their inclusion in the last term of eq 3 did

Table 1. Parameters Determining the Analytic Form, eq 3, of the Born−Oppenheimer Potential for H_2[a]

b_0	−246.146616782077	b_{11}	19.870410304616
b_1	−122.890180187858	b_{12}	−7.564322211157
b_2	−162.863251799668	b_{13}	2.089842241100
b_3	−67.028576007896	b_{14}	−0.400842621727
b_4	−58.308248409124	b_{15}	0.047594467110
b_5	3.483076932756	b_{16}	−0.002719925287
b_6	−52.461380739836	β	0.584358199608
b_7	59.254861689279	γ	3.338428574260
b_8	−70.780756953312	η	2.561607545
b_9	59.254901002422	a_2	5.258436256979
b_{10}	−39.529747868821	a_3	−1.499067595467

[a] All parameters are in atomic units.

not lead to further improvement of the fit [with the fixed form of the short-range part of $V(R)$]. It should be noted that the values of C_{24}, C_{25}, and C_{26} reported later by Ovsiannikov and Mitroy[40] with a smaller number of digits cannot be used in our fit.

The three nonlinear parameters β, γ, η and 19 linear ones a_2, a_3, b_0, ..., b_{16} were obtained by least-squares fitting the right hand side (rhs) of eq 3 to the energies computed by Sims and Hagstrom[41] for 47 internuclear distances R ranging from 0.4 to 6.0 bohr. In the vicinity of the minimum of the potential well, these energies have an error on the order of 10^{-6} cm^{-1},[41] while for $R = 6.0$, where the basis set used by Sims and Hagstrom is least adequate, the error is smaller than 2×10^{-5} cm^{-1}.[42] For 27 distances outside the range covered by Sims and Hagstrom, we used values obtained by Cencek[42] using a 1200-term fully optimized Gaussian geminal basis set. These values have an error smaller than 2×10^{-5} cm^{-1}.[42] The linear parameters a_0, a_1 were constrained by the relations:

$$\begin{aligned} a_0 &= E_{\mathrm{He}} - 2E_{\mathrm{H}} - b_0 + \gamma \\ a_1 &= 2a_0 + \gamma b_0 - b_1 + \beta - \frac{\gamma^2}{2} + \sum_{n=6}^{26} \frac{C_n \eta^{n+1}}{(n+1)!} \end{aligned} \tag{4}$$

required to ensure the right behavior of $V(R)$ at small distances:

$$V(R) = \frac{1}{R} + E_{\mathrm{He}} - 2E_{\mathrm{H}} + \boldsymbol{O}(R^2) \tag{5}$$

with $E_{\mathrm{He}} = -2.903724377034119$ and $E_{\mathrm{H}} = -0.5$ being atomic energies of helium and hydrogen (assuming infinite nuclear mass). The error of our fit is 5×10^{-5} cm^{-1} at the bottom of the potential well and is even smaller at larger distances. The fit parameters obtained by us are listed in Table 1. A code generating $V(R)$ is available upon request.

The dissociation energy D_0^{BO} computed using the analytic Born−Oppenheimer potential generated in this way is 36 112.59273 cm^{-1} (using the conversion factor 1 hartree = 219 474.631 37 cm^{-1}[31]). We estimate that the error of this value is 0.00010 cm^{-1}. Since the potential points have substantially smaller inaccuracies and since the numerical integration of the radial Schrödinger equation with an analytic potential does not introduce a significant error, most of the uncertainty of D_0^{BO} results from the fitting procedure.

Accurate values of the adiabatic $\delta D_0^{\mathrm{ad}} = 5.77111$ cm^{-1} and the nonadiabatic $\delta D_0^{\mathrm{na}} = 0.43391$ cm^{-1} corrections to D_0^{BO} were recently computed by two of us[43] using a perturbation method formulated in ref 44 (the proton mass $m_{\mathrm{p}} = 1\,836.15267247\ m_{\mathrm{e}}$ was assumed[31] in obtaining these numbers). The computation of the adiabatic correction reported in refs 43 and 44 was carried out using a novel, very stable numerical procedure,[44] avoiding entirely the cumbersome differentiation of the electronic wave function. With basis sets ranging from 600 to 1800 fully optimized Gaussian geminals, the accuracy of at least five significant figures for δD_0^{ad} was achieved. Therefore, we can assume that the error of δD_0^{ad} is smaller than 0.00010 cm^{-1}. Also all five figures of the nonadiabatic correction δD_0^{na} appear to be converged with regard to the extension of the basis set. However, the fourth- and higher-order effects neglected in the perturbation procedure of ref 43 may be of the order of 0.0001−0.0002 cm^{-1}. In fact, the value $\delta D_0^{\mathrm{na}} = 0.43391$ cm^{-1} differs from the earlier, methodologically very different, calculation of Wolniewicz by 0.0002 cm^{-1}. Therefore, we assign the uncertainty of 0.00020 cm^{-1} to the value $\delta D_0^{\mathrm{na}} = 0.43391$ cm^{-1}.

Adding D_0^{BO}, δD_0^{ad}, and δD_0^{na}, we find that the nonrelativistic dissociation energy amounts to $D_0^{(0)} = 36\,118.7978(2)$ cm^{-1}, where the uncertainty (given in the parentheses as the error in the last digit) is calculated by quadratically adding the errors of summed contributions. Our result for $D_0^{(0)}$ is consistent with the value 36 118.79774(1) cm^{-1} obtained very recently[45] using 10 000 extensively optimized Gaussians (and more than a year of massively parallel computing). The accuracy achieved in ref 45, however impressive, is not relevant for our purposes since the experimental uncertainty of D_0 and, even more so, the uncertainty of the relativistic and QED contributions to D_0 are 2 orders of magnitude larger than the error of the large-scale variational calculations of ref 45.

2.2. Lowest-Order Relativistic Contribution. The lowest-order, α^2 relativistic correction to the nonrelativistic energy is expressed by the expectation value of the Breit−Pauli Hamiltonian[46,47] over the nonrelativistic wave function ψ. When the electrons and nuclei are in their singlet states and when the terms containing the proton charge radius and the so-called recoil terms,[48,49] (of the order of $(m_{\mathrm{e}}/m_{\mathrm{p}})^n\alpha^2$, $n = 1, 2, 3$) are neglected, this correction is given by the sum of four terms:

$$E^{(2)} = -\frac{1}{4}\langle \mathbf{p}_1^4 \rangle + 2\pi\langle \delta(\mathbf{r}_{1a}) \rangle + \pi\langle \delta(\mathbf{r}_{12}) \rangle - \frac{1}{2}\left\langle \mathbf{p}_1 \frac{1}{r_{12}} \mathbf{p}_2 + \mathbf{p}_1 \cdot \mathbf{r}_{12} \frac{1}{r_{12}^3} \mathbf{r}_{12} \cdot \mathbf{p}_2 \right\rangle \tag{6}$$

referred to successively as the mass−velocity, the one- and two-electron Darwin, and the Breit contributions (the contact spin−spin interaction is included in the two-electron Darwin term). In eq 6, $\mathbf{p}_i$ is the momentum operator for the ith electron, $\mathbf{r}_{1a}$ is the vector pointing from nucleus a to electron 1, $\mathbf{r}_{12}$ is the vector pointing from electron 2 to electron 1, and $\delta(\mathbf{r})$ is the three-dimensional Dirac distribution. We made use of the fact that the wave function ψ employed to compute the expectation values is symmetric in the spatial electronic and nuclear coordinates. When computing the expectation values in eq 6, we used the adiabatic function $\psi_{\mathrm{ad}} = \chi(R)\psi_{\mathrm{el}}(\mathbf{r}_1, \mathbf{r}_2; \mathbf{R})$, where $\psi_{\mathrm{el}}(\mathbf{r}_1, \mathbf{r}_2; \mathbf{R})$ is the electronic wave function depending parametrically on the vector $\mathbf{R}$ joining the nuclei, and $\chi(R)$ is the solution of the radial Schrödinger equation with the potential $V(R)$ plus the adiabatic correction to $V(R)$.[44] With this approximation for ψ, the expectation values in eq 6 are obtained by averaging the R dependent electronic expectation values, e.g., $2\pi\langle\psi_{\mathrm{el}}|\delta(\mathbf{r}_{1a})|\psi_{\mathrm{el}}\rangle \equiv D_1(R)$ with the weight function given by the square of $\chi(R)$. This adiabatic procedure is justified since, as discussed in Section 3, the neglected cross relativistic−nonadiabatic terms can be expected to be of the order of $(m_e/m_p)\alpha^2$, and therefore, 3 orders of magnitude smaller than the relativistic correction of eq 6. The R dependent electronic expectation values corresponding to the four successive terms in eq 6 will be denoted by us as $P(R)$, $D_1(R)$, $D_2(R)$, and $B(R)$. These radial functions were computed by Wolniewicz[50] using the basis of Kolos and Wolniewicz.[51] They were tabulated[50] for 55 internuclear distances ranging from $R = 0.2$ to 12.0 bohr in the form of functions $\varepsilon_k(R)$ related to ours by $\varepsilon_1(R) = P(R)$, $\varepsilon_2 = B(R)$, $\varepsilon_4(R) = D_1(R) - D_2(R)$, $\varepsilon_5(R) = 2D_2(R)$.

We recomputed these radial functions using extensively optimized sets of Gaussian geminals and paying special attention[52] to larger internuclear separations. We also computed the constants determining the asymptotic behavior of $P(R)$, $D_1(R)$, and $B(R)$ at large R. The first three constants (at $1/R^6$, $1/R^8$, and $1/R^{10}$), fixing $P(R)$ and $D_1(R)$ at large R were already reported in ref 52 [$D_2(R)$ vanishes exponentially at large R].

For the Breit correction $B(R)$, we considered only the first two terms in the asymptotic expansion $B(R) = W_4R^{-4} + W_6R^{-6} + \cdots$. The constants W_4 and W_6 are given by the expressions:[53,54]

$$W_4 = -2\langle\varphi_0|z_{1a}z_{2b}\boldsymbol{R}_0p_{z1}p_{z2}|\varphi_0\rangle \tag{7}$$

and

$$\begin{aligned} W_6 \;=\; & -9\langle\varphi_0|(Q_2^0)_{1a}z_{2b}\boldsymbol{R}_0(z_{1a}p_{z1} + p_{z1}z_{1a})p_{z2}|\varphi_0\rangle \\ & -\frac{12}{5}\langle\varphi_0|z_{1a}z_{2b}\boldsymbol{R}_0[2r_{1a}^2p_{z1} - z_{1a}(\mathbf{r}_{1a}\cdot\mathbf{p}_1)]p_{z2}|\varphi_0\rangle \end{aligned} \tag{8}$$

where ϕ_0 is the product of atomic wave functions, $\boldsymbol{R}_0 = (\mathrm{H}_a + \mathrm{H}_b - E_a - E_b)^{-1}$ is the reduced resolvent for two noninteracting hydrogen atoms, z_{1a}, z_{2b}, p_{z1}, and p_{z2} are the z components of the vectors $\mathbf{r}_{1a}$, $\mathbf{r}_{2b}$, $\mathbf{p}_1$, and $\mathbf{p}_2$, and finally, $(Q_2^0)_{1a} = 1/2(3z_{1a}^2 - r_{1a}^2)$ is the quadrupole moment operator. We computed W_4 and W_6 using the spd part of the Dunning's one-electron Gaussian basis set of the sextuple-ζ quality with double augmentation, d-aug-cc-pV6Z.[55] The atomic orbitals and all the necessary integrals were obtained using the DALTON suite of codes.[56] The values of both coefficients were calculated using the sum-over-states technique with a code written especially for this purpose. All excited states resulting form the chosen basis set were included in the summation defining $\boldsymbol{R}_0$. We found that $W_4 = 0.4627(7)$ and $W_6 = 3.995(7)$ atomic units. The proposed error bars were determined by observing changes of the W_4 and W_6 values obtained with d-aug-cc-pV*XZ* bases, $X = \mathrm{T}$, Q, 5, and 6, and by making a comparison with the results computed using the alternative form of eqs 7 and 8 in which the linear momentum operators are replaced by operators corresponding to the Cartesian coordinates.[53,54]

Table 2. Electronic Bethe Logarithm, ln $K^{\mathrm{el}}(R)$, and the Electronic Expectation Values of $\delta(\mathbf{r}_{ia})$, $\delta(\mathbf{r}_{12})$, and $P(r_{12}^{-3})$ for H_2 as Functions of Internuclear Separation, R[a]

R	ln K^{el}	$\delta(\mathbf{r}_{ia})$	$\delta(\mathbf{r}_{12})$	$P(r_{12}^{-3})$
0.0	4.37016	3.62086	0.10635	0.98927
0.1	3.765	2.88530	0.10157	0.98082
0.2	3.526	2.28447	0.09137	0.96236
0.4	3.279	1.50399	0.06887	0.88474
0.6	3.1596	1.06778	0.05076	0.77747
0.8	3.09331	0.80828	0.03767	0.66964
1.0	3.05490	0.64410	0.02835	0.57115
1.1	3.04206	0.58427	0.02473	0.52685
1.2	3.03215	0.53496	0.02164	0.48593
1.3	3.02448	0.49397	0.01901	0.44828
1.4	3.01855	0.45967	0.01674	0.41430
1.5	3.01396	0.43079	0.01479	0.38169
1.6	3.01040	0.40636	0.01309	0.35199
1.7	3.00763	0.38565	0.01161	0.32500
1.8	3.00547	0.36805	0.01032	0.30005
1.9	3.00377	0.35309	0.00918	0.27685
2.0	3.00240	0.34040	0.00817	0.25544
2.2	3.00034	0.32062	0.00649	0.21731
2.4	2.99878	0.30686	0.00514	0.18412
2.6	2.99742	0.29779	0.00406	0.15552
2.8	2.99610	0.29243	0.00319	0.13036
3.0	2.99476	0.29000	0.00247	0.10847
3.5	2.99137	0.29236	0.00124	0.06613
4.0	2.98848	0.29997	0.00057	0.03881
4.5	2.98650	0.30722	0.00024	0.02277
5.0	2.98534	0.31220	0.00010	0.01390
5.5	2.98473	0.31510	0.00004	0.00903
6.0	2.98442	0.31667	0.00001	0.00625
7.0	2.98420	0.31788	0.00000	0.00347
8.0	2.98415	0.31819	0.00000	0.00219
10.0	2.98413	0.31829	0.00000	0.00107
12.0	2.98413	0.31831	0.00000	0.00061

[a] All values in atomic units.

Except for large distances, $R > 10$ bohr, our values of $P(R)$ and $D_1(R)$ agree very well with those of Wolniewicz, so we used Wolniewicz's values (available for a larger number of distances) in computing the averages $\langle P(R)\rangle$ and $\langle D_1(R)\rangle$. For $R > 10.0$ bohr, we used our values, which appear to agree somewhat better with the exact asymptotics. For $R > 12.0$, we applied the three-term (undamped) asymptotic expansion with the constants (at $1/R^6$, $1/R^8$, and $1/R^{10}$) published earlier by the three of us.[52] By observing the basis set convergence patterns and by comparing our values of $P(R)$ and $D_1(R)$ with those published by Wolniewicz, we estimate that the computed dissociation energy contributions due to the mass−velocity and one-electron Darwin terms, amounting to 4.4273 and −4.9082 cm^{-1}, respectively, have the uncertainty of 0.0002 cm^{-1} each.

For the two-electron Darwin term, we found that our values of $D_2(R)$, computed with a basis set of 1 200 fully optimized Gaussian geminals, are slightly different than those of Wolniewicz.[50] The observed basis set convergence pattern and the independent calculations of Cencek[42] suggest that our values, listed in Table 2, are more accurate (especially at smaller values of R), and we used them to calculate

$\langle D_2(R)\rangle$. We estimate that the dissociation energy contribution $-\alpha^2\langle D_2(R)\rangle = -0.5932$ cm^{-1} computed using these values has an uncertainty of 0.0001 cm^{-1}.

For $R \leq 5.0$ bohr, our values of $B(R)$ agree very well with those of Wolniewicz, and we used the latter in calculating $B(R)$. For $R > 5.0$ bohr, however, the Wolniewicz's values appear to be less accurate, deviating significantly from the correct asymptotics at large R. Therefore, for $R > 5.0$ bohr we used the analytic fit:

$$B(R) = e^{-bR}(A_0 + A_1R + A_2R^2 + A_3R^3 + A_4R^4) + \frac{W_4}{R^4} + \frac{W_6}{R^6} \quad (9)$$

with parameters $b = 1.351860240$, $A_0 = 2.077615180$, $A_1 = -2.519175275$, $A_2 = 0.577315005$, $A_3 = -0.051870326$, and $A_4 = 0.001715821$, all in atomic units, adjusted to values computed by us for $R > 5.0$ bohr. We estimate that the resulting contribution to the dissociation energy $-\alpha^2\langle B(R)\rangle = 0.5422$ cm^{-1} has an uncertainty of 0.0001 cm^{-1}.

2.3. QED Contribution. The lowest-order QED correction, $\alpha^3 E^{(3)}$, to the energy of an atomic or molecular bound state is given by[25−27]

$$E^{(3)} = \frac{16}{3}\left(\frac{19}{30} - 2\ln\alpha - \ln K\right)\langle\delta(\mathbf{r}_{1a})\rangle + \left(\frac{164}{15} + \frac{14}{3}\ln\alpha\right)\langle\delta(\mathbf{r}_{12})\rangle - \frac{7}{6\pi}\langle P(r_{12}^{-3})\rangle \quad (10)$$

where the expectation values are computed with the eigenfunction ψ of the nonrelativistic Hamiltonian H. $P(r_{12}^{-3})$ is the distribution defined in atomic units by

$$\langle\varphi_1|P(r_{12}^{-3})\varphi_2\rangle = \lim_{a\to 0}\,[\langle\varphi_1|\theta(r_{12} - a)r_{12}^{-3}\varphi_2\rangle + 4\pi(\gamma + \ln a)\langle\varphi_1|\delta(\mathbf{r}_{12})\varphi_2\rangle] \quad (11)$$

where $\theta(x)$ is the Heaviside step function, and γ is the Euler−Mascheroni constant. The so-called Bethe logarithm, $\ln K$, in eq 10 is defined as

$$\ln K = \frac{\langle\psi|\mathbf{j}(H - E^{(0)})\ln[(H - E^{(0)})/Ry_\infty]\,\mathbf{j}\psi\rangle}{\langle\psi|\mathbf{j}(H - E^{(0)})\,\mathbf{j}\psi\rangle} \quad (12)$$

where $\mathbf{j} = -\mathbf{p}_1/m_e - \mathbf{p}_2/m_e + \mathbf{p}_a/m_p + \mathbf{p}_b/m_p$ is the electric current operator for the system ($\mathbf{p}_a$ and $\mathbf{p}_b$ are proton momenta), and $\mathrm{Ry}_\infty = \alpha^2 m_e c^2/2 = 1/2$ hartree is the Rydberg constant. The expectation values $\langle\delta(\mathbf{r}_{1a})\rangle$ and $\langle\delta(\mathbf{r}_{12})\rangle$ are already known from the calculation of the α^2 contribution, so the only new quantities to be calculated are the Bethe logarithm $\ln K$ and the so-called Araki−Sucher term — the last on the rhs of eq 10.

The evaluation of eq 12 for the four-body system using an accurate nonadiabatic wave function ψ appears to be very demanding computationally and was not attempted. Instead we used an adiabatic approximation to $\ln K$ defined as

$$\ln K^{\mathrm{ad}} = \frac{\langle\ln K^{\mathrm{el}}(R)D_1(R)\rangle}{\langle D_1(R)\rangle} \quad (13)$$

where $D_1(R)$ is the already computed electronic expectation value of $2\pi\delta(\mathbf{r}_{1a})$, and the averaging over R is carried out with the adiabatic nuclear wave function $\chi(R)$. The R dependent electronic Bethe logarithm, $\ln K^{\mathrm{el}}(R)$, appearing in eq 13, is defined exactly by eq 12 but with ψ replaced by the electronic wave function $\psi_{\mathrm{el}}(\mathbf{r}_1, \mathbf{r}_2; \mathbf{R})$, H by the electronic Hamiltonian H^{el}, $E^{(0)}$ by the Born−Oppenheimer energy $-2\mathrm{Ry}_\infty + V(R)$, and $\mathbf{j}$ by the total electronic momentum operator $\mathbf{p}_1 + \mathbf{p}_2$. Note that after these substitutions, the denominator in eq 12 becomes equal to $4D_1(R)$.

One can ask how well does this simple adiabatic approximation for $\ln K$ work? To answer this question we used eq 13 to compute $\ln K^{\mathrm{ad}}$ for the H_2^+ ion using the values of $\ln K^{\mathrm{el}}(R)$ reported in ref 30 (note that the definition of $\ln K$ adopted in this reference differs from ours by ln 2). The obtained adiabatic value $\ln K^{\mathrm{ad}} = 3.01276$ agrees very well with the result $\ln K = 3.01225$ of the complete nonadiabatic calculation of Korobov.[21] In fact, the adiabatic value (obtained with the real electron mass m_e) should be corrected by $\ln(\mu/m_e)$, where $\mu = m_e(1 + m_e/m_p)^{-1}$ is the reduced electron mass (see ref 25, p. 101). With this correction, the adiabatic value, equal now to 3.01222, differs only in 1 part per 10^5 from the result of Korobov's calculation. Similarly excellent agreement is observed for the excited vibrational levels. Since using this reduced electron mass correction gives an energy effect of the order of $(m_e/m_p)\alpha^3$, much smaller than the neglected relativistic recoil effects, we did not include this correction in our H_2 calculations.

To compute $\ln K^{\mathrm{el}}(R)$, we followed closely the technique described in refs 57−59. The present work is the first molecular application of this technique and probably the first calculation of the Bethe logarithm for a molecule other then H_2^+ and HD^+. The method employed by us is based on the integral representation of $\ln K$ introduced by Schwartz[60] and involves essentially an integration over the photon momenta k. Using large Gaussian geminal bases fully optimized at each value of R and k (by minimizing the relevant Hylleraas-type functionals) allows for a very efficient modeling of perturbed wave functions at different k and R dependent length scales. The mathematical completeness of Gaussian geminal bases for functions of Σ and Π symmetries, appearing in our calculations, is guaranteed by theorems proved in refs 61, 62. By inspecting the basis convergence pattern, we found that the values of $\ln K^{\mathrm{el}}(R)$, obtained with 3000-term geminal bases, and listed in Table 2, may be inaccurate only at the last figure given in this table. It may be of some interest to note that our values of $\ln K^{\mathrm{el}}(R)$ agree rather well with the values one can obtain using approximate models proposed by Garcia[28] and Bishop and Cheung[29] and used by Wolniewicz.[13] In fact, the Garcia model works somewhat better underestimating $\ln K^{\mathrm{el}}(R)$ by 2% at $R = 1$ bohr and even less for larger distances. The model of Bishop and Cheung overestimates $\ln K^{\mathrm{el}}(R)$ by 4% at $R = 1$ bohr, by 2% at the minimum of the potential well, and by less than that at larger internuclear separations. Note, however, that the good performance of these models does not hold generally, since they do not work so well for H_2^+.[30]

We obtained a very accurate analytic fit of $\ln K^{\mathrm{el}}(R)$ interpolating between the atomic hydrogen, $\ln K_{\mathrm{H}}$, and

Table 3. Parameters Determining the Analytic Form, eq 14, of the Bethe Logarithm, ln $K^{\mathrm{el}}(R)$[a]

ln K_{He}	4.370160222
ln K_{H}	2.984128555
L_6	2.082773197
A_1	−2.296997851
A_2	2.791145918
A_3	−1.589533050
A_4	0.408542881
b	2.292743496

[a] All parameters are in atomic units.

helium, ln K_{He}, values and exhibiting the correct L_6/R^6 fall off at large R. The asymptotic constant L_6 was calculated independently from appropriate perturbation theory expressions using the Slater basis set. The specific form of the fit function is

$$\ln K^{\mathrm{el}}(R) = \ln K_{\mathrm{H}} + e^{-bR}(\ln K_{\mathrm{He}} - \ln K_{\mathrm{H}} + A_1R + A_2R^2 + A_3R^3 + A_4R^4) + \frac{f_6(R)L_6}{R^6} \quad (14)$$

The parameters of the fit are given in Table 3. For $R > 1$ bohr, the error of this fit is of the order of 10^{-4} (at few points in the vicinity of $R = 3$ bohr it reaches 4×10^{-4}), but using the fit function in evaluating the formula (13) leads to errors much smaller than 0.0001.

The value of ln K^{ad}, found using eq 14 and our values of $D_1(R)$, amounts to 3.0188 and has an uncertainty smaller than 0.0001. Using this value, we can compute the dissociation energy contribution from the first term in eq 10, referred to as the one-electron Lamb shift. This term, dominating the total α^3 contribution, is equal to −0.2241 cm^{-1}, and we estimate its uncertainty as 0.0001 cm^{-1}. It is worthwhile to note that using the atomic hydrogen value of ln K, which is a natural and inexpensive approximation, one obtains −0.2277 cm^{-1} instead of −0.2241 cm^{-1}, i.e., a value which is not sufficiently accurate for our purpose. Thus, including the correct R dependence of the electronic Bethe logarithm is essential for a meaningful comparison with high-precision experimental data. The second term in eq 10, which we refer to as the two-electron Lamb shift, gives only 0.0166 cm^{-1} with an uncertainty smaller than 0.0001 cm^{-1}.

The Araki−Sucher term, the last in eq 10, was also obtained in the adiabatic approximation by computing the R-dependent electronic expectation value $A(R) = -(7/6\pi)\langle\psi_{\mathrm{el}}|P(r_{12}^{-3})\,\psi_{\mathrm{el}}\rangle$ and subsequently averaging $A(R)$ with the square of the adiabatic nuclear wave function $\chi(R)$. The numerical calculation was performed using Gaussian geminal basis. The needed matrix elements of the distribution $P(r_{12}^{-3})$ between Gaussian geminal functions located at points **P** and **T** in the bra and **R** and **Q** in the ket:

$$I = \lim_{\lambda\to 0}\int \exp(-a_1r_{1P}^2 - b_1r_{2T}^2 - c_1r_{12}^2)[\theta(r_{12}-\lambda)r_{12}^{-3} + 4\pi(\gamma + \ln\lambda)\delta(\mathbf{r}_{12})]\exp(-a_2r_{1R}^2 - b_2r_{2Q}^2 - c_2r_{12}^2)\mathrm{d}\mathbf{r}_1\mathrm{d}\mathbf{r}_2 \quad (15)$$

were obtained from the formula:

$$I = W_1W_2\frac{2\pi^{5/2}}{(a+b)^{3/2}}\exp\left[-\frac{ab}{a+b}(\mathbf{F}\text{-}\mathbf{H})^2\right] \times \left[\gamma - \ln\left(\frac{\xi}{a+b}\right) + g\left(\frac{a^2b^2(\mathbf{F}\text{-}\mathbf{H})^2}{\xi(a+b)}\right)\right] \quad (16)$$

where

$$a = a_1 + a_2 \qquad b = b_1 + b_2 \qquad c = c_1 + c_2 \qquad \xi = ab + bc + ca \quad (17)$$

and

$$\mathbf{F} = \frac{a_1\mathbf{P} + a_2\mathbf{R}}{a_1 + a_2} \qquad W_1 = \exp\left[-\frac{a_1a_2}{a_1+a_2}(\mathbf{P}\text{-}\mathbf{R})^2\right] \quad (18)$$

$$\mathbf{H} = \frac{b_1\mathbf{T} + b_2\mathbf{Q}}{b_1 + b_2} \qquad W_2 = \exp\left[-\frac{b_1b_2}{b_1+b_2}(\mathbf{T}\text{-}\mathbf{Q})^2\right] \quad (19)$$

The function $g(x)$ appearing in eq 16 is defined as an integral involving the usual Boys function $F_0(x) = (\pi/x)^{1/2}\,\mathrm{erf}(\sqrt{x})/2$:

$$g(x) = \int_0^x \frac{1}{t}[e^t\mathrm{F}_0(t) - 1]\mathrm{d}t \quad (20)$$

To compute $g(x)$ we used the following expansions:

$$g(x) = \sum_{k=1}^{n}\frac{2^k}{(2k+1)!!k}x^k + \boldsymbol{O}(x^{n+1}) \quad (21)$$

$$g(x) = \frac{\sqrt{\pi}e^x}{2x^{3/2}}\sum_{k=0}^{n}\frac{(2k+1)!!}{2^k}x^{-k} + \boldsymbol{O}(x^{-(n+1)}) \quad (22)$$

used, respectively, for small and medium and for large values of the argument x. To independently verify our calculations we computed $\langle\psi_{\mathrm{el}}|P(r_{12}^{-3})\,\psi_{\mathrm{el}}\rangle$ using also the integral transform method of reference 63 obtaining the same results at basis set convergence. The values of $\langle\psi_{\mathrm{el}}|P(r_{12}^{-3})\,\psi_{\mathrm{el}}\rangle$ computed with an extensively optimized 1200-term explicitly correlated Gaussian basis set are given in Table 2. We estimate that their accuracy is better than one unit in the last digit shown in the table.

The integral $\langle\psi_{\mathrm{el}}|P(r_{12}^{-3})\,\psi_{\mathrm{el}}\rangle$ exhibits a slow R^{-3} decay at large R. To compute it for values of R larger than 12.0 bohr, we used its asymptotic expansion:

$$\langle\psi_{\mathrm{el}}|P(r_{12}^{-3})\psi_{\mathrm{el}}\rangle = \frac{1}{R^3} + \frac{6}{R^5} + \frac{75}{R^7} + \boldsymbol{O}(R^{-8}) \quad (23)$$

Using the values given in Table 2 and the asymptotic formula (eq 23), we found that the Araki−Sucher contribution to the dissociation energy $-\alpha^3\langle A(R)\rangle$ amounts to 0.0127 cm^{-1} with an uncertainty of one unit at the last digit. This contribution has not been computed before for H_2. It should be noted that in his calculations Wolniewicz[50] neglected also the contribution from the first part (164/15) $\langle\delta(\mathbf{r}_{12})\rangle$ of the two-electron Lamb shift, amounting to −0.01457 cm^{-1}.

Calculation of the complete α^4 contribution to the dissociation energy is a very complex task[32,33] and could not be carried out for the purpose of this investigation. It is well-

Table 4. Dissociation Energies for H_2 and D_2 (in cm^{-1}) Compared with Experimental Data

		H_2	D_2
α^0	Born−Oppenheimer	36112.5927(1)	36746.1623(1)
	adiabatic	5.7711(1)	2.7725(1)
	nonadiabatic	0.4339(2)	0.1563(2)
	total α^0	36118.7978(2)	36749.0910(2)
α^2	mass−velocity	4.4273(2)	4.5125(2)
	one-el. Darwin	−4.9082(2)	−4.9873(2)
	two-el. Darwin	−0.5932(1)	−0.5993(1)
	Breit	0.5422(1)	0.5465(1)
	total α^2	−0.5319(3)	−0.5276(3)
$\alpha^2 m_e/m_p$	estimate	0.0000(4)	0.0000(2)
α^3	one-el. Lamb shift	−0.2241(1)	−0.2278(1)
	two-el. Lamb shift	0.0166(1)	0.0167(1)
	Araki−Sucher	0.0127(1)	0.0128(1)
	total α^3	−0.1948(2)	−0.1983(2)
$\alpha^3 m_e/m_p$	estimate	0.0000(2)	0.0000(1)
α^4	one-loop term	−0.0016(8)	−0.0016(8)
total theory		36 118.0695(10)	36 748.3633(9)[a]
expt.	ref 15	36 118.06(4)	36 748.32(7)
expt.	ref 16	36 118.062(10)[b]	36 748.343(10)
expt.	ref 17	36 118.0696(4)	

[a] This value includes the −0.0002 cm^{-1} correction for the finite size of the deuteron (the charge radius of 2.14 fm was assumed). The corresponding correction for the H_2 molecule is smaller than 0.0001 cm^{-1} and can be neglected for our purposes. [b] In the footnote to Table III the authors of ref 16 report also the value 36 118.073(4) cm^{-1} contingent on the assumption that a particular resonance is a bound state and not a quasi-bound, above threshold state.

known,[33] however, that this α^4 contribution is dominated by the one-loop term given by

$$E^{(4)}_{\text{1-loop}} = 4\pi\left(\frac{427}{96} - 2\ln 2\right)\langle\delta(\mathbf{r}_{1a})\rangle \tag{24}$$

The corresponding correction to the dissociation energy is −0.0016 cm^{-1}, and we estimate that it differs from the exact value of the complete $\alpha^4 E^{(4)}$ contribution by less than 50%. We also verified that the α^4, α^5, and higher-order QED corrections due to retardation and taken into account by the Casimir−Polder formula[64] are smaller than 0.0001 cm^{-1}, i.e., are well within the error bars assumed for the complete $\alpha^4 E^{(4)}$ contribution.

3. Results and Discussion

Dissociation energies for the H_2 and D_2 molecules are presented in Table 4 together with all components computed by us. The experimental dissociation energies shown for comparison are already corrected for the effects of hyperfine interactions, i.e., the true energies of atoms into which the molecule dissociate are replaced by the center of gravity of the hyperfine structure of the $1\,^2S_{1/2}$ atomic states. This means that in the case of H_2 we must not subtract the 2×0.0355 cm^{-1} correction corresponding to the difference between this center of gravity and the $F = 0$ hyperfine level of hydrogen atom.

The error bars of all computed components were discussed in Section 2. Here we still have to estimate the relativistic nonadiabatic/recoil corrections that have not been computed. Within the perturbation formalism of ref 44, the leading nonadiabatic contribution to each of the four terms in eq 6 is given by the expression:

$$2\langle\psi_{\text{el}}\chi|W\frac{1}{(E_{\text{el}} - H_{\text{el}})'}H_n|\psi_{\text{el}}\chi\rangle \tag{25}$$

where W stands for $\mathbf{p}_1^4/4$, $2\pi\delta(\mathbf{r}_{1a})$, $\pi\delta(\mathbf{r}_{12})$ or for the Breit operator,

$$H_n = -\frac{1}{m_p}\nabla^2_{\mathbf{R}} + \frac{1}{4m_p}(\mathbf{p}_1 + \mathbf{p}_2)^2 \tag{26}$$

H_{el} is the electronic Hamiltonian, E_{el} is the eigenvalue of H_{el} corresponding to the wave function ψ_{el}, $\mathbf{R}$ is the vector joining the nuclei, and the prime indicates the orthogonalization to ψ_{el}. The term involving $(\mathbf{p}_1 + \mathbf{p}_2)^2$ can be obtained by averaging the R dependent function:

$$\frac{1}{2m_p}\left\langle\psi_{\text{el}}\middle|W\frac{1}{(E_{\text{el}} - H_{\text{el}})'}(\mathbf{p}_1 + \mathbf{p}_2)^2\middle|\psi_{\text{el}}\right\rangle_{\text{el}} \tag{27}$$

with $4\pi R^2\chi^2(R)$. The bracket $\langle\cdots\rangle_{\text{el}}$ denotes the integration over electronic coordinates only. Since the integral in eq 27 is mass independent the corresponding contribution to the energy is clearly of the order of $\alpha^2 m_e/m_p$. The term involving $\nabla^2_{\mathbf{R}}$ can also be written in terms of mass independent radial functions. To see that we note that this term can be expressed as the sum of two terms:

$$-\frac{2}{m_p}\int\chi^2(R)\left\langle\psi_{\text{el}}\middle|W\frac{1}{(E_{\text{el}} - H_{\text{el}})'}\middle|\nabla^2_{\mathbf{R}}\psi_{\text{el}}\right\rangle_{\text{el}} d^3R \\ -\frac{4}{m_p}\left\langle\psi_{\text{el}}\chi\middle|\mathrm{W}\frac{1}{(E_{\text{el}} - H_{\text{el}})'}\middle|\nabla_{\mathbf{R}}\psi_{\text{el}}\nabla_{\mathbf{R}}\chi\right\rangle \tag{28}$$

The first one is explicitly in the form of an average of a mass independent radial function and is clearly of the order of $\alpha^2 m_e/m_p$. Performing integration by parts the mass dependent gradient of χ in the second term can be eliminated, and this term can be written as an average of the radial function:

$$\frac{2}{m_p}\langle\nabla_{\mathbf{R}}\psi_{\text{el}}|W\frac{1}{(E_{\text{el}} - H_{\text{el}})'}|\nabla_{\mathbf{R}}\psi_{\text{el}}\rangle_{\text{el}} + \\ \frac{2}{m_p}\langle\psi_{\text{el}}|\nabla_{\mathbf{R}}W\frac{1}{(E_{\text{el}} - H_{\text{el}})'}|\nabla_{\mathbf{R}}\psi_{\text{el}}\rangle_{\text{el}} \tag{29}$$

proportional to $1/m_p$. This term is, thus, also of the order of $\alpha^2 m_e/m_p$.

Since all relativistic nonadiabatic/recoil terms are of the order of $\alpha^2 m_e/m_p$, we decided to estimate their magnitude by scaling the total α^2 correction by the factor m_e/m_p. We view this estimate as a conservative one since for separated hydrogen atoms the $\alpha^2 m_e/m_p$ contributions to the mass−velocity, Darwin, and Breit terms (equal to $5\alpha^2 m_e/m_p$, $-3\alpha^2 m_e/m_p$, and $-2\alpha^2 m_e/m_p$) add up exactly to zero, and this cancellation must persist to a significant degree when the atoms are bound. The resulting estimate of the total relativistic nonadiabatic/recoil correction is ± 0.0000(4) and gives the second largest (after the α^4 term) contribution to the error budget of our calculation. We applied the same scaling procedure to the QED contribution of the order $\alpha^3 m_e/m_p$.

The results of Table 4 show that the dissociation energy of H_2 computed by us, amounting to 36 118.0695(10) cm^{-1}, is not only within the rather wide error bars of the experimental determinations from the Eyler group[15,16] but agrees impresively well with the very precise hybrid, experimental−theoretical value of 36 118.0696(4) cm^{-1} determined recently by Liu et al.[17] The difference between the experiment and our theoretical prediction is only 1 unit at the ninth decimal place. It should be emphasized that the theoretical input used in ref 17 can be viewed as very reliable (it contains data from extremely high-accuracy calculations for the H_2^+ ion)[21−23] and is totally independent of the results of present calculations. The fact that the experimental value lies rather close to the center of the energy range determined by our error bars may not be accidental. We believe that as a result of the cancellation of terms (complete at the separated atoms limit), the actual value of the $\alpha^2 m_e/m_p$ contribution is smaller than our estimate, and that our estimate of the uncertainty of the α^4 contribution is very conservative. Before the α^4 contribution and the relativistic nonadiabatic/recoil terms are accurately calculated it will be very difficult to further reduce the uncertainty of the theoretical value of the dissociation energy. It may be interesting to observe that the achieved agreement with experiment would have been impossible without the inclusion of the Araki−Sucher term, the radial dependence of the electronic Bethe logarithm, and the one-loop α^4 contribution.

The dissociation energy for D_2 was computed using the same method as for H_2 and the same approach to estimate the $\alpha^2 m_e/m_d$ and $\alpha^3 m_e/m_d$ terms (we assumed that m_d = 3 670.4829654 m_e).[42] These terms are smaller for D_2, so in this case, 90% of the error budget comes from the uncertainty in the value of the α^4 contributions other than the one-loop term included in our calculations. For D_2, the agreement with the most recent experimental value[16] is not satisfactory despite the large experimental uncertainty (25 times larger than for H_2). The observed discrepancy is, however, only 2σ (experimental). A more precise experiment should be possible now and could shed some light on the reason of this small discrepancy.

To demonstrate better the level of accuracy of our calculations, we also computed the energy differences between the ground-state energy of H_2 and energies of the first rotationally and vibrationally excited states. These energies are shown in Table 5 and compared with the experimental results. Both the theoretical and experimental energies of the $J = 1$ state refer to the center of gravity of the hyperfine structure, so we did not have to consider nuclear spin interactions in computing the rotational (ortho−para) energy difference.

In computing small energy differences, there is a significant cancellation of errors, so the error bars for some contributions are smaller than for the dissociation energy. These error bars were estimated by performing computations with several reasonable approximations to the radial functions [like $V(R)$, $D_1(R)$, or $D_2(R)$] and observing the resulting scatter of energy differences. We assumed that the error of the nonadiabatic contribution is twice as large as the error of the adiabatic contribution, as suggested by the observed ratio of uncertainties for the individual energy levels.

Table 5. The Energy Differences (in cm^{-1}) between the Ground-State Energy of H_2 and Energies of the First Rotationally and Vibrationally Excited States

		$J = 0 \rightarrow 1$	$v = 0 \rightarrow 1$
α^0	Born−Oppenheimer	118.55558(2)	4 163.4035(1)
	adiabatic	−0.06365(4)	−1.4029(1)
	nonadiabatic	−0.00667(8)	−0.8365(2)
	total α^0	118.48526(9)	4 161.1641(2)
α^2	mass−velocity	0.02713(4)	0.5341(2)
	one-el. Darwin	−0.02383(4)	−0.4994(2)
	two-el. Darwin	−0.00160(2)	−0.0391(1)
	Breit	0.00088(2)	0.0279(1)
	total α^2	0.00258(6)	0.0235(3)
α^3	one-el. Lamb shift	−0.00109(2)	−0.0231(1)
	two-el. Lamb shift	0.00004(1)	0.0011(1)
	Araki−Sucher	0.00002(1)	0.0007(1)
	total α^3	−0.00103(2)	−0.0213(2)
α^4	one-loop term	−0.00001(1)	−0.0002(2)
total theory		118.48680(11)	4 161.1661(5)
experiment		118.48684(10)[a]	4 161.1660(3)[b]

[a] Ref 18. [b] Ref 65.

The inspection of the last two rows of Table 5 shows that the theoretical and experimental values of the ortho−para energy gap differ only by 0.00004 cm^{-1}, which is much less than the error of either the theoretical and experimental determinations. This excellent agreement is very gratifying since the ortho−para energy difference was employed in ref 17 to obtain the most precise experimental value of the dissociation energy to date.

The results presented in Table 5 show also an excellent agreement (up to seventh significant digit) between the theoretical and experimental vibrational energy difference. The experimental value, which has a very small uncertainty of 0.0003 cm^{-1}, differs only by 0.0001 cm^{-1} from the theoretical result and lies well within the error bars of the latter. It appears that the new evaluation of experimental data reported in ref 65 leads indeed to a much more accurate result than the older value measured by Dabrowski,[66] amounting to 4 161.14 cm^{-1} and lying about 30σ (theoretical) off our result.

Acknowledgment. The authors thank W. Cencek and L. Wolniewicz for making available their unpublished results.

Note Added after ASAP Publication. This paper was published ASAP on September 30, 2009. A correction was made in the Method section to clarify calculation procedures, and a portion of eq 16 was corrected as well. The revised paper was reposted on October 1, 2009. Additional corrections were made referring to equation 3 instead of equation 6 and the journal title for reference 57 corrected. The updated version was reposted on October 7, 2009.

Appendix

A calculation of the complete α^2 contribution to the ground-state energy of H_2 without the adiabatic approximation, i.e., including the relativistic nonadiabatic/recoil effects, has already been presented in the literature[65] and we made an effort to use the results of ref 65 to extract the magnitude of the $\alpha^2 m_e/m_p$ contribution to the dissociation energy. This was not an easy task since the authors of ref 65 included partly the α^3 QED contribution (by using the anomalous magnetic moment of electron in their α^2 Hamiltonian) and because they provided two values of their relativistic energy differing by 0.0083 cm^{-1}: one obtained as the sum of the mass−velocity, Darwin, Breit and spin−spin contributions from their table 3 and the other which could be calculated as the difference between the 5th and 2nd column in their table 2.

We were able to eliminate the α^3 contributions from their Darwin energies, and after subtracting the correct atomic values, we found that their mass−velocity, one-electron Darwin, two-electron Darwin, and Breit contributions to the dissociation energy differ from ours by −0.0030, −0.0032, −0.0043, and 0.0020 cm^{-1}. The sum of these four contributions amounts to −0.0085 cm^{-1}. This value is by an order of magnitude larger than our estimate of the $\alpha^2 m_e/m_p$ contribution. If we added this additional −0.0085 cm^{-1} to our dissociation energy, the disagreement with experiment would increase to 9σ. However, the total relativistic energy from their table 2, after eliminating the α^3 terms (using results from their table 3), differs from our α^2 contribution by only −0.0002 cm^{-1}. This magnitude of the $\alpha^2 m_e/m_p$ effect is within our error bars and including it would not affect the comparison with the experimental results. For the reasons discussed above, we did not use the results of ref 65 in our theoretical determination of the dissociation energy of H_2.

References

(1) Heitler, W.; London, F. *Z. Phys.* **1927**, *44*, 455.

(2) James, H. M.; Coolidge, A. S. *J. Chem. Phys.* **1933**, *1*, 825.

(3) James, H. M.; Coolidge, A. S. *J. Chem. Phys.* **1935**, *3*, 129.

(4) Richardson, O. W.; Davidson, P. M. *Proc. R. Soc. A* **1929**, *123*, 466.

(5) Kolos, W.; Wolniewicz, L. *J. Chem. Phys.* **1964**, *41*, 3663.

(6) Kolos, W.; Wolniewicz, L. *Phys. Rev. Lett.* **1968**, *20*, 243.

(7) Kolos, W.; Wolniewicz, L. *J. Chem. Phys.* **1968**, *49*, 404.

(8) Herzberg, G.; Monfils, A. *J. Mol. Spectrosc.* **1960**, *5*, 482.

(9) Herzberg, G. *J. Mol. Spectrosc.* **1970**, *33*, 147.

(10) Stwalley, W. C. *Chem. Phys. Lett.* **1970**, *6*, 241.

(11) Kolos, W.; Szalewicz, K.; Monkhorst, H. J. *J. Chem. Phys.* **1986**, *84*, 3278.

(12) Kolos, W.; Rychlewski, J. *J. Chem. Phys.* **1993**, *98*, 3960.

(13) Wolniewicz, L. *J. Chem. Phys.* **1995**, *103*, 1792.

(14) Balakrishnan, A.; Smith, V.; Stoicheff, B. P. *Phys. Rev. Lett.* **1992**, *68*, 2149.

(15) Eyler, E. E.; Melikechi, N. *Phys. Rev. A: At., Mol., Opt. Phys.* **1993**, *48*, R18.

(16) Zhang, Y. P.; Cheng, C. H.; Kim, J. T.; Stanojevic, J.; Eyler, E. E. *Phys. Rev. Lett.* **2004**, *92*, 203003.

(17) Liu, J.; Salumbides, E. J.; Hollenstein, U.; Koelemeji, J. C. J.; Eikema, K. S. E.; Ubachs, W.; Merkt, F. *J. Chem. Phys.* **2009**, *130*, 174306.

(18) Jennings, D. E.; Bragg, S. L.; Brault, J. W. *Astrophys. J.* **1984**, *282*, L85.

(19) Hannemann, S.; Salumbides, E. J.; Witte, S.; Zinkstok, R. T.; van Duijn, E.-J.; Eikema, K. S. E.; Ubachs, W. *Phys. Rev. A: At., Mol., Opt. Phys.* **2006**, *74*, 062514.

(20) Osterwalder, A.; Wüest, A.; Merkt, F.; Jungen, C. *J. Chem. Phys.* **2004**, *121*, 11810.

(21) Korobov, V. I. *Phys. Rev. A: At., Mol., Opt. Phys.* **2006**, *73*, 024502.

(22) Korobov, V. I. *Phys. Rev. A: At., Mol., Opt. Phys.* **2006**, *74*, 052506.

(23) Korobov, V. I. *Phys. Rev. A: At., Mol., Opt. Phys.* **2008**, *77*, 022509.

(24) Karr, J.-P.; Bielsa, F.; Douillet, A.; Gutierrez, J. P.; Korobov, V. I.; Hilico, L. *Phys. Rev. A: At., Mol., Opt. Phys.* **2008**, *77*, 063410.

(25) Bethe, H. A.; Salpeter, E. E. *Quantum Mechanics of One- and Two-Electron Systems*; Springer: Berlin, Germany, 1975.

(26) Araki, H. *Prog. Theor. Phys.* **1957**, *17*, 619.

(27) Sucher, J. *Phys. Rev.* **1958**, *109*, 1010.

(28) Garcia, J. D. *Phys. Rev.* **1966**, *14*, 66.

(29) Bishop, D. M.; Cheung, L. M. *J. Phys. B* **1978**, *11*, 3133.

(30) Bukowski, R.; Moszynski, R.; Jeziorski, B.; Kołos, W. *Int. J. Quantum Chem.* **1992**, *42*, 287.

(31) CODATA, The Committee on Data for Science and Technology http://www.codata.org/ (accessed Aug 26, 2009).

(32) Pachucki, K. *Phys. Rev. A: At., Mol., Opt. Phys.* **2005**, *71*, 012503.

(33) Pachucki, K. *Phys. Rev. A: At., Mol., Opt. Phys.* **2006**, *74*, 022512.

(34) Kolos, W.; Wolniewicz, L. *Rev. Mod. Phys.* **1963**, *35*, 473.

(35) Bubin, S.; Adamowicz, L. *J. Chem. Phys.* **2003**, *118*, 3079.

(36) Kolos, W. *Adv. Quantum Chem.* **1970**, *5*, 99.

(37) Kutzelnigg, W. *Mol. Phys.* **1997**, *90*, 909.

(38) Tang, K. T.; Toennies, J. P. *J. Chem. Phys.* **1984**, *80*, 3726.

(39) Mitroy, J.; Ovsiannikov, V. D. *Chem. Phys. Lett.* **2005**, *412*, 76.

(40) Ovsiannikov, V. D.; Mitroy, J. *J. Phys. B* **2006**, *39*, 159.

(41) Sims, J.; Hagstrom, S. *J. Chem. Phys.* **2006**, *124*, 094101.

(42) Cencek, W. 2003, private communication.

(43) Pachucki, K.; Komasa, J. *J. Chem. Phys.* **2009**, *130*, 164113.

(44) Pachucki, K.; Komasa, J. *J. Chem. Phys.* **2008**, *129*, 034102.

(45) Bubin, S.; Leonarski, F.; Stanke, M.; Adamowicz, L. *Chem. Phys. Lett.* **2009**, *477*, 12.

(46) Pachucki, K. *Phys. Rev. A: At., Mol., Opt. Phys.* **2004**, *69*, 052502.

(47) Pachucki, K. *Phys. Rev. A: At., Mol., Opt. Phys.* **2007**, *76*, 022106.

(48) Stone, A. P. *Proc. Phys. Soc. (London)* **1961**, *77*, 786.

(49) Stone, A. P. *Proc. Phys. Soc. (London)* **1963**, *81*, 868.

(50) Wolniewicz, L. *J. Chem. Phys.* **1993**, *99*, 1851–1868.

(51) Kolos, W.; Wolniewicz, L. *J. Chem. Phys.* **1966**, *45*, 509.

(52) Piszczatowski, K.; Lach, G.; Jeziorski, B. *Phys. Rev. A: At., Mol., Opt. Phys.* **2008**, *77*, 062514.

(53) Meath, W. J.; Hirschfelder, J. O. *J. Chem. Phys.* **1966**, *44*, 3197.

(54) Pachucki, K. *Phys. Rev. A: At., Mol., Opt. Phys.* **2005**, *72*, 062706.

(55) Woon, D. E.; Dunning, T. H., Jr. *J. Chem. Phys.* **1994**, *100*, 2975.

(56) *DALTON, a Molecular Electronic Structure Program*, Release 2.0, 2005; http://www.kjemi.uio.no/software/dalton/dalton.html.

(57) Pachucki, K.; Komasa, J. *Phys. Rev. A: At., Mol., Opt. Phys.* **2003**, *68*, 042507.

(58) Pachucki, K.; Komasa, J. *Phys. Rev. Lett.* **2004**, *92*, 213001.

(59) Pachucki, K.; Komasa, J. *J. Chem. Phys.* **2006**, *125*, 294394.

(60) Schwartz, C. *Phys. Rev.* **1961**, *123*, 1700.

(61) Jeziorski, B.; Bukowski, R.; Szalewicz, K. *Int. J. Quantum Chem.* **1997**, *61*, 769.

(62) Hill, R. N. *Int. J. Quantum Chem.* **1998**, *68*, 357.

(63) Pachucki, K.; Cencek, W.; Komasa, J. *J. Chem. Phys.* **2005**, *122*, 184101.

(64) Casimir, H. B. G.; Polder, D. *Phys. Rev.* **1948**, *73*, 360.

(65) Stanke, M.; Kedziera, D.; Bubin, S.; Molski, M.; Adamowicz, L. *J. Chem. Phys.* **2008**, *128*, 114313.

(66) Dabrowski, I. *Can. J. Phys.* **1984**, *62*, 1639.

CT900391P

J. Chem. Theory Comput. **2009,** *5,* 3049–3059 **3049**

JCTC Journal of Chemical Theory and Computation

Can Induced Orbital Paramagnetism Be Controlled by Strong Magnetic Fields?

G. I. Pagola,*,† M. B. Ferraro,† and P. Lazzeretti‡

Departamento de Física, Facultad de Ciencias Exactas y Naturales, Universidad de Buenos Aires, Ciudad Universitaria, Pab. I, (1428) Buenos Aires, Argentina, and

Dipartimento di Chimica dell'Universita degli Studi di Modena e Reggio Emilia, Via Campi 183, 41100 Modena, Italy

Received July 30, 2009

Abstract: Magnetic hypersusceptibilities and hypershielding at the nuclei of BH, CH^+, C_4H_4, and C_8H_8 molecules in the presence of an external spatially uniform, time-independent magnetic field have been investigated accounting for cubic response contributions via Rayleigh−Schrödinger perturbation theory. Numerical estimates have been obtained at the coupled Hartree−Fock and density-functional levels of theory within the conventional common-origin approach, using extended gaugeless basis sets. The fundamental role of electron correlation effects was assessed. Critical values of the applied magnetic field at which transition from paramagnetic to diamagnetic behavior would occur were estimated. It is shown that perturbative methods may successfully be employed to estimate the interaction energy for big cyclic molecules.

I. Introduction

Strong magnetic fields are well-known to severely modify the structure and properties of matter. This holds not only for bulk systems where extraordinary phenomena such as, for example, the quantum Hall effect, have been discovered but, in particular, for the elementary constituents of matter, that is, atoms and molecules.[1]

Recently, the response of atoms and molecules to strong magnetic fields became a subject of increasing interest in different areas of physics such as astrophysics and atomic, molecular, and solid-state physics. Bound-particle systems in external magnetic fields show a number of intriguing features which are not observable in field-free space and which manifest themselves at the level of the basic equations of motion.

Observations of radio pulsars and accreting neutron stars in X-ray binaries, possessing surface fields in excess of 10^8 T, and the detection of magnetic white dwarf stars with superstrong fields have further increased interest in this area. A "magnetar" with a magnetic field stronger than any other known object in the universe, the soft gamma repeater known as SGR 1900+14, lying 20 000 light years away, has been discovered in the constellation of Aquila.[2] Magnetic fields as big as 800 trillion times that of the Earth cause the surface of magnetars to ripple and crack, releasing strong bursts of radiation.

A review of atoms in strong magnetic fields, reporting tabulations of numerical data, is available in a monograph by Ruder et al.[3] Other references are the conference proceedings on *Atoms and Molecules in Strong External Fields* edited by Schmelcher and Schweizer[4] and the special issue of the *International Journal of Quantum Chemistry* dedicated to the properties of molecules in strong magnetic fields, edited by Runge and Sabin.[5] An extensive review on atoms, molecules, and bulk matter has been reported by Lai.[1]

Atoms and molecules in strong magnetic fields are also of interest from a purely theoretical point of view.[6,7] The difficulty in theoretically treating atoms in strong magnetic fields lies in the fact that a strong rearrangement of the electronic wave function takes place, which is particularly dramatic in the so-called intermediate regime, in which matter interacts with fields from 10^3 to 10^5 T. In the presence of fields of this strength, magnetic and Coulomb forces are of nearly equal importance: neither can be treated as a

---

* Corresponding author e-mail: gpagola@df.uba.ar.

† Universidad de Buenos Aires.

‡ Universita degli Studi di Modena e Reggio Emilia.

10.1021/ct900390s CCC: $40.75

perturbation of the other. Due to the competition of the spherically symmetric Coulomb potential, and the cylindrically symmetric magnetic field interaction, the problem is formally non-integrable.

The "strong field" regime is typical of a situation in which the Lorentz force is on the order of magnitude of or greater than the Coulomb binding force. For a hydrogen atom in the ground state, the corresponding field strength cannot be reached in the laboratory, but only in astrophysical objects. However, the strong magnetic field regime is accessible in the laboratory for highly excited Rydberg states of atoms.[3,4,8]

In molecules, difficulties arise from nonseparability of the center of mass and internal motion,[7] and the screened Born−Oppenheimer approximation[6,9] has been advocated to guarantee the validity of an adiabatic approximation in the presence of magnetic fields. Most studies of molecules in strong magnetic fields have been restricted to hydrogen molecular ion H_2^+.[10−16] There exist some investigations dealing with the electronic structure of the neutral molecule H_2 in the presence of a strong magnetic field.[17−23]

Highly excited states of H_2 were studied for a field strength of 4.7 T by Monteiro and Taylor.[17] For intermediate field strengths, two studies of almost qualitative character examined the potential energy curve of the lowest $^1\Sigma_g$ state.[18,19] A few investigations were performed at the high field limit,[20−24] where the magnetic forces dominate over the Coulomb forces. The ground state of the H_2 molecule in the parallel configuration, in which the internuclear and magnetic field axes coincide, has been investigated by Kravchenko and Liberman,[25,26] and by Detmer et al.[25,27,28]

According to the fundamental results arrived at in ref 26 using a fully numerical Hartree−Fock approach, the ground state of H_2 in a magnetic field below 4.2×10^4 T is the strongly bound singlet state $^1\Sigma_g$. For magnetic fields stronger than 3×10^6 T, the ground state becomes the strongly bound triplet $^3\Pi_u$, and for magnetic fields between 4.2×10^4 T and 3×10^6 T, the symmetry of the ground state is the triplet state $^3\Sigma_u$, which is characterized by repulsion at intermediate internuclear distances and by a weak quadrupole−quadrupole interaction between atoms at large internuclear separation. In this region of magnetic field strength, the hydrogen molecule is bound weakly, if at all; the hydrogen atoms behave like a weakly nonideal gas of Bose particles and can form a superfluid phase.

Nonperturbative Hartree−Fock calculations on molecules in strong magnetic fields were recently reported using London orbitals by Tellgren et al. For a number of molecules, plots of the interaction energy as a function of the magnetic field were shown.[29,30] Highly nonlinear behavior was discovered for closed-shell paramagnetic species BH and CH^+, which would become diamagnetic for field strengths higher than 0.22 and 0.45 au, respectively. Surprisingly

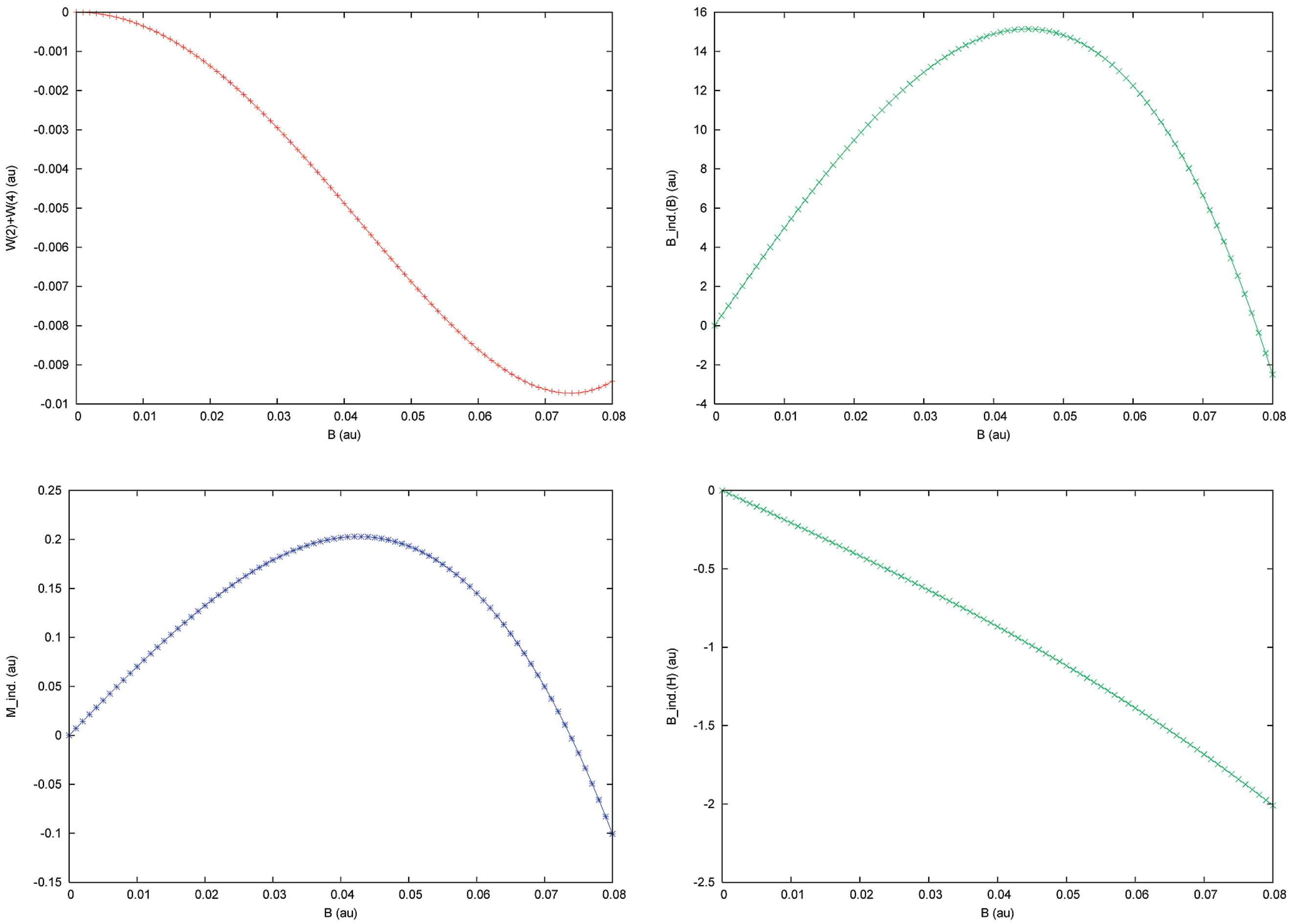

Figure 1. Response properties of the BH molecule in a magnetic field normal to the bond direction. Top left: Magnetic interaction energy. Top right: Magnetic field induced at the boron nucleus. Bottom left: Induced magnetic moment. Bottom right: Magnetic field induced at the hydrogen nucleus.

Table 1. Magnetic Hypershielding,[a] $\Sigma^{B}_{\alpha\beta\gamma\delta}$, and Shielding,[b] $\sigma^{B}_{\alpha\beta}$, of the Boron Nucleus in the BH Molecule

method	component[c]	$\Sigma^B(B)$[d]	$\Sigma^B(H)$[d]
CHF (CO)	xxxx	5.043×10^5	5.043×10^5
	xxyy	1.681×10^5	1.681×10^5
	xxzz	-3.009×10^4	-3.009×10^4
	zxxz	-3.600×10^4	-3.600×10^4
	zzzz	45.0	45.0
	$\langle\Sigma^B\rangle$	2.425×10^5	2.425×10^5
DFT (KT3)	xxxx	3.808×10^5	4.252×10^5
	xxyy	1.269×10^5	1.417×10^5
	xxzz	-2.143×10^4	-2.143×10^4
	zxxz	-2.572×10^4	-2.572×10^4
	zzzz	47.89	47.89
	$\langle\Sigma^B\rangle$	1.843×10^5	2.079×10^5

method	CHF(CO)	DFT(KT3)
component[e]	$\sigma^B(B)$[d]	$\sigma^B(B)$[d]
xx	−506.7	−398.7
zz	198.9	202.4
$\langle\sigma^B\rangle$	−271.5	−198.3
component	$\sigma^B(H)$[d]	$\sigma^B(H)$[d]
xx	−506.6	−398.6
zz	198.9	202.4
$\langle\sigma^B\rangle$	−271.5	−198.3

[a] In ppm SI atomic units. The conversion factor to SI units is $1.80997698 \times 10^{-11}$ T^{-2}, using the CODATA values of the fundamental constants 2002.[83] Coordinates in bohr: H (0, 0, −2.1120108509); B (0, 0, 0.19333975910). [b] In ppm. [c] Only components contributing to the average property are reported. yyyy = xxxx, xxyy = yxxy, xxzz = yyzz, zxxz = zyyz by symmetry. [d] Common origin results; the gauge origin is indicated between parentheses. [e] xx = yy by symmetry.

Table 2. Magnetic Hypershielding, $\Sigma^{H}_{\alpha\beta\gamma\delta}$, and Shielding, $\sigma^{H}_{\alpha\beta}$, of the Hydrogen Nucleus in the BH Molecule[a]

method	component	$\Sigma^H(H)$	$\Sigma^H(B)$
CHF (CO)	xxxx	4252	4242
	xxyy	1417	1414
	xxzz	−277.6	−277.7
	zxxz	−4299	−4298
	zzzz	24.55	24.55
	$\langle\Sigma^H\rangle$	442.1	436.8
DFT (KT3)	xxxx	7857	5898
	xxyy	2619	1966
	xxzz	−350.1	−350.2
	zxxz	−3081	−3082
	zzzz	27.90	27.90
	$\langle\Sigma^H\rangle$	2823	1778

method	CHF(CO)	DFT(KT3)
component	$\sigma^H(H)$	$\sigma^H(H)$
xx	20.58	18.25
zz	33.93	34.18
$\langle\sigma^H\rangle$	25.03	23.56
component	$\sigma^H(B)$	$\sigma^H(B)$
xx	20.56	18.23
zz	33.93	34.10
$\langle\sigma^H\rangle$	25.02	23.55

[a] See footnotes a−e of Table 1 for the use of symbols, units, and abbreviations.

enough, the curve for BH in the presence of a perpendicular field indicates that, for a field as big as 0.4 au, that is, $\approx 10^5$ T, the interaction energy would vanish, as happens for the molecule in the absence of magnetic perturbation, see Figure 1d of ref 29.

II. Perturbation Theory Approach to Cubic Response

Perturbation theory, which is applicable in the weak field regime, breaks down in the intermediate field regime. However, for a time, standard perturbative methods were taken into account for predicting observable phenomena in a terrestrial environment.[31] Ramsey[32] considered possible deviations from linear dependence of the resonance frequencies on the strength of the external magnetic field in nuclear magnetic resonance (NMR) spectroscopy. Bendall and Doddrell reported an experimental observation of a field-dependent ^{59}Co chemical shift in two compounds.[31] Źaucer and Aźman[33] suggested that departures from linear dependence between the induced magnetic dipole moment and the applied field can arise in a molecule, due to magnetic field dependence of the magnetic susceptibility. Magnetic field-dependent nuclear spin−spin coupling was discussed by Raynes and Stevens via fourth-order perturbation theory.[34]

A few semiempirical[35,36] and ab initio calculations[37] have been carried out. Theoretical aspects of the magnetic-field dependence of quadrupole splitting in ^{131} Xe were considered by Vaara and Pykkö, who presented accurate numerical predictions[38] in good agreement with corresponding experimental values.[39] Theoretical and computational studies on nuclear magnetic shielding in closed-shell atoms as a function of even powers of a perturbing magnetic field were reported by Vaara and co-workers,[40] and the magnetic-field dependence of ^{59}Co nuclear magnetic shielding in Co(III) complexes was investigated.[41] Nonlinear ring currents and the effect of strong magnetic fields on π-electron circulation were analyzed by Soncini and Fowler.[42]

Increasing attention is being paid to nonlinear magnetic response[43] in view of possible technological applications, for example, a semiconductor-to-metal switch, which can be operated via the Aharonov-Bohm effect in carbon nanocylinders whose axes are aligned along a strong magnetic field,[44,45] the quantum Hall effect observed in graphene sheets at room temperature,[46] and the field-induced change of the electronic band structure of CeBiPt evidenced by electrical-transport measurements in pulsed magnetic fields.[47]

A systematic study of molecular response to intense magnetic fields in the lower limit of the intermediate regime has recently been undertaken to rationalize the phenomenology induced in the electron distribution of diamagnetic atoms and molecules: a computational approach to nonlinear magnetic field dependence of magnetic susceptibility and electric and magnetic nuclear shielding has been developed in a series of papers within the framework of the Rayleigh−Schrödinger perturbation theory, allowing for the conventional common origin (CO) choice, gaugeless basis sets, and coupled Hartree−Fock approximation.[48−55]

The present study attempts to evaluate fourth-rank hypermagnetizability and nuclear magnetic hypershielding tensors in some closed-shell systems characterized by induced orbital paramagnetism,[56] the BH molecule,[56−69] the CH$^+$ cation,[68−70] and two planar unsaturated hydrocarbons exhibiting π paramagnetism, cyclobutadiene C_4H_4,[71,72] and flattened cy-

Table 3. Magnetic Hypersusceptibility,[a] $X_{\alpha\beta\gamma\delta}$, and Susceptibility,[b] $\chi_{\alpha\beta}$, of the BH Molecule

method	component[c]	$X(H)$[d]	$X(\mathrm{CM})$[d]
CHF (CO)	xxxx	−7882	−7881
	xxyy	−2627	−2627
	xxzz	400.2	400.2
	zzzz	36.02	36.02
	$\langle X \rangle$	−3876	−3875
DFT (KT3)	xxxx	−6962	−5902
	xxyy	−2320	−1967
	xxzz	277.8	277.9
	zzzz	41.28	41.28
	$\langle X \rangle$	−3483	−2918

method	CHF(CO)	DFT(KT3)
component[e]	$\chi(H)$[d]	$\chi(\mathrm{H})$[d]
xx	7.15	5.44
zz	−2.51	−2.50
$\langle \chi \rangle$	3.93	2.80
component[e]	$\chi(\mathrm{CM})$[d]	$\chi(\mathrm{CM})$[d]
xx	7.15	5.44
zz	−2.51	−2.50
$\langle \chi \rangle$	3.93	2.79

[a] In SI atomic units. The conversion factor to SI units is $1.42825951 \times 10^{-39}$ JT^{-4} per molecule, see ref 83. [b] In SI atomic units. The conversion factor to SI units is $7.891036\,60 \times 10^{-29}$ JT^{-2}, see ref 83. [c] Only components contributing to the average property are reported. yyyy = xxxx and xxzz = yyzz by symmetry. [d] Common origin results; the gauge origin is indicated between parentheses. [e] xx = yy by symmetry.

Table 4. Magnetic Hypershielding, $\Sigma^{C}_{\alpha\beta\gamma\delta}$, and Shielding, $\sigma^{C}_{\alpha\beta}$, of the Carbon Nucleus in the CH$^+$ Cation[a]

method	component	$\Sigma^{\mathrm{C}}(C)$	$\Sigma^{\mathrm{C}}(H)$
CHF (CO)	xxxx	2.642×10^{6}	2.618×10^{6}
	xxyy	8.807×10^{5}	8.727×10^{5}
	xxzz	-1.103×10^{5}	-1.095×10^{5}
	zxxz	-1.307×10^{5}	-1.297×10^{5}
	zzzz	14.99	14.99
	$\langle \Sigma^{\mathrm{C}} \rangle$	1.313×10^{6}	1.301×10^{6}
DFT (KT3)	xxxx	8.983×10^{5}	9.665×10^{5}
	xxyy	2.994×10^{5}	3.222×10^{5}
	xxzz	-4.820×10^{4}	-4.821×10^{4}
	zxxz	-5.749×10^{4}	-5.750×10^{4}
	zzzz	15.68	15.68
	$\langle \Sigma^{\mathrm{C}} \rangle$	4.368×10^{5}	4.732×10^{5}

method	CHF(CO)	DFT(KT3)
component	$\sigma^{\mathrm{C}}(C)$	$\sigma^{\mathrm{C}}(C)$
xx	−2051	−1276
zz	247.0	250.4
$\langle \sigma^{\mathrm{C}} \rangle$	−1285	−767.0
component	$\sigma^{\mathrm{C}}(H)$	$\sigma^{\mathrm{C}}(H)$
xx	−2047	−1276
zz	247.0	250.4
$\langle \sigma^{\mathrm{C}} \rangle$	−1282	−767.1

[a] See footnotes a−e of Table 1 for the use of symbols, units, and abbreviations. Coordinates in bohr: H (0, 0, 0); C (0, 0, 2.1370912849).

Table 5. Magnetic Hypershielding, $\Sigma^{H}_{\alpha\beta\gamma\delta}$, and Shielding, $\sigma^{H}_{\alpha\beta}$, of the Hydrogen Nucleus in the CH$^+$ Cation[a]

method	component	$\Sigma^{\mathrm{H}}(H)$	$\Sigma^{\mathrm{H}}(C)$
CHF (CO)	xxxx	-2.032×10^{4}	-2.034×10^{4}
	xxyy	−6773	−6779
	xxzz	789.0	789.1
	zxxz	−7665	−7659
	zzzz	5.86	5.86
	$\langle \Sigma^{\mathrm{H}} \rangle$	-1.359×10^{4}	-1.359×10^{4}
DFT (KT3)	xxxx	−4295	−4966
	xxyy	−1432	−1655
	xxzz	231.9	232.0
	zxxz	−3320	−3317
	zzzz	7.42	7.42
	$\langle \Sigma^{\mathrm{H}} \rangle$	−3525	−3881

method	CHF(CO)	DFT(KT3)
component	$\sigma^{\mathrm{H}}(H)$	$\sigma^{\mathrm{H}}(H)$
xx	35.79	27.63
zz	30.17	30.56
$\langle \sigma^{\mathrm{C}} \rangle$	33.92	28.61
component	$\sigma^{\mathrm{H}}(C)$	$\sigma^{\mathrm{H}}(C)$
xx	35.65	27.50
zz	30.17	30.56
$\langle \sigma^{\mathrm{H}} \rangle$	33.82	28.52

[a] See footnotes a−e of Table 1 for the use of symbols, units, and abbreviations.

clo-octatetraene (COT) C_8H_8. A "clamped" planar structure of COT is annelated with perfluorocyclobuteno moieties[73] and with bicyclo[2.1.1] hex-2-ene groups.[74,75]

The scope of the present research is (i) to investigate the reliability and the limits of approaches neglecting contributions higher than a cubic response's; (ii) to compare fourth-rank hypermagnetizabilities and hypershieldings as properties suitable for experimental detection of nonlinear behavior; (iii) to estimate the contribution of electron correlation to fourth-rank magnetic tensors via density functional theory (DFT), allowing for the Keal-Tozer KT3 functional;[76,77] and (iv) to investigate whether induced orbital paramagnetism can be controlled by applying a magnetic field of increasing strength.

The approaches employed are outlined in section III. Numerical estimates of the fourth-rank hypershieldings for the molecules BH, C_4H_4, and C_8H_8 and the CH$^+$ cation, and a discussion of results are also reported in section III.

III. Calculation of Fourth-Rank Magnetic Tensors

The energy of a closed-shell molecule in the electronic reference state a, in the presence of an external spatially uniform and time-independent magnetic field **B** and of an intramolecular permanent magnetic dipole m_I at nucleus I can be written as a Taylor series:[48−55]

$$W_a = W_a^{(0)} + W_a^{(2)} + W_a^{(4)} + \ldots = W_a^{(0)} - \frac{1}{2}\chi_{\alpha\beta}B_\alpha B_\beta - \frac{1}{24}X_{\alpha\beta\gamma\delta}B_\alpha B_\beta B_\gamma B_\delta + \ldots + \sigma^I_{\alpha\beta} m_{I\alpha} B_\beta + \frac{1}{6}\Sigma^I_{\alpha\beta\gamma\delta} m_{I\alpha} B_\beta B_\gamma B_\delta + \ldots \quad (1)$$

where $W_a^{(0)}$ is the energy of the isolated molecule, $\chi_{\alpha\beta}$ is the magnetic susceptibility, and $\sigma^I_{\alpha\beta}$ is the magnetic shielding at nucleus I. The fourth-rank tensors $X_{\alpha\beta\gamma\delta}$ and $\Sigma^I_{\alpha\beta\gamma\delta}$ account for nonlinear response in **B**. The explicit expressions needed to calculate these quantities contain 10 propagators, see eq 18 of ref 48 and eq 28 of ref 53. Einstein's convention of summing over repeated Greek indices is in force throughout this paper.

Table 6. Magnetic Hypersusceptibility,[a] $X_{\alpha\beta\gamma\delta}$, and Susceptibility, $\chi_{\alpha\beta}$, of the CH$^+$ Cation

Method	Component	X (H)	X (CM)
CHF (CO)	xxxx	-1.452×10^4	-1.451×10^4
	xxyy	−4839	−4836
	xxzz	574.2	573.8
	zzzz	4.57	4.57
	⟨X⟩	−7282	−7279
DFT (KT3)[c]	xxxx	−5435	−4880
	xxyy	−1812	−1627
	xxzz	242.8	242.5
	zzzz	4.79	4.79
	⟨X⟩	−2703	−2408

method	CHF(CO)	DFT(KT3)
component	$\chi(H)$	$\chi(H)$
xx	10.59	6.30
zz	−1.44	−1.44
⟨χ⟩	6.58	3.72
component	$\chi(CM)$	$\chi(CM)$
xx	10.59	6.29
zz	−1.44	−1.44
⟨χ⟩	6.58	3.72

[a] See footnotes a−e of Table 3 for the use of symbols, units, and abbreviations.

The induced orbital magnetic dipole is

$$\langle \hat{m}_\alpha \rangle = -\frac{\partial W_a}{\partial B_\alpha} = \chi_{\alpha\beta} B_\beta + \frac{1}{6} X_{\alpha\beta\gamma\delta} B_\beta B_\gamma B_\delta + \ldots - \sigma^I_{\beta\alpha} m_{I\beta} - \frac{1}{2} \Sigma^I_{\beta\alpha\gamma\delta} m_{I\beta} B_\gamma B_\delta + \ldots \quad (2)$$

The magnetic field induced at the nucleus in question by the n electrons responding to the perturbation is

$$\langle \hat{B}^n_{I\alpha} \rangle = -\frac{\partial W_a}{\partial m_{I\alpha}} = -\sigma^I_{\alpha\beta} B_\beta - \frac{1}{6} \Sigma^I_{\alpha\beta\gamma\delta} B_\beta B_\gamma B_\delta + \ldots = -\int \sigma^I_{\alpha\beta}(\mathbf{B})\, \mathrm{d}B_\beta \quad (3)$$

where

$$\sigma^I_{\alpha\beta}(\mathbf{B}) = \sigma^I_{\alpha\beta} + \frac{1}{2} \Sigma^I_{\alpha\beta\gamma\delta} B_\gamma B_\delta + \ldots \quad (4)$$

is the field-dependent magnetic shielding at nucleus I. For the species BH and CH$^+$ characterized by diamagnetism in the z bond direction, that is, $\chi_{\parallel} \equiv \chi_{zz} < 0$, and strong paramagnetism in the radial direction, we will consider only terms depending on $B_\perp$, rewriting eq 1 in the truncated form

$$W_a - W_a^{(0)} \approx W_a^{(2)} + W_a^{(4)} \approx -\frac{1}{2} \chi_\perp B_\perp^2 + \frac{1}{24} |X_\perp| B_\perp^4 \quad (5)$$

where the perpendicular components of the susceptibility are denoted $\chi_\perp \equiv \chi_{xx} = \chi_{yy} > 0$ and $X_\perp \equiv X_{xxxx} = X_{yyyy} < 0$. The interaction energy (eq 5) has a local maximum $W_a^{(2)} + W_a^{(4)} = 0$ for $B_\perp = 0$, an inflection point for $B_\perp \equiv B_s = \surd(2\chi_\perp/|X_\perp|)$, a minimum $-3\chi_\perp^2/(2|X_\perp|)$ for $B_\perp \equiv B_m = \surd(6\chi_\perp/|X_\perp|)$. It vanishes also for $B_\perp \equiv B_c = \surd(12\chi_\perp/|X_\perp|)$, and it becomes positive, that is, destabilizing, beyond this field value.

The orbital magnetic dipole induced by $B_\perp$ in the radial direction of the BH molecule

$$\langle \hat{m}_\perp \rangle = \chi_\perp B_\perp + \frac{1}{6} X_\perp B_\perp^3 + \ldots \quad (6)$$

reaches its maximum paramagnetic value $\langle m_s \rangle = (2/3)\chi_\perp \surd(2\chi_\perp/|X_\perp|)$ at the inflection point of the interaction energy, B_s. It vanishes at $B_\perp = 0$ and for $B_\perp = B_m$, where transition from paramagnetic to diamagnetic response occurs. For instance, using the theoretical CHF results reported in Table 3, $\chi_\perp = 7.15$ au and $X_\perp = -7882$ au, we find $B_s \approx 4.3 \times 10^{-2}$ au and $\langle m_s \rangle \approx 0.20$ au, compare Figure 1.

The radial component of magnetic field induced at nucleus I by $B_\perp$ applied perpendicular to the BH bond is

$$\langle \hat{B}^n_{I\perp} \rangle = -\sigma^I_\perp B_\perp - \frac{1}{6} \Sigma^I_\perp B_\perp^3 + \ldots \quad (7)$$

indicating by $\sigma^I_\perp$ and $\Sigma^I_\perp$ the perpendicular components of nuclear shielding and hypershielding. If I is either H or B, with $\sigma^I_\perp$ and $\Sigma^I_\perp$ of opposite sign, then an extremum point of $\langle \hat{B}^n_{I\perp} \rangle$ occurs at $B^*_\perp = \surd(|2\sigma^I_\perp/\Sigma^I_\perp|)$. Relationships similar to 5−7 hold for the other systems studied.

Magnetic susceptibilities and hypersusceptibilities, magnetic shielding, and hypershieldings at the nuclei have been calculated for BH, CH$^+$, C$_4$H$_4$, and C$_8$H$_8$ at two levels of

Table 7. Magnetic Hypershielding, $\Sigma^C_{\alpha\beta\gamma\delta}$, and Shielding, $\sigma^C_{\alpha\beta}$, of the Carbon Nucleus in the C$_4$H$_4$ Molecule[a]

method	component	$\Sigma^C(C)$	$\Sigma^C(CM)$
CHF (CO)	xxxx	7751	7728
	xxyy	−2727	−2719
	xxzz	−1808	−1805
	yxxy	-1.884×10^4	-1.890×10^4
	yyyy	−1900	−1863
	yyzz	916.4	893.6
	zxxz	5454	5424
	zyyz	2559	2550
	zzzz	1.252×10^4	1.250×10^4
	$\langle \Sigma^C \rangle$	785.6	761.5
DFT (KT3)	xxxx	1.253×10^4	1.229×10^4
	xxyy	−2029	−2090
	xxzz	−1232	−1305
	yxxy	-1.726×10^4	-1.642×10^4
	yyyy	1151	1075
	yyzz	1361	1405
	zxxz	5831	6309
	zyyz	2673	2713
	zzzz	1.231×10^4	1.208×10^4
	$\langle \Sigma^C \rangle$	3066	3211

method	CHF(CO)	DFT(KT3)
component	$\sigma^C(C)$	$\sigma^C(C)$
xx	124.2	108.1
yy	107.0	94.23
yz	−69.37	−56.46
zy	28.51	28.29
zz	−106.6	−66.40
$\langle \sigma^C \rangle$	41.53	45.32
component	$\sigma^C(H)$	$\sigma^C(H)$
xx	124.1	108.0
yy	106.9	94.18
yz	−69.32	−56.42
zy	28.67	28.49
zz	−106.7	−66.57
$\langle \sigma^C \rangle$	41.42	45.21

[a] See footnotes a−e of Table 1 for the use of symbols, units, and abbreviations. Coordinates in bohr: H (0, 2.69820955550, 2.9255001457); C (0, 1.2552449153, 1.4870179359).

Table 8. Magnetic Hypershielding, $\Sigma^{H}_{\alpha\beta\gamma\delta}$, and Shielding, $\sigma^{H}_{\alpha\beta}$, of the Hydrogen Nucleus in the C_4H_4 Molecule[a]

method	component	$\Sigma^H(H)$	$\Sigma^H(CM)$
CHF (CO)	xxxx	−1410	−1493
	xxyy	57.94	26.24
	xxzz	55.54	31.05
	yxxy	−941.3	−958.5
	yyyy	−132.6	−180.9
	yyzz	−57.33	−74.16
	zxxz	170.6	158.2
	zyyz	−63.49	−76.61
	zzzz	504.5	460.6
	$\langle\Sigma^H\rangle$	−363.3	−421.5
DFT (KT3)	xxxx	−907.6	−1981
	xxyy	176.7	8.86
	xxzz	132.1	17.18
	yxxy	−829.0	−952.1
	yyyy	225.7	−75.79
	yyzz	43.00	−49.71
	zxxz	237.2	115.1
	zyyz	43.64	−51.34
	zzzz	720.0	475.0
	$\langle\Sigma^H\rangle$	−31.66	−498.8

method	HF(CO)	DFT(KT3)
component	$\sigma^H(H)$	$\sigma^H(H)$
xx	28.04	28.15
yy	28.77	27.56
zz	21.21	21.90
$\langle\sigma^C\rangle$	26.00	25.87
component	$\sigma^H(CM)$	$\sigma^H(CM)$
xx	27.61	27.70
yy	28.57	27.38
zz	21.01	21.72
$\langle\sigma^H\rangle$	25.73	25.60

[a] See footnotes a−e of Table 1 for the use of symbols, units, and abbreviations.

Table 9. Magnetic Hypersusceptibility,[a] $X_{\alpha\beta\gamma\delta}$, and Susceptibility, $\chi_{\alpha\beta}$, of the C_4H_4 Molecule

method	component	$X(C)$	$X(CM)$
CHF (CO)	xxxx	−3869	−3847
	xxyy	−81.99	−72.78
	xxzz	39.09	46.01
	yyyy	−431.7	−405.7
	yyzz	−41.50	−36.16
	zzzz	−146.7	−139.5
	$\langle X\rangle$	−923.3	−903.6
DFT (KT3)	xxxx	−5329	−4999
	xxyy	−222.6	−158.4
	xxzz	−5.57	25.71
	yyyy	−563.8	−454.0
	yyzz	−85.26	−59.48
	zzzz	−223.0	−182.2
	$\langle X\rangle$	−1348	−1204

method	HF(CO)	DFT(KT3)
component	$\chi(C)$	$\chi(C)$
xx	−0.78	−0.13
yy	−4.60	−4.21
zz	−5.27	−5.20
$\langle\chi\rangle$	−3.55	−3.18
component	$\chi(CM)$	$\chi(CM)$
xx	−0.77	−0.12
yy	−4.59	−4.21
zz	−5.26	−5.19
$\langle\chi\rangle$	−3.54	−3.17

[a] See footnotes a−e of Table 3 for the use of symbols, units, and abbreviations.

Table 10. Magnetic Hypershielding, $\Sigma^{C}_{\alpha\beta\gamma\delta}$, and Shielding, $\sigma^{C}_{\alpha\beta}$, of the Carbon Nucleus in the C_8H_8 Molecule[a]

method	CHF(CO)	DFT(KT3)
component	$\Sigma^C(C)$	$\Sigma^C(C)$
xxxx	7211	7883
xxyy	2249	2124
xxzz	-4.655×10^4	-8.584×10^4
yxxy	2853	2831
yyyy	4512	4597
yyzz	2.215×10^4	5.021×10^4
zxxz	1134	2526
zyyz	−835.9	−409.1
zzzz	8.016×10^4	5.561×10^4
$\langle\Sigma^C\rangle$	1.458×10^4	1.080×10^5

method	CHF(CO)	DFT(KT3)
component	$\sigma^C(C)$	$\sigma^C(C)$
xx	−2.40	−0.26
yy	24.72	36.73
zz	143.3	106.4
$\langle\sigma^C\rangle$	55.20	47.61

[a] See footnotes a−e of Table 1 for the use of symbols, units, and abbreviations. Coordinates in bohr: H (5.1668362830, 2.1620413390, 0); C (3.2324200158 1.40696913683, 0).

Table 11. Magnetic Hypershielding, $\Sigma^{H}_{\alpha\beta\gamma\delta}$, and Shielding $\sigma^{H}_{\alpha\beta}$, of the Hydrogen Nucleus in the C_8H_8 Molecule[a]

Method	CHF(CO)	DFT(KT3)
component	$\Sigma^H(H)$	$\Sigma^H(H)$
xxxx	446.9	762.7
xxyy	122.1	308.9
xxzz	−1440	−2473
yxxy	66.00	250.0
yyyy	42.0	888.1
yyzz	503.3	1981
zxxz	72.75	195.2
zzzz	-3.323×10^4	-2.033×10^5
$\langle\Sigma^H\rangle$	-6.690×10^3	-4.029×10^4

method	CHF(CO)	DFT(KT3)
component	$\sigma^H(H)$	$\sigma^H(H)$
xx	27.94	27.17
yy	30.63	30.29
zz	33.12	41.03
$\langle\sigma^H\rangle$	30.56	32.83

[a] See footnotes a−e of Table 1 for the use of symbols, units, and abbreviations.

Table 12. Magnetic Hypersusceptibility,[a] $X_{\alpha\beta\gamma\delta}$, and Susceptibility, $\chi_{\alpha\beta}$, of the C_8H_8 Molecule

method	CHF(CO)	DFT(KT3)
component	$X(CM)$	$X(CM)$
xxxx	−477.1	−818.7
xxyy	−166.1	−303.8
xxzz	−554.5	−1459
zzzz	-1.393×10^5	-8.492×10^5
$\langle X\rangle$	-2.857×10^4	-1.715×10^5

method	CHF(CO)	DFT(KT3)
component	$\chi(CM)$	$\chi(CM)$
xx	−12.25	−11.34
zz	16.78	48.83
$\langle\chi\rangle$	−2.57	8.72

[a] See footnotes a−e of Table 3 for the use of symbols, units, and abbreviations.

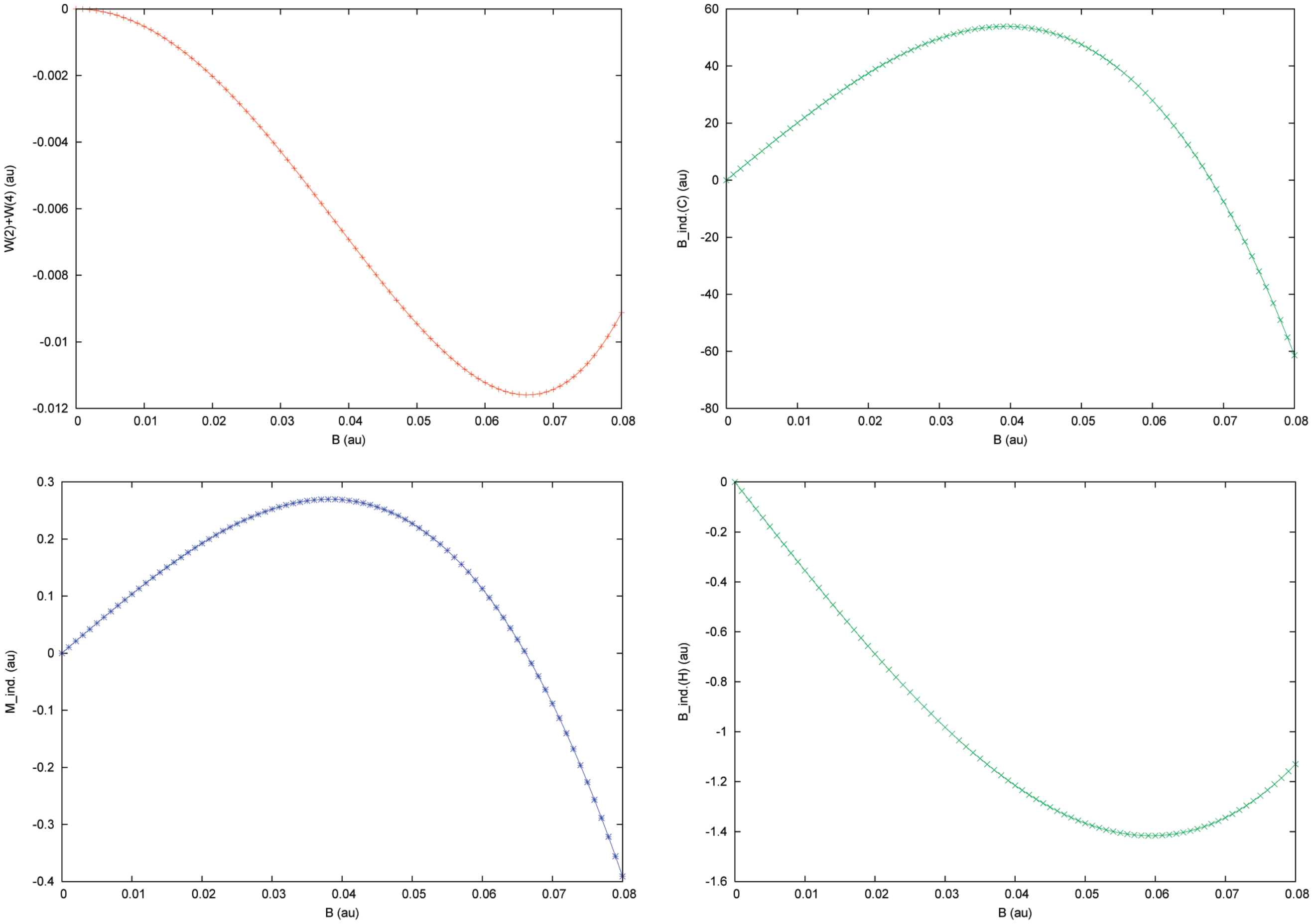

Figure 2. Response properties of the CH^+ cation in a magnetic field normal to the bond direction. Top left: Magnetic interaction energy. Top right: Magnetic field induced at the carbon nucleus. Bottom left: Induced magnetic moment. Bottom right: Magnetic field induced at the hydrogen nucleus.

accuracy, coupled Hartree−Fock (CHF), equivalent to random-phase approximation (RPA), and DFT, allowing for the KT3 functional,[76,77] implemented in the DALTON package.[78] The KT3 functional was found to be the most efficient for calculating shielding constants in a series of small molecules[79] and for studies of hydrogen bonding.[80] Calculated values for tensor components are reported in Tables 1−12. The isotropic term $\langle \Sigma^I \rangle$ is defined:

$$\langle \Sigma \rangle^I = \frac{1}{15}[\Sigma^I_{\alpha\alpha\beta\beta} + \Sigma^I_{\alpha\beta\alpha\beta} + \Sigma^I_{\alpha\beta\beta\alpha}] \qquad (8)$$

and $\langle X \rangle$ is analogously defined.

We give data needed to reproduce our calculations of the properties in eqs 1−7. Gaussian basis sets used for the BH molecule are as follows: for B, the 13s set from ref 81 plus one s with exponent 0.022845; the 8p set from ref 81 plus a 3p set of functions with exponents 880.0, 220.0, and 0.01588267; the 8d set with exponents 29.97, 9.99, 3.33, 1.110, 0.402, 0.145, 0.048333, and 0.016111; the 5f set with exponents 2.646, 0.882, 0.311, 0.103667, and 0.03455567; for H, the 10s set from ref 81; the 6p set with exponents 18.807, 6.269, 2.292, 0.838, 0.292, and 0.09733; the 3d set with exponents 3.171, 1.057, and 0.3523. Gaussian basis sets used for the CH^+ and C_4H_4 molecules are as follows: for C, the 13s set from ref 81, the 8p set from ref 81 plus a 2p set of functions with exponents 1512.9 and 355.1; the 5d set with exponents 5.262, 1.848, 0.649, 0.228, and 0.08; and the 2f set with exponents 1.419 and 0.485; for H, the 10s set from ref 81, the 4p set with exponents 6.269, 2.292, 0.838, and 0.292; one d function with exponent 1.057. The Gaussian basis set used for the C_8H_8 molecule was the truncated aug-cc-pCVTZ, (12s7p3d2f/6s3p2d) → 6s5p3d2f/4s3p2d basis set from ref 52. The molecular geometries for BH, and CH^+ were optimized at the HF scheme with the same basis set employed in the calculations; that of C_4H_4 was optimized at the B3LYP[82] level of theory, with the same basis set employed in the calculations. The molecular geometry of cyclo-octatetraene was taken from ref 52. The interaction energy, eq 5; induced orbital magnetic moment, eq 6; and magnetic field induced at the nuclei, eq 7, are displayed in Figures 1−4 as a function of the applied magnetic field.

Within the assumption of cubic response, the values of magnetic field $B_\perp = B_m$ at which a transition from the paramagnetic to diamagnetic response would take place (corresponding to a change of sign in eq 6 for the induced moment) are, in atomic units (1 au of magnetic flux density $\hbar/ea_0^2 = 2.35051742 \times 10^5$ T from ref 83), $\approx 7.4 \times 10^{-2}$, $\approx 6.6 \times 10^{-2}$, and $\approx 2.7 \times 10^{-2}$, respectively, for BH, CH^+, and C_8H_8, within the CHF approximation, see the red and blue curves in Figures 1, 2, and 4. Since $\chi_\perp$ and $X_\perp$ have the same sign in C_4H_4, no transition was observed in Figure 3.

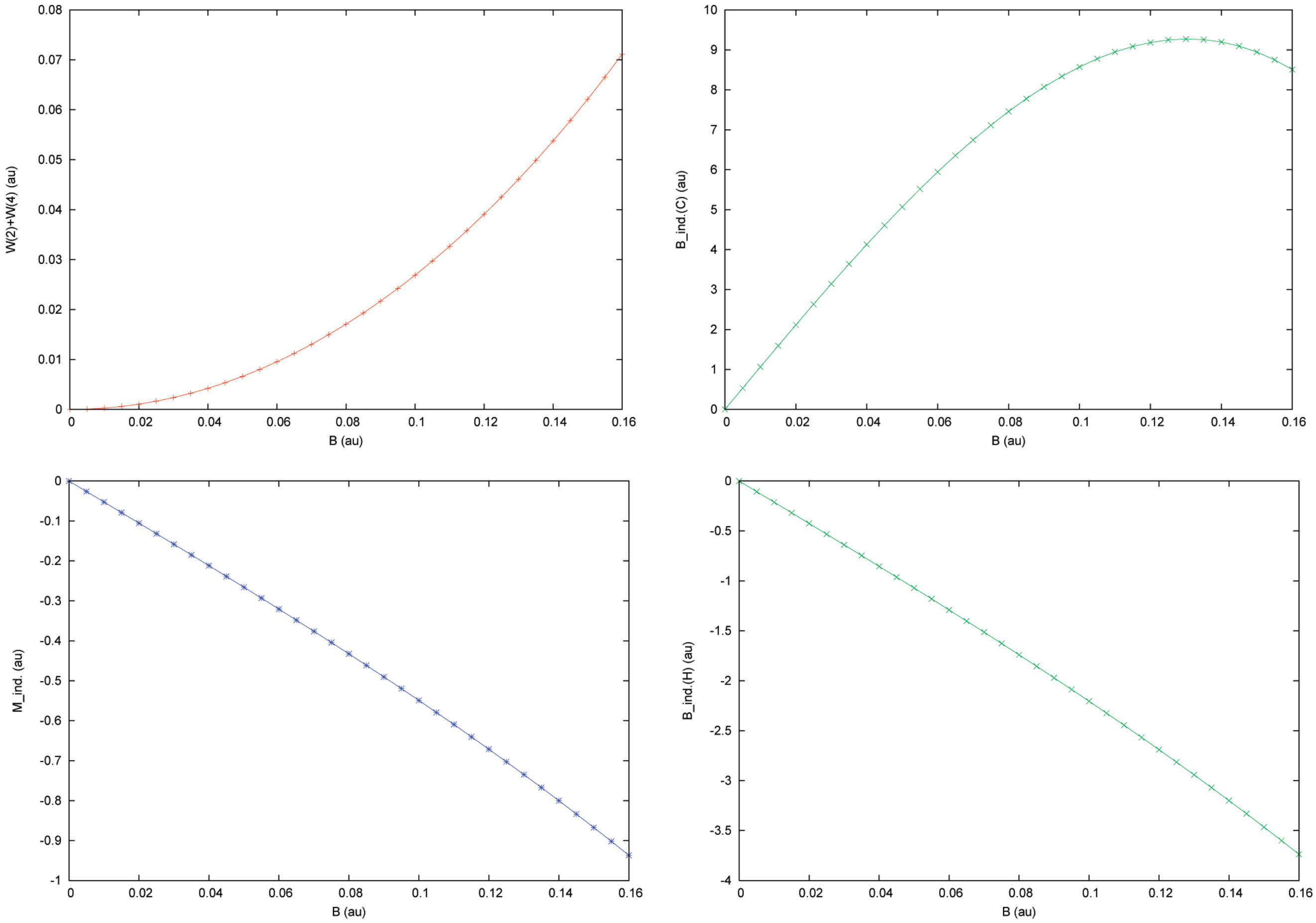

Figure 3. Response properties of the C_4H_4 molecule in a magnetic field normal to the molecular plane. Top left: Magnetic interaction energy. Top right: Magnetic field induced at the carbon nucleus. Bottom left: Induced magnetic moment. Bottom right: Magnetic field induced at the hydrogen nucleus.

Analogously, the values of $B^{*}_{\perp}$, in atomic units, corresponding to a change of sign of $\langle \hat{B}^{n}_{H\perp} \rangle$ in eq 7, are $\approx 5.9 \times 10^{-2}$ and $\approx 4.5 \times 10^{-2}$, for CH^+ and C_8H_8 at the CHF level, respectively. $\sigma^{H}_{\perp}$ and $\Sigma^{H}_{\perp}$ have the same sign in BH and C_4H_4, compare for the monotonically decreasing green curves in Figures 1 and 3.

The values of $B^{*}_{\perp}$, in atomic units, for a sign inversion of the shielding of the heavier nucleus are $\approx 4.5 \times 10^{-2}$, $\approx 3.9 \times 10^{-2}$, and ≈ 0.13, for BH, CH^+, and C_4H_4. The green curve for the shielding of the C nucleus in C_8H_8 decreases monotonically in Figure 4.

We observe that, within the assumption of cubic response, that is, neglecting higher nonlinear contributions, and within the CHF approximation, the critical B_m values of external magnetic field at which transition from induced orbital paramagnetism to diamagnetic behavior would occur in BH, ≈ 0.074 au, and CH^+, ≈ 0.066 au, are much smaller than those predicted by Tellgren et al.,[30] 0.25 and 0.45 au, respectively. This seems to imply that perturbative approaches like those employed in the present investigations are basically unsuitable to describe a nonlinear response to extra-strong magnetic fields of diatomics such as BH and CH^+, characterized by strong radial paramagnetism.

However, on increasing the size of the perturbed system, the discrepancies between the predictions in ref 30 and ours become smaller; compare the values for the clamped COT molecule, ≈ 0.035 au, estimated by Tellgren et al. with $B_m \approx 0.027$ obtained here. This trend is expected, since the magnitude of the critical field $B_\perp = B_m$ decreases with the area of the system. In fact, orbital magnetism is proportional to the external magnetic flux; so that B_m varies approximately as the inverse of the area of the molecule.[30] Therefore, perturbative approaches like those applied here are accurate and can safely be used to rationalize a nonlinear response in systems spread over a large surface, which are most interesting for practical applications.[43−46]

On the other hand, the radial component $\chi_\perp$ of the second-rank magnetizability of BH is known to be affected by electron correlation, as demonstrated by multiconfiguration self-consistent-field calculations.[69] Also, the KT3 results in Table 3 indicate that paramagnetism is lowered with respect to CHF. A similar reduction of $\chi_\perp$ for the CH^+ cation is observed in Table 6. Correlation contributions dramatically influence both hypermagnetizabilities and hypershieldings according to the present investigations. Tables 1−6 show that the *xxxx*, *xxyy*, *xxzz*, and *zxxz* components of magnetic tensors are most affected.

Although the KT3 predictions obtained via the gaugeless basis sets depend strongly on the origin assumed in the calculation, much more than the corresponding CHF (which would be origin-independent for a complete basis set), inspection of the tables shows that electron correlation

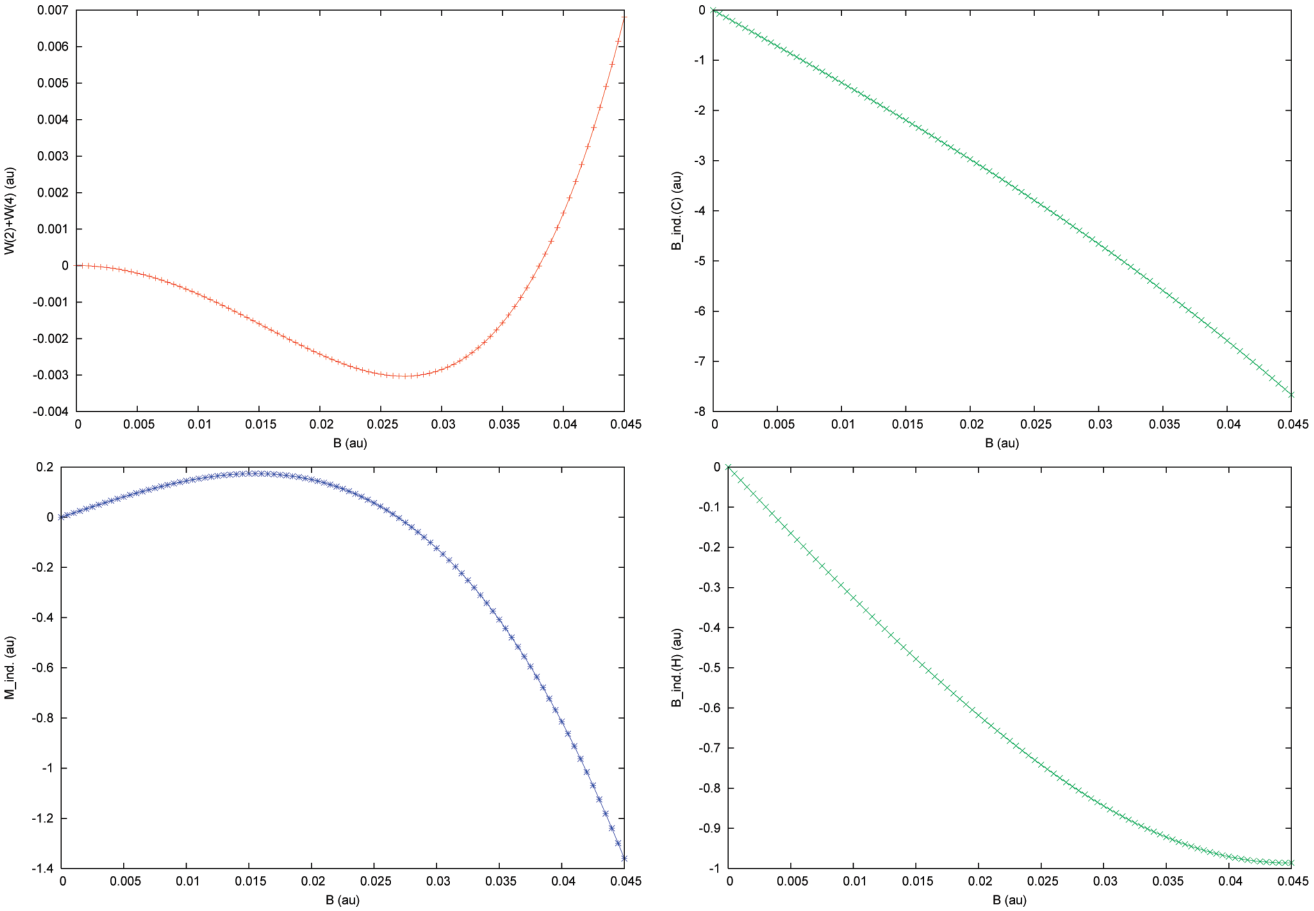

Figure 4. Response properties of the C_8H_8 molecule in a magnetic field normal to the molecular plane. Top left: Magnetic interaction energy. Top right: Magnetic field induced at the carbon nucleus. Bottom left: Induced magnetic moment. Bottom right: Magnetic field induced at the hydrogen nucleus.

provides a huge positive contribution to $X_\perp$ of paramagnetic diatomics. The difference between CHF and DFT KT3 estimates is as big as $\approx 2 \times 10^3$ au for BH and $\approx 1 \times 10^4$ au for CH^+, for the gauge origin on the center of mass. Quite remarkably, the correlation contributions to $X_\perp \equiv X_{zzzz}$ of cyclobutadiene and COT are negative. However, for the gauge origin on the center of mass, we calculated ≈ -43 au for the former, see Table 9, and $\approx -7 \times 10^5$ au for the latter, Table 12, at the KT3 level. Enormous changes were found also for $\Sigma^I_\perp$, KT3 estimates being in many cases an order of magnitude smaller than those of CHF.

Notwithstanding the evident lack of accuracy of our common origin KT3 calculations of $X_\perp$ and $\Sigma_\perp$, the results obtained here indicate that either perturbative or nonperturbative[30] calculations not taking electron correlation into account are limitedly reliable for predicting critical values of the applied magnetic field B_m at which the interaction energy changes sign in systems such as BH and CH^+. One can therefore conclude that transition from orbital induced paramagnetism[56] to diamagnetism should occur at much smaller values of critical B_m than those predicted by CHF or RPA calculations not taking electron correlation into account.

Eventually, the magnitude of theoretical values obtained in this study and in a previous one for nitroso and diazene compounds[55] seem to indicate that nuclear magnetic hypershieldings can be better candidates than hypermagnetizabilities for experimental detection of nonlinear magnetic response. Nuclear magnetic resonance spectroscopy would yield the best practical option.[31,32]

IV. Concluding Remarks and Outlook

The present study provides reasonable answers to the basic questions (i−iv) raised in section II: (i) Perturbative CHF-RPA approaches to nonlinear response neglecting contributions higher than fourth order in the applied magnetic field may be insufficiently reliable for accurate estimates of interaction energy in closed-shell compounds of a small size such as BH and CH^+, characterized by strong induced orbital paramagnetism in the singlet ground state. The interpretation of the highly nonlinear behavior, and the prediction of the magnetic field values $B_\perp = B_m$ and $B_\perp = B^*_\perp$, at which transition from paramagnetism to diamagnetism would occur in these systems, seems to require hypermagnetizability and hypershielding tensors higher than the fourth-order $X_{\alpha\beta\gamma\delta}$ and $\Sigma^I_{\alpha\beta\gamma\delta}$ in eqs 1−4. However, the CHF perturbation method turns out to be useful for molecules as big as clamped C_8H_8, for which satisfactory agreement with nonperturbative calculations[29,30] was obtained. (ii) A nonlinear response can in principle be detected by measuring magnetic-field-dependent magnetizabilities and hypermagnetizabilities via a superconducting quantum interference device (SQUID). On the other hand, according to previous studies,[55] deviations from a linear response would more easily be observed by measurements of magnetic hypershielding at the nuclei via NMR spectroscopy. The magnitude of calculated $\Sigma^I_{\alpha\beta\gamma\delta}$ is big in clamped C_8H_8, suggesting that compounds containing this moiety may be potential candidates for detection. Cyclic species with bigger area are best suited for experimental observation of nonlinear contributions to a global molecular property such as the interaction energy $W_a - W_a^{(0)}$, eq 1, and for determination of the critical field B_m, as B_m decreases with system area. However, nonlinear response can in principle be observed also in small-sized species by investigating local effects on nuclear hypershielding. (iii) According to the present study, correlation plays a major role, and it dramatically affects the magnitude of calculated fourth-rank response tensors. Therefore, reliable predictions of hypermagnetizabilities and magnetic hypershielding at the nuclei would only be obtained by theoretical methods accounting for electron correlation. Furthermore, values of $X_\perp$ predicted via KT3 in BH and in CH^+ are smaller than CHF's, which seems to imply that, at variance with (i), perturbative approaches limited to cubic response may be applicable at levels of theory taking electron correlation into account. In these diatomics, $\Sigma^I_\perp$ calculated via DFT methods for boron and carbon are also smaller than CHF's. (iv) Therefore, allowing for the previous points, the answer to the question posed in the title is likely to be in the affirmative: induced orbital paramagnetism of some closed-shell species selected ad hoc can be controlled, and transition from paramagnetic to diamagnetic behavior can probably be observed in a terrestrial laboratory.

Eventually, highly excited hydrogen atoms and Rydberg molecules in strong magnetic fields are a paradigm of a real system, showing the signature of quantum chaos.[84−86] These species become chaotic as soon as the interaction of the electron with the magnetic field is of the same order of magnitude as the Coulomb interaction with the nucleus. The classical trajectories of the atomic electron undergo a transition from regularity to chaos as the field strength increases. Therefore, the interplay of regularity and chaos for highly excited Rydberg atoms and molecules in strong magnetic fields would possibly make difficult, or even preclude, in the majority of cases, experimental determination of hypermagnetizabilities and nuclear hypershieldings of rank higher than the fourth, and rationalization of nonlinear effects beyond the cubic in the field strength, either via perturbation theory or nonperturbative techniques, may become problematic.

Acknowledgment. The authors would like to thank Dr. S. Pelloni for helpful comments. Financial support to this work from the Italian MURST (Ministero dell'Universita e della Ricerca Scientifica e Tecnologica), via 60% funds, from the University of Buenos Aires, and from the Argentinian CONICET, is gratefully acknowledged.

References

(1) Lai, D. *Rev. Mod. Phys.* **2001**, *73*, 629–661.

(2) Reichhardt, T. *Nature* **1998**, *395*, 529–529.

(3) Ruder, H.; Wunner, G.; Herold, H.; Geyer, F. *Atoms in Strong Magnetic Fields*; Springer-Verlag: Berlin, 1994.

(4) Schmelcher, P.; Schweizer, W. *Atoms and Molecules in Strong External Fields*; Plenum Press: New York, 1998.

(5) Runge, K.; Sabin, J. R. *Int. J. Quantum Chem.* **1997**, *64*, 495–496, and references therein. .

(6) Schmelcher, P.; Cederbaum, L. S.; Kappes, U. In *Conceptual Trends in Quantum Chemistry*; Kryachko, E. S., Calais, J.-L., Eds.; Kluwer Academic: Dordrecht, Ther Netherlands, 1994.

(7) Schmelcher, P.; Cederbaum, L. S. In *Atoms and Molecules in Intense Fields*; Cederbaum, L. S., Kulander, K. C., March, N. H., Eds.; Springer: New York, 1997; Springer Series: Structure and Bonding, Vol. 86.

(8) Friedrich, H.; Wintgen, D. *Phys. Rep.* **1989**, *183*, 37–79.

(9) Schmelcher, P.; Cederbaum, L. S.; Meyer, H.-D. *Phys. Rev. A* **1988**, *38*, 6066–6079.

(10) Wille, U. *Phys. Rev. A* **1988**, *38*, 3210–3235.

(11) Kappes, U.; Schmelcher, P.; Pacher, T. *Phys. Rev. A* **1994**, *50*, 3775–3781.

(12) Kappes, U.; Schmelcher, P. *Phys. Rev. A* **1995**, *51*, 4542–4557.

(13) Kappes, U.; Schmelcher, P. *Phys. Rev. A* **1996**, *53*, 3869–3883.

(14) Kappes, U.; Schmelcher, P. *Phys. Rev. A* **1996**, *54*, 1313–1317.

(15) Kappes, U.; Schmelcher, P. *Phys. Lett. A* **1996**, *210*, 409–415.

(16) Kravchenko, Y. P.; Liberman, M. A. *Phys. Rev. A* **1997**, *55*, 2701–2710.

(17) Monteiro, T.; Taylor, K. *J. Phys. B* **1990**, *23*, 427–439.

(18) Basile, S.; Trombetta, F.; Ferrante, G. *Nuovo Cimento D* **1990**, *9*, 457.

(19) Turbiner, A. *JETP Lett.* **1983**, *38*, 618.

(20) Korolev, A. V.; Liberman, M. A. 1992, *45*, 1762−1766.

(21) Lai, D.; Salpeter, E. E.; Shapiro, S. L. *Phys. Rev. A* **1992**, *45*, 4832–4847.

(22) Ortiz, G.; Jones, M. D.; Ceperley, D. M. *Phys. Rev. A* **1995**, *52*, R3405–R3408.

(23) Lai, D.; Salpeter, E. E. *Phys. Rev. A* **1996**, *53*, 152–167.

(24) Demeur, M.; Heenen, P.-H.; Godefroid, M. *Phys. Rev. A* **1994**, *49*, 176–183.

(25) Kravchenko, Y. P.; Liberman, M. A. *Phys. Rev. A* **1997**, *56*, R2510–R2513.

(26) Kravchenko, Y. P.; Liberman, M. A. *Phys. Rev. A* **1998**, *57*, 3403–3418.

(27) Detmer, T.; Schmelcher, P.; Diakonos, F. K.; Cederbaum, L. S. *Phys. Rev. A* **1997**, *56*, 1825–1838.

(28) Detmer, T.; Schmelcher, P.; Cederbaum, L. S. *Phys. Rev. A* **1998**, *57*, 1767–1777.

(29) Tellgren, E. I.; Soncini, A.; Helgaker, T. *J. Chem. Phys.* **2008**, *129*, 154114.

(30) Tellgren, E. I.; Soncini, A.; Helgaker, T. *Phys. Chem. Chem. Phys.* **2009**, *11*, 5489–5498.

(31) Bendall, M. R.; Doddrell, D. M. *J. Magn. Reson.* **1979**, *33*, 659–663.

(32) Ramsey, N. F. *Phys. Rev. A* **1970**, *1*, 1320–1322.

(33) Źaucer, M.; Aźman, A. *Phys. Rev. A* **1977**, *16*, 475–476.

(34) Raynes, W. T.; Stevens, S. J. *Magn. Reson. Chem.* **1992**, *30*, 124–128.

(35) Doddrell, D. M.; Pegg, D. T.; Bendall, M. R. *Aust. J. Chem.* **1979**, *32*, 1219–1230.

(36) Endo, K.; Yamamoto, K. *J. Phys. Soc. Jpn.* **1995**, *64*, 4053–4054.

(37) Boucekkine, A.; Boucekkine-Yaker, G.; Achour, M. N.; Berthier, G. *THEOCHEM* **1988**, *166*, 109–112.

(38) Vaara, J.; Pyykkö, P. *Phys. Rev. Lett.* **2001**, *86*, 3268–3271.

(39) Meersmann, T.; Haake, M. *Phys. Rev. Lett.* **1998**, *81*, 1211–1214.

(40) Vaara, J.; Manninen, P.; Lounila, J. *Chem. Phys. Lett.* **2003**, *372*, 750–757.

(41) Manninen, P.; Vaara, J. *Phys. Rev. A* **2004**, *69*, 022503−07.

(42) Soncini, A.; Fowler, P. W. *Chem. Phys. Lett.* **2004**, *400*, 213–220.

(43) Compernolle, S.; Chibotaru, L. F.; Ceulemans, A. *Chem. Phys. Lett.* **2006**, *428*, 119–124.

(44) Zaric, S.; Ostojic, G. N.; Kono, J.; Shaver, J.; Moore, V. C.; Strano, M. S.; Hauge, R. H.; Smalley, R. E.; Wei, X. *Science* **2004**, *304*, 1129–1131.

(45) Coskun, U. C.; Wei, T.-C.; Vishveshwara, S.; Goldbart, P. M.; Bezryadin, A. *Science* **2004**, *304*, 1132–1134.

(46) Novoselov, K. S.; Jiang, Z.; Zhang, Y.; Morozov, S. V.; Stormer, H. L.; Zeitler, U.; Maan, J. C.; Boebinger, G. S.; Kim, P.; Geim, A. K. *Science* **2004**, *315*, 1379.

(47) Kozlova, N.; Hagel, J.; Doerr, M.; Wosnitza, J.; Eckert, D.; Müller, K.-H.; Schultz, L.; Opahle, I.; Elgazzar, S.; Richter, M.; Goll, G.; v.; Löhneysen, H.; Zwicknagl, G.; Yoshino, T.; Takabatake, T. *Phys. Rev. Lett.* **2005**, *95*, 086403.

(48) Pagola, G. I.; Caputo, M. C.; Ferraro, M. B.; Lazzeretti, P. *J. Chem. Phys.* **2004**, *120*, 9556–9560.

(49) Pagola, G. I.; Caputo, M. C.; Ferraro, M. B.; Lazzeretti, P. *Chem. Phys. Lett.* **2004**, *400*, 133–138.

(50) Pagola, G. I.; Caputo, M. C.; Ferraro, M. B.; Lazzeretti, P. *J. Chem. Phys.* **2005**, *122*, 074318−1/6.

(51) Pagola, G. I.; Caputo, M. C.; Ferraro, M. B.; Lazzeretti, P. *Chem. Phys. Lett.* **2005**, *408*, 403–408.

(52) Pagola, G. I.; Pelloni, S.; Caputo, M. C.; Ferraro, M. B.; Lazzeretti, P. *Phys. Rev. A* **2005**, *72*, 033401:1−8.

(53) Pagola, G. I.; Caputo, M. C.; Ferraro, M. B.; Lazzeretti, P. *Phys. Rev. A* **2006**, *74*, 022509−1-7.

(54) Caputo, M. C.; Ferraro, M. B.; Pagola, G. I.; Lazzeretti, P. *J. Chem. Phys.* **2007**, *126*, 154103−1/9.

(55) Boyd, J.; Pagola, G. I.; Caputo, M. C.; Ferraro, M. B.; Lazzeretti, P. *J. Chem. Theor. Comput.* **2009**, *5*, 1343–1349.

(56) Riess, J. *Ann. Phys.* **1970**, *57*, 301–321.

(57) Stevens, R. M.; Lipscomb, W. N. *J. Chem. Phys.* **1965**, *42*, 3666–3669.

(58) Hegstrom, R. A.; Lipscomb, W. N. *J. Chem. Phys.* **1966**, *45*, 2378–2383.

(59) Hegstrom, R. A.; Lipscomb, W. N. *Rev. Mod. Phys.* **1968**, *40*, 354–358.

(60) Lipscomb, W. N. *MTP Int. Rev. Sci. Phys. Chem.* **1972**, *1*, 167.

(61) Heller, D. F.; Hirschfelder, J. O. *J. Chem. Phys.* **1977**, *66*, 1929–1933.

(62) Źaucer, M.; Pumpernik, D.; Hladnik, M.; Aźman, A. *Chem. Phys. Lett.* **1977**, *48*, 139–140.

(63) Jaszuński, M. *Theor. Chim. Acta* **1978**, *48*, 323–329.

(64) Corcoran, C. T.; Hirschfelder, J. O. *J. Chem. Phys.* **1980**, *72*, 1524–1528.

(65) Schindler, M.; Kutzelnigg, W. *J. Chem. Phys.* **1982**, *76*, 1919–1933.

(66) Daborn, G. T.; Handy, N. C. *Mol. Phys.* **1983**, *49*, 1277–1288.

(67) Sauer, S. P. A.; Oddershede, J.; Geertsen, J. *Mol. Phys.* **1992**, *76*, 445–465.

(68) Sauer, S. P. A.; Enevoldsen, T.; Oddershede, J. *J. Chem. Phys.* **1993**, *98*, 9748–9757.

(69) Ruud, K.; Helgaker, T.; Bak, K. L.; Jørgensen, P.; Olsen, J. *Chem. Phys.* **1995**, *195*, 157–169.

(70) Fowler, P. W.; Steiner, E. *Mol. Phys.* **1991**, *74*, 1147–1158.

(71) Bally, T.; Masamune, S. *Tetrahedron* **1980**, *36*, 343–370.

(72) Pelloni, S.; Ligabue, A.; Lazzeretti, P. *Org. Lett.* **2004**, *6*, 4451–4454.

(73) Einstein, F. W. B.; Willis, A. C.; Cullen, W. R.; Soulen, R. L. *J. Chem. Soc. Chem. Comm.* **1981**, 526–528.

(74) Matsuura, A.; Komatsu, K. *J. Am. Chem. Soc.* **2001**, *123*, 1768–1769.

(75) Nishinaga, T.; Uto, T.; Matsuura, R. I. A.; Treitel, N.; Rabinovitz, M.; Komatsu, K. *Chem.—Eur. J.* **2001**, *14*, 2067–2074.

(76) Keal, W.; Tozer, D. J. *J. Chem. Phys.* **2003**, *119*, 3015–3024.

(77) Keal, W.; Tozer, D. J. *J. Chem. Phys.* **2004**, *121*, 5654–5660.

(78) DALTON, An Electronic Structure Program, release 2.0 http://www.kjemi.uio.no/software/dalton/ (accessed September 2009).

(79) Ligabue, A.; Sauer, S. P. A.; Lazzeretti, P. *J. Chem. Phys.* **2007**, *126*, 154111–14.

(80) Kongsted, J.; Aidas, K.; Mikkelsen, K. V.; Sauer, S. P. A. *J. Chem. Theory Comput.* **2008**, *4*, 267–277.

(81) van Duijneveldt, F. B. *Gaussian Basis Sets for the Atoms H-Ne for Use in Molecular Calculations*; Research Report RJ 945, IBM: Armonk, NY, 1971.

(82) Becke, A. D. *J. Chem. Phys.* **1993**, *98*, 5648–5652.

(83) Mohr, P. J.; Taylor, B. N. *Rev. Mod. Phys.* **2005**, *77*, 1–107.

(84) Matzkin, A.; Monteiro, T. S. *Phys. Rev. Lett.* **2001**, *87*, 143002–05.

(85) Matzkin, A.; Dando, P. A.; Monteiro, T. S. *Phys. Rev. A* **2002**, *66*, 013410−21.

(86) Matzkin, A.; Dando, P. A.; Monteiro, T. S. *Phys. Rev. A* **2003**, *67*, 023402−08.

CT900390S

JCTC Journal of Chemical Theory and Computation

Assessment of Orbital-Optimized, Spin-Component Scaled Second-Order Many-Body Perturbation Theory for Thermochemistry and Kinetics

Frank Neese,*,†,§ Tobias Schwabe,‡ Simone Kossmann,† Birgitta Schirmer,‡ and
Stefan Grimme*,‡

Lehrstuhl für Theoretische Chemie, Institut für Physikalische und Theoretische Chemie, Universität Bonn, Wegelerstrasse 12, D-53115 Bonn, Germany, Max-Planck Institut für Bioanorganische Chemie, Stiftstrasse 34-36, D-45470 Mülheim an der Ruhr, Germany, and Abteilung Theoretische Chemie, Organisch-Chemisches Institut, Westfälische Wilhelms-Universität, Corrensstrasse 40, D-48149 Münster, Germany

Received June 29, 2009

Abstract: An efficient implementation of the orbital-optimized second-order Møller−Plesset perturbation theory (OO-MP2) within the resolution of the identity (RI) approximation is reported. Both conventional MP2 and spin-component scaled (SCS-MP2) variants are considered, and an extensive numerical investigation of the accuracy of these approaches is presented. This work is closely related to earlier work of Lochan, R. C.; Head-Gordon, M. *J. Chem. Phys.* **2007**, *126*. Orbital optimization is achieved by making the Hylleraas functional together with the energy of the reference determinant stationary with respect to variations of the double excitation amplitudes and the molecular orbital rotation parameters. A simple iterative scheme is proposed that usually leads to convergence within 5−15 iterations. The applicability of the method to larger molecules (up to ~1000−2000 basis functions) is demonstrated. The numerical results show that OO-SCS-MP2 is a major improvement in electronically complicated situations, such as represented by radicals or by transition states where spin contamination often greatly deteriorates the quality of the conventional MP2 and SCS-MP2 methods. The OO-(SCS-)MP2 approach reduces the error by a factor of 3−5 relative to the standard (SCS-)MP2. For closed-shell main group elements, no significant improvement in the accuracy relative to the already excellent SCS-MP2 method is observed. In addition, the problems of all MP2 variants with 3d transition-metal complexes are not solved by orbital optimization. The close relationship of the OO-MP2 method to the approximate second-order coupled cluster method (CC2) is pointed out. Both methods have comparable computational requirements. Thus, the OO-MP2 method emerges as a very useful tool for computational quantum chemistry.

Introduction

Second-order many-body perturbation theory (MBPT2) occupies an important place in quantum chemistry. It is known to greatly improve upon the results of Hartree−Fock (HF) self-consistent field calculations and is the simplest wave function based ab initio method. With the Mϕller-Plesset (MP) choice of the zero-order Hamiltonian,[1,2] the method is known as MP2 and has been widely used in computational chemistry. The pertinent features of MP2 are well-known:[3,4]

a. MP2 is size consistent but not variational or even stationary with respect to the wave function parameters.
b. MP2 recovers 80−90% of the basis set correlation energy.
c. MP2 scales as the fifth power of the molecular size, e.g., as $O(N^5)$. It is, therefore, intermediate in computational

---

* Corresponding authors. Telephone: +49-228-73-2351 (F.N.) and +49-251-83-36512 (S.G.). Fax: +49-228-739064 (F.N.) and +49-251-83 36515 (S.G.). E-mail: theochem@thch.uni-bonn.de (F.N.) and grimmes@uni-muenster.de (S.G.).

† Lehrstuhl für Theoretische Chemie, Institut für Physikalische und Theoretische Chemie.

§ Max-Planck Institut für Bioanorganische Chemie.

‡ Abteilung Theoretische Chemie, Organisch-Chemisches Institut.

10.1021/ct9003299 CCC: $40.75

complexity between the HF theory (formally $O(N^4)$, practically $O(N^2)$) and the more rigorous coupled cluster (CC)[5,6] or coupled electron pair (CEPA)[7−9] methods that require at least an iterative $O(N^6)$ process, if only single and double excitations from the HF reference determinant are included (CCSD).
d. MP2 applied to closed-shell organic molecules often yields fairly good structures, but energetics that are slightly worse than with common density functionals.[10]
e. MP2 applied to open-shell molecules or to transition-metal complexes yields distinctly less accurate results.[11]
f. With a HF reference, the first-order MP2 wave function only contains double excitation amplitudes. Hence, MP2 does not incorporate any orbital relaxation in the electron correlation field.

A great deal of effort has been invested into making MP2 computationally affordable for general computational chemistry applications, and consequently, a number of highly efficient MP2 approaches exist. Early on, Almlöf and Saebo demonstrated that MP2 can be done in an integral direct fashion, thus, avoiding the storage of $O(N^4)$ intermediates on disk.[12] Head-Gordon,[13,14] Ahlrichs, and others have reported modifications of the original direct algorithm. The most efficient semidirect algorithm has probably been developed by Pulay and co-workers and does *not* avoid storage of $O(N^4)$ quantities on disk.[15−19] The scaling of their method is still $O(N^5)$, and it completely reproduces the canonical result. Pulay and co-workers have reported very large MP2 calculations with more than 2 000 basis functions on the basis of a parallelized code.[20]

More recently, Ochsenfeld and co-workers have developed a linear scaling integral direct MP2 code.[21,22] Their strategy is based on the Laplace transformation technique introduced originally by Almlöf[23] and discussed in detail by Häser and Almlöf,[24] Häser,[25] and Scuseria.[26] Microhartree accuracy (relative to the canonical result) MP2 calculations with more than 10 000 basis functions have been reported by Ochsenfeld et al.,[27] and a gradient code has also been developed along the same lines.[28]

A number of efficient approximate MP2 treatments are available. One of the first, and still widely used, approximations is the resolution of the identity (RI, equivalently density fitting, DF) technique in which products of orbitals are expanded in an auxiliary basis set.[29] The RI approximation to MP2 (RI-MP2) was first reported by Feyereisen et al.[30] and was based on the results of Vahtras, Feyereisen, and Almlöf, who showed that the RI technique performs best in the Coulomb metric.[31] Häser and Weigend optimized fitting basis sets for RI-MP2 calculation for almost the entire periodic table.[32,33] They are optimally used together with the segmented Gaussian basis sets developed by the Karlsruhe group.[32,34−36] The error introduced by the RI approximation is usually smaller than 0.1 mEh/atom and is very smooth, such that it essentially cancels in chemically relevant energy differences (typical RI errors in energy differences amount to only 0.02 kcal mol^{-1}). The RI technique leads to dramatic speedups of MP2 calculations, in particular, if large basis sets are used, the savings compared to the canonical calculation amount to 1−2 orders of magnitude. It does, however, not reduce the formal scaling that remains at the $O(N^5)$ level. Nevertheless, the prefactor for RI-MP2 is so small that, in the range up to at least 2 000 basis functions, the preceding HF calculation still dominates the overall computational effort.

Linear scaling approximate MP2 methods (as opposed to the linear scaling full accuracy MP2 method pursued by Ochsenfeld et al.) have been developed by a number of groups. The most efficient of these have probably been reported by Werner, Schütz and co-workers,[37−41] who used the correlation domain concept of Pulay and Saebo.[42−44] The LMP2 technique has been developed in combination with the standard four index repulsion integrals and together with the DF technique where further dramatic savings are realized.[37,38]

A different approach has been pursued by Friesner and co-workers, who have developed low-order scaling pseudospectral techniques for MP2 calculations that are also characterized by a small error and a low prefactor.[45] We have previously reported a hybrid technique where the HF energy is obtained with a combination of RI and seminumerical integration and the MP2 energy is calculated within the RI framework.[46,47] The technique has been termed RIJCOSX, and it has been shown that it leads to speedups of about a factor of 15 for basis sets of triple-ζ quality compared to standard RI-MP2 calculations.

Overall, it is clear that the development of MP2 has reached a stage where MP2 energies can be obtained faster than the HF energy itself for many chemically interesting systems. Hence, the domain of applicability of MP2 is similar to that of density functional theory (DFT). However, DFT is still more frequently used than MP2, perhaps because it proves to be more robust when applied to electronically difficult situations, such as presented by open-shell systems and by transition-metal complexes. Furthermore, widely used quantum chemistry software packages still use non-RI, disk-based MP2 algorithms so that the calculations remain very time, memory, and disk space consuming.

Given the efficiency of the MP2 technique it seems natural to look for extensions that improve the accuracy of the MP2 method while not worsening the computational scaling. Perhaps the most successful of these techniques has been the spin-component scaled MP2 method (SCS-MP2) previously proposed by one of us.[48−50] SCS-MP2 has proven to be a robust, efficient, and accurate technique when applied to closed-shell main group systems. However, it has also shown some deficiencies in the calculation of activation and reaction energies involving open-shell molecules.[9,51] A modification of the SCS-MP2 idea that reduces the scaling behavior to $O(N^4)$ has been proposed by Head-Gordon and co-workers and has been termed SOS-MP2.[52−54]

A second successful extension of MP2 has been the proposals of double-hybrid DFT (DHDF),[55−57] and third-order spin-component scaled perturbation theory.[58] The DHDFs have quickly gained popularity in the computational chemistry community and, to some extent, combine the best features of DFT and MP2 in terms of robustness, efficiency, and accuracy.[59] Because neither (SCS-)MP2 nor DHDF methods are variational or even stationary, the formulation of analytic gradients is more involved,[59] and hence, structure optimizations on the basis of these methods are more expensive than with conventional DFT.

One notorious problem with MP2 has been its inability to calculate response properties since it 'inherits' the poor pole structure of the HF method. This has been the motivation for the introduction of second-order polarization propagator approaches (SOPPA) that are broadly consistent with MP2 ground states.[60,61] Another workaround has been the development of a second-order CC method that has been termed CC2 by its developers.[62] Response properties of the CC2 method are readily formulated within the standard CC hierarchy.[63] CC2 has the same scaling as MP2 but requires an iterative process. It is, hence, more expensive than MP2 itself. The accuracy of CC2 for ground-state energies and for structures appears to be similar (or slightly worse) to that of MP2.[64,65] Thus, its main strength is the calculation of response properties, such as excitation energies.[66-69] Efficient techniques based on the RI approximation have been developed by Hättig and co-workers and are available in the TurboMole program.[66,67,70] In addition, spin-component scaling with emphasis on excited-state calculations has been investigated in the CC2 framework as well.[65] More recently, Schütz and co-workers have reported local CC2 methods and have combined them with DF and Laplace techniques.[71,72]

In the present work, we investigate another modification of the MP2 technique that, in our opinion, suggests itself: the orbital-optimized MP2 technique (OO-MP2). Thus, one bases the calculation on the well-known Hylleraas functional[73] which is made stationary with respect to both amplitude variations and orbital rotations. Hence, a fully stationary energy, which simplifies the calculation of first-order properties is obtained. Closely related ideas have previously been pursued by Adamowicz and Bartlett,[74-79] Head-Gordon and co-workers[52,80] and Kollmar.[81] In ref 52, orbital optimization as been applied to the opposite-spin scaled MP2 method (dubbed O2), and encouraging results for atomization energies and vibrational frequencies of open-shell systems have been reported. Noteworthy is the substantial reduction of spin contamination for small molecules by the OO procedure. It was also pointed out that OO-MP2 is not bounded from below, and hence, in worst case the energy could 'run away' to infinity. However, importantly, the recent analysis of Head-Gordon and co-workers shows that with orbital optimization methods, the stability of MP2-type procedures is greatly enhanced by turning a first derivative discontinuity problem into a second derivative discontinuity problem.[80] Hence, in or close to symmetry-breaking situations orbital optimization will be essential.

In this paper, we perform additional detailed benchmark studies of the orbital optimization technique and pursue the original (and generally more accurate) spin-component scaling technique as opposed to opposite-spin scaling that has been pursued in ref 52. An efficient RI-based implementation of the OO-RI-MP2 and OO-RI-SCS-MP2 techniques into the ORCA program package is reported, and both approaches are characterized through detailed benchmark calculations. The relationship between OO-MP2 and CC2 will be pointed out in the discussion.

The evaluation will focus on those cases where MP2 itself (and also to some extent SCS-MP2) are more difficult to apply. Thus, special attention will be devoted to open-shell systems where spin contamination in the UHF reference often significantly deteriorates the quality of the subsequent MP2 correction.[9,82]

A suitable test set is provided by the radical stabilization energies (RSE, see also ref 83) of organic systems. Two sets of radicals will be investigated. The first set has been proposed in an extensive study by Zipse,[84] who thoroughly investigated trends in RSE for different types of substituents. The second set of test cases is taken from the investigation of Hemelsoet et al.[85] They reported that dissociation energies for C−H bonds in methyl groups connected to aromatic hydrocarbons are particularly strongly affected by spin contamination. All kinds of open-shell transition states represent cases where significant spin contamination may occur. As benchmark for transition states, the hydrogen transfer barrier heights of the HTBH38 set from Zhao et al. have been selected.[86]

In order to judge whether the orbital optimization approach also provides an improvement over the well-established SCS-MP2 method for closed shell systems, a restricted set of such systems has also been included in the study. The test set includes some prototypical main group reactions that have already been investigated in the original parametrization of the SCS-MP2 method.[49] Further, ligand binding energies of some transition-metal complexes will be studied. For these systems, it is commonly claimed that second-order perturbation methods are insufficient, and higher-order correlation methods are required in order to reach quantitative accuracy.[87]

1. Theory

Throughout this paper, indices *i*,*j*,*k* refer to occupied orbitals in the reference determinant, *a*,*b*,*c* refer to virtual orbitals, and *p*,*q*,*r* refer to general orbitals from either set, while *P* and *Q* denote auxiliary basis functions. The MP2 energy can be regarded as being stationary with respect to the MP2 amplitudes, since they can be considered as having been optimized through the minimization of the Hylleraas functional:[88]

$$E_{\mathrm{MP2}} = \min_{\mathbf{t}}\{2\langle\Psi_1|\hat{H}|\Psi_0\rangle + \langle\Psi_1|\hat{H}_0 - E_0|\Psi_1\rangle\} \quad (1)$$

$\hat{H}_0$ is the zero-order Hamiltonian, as proposed by Møller and Plesset, Ψ_0 is the reference determinant, Ψ_1 is the first-order wave function, and $E_1 = E_{\mathrm{HF}} = \langle\Psi_{\mathrm{HF}}|\hat{H}|\Psi_{\mathrm{HF}}\rangle$ is the reference energy. The quantities **t** collectively denote the MP2 amplitudes.

The fundamental idea of the OO-MP2 method is to not only minimize the MP2 energy with respect to the MP2 amplitudes but also to minimize the total energy with respect to changes in the orbitals. Since the MP2 energy is not variational with respect to the MO coefficients, no orbital relaxation due to the correlation field is taken into account. If the reference determinant is poor, then the low-order perturbative correction becomes unreliable. This may be alleviated to a large extent by choosing better orbitals in the reference determinant. Numerical evidence for the correctness of this assumption will be presented below.

In order to allow for orbital relaxation, the Hylleraas functional can be regarded as a functional of the wave function amplitudes **t** and the orbital rotation parameters **R** that will be defined below. Through a suitable parametrization, it becomes unnecessary to ensure orbital orthonormality through Lagrange multipiers. The functional that we minimize reads:

$$\mathscr{H}\{\mathbf{t},\mathbf{R}\} = E_0[\mathbf{R}] + 2\langle\Psi_1|\hat{H}|\Psi_0\rangle + \langle\Psi_1|\hat{H}_0 - E_0[\mathbf{R}]|\Psi_1\rangle \tag{2}$$

Ψ_0 is the reference determinant. However, it does no longer correspond to the HF determinant. Hence, the reference energy $E_0[\mathbf{R}] = \langle\Psi_0[\mathbf{R}]|\hat{H}|\Psi_0[\mathbf{R}]\rangle$ also changes during the variational process and is no longer stationary with respect to the HF MO coefficients. Obviously, $E_0[\mathbf{R}] \geq E_{\mathrm{HF}}$ since the HF determinant is, by construction, the single determinant with the lowest expectation value of the full Hamiltonian.

The reference energy is given as

$$E_0[\mathbf{R}] = \sum_i \langle i|h|i\rangle + \frac{1}{2}\sum_{ij}\langle ij||ij\rangle \tag{3}$$

The first-order wave function excluding single excitations is

$$|\Psi_1\rangle = \frac{1}{4}\sum_{ijab} t_{ab}^{ij}|\Psi_{ij}^{ab}\rangle \tag{4}$$

A conceptually important point is that Brillouin's theorem[89] is no longer obeyed since the Fock matrix will contain off-diagonal blocks. Under these circumstances, the first-order wave function would contain contributions from single excitations. Since the orbital optimization brings in all important effects of the singles, we prefer to leave them out of the treatment. Any attempt to the contrary will destroy the convergence properties. We have, nevertheless, contemplated to include the single excitations perturbatively:

$$E_{\mathrm{singles}}^{(2)} = -\sum_{ia}\frac{|F_{ia}|^2}{\varepsilon_a - \varepsilon_i} \tag{5}$$

The perturbative nature of this correction would destroy the stationary nature of the total energy and is, hence, not desirable. Furthermore, results with inclusion of single excitation contributions represent no improvement to the results reported below. They will, therefore, not be documented below and, henceforth, be omitted from the OO-MP2 method by default.

The explicit form of the OO-MP2 Hylleraas functional employing the RI approximation (OO-RI-MP2) becomes

$$\mathscr{L}_{\mathrm{OO}}[\mathbf{t},\mathbf{R}] = \sum_i \langle i|\hat{h}|i\rangle + \frac{1}{2}\sum_{ij}\langle ij||ij\rangle + \sum_{iaP}(ia|P)\Gamma_{ia}^{\prime P} + \sum_{ij}D_{ij}F_{ij} + \sum_{ab}D_{ab}F_{ab} \tag{6}$$

with

$$\Gamma_{ia}^{\prime P} = \sum_Q V_{PQ}^{-1}\sum_{jb}(Q|jb)t_{ab}^{ij} \tag{7}$$

$$(ia|P) = \int\int \psi_i(\mathbf{r}_1)\psi_a(\mathbf{r}_1)\frac{1}{|\mathbf{r}_1 - \mathbf{r}_2|}\eta_P(\mathbf{r}_2)\mathrm{d}\mathbf{r}_1\mathrm{d}\mathbf{r}_2 \tag{8}$$

$$(P|Q) = V_{PQ} = \int\int \eta_P(\mathbf{r}_1)\frac{1}{|\mathbf{r}_1 - \mathbf{r}_2|}\eta_Q(\mathbf{r}_2)\mathrm{d}\mathbf{r}_1\mathrm{d}\mathbf{r}_2 \tag{9}$$

Here, $\{\psi\}$ is the set of orthonormal molecular orbitals and $\{\eta\}$ denotes the auxiliary basis set. F_{pq} denotes a Fock matrix element:

$$F_{pq} = \langle p|\hat{h}|q\rangle + \sum_k \langle pk||qk\rangle \tag{10}$$

and it is insisted that the orbitals diagonalize the occupied and virtual subspaces, respectively:

$$\begin{aligned} F_{ij} &= \delta_{ij}F_{ii} &&= \delta_{ij}\varepsilon_i \\ F_{ab} &= \delta_{ab}F_{aa} &&= \delta_{ab}\varepsilon_a \end{aligned} \tag{11}$$

The MP2 like density blocks are

$$\begin{aligned} D_{ij} &= -\frac{1}{2}\sum_{kab} t_{ab}^{ik}t_{ab}^{jk} \\ D_{ab} &= \frac{1}{2}\sum_{ijc} t_{ac}^{ij}t_{bc}^{ij} \end{aligned} \tag{12}$$

where the MP2 amplitudes in the case of a block diagonal Fock matrix are obtained through the condition $(\partial\mathscr{L}_{\mathrm{OO}})/(\partial t_{ab}^{ij}) = 0$:

$$t_{ab}^{ij} = -\frac{\langle ij||ab\rangle}{\varepsilon_a + \varepsilon_b - \varepsilon_i - \varepsilon_j} \tag{13}$$

The orbital changes are parametrized by an anti-Hermitian matrix **R** and an exponential Ansatz:

$$\begin{aligned} \mathbf{c}^{\mathrm{new}} &= \mathbf{c}^{\mathrm{old}}\exp(\mathbf{R}) \\ \mathbf{R} &= \begin{pmatrix} 0 & \mathbf{R}_{ia} \\ -\mathbf{R}_{ia} & 0 \end{pmatrix} \end{aligned} \tag{14}$$

The orbitals changes to second order are

$$\begin{aligned} \exp(\mathbf{R})|i\rangle &= |i\rangle + \sum_a R_{ai}|a\rangle - \frac{1}{2}\sum_{jb}R_{bi}R_{bj}|j\rangle + ... \\ \exp(\mathbf{R})|a\rangle &= |a\rangle - \sum_i R_{ai}|i\rangle - \frac{1}{2}\sum_{jb}R_{aj}R_{bj}|b\rangle + ... \end{aligned} \tag{15}$$

Through this Ansatz it is ensured that the orbitals remain orthonormal and that no Lagrangian multipliers need to be introduced. The first-order expansion of the Fock operator due to the orbital rotations is

$$F_{pq}[\mathbf{R}] = F_{pq}[0] + R_{pq}^{(1)} + \sum_r R_{rp}F_{rq}[0] + R_{rq}F_{pr}[0] \tag{16}$$

$$R_{pq}^{(1)} = \sum_{kc} R_{ck}\{\langle pc||qk\rangle + \langle pk||qc\rangle\} \tag{17}$$

The first-order energy change becomes ($h_{pq} \equiv \langle p|\hat{h}|q\rangle$, $g_{pqrs} \equiv \langle pq||rs\rangle$):

$$\begin{aligned}\mathscr{L}_{OO}[\mathbf{t},\mathbf{R}] \;=\;& \sum_{ic} R_{ci}(h_{ci}+h_{ic}) + \frac{1}{2}\sum_{ijc} R_{ci}(g_{cjij}+g_{ijcj}) + \\ & R_{cj}(g_{icij}+g_{ijic}) \\ +\;& 2\sum_{iacP} R_{ci}(ac|P)\Gamma'^{P}_{ia} - 2\sum_{ikaP} R_{ak}(ik|P)\Gamma'^{P}_{ia} \\ -\;& 2\sum_{ij} D_{ij}(R^{(1)}_{ij} + \sum_{c}(R_{ci}F_{cj} + R_{cj}F_{ic})) \\ +\;& 2\sum_{ab} D_{ab}(R^{(1)}_{ab} - \sum_{c}(R_{ak}F_{kb} + R_{bk}F_{ak}))\end{aligned} \tag{18}$$

The condition for the energy functional to be stationary, with respect to the orbital rotations, ($\partial\mathscr{L}_{\mathrm{OO}}[\mathbf{t},\mathbf{R}]/\partial R_{ai} = 0$) yields the expression for the orbital gradient and, hence, the expression for the OO-RI-MP2 Lagrangian.

$$\begin{aligned}\frac{\partial\mathscr{L}_{OO}[\mathbf{t},\mathbf{R}]}{\partial R_{ai}} \;\equiv\;& g_{ai} = 2F_{ai} + 2\sum_{j} D_{ij}F_{aj} - \\ & 2\sum_{b} D_{ab}F_{ib} + R^{(1)}(\mathbf{D})_{ai} \\ +\;& 2\sum_{cP}(ac|P)\Gamma'^{P}_{ia} - 2\sum_{kP}(ik|P)\Gamma'^{P}_{ia}\end{aligned} \tag{19}$$

The goal of the orbital optimization process is to bring this gradient to zero. There are obviously many ways to achieve this. In our experience, the following simple procedure is essentially satisfactory. We first build a matrix **B** in the current MO basis with the following structure:

$$\begin{aligned}\mathbf{B}_{ij} &= \delta_{ij}F_{ii} \\ \mathbf{B}_{ab} &= \delta_{ab}(F_{aa} + \Delta) \\ \mathbf{B}_{ai} &= \mathbf{B}_{ia} = g_{ai}\end{aligned} \tag{20}$$

where Δ is a level shift parameter. The occupied/occupied and virtual/virtual blocks of this matrix are arbitrary, but their definition has a bearing on the convergence properties of the method. The orbital energies of the block diagonalized Fock matrix appear to be a logical choice. If the gradient is zero, then the **B** matrix is diagonal. Hence, one obtains an improved set of orbitals by diagonalizing **B**. In order to accelerate convergence, a standard DIIS scheme is used.[90,91] However, in order to carry out the DIIS extrapolation of the **B**-matrix, it is essential that a common basis is used that does not change from iteration to iteration. Since the **B** matrix itself is defined in the molecular orbitals of the current iteration, we choose as a common set of orthonormal orbitals the MOs of the HF calculation. The extrapolation is carried out in this basis, and the extrapolated **B** matrix is transformed back to the current set of MOs prior to diagonalization. Obviously, the same strategy can be used for orbital optimization in any method for which an orbital gradient is available.

For well-behaved cases this simple scheme converges in 5–10 iterations. Transition metals and more complicated molecules may require up to 20 iterations and level shifting in order to achieve convergence.

It has been argued by Rice et al.[92] and by Scuseria and Schaefer,[93] that one would obtain a Newton–Raphson-like scheme by regarding g_{ai} as an electronic perturbation and solve a set of coupled-perturbed HF equations in order to obtain new orbital rotation parameters. We have implemented this scheme and found it to be not competitive with the simple DIIS scheme. Each orbital update requires the expensive solution of the CPHF equations. Yet, the convergence is no better or worse than that of the DIIS scheme. This makes sense, the method is not a true Newton–Raphson procedure, because the SCF Hessian is used in place of the much more elaborate OO-MP2 electronic Hessian. The true Newton–Raphson method requires the exact second derivatives of the total energy with respect to the orbital rotation parameters. The CPHF method simply contains the second derivative of the energy of the reference determinant with respect to these rotations and, hence, misses substantial contributions that come from the dynamic correlation part. Since the Hessian is not the exact one, quadratic convergence does not occur. In fact, convergence is at best linear, and the scheme is overall too expensive for large-scale applications.

To illustrate this point, the performance of the (quasi) Newton–Raphson procedure is compared to the DIIS scheme for the glycine molecule in the TZVPP basis and the TZVPP/C auxbasis (411 basis functions, 986 auxiliary basis functions). The time for the DIIS extrapolation is negligible compared to the total time of the iterative OO-MP2 procedure. By contrast, the Newton–Raphson procedure amounts to about 20% of the total OO-MP2 calculation time. Whereas the DIIS extrapolation takes about 1 s per OO-MP2 cycle, the solution of the CPSCF equations takes about 680 s per cycle (10 cycles for energy convergence to 10^{-7} E_h are required in both schemes).

We note, in passing, that upon convergence the sum of the matrix **D** and the density of the reference determinant $P_{\mu\nu} = \sum_i c_{\mu i}c_{\nu i}$ form the true one-particle density matrix of the OO-MP2 approach that can be used for property or gradient calculations. This will be investigated in detail elsewhere.

2. Implementation and Timings

The OO-RI-MP2 and OO-RI-SCS-MP2 methods have been implemented in closed-shell and spin-unrestricted versions into a development version of the ORCA program package. The implementation is based on the previously reported parallelized gradient code for RI-MP2 and DHDF methods.[59] Since the details have been documented in the previous publication, we only briefly discuss the timings for a medium-sized test case, the cocaine molecule with the TZVP basis set (43 atoms, 544 basis functions, 1 025 auxiliary functions).

The RHF calculation takes 105 min and converges in 15 cycles to an accuracy of 10^{-9} E_h (single CPU of a MacPro 3.1; operating system OS X 10.5, 2 quad-core Intel XEON 3.0 GHZ CPUs that have 12 MB level 2 cache). The RI-MP2 calculation takes only 2 min. The effort for the OO-RI-MP2 method is obviously higher. In addition to its iterative nature, the necessary terms for the orbital gradient must be calculated, which involves the calculation of the response operator (eq 17), the unrelaxed density (eq 12), and

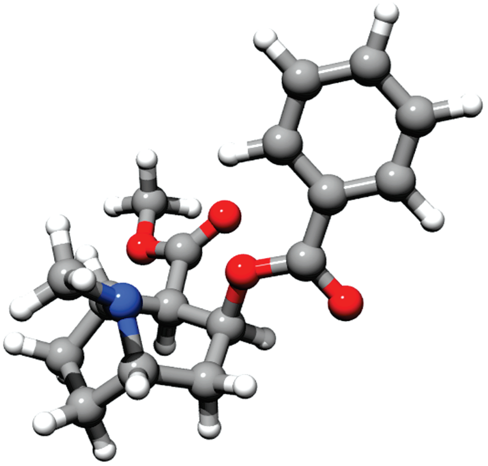

Figure 1. Structure of the cocaine molecule used in the benchmark calculations (43 atoms, 976 basis functions with TZVPP, 976 and 1025 auxiliary functions).

the two external/internal contributions (eq 19), all of which are expensive.

In this example, there are 16 orbital iterations required to converge the energy to about 10^{-9} E_h, which takes 12.2 h. No single term is dominating the calculation time. The construction of the Fock (13%) and response (16%) operators as well as the calculation of the (*ia|jb*) integrals (15%), the virtual part of the Lagrangian (15%), the internal part of the density (13%) and the calculation of the three-index, two particle density (15%) all take about the same amount of time. The remaining time goes, in about equal parts, to the three-index integral transformation, the virtual part of the density as well as the internal part of the Lagrangian.

Thus, the effort for the total calculation is substantially higher than that for a RI-MP2 calculation (by a factor typically 8−12), but the calculations are feasible even for larger molecules. As will be explained in a different context, the computational effort can be significantly reduced by additional approximations.

In order to illustrate that the effort for a RI-OO-MP2 calculation is still substantially lower than that of a CCSD calculation, we have compared the timings for the tyrosine molecule with the TZVP basis set (313 basis functions). We emphasize that the ORCA CCSD program has state of the art performance such that the comparison is fair. The time required to complete the OO-RI-MP2 calculation is 5 353 s, while the CCSD calculation takes 66 299 s. This shows that the effort for orbital-optimized MP2 calculations is intermediate between that of CCSD and that of MP2 (RI-MP2: 1 016 s including SCF). Also, the computational scaling for MP2 (with or without orbital optimization) is $O(N^5)$ while CCSD is well-known to scale as $O(N^6)$.

3. Calculations

3.1. Computational Details. Unless otherwise noted, all geometries were optimized without constraints at the B3LYP[94−97]/TZVP[35] level using the TurboMole program suite (Version 5.9).[98,99] For the larger systems in the RSE set, an empirical dispersion correction[100−102] was added (B3LYP-D). The transition-metal complexes were optimized using RI-BP86[95,103]/TZVP together with matching auxiliary basis sets[104] and TurboMole multigrid 'm4'.[105] Single point energies were computed at each given level of theory at the optimized geometries. The exception are the systems from the HTBH38 test set that were taken in an unchanged way from the literature.[86] B2PLYP-D[106,107] BDEs for the polycyclic aromatic hydrocarbons were also calculated with the TurboMole program. In these calculations, the TZVPP basis was used together with matching auxiliary basis sets and RI approximation for the Coulomb-exchange part[108] as well as for the second-order perturbation part.

OO-MP2 and OO-SCS-MP2 calculations were carried out with a development version of the ORCA program system.[109] As explained above, the RI approximation was used throughout together with the auxiliary basis sets of Weigend et al.[108] Reaction energies, barrier heights, and RSE are based on the QZVP basis set.[34] All other calculations employed the TZVPP basis set.

Ligand dissociation energies for the carbonyl systems were computed with the RICC program developed in Münster, Germany, at the SCS-MP3[58]/TZVPP level of theory (or equivalently also with the ORCA program).

Reference data for the RSE were calculated at the CCSD(T) level together with the standard two-point basis set extrapolation scheme of Helgaker, Klopper, and co-workers.[110,111] For the extrapolation the Dunning basis sets, cc-pVDZ and cc-pVTZ are applied.[112−114] These calculations were carried out using MOLPRO 2006.[115]

All open-shell species were treated in the spin-unrestricted formalism.

3.2. Reaction Energies. In order to assess the performance of OO-SCS-MP2 for thermochemical applications, a set of reactions constructed from the molecules of the G2 set was investigated.[4] In our opinion, this data are more relevant for chemical applications than atomization energies, as discussed in detail in ref 49. The present test set is a subset of the one that has been used to parametrize SCS-MP2. Only transition states and protonation reactions have been omitted but will be discussed below. Furthermore, reactions involving ozone are omitted as well due to the multireference character of O_3.

It is evident from the results in Table 1 that OO-MP2 is not an improvement over MP2 itself. The mean average deviations of both methods are almost identical, but for OO-MP2, the error range is even larger than that of MP2. Interestingly, the errors of MP2 and OO-MP2 are almost always of opposite signs. Hence, it appears that OO-MP2 is overcorrecting the MP2 results. Turning now to the spin-component scaled results, Table 1 demonstrates that OO-SCS-MP2 improves upon the already excellent results of SCS-MP2. The mean absolute deviation (MAD) drops from 2.5 to 2.2 kcal mol^{-1}. However, at the same time, the error range increases. It was hypothesized that this problem might be alleviated by reoptimization of the two SCS-MP2 scaling parameters. Thus, the calculations were repeated for the entire test set for a collection of systematically varied scaling parameters. The statistical results of this investigation are collected in Table 2. It is apparent that the achievable improvements through reoptimization of the SCS-MP2

Table 1. Reaction Energies for Closed-Shell Molecules[a]

	reaction	ref[b]	deviation			
			SCS-MP2[c]	OO-SCS-MP2[c]	MP2	OO-MP2
1	$F_2 + H_2 \rightarrow 2\ HF$	−132.9	−5.9	−2.6	−10.0	7.8
2	$F_2O + H_2 \rightarrow F_2 + H_2O$	−67.5	−4.5	−1.3	−4.9	1.1
3	$H_2O_2 + H_2 \rightarrow 2\ H_2O$	−85.9	−3.9	−2.2	−5.8	4.9
4	$CO + H_2 \rightarrow CH_2O$	−3.9	−1.3	−0.7	−1.6	2.1
5	$CO + 3\ H_2 \rightarrow CH_4 + H_2O$	−62.3	−2.3	0.1	−4.1	3.7
6	$N_2 + 3\ H_2 \rightarrow 2\ NH_3$	−36.7	0.0	2.2	−2.1	2.0
7	$^1CH_2 + H_2 \rightarrow CH_4$	−128.2	−3.9	−3.9	−7.6	9.4
8	$N_2O + H_2 \rightarrow N_2 + H_2O$	−80.2	0.2	6.1	3.5	−11.3
9	$HNO_2 + 3\ H_2 \rightarrow 2\ H_2O + NH_3$	−119.8	−6.8	1.0	−10.5	2.7
10	$C_2H_2 + H_2 \rightarrow C_2H_4$	−48.8	1.4	2.1	1.6	−1.8
11	$CH_2{=}CO + 2\ H_2 \rightarrow CH_2O + CH_4$	−42.9	0.2	1.9	1.7	−3.6
12	$BH_3 + 3\ HF \rightarrow BF_3 + 3\ H_2$	−94.0	2.9	1.5	0.9	0.2
13	benzene + 3 H_2 → cyclohexane	−69.4	2.7	2.3	4.1	−3.1
14	$HCO{-}OH \rightarrow CO_2 + H_2$	1.2	−1.5	−3.0	−1.6	2.8
15	$CO + H_2O \rightarrow CO_2 + H_2$	−6.7	−1.8	−4.3	−3.5	7.2
16	$C_2H_2 + HF \rightarrow CH_2{-}\ CHF$	−26.9	2.7	2.6	3.2	−2.6
17	$HCN + H_2O \rightarrow CO + NH_3$	−12.7	2.7	2.4	3.5	−3.6
18	$HCN + H_2O \rightarrow HCO{-}NH_2$	−21.0	1.3	0.6	0.3	1.9
19	$HCONH_2 + H_2O \rightarrow HCOOH + NH_3$	0.4	1.0	0.6	1.3	−1.0
20	$HCN + NH_3 \rightarrow N_2 + CH_4$	−38.3	0.4	0.4	1.5	−1.9
21	$CO + CH_4 \rightarrow CH_3{-}CHO$	4.2	−1.2	−1.0	−2.4	3.6
22	$N_2 + F_2 \rightarrow N_2F_2$	17.6	3.8	3.6	0.6	1.5
23	$BH_3 + 2\ F_2 \rightarrow BF + 3\ HF$	−246.1	−6.4	−0.9	−15.2	10.8
24	$2\ BH_3 \rightarrow B_2H_6$	−43.0	1.4	1.0	−1.8	4.5
25	$2\ ^1CH_2 \rightarrow C_2H_4$	−198.4	−7.5	−8.3	−14.3	1 8.1
26	$CH_3{-}O{-}NO \rightarrow CH_3{-}NO_2$	−3.1	−3.4	−2.1	−5.5	3.3
27	$CH_2{=}C \rightarrow C_2H_2$	−44.6	−5.9	−5.8	−8.2	8.5
28	allene → propyne	−1.5	−2.7	−2.6	−3.2	3.1
29	Cyclopropene → propyne	−23.9	−0.2	−0.7	0.1	0.1
30	oxirane → CH_3CHO	−26.8	0.9	0.2	1.6	−0.9
31	vinyl alcohol → CH_3CHO	−10.1	−0.1	−0.6	−1.0	1.5
32	cyclobutene → 1,3- butadiene	−11.6	1.3	0.9	2.3	−2.2
33	$C_2H_4 + {}^1CH_2 \rightarrow C_3H_6$	−106.5	−5.9	−5.6	−11.6	1 3.8
34	$C_2H_2 + C_2H_4$ → cyclobutene	−31.5	−0.5	0.4	−2.8	3.3
35	*cis*-1,3 butadiene + C_2H_4 → cyclohexene	−44.4	6.7	6.4	2.5	−1.5
36	3 C_2H_2 → benzene	−151.1	0.2	2.5	−7.3	7.7
37	$^3CH_2 \rightarrow {}^1CH_2$	9.9	−1.7	−1.2	4.5	−5.0
38	$2\ NH_3 \rightarrow (NH_3)_2$	−3.1	0.5	0.4	−0.1	0.2
39	$2\ H_2O \rightarrow (H_2O)_2$	−5.2	0.5	0.4	0.1	0.2
40	$2\ HF \rightarrow (HF)_2$	−4.7	1.5	1.4	0.1	0.1
	MD		−0.9	−0.1	−2.3	−2.2
	MAD		2.5	2.2	4.0	4.1
	$\Delta_{\text{min-max}}$		14.2	14.7	19.7	29.4

[a] Given are the reference values (ref) and the deviations (*E*(method) − *E*(reference)) for SCS-MP2 and OO-SCS-MP2. The mean deviation (MD), the mean absolute deviation (MAD), and the error range ($\Delta_{\text{min-max}}$ = maximum deviation − minimum deviation) are also listed. All energies are in kcal mol^{-1}. [b] QCISD(T) with QZVP basis for heavy atoms (TZVP for H) on B3LYP/TZVP geometries taken from ref 49. [c] With QZVP basis set on B3LYP/TZVP geometries.

Table 2. Statistical MD and MAD (in parentheses) Values for the Reaction Set for Different Combinations of Same Spin (c_{ss}) and Opposite Spin (c_{os}) Scaling Parameters in OO-SCS-MP2[a]

	c_{os}		
c_{ss}	1.15	1.20	1.25
0.30	0.0 (2.0)	0.0 (2.1)	0.0 (2.3)
0.35	−0.2 (2.1)	−0.2 (2.2)	−0.1 (2.3)
0.40	−0.3 (2.1)	−0.3 (2.3)	−0.3 (2.4)

[a] All values in kcal mol^{-1}.

parameters are marginal. Thus, we prefer to keep the method as simple as possible and to keep the original SCS-MP2 scaling parameters also for OO-SCS-MP2. All remaining calculations have been performed in this way.

3.3. Transition-Metal Complexes. As a more challenging test, the performance of OO-SCS-MP2 is tested for a selection of organometallic transition-metal complexes. In transition-metal carbonyls, the metal−ligand bonds are still strong but are nevertheless difficult to describe with high accuracy by wave-function methods. Experience indicates that at least third-order perturbation contributions must be accounted for in order to correctly treat these bonds.[87] Hence, they provide a particularly challenging test set for OO-SCS-MP2.

Our results obtained with the SCS-MP3,[58] SCS-MP2 and OO-SCS-MP2 methods in conjunction with the TZVPP basis set are shown in Table 3. The CCSD(T) data serve as the reference in this case. They are extremely well reproduced by SCS-MP3, that is, in essentially quantitative agreement. The otherwise very successful LPNO-NCPF/1 method, on

Table 3. Ligand Dissociation Energies D_e (in kcal mol^{-1}) Based on BP86/TZVPP Geometries[a]

dissociation reaction	D_e						
	CCSD(T)	LPNO-NCPF/1	SCS-MP3	OO-SCS-MP2	SCS-MP2	OO-MP2	MP2
$[Cr(CO)_6] \rightarrow [Cr(CO)_5] + CO$	42.0	34.9	41.6	44.1	50.3	59.2	46.8
$[Cr(CO)_5(C_2H_4)] \rightarrow [Cr(CO)_5] + C_2H_4$	30.2	23.9	28.1	39.6	36.3	46.0	46.8
$[Cr(CO)_5(CS)] \rightarrow [Cr(CO)_5] + CS$	74.4	65.6	76.4	89.8	89.7	100.9	107.9
$[Ni(CO)_4] \rightarrow [Ni(CO)_3] + CO$	29.4[b]	22.9	22.1	61.2	43.9	55.6	89.1

[a] For the single point energies the TZVPP basis set was also applied. [b] The T1 diagnostic is 0.031 for both $Ni(CO)_3$ and $Ni(CO)_4$.

Table 4. Barrier Heights for Hydrogen Transfer Reactions[a]

	reaction	lit[b]	deviation			
			SCS-MP2[c]	OO-SCS-MP2[c]	MP2	OO-MP2
1	$H + HCl \rightarrow TS1$	5.7	3.7	2.5	5.1	5.7
2	$H_2 + Cl \rightarrow TS1$	8.7	1.8	0.9	−0.1	−2.1
3	$OH + H_2 \rightarrow TS2$	5.1	4.9	1.1	2.3	−2.9
4	$H_2O + H \rightarrow TS2$	21.2	8.0	4.3	10.1	7.7
5	$CH_3 + H_2 \rightarrow TS3$	12.1	2.2	1.0	0.8	−1.0
6	$CH_4 + H \rightarrow TS3$	15.3	4.0	2.6	4.4	5.0
7	$OH + CH4 \rightarrow TS4$	6.7	4.4	−0.4	1.2	−4.8
8	$H_2O + CH_3 \rightarrow TS4$	19.6	5.6	1.3	5.4	−0.2
9/10	$H + H_2 \rightarrow TS5$	9.6	3.7	2.9	3.5	4.5
11	$OH + NH_3 \rightarrow TS6$	3.2	7.3	−0.3	3.7	−5.7
12	$H_2O + NH_2 \rightarrow TS6$	12.7	8.3	1.1	6.0	−3.1
13	$HCl + CH_3 \rightarrow TS7$	1.7	2.3	0.8	1.1	−1.0
14	$Cl + CH_4 \rightarrow TS7$	7.9	2.2	0.7	−0.5	−2.8
15	$OH + C_2H_6 \rightarrow TS8$	3.4	5.4	0.2	2.4	−4.6
15	$H_2O + C_2H_5 \rightarrow TS8$	19.9	6.0	1.5	6.0	0.0
16	$F + H_2 \rightarrow TS9$	1.8	4.6	1.7	3.1	−1.2
17	$HF + H \rightarrow TS9$	33.4	7.5	5.1	11.7	10.5
18	$O + CH_4 \rightarrow TS10$	13.7	5.8	1.9	3.8	−0.4
19	$OH + CH_3 \rightarrow TS10$	8.1	5.5	2.3	4.0	0.4
20	$H + PH_3 \rightarrow TS11$	3.12	2.8	2.0	2.5	3.4
21	$H_2 + PH_2 \rightarrow TS11$	23.2	3.3	3.0	1.4	0.5
22	$H + OH \rightarrow TS12$	10.7	6.8	3.5	6.9	5.4
23	$H_2 + O \rightarrow TS12$	13.1	5.2	1.5	3.0	−1.4
24	$H + H_2S \rightarrow TS13$	3.5	3.5	2.5	3.2	4.0
25	$H_2 + HS \rightarrow TS13$	17.3	2.1	1.4	−0.6	−2.2
26	$O + HCl \rightarrow TS14$	9.8	8.7	2.6	6.1	−1.8
27	$OH + Cl \rightarrow TS14$	10.4	8.3	3.0	4.7	−2.8
28	$NH_2 + CH_3 \rightarrow TS15$	8.0	5.1	2.4	3.1	0.0
29	$NH + CH_4 \rightarrow TS15$	22.4	3.3	0.4	1.9	−1.4
30	$NH_2 + C_2H_5 \rightarrow TS16$	7.5	6.2	3.6	4.1	1.0
31	$NH + C_2H_6 \rightarrow TS16$	18.3	5.2	1.9	3.4	−0.3
32	$C_2H_6 + NH_2 \rightarrow TS17$	10.3	4.4	1.2	1.4	−2.8
33	$C_2H_5 + NH_3 \rightarrow TS170$	17.4	4.1	1.2	2.7	−0.8
34	$NH_2 + CH_4 \rightarrow TS18$	14.5	2.7	−0.2	−0.2	−3.8
35	$NH_3 + CH_3 \rightarrow TS18$	17.8	3.1	0.3	1.8	−1.6
37/38	*s-trans cis*-$C_5H_8 \rightarrow TS19$	38.4	1.5	1.4	−2.8	−5.2
	MD		4.6	1.7	3.1	−0.2
	MAD		4.6	1.8	3.5	2.9
	$\Delta_{\text{min-max}}$		6.9	5.5	14.5	16.2

[a] Given are the reference values from the literature and the deviations ($\Delta E^{\ddagger}$(method) − $\Delta E^{\ddagger}$(reference)) for SCS-MP2 and OO-SCS-MP2. The mean deviation (MD), the mean absolute deviation (MAD), and the error range ($\Delta_{\text{min-max}}$) are listed at the bottom. All energies in kcal mol^{-1}. [b] Best estimates from experiment and theory taken from ref 49. [c] With QZVP basis set on geometries taken from ref 49.

the other hand, systematically underestimates all binding energies by 6−9 kcal/mol. Turning to the SCS-MP2 and OO-SCS-MP2 data, it is evident from the data in Table 3 that orbital optimization is not able to improve the description of the complex electronic situation in these transition-metal carbonyl complexes. Given the success of the SCS-MP3 method, the most likely explanation is that it is necessary to correctly account for electron pair−pair couplings that are invariably neglected in any MBPT2 variant. Hence, the results of OO-SCS-MP2 and SCS-MP2 are of about the same quality and both show significant deviations from the reference values, in particular for $Ni(CO)_4$. Comparison to the nonscaled MP2 and OO-MP2 shows that spin-component scaling brings in a substantial improvement, which is, however, not enough to render the results chemically accurate. The smallness of the test set does not allow for a statistical evaluation.

3.4. Barrier Heights. In the next step of the evaluation, barrier heights from the HTBH38 benchmark set are considered. As has recently been pointed out by Zheng et al.,[116] reaction barriers are particularly challenging for MP2 methods. Our results are collected in Table 4. Note that, for two of the reactions, reactant and product are identical (entries 9, 10 and 37, 38). They are listed only once but are considered individually for the statistical evaluations in order to maintain consistency with the previous evaluations for this benchmark test.[49]

It becomes evident from the data in Table 4 that OO-SCS-MP2 provides particularly accurate results for these barriers. The MAD from the reference values decreases from 4.6 to only 1.7 kcal mol^{-1} in comparison with SCS-MP2. Interestingly, the comparison of MP2 and OO-MP2 reveals that the improvement by orbital optimization alone is rather moderate. Hence, it is the combination of orbital optimization and spin-component scaling that renders the method accurate. The results for OO-SCS-MP2 are almost as good as those delivered by the previously evaluated CEPA methods that are computationally much more demanding[9] (unless efficient approximations are employed).[117] In fact, the MAD of 1.7 kcal/mol for OO-SCS-MP2 is of the same size as what is obtained with the best current (and highly parametrized) density functionals and is much better than B3LYP, which provides an MAD of about 4 kcal/mol^{-1} for this benchmark.[118] Interestingly, OO-SCS-MP2 and SCS-MP2 themselves tend to overestimate barrier heights, especially when one of the reactants is a hydrogen atom, while the corresponding back reaction barriers are described better.

3.5. Radical Stabilization Energies. We now turn to the systems that the OO-SCS-MP2 method was mainly designed for. These are the reactions of radical species. In the evaluation reactions of the general homodesmotic type:

$$R{-}H + CH_3{\cdot} \rightarrow R{\cdot} + CH_4 \qquad (21)$$

are considered. If the reaction is exothermic, the rest R stabilizes the radical better than a methyl group. For our investigation, we took the set of R groups, as previously proposed in the study of Zipse.[84] However, we believe that it is desirable to obtain more rigorous reference values than those provided by the earlier restricted open-shell MP2 (ROMP2) calculations.[84] Therefore, we have turned to CCSD(T) calculations in combination with basis set extrapolation. For simplicity and since we only compare theoretical data among each other, ZPVE and thermal effects were not considered. The new reference data together with the results of OO-SCS-MP2 and SCS-MP2 calculations are collected in Table 5.

As in the case of reaction barriers, it is observed that OO-SCS-MP2 drastically improves upon the results of SCS-MP2. The MAD value drops by about a factor of 3 from 4.7 to 1.5 kcal mol^{-1}, and at the same time, the error range is reduced from 43.4 kcal mol^{-1} (SCS-MP2) to only 16.3 kcal mol^{-1} (OO-SCS-MP2), again a factor of 3. In addition, in this case OO-MP2 also improves substantially upon MP2. It is, in fact, the most accurate method for this test set.

For judging the effect of spin contamination, the $\langle S^2 \rangle$ values for the UHF reference are also listed in Table 5. Clearly, if the reference suffers from spin contamination, then the SCS-MP2 results are strongly biased. OO-SCS-MP2, on the other hand, decreases this effect to a remarkable extent. This is in agreement with the results of ref 52. Unfortunately, we have not yet implemented the calculation of the $\langle S^2 \rangle$ value on the basis of OO-SCS-MP2, which would allow us to judge the precise extent of residual spin contamination. Nevertheless, the behavior of SCS-MP2 versus OO-SCS-MP2 is visualized in Figure 2.

3.6. Bond Dissociation Energies in Polycyclic Aromatic Hydrocarbons. Encouraged by the performance of OO-SCS-MP2 for the RSE test set, we have turned to study bond dissociation energies in polcyclic hydrocarbons as another challenging application of the method. Here, it is demonstrated that OO-SCS-MP2 can be applied to larger systems in conjunction with sufficiently saturated basis sets.

In the test reactions, the C−H bond in a methyl group is broken which leads to a benzyl type radical (Figure 3). The design of the test set goes back to an investigation of Hemelsoet et al.,[85] who reported that these systems significantly suffer from spin contamination.

The results of our computations are collected in Table 6. In agreement with the results of Hemelsoet et al.,[85] very large deviations from the expected $\langle S^2 \rangle$ value of 0.75 are found. This leads to such a large bias for the SCS-MP2 results that these are rendered essentially useless. Again, however, OO-SCS-MP2 yields greatly improved the results. However, they cannot be directly compared to the results of ref 85 because, in the previous study, vibrational and thermal corrections were added, and a basis set of only double-ζ quality was used. Since this puts some doubt on the accuracy of the results in ref 85, we also computed B2-PLYP-D values for these reactions. These should also be much less influenced by spin contamination because the Kohn−Sham determinant is usually much less prone to symmetry breaking and spin contamination than that of the UHF wave function. Hence, the results are considered to be more reliable. Indeed, the corresponding $\langle S^2 \rangle$ values in Table 6 deviate less strongly from 0.75 but still indicate significant problems with the reference.

On an absolute scale both methods, OO-SCS-MP2 and B2-PLYP-D, differ by about 5 kcal mol^{-1}, but the trends are the same. There is a slight increase in BDE of 1 kcal mol^{-1} from **5−13** to **5−14**, then a larger increase of 10 kcal mol^{-1} to **5−1**, and the bond in **5−2** is less stable by about 2 kcal mol^{-1}. The step from **10−14** to **10−1** leads to an increase of about 6 kcal mol^{-1} in BDE, and there is almost no difference between **10−1** and **10−12**. Both methods are in qualitative agreement with the findings of Hemelsoet et al. We note, in passing, that their B2-PLYP results do *not* show the same trend. The reason for this discrepancy is not clear.

4. Discussion

In this work, the orbital-optimized MP2 method has been developed into a useful tool for computational quantum chemistry. The motivation for the work is to improve upon the results of the second-order many-body perturbation theory through incorporation of orbital relaxation effects to all orders, while maintaining acceptable computational efficiency. This goal is clearly reached by the OO-MP2 method that, as we have demonstrated here, can be applied in reasonable turnaround times to molecules of significant size. The effort for a OO-RI-MP2 calculation is nevertheless substantially higher than that of a RI-MP2 (RI-SCS-MP2) calculation due to its iterative nature and to the extra terms required to obtain the orbital gradient. The ratio for a reasonably large calculation has been found to be 8−12 in

Table 5. Reference Radical Stabilization Energies Together with the Deviations (RSE(method) − RSE(reference)) for SCS-MP2 and OO-SCS-MP2 are given in kcal mol^{-1} [a]

		deviation				
substituent	ref[b]	SCS-MP2[c]	OO-SCSMP2[c]	MP2	OO-MP2	$<S^2>$[d]
$\cdot CH_2-C_6H_5$	−15.2	22.9	0.7	24.4	0.5	1.335
$CH_2{=}C\cdot-CN$	1.9	30.1	0.8	27.3	−1.1	1.385
$\cdot CF{=}CH_2$	6.8	7.8	0.5	6.0	−0.7	0.934
$\cdot CH_2-CCl_3$	7.4	4.2	1.5	7.1	4.6	0.825
$\cdot CH_2-CF_2-CH_3$	0.1	0.5	0.1	0.5	−0.1	0.762
$\cdot CH_2-CF_3$	1.4	0.5	0.1	0.5	−0.1	0.762
$\cdot CH_2-CH_2-Cl$	−3.2	1.4	0.4	1.4	0.2	0.774
$\cdot CH_2-CH_2-F$	−1.3	0.4	−0.1	0.3	−0.3	0.763
$\cdot CH_2-CH_2-OH$	−1.8	0.6	0.2	0.4	−0.1	0.764
$\cdot CH_2-CH{=}CH_2$	−17.5	6.9	1.0	6.0	0.1	0.951
$\cdot CH_2-CHO$	−10.0	9.7	0.7	9.6	0.2	0.927
$\cdot CH_2-CN$	−8.6	11.6	0.7	10.9	0.0	0.938
$\cdot CH_2-CO-CH_3$	−8.7	8.5	0.6	8.4	0.2	0.909
$\cdot CH_2-CO\text{-}NH_2$	−6.3	1.9	−0.1	1.8	−0.3	0.793
$\cdot CH_2-CO-NH-CH_3$	−6.3	4.0	−0.2	1.6	−0.5	0.786
$\cdot CH_2-CO-O-CH_3$	−6.6	2.5	0.0	2.4	−0.3	0.802
$\cdot CH_2-CO-OH$	−6.4	2.7	0.1	2.6	−0.1	0.807
$\cdot CH_2-CH(-CH_2)_2$	−3.0	0.6	0.1	0.5	−0.1	0.763
$\cdot CH_2-F$	−3.9	1.0	0.2	0.3	−0.8	0.762
$\cdot CH_2-NH_2$	−12.0	0.8	−0.4	0.1	−1.4	0.763
$\cdot CH_2-NH_3^+$	4.7	0.6	0.3	0.2	−0.1	0.763
$\cdot CH_2-NH-CH_3$	−12.6	0.9	−0.5	0.3	−1.5	0.764
$\cdot CH_2-NH-CHO$	−11.1	1.7	0.2	1.0	−0.7	0.777
$\cdot CH_2-NH-OH$	−8.6	1.8	−0.4	0.9	−1.7	0.772
$\cdot CH_2-N(-CH_3)_2$	−12.8	1.2	−0.5	0.6	−1.3	0.764
$\cdot CH_2-NO_2$	−3.3	2.3	0.1	1.6	−0.7	0.787
$\cdot CH_2-O-CF_3$	−3.9	1.4	0.4	0.7	−0.4	0.764
$\cdot CH_2-O-CH_3$	−2.7	0.9	0.1	0.4	−0.5	0.763
$\cdot CH_2-O-CHO$	−5.9	1.3	0.4	0.6	−0.6	0.765
$\cdot CH_2-CO-O-CH_3$	−6.2	1.5	0.3	0.7	−0.8	0.766
$\cdot CH_2-OH$	−4.2	0.9	0.2	0.2	−0.6	0.762
$\cdot CH_2-PH_3^+$	0.7	0.2	0.1	0.5	0.3	0.762
$\cdot CH_2-S-CH_3$	−10.8	1.4	−0.7	0.7	−1.8	0.773
$\cdot CH_2-S-CHO$	−8.4	1.6	−0.5	1.0	−1.7	0.776
$\cdot CH_2-SH_2^+$	2.7	0.5	0.0	0.2	−0.4	0.765
$\cdot CH_2-SH$	−9.4	1.1	−0.6	0.5	−1.6	0.772
$\cdot CH_2-SO-O-CH_3$	0.0	0.9	−0.4	0.9	−0.9	0.763
$\cdot CH_2-SO-CH_3$	−2.9	1.2	−0.3	1.0	−1.0	0.771
$NH_2-CH\cdot-CN$	−22.5	10.3	−0.4	8.8	−2.3	0.908
$NH_2-CH\cdot-CO-NH_2$	−24.1	1.2	−1.0	0.0	−2.7	0.776
$NH_2-CH\cdot-CO-OH$	−25.4	1.4	−1.0	0.0	−2.8	0.779
$\cdot CH_2-C{\equiv}CH$	−13.1	10.7	0.9	9.5	0.1	0.960
$\cdot C(-CH_3)_3$	−6.4	1.5	0.6	1.3	0.1	0.767
$\cdot CH_2-C(-CH_3)_3$	−2.3	0.8	0.3	0.8	0.2	0.763
MD		3.8	0.1	3.3	−0.5	
MAD		3.8	0.4	3.3	0.8	
$\Delta_{\text{min-max}}$		29.9	2.5	27.2	7.4	

[a] The $<S^2>$ values are taken from the unrestricted Hartree−Fock calculation. The mean deviation (MD), the mean absolute deviation (MAD), and the error range ($\Delta_{\text{min-max}}$) are listed at the bottom. [b] CCSD(T)/CBS(D→T). [c] QZVP basis set on B3LYP/TZVP geometries. [d] The theoretical value is always 3/4.

this work. As will be developed in detail elsewhere, this ratio improves in analytic gradient calculations where all of these terms also have to be calculated for RI-MP2.

The results of an extensive numerical evaluation of the OO-MP2 and OO-SCS-MP2 methods indicate that they do drastically improve the accuracy (and stability) of the parent nonorbital-optimized methods in electronically difficult situations. The errors typically decrease by a factor of 3 to 5. This is particularly evident for open-shell species and transition states and less so for transition-metal complexes. For standard main group closed-shell species, the results of orbital-optimized and conventional MP2 methods is, however, comparable, and it is questionable whether the extra effort for the orbital optimization is well invested. The consistent improvement offered by spin-component scaling in the conventional MP2 method persists in the OO-MP2 approach, and it was found in this work that very little, if anything, can be gained through reoptimization of the SCS-MP2 same-spin and opposite-spin scaling parameters.

Thus, there is a well-defined domain of applicability for OO-(SCS)-MP2 that is intermediate between the conventional MP2 and the more rigorous coupled-cluster approaches. The cost for OO-(SCS)-MP2 is also intermediate between these extremes. In many cases, the much better orbitals delivered by the OO-(SCS)-MP2 method may also be advantageous for coupled cluster investigations, in particular for open-shell transition-metal complexes. This subject will be investigated elsewhere.

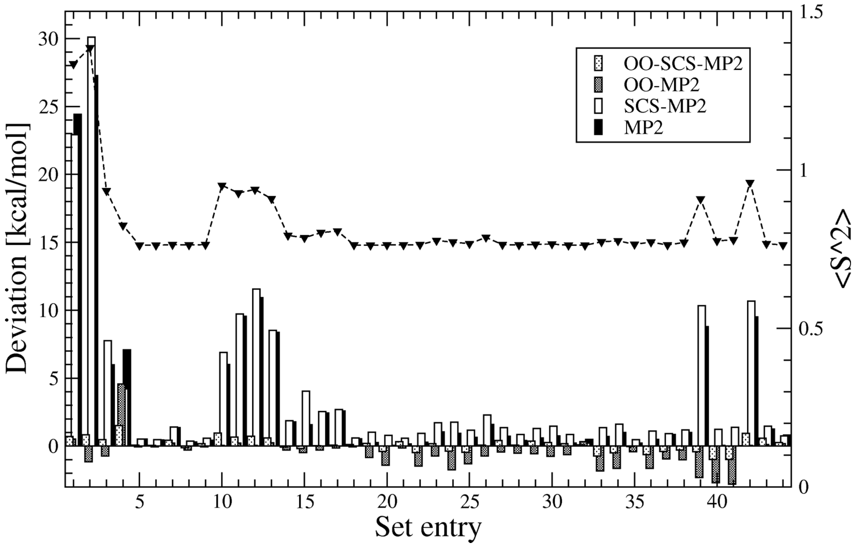

Figure 2. Errors of the methods under investigation for the RSE set (RSE(theory) - RSE(reference)). In order to demonstrate the relation of the error with spin contamination, the <S^2> value for each UHF reference is plotted on top.

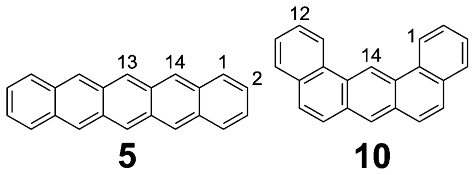

Figure 3. Polycyclic aromatic hydrocarbons. Methylated positions, where bond dissociations in the methyl group are considered, are indicated by numbers.

Table 6. Bond Dissociation Energies for the C−H bond of the Methyl Group of Polycyclic Aromatic Hydrocarbons Based on Single Point Energies with the TZVPP Basis on B3LYP-D/TZVP Geometries[a]

	BDE			BDE	
system	SCS-MP2	OO-SCS-MP2	<S^2>[b]	B2PLYP-D	<S^2>[b]
5−13	183.0	85.4	3.509	90.8	0.896
5−14	180.8	86.4	3.469	91.9	1.361
5−1	189.7	95.7	3.689	103.8	0.757
5−2	187.5	94.1	3.656	102.0	0.850
10−14	187.5	90.4	3.303	94.4	1.112
10−1	115.6	97.3	1.483	99.4	1.046
10−12	194.6	97.2	3.377	98.9	0.757

[a] The <S^2> from the unrestricted Hartree−Fock and DFT calculation is also given. Energies in kcal mol^{-1}. [b] The theoretical value is always 3/4.

Methodologically, the OO-MP2 method is closely related to the CC2 coupled cluster variant. The CC2 doubles amplitude equations correspond to the conventional MP2 residual, eq 22[72] (but with integrals that are 'dressed' with t_1 amplitudes). In order to emphasize the similarities between the OO-MP2 and CC2 methods, one may write the CC2 singles residual and the OO-MP2 orbital gradient in the following forms:

CC2-singles residual:

$$\sigma_a^i = \tilde{F}'_{ai} + \frac{1}{2}\sum_{lcd}\tau_{cd}^{il}\overline{\langle al||cd\rangle} - \frac{1}{2}\sum_{kld}\tau_{ad}^{kl}\overline{\langle kl||id\rangle} \tag{22}$$

$$\tau_{cd}^{il} = t_{cd}^{il} + t_c^i t_d^l \tag{23}$$

$$\overline{\langle al||cd\rangle} = \langle al||cd\rangle - \sum_k \langle kl||cd\rangle t_a^k \tag{24}$$

$$\overline{\langle kl||id\rangle} = \langle kl||id\rangle + \sum_c \langle kl||cd\rangle t_c^i \tag{25}$$

OO-MP2 orbital gradient:

$$R_{ai} = \hat{F}_{ai} + \sum_{ldc} t_{cd}^{il}\langle al||cd\rangle - \sum_{kld} t_{ad}^{kl}\langle kl||id\rangle \tag{26}$$

Thus, in both approaches, an effective one-particle Fock matrix enters the quantity to be brought to zero together with three internal and three external integrals contracted in an identical way with double excitation amplitudes. The difference is that in CC2 one uses a fixed set of SCF orbitals and obtains integrals and amplitudes that are dressed in a nonlinear way with t_1 amplitudes. In the OO-MP2 technique, one has orbitals that change in each iteration, but one may well think of the changes as a "dressing" of the SCF orbitals with orbital rotation parameters. In CC2, one needs to do a "dressing transformation" in each iteration, while in OO-MP2 a new integral transformation is required. The dressing of the integrals and amplitudes in CC2 is, in fact, relaxing the orbitals. In a Brückner sense, one could even absorb the t_1 amplitudes into the orbitals in each iteration. The similarity transformed integrals that are usually used in CC2 implementations expose this feature rather clearly. If the t_1 operator, $\hat{t}_1 = \sum_{ia} t_a^i a_a^+ a_i$, would now be replaced by the full orbital rotation operator, $\hat{\kappa} = \sum_{ai}\kappa_{ai}(a_a^+ a_i - a_i^+ a_a)$, then one would fully relax to orbital-optimized CC2 that must resemble OO-MP2. A highly interesting discussion of orbital-optimized coupled cluster theory has been given by Köhn and Olsen.[119]

The effective Fock matrices are given by

CC2:

$$\tilde{F}'_{ai} = F_{ai} - \sum_{kc}(F_{kc}\tau^{ik}_{ca} + t^{k}_{c}\langle ak||ic\rangle) + \sum_{c} F_{ac}t^{i}_{c} - \sum_{k} F_{ik}t^{k}_{a} + \frac{1}{2}\sum_{kcd} t^{k}_{c}t^{i}_{d}\langle ak||cd\rangle - \frac{1}{2}\sum_{klc} t^{l}_{a}t^{k}_{c}\langle lk||ic\rangle \quad (27)$$

OO-MP2:

$$\hat{F}_{ai} = F_{ai} + \sum_{j} D_{ij}F_{aj} - \sum_{b} D_{ab}F_{ib} + \sum_{cd} D_{cd}\langle ca||di\rangle + \sum_{kl} D_{kl}\langle ka||li\rangle \quad (28)$$

again, similar terms can be recognized. The computational effort for both methods must, for optimal implementations, be rather similar. However, the stationary properties of the OO-MP2 method make it more efficient for the calculation of first-order and perhaps also of response properties. This subject will be investigated elsewhere. From this point of view, one may regard OO-MP2 as an improved or, at least, modified second-order coupled-cluster-type theory.

In conclusion, this work evaluates a wave function based second-order ab initio method that complements existing approaches such as MP2, SCS-MP2, B2PLYP, or CC2.

References

(1) Möller, C.; Plesset, M. S. *Phys. Rev.* **1934**, *46*, 618.

(2) Binkley, J. S.; Pople, J. A. *Int. J. Quantum Chem.* **1975**, *9*, 229–236.

(3) Szabo, A.; Ostlund, N. S. *Modern Quantum Chemistry. Introduction to Advanced Electronic Structure Theory*; McGraw-Hill: New York, 1989.

(4) Cremer, D. In *Encyclopedia of Computational Chemistry*; Schleyer, P. V., Ed.; John Wiley & Sons: Chichester, U.K., 1998; Vol. 3, p 1706−1735.

(5) Bartlett, R. J. *Rev. Mod. Phys.* **2007**, *79*, 291–352.

(6) Crawford, T. D.; Schaefer, H. F. *Rev. Comp. Chem.* **2000**, *14*, p 33–136.

(7) Meyer, W. *Int. J. Quant.Chem. Symp.* **1971**, *341*, 341.

(8) Kutzelnigg, W. In *Modern Theoretical Chemistry*; Schaefer, H. F., Ed.; Plenum Press: New York, 1977.

(9) Neese, F.; Wennmohs, F.; Hansen, A.; Grimme, S. *Acc. Chem. Res.* **2009**, *42,* 641−648.

(10) Grimme, S. *J. Phys. Chem. A* **2005**, *109*, 3067–3077.

(11) Taylor, P. R. In *Lecture Notes in Quantum Chemistry*; Roos, B. O., Ed.; Springer: Berlin, Germany, 1992, p 336.

(12) Saebo, S.; Almlöf, J. *Chem. Phys. Lett.* **1989**, *154*, 83–89.

(13) Head-Gordon, M.; Pople, J. A.; Frisch, M. J. *Chem. Phys. Lett.* **1988**, *153*, 503–506.

(14) Haase, F.; Ahlrichs, R. *J. Comput. Chem.* **1993**, *14*, 907–912.

(15) Ishimura, K.; Pulay, P.; Nagase, S. *J. Comput. Chem.* **2006**, *27*, 407–413.

(16) Saebo, S.; Baker, J.; Wolinski, K.; Pulay, P. *J. Chem. Phys.* **2004**, *120*, 11423–11431.

(17) Baker, J.; Pulay, P. *J. Comput. Chem.* **2002**, *23*, 1150–1156.

(18) Saebo, S.; Pulay, P. *J. Chem. Phys.* **2001**, *115*, 3975–3983.

(19) Pulay, P.; Saebo, S.; Wolinski, K. *Chem. Phys. Lett.* **2001**, *344*, 543–552.

(20) Baker, J.; Wolinski, K.; Malagoli, M.; Kinghorn, D.; Wolinski, P.; Magyarfalvi, G.; Saebo, S.; Janowski, T.; Pulay, P. *J. Comput. Chem.* **2009**, *30*, 317–335.

(21) Lambrecht, D. S.; Doser, B.; Ochsenfeld, C. *J. Chem. Phys.* **2005**, 123.

(22) Doser, B.; Lambrecht, D. S.; Kussmann, J.; Ochsenfeld, C. *J. Chem. Phys.* **2009**, *130*, 064107.

(23) Almlöf, J. *Chem. Phys. Lett.* **1991**, *181*, 319–320.

(24) Haser, M.; Almlöf, J. *J. Chem. Phys.* **1992**, *96*, 489–494.

(25) Häser, M. *Theoret. Chim. Acta* **1993**, *87*, 147.

(26) Ayala, P. Y.; Kudin, K. N.; Scuseria, G. E. *J. Chem. Phys.* **2001**, *115*, 9698–9707.

(27) Doser, B.; Lambrecht, D. S.; Ochsenfeld, C. *Phys. Chem. Chem. Phys.* **2008**, *10*, 3335.

(28) Schweizer, S.; Doser, B.; Ochsenfeld, C. *J. Chem. Phys.* **2008**, *127*, 154101.

(29) Kendall, R. A.; Früchtl, H. A. *Theor. Chem. Acc.* **1997**, *97*, 158.

(30) Feyereisen, M.; Fitzgerald, G.; Komornicki, A. *Chem. Phys. Lett.* **1993**, *208*, 359–363.

(31) Vahtras, O.; Almlöf, J.; Feyereisen, M. W. *Chem. Phys. Lett.* **1993**, *213*, 514–518.

(32) Weigend, F.; Ahlrichs, R. *Phys. Chem. Chem. Phys.* **2005**, *7*, 3297–3305.

(33) Weigend, F.; Häser, M.; Patzelt, H.; Ahlrichs, R. *Chem. Phys. Lett.* **1998**, *294*, 143–152.

(34) Weigend, F.; Furche, F.; Ahlrichs, R. *J. Chem. Phys.* **2003**, *119*, 12753–12762.

(35) Schäfer, A.; Huber, C.; Ahlrichs, R. *J. Chem. Phys.* **1994**, *100*, 5829–5835.

(36) Schäfer, A.; Horn, H.; Ahlrichs, R. *J. Chem. Phys.* **1992**, *97*, 2571–2577.

(37) Schütz, M.; Werner, H.-J.; Manby, F. R. *J. Chem. Phys.* **2004**, *121*, 737.

(38) Werner, H.-J.; Manby, F. R.; Knowles, P. J. *J. Chem. Phys.* **2003**, *118*, 8149.

(39) Hetzer, G.; Schütz, M.; Stoll, H.; Werner, H. J. *J. Chem. Phys.* **2000**, *113*, 9443–9455.

(40) Rauhut, G.; Pulay, P.; Werner, H. J. *J. Comput. Chem.* **1998**, *19*, 1241–1254.

(41) El Azhary, A.; Rauhut, G.; Pulay, P.; Werner, H. J. *J. Chem. Phys.* **1998**, *108*, 5185–5193.

(42) Pulay, P. *Chem. Phys. Lett.* **1983**, *100*, 151–154.

(43) Saebo, S.; Pulay, P. *Annu. Rev. Phys. Chem.* **1993**, *44*, 213–236.

(44) Saebo, S.; Pulay, P. *Chem. Phys. Lett.* **1985**, *113*, 13–18.

(45) Friesner, R. A. *Proc. Natl. Acad. Sci. U.S.A.* **2005**, *102*, 6648–6653.

(46) Neese, F.; Wennmohs, F.; Hansen, A.; Becker, U. *Chem. Phys.* **2009**, *356*, 98–109.

(47) Neese, F. *J. Comput. Chem.* **2003**, *24*, 1740–1747.

(48) Grimme, S. *J. Chem. Phys.* **2003**, *109*, 3067–3077.

(49) Grimme, S. *J. Chem. Phys.* **2003**, *118*, 9095.

(50) Gerenkamp, M.; Grimme, S. *Chem. Phys. Lett.* **2004**, *392*, 229–235.

(51) Zheng, J.; Zhao, Y.; Truhlar, D. G. *J. Chem. Theo. Comp.* **2009**, *5*, 808–821.

(52) Lochan, R. C.; Head-Gordon, M. *J. Chem. Phys.* **2007**, 126.

(53) Lochan, R. C.; Jung, Y.; Head-Gordon, M. *J. Phys. Chem. A* **2005**, *109*, 7598–7605.

(54) Jung, Y. S.; Lochan, R. C.; Dutoi, A. D.; Head-Gordon, M. *J. Chem. Phys.* **2004**, *121*, 9793–9802.

(55) Grimme, S.; Steinmetz, M.; Korth, M. *J. Org. Chem.* **2007**, *72*, 2118–2126.

(56) Schwabe, T.; Grimme, S. *Phys. Chem. Chem. Phys.* **2006**, *38*, 4398.

(57) Grimme, S.; Mück-Lichtenfeld, C.; Würthwein, E.-U.; Ehler, A. W.; Goumans, T. P. M.; Lammertsma, K. *J. Phys Chem. A* **2006**, *110*, 2583–2586.

(58) Grimme, S. *J. Comput. Chem.* **2003**, *24*, 1529–1537.

(59) Neese, F.; Schwabe, T.; Grimme, S. *J. Chem. Phys.* **2007**, *126*, 124115.

(60) Nielsen, E. S.; Jørgensen, P.; Oddershede, J. *J. Chem. Phys.* **1980**, *73*, 6238.

(61) Oddershede, J.; Jørgensen, P.; Yeager, D. *Comp. Phys. Rep.* **1984**, *2*, 33.

(62) Christiansen, O.; Koch, H.; Jorgensen, P. *Chem. Phys. Lett.* **1995**, *243*, 409–418.

(63) Christiansen, C.; Jørgensen, P.; Hättig, C. *Int. J. Quantum Chem.* **1998**, *68*, 1.

(64) Hättig, C. *J. Chem. Phys.* **2003**, *118*, 7751–7761.

(65) Hellweg, A.; Grün, S. A.; Hättig, C. *Phys. Chem. Chem. Phys.* **2008**, *10*, 4119–4127.

(66) Hättig, C.; Weigend, F. *J. Chem. Phys.* **2000**, *113*, 5154.

(67) Hald, K.; Hattig, C.; Yeager, D. L.; Jorgensen, P. *Chem. Phys. Lett.* **2000**, *328*, 291–301.

(68) Christiansen, O.; Koch, H.; Jorgensen, P.; Helgaker, T. *Chem. Phys. Lett.* **1996**, *263*, 530–539.

(69) Koch, H.; Christiansen, O.; Jorgensen, P.; Olsen, J. *Chem. Phys. Lett.* **1995**, *244*, 75–82.

(70) Hättig, C. *Adv. Quant. Chem.* **2005**, *50*, p 37–60.

(71) Kats, D.; Korona, T.; Schutz, M. *J. Chem. Phys.* **2007**, 127.

(72) Kats, D.; Korona, T.; Schütz, M. *J. Chem. Phys.* **2006**, *125*, 104106.

(73) Pulay, P.; Saebo, S. *Theo. Chim. Acta* **1986**, *69*, 357–368.

(74) Adamowicz, L.; Bartlett, R. J. *J. Chem. Phys.* **1987**, *86*, 6314.

(75) Adamowicz, L.; Bartlett, R. J. *Phys. Rev. A: At., Mol., Opt. Phys.* **1988**, *37*, 1.

(76) Adamowicz, L.; Bartlett, R. J.; Sadlej, A. J. *J. Chem. Phys.* **1988**, *88*, 5749.

(77) Adamowicz, L. *J. Comput. Chem.* **1989**, *10*, 928.

(78) Adamowicz, L. *J. Phys. Chem.* **1990**, *93*, 1780.

(79) Adamowicz, L. *Int. J. Quant. Chem. Symp. Ser.* **1991**, *25*, 71.

(80) Kurlancheek, W.; Head-Gordon, M. *Mol. Phys.* **2009**, *107*, 1223–1232.

(81) Kollmar, C., The MP2O method.

(82) Parkinson, C. J.; Mayer, P. M.; Radom, L. *Theor. Chem. Acc.* **1999**, *102*, 92.

(83) Menon, A. S.; Wood, G. P. F.; Moran, D.; Radom, L. *J. Phys. Chem. A* **2007**, *111*, 13638–13644.

(84) Zipse, H. *Top. Curr. Chem.* **2006**, *263*, 163–189.

(85) Hemelsoet, K.; Van Speybroeck, V.; Waroquier, M. *J. Phys. Chem. A* **2008**, *112*, 13566–13573.

(86) Zhao, Y.; Lynch, B. J.; Truhlar, D. G. *Phys. Chem. Chem. Phys.* **2005**, *7*, 43–52.

(87) Hyla-Kryspin, I.; Grimme, S. *Organometallics* **2004**, *23*, 5581–5592.

(88) Hylleraas, E. A. *Z. Phys. A* **1930**, *65*, 209.

(89) Brillouin, L. *J. Phys.* **1932**, *3*, 373.

(90) Pulay, P. *Chem. Phys. Lett.* **1980**, *73*, 393–398.

(91) Pulay, P. *J. Comput. Chem.* **1982**, *3*, 556–560.

(92) Rice, J. E.; Amos, R. D.; Handy, N. C.; Lee, T. J.; Schaefer, H. F. *J. Chem. Phys.* **1986**, *85*, 963.

(93) Scuseria, G. E.; Schaefer, H. F. *Chem. Phys. Lett.* **1987**, *142*, 354–358.

(94) Becke, A. D. *J. Chem. Phys.* **1993**, *98*, 1372–1377.

(95) Becke, A. D. *Phys. Rev. A* **1988**, *38*, 3098–3100.

(96) Lee, C.; Yang, W.; Parr, R. G. *Phys. Rev. B: Solid State* **1988**, *37*, 785.

(97) Devlin, F. J.; Stephens, P. J.; Cheeseman, J. R.; Frisch, M. J. *J. Phys. Chem. A* **1997**, *101*, 6322–6333.

(98) Ahlrichs, R.; Bar, M.; Haser, M.; Horn, H.; Kolmel, C. *Chem. Phys. Lett.* **1989**, *162*, 165–169.

(99) Ahlrichs, R.; Bär, M.; Baron, H. P.; Bauernschmitt, R.; Böcker, S.; Ehrig, M.; Eichkorn, K.; Elliott, S.; Furche, F.; Haase, F.; Häer, M.; Horn, H.; Huber, C.; Huniar, U.; Kattannek, M.; Kölmel, C.; Kollwitz, M.; May, K.; Ochsenfeld, C.; öhm, H.; Schäfer, A.; Schneider, U.; Treutler, O.; von Arnim, M.; Weigend, F.; Weis, P.; Weiss, H.; *(Version 5.9) ed.* 2008.

(100) Grimme, S.; Antony, J.; Schwabe, T.; Muck-Lichtenfeld, C. *Org. Biomol. Chem.* **2007**, *5*, 741–758.

(101) Grimme, S. *J. Comput. Chem.* **2006**, *27*, 1787–1799.

(102) Antony, J.; Grimme, S. *Phys. Chem. Chem. Phys.* **2006**, *8*, 5287–5293.

(103) Perdew, J. P. *Phys. Rev. B: Solid State* **1986**, *33*, 8822–8824.

(104) Eichkorn, K.; Treutler, O.; öhm, H.; Häser, M.; Ahlrichs, R. *Chem. Phys. Lett.* **1995**, *240*, 283–290.

(105) Treutler, O.; Ahlrichs, R. *J. Chem. Phys.* **1995**, *102*, 346–354.

(106) Grimme, S. *J. Chem. Phys.* **2006**, *124*, 34108.

(107) Schwabe, T.; Grimme, S. *Phys. Chem. Chem. Phys.* **2006**, *8*, 4398–4401.

(108) Weigend, F. *Phys. Chem. Chem. Phys.* **2006**, *8*, 1057.

(109) Neese, F.; Becker, U.; Ganyushin, D.; Kossmann, S.; Hansen, A.; Liakos, D.; Petrenko, T.; Riplinger, C.; Wennmohs, F.; *Version 2.7.0 ed.* University of Bonn, Germany, 2009.

(110) Halkier, A.; Helgaker, T.; Jorgensen, P.; Klopper, W.; Koch, H.; Olsen, J.; Wilson, A. K. *Chem. Phys. Lett.* 1998*286*, 243–252.

(111) Helgaker, T.; Klopper, W.; Koch, H.; Noga, J. *J. Chem. Phys.* **1997**, *106*, 9639.

(112) Dunning, T. H. *J. Chem. Phys.* **1994**, *100*, 5829.

(113) Dunning, J. T. H. *J. Chem. Phys.* **1989**, *90*, 1007.

(114) Dunning, J. T. H. *J. Chem. Phys.* **1980**, *90*, 1007.

(115) Werner, H.-J.; Knowles, P. J.; Lindh, R.; Manby, F. R.; Schütz, M.; Celani, P.; Korona, T.; Rauhut, G.; Amos, R. D.; Bernhardsson, A.; Berning, A.; Cooper, D. L.; Deegan, M. J. O.; Dobbyn, A. J.; Eckert, F.; Hampel, C.; Hetzer, G.; Lloyd, A. W.; McNicholas, S. J.; Meyer, W.; Mura, M. E.; Nicklaβ, A.; Palmieri, P.; Pitzer, R.; Schumann, U.; Stoll, H.; Stone, A. J.; Tarroni, R.; Thorsteinsson, T.;2006.1 ed. 2006.

(116) Zheng, J.; Zhao, Y.; Truhlar, D. G. *J. Chem. Theo. Comp.* **2009**, *5*, 808–821.

(117) Neese, F.; Wennmohs, F.; Hansen, A. *J. Chem. Phys.* **2009**, *130*, 114108.

(118) Zhao, Y.; Truhlar, D. G. *J. Chem. Theor. Comp.* **2008**, *4*, 1849–1868.

(119) Köhn, A.; Olsen, J. *J. Chem. Phys.* **2005**, 122.

CT9003299

3074 J. Chem. Theory Comput. 2009, 5, 3074–3078

JCTC Journal of Chemical Theory and Computation

Phase-Dependent Photocatalytic Ability of TiO_2: A First-Principles Study

Hui Pan,[*,†] Baohua Gu,[†] and Zhenyu Zhang

Environmental Science Division, Material Science & Technology Division, Oak Ridge National Laboratory, Oak Ridge, Tennessee 37831, and Department of Physics and Astronomy, University of Tennessee, Knoxville, Tennessee 37996

Received May 25, 2009

Abstract: The electronic properties of defected TiO_2 were investigated using the first-principles calculations based on density functional theory and generalized gradient approximation. Three typical defects, oxygen vacancy, titanium interstitial, and titanium vacancy, were considered in three TiO_2 polymorphs, anatase, rutile, and brookite, respectively. Our calculations demonstrated that the defect band is formed by removing an oxygen atom from or inserting an interstitial Ti atom into the TiO_2 lattice, which is responsible for the improvement of photocatalytic ability due to the enhanced visible-light absorption. Our calculations further revealed that the defect formation energy increases as following brookite, anatase, and rutile, indicating that defects are easy to be created in brookite TiO_2. The relatively high defect density and wide defect band contribute to the better photocatalytic performance of brookite TiO_2 in visible light.

Introduction

Titanium dioxide (TiO_2) finds wide applications in pigment, photocatalyst, photovoltaic materials, gas sensor, electrical circuit varistor, biocompatible material for bone implants, and spacer material for magnetic spin valve systems.[1−4] TiO_2, as a photocatalyst, has attracted substantial interest and been widely studied since 1972.[5] The photocatalytic ability of TiO_2 strongly depends on the crystal structure, morphology, and size. TiO_2 has commonly three crystalline polymorphs: anatase, brookite, and rutile. Generally, the performance of anatase TiO_2 is recognized to be better than the rutile counterpart.[6−8] The photocatalytic performance of anatase TiO_2 was attributed to the shallow electronic levels induced by oxygen vacancy.[8] Recently, it has been illustrated that brookite TiO_2 is more electrochemically active than anatase TiO_2.[9−11] It has been argued that the defects, such as oxygen vacancy, may make a contribution to the photocatalytic ability,[12−14] because the defect, as a "local factor", interacts with the adsorbed molecules and allows effective charge transfer between the H_2O and the TiO_2 surface.[14,15] More recently, Wendt et al. reported that the defect state (Ti*3d*) in the bandgap of titania was attributed to Ti interstials and resulted in narrowing the bandgap,[16] which played a key role in providing the electronic charge required for O_2 adsorption and dissociation. To date, the mechanism for the phase-dependent photocatalytic ability has not been clarified. The understanding of the origin should help the searching of photocatalyst with high efficiency. In this work, we systematically studied the effects of the defects on the electronic properties of TiO_2 by first-principles calculations. The first-principles calculations confirmed that the defects whose states were located within the bandgap can result in the improvement of visible-light absorption and revealed the origin of the phase-dependent photocatalytic ability of TiO_2.

Methods

The first-principles calculation based on the density functional theory[17] and the Perdew-Burke-Eznerhof generalized gradient approximation (PBE-GGA)[18] was carried out to find the mechanism of the phase-dependent photocatalytic performance of TiO_2. The projector augmented wave (PAW) scheme[19,20] as incorporated in the Vienna *ab initio* simulation package (VASP)[21] was used in the study. The Monkhorst and Pack scheme of k point sampling was used for integration

---

[*] Corresponding author e-mail: panh@ihpc.a-star.edu.sg.

[†] Environmental Science.

[‡] Material Science & Technology Divisions, ORNL.

[§] University of Tennessee.

10.1021/ct9002724 CCC: \$40.75

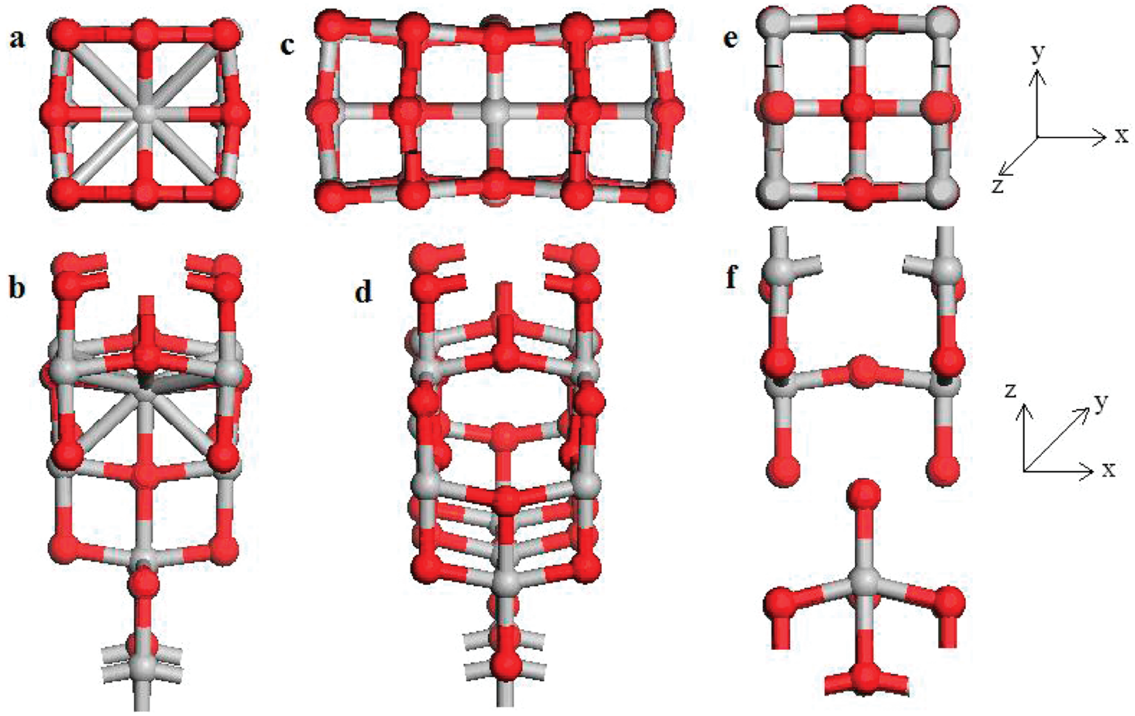

Figure 1. The local structures: (a) and (b) around Ti interstitial, (c) and (d) around oxygen vacancy, and (e) and (f) around Ti vacancy after geometry optimization.

over the first Brillouin zone.[22] The GGA+U method was used to treat *3d* electrons of Ti with the Hubbard on-site Coulomb interaction parameter (U-J) of 6 eV.[23] A 3 × 3 × 3 grid for k-point sampling and an energy cutoff of 380 eV were consistently used in our calculations. Good convergence was obtained with these parameters, and the total energy was converged to 2.0×10^{-5} eV/atom. The bulk anatase, brookite, and rutile TiO_2 structures are modeled with a 3 × 3 × 1, 1 × 2 × 2, 2 × 2 × 3 supercell containing 36 Ti atoms and 72 O atoms, 32 Ti atoms and 64 O atoms, 24 Ti atoms and 48 O atoms, respectively. The oxygen or titanium vacancy is modeled by removing oxygen or titanium atom from the supercell. The titanium interstitial is created by adding interstitial Ti atom into the supercell.

Results and Discussion

The local structure around the defect is distorted, such as bond extension, after geometry optimization. For anatase TiO_2 (a-TiO_2), the atoms surrounding the Ti interstitial (Ti_i) are pushed away with the change of the Ti−O bond length within 1.5% (Figure 1a,b). The effect of oxygen vacancy (V_O) on the local structure is different from that of Ti interstitial. V_O attracts the nearest Ti atoms and the oxygen atoms bonded with the Ti atoms in the x direction, while it pushes the oxygen atoms out in the y direction (Figure 1c,d). The change of the bond length in the local structure induced by V_O is within 1%. The Ti vacancy (V_{Ti}) slightly stretches the nearest oxygen atoms and Ti atoms (bonded with the nearest oxygen atoms) in all directions (Figures 1e,f) with a change of bond length within 0.5%. For brookite TiO_2 (b-TiO_2), the defect-induced distortion on the local structure is much less than that in a-TiO_2. The bond length around Ti_i is slightly extended within 0.5%, and the distortion induced by V_{Ti} or V_O is within 0.6%. The changes of bond length in the local structures of rutile TiO_2 (r-TiO_2) around Ti_i and V_O are within 1% and 0.5%, respectively. The Ti−O bond length in the local structure is reduced by 4% after removing one Ti atom from rutile TiO_2. The effect of Ti_i on the local structure decreases following a-TiO_2, r-TiO_2, and b-TiO_2.

The defects affect not only the local structure but also the electronic properties of TiO_2. Figure 2 shows the total and partial density of states (DOS and PDOS) of a-TiO_2 with and without defects. The calculated bandgap of perfect a-TiO_2 is about 2.72 eV (Figure 2a). The analysis of PDOS indicates that the valence top states and conduction bottom states of the perfect a-TiO_2 are mainly attributed to the oxygen *2p* states and Ti *3d* electrons, respectively (Figure 2b). For a-TiO_2 with a Ti interstitial, an intermediate band within the bandgap, defect states, can be observed in DOS of a-TiO_2 with Ti_i, which is close to the conduction band bottom (Figure 2c) and attributed to the interstitial Ti *3d* and oxygen (near the Ti_i) *2p* electrons (Figure 2d). The oxygen vacancy can also introduce an additional band into the bandgap, located almost at the middle of the bandgap (Figure 2e). The defect states induced by the oxygen vacancy are mainly attributed to the Ti *3d* electrons due to the unsaturated bonds after removing the oxygen atom (Figure 2f). The bandgap of a-TiO_2 is slightly reduced to 2.64 eV by removing the Ti atom from the lattice (Figure 2g). The Fermi level is within the valence band (Figure 2g), indicating that a-TiO_2 with V_{Ti} is a p-type semiconductor, consistent with the experimental reports.[14] The PDOS analysis indicated that the valence band top and conduction band bottom states of a-TiO_2 with V_{Ti} are mainly attributed to oxygen *2p* orbitals and Ti *3d* electrons, respectively (Figure 2h), similar to those of perfect a-TiO_2 (Figure 2b). For perfect r-TiO_2, the

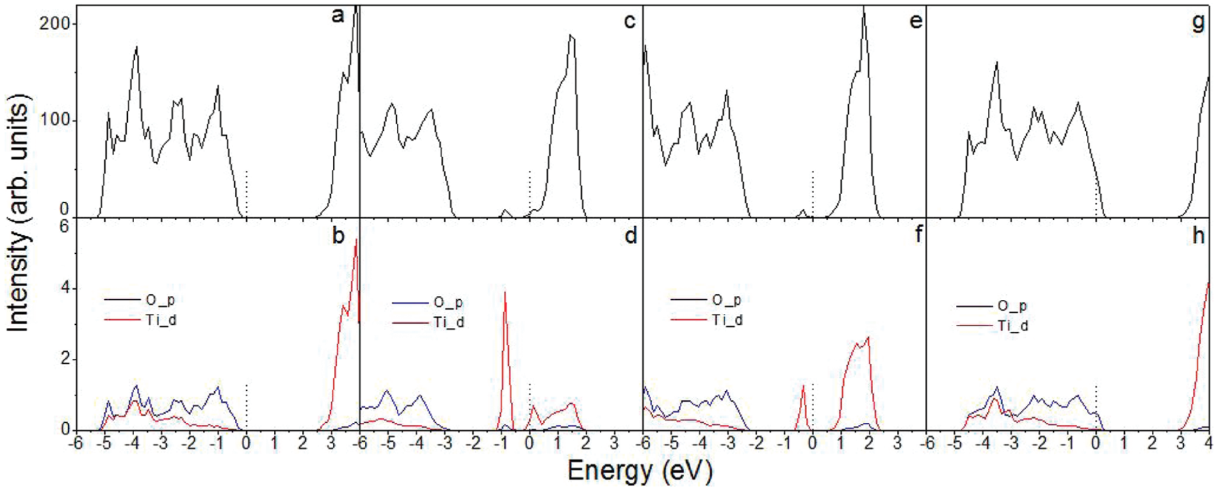

Figure 2. The calculated density of states (DOS) of a-TiO_2: (a) perfect, and with (b) Ti interstitial, (c) oxygen vacancy, and (d) Ti vacancy, and the calculated partial density of states (PDOS) of a-TiO_2 without defect (e) and with defect: (f) Ti interstitial, (g) oxygen vacancy, and (h) Ti vacancy.

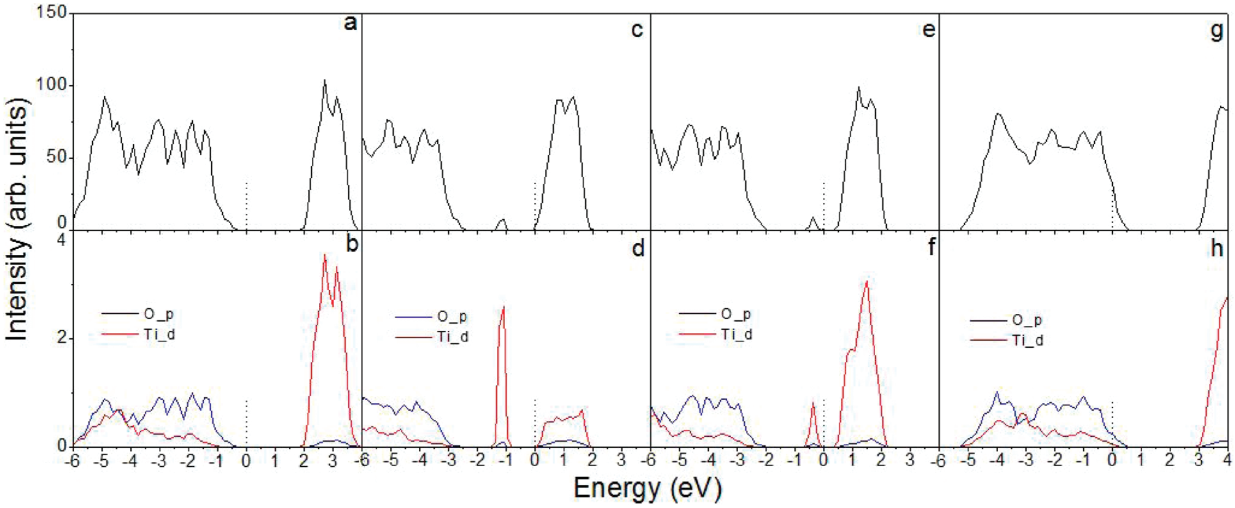

Figure 3. The DOS of r-TiO_2: (a) perfect, and with (b) Ti interstitial, (c) oxygen vacancy, and (d) Ti vacancy, and the PDOS of r-TiO_2 without defect (e) and with defect: (f) Ti interstitial, (g) oxygen vacancy, and (h) Ti vacancy.

calculated bandgap is 2.36 eV, as indicated in the DOS of r-TiO_2 (Figure 3a). The PDOS of perfect r-TiO_2 shows that the oxygen *2p* and Ti *3d* electrons are contributed to the valence top and conduction bottom states, respectively (Figure 3b). It was found that an intermediate band within the bandgap is formed by introducing Ti_i or V_O into the r-TiO_2 (Figure 3c,e) lattice, which is mainly attributed to Ti *3d* electrons (Figures 3d,f). The r-TiO_2 can also be a p-type semiconductor if removing a Ti atom from its supercell (Figure 3g). For perfect b-TiO_2, the calculated bandgap is 2.64 eV (Figure 4a), with its valence top and conduction bottom stated originating from the oxygen *2p* states and Ti *3d* electrons, respectively (Figure 4b). For defected b-TiO_2, similar results can be obtained. The Ti_i or V_O states form the intermediate band within the bandgap of b-TiO_2 (Figure 4c,e), mainly attributing to the Ti *3d* electrons (Figure 4d,f), and the V_{Ti} shifts the Fermi level down into the valence band (Figure 4g). Our calculations demonstrated that the intermediate band within the bandgap can be formed by creating V_O or Ti_i in the TiO_2 lattice, and the Fermi level is shifted into the valence band due to the formation of V_{Ti}, regardless of the crystal structure. However, it was found that the gap between the Ti_i defect band top and the conduction band bottom of b-TiO_2 (~0.12 eV, Figure 4c) (the PDOS shows that there is almost gapless between the defect and the conduction bands (Figure 4d)) is much less than those of a-TiO_2 (~0.57 eV, Figure 2c) and r-TiO_2 (1.0 eV, Figure 3c), and the Ti_i defect states occupy a width of ~0.61 eV in the bandgap of b-TiO_2, which may contribute to the better photocatalytic performance of b-TiO_2 due to the maximum absorption of sunlight induced by bandgap narrowing.

Figure 5 shows the formation energies of three-type defects in the three TiO_2 structures, which is estimated from

$$E_f = E_{tot}(TiO_2 + defect) - E_{tot}(TiO_2) + \mu_O(or \pm \mu_{Ti})$$

where $E_{tot}(TiO_2+defect)$ and $E_{tot}(TiO_2)$ are total energies of the TiO_2 with and without defect, respectively. μ_O and μ_{Ti} are the chemical potentials of O and Ti, respectively. $\mu_O = {}^1/_2\mu(O_2)$ and $\mu_{Ti} = \mu(Ti_{Bulk})$. The detailed numbers were provided in Table 1. We can see that the formation V_{Ti} requires higher energy than that of V_O or Ti_i, indicating V_{Ti}

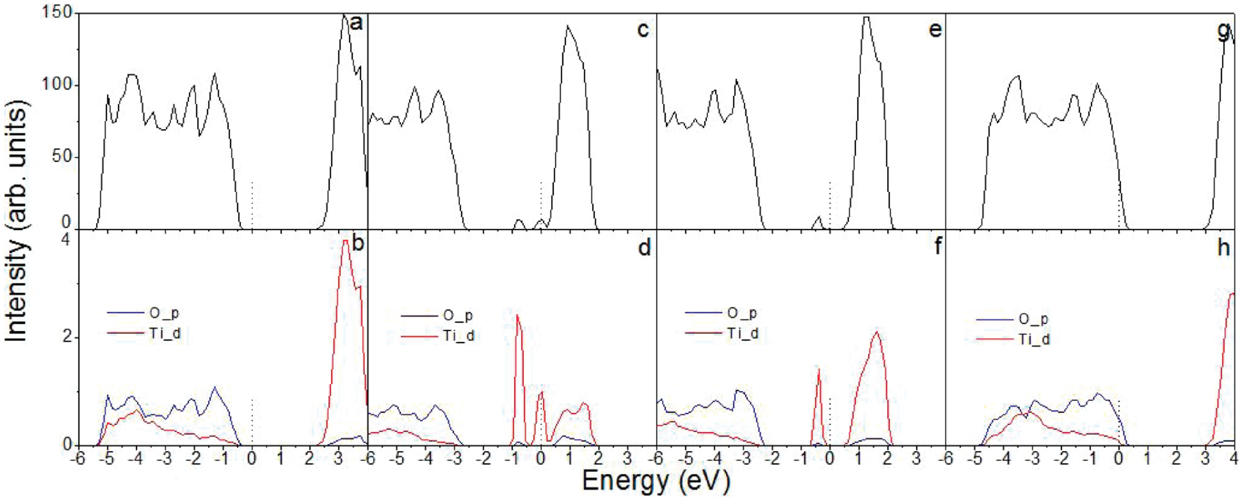

Figure 4. The DOS of b-TiO$_2$: (a) perfect, and with (b) Ti interstitial, (c) oxygen vacancy, and (d) Ti vacancy, and the PDOS of b-TiO$_2$ without defect (e) and with defect: (f) Ti interstitial, (g) oxygen vacancy, and (h) Ti vacancy.

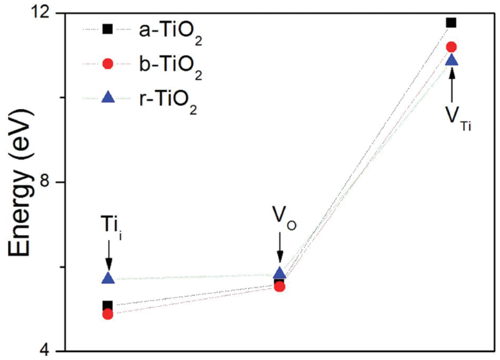

Figure 5. The formation energy of defect in the three TiO$_2$ structures.

Table 1. Calculated Formation Energies of Defects

	Ti$_i$ (eV)	V$_O$ (eV)	V$_{Ti}$ (eV)
a-TiO2	5.07	5.58	11.76
b-TiO2	4.87	5.52	11.19
r-TiO2	5.70	5.82	10.86

is difficult to be created under moderate conditions. Experimentally, V$_{Ti}$ can only be formed at elevated heating temperature and in oxygen ambiance,[14] consistent with our calculation results. The relatively low formation energies of V$_O$ and Ti$_i$ demonstrate the fact that TiO$_2$ is a nonstoichiometric compound with oxygen deficiency. Generally, the defect formation energy decreases with the trend of V$_{Ti}$, V$_O$, and Ti$_i$ for the same TiO$_2$. The formation energies of V$_{Ti}$ and V$_O$ increase with the TiO$_2$ structures changing from brookite to anatase, further to rutile. The relatively low formation energy of Ti$_i$ in b-TiO$_2$ indicates that its formation in b-TiO$_2$ is easier than that in a-TiO$_2$ and r-TiO$_2$, and b-TiO$_2$ may be produced under Ti-rich condition. In Ti-rich condition, the Ti interstitial is the dominant defect, which may trigger the formation of brookite structure due to its lower formation energy in b-TiO$_2$ (Figure 5).

From the calculated electronic properties of the defected TiO$_2$ and the defect formation energy, we may reveal the origin of the phase-dependent photocatalytic ability of TiO$_2$. The Ti$_i$ and V$_O$ are the most common defects in a-TiO$_2$ and r-TiO$_2$ due to their relatively low formation energies (Figure 5). However, the formation of Ti$_i$ and V$_O$ in a-TiO$_2$ is easier than those in r-TiO$_2$ because their formation energies in a-TiO$_2$ are less than those in r-TiO$_2$ (Figure 5). The relatively low formation energies of titanium interstitial and oxygen vacancy (E$_f$) in a-TiO$_2$ indicate that the defect density ($exp(-E_f/k_BT)$) is high, and the intermediate defect band within the bandgap induced by Ti$_i$ or V$_O$ in a-TiO$_2$ results in the maximally utilization of the sunlight (Figure 2), which should attribute to the improved photocatalytic performance of a-TiO$_2$. The observation of further improvement of photocatalytic ability in b-TiO$_2$ is also contributed to the easy formation of defects, increased defect density and enhanced light absorption. The relatively low formation energies of Ti$_i$ and V$_O$ in b-TiO$_2$ indicate that their densities are higher than those in a- and r-TiO$_2$. The defect states induced by the two-type defects may result in a broad defect band, even crossing the small gap and overlapping with the conduction band bottom (Figure 4c), i.e. the bandgap narrowing, similar to the doping effect. The defect-induced bandgap narrowing and the relatively high defect density due to lower defect formation energy in b-TiO$_2$ greatly enhance the photocatalytic performance of b-TiO$_2$ in visible light.

Conclusions

In summary, a systematic study of the defect effect on the photocatalytic ability of TiO$_2$ was carried out based on first-principles calculations. We found that the intermediate band induced by defect, Ti interstitial, or oxygen vacancy is located within the bandgap, responsible for the enhancement of visible-light absorption. The calculation on the defect formation energy indicated that titanium interstitial and oxygen vacancy are easy to be formed due to their lower formation energies. The formation energies of oxygen vacancy and Ti interstitial decrease as rutile, anatase, and brookite, revealing the mechanism of phase-dependent photocatalytic ability of TiO$_2$. The low formation energy of Ti interstitial in b-TiO$_2$ indicated that b-TiO$_2$ may be easily produced in Ti-rich condition. The better photocatalytic performance in b-TiO$_2$ in visible light is attributed to the relatively high defect density, broad defect states in the bandgap, and bandgap narrowing.

Acknowledgment. This work was sponsored by the Office of Basic Energy Sciences, Division of Materials Sciences and Engineering and Laboratory Directed Research and Development (LDRD) Program of Oak Ridge National Laboratory (ORNL), which is managed by UT-Battelle LLC for the U.S. Department of Energy under contract No. DE-AC05-00OR22725. The DFT calculations were performed at the Computational Center of Science (CCS) of ORNL.

References

(1) Fujishima, A.; Hashimoto, K.; Watanabe, T. *TiO2 Photocatalysis. Fundamentals and applications*; BKC, Inc.: Tokyo, 1999; pp 14−176.

(2) Chen, X.; Mao, S. S. *Chem. Rev.* **2007**, *107*, 2891.

(3) Pfaff, G.; Reynders, P. *Chem. Rev.* **1999**, *99*, 1963.

(4) Linsebigler, A. L.; Lu, G.; Yates, J. T. *Chem. Rev.* **1995**, *95*, 735.

(5) Fujishima, A.; Honda, K. *Nature* **1972**, *238*, 37.

(6) Hoffmann, M. R.; Martin, S. T.; Choi, W.; Bahnemann, D. W. *Chem. Rev.* **1995**, *95*, 69.

(7) Hagfeldt, A.; Gratzel, M. *Chem. Rev.* **1995**, *95*, 49.

(8) Mattioli, G.; Filippone, F.; Alippi, P.; Bonapasta, A. A. *Phys. Rev. B* **2008**, *78*, 241201.

(9) Koelsch, M.; Cassaignon, S.; Guillemoles, J. F.; Jolivet, J. R. *Thin Solid Films* **2002**, *403*, 312.

(10) Shibata, T.; Irie, H.; Ohmori, M.; Nakajima, A.; Watanabe, T.; Hashimoto, K. *Phys. Chem. Chem. Phys.* **2004**, *6*, 1359.

(11) Iskandar, F.; Nandiyanto, A. B. D.; Yun, K. M.; Hogan, C. J., Jr.; Okuyama, K.; Biswas, P. *Adv. Mater.* **2007**, *19*, 1408.

(12) Lin, Z.; Orlov, A.; Lambert, R. M.; Payne, M. C. *J. Phys. Chem. B* **2005**, *109*, 20948.

(13) Serpone, N. *J. Phys. Chem. B* **2006**, *110*, 24287.

(14) Nowontny, M. K.; Sheppard, L. R.; Bak, T.; Nowontny, J. *J. Phys. Chem. C* **2008**, *112*, 5275.

(15) Nowontny, J.; Bak, T.; Nowontny, M. K. *J. Phys. Chem. B* **2006**, *110*, 21560.

(16) Wendt, S.; Sprunger, P. T.; Lira, E.; Madsen, G. K. H.; Li, Z.; Hansen, J. Ø.; Matthiesen, J.; Blekinge-Rasmussen, A.; Lægsgaars, E.; Hammer, B.; Besenbacger, F. *Science* **2008**, *320*, 1755.

(17) Hohenberg, P.; Kohn, W. *Phys. Rev.* **1964**, *136*, B864.

(18) Perdew, J. P.; Burke, K.; Ernzerhof, M. *Phys. Rev. Lett.* **1996**, *77*, 3865.

(19) Blöchl, P. E. *Phys. Rev. B* **1994**, *50*, 1795.

(20) Kresse, G.; Joubert, D. *Phys. Rev. B* **1999**, *59*, 1758.

(21) Kresse, G.; Furthmüller, J. *Phys. Rev. B* **1996**, *54*, 11169.

(22) Monkhorst, H. J.; Pack, J. D. *Phys. Rev. B* **1976**, *23*, 5188.

(23) Anisimov, V. I.; Aryasetiawan, F.; Lichtenstein, A. I. *J. Phys.: Condens. Matter* **1997**, *9*, 767.

CT9002724

JCTC Journal of Chemical Theory and Computation

Hydrogen Interaction in Ti-Doped $LiBH_4$ for Hydrogen Storage: A Density Functional Analysis

Jianjun Liu and Qingfeng Ge*

Department of Chemistry and Biochemistry, Southern Illinois University, Carbondale, Illinois 62901

Received June 4, 2009

Abstract: Density functional theory studies have been carried out to investigate the energetics and structures of Ti-doped $LiBH_4$ (001), (100), and (010) surfaces. The possibilities of Ti occupying various positions at these surfaces leading to substitution, surface adsorption, and interstitial insertion are examined. Among all possible structures, a Ti atom energetically prefers to occupy interstitial positions involving three or four BH_4^- hydrides and to stay above the top layer of B atoms. The most stable species on the three surfaces have a similar local structure, described as $TiB_2H_8-nBH_4$ ($n = 1, 2$), with varying spin states. Molecular orbital analysis for the local structures showed that the structural stability could be attributed to the symmetry-adapted orbital overlap between Ti and “inside” B−H bonds. Furthermore, the hydrogen desorption energies from many positions in these local complex structures were reduced significantly with respect to that from the clean surface. The most favorable hydrogen desorption pathways are found to lead to triplet dehydrogenation products. Therefore, the triplet $TiB_2H_8-BH_4$ in (001) and $TiB_2H_8-2BH_4$ in (010) can desorb hydrogen in molecular form, while the quintet $TiB_2H_8-BH_4$ in (100) must first desorb hydrogen atoms, followed by the formation of a hydrogen molecule in the gas phase. The catalytic effect of Ti doped in $LiBH_4$ has been compared with that in $NaAlH_4$.

1. Introduction

Many attempts have been made to develop new materials with high hydrogen storage capacities in order to meet the demand of commercial vehicles powered by H_2/O_2 proton exchange membrane fuel cells.[1−3] Lithium borohydride ($LiBH_4$) has been an attractive candidate due to its intrinsically high gravimetric and volumetric hydrogen capacities (18.2 wt %, 121 kg/m^3).[2] Unfortunately, pure $LiBH_4$ material is too stable and only liberates 2% of the hydrogen even at the melting point (541−559 K).[4] For $LiBH_4$, the partial decomposition to $LiH(s) + B(s) + 3/2H_2(g)$ has a standard enthalpy of 100.3 kJ/mol.[5] The highly endothermic reaction indicates that dehydrogenation of $LiBH_4$ must be performed at elevated temperatures. The experimental results of Züttel et. al showed that a significant hydrogen desorption peak started at 673 K and reached its maximum value around 773 K.[6] In order to use $LiBH_4$ as a practical hydrogen storage material, the enthalpy of the dehydrogenation reaction has to be reduced, by either stabilizing the dehydrogenated state or destabilizing the hydrogenated state.

Many compounds which bind strongly to borohydrides or provide a source to allow partial substitution of Li cations have been mixed with $LiBH_4$. Züttel et al. found that 75% $LiBH_4$ mixed with 25% SiO_2 can reduce the initial hydrogen release temperature from 673 to 523 K.[6] On the other hand, the rehydrogenation reaction will not occur under mild conditions. The same authors reported that synthesizing $LiBH_4$ from its elements under conditions up to 923 K and 150 bar of H_2 pressure was unsuccessful.[6] Mixing compounds with cations of similar size to Li but having a higher valence, such as Mg^{2+}, was also attempted.[7] The temperature of the dehydrogenation reaction was lowered by approximately 30 K when Li in $LiBH_4$ was partially substituted by Mg^{2+}. Vajo et al. reported a more complicated mixture of $LiBH_4$ and $LiH + 0.5MgB_2$, doped with 2−3 mol % $TiCl_3$. They showed that 9 wt % hydrogen was adsorbed at 627 K

---

* Corresponding author e-mail: qge@chem.siu.edu.

10.1021/ct900287r CCC: $40.75

and 100 bar, neglecting the weight of $TiCl_3$.[8] Their P−C−T isotherms demonstrated that the addition of MgH_2 reduced the rehydrogenation/dehydrogenation enthalpy by ∼25 kJ/(mol H_2) compared with the pure $LiBH_4$ material. A finding relevant to the present study is that their initial experiments without $TiCl_3$ displayed poor kinetic performance. Recently, Au et al. showed that $LiBH_4$ modified by metal oxides or metal chlorides, such as TiO_2 and $TiCl_3$, could reduce the dehydrogenation temperature and achieve rehydrogenation under moderate conditions.[9,10] Modified $LiBH_4$ releases 9 wt % H_2, starting as low as 473 K, which is significantly lower than the hydrogen-releasing temperature of 673 K for pure $LiBH_4$. After being dehydrogenated, the modified $LiBH_4$ can absorb 7−9 wt % H_2 at 873 K and 70 bar, a significant improvement from 923 K and 150 bar for pure $LiBH_4$. Very recently, Fang et al. reported that a mechanically milled $3LiBH_4/TiF_3$ mixture released 5−6 wt % hydrogen at temperatures of 343−363 K.[11] Similarly, the use of other dopants has been attempted to reduce the hydrogen desorption temperature of MgH_2.[12,13] Clearly, the addition of Ti compounds (TiO_2, $TiCl_3$, and TiF_3) results in a strong improvement for hydrogen desorption and, to a lesser extent, for rehydrogenation. On the other hand, the improvement brought by these additives to $LiBH_4$ is not sufficient to make $LiBH_4$ viable as a practical hydrogen storage medium in spite of its structural similarity to $NaAlH_4$. Chemically, boron holds onto its hydrogen atoms tighter in $LiBH_4$ than aluminum does in $NaAlH_4$. A comparative study of Ti-doped $LiBH_4$ and $NaAlH_4$ would provide some insights into the effect of doped Ti on hydrogen interactions in these materials. Previously, we identified an interstitial $TiAl_3H_{12}$ complex structure to be the most stable species in both Ti-doped $NaAlH_4$(001) and (100) surfaces.[14,15] Hydrogen desorption energies from many positions of the $TiAl_3H_{12}$ complex structure were reduced considerably as compared with that from an undoped surface. Our prediction of the complex structure was confirmed subsequently by an experimental study: the interstitial structure was shown to account for 75% of all Ti doped in $NaAlH_4$.[16] Furthermore, we studied 3d-transition-metal (TM)-doped $NaAlH_4$(001) and found that the stability of $TMAl_3H_{12}$ and its desorption energies correlate with the 18-electron rule.[17] The coordination chemistry of a transition metal with tetrahydroborate ligands has been extensively discussed in the literature.[18−23] The electron-counting rule and electronic structure analysis were used to explain the stability of molecular complexes such as $Ti(BH_4)_3$.[18,20,23,24] Considering that $Ti(BH_4)_n$ may be formed in Ti-doped $LiBH_4$, it is expected that the explanation and analysis applied in $Ti(BH_4)_3$ can be helpful in understanding the stability of local structures in Ti-doped $LiBH_4$. On the other hand, we expect some discrepancies between $Ti(BH_4)_n$ in Ti-doped $LiBH_4$ and the complex $Ti(BH_4)_3$ because of the different ligand charge. Furthermore, electron redistribution in a saltlike solid-state complex may cause the electron-counting rule to be different from that of the isolated clusters. The creation of the surface will further change the local environment of the ions, especially in regions close to the surface.

Herein, we explored the effect of added Ti to the B−H interaction in $LiBH_4$ on the basis of various surface models. We examined the structures and the stabilities of $LiBH_4$ (001), (100), and (010) surfaces doped with a Ti atom. On the basis of the most stable structures, we computed the hydrogen desorption energies and compared them with those of undoped $LiBH_4$ surfaces. We also compared the effect of doped Ti in $LiBH_4$ surfaces with that in $NaAlH_4$ surfaces and identified key differences between the two systems.

2. Computational Details

Periodic density functional theory (DFT) calculations with spin-polarization were carried out using the VASP code.[25,26] The electron−ion interactions were described by the projector augmented wave (PAW).[27] The valence electrons of Li $2s^12p^0$, B $2s^22p^1$, H $1s^1$, and Ti $3d^34s^1$ were treated explicitly with a plane-wave basis set at a cutoff energy of 400 eV. The exchange-correlation energy was calculated with the PBE form of the generalized gradient-corrected functional.[28,29] The surface Brillouin zone was sampled with the K points generated by the Monkhorst−Pack scheme and with a space less than 0.05 $Å^{-1}$.[30] Similar parameters have been used in our previous calculations, in which test results were consistent with experimental observation.[14,15,17,31,32]

The supercell structures of clean $LiBH_4$ surfaces were built from the optimized bulk structure.[32] The vacuum spaces in all surface calculations are larger than 15 Å along the z direction. The geometries of slabs were optimized by the quasi-Newton or conjugate-gradient method as implemented in VASP. A Gaussian electronic smearing of 0.1 eV was employed to improve the convergence of electronic self-consistent cycles. The convergence criteria for energy and force are 1.0×10^{-6} eV and 0.05 eV/Å, respectively. Six layers of B atoms were included in the slabs, simulating the surfaces. The Li and B atoms in the bottom two layers of the slab were fixed at their corresponding bulk positions, while the Li and B atoms in the top four layers as well as all of the hydrogen atoms were allowed to relax according to the Hellman-Feynman forces. The total energies of the relaxed slabs were used as references to calculate the binding energy for Ti doped in different positions. The reference energy of the Ti atom was calculated by placing a Ti atom in a large box with spin-polarization. The converged self-consistent field cycles resulted in a Ti atom with a quintet multiplicity, consistent with the electronic ground state of the Ti atom.[33] The electronic structures of local structures were calculated using Gaussian03 without further optimization and analyzed with GaussView 3.0.[34] The atomic electronic charges were determined according to the Bader's scheme implemented by Henkelman and Jonsson.[35]

3. Results and Discussion

3.1. Energetics and Structures of Ti-Doped $LiBH_4$. A number of experimental studies of $TiCl_3$-doped sodium alanates indicated that Ti was reduced to zero valence and dispersed into the host materials.[36−42] We therefore chose to study the Ti atom interaction with the $LiBH_4$ surfaces. The slabs of three clean surfaces, that is, (001), (100), and

(010), were optimized first. The unit cells of these surfaces have lateral dimensions of 7.1065 × 8.6532, 8.6532 × 6.6140, and 6.6140 × 7.1065 Å^2, respectively.[32] The clean (100) and (010) surfaces have a surface energy of ~0.12 J/m^2 and are significantly more stable than the (001) surface.[32] On the basis of the relaxed clean surfaces, several possible positions for adding Ti in the $LiBH_4$ surfaces were considered. The relaxed structures are shown in Figure 1a, the (001) surface, 1b, the (100) surface, and 1c, the (010) surface. The binding energy and Bader charge of Ti are also given in each structure. In all of the structures, Ti loses electrons and becomes positively charged. Furthermore, the Bader charge on Ti depends on its depth/position and coordination with the BH_4^- units. According to the final position of the Ti atom, the relaxed structures were classified as interstitial insertion, surface adsorption, and substitution of Li, which were prefixed with *Inter*, *Surf*, and *Sub*, respectively. We note that *Surf* corresponds to the structures in which Ti interacts with BH_4^- through H only. In order to account for the local geometric structures, we categorized the arrangements of the BH_4^- ligands around the Ti atom into T-shape, linear, triangle, and square. The binding energies, the depth of the Ti atom with respect to the surface layer B atoms, as well as the local geometric shape are all summarized in Table 1.

For Ti-doped $LiBH_4$ (001) surface, *Inter_1*, with a binding energy of −2.598 eV, is energetically the most stable among all relaxed structures of the Ti-doped $LiBH_4$ (001) surface. In *Inter_1*, Ti connects with two BH_4^- units in the first layer via Ti−B and Ti−H bonds and interacts with a third BH_4^- unit in the second layer through a Ti−H bond, as shown in Figure 1a. The local structure of *Inter_1* is referred to as $TiB_2H_8-BH_4$, distinguishing the BH_4^- unit in the second layer from those in the top layer. The Ti atom and three BH_4^- ligands form a T-shape geometric arrangement. *Inter_5*, which has a similar local structure to *Inter_1*, is 1.374 eV less stable. The obvious difference between *Inter_5* and *Inter_1* is the location of the Ti in the former with respect to the surface: Ti is situated 4.387 Å below the first layer B atoms in *Inter_5*, whereas the Ti depth is only 0.343 Å in *Inter_1*. In fact, there is a correlation between the depth of Ti in the slab and the stability of the structure for the same type of doping mode (interstitial insertion, surface absorption, and substitution) in the same surface.

The slab representing the $LiBH_4$ (100) surface has a double-layered arrangement, that is, the layer spacing alternates between large and small. This resulted in two possible slab models for the surface: one with an arrangement of a small interlayer spacing between the top and second layers and a large one between the second and the third layers and another with the reversed arrangement. Our results show that the first one is 0.121 eV more stable than the second. Therefore, we chose the first arrangement as our model for the (100) surface.

Doped Ti interacts primarily with the BH_4^- units in the first two layers. Again, *Inter_1* is the most stable structure among all of the relaxed structures of the Ti-doped $LiBH_4$ (100) surface and has a binding energy of −1.608 eV. Three surrounding BH_4^- units and the Ti atom form a T-shape local arrangement. We note that the local structure of *Inter_1* in the (100) surface is very similar to that of *Inter_1* in the (001) surface and can also be denoted as $TiB_2H_8-BH_4$. As shown in Figure 1b, the substitutional doping (*Sub_1* and *Sub_2*) seems to result in local structures similar to those in interstitial insertion. However, these structures are much less stable. The reduced stabilities of these structures are related to the displacement of Li cations, which costs a significant amount of energy. The weaker electron-donating ability of Ti relative to that of Li causes fewer electrons to be donated from Ti to the sp^3 orbitals of BH_4^-, leading to an incomplete occupancy of the bonding orbitals.

The results of doping Ti in the $LiBH_4$ (010) surface are similar; that is, the interstitial insertion is energetically the most favorable doping mode. In *Inter_1* formed on the (010) surface, two BH_4^- units in the second layer share their interactions with the two BH_4^- units in the top layer, forming a $TiB_2H_8-2BH_4$ local complex. The binding energy of this structure is −1.709 eV. Geometrically, $TiB_2H_8-2BH_4$ forms a square arrangement.

In summary, doped Ti prefers the interstitial position formed by three or four BH_4^- units, forming a $TiB_2H_8-BH_4$ complex in the (001) and (100) surfaces and a $TiB_2H_8-2BH_4$ complex in (010). In the most stable structures, Ti sits in the first layer of the $LiBH_4$ surface. The detailed local structures are replotted in Figure 2 by removing other Li atoms and other BH_4^- units that are not directly connected to the Ti atom. The atoms in those structures are numbered in Figure 2 and will be referred to as such in the following sections. Although $TiB_2H_8-BH_4$ (T-shape) and $TiB_2H_8-2BH_4$ (square) have different geometric arrangements, the main part of the structures, TiB_2H_8, is very similar in the three structures. In fact, the linear TiB_2H_8 is the main constituent of the structure and determines the stability of the structures. This analysis is supported by the fact that the binding energies of *Inter_1* and *Inter_2* in the Ti-doped $LiBH_4$ (001) surface only differ by 0.189 eV. However, these binding energies are much smaller than that of Ti in the $TiAl_3H_{12}$ structure formed upon doping Ti in $NaAlH_4$ (−4.182 eV).[14] We showed that doping Ti in $NaAlH_4$ would become thermodynamically unfavorable if bulk Ti was used as a reference state.[17] Doping Ti in $LiBH_4$ will be more endothermic than in $NaAlH_4$.

3.2. Hydrogen Desorption from $TiB_2H_8-BH_4$ and $TiB_2H_8-2BH_4$.

Many experiments showed that the Ti-containing compounds in alanate-based materials enhanced the dehydrogenation kinetics and improved the rehydrogenation conditions.[16,37,40,43−46] We attributed the reduction in dehydrogenation temperatures to the formation of the $TiAl_3H_{12}$ complex. We showed that hydrogen desorption energies from many positions of the complex were reduced compared to the undoped surfaces. Furthermore, our analyses indicated that the effect was not localized to the complex structure. Herein, we examined the effect of doped Ti in $LiBH_4$ on dehydrogenation on the basis of the most stable structures: $TiB_2H_8-BH_4$ on (001) and (100) and $TiB_2H_8-2BH_4$ on (010).

We note that the most stable structures carry net magnetic moments. Our further analyses of local spin-density showed

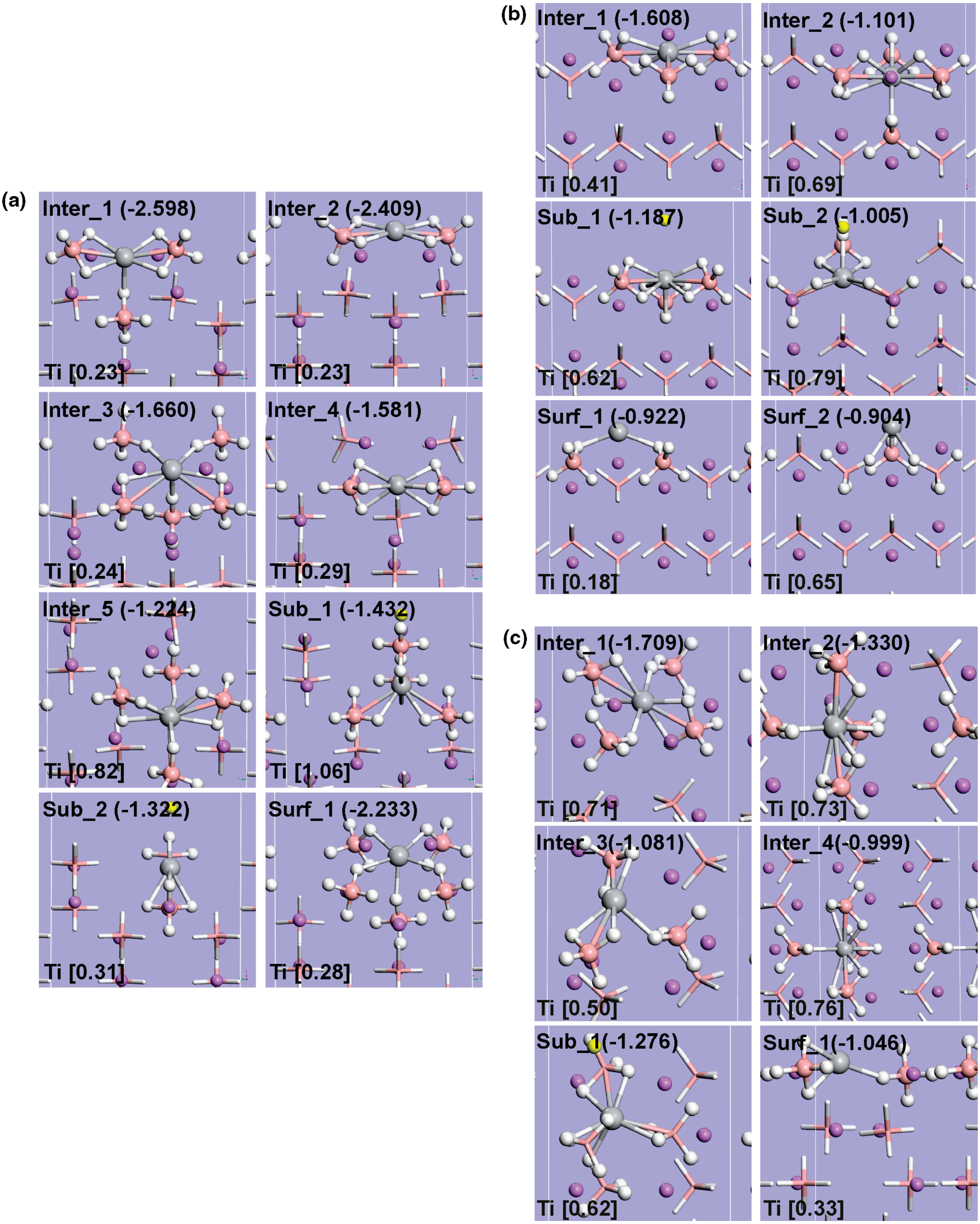

Figure 1. The DFT-GGA relaxed structures of Ti doped in the (a) (001), (b) (100), and (c) (010) surface of $LiBH_4$. The binding energy and net Bader charge of Ti are given in the top-left and bottom-left corners of each structure, respectively. The white, peach, purple, and gray balls represent H, B, Li, and Ti atoms, respectively. The yellow ball in the substitution structures represents the Li atom substituted by the Ti atom.

that the magnetic moments were largely localized to Ti, with some residual spins (1 to 2 orders of magnitude lower than on Ti) on the neighboring BH_4^- units but limited to the $TiB_2H_8{-}nBH_4$ (n = 1, 2) local structures. The resulting magnetic moments are integers in most cases. Even in the few cases of noninteger values, they are within 0.01 from the closest integer. Therefore, we borrowed the terms that have been used to describe isolated molecules and considered

Table 1. Binding Energies, Depth of Ti with Respect to the First Layer of B, and Shape of Local Structures in the Ti-Doped $LiBH_4$ (001), (100), and (010) Surfaces

species	depth	ligand	binding energy (eV) singlet	binding energy (eV) triplet	binding energy (eV) quintet
		Ti-Doped $LiBH_4$ (001)			
Inter_1	−0.343	T-shaped	−2.256	−2.598	−2.580
Inter_2	+0.233	linear	−2.181	−2.409	−2.205
Inter_3	−0.743	square	−1.475	−1.660	−1.716
Inter_4	−2.048	linear	−1.261	−1.442	−1.581
Inter_5	−4.387	T-shaped	−1.154	−1.224	−1.205
Sub_1	−2.053	triangle		−1.432	−1.422
Sub_2	−0.445	linear	−1.048	−1.315	−1.322
Surf_1	−0.547	square		−2.132	−2.233
		Ti-Doped $LiBH_4$ (100)			
Inter_1	−0.059	T-shaped	−1.010	−1.392	−1.608
Inter_2	−0.937	T-shaped	−0.598	−0.870	−1.101
Sub_1	−0.095	T-shaped	−0.987	−1.187	−0.834
Sub_2	−1.233	triangle	−0.873	−1.005	−0.881
Surf_1	+1.148	linear	−0.213	−0.922	−0.790
Surf_2	+1.233	triangle	−0.242	−0.481	−0.904
		Ti-Doped $LiBH_4$ (010)			
Inter_1	−0.907	square	−1.594	−1.709	−1.444
Inter_2	−2.399	T-shape	−1.093	−1.330	−1.270
Inter_3	−0.699	triangle	−0.670	−0.924	−1.081
Inter_4	−4.431	T-shape	−0.779	−0.999	−0.408
Sub_1	−1.920	triangle	−1.106	−1.276	−1.060
Surf_1	+0.226	linear	−0.655	−0.872	−1.046

the unit cell in a singlet (zero unpaired electron), triplet (two unpaired electrons), or quintet (four unpaired electrons) state.

We expected that the spin states would play some roles in hydrogen desorption. We calculated the hydrogen desorption energies from various positions of the $TiB_2H_8-nBH_4$ complex structures. We considered the products in different spin states and listed the desorption energies accordingly in Table 2. The numbering of hydrogen atoms in Table 2 was labeled in the local structures shown in Figure 2. For clarity, the lower-energy and, therefore, favorable product states are given in bold. We stress that all of our calculations have been done with the periodic boundary condition using the VASP program. The cluster structures were used for clarity in the presentations. Following the convention that we developed in treating the $TiAl_3H_{12}$ complex, the hydrogen atoms were classified into outside hydrogen atoms ($H_5 \sim H_8$), inside hydrogen atoms ($H_9 \sim H_{12}$), and mixed hydrogen atoms ($H_1 \sim H_4$), according to their relative positions to Ti. As a reference, the hydrogen desorption energies from the undoped (001), (100), and (010) surfaces were calculated as 3.676, 3.856, and 3.768 eV, respectively, and all led to a singlet product state.[32] In general, all hydrogen desorption energies listed in Table 2 are significantly lower than those of the corresponding clean surfaces. The lower desorption energies may favor a quick release of hydrogen from the system, which is consistent with the experimental observation.[11] We believe that the doped Ti in $LiBH_4$ can improve the thermodynamics by reducing dehydrogenation energies and may enhance the dehydriding and rehydriding kinetics through the complex active centers. Although the activation barrier of the elementary step provides some kinetics information about the process, an overall kinetic description needs all of the steps involved in the complicated network of reactions. These steps include hydrogen recombination and desorption as well as hydrogen migration and phase transition. This is beyond the scope of the present paper.

We used S, T, and Q to denote the singlet, triplet, and quintet states, respectively, and summarized possible reactions involved in dehydrogenation into the following reactions:

$$S \rightarrow S + H_2 \tag{R1}$$

$$S \rightarrow S + H + H \rightarrow S + H_2 \tag{R2}$$

$$T \rightarrow T + H_2 \tag{R3}$$

$$T \rightarrow S + H + H \rightarrow S + H_2 \tag{R4}$$

$$Q \rightarrow Q + H_2 \tag{R5}$$

$$Q \rightarrow T + H + H \rightarrow T + H_2 \tag{R6}$$

Reactions R1, R3, and R5 represent one-step pathways for forming a hydrogen molecule, while eqs R2, R4, and R6 are two-step pathways which involve desorbing atomic hydrogen first and recombining the desorbed hydrogen atoms in the gas phase. Along the two-step pathways, the spin state may change as the reaction progresses. For example, triplet $TiB_2H_8-BH_4$ on the (001) surface and $TiB_2H_8-2BH_4$ on the (010) surface can form a singlet product following the H atom desorption, R4, whereas the quintet $TiB_2H_8-BH_4$ on the (100) surface can lead to a triplet product, R6. The desorption energies listed in Table 2 are the overall reaction energies of R3−R6. A triplet product state is energetically more favorable than the singlet product state in the Ti-doped $LiBH_4$ (001) surface. Therefore, we expect that the dehydrogenation of triplet $TiB_2H_8-BH_4$ on the (001) surface will follow the one-step mechanism described in reaction R3 and desorb a hydrogen molecule from the Ti catalytic center. As shown in Table 2, the inside hydrogen atoms (H9−H12) have a much higher desorption energy than those from other positions but are still lower than that of the undoped clean surface. As discussed later, the structural stability really depends on the orbital overlap between inside B−H bonds and Ti. Desorption of inside hydrogen atoms results in a relatively higher desorption energy due to the reduced orbital overlap between Ti and inside B−H bonds.

In contrast, from the quintet $TiB_2H_8-BH_4$ of the Ti-doped $LiBH_4$ (100) surface, the triplet product state upon desorbing hydrogen is favored. Therefore, the quintet $TiB_2H_8-BH_4$ on surface (100) may have a two-step dehydrogenation mechanism, described in reaction R6. Hydrogen atoms are first released from the $TiB_2H_8-BH_4$ cluster and then combine to form a hydrogen molecule in the gas phase. An exception is that some inside hydrogen pairs such as H10−H11 and H10−H12 show much lower desorption energies than the corresponding pairs in the Ti-doped $LiBH_4$ (001) surface. A careful examination revealed that hydrogen desorption from these positions of $TiB_2H_8-BH_4$ in the (100) surface led to outside hydrogen atoms being transferred to inside positions. In contrast, a similar hydrogen transfer was not found in the triplet $TiB_2H_8-BH_4$ in the (001) surface.

For the triplet $TiB_2H_8-2BH_4$ of the Ti-doped $LiBH_4$ (010) surface, the majority of hydrogen desorption pathways still led to triplet states. Desorption of H1−H2, H3−H4, and

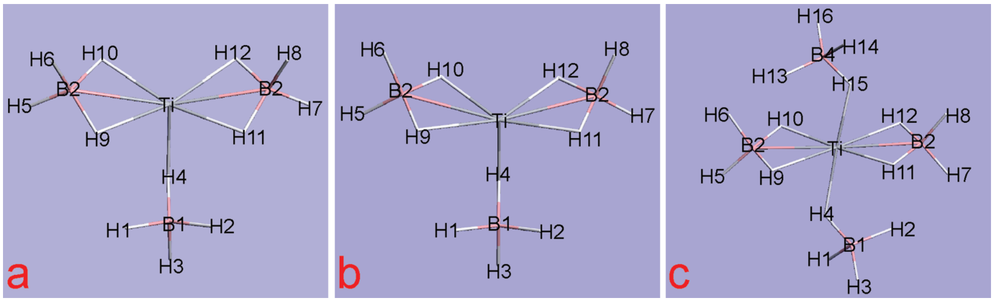

Figure 2. Local structures of the most stable species in the Ti-doped (a) $LiBH_4$(001), (b) $LiBH_4$ (100), and (c) $LiBH_4$ (010).

Table 2. Hydrogen Desorption Energies (unit: eV) of the Most Stable Species in Ti-Doped $LiBH_4$ (001), (100), and (010) Surfaces

	triplet $TiB_2H_8-BH_4$ (001)		quintet $TiB_2H_8-BH_4$ (100)		triplet TiB_2H_8-$2BH_4$ (010)	
	singlet	triplet	triplet	quintet	singlet	triplet
H1−H2	1.092	**0.915**	**−0.028**	1.749	**0.210**	0.389
H3−H4	N/A	**1.193**	**0.587**	1.664	**0.150**	0.387
H5−H6	2.477	**2.312**	**0.698**	1.896	0.473	**0.403**
H5−H7	1.363	**1.070**	**0.463**	2.520	0.550	**0.459**
H6−H7	1.217	**1.095**	**0.513**	2.246	0.759	**0.718**
H6−H8	1.219	**1.088**	**0.557**	2.790	**0.185**	0.221
H9−H10	N/A	N/A	N/A	2.324	0.568	**0.480**
H9−H11	1.510	**1.269**	**2.089**	2.532	0.594	**0.527**
H10−H11	2.101	**1.901**	**0.551**	2.079	0.859	**0.718**
H10−H12	**2.182**	2.248	**0.528**	2.182	0.431	**0.320**

H6−H8 resulted in singlet states. We consider the singlet and triplet states as the competitive hydrogen desorption pathways due to the very similar desorption energies. We would point out that the triplet $TiB_2H_8-2BH_4$ in the (010) surface has lower desorption energies than the triplet and quintet $TiB_2H_8-BH_4$ in the (001) and (100) surfaces, respectively.

3.3. Comparison of Ti-Doped $LiBH_4$ with Ti-Doped $NaAlH_4$. As we stated in the Introduction, the improvement by adding Ti compounds in $LiBH_4$ is not as efficient as doping Ti compounds in $NaAlH_4$.[9,10] A comparison of Ti-doped $LiBH_4$ and Ti-doped $NaAlH_4$ will help to understand the changes that Ti induces in B−H interactions and how these changes affect subsequent dehydriding/rehydriding reactions. Our previous studies of Ti-doped $NaAlH_4$ showed that doped Ti prefers to occupy the interstitial site and interacts with surrounding AlH_4^-, forming a $TiAl_3H_{12}$ species.[14,15] We further suggested the role of the $TiAl_3H_{12}$ complex in dehydriding and hydriding sodium alanate-based hydrogen storage materials.[17]

First of all, our results indicate that Ti energetically prefers to occupy the interstitial positions in both $NaAlH_4$ and $LiBH_4$ surfaces, although the detailed structures of the local complexes in $LiBH_4$ are different from that of Ti-doped $NaAlH_4$. We used $TiB_2H_8-nBH_4$ to represent the complex structures formed from doping Ti in $LiBH_4$. The stability of these species may play an important role in their reactivity for the dehydriding/hydriding reactions. On the other hand, hydrogen desorption energies in both Ti-doped $LiBH_4$ and $NaAlH_4$ were also reduced significantly with respect to that from their corresponding undoped clean surfaces. Dehydriding the $TiB_2H_8-nBH_4$ ($n = 1-2$) species would lead to the formation of TiB_n ($n = 2-3$), which is consistent with the experimental observation.[10]

There are also distinctive discrepancies between Ti-doped $NaAlH_4$ and Ti-doped $LiBH_4$. First, the bond activation by Ti in $LiBH_4$ is much less dramatic than that in $NaAlH_4$. In Ti-doped $LiBH_4$, the inside B−H bonds were only slightly elongated (about 0.02−0.04 Å) compared with the B−H bond in the clean surface. In contrast, two inside A−H bonds in $TiAl_3H_{12}$ of Ti-doped $NaAlH_4$ surfaces were broken, and the dissociated H atoms were transferred to Ti.[14,15] To understand the electronic origin of the difference, we analyzed the densities of state (DOSs) of the most stable interstitial structures (*Inter_1*) on each Ti-doped $LiBH_4$ surface. The DOSs of $TiB_2H_8-BH_4$ in the (001) surface, $TiB_2H_8-BH_4$ in the (100) surface, and TiB_2H_8-$2BH_4$ in the (010) surface were plotted in Figure 3a−c. In each DOS plot, we included the Ti atom, the boron atoms (B1 and B2) of the neighboring BH_4^- units, and the hydrogen atoms (H4, H9, and H10) connected with Ti. The bond-activation difference can be attributed to the back-donation of electrons from the d orbitals of Ti to antibonding orbitals of the B−H bond. In the previous analysis of Ti-doped $NaAlH_4$, we attributed some new peaks at −2 to 0 eV in Al1- and Al2-DOS to electron backdonation from Ti d orbitals to A−H antibonding orbitals.[17] However, similar electron backdonation was not found in the Ti-doped $LiBH_4$ surfaces, although electron donation from bonding orbitals of B−H to the empty orbital of Ti occurred, as shown in low-energy regions (−8∼−6 eV) of Ti-DOS. A lack of backdonation in Ti-doped $LiBH_4$ may be due to the considerable gap between the occupied orbital of Ti and virtual orbitals of BH_4^-. We have demonstrated that the electron back-donation played a dominant role in H−H and A−H bond activation in transition-metal-catalyzed $NaAlH_4$.[17] In the case of Ti-doped $LiBH_4$, the weak backdonation is the main reason for the observed low reactivity.[9,10] Fe and Mo, which have a

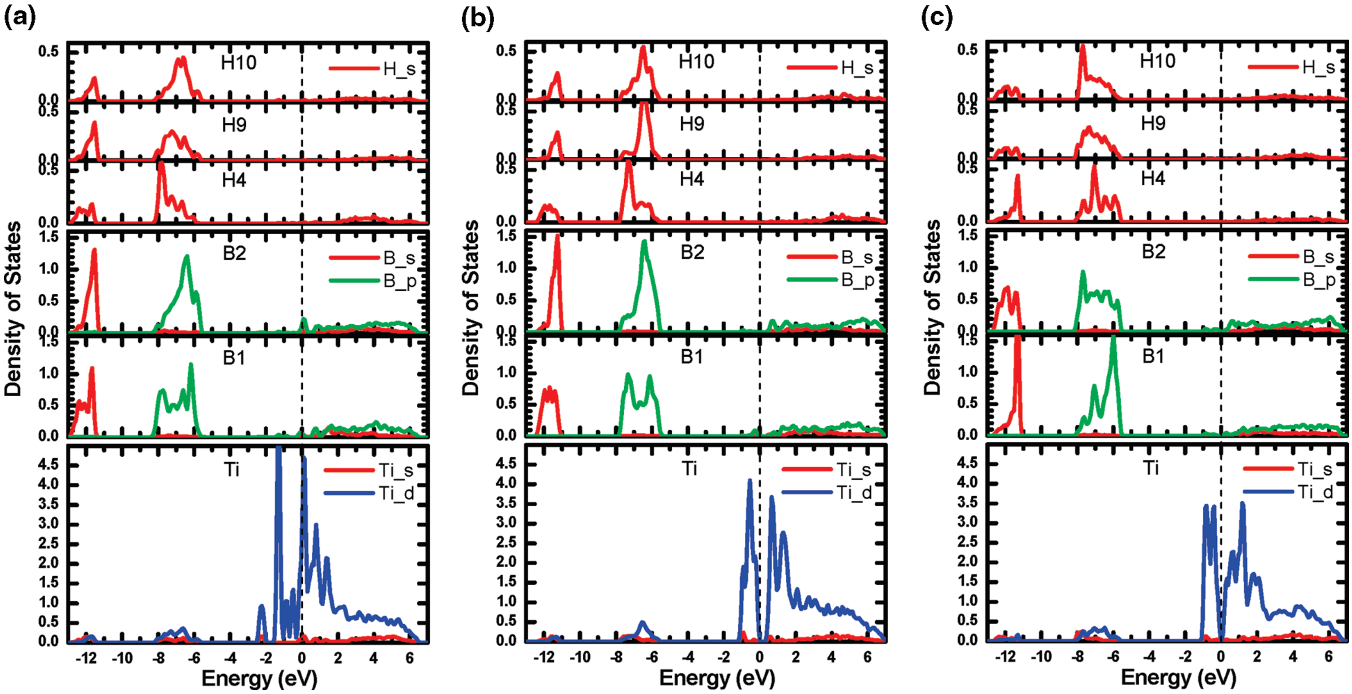

Figure 3. Local densities of state (DOSs) of the H, B, and Ti atoms in the most stable structures, that is, triplet $TiB_2H_8-BH_4$ in the (001) surface, quintet $TiB_2H_8-BH_4$ in the (100) surface, and triplet TiB_2H_8-$2BH_4$ in the (010) surface.

stronger backdonation capability from their occupied orbitals to the virtual orbitals of BH_4^-, may be better catalysts to activate the B−H bonds.[47,48]

Another difference in the two systems lies in the correlation of stability of local structures with the 18-electron rule. The XH_4^- (X = B, Al) ligands can act as a two-, four-, and six-electron donor by coordination of Ti through one, two, or three X−H bonds.[17,19,20,49] Usually, the stability of relaxed structures can be simply predicted by applying the electron-counting rule.[50,51] The total number of electrons surrounding Ti can be calculated by adding its valence electrons and the electrons shared with the ligands. For Ti, 18 electrons are needed to fill the five d orbitals, one s orbital, and three p orbitals in order to reach a closed-shell configuration. In some cases, the complex in a high-spin state accommodates fewer electrons. For example, a 16-electron complex in a triplet state is the most stable. Deviation from this number resulted in less stable structures and, therefore, lower binding energies.[18,19] Unfortunately, the stability order of relaxed structures in the Ti-doped $LiBH_4$ (001) surface does not follow this electron-counting rule. There are a total of 14 electrons surrounding the Ti atom in the most stable structure *Inter_1* of the (001) surface. However, the triplet state is the lower-energy spin-state for *Inter_1*. Similarly, both *Inter_3* and *Inter_4* in the (001) surface have 16 electrons and are in the quintet state instead of the triplet state. Therefore, the electron-counting rule is not strictly applicable in predicting the structural stability of Ti-doped $LiBH_4$. However, in the TM-doped $NaAlH_4$, the stability of most structures was found to follow the 18-electron rule.[17] The difference between Ti-doped $LiBH_4$ and $NaAlH_4$ could be understood by comparing the DOSs of the two systems. In the Ti-doped $NaAlH_4$, there is a very small gap (about 1.5 eV) from the bonding orbitals of Al−H to the d orbitals of Ti. Electrons in these orbitals can be shared, thereby satisfying the closed-shell requirement. On the other hand, there is about a 4 eV gap between the bonding orbitals of B−H and the d orbitals of Ti, as shown in the DOS figures of the Ti-doped $LiBH_4$ surfaces. The large gap makes the electrons in the B−H bond less available to the empty d orbitals of Ti.

We explored further the relationship of stability with the coordination modes of the local structures. First of all, we focus on a linear TiB_2H_8 structure (*Inter_2*) with a double η^2 coordinate mode. Figure 4 shows schematically the molecular orbital overlap between two BH_4^- ligands and the central Ti atom. We did not display the low-energy orbitals formed by the B s orbital and the four remaining H s ones because they were localized mainly on the ligands and interact poorly with transition metals. We only showed the overlaps between Ti d orbitals and ligand orbitals constructed by B p and H s. Under D_{2h} symmetry, two BH_4^- units generate three types of orbitals with the symmetry b_{1g}, b_{2u}, and b_{3u}. According to the orbital symmetry-adapting rule, the ligand orbitals with the symmetries of b_{2u} and b_{3u} only interact poorly with Ti 4s or 4p orbitals. Therefore, the ligand orbitals of b_{2u} and b_{3u} contribute little to the stability of TiB_2H_8. Although symmetrically allowed, the molecular orbital HOMO−1 that is constructed by the Ti d orbital and "outside" B−H bonding orbitals only shows a weak overlap. On the other hand, the molecular orbital HOMO−5 exhibits a significant orbital overlap between Ti d_{xz} and "inside" B−H bonding orbitals. Such an orbital overlap contributes significantly to the stability of the structure.

Another linear TiB_2H_8 structure, *Inter_4* in Ti-doped $LiBH_4$ (001), has a double η^3 coordination mode with a smaller binding energy (−1.581 eV) than that of *Inter_2* (double η^2, −2.409 eV). We also displayed its molecular orbitals, showing the interaction between Ti and two ligands in Figure 4. Under D_{3h} symmetry, two BH_4^- units generate

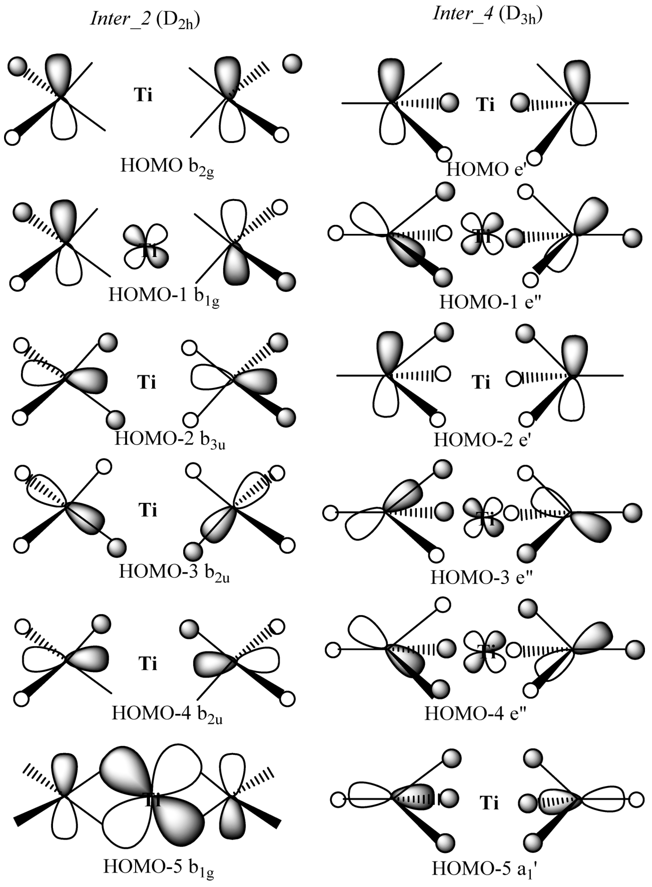

Figure 4. Schematic frontier molecular orbitals of TiB_2H_8 in *Inter_2* and *Inter_4* of Ti-doped $LiBH_4$(001). *Inter_2* and *Inter_4* have a double η^2 coordinate with D_{2h} symmetry and a double η^3 coordinate with D_{3h} symmetry, respectively.

three types of orbitals with the symmetries a_1', e', and e''. However, we expect the ligand orbitals with symmetries a_1' and e' not to make a major contribution to the structural stability. Only e'' orbitals generated by the two ligands are able to overlap with π-type orbitals of Ti. These orbital overlaps are very small because the ligand orbitals are not symmetric and some of the electrons are distributed in the terminal atoms. Therefore, the calculated binding energies of *Inter_4* are much smaller than that of *Inter_2*. For the isolated complexes such as $Ti(BH_4)_3$, ab initio calculations have shown that η^2 and η^3 structures are not much different in binding energy for some transition metals.[23,52−55] Obviously, there is a large difference of stability related to η^2 and η^3 ligands between the isolated complexes $Ti(BH_4)_3$ and $TiB_2H_8{-}n BH_4^-$ in a solid-state environment.

Finally, $TiB_2H_8{-}n BH_4$ (n = 1,2) in Ti-doped $LiBH_4$ surfaces is isolated from neighboring BH_4^- units. This is in direct contrast with the $TiAl_3H_{12}$ structure formed in Ti-doped $NaAlH_4$ which links to the neighboring AlH_4^- units and facilitates hydrogen desorption and transfer.[15] This structure difference may offer an explanation for the different amounts of added Ti in $NaAlH_4$ and $LiBH_4$. Experimentally, only ∼4 mol % $TiCl_3$ was needed for $NaAlH_4$,[38,43,56−58] whereas 25 mol % $TiCl_3$ or TiO_2 was required to achieve significant reduction in the hydrogen desorption temperature for $LiBH_4$.[9,10]

4. Conclusions

In the present paper, we have studied the energetics and structures of Ti-doped $LiBH_4$ (001), (100), and (010) surfaces using DFT-PBE methods with the plane-wave basis set and PAW potential. On the basis of our results and analysis, we conclude the following:

(1) Ti prefers occupying the interstitial positions among three or four BH_4^- hydrides, forming local complex structures of $TiB_2H_8{-}n BH_4$ (n = 1, 2) with the high-spin states. The stability of these structures can be explained by orbital overlap between Ti and "inside" B−H bonds.

(2) The desorption energies from many positions of these stable complex structures are reduced significantly with respect to those from the clean surface. The triplet $TiB_2H_8{-}BH_4$ in (001) and $TiB_2H_8{-}2BH_4$ in (010) can desorb hydrogen in the form of a H_2 molecule, while the quintet $TiB_2H_8{-}BH_4$ in (100) preferably desorbs atomic hydrogen.

(3) A comparison between Ti interaction with B−H and A−H revealed that the low reactivity of Ti-doped $LiBH_4$ is a result of the weak back-donation from d orbitals of Ti to the antibonding orbitals of BH_4^-.

Acknowledgment. This work was supported by U.S. Department of Energy, Basic Energy Science grant DE-FG02-05ER46231.

References

(1) Seayad, A. M.; Antonelli, D. M. *Adv. Mater.* **2004**, *16*, 765.

(2) Schlapbach, L.; Züttel, A. *Nature* **2001**, *414*, 353.

(3) Orimo, S.; Nakamura, Y.; Eliseo, J. R.; Züttela, A.; Jensen, C. M. *Chem. Rev.* **2007**, *107*, 4111.

(4) Fedneva, E. M.; Alpatova, V. L.; Mikheeva, V. I. *Russ. J. Inorg. Chem.* **1964**, *9*, 826.

(5) Lide, D. R. *CRC Handbook of Chemistry and Physics*; CRC Press: Boca Raton, FL, 2004; Vol. 84.

(6) Züttel, A.; Rentsch, S.; Fischer, P.; Wenger, P.; Sudan, P.; Mauron, P.; Emmenegger, C. *J. Alloys Compd.* **2003**, *356−357*, 515.

(7) Orimo, S.; Nakamori, Y.; Züttel, A. *Mater. Sci. Eng.* **2004**, *B108*, 51.

(8) Vajo, J. V.; Skeith, S. L.; Mertens, F. *J. Phys. Chem. B* **2005**, *109*, 3719.

(9) Au, M.; Jurgensen, A.; Zeigler, K. *J. Phys. Chem. B* **2006**, *110*, 26482.

(10) Au, M.; Jurgensen, A. *J. Phys. Chem. B* **2006**, *110*, 7062.

(11) Fang, Z. Z.; Ma, L. P.; Kang, X. D.; Wang, P. J.; Wang, P.; Cheng, H. M. *Appl. Phys. Lett.* **2009**, *94*, 044104.

(12) Kelkar, T.; Pal, S. *J. Mater. Chem.* **2009**, *19*, 4348.

(13) Kelkar, T.; Pal, S.; Kanhere, D. G. *ChemPhysChem* **2008**, *9*, 928.

(14) Liu, J.; Ge, Q. *Chem. Commun.* **2006**, 1822.

(15) Liu, J.; Ge, Q. *J. Phys. Chem. B* **2006**, *110*, 25863.

(16) Balde, C. P.; Stil, H. A.; van der Ederden, A. M. J.; de Jong, K. P.; Bitter, J. H. *J. Phys. Chem. B.* **2007**, *111*, 2797.

(17) Liu, J.; Han, Y.; Ge, Q. *Chem.—Eur. J.* **2009**, *15*, 1685.

(18) Volatron, F.; Duran, M.; Lledos, A.; Jean, Y. *Inorg. Chem.* **1993**, *32*, 951.

(19) Lledos, A.; Duran, M.; Jean, Y.; Volatron, F. *Inorg. Chem.* **1991**, *30*, 4440.

(20) Dain, C. J.; Downs, A. J.; Goode, M. J.; Evans, D. G.; Nicholls, K. T.; Rankin, D. W. H.; Robertson, H. E. *J. Chem. Soc., Dalton Trans.* **1991**, *4*, 967.

(21) Hitchkock, A. P.; Hao, N.; Werstiuk, N. H.; Mcglinchey, M. J.; Ziegler, T. *Inorg. Chem.* **1982**, *21*, 793.

(22) Mancini, M.; Bougeard, P.; Burns, R. C.; Mlekuz, M.; Sayer, B. G.; Thompson, J. I. A.; Mcglinchey, M. J. *Inorg. Chem.* **1984**, *23*, 1072.

(23) Jarid, A.; Lledos, A.; Jean, Y.; Volatron, F. *Inorg. Chem.* **1993**, *32*, 4695.

(24) Íñiguez, J.; Yildirim, T.; Udovic, T. J.; Sulic, M.; Jensen, C. M. *Phys. Rev. B* **2004**, *70*, 060701(R).

(25) Kresse, G.; Furthmiiller, J. *Comput. Mater. Sci.* **1996**, *6*, 15.

(26) Kresse, G.; Furthmü ller, J. *Phys. Rev. B* **1996**, *54*, 11169.

(27) Kresse, G.; Joubert, D. *Phys. Rev. B* **1999**, *70*, 1758.

(28) Perdew, J. P.; Burke, K.; Ernzerhof, M. *Phys. Rev. Lett.* **1996**, *77*, 3865.

(29) Perdew, J. P.; Burke, K.; Wang, Y. *Phys. Rev. B: Condens. Matter* **1996**, *54*, 16533.

(30) Monkhorst, H. J.; Pack, J. D. *Phys. Rev. B* **1976**, *13*, 5188.

(31) Liu, J.; Ge, Q. *J. Alloys Compd.* **2007**, *446*−*447*, 267.

(32) Ge, Q. *J. Phys. Chem. A.* **2004**, *108*, 8682.

(33) Philipsen, P. H. T.; Baerends, E. J. *Phys. Rev. B* **1996**, *54*, 5326.

(34) Frisch, M. J.; Trucks, G. W.; Schlegel, H. B.; Scuseria, G. E.; Robb, M. A.; Cheeseman, J. R.; Montgomery, J. A., Jr.; Vreven, T. K. K. N.; Burant, J. C.; Millam, J. M.; Iyengar, S. S.; Tomasi, J.; Barone, V.; Mennucci, B.; Cossi, M.; Scalmani, G.; Rega, N.; Petersson, G. A.; Nakatsuji, H.; Hada, M.; Ehara, M.; Toyota, K.; Fukuda, R.; Hasegawa, J.; Ishida, M.; Nakajima, T.; Honda, Y.; Kitao, O.; Nakai, H.; Klene, M.; Li, X.; Knox, J. E.; Hratchian, H. P.; Cross, J. B.; Bakken, V.; Adamo, C.; Jaramillo, J.; Gomperts, R.; Stratmann, R. E.; Yazyev, O.; Austin, A. J.; Cammi, R.; Pomelli, C.; Ochterski, J. W.; Ayala, P. Y.; Morokuma, K.; Voth, G. A.; Salvador, P.; Dannenberg, J. J.; Zakrzewski, V. G.; Dapprich, S.; Daniels, A. D.; Strain, M. C.; Farkas, O.; Malick, D. K.; Rabuck, A. D.; Raghavachari, K.; Foresman, J. B.; Ortiz, J. V.; Cui, Q.; Baboul, A. G.; Clifford, S.; Cioslowski, J.; Stefanov, B. B.; Liu, G.; Liashenko, A.; Piskorz, P.; Komaromi, I.; Martin, R. L.; Fox, D. J.; Keith, T.; Al-Laham, M. A.; Peng, C. Y.; Nanayakkara, A.; Challacombe, M.; Gill, P. M. W.; Johnson, B.; Chen, W.; Wong, M. W.; Gonzalez, C.; Pople, J. A. *Gaussian 03*, revision C. 02; Gaussian, Inc: Wallingford, CT, 2004.

(35) Henkelman, G. A., A.; Jonsson, H. *Comput. Mater. Sci.* **2006**, *36*, 354.

(36) Balema, V. P.; Wiench, J. M.; Dennis, K. W.; Pruski, M. *J. Alloys Compd.* **2001**, *329*, 108.

(37) Sandrock, G.; Gross, K. J.; Thomas, G. *J. Alloys Compd.* **2002**, *339*, 299.

(38) Majzoub, E. H.; Gross, K. J. *J. Alloys Compd.* **2003**, *356*−*357*, 363.

(39) Bellosta von Colbe, J. M.; Bogdanovic, B.; Felderhoff, M.; Pommerin, A.; Schüth, F. *J. Alloys Compd.* **2004**, *370*, 104.

(40) Felderhoff, M.; Klementiev, K.; Grünert, W.; Spliethoff, B.; Tesche, B.; Bellosta von Colbe, J. M.; Bogdanovic, B.; Härtel, M.; Pommerin, A.; Schüth, F.; Weidenthaler, C. *Phys. Chem. Chem. Phys.* **2004**, *6*, 4369.

(41) Graetz, J.; Reilly, J. J.; Johnson, J.; Ignatov, A. Y.; Tyson, T. A. *Appl. Phys. Lett.* **2004**, *85*, 500.

(42) Leon, A.; Kircher, O.; Rothe, J.; Fichtner, M. *J. Phys. Chem. B.* **2004**, *108*, 16372.

(43) Bogdanovic, B.; Schwickardi, M. *J. Alloys Compd.* **1997**, *253*−*254*, 1.

(44) Streukens, G.; Bogdanovic, B.; Felderhoff, M.; Schuth, F. *Phys. Chem. Chem. Phys.* **2006**, *8*, 2889.

(45) Bogdanovic, B.; Felderhoff, M.; Germann, M.; Hartel, M.; Pommerin, A.; Schuth, F.; Weidenthaler, C.; Zibrowius, B. *J. Alloys Compd.* **2003**, *350*, 246.

(46) Kircher, O.; Fichtner, M. *J. Alloys Compd.* **2005**, *404*−*406*, 339.

(47) McNamara, W. F.; Duesler, E. N.; Paine, R. T.; Ortiz, J. V.; Kolle, P.; Noth, H. *Organometallics* **1986**, *5*, 380.

(48) Khasnis, D. V.; Toupet, L.; Dixneuf, P. H. *J. Chem. Soc., Chem. Commun.* **1987**, 230.

(49) Demachy, I.; Volatron, F. *Inorg. Chem.* **1994**, *33*, 3965.

(50) Langmuir, I. *Science* **1921**, *54*, 59.

(51) Mingos, D. M. P. *J. Organomet. Chem.* **2004**, *689*, 4420.

(52) Ariafard, A.; Amini, M. M. *J. Orgamomet. Chem.* **2005**, *690*, 84.

(53) Xu, Z.; Lin, Z. *Inorg. Chem.* **1996**, *35*, 3964.

(54) Musaev, D. G.; Morokuma, K. *Organometallics* **1995**, *14*, 3327.

(55) Goebbert, D. J.; Hernandez, H.; Francisco, J. S.; Wenthold, P. G. *J. Am. Chem. Soc.* **2005**, *127*, 11684.

(56) Bogdanovic, B.; Brand, R. A.; Marjanovic, A.; Schwickardi, M.; Tolle, J. *J. Alloys Compd.* **2000**, *302*, 36.

(57) Gross, K. J.; Guthrie, S.; Takara, S.; Thomas, G. *J. Alloys Compd.* **2000**, *297*, 270.

(58) Gross, K. J.; Majzoub, E. H.; Spangler, S. W. *J. Alloys Compd.* **2003**, *356*−*357*, 423.

CT900287R

JCTC Journal of Chemical Theory and Computation

Electronic Structure and Reactivity of Boron Nitride Nanoribbons with Stone-Wales Defects

Wei Chen,[†] Yafei Li,[‡] Guangtao Yu,[§] Zhen Zhou,*[,‡] and Zhongfang Chen*[,†]

Department of Chemistry, Institute for Functional Nanomaterials, University of Puerto Rico, Rio Piedras Campus, San Juan, Puerto Rico 00931, Institute of New Energy Material Chemistry, Institute of Scientific Computing, Nankai University, Tianjin 300071, P. R. China, and The State Key Laboratory of Theoretical and Computational Chemistry, Institute of Theoretical Chemistry, Jilin University, Changchun 130023, P.R. China

Received July 27, 2009

Abstract: Gradient-corrected density functional theory (DFT) computations were performed to investigate the geometry, electronic property, formation energy, and reactivity of Stone−Wales (SW) defects in zigzag-edge and armchair-edge boron nitride nanoribbons (BNNRs). The formation energies of SW defects increase with an increase in the widths of BNNRs and are orientation-dependent. SW defects considerably reduce the band gaps of BNNRs independent of the defect orientations. In addition, the local chemical reactivity of SW defects and edge sites in zigzag-edge and armchair-edge BNNRs was probed with the CH_2 cycloaddition reaction. Independent of the nanoribbon types and the SW defect orientations, the reactions at SW defect sites are more exothermic than those at the center of perfect BNNRs, and the newly formed B−B and N−N bonds are the most reactive sites, followed by the 5−7 ring fusions.

1. Introduction

Since its experimental discovery in 2004,[1,2] graphene, a single atomic layer of graphite, has brought us a new revolution in materials science due to its many charming, unusual properties.[3−6] For example, graphene is the strongest material ever measured,[3] chemically stable and inert, and conducts electricity better than any other known material at room temperature.[5] These outstanding mechanical, chemical, and electronic properties have stimulated great interest and extensive experimental and theoretical research on the graphene-based materials family.[7−31] As one important member of this family, graphene nanoribbons (GNRs), a new type of one-dimensional (1-D) graphene-based material, have been synthesized by cutting the two-dimensional graphene.[1] The electronic and magnetic properties of GNRs have been widely studied.[15−31] The tight-binding computational results showed that, depending upon the width and orientation of the edges, the H-terminated GNRs can be semiconducting or metallic.[16−18] While more reliable first-principles calculations revealed a nonzero band gap for GNRs independent of the width and orientation of the edges.[19,24,25] In particular, this theoretical prediction was confirmed by the recent experiments.[27,28] Moreover, the zigzag GNRs are magnetic,[22,24] and applying electric field[29] or edge-modifications[30,31] renders them half-metallic.

Inspired by the intensive studies on GNRs, researchers have also broadened the field to inorganic nanoribbons, such as BN,[32] BNC,[33] B,[34] BC_3,[35] B_2C,[36] SiC,[37] ZnO,[38] and MoS_2[39] nanoribbons. Among them, as an analogy to GNRs structurally, BN nanoribbons (BNNRs) have attracted more attention.[32,40−47] Note that single-layer and few-atomic-layer hexagonal BN sheets have been experimentally realized.[48−52] In particular, Meyer et al.[51] synthesized the clean single-layer hexagonal boron nitride graphene and reported atomic resolution imaging. Zhi et al.[52] achieved large-scale fabrication of boron nitride nanosheets (as thin as three layers), and these inorganic sheets were utilized to improve thermal and mechanical properties of the polymeric composites.

---

* Corresponding author e-mail: zhouzhen@nankai.edu.cn (Z.Z.); zhongfangchen@gmail.com (Z.C.).

[†] University of Puerto Rico.

[‡] Nankai University.

[§] Jilin University.

10.1021/ct900388x CCC: $40.75

Therefore, similar to the case of GNRs, it is highly possible that the BNNRs may be synthesized by cutting single-layer hexagonal BN. Due to the large ionicity of BN, BNNRs may possess novel properties different from those of GNRs. Theoretically, perfect BNNRs have been predicted to present semiconductor behavior, regardless of their width and orientation of the edges.[40] The H-terminated BNNRs are nonmagnetic,[40] while the bare zigzag BNNRs are magnetic.[32,46] An applied transverse electric field can induce electron reorganization and control the band gap of bare zigzag BNNRs to produce a metallic−semiconducting−half-metallic transition.[32] The half-metallicity is also found in BNNRs with only the B edge passivated with hydrogen.[46,47] These open promising opportunities for the application of BNNRs in electro-optical devices.

Perfect nanomaterials exhibit attractive physical and chemical properties; however, defects are inevitable in reality, such as vacancies, adatoms, and topological defects, which may impact significantly the electronic properties and chemical reactivity of nanomaterials.[53−66] A well-known example is the Stone−Wales (SW) defect, which is comprised of two pairs of five-membered and seven-membered rings (5−7−7−5) formed by rotating one bond of the traditional six-membered ring by 90°.[67] The effect of SW defects on the electronic and mechanical properties of carbon nanotubes (CNTs), BN nanotubes (BNNTs), and GNRs has drawn considerable attention, especially in terms of chemical reactivity.[55,56,61,62,64−66] All of these studies show that the SW defects play an important role in the structural reconstruction, electronic properties, and chemical reactivity of nanomaterials. To the best of our knowledge, however, no investigations have been performed on the electronic properties and chemical reactivity of BNNRs with SW defects.

In this study, we carried out systematic first-principles computations to investigate the formation energies and electronic properties of zigzag and armchair BNNRs with SW defects. Because of the stronger reactivity, carbene (CH_2) is used as a probe to examine the chemical reactivity of SW defect sites in BNNRs with different edges. In particular, we focus on the effects of the SW defects and defect orientation on the formation energies, band structures, and chemical reactivity of these BNNRs.

2. Computational Methods

The generalized gradient approximation with the PW91 functional[68] and a 360 eV cutoff for the plane-wave basis set were employed for all of the DFT computations with the Vienna *ab initio* simulation package (VASP).[69−72] The ultrasoft pseudopotentials[73] were used to model the electron−ion interactions. Interactions between SW defects and their images were avoided in our computational supercell models, for which the distance between two SW defects is longer than 10 Å in both zigzag BNNRs (zBNNRs) and armchair BNNRs (aBNNRs). The edges of BNNRs are terminated by hydrogen atoms to remove dangling bonds. Five *k* points were used for sampling the 1-D Brillouin zone, and the convergence threshold was set as 10^{-4} eV in energy and 10^{-3} eV/Å in force. The positions of all of the atoms in the supercell were fully relaxed during the geometry optimizations. On the basis of the equilibrium structures, 21 *k* points were used to compute band structures.

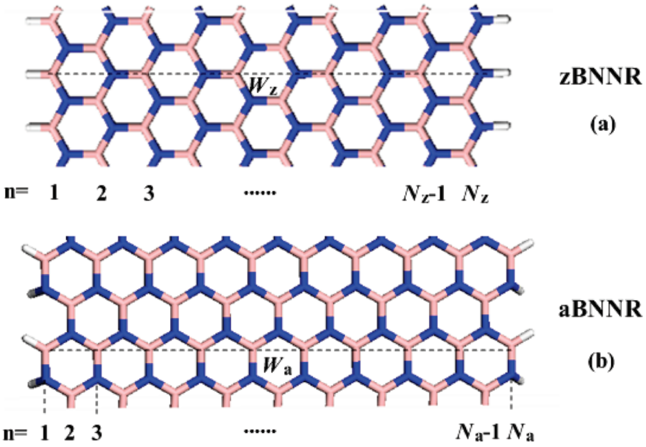

Figure 1. Geometric structure for H-terminated BN nanoribbons: (a) zigzag-edged and (b) armchair-edged. The blue, pink, and white colors represent N, B, and H atoms, respectively.

Defect formation energies (energies required to form SW defects) are defined as

$$E_F = E_{SW} - E_{perfect} \tag{1}$$

where E_{SW} and $E_{perfect}$ are the total energy of the BNNR containing a SW defect and that of the perfect BNNR, respectively. Note that this definition does not take into account the energy barrier height for the formation of the SW defect, which may be higher than the calculated formation energy on the basis of the ground state energy differences. The reaction energy for the cycloaddition of CH_2 group is estimated as

$$E_R = E_{total} - E_{BNNR} - E_{CH_2} \tag{2}$$

where E_{total}, E_{BNNR}, and E_{CH_2} are the total energy of the CH_2-added BNNR, the pristine BNNR, and the CH_2 group, respectively.

3. Results and Discussion

3.1. Geometric Structures of SW Defects in zBNNRs and aBNNRs. By convention, as shown in Figure 1, the structures of zBNNRs and aBNNRs are classified by the number of zigzag chains N_z and dimer lines N_a across the ribbon width, respectively. Figure 2 represents the perfect and defective structures of 8-zBNNR and 11-aBNNR. There are two kinds of B−N bonds in zBNNRs and aBNNRs. One is parallel or perpendicular to the axis, and the other is slanted. These are denoted by bond "1" and bond "2" in Figure 2a and d, respectively. Consequently, two types of SW defects for each of the BNNRs (labeled as SW-1 and SW-2) are possible via rotating bonds 1 or 2 by 90°, and new B−B and N−N bonds appear in all of the defective BNNRs. These new B−B and N−N bonds in 8-zBNNR with SW-1 (1.663 and 1.433 Å) are slightly shorter than those in 8-zBNNR with SW-2 (1.664 and 1.439 Å), while the corresponding B−B and N−N bonds in 11-aBNNR with SW-1 (1.672 and 1.443 Å) are somewhat longer than those

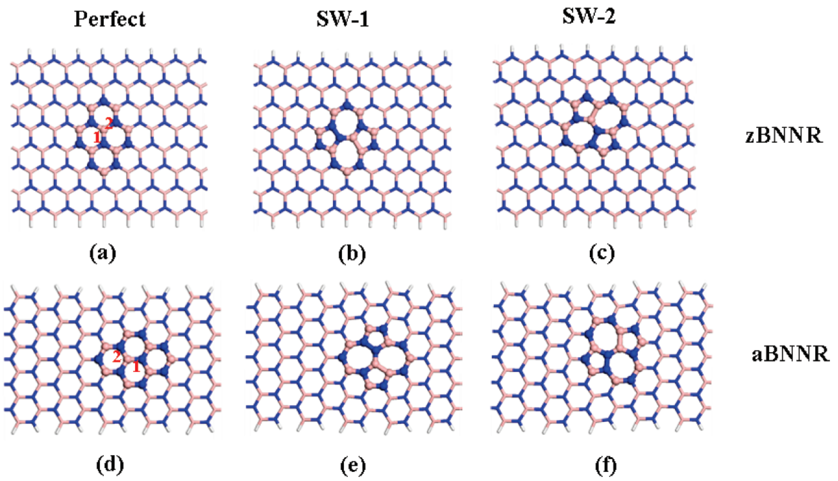

Figure 2. Optimized structures of BNNRs: (a, d) perfect and (b/e, c/f) with various SW defects.

Table 1. Bond Lengths, Pyramidalization Angles, and Formation Energies Related to SW Defects in 8-zBNNRs and 11-aBNNRs

species		d_{B-N} (Å)	d_{B-B} (Å)	d_{N-N} (Å)	Θ_p (degree)		E_F (eV)
					B^a	N^b	
zBNNRs	perfect	1.446^c 1.443^d					
	SW-1	1.353^e	1.663	1.433	0.15	0.18	6.50
	SW-2	1.363^e	1.664	1.439	0.75	1.60	6.31
aBNNRs	perfect	1.448^c 1.446^d					
	SW-1	1.365^e	1.672	1.443	0.54	0.15	6.30
	SW-2	1.367^e	1.668	1.435	0.18	0.62	5.96

[a] The B atom at the 7−7 ring fusions of SW defects. [b] The N atom at the 7−7 ring fusions of SW defects. [c] Bond 1. [d] Bond 2 (see Figure 2a and d). [e] The B−N bonds at the 7−7 ring fusions of SW defects.

in 11-aBNNR with SW-2 (1.668 and 1.435 Å, respectively). Moreover, the B−N bonds at the 7−7 ring fusions of SW defects in all defective BNNRs are shorter than those in perfect BNNRs. For the defective BNNRs, most of the bonds are slightly longer than the corresponding bonds in BNNTs with SW defects due to local curvatures of BNNTs.[65]

Usually, the pyramidalization angle ($\Theta_p = \theta_{\sigma\pi} - 90°$) is used to measure the degree of sp^3 hybridization of an atom, where $\theta_{\sigma\pi}$ is the angle between σ and π bonds.[74−76] Note that perfect BNNRs have no pyramidalization angle because of their π-conjugated planar structures. However, the Θ_p angle can describe the degree of sp^3 hybridization for the B and N atoms at the 7−7 ring fusions of SW defects, where the B and N atoms are slightly outward from the plane due to the formation of SW defects (Table 1). Obviously, these Θ_p angles may reflect the structural deformation owing to the defect formation. As shown in Table 1, the respective Θ_p angles of the B and N atoms at the SW-1 site are 0.15 and 0.18° for zBNNRs and 0.54 and 0.15° for aBNNRs, while the corresponding values at the SW-2 site are 0.75 and 1.60° for zBNNRs and 0.18 and 0.62° for aBNNRs, respectively. Clearly, the orientation of SW defects in BNNRs has different effects on the Θ_p angles: independent of the orientation of the edges in BNNRs, the deviations of the B and N atoms at the 7−7 ring fusions of SW-1 sites are less than those of SW-2 sites. Note that deviations can be directly reflected by Θ_p angles in BNNRs. These tiny deviations of the B and N atoms at the 7−7 ring fusions of SW defects may influence the formation energies of SW defects in BNNRs. As shown in Table 1, in contrast to the BNNRs with SW-1, the more deformed BNNRs with SW-2 are more favorable energetically and possess smaller defect formation energy, independent of the orientation of the edges.

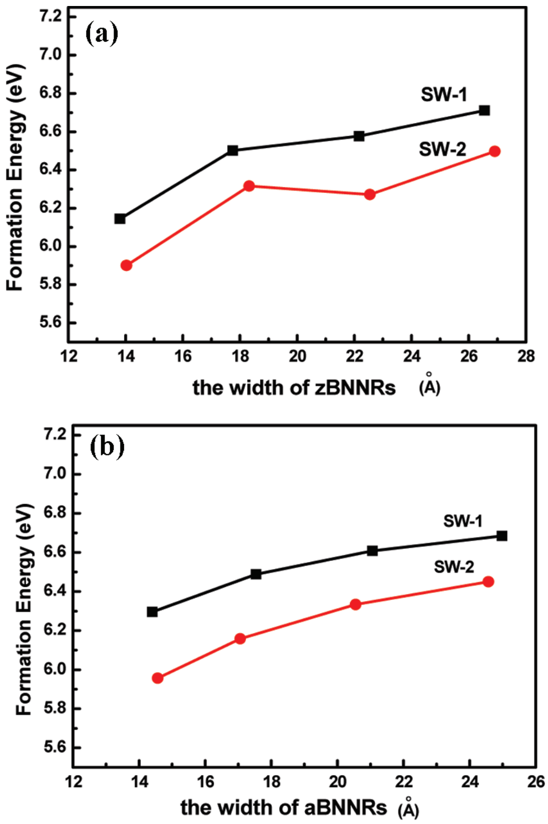

Figure 3. Formation energies of SW defects as a function of the widths of BNNRs: (a) zBNNRs and (b) aBNNRs.

3.2. Formation Energies of SW Defects in zBNNRs and aBNNRs with Different Widths. The formation energies of SW defects in CNTs[77,78] and BNNTs[65] have been reported, which depend not only on the defect orientations but also on the tube radii. It has been pointed out that SW defects form with more difficulty in larger-diameter BNNTs

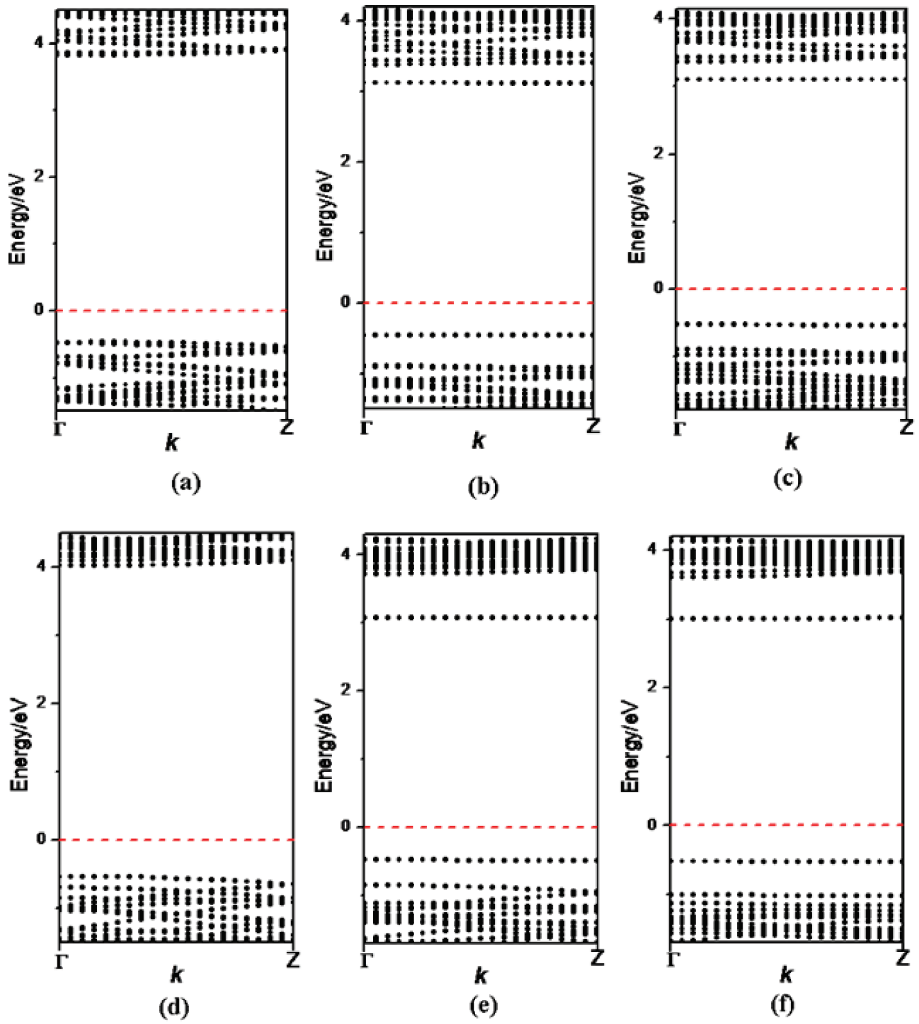

Figure 4. Band structures of 8-zBNNRs—perfect (a), with SW-1 (b), and with SW-2 (c)—11-aBNNRs: perfect (d), with SW-1 (e), and with SW-2 (f).

and CNTs.[65,78] Also, in the BN graphene sheet, the formation energy of SW defects is up to 7.28 eV.[65] Naturally, it can be expected that forming SW defects in BNNRs will be more difficult than in BNNTs,[65] which is supported by our present computations.

We computed the formation energies of SW defects in zBNNRs and aBNNRs as a function of the ribbon width (Figure 3), for which both kinds of SW defects (SW-1 and SW-2) in a series of zBNNRs and aBNNRs with various widths ($N_z = 6, 8, 10, 12$ and $N_a = 11, 13, 16, 19$) were considered. Our computations show that the formation energies of both SW-1 and SW-2 increase with increasing widths of zBNNRs and aBNNRs (Figure 3). The narrowest ribbons have the lowest formation energies of SW defects, which are 6.14 eV for SW-1 in 6-zBNNR, 5.90 eV for SW-2 in 6-zBNNR, 6.30 eV for SW-1 in 11-aBNNR, and 5.96 eV for SW-2 in 11-aBNNR. When their widths are the same, the formation energies of SW-1 are always larger than those of SW-2 in all of the zBNNRs and aBNNRs. Obviously, the orientation of the SW defect has different effects on the formation energies of both zBNNRs and aBNNRs. The SW-2 defect is closer to the edges than SW-1 defect in both types of BNNRs (Figure 2). Consequently, the SW-2 defect is easier to form than the SW-1 defect due to the easier deformation of the edge, and the more deformed BNNRs with SW-2 defect possess a smaller formation energy, as shown in Table 1.

3.3. Band Structures of zBNNRs and aBNNRs with SW Defects. Similar to BNNTs,[65] the electronic band structures of perfect and defective zBNNRs and aBNNRs show typical semiconductor behavior (Figure 4). The perfect BNNRs display a 4.56 eV direct band gap for 11-aBNNR and a 4.28 eV indirect band gap for 8-zBNNR (Figure 4a and d), which are reasonably consistent with the results reported by Du et al.[40]

Previous theoretical studies pointed out that the electronic band structures of BNNTs can only be modified slightly at the presence of some defects.[57−59,65] However, different from the BNNTs with SW defects,[65] the formation of SW defects in BNNRs has significant effects on their electronic band structures, although all of the BNNRs with SW defects still retain typical wide-band-gap semiconductor character. As shown in Figure 4, introducing SW defects in perfect BNNRs leads to new levels of the top valence band and the bottom conduction band. Consequently, the band gaps of BNNRs with SW defects are reduced significantly, by 0.71, 0.65, 1.00, and 1.03 eV, respectively, for 8-zBNNR with SW-1, 8-zBNNR with SW-2, 11-aBNNR with SW-1, and 11-

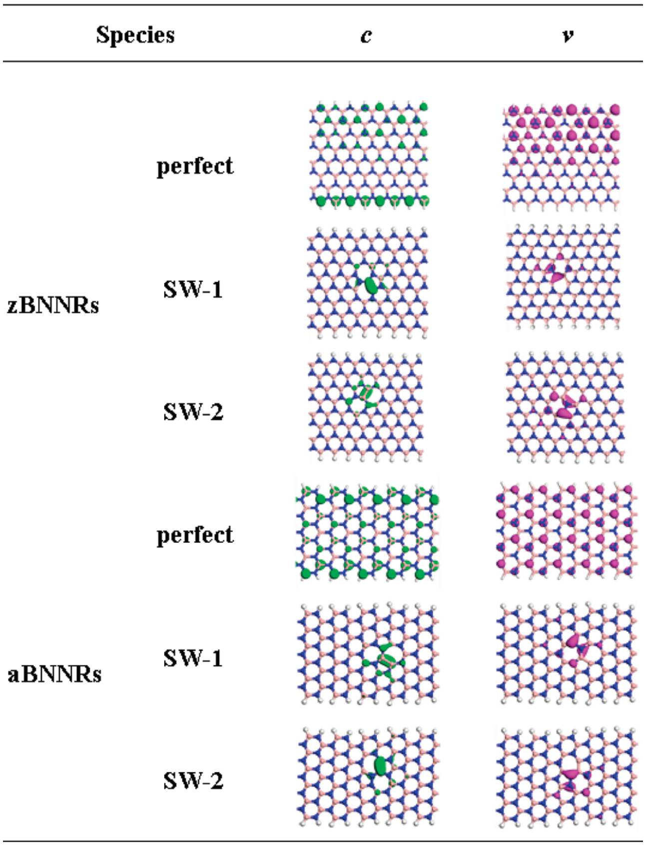

Figure 5. Electron density isosurfaces of the highest-energy valence (*v*) and the lowest-energy conduction (*c*) bands of perfect and defective zBNNRs and aBNNRs.

aBNNR with the SW-2 defect. The orientation of SW defects has almost no effect on the band gap reduction of zBNNRs and aBNNRs.

To clearly examine the character of these new levels in defective BNNRs, we plotted the electron density isosurfaces of the valence bands and conduction bands of perfect and defective BNNRs (Figure 5). For the perfect zBNNR, its top valence band is mainly from N atoms close to and on the N edge, while its bottom conduction band is mainly from the B atoms of the B edge; in contrast, for perfect aBNNR, the top valence band and bottom conduction band originate from almost all of the N atoms and all of the B atoms, respectively. Obviously, the edge orientation of perfect BNNRs affects the composition of their top valence bands and bottom conduction bands. In comparison with perfect BNNRs, for all of the defective BNNRs, independent of the edge and defect orientation, the top valence bands originate mainly from the N atoms in the N−N bonds at the SW defects sites, while the bottom conduction bands are mainly from the B atoms in the B−B bonds at the SW defects sites. Obviously, the reduction of the band gap of BNNRs with SW defects is due to the localized defect states appearing within the gap of the pristine BNNRs, instead of the shifting of the original valence and conductance bands. This is similar to the case of the BNNTs with SW defects reported by Li et al.[65] However, compared with the defective BNNTs, BNNRs with SW defects show a much larger reduction of band gaps, which indicates that the newly formed N−N bonds and B−B bonds of SW defect sites are more unfavorable due to the planar structures of BNNRs.

Additionally, the introduction of SW defects obviously reduces the band gaps of defective BNNRs, which implies that the band gap of BNNRs is not so robust. As a result, it is reasonable for us to suppose that the band gap of BNNRs may be further reduced, even close to having metal behavior, such as by chemical modification. These interesting electronic properties will make BNNRs promising materials for many potential applications, particularly in nanoelectronics.

3.4. Chemical Reactivity of SW Defects in zBNNRs and aBNNRs. Defects sites are usually considered as the center of chemical reactions in nanomaterials. The chemical reactivities of SW defects in CNTs and BNNTs have been widely investigated,[61,62,64,65,79,80] in which some small species such as CH_2, O, O_3, and CO are deemed to be excellent adsorbates due to their high reactivity. A previous theoretical study, reported by Lu et al., indicated that the central C−C bond of the SW-defect site in CNTs is less reactive than all of the other sites.[61] However, An et al. found that the SW defects in BNNTs are more reactive than the perfect sites.[64] These different chemical reactivities are related to the local deformation, characterized with the pyramidalization angles Θ_p of the involved atoms. The increased Θ_p angle has a significant contribution to high chemical reactivities.

In this work, carbene cycloaddtions were used to probe the chemical reactivity of SW defect sites in zBNNRs and aBNNRs. Some characteristic sites related to SW defects were considered, as well as two sites on the edges of perfect and defective BNNRs, because the edge plays an important role in nanoribbons.[26,27] All of the addition sites on the perfect and defective BNNRs with the different edges are illustrated in Figure 6. Some typical structures of CH_2 cycloaddition to perfect BNNRs and the B−B, N−N, and 7−7 ring fusion sites in defective BNNRs are shown in Figure S1 (Supporting Information). Our calculated reaction energies in Tables 2 and 3 reveal that these CH_2 cycloadditions are favorable thermodynamically. The chemical reactivities of the B−N bonds on edges are higher than those in the center for perfect BNNRs. In defective BNNRs, the chemical reactivities of the bonds related to SW defects are comparable to or even higher than those of the bonds on the edges due to the existence of tiny pyramidalization angles for the related atoms in SW defect sites. In particular, the newly formed B−B and N−N bonds are the most reactive sites in defective BNNRs due to their energetically unfavorable character. Among all of the sites including 7−7, 6−7, 5−7, and 5−6 ring fusions, the chemical reactivity of 5−7 ring fusion sites (sites 4 and 5) are higher than those of other sites, followed by 6−7 ring fusion sites. All of the above results are independent of the type of BNNRs.

4. Conclusion

SW defects in a series of zBNNRs and aBNNRs were investigated by means of DFT computations. By rotating different B−N bonds, two kinds of SW defects (named SW-1 and SW-2) for zBNNRs and aBNNRs were considered. The formation of the SW defects in all BNNRs changes the local

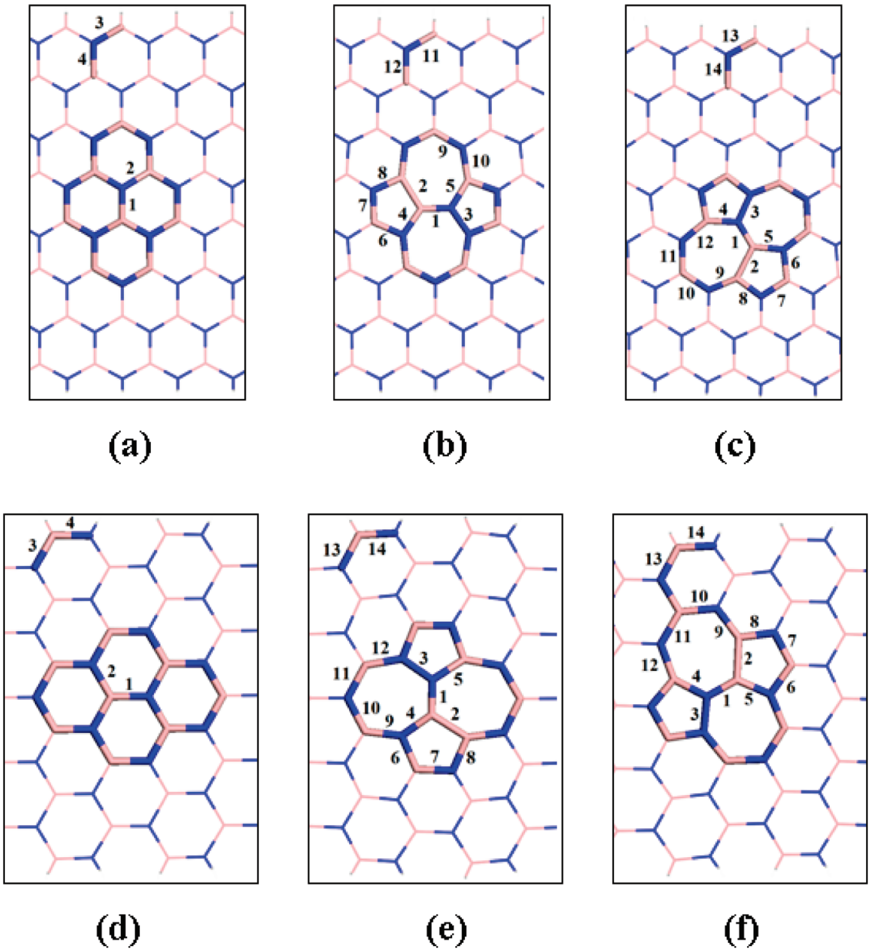

Figure 6. Possible sites for cycloadditions of CH_2 to perfect and defective BNNRs: (a−c) for zBNNRs and (d−f) for aBNNRs.

Table 2. CH_2 Cycloaddition Reaction Energies (eV) on Corresponding Sites (Figure 6a−c) in the Perfect and Defective 8-zBNNRs

reaction sites	perfect	SW-1	SW-2
1	−1.60	−2.27	−2.22
2	−1.62	−4.62	−4.54
3	−2.33	−4.81	−4.64
4	−2.02	−2.93	−3.13
5		−3.13	−2.79
6		−2.07	−2.12
7		−2.36	−2.20
8		−2.42	−2.46
9		−2.53	−2.24
10		−3.03	−2.27
11		−2.08	−2.49
12		−2.06	−2.89
13			−2.43
14			−2.06

Table 3. CH_2 Cycloaddition Reaction Energies on Corresponding Sites (Figure 6d−f) in the Perfect and Defective 11-aBNNRs

reaction sites	perfect	SW-1	SW-2
1	−1.62	−2.22	−2.09
2	−1.62	−4.45	−4.38
3	−2.45	−4.69	−4.51
4	−2.36	−2.77	−2.89
5		−3.08	−2.63
6		−2.12	−1.97
7		−2.16	−2.14
8		−2.40	−2.33
9		−2.02	−2.07
10		−2.13	−2.52
11		−2.40	−2.52
12		−2.58	−2.82
13		−2.47	−1.97
14		−2.42	−2.34

curvature at defect sites and results in small pyramidalization angles of the related atoms. Compared with BNNTs, BNNRs show larger formation energies of SW defects due to their planar structures. The SW orientations have an impact on their formation energies, and SW-2 defects are preferred energetically over SW-1 defects in BNNRs, independent of the edge orientation. The chemical reactivity of SW defects in BNNRs was investigated by using the CH_2 cycloaddition reactions. All of the CH_2 cycloadditions in perfect and defective BNNRs are exothermic and favorable thermodynamically. The reactions at SW defects sites are more exothermic than those in the center of perfect BNNRs. The newly formed B−B and N−N bonds are the most reactive sites, followed by the 5−7 ring fusions, irrespective of the types of ribbon edges. Moreover, independent of the SW defect orientation, the formation of SW defects significantly narrows the energy gaps of the defective BNNRs, though they still retain typical wide-band-gap semiconductor behavior. It is indicated that the band gap of BNNRs is not so robust, and it is highly possible to further reduce their band gap by chemical modification. These findings are useful to design new nanodevices on the basis of BNNRs.

Acknowledgment. This work was supported in the U. S. A. by NSF Grant CHE-0716718, the Institute for Functional Nanomaterials (NSF Grant 0701525), and the U.S. Environmental Protection Agency (EPA Grant No. RD-83385601), and in China by NSFC (20873067) and NCET. GT.Y. thanks the start-up fund (450080011085) from Jilin University.

Supporting Information Available: The structures of the CH_2 cycloaddition at some characteristic sites of perfect and defective BNNRs. This material is available free of charge via the Internet at http://pubs.acs.org.

References

(1) Novoselov, K. S.; Geim, A. K.; Morozov, S. V.; Jiang, D.; Zhang, Y.; Dubonos, S. V.; Grigoreva, I. V.; Firsov, A. A. *Science* **2004**, *306*, 666–669.

(2) Novoselov, K. S.; Jiang, D.; Schedin, F.; Booth, T. J.; Khotkevich, V. V.; Morozov, S. V.; Geim, A. K. *Proc. Natl. Acad. Sci. U. S. A.* **2005**, *102*, 10451–10453.

(3) Lee, G.; Wei, X.; Kysar, J. W.; Hone, J. *Science* **2008**, *321*, 385–388.

(4) Zhang, Y.; Tan, Y.-W.; Stormer, H. L.; Kim, P. *Nature* **2005**, *438*, 201–204.

(5) Ponomarenko, L. A.; Schedin, F.; Katsnelson, M. I.; Yang, R.; Hill, E. W.; Novoselov, K. S.; Geim, A. K. *Science* **2008**, *320*, 356–358.

(6) Kan, E. J.; Li, Z. Y.; Yang, J. L. *Nano* **2008**, *3*, 433–442.

(7) Elias, D. C.; Nair, R. R.; Mohiuddin, T. M. G.; Morozov, S. V.; Blake, P.; Halsall, M. P.; Ferrairi, A. C.; Boukhvalov, D. W.; Katsnelson, M. I.; Geim, A. K. *Science* **2009**, *323*, 610–613.

(8) Berger, C.; Song, Z.; Li, X.; Wu, X.; Brown, N.; Naud, C.; Mayou, D.; Li, T.; Hass, J.; Marchenkov, A. N.; Conrad, E. H.; First, P. N.; Heer, W. A. D. *Science* **2006**, *312*, 1191–1196.

(9) Ci, L.; Xu, Z.; Wang, L.; Gao, W.; Ding, F.; Kelly, K.; Yakobson, B. I.; Ajayan, P. *Nano Res.* **2008**, *1*, 116–122.

(10) Chen, Z.; Lin, Y.; Rooks, M. J.; Avouris, P. *Physica E* **2007**, *40*, 228–232.

(11) Singh, A. K.; Yakobson, B. I. *Nano Lett.* **2009**, *9*, 1540–1543.

(12) Boukhvalov, D. W.; Katsnelson, M. I.; Lichtenstein, A. I. *Phys. Rev. B* **2008**, *77*, 035427.

(13) Li, Y.; Zhou, Z.; Shen, P.; Chen, Z. *J. Phys. Chem. C* **2009**, *113*, 15043–15045.

(14) Li, Y.; Zhou, Z.; Shen, P.; Chen, Z. *ACS Nano* **2009**, *3*, 1952–1958.

(15) Ezawa, M. *Phys. Rev. B* **2006**, *73*, 045432.

(16) Fujita, M.; Wakabayashi, K.; Nakada, K.; Kusakabe, K. *J. Phys. Soc. Jpn.* **1996**, *65*, 1920–1923.

(17) Wakabayashi, K.; Fujita, M.; Ajiki, H.; Sigrist, M. *Phys. Rev. B* **1999**, *59*, 8271–8282.

(18) Nakada, K.; Fujita, M.; Dresselhaus, G.; Dresselhaus, M. S. *Phys. Rev. B* **1996**, *54*, 17954–17961.

(19) Son, Y.; Cohen, M.; Louie, S. *Phys. Rev. Lett.* **2006**, *97*, 216803.

(20) Ezawa, M. *Physica E* **2008**, *40*, 1421–1423.

(21) Ezawa, M. *Phys. Rev. B* **2007**, *76*, 245415.

(22) Kudin, K. N. *ACS Nano* **2008**, *2*, 516–522.

(23) Wassman, T.; Seitsonen, A. P.; Saitta, A. M.; Lazzeri, M.; Mauri, F. *Phys. Rev. Lett.* **2008**, *101*, 096402.

(24) Barone, V.; Hod, O.; Scuseria, G. E. *Nano Lett.* **2006**, *6*, 2748–2754.

(25) Jiang, D. E.; Sumpter, B. G.; Dai, S. *J. Chem. Phys.* **2007**, *127*, 124703.

(26) Jiang, D. E.; Sumpter, B. G.; Dai, S. *J. Chem. Phys.* **2007**, *126*, 134701.

(27) Ritter, K. A.; Lyding, J. W. *Nat. Mater.* **2009**, *8*, 235–242.

(28) Li, X. L.; Wang, X. R.; Zhang, L.; Lee, S. W.; Dai, H. J. *Science* **2008**, *319*, 1229–1232.

(29) Son, Y. W.; Cohen, M. L.; Louie, S. G. *Nature (London)* **2006**, *444*, 347–349.

(30) Hod, O.; Barone, V.; Peralta, J. E.; Scuseria, G. E. *Nano Lett.* **2007**, *7*, 2295–2299.

(31) Kan, E. J.; Li, Z. Y.; Yang, J. L.; Hou, J. G. *J. Am. Chem. Soc.* **2008**, *130*, 4224–4225.

(32) Barone, V.; Peralta, J. E. *Nano Lett.* **2008**, *8*, 2210–2214.

(33) Nakamura, J.; Nitta, T.; Natori, A. *Phys. Rev. B* **2005**, *72*, 205429.

(34) Ding, Y.; Yang, X.; Ni, J. *Appl. Phys. Lett.* **2008**, *93*, 043107.

(35) Ding, Y.; Wang, Y. L.; Ni, J. *Appl. Phys. Lett.* **2009**, *94*, 073111.

(36) Wu, X.; Pei, Y.; Zeng, X. C. *Nano Lett.* **2009**, *9*, 1577–1582.

(37) Sun, L.; Li, Y.; Li, Z.; Li, Q.; Zhou, Z.; Chen, Z.; Yang, J.; Hou, J. G. *J. Chem. Phys.* **2008**, *129*, 174114.

(38) Botello-Méndez, A. R.; López-Urías, F.; Terrones, M.; Terrones, H. *Nano Lett.* **2008**, *8*, 1562–1565.

(39) Li, Y.; Zhou, Z.; Zhang, S.; Chen, Z. *J. Am. Chem. Soc.* **2008**, *130*, 16739–16744.

(40) Du, A.; Smith, S. C.; Lu, G. *Chem. Phys. Lett.* **2007**, *447*, 181–186.

(41) Zhang, Z.; Guo, W. *Phys. Rev. B* **2008**, *77*, 075403.

(42) Park, C. H.; Louie, S. G. *Nano Lett.* **2008**, *8*, 2200–2203.

(43) Jin, C.; Lin, F.; Suenaga, K.; Iijima, S. *Phys. Rev. Lett.* **2009**, *102*, 195505.

(44) Wu, X.; Wu, M.; Zeng, X. C. *Front. Phys. China* **2009**, *4* (3), 367–372.

(45) Ding, Y.; Wang, Y. L.; Ni, J. *Appl. Phys. Lett.* **2009**, *94*, 233107.

(46) Lai, L.; Lu, J.; Wang, L.; Luo, G.; Zhou, J.; Qin, R.; Gao, Z.; Mei, W. N. *J. Phys. Chem. C* **2009**, *113*, 2273–2276.

(47) Zheng, F.; Zhou, G.; Liu, Z.; Wu, J.; Duan, W.; Gu, B.; Zhang, S. B. *Phys. Rev. B* **2008**, *78*, 205415.

(48) Nagashima, A.; Tejima, N.; Gamou, Y.; Kawai, T.; Oshima, C. *Phys. Rev. Lett.* **1995**, *75*, 3918–3921.

(49) Pacilé, D.; Meyer, J. C.; Girit, C.; Zettl, A. *Appl. Phys. Lett.* **2008**, *92*, 133107.

(50) Han, W.-Q.; Wu, L.; Zhu, Y.; Watanabe, K.; Taniguchi, T. *Appl. Phys. Lett.* **2008**, *93*, 223103.

(51) Meyer, J. C.; Chuvilin, A.; Algara-Siller, G.; Biskupek, J.; Kaiser, U. *Nano Lett.* **2009**, *9*, 2683–2689.

(52) Zhi, C.; Bando, Y.; Tang, C.; Kuwahara, H.; Golberg, D. *Adv. Mater.* **2009**, *21*, 2889–2893.

(53) Wei, D.; Liu, Y.; Wang, Y.; Zhong, H.; Huang, L.; Yu, G. *Nano Lett.* **2009**, *9*, 1752–1758.

(54) Chandra, N.; Namilae, S.; Shet, C. *Phys. Rev. B* **2004**, *69*, 094101.

(55) Wang, C. C.; Zhou, G.; Liu, H. T.; Wu, J.; Qiu, Y.; Gu, B. L.; Duan, W. H. *J. Phys. Chem. B* **2006**, *110*, 10266–10271.

(56) Chakrapani, N.; Zhang, Y. M.; Nayak, S. K.; Moore, J. A.; Carroll, D. L.; Choi, Y. Y.; Ajayan, P. M. *J. Phys. Chem. B* **2003**, *107*, 9308–9311.

(57) Piquini, P.; Baierle, R. J.; Schmidt, T. M.; Fazzio, A. *Nanotechnology* **2005**, *16*, 827–831.

(58) Schmidt, T. M.; Baierle, R. J.; Piquini, P.; Fazzio, A. *Phys. Rev. B* **2003**, *67*, 113407.

(59) Zobelli, A.; Ewels, C. P.; Gloter, A.; Seifert, G.; Stephan, O.; Csillag, S.; Colliex, C. *Nano Lett.* **2006**, *6*, 1955–1960.

(60) Ren, Y.; Xiao, T.; Liao, K. *Phys. Rev. B* **2006**, *74*, 045410.

(61) Lu, X.; Chen, Z.; Schleyer, P. v. R. *J. Am. Chem. Soc.* **2005**, *127*, 20–21.

(62) Bettinger, H. F. *J. Phys. Chem. B* **2005**, *109*, 6922–6924.

(63) Dinadayalane, T. C.; Leszczynski, J. *Chem. Phys. Lett.* **2007**, *434*, 86–91.

(64) An, W.; Wu, X.; Yang, J. L.; Zeng, X. C. *J. Phys. Chem. C* **2007**, *111*, 14105–14112.

(65) Li, Y. F.; Zhou, Z.; Golberg, D.; Bando, Y.; Schleyer, P. v. R.; Chen, Z. F. *J. Phys. Chem. C* **2008**, *112*, 1365–1370.

(66) Boukhvalov, D. W.; Katsnelson, M. I. *Nano. Lett.* **2008**, *8*, 4373–4379.

(67) Stone, A. J.; Wales, D. J. *Chem. Phys. Lett.* **1986**, *128*, 501–503.

(68) Perdew, J. P.; Chevary, J. A.; Vosko, S. H.; Jackson, K. A.; Pederson, M. R.; Singh, D. J.; Fiolhais, C. *Phys. Rev. B* **1992**, *46*, 6671–6687.

(69) Kresse, G.; Hafner, J. *Phys. Rev. B* **1993**, *47*, 558–561.

(70) Kresse, G.; Hafner, J. *Phys. Rev. B* **1994**, *49*, 14251–14269.

(71) Kresse, G.; Furthmuller, J. *Comput. Mater. Sci.* **1996**, *6*, 15–50.

(72) Kresse, G.; Furthmuller, J. *Phys. Rev. B* **1996**, *54*, 11169–11186.

(73) Vanderbilt, D. *Phys. Rev. B* **1990**, *41*, 7892–7895.

(74) Haddon, R. C. *J. Am. Chem. Soc.* **1986**, *108*, 2837–2842.

(75) Haddon, R. C. *J. Am. Chem. Soc.* **1987**, *109*, 1676–1685.

(76) Haddon, R. C. *J. Am. Chem. Soc.* **1990**, *112*, 3385–3389.

(77) Yang, S. H.; Shin, W. H.; Kang, J. K. *J. Chem. Phys.* **2006**, *125*, 084705.

(78) Pan, B. C.; Yang, W. S.; Yang, J. L. *Phys. Rev. B* **2000**, *62*, 12652–12655.

(79) Horner, D. A.; Redfern, P. C.; Sternberg, M.; Zapol, P.; Curtiss, L. A. *Chem. Phys. Lett.* **2007**, *450*, 71–75.

(80) Ouyang, F. P.; Huang, B.; Li, Z.; Xiao, J.; Wang, H.; Xu, H. *J. Phys. Chem. C* **2008**, *112*, 12003–12007.

CT900388X

3096 J. Chem. Theory Comput. 2009, 5, 3096–3104

JCTC Journal of Chemical Theory and Computation

How Does the Relocation of Internal Water Affect Resonance Raman Spectra of Rhodopsin? An Insight from CASSCF/Amber Calculations

Tadeusz Andruniów*,† and Massimo Olivucci‡,§

Quantum Chemistry and Molecular Modelling Lab, Institute of Physical and Theoretical Chemistry, Wroclaw University of Technology, Wyb. Wyspianskiego 27, 50-370 Wroclaw, Poland, Dipartimento di Chimica, Università di Siena, via Aldo Moro 2, 53100 Siena, Italy, and Chemistry Department, Bowling Green State University, Bowling Green, Ohio 43403

Received February 9, 2009

Abstract: The effect of relocation of the W2 crystallographic water in bovine rhodopsin has been investigated by comparing and analyzing simulated resonance Raman spectra of 1HZX- and 1U19-based quantum mechanics/molecular mechanics (CASSCF/MM) models. The main target is to explore the sensitivity of the simulated resonance Raman spectra to protein cavity change. In particular, we focus on a quantitative investigation of the changes in the vibrational activity of rhodopsin induced by modifications in the protein cavity structure and in the water position. Comparison of the simulated RR spectra of the *Rh-1U19* and *Rh-1HZX* models with the measured spectrum of rhodopsin reveals that the *Rh-1U19* model provides a slightly better rhodopsin model consistently with the simulations of the absorption maxima. On the other hand, and irrespective of the comparison with the experimental data, the analysis of two different computational models for the same protein and chromophore makes it possible to investigate and disentangle the relationship between structural features and change in the RR intensities in an unusually detailed way.

Introduction

The visual pigment rhodopsin is a G protein-coupled receptor responsible for dim-light vision in vertabrates. Rhodopsin contains an 11-*cis* retinal chromophore bound to a lysine residue via a protonated Schiff base linkage (PSB11). The biological activity of rhodopsin is triggered by the ultrafast light-induced *cis*−*trans* isomerization of the chromophore that initiates the vision process. The isomerization reaction is very efficient and extremely fast - the chromophore isomerizes to the *all-trans* photoproduct within a few picoseconds and with a quantum yield of 0.67.[1]

Since Palczewski and co-workers reported the first X-ray crystal structure of bovine rhodopsin at 2.8 Å resolution (1F88), there has been an ever increasing interest in diffraction studies on rhodopsin. Indeed, a year later, an improved model (1HZX) from the same groups[3] revealed some missing residues from the original structure. 1HZX contains only one internal water molecule (W1), positioned between PSB11 and the Glu181 residue. Soon after, two additional crystallographic structures, resolved at 2.6[4] and 2.2 Å[5] (1L9H and 1U19, respectively), were deposited in the ProteinDataBank archive. The 1HZX location of W1 is retained in 1L9H and 1U19. However, both 1L9H and 1U19 report a newly identified water molecule (W2) placed close to PSB11 and the chromophore carboxylate counterion Glu113. It is believed that internal water molecules may have an important role in regulating the activity of rhodopsin.[4]

A recent computational study on bovine rhodopsin[6] has investigated the effect of relocation of the W2 crystallographic water by comparing and analyzing the vertical excitation energy of the 1HZX- and 1U19-based quantum

---

* Corresponding author e-mail: andruniow@mml.ch.pwr.wroc.pl.

† Wroclaw University of Technology.

‡ Università di Siena.

§ Bowling Green State University.

10.1021/ct900071c CCC: $40.75

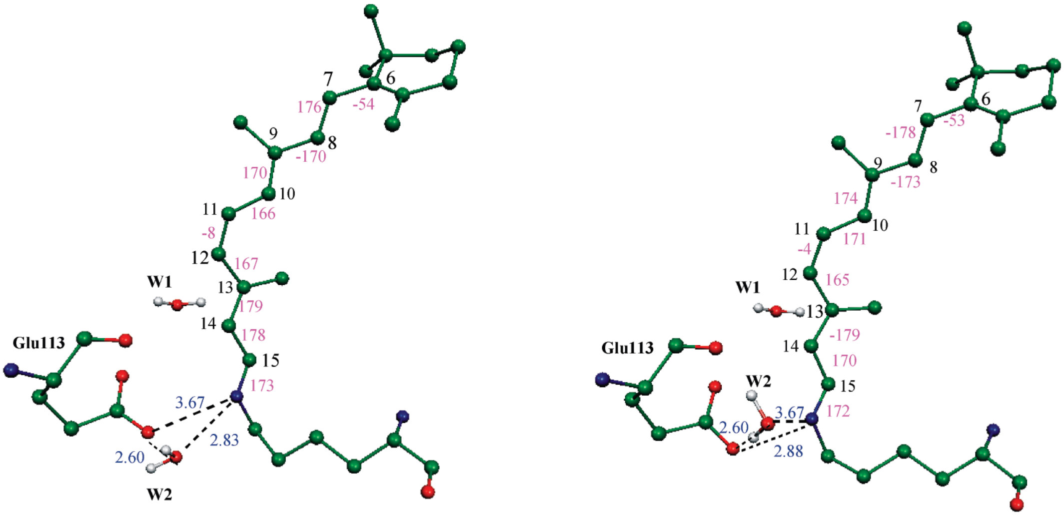

Rh-1HZX *Rh-1U19*

Figure 1. 11-*cis* retinal frameworks with Glu113 and W1 and W2 molecules. The ground-state optimized structure on the left corresponds to *Rh-1HZX*, while the structure on the right corresponds to *Rh-1U19*. Dihedral angles (in degrees) are indicated in pink. Some critical distances between W2 water and the Schiff base region and/or the counterion are in blue (in Å).

mechanics/molecular mechanics models (see Figure 1). Using CASSCF/Amber optimized structures of such models and subsequent single-point CASPT2//CASSCF/Amber computations the authors have been able to compute a red-shifting effect moving the absorption maximum from 479 nm (59.8 kcal·mol^{-1} vertical excitation energy) for the 1HZX-based model (*Rh-1HZX*) to 513 nm (55.7 kcal·mol^{-1} vertical excitation energy) for the 1U19-based model (*Rh-1U19*). Since the observed absorption maximum is 498 nm (57.4 kcal· mol^{-1} vertical excitation energy) the 1U19-based model leads to a smaller −1.8 kcal·mol^{-1} red-shifted error. A comparative analysis of the two models reveals that the change in absorption maximum is not due to a single structural change such as W2 relocation but to simultaneous changes in the PSB11-counterion distance and to a substantial PSB11 chain displacement within the (modestly) different protein cavity structures.

Resonance Raman (RR) spectroscopy is a powerful experimental technique for probing the structural changes of chromophores. In fact, even limited changes in the chromophore structure, or in the relationship of the chromophore with its environment, usually result in clear changes in the spectrum vibrational pattern and intensities. RR spectra are generated via electronic excitation in the Franck−Condon vicinity and display the intensity of vibrational modes coupled to the electronic transition. Moreover, RR spectra provide detailed information on the difference of the ground and excited state molecular structures of the chromphore as well as on its initial excited state dynamics. In the past, the RR studies of the PSB11 retinal chromophore of rhodopsin were very useful in identifying the photoreaction intermediates and the initial excited-state dynamics of the photoisomerization process.[1] In these studies the effect of the protein environment was scrutinized by comparing the RR spectra of PSB11 in solution and in the protein.[7−9]

In this article we report simulations of RR spectra of rhodopsin for *Rh-1HZX* and *Rh-1U19* models (Figure 1) using the CASSCF/Amber method to calculate the ground state force field. The main target is to explore the sensitivity of the simulated RR spectra to protein cavity changes. In particular, we focus on a quantitative investigation of the changes in the vibrational activity of rhodopsin induced by modifications in the protein cavity structure and in the water position. A comparison of the simulated RR spectra of *Rh-1U19* and *Rh-1HZX* models reveals that there are non negligible differences in vibrational frequencies and intensity distribution in both spectra. The results also show that the *Rh-1U19* model allows for a slightly more detailed reproduction of the experimental RR spectrum consistently with the simulations of the absorption maxima. On the other hand, and irrespective of the comparison with the experimental data, the analysis of two different computational models for the same protein and chromophore makes it possible to investigate and disentangle the relationship between structural features and change in the RR intensities in an unusually detailed way.

Models and Methods

The first model (*Rh-1HZX*) investigated in this study is based on monomer A of 1HZX crystal structure. In addition to one internal water molecule present in the original protein structure, the second internal water molecule was introduced following a suggestion by Kandori et al.[10] This model was utilized in our early studies on rhodopsin.[11−13] The second model (*Rh-1U19*) was prepared, using the same procedures, from 1U19 crystal structure that comprises two resolved water molecules close to the chromophore binding site. As displayed in Figure 2, the position of W2 in *Rh-1U19* differs significantly from that seen in *Rh-1HZX*. Even though W2 is invariably hydrogen-bonded to the O1 carboxylate oxygen of Glu113 counterion in both structures, its position is strongly shifted to the opposite side of Glu113 in *Rh-1U19* relative to *Rh-1HZX* models.

The retinal chromophore bears a net positive charge counterbalanced by a negative charge of Glu113 residue. The

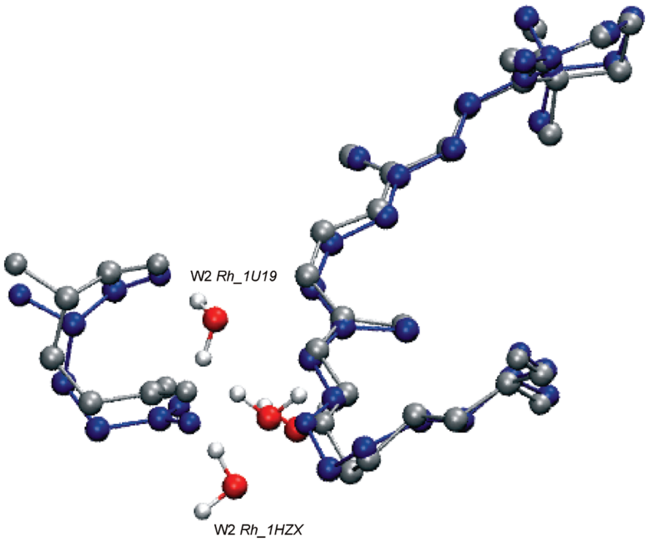

Figure 2. Superposition of the ground-state optimized *Rh-1HZX* (in silver) and *Rh-1U19* (in blue) 11-*cis* retinal chromophores. Notice a different orientation of the W2 molecule in both rhodopsin models.

rest of the protein cavity is set to neutral. Even though there is conflicting evidence in the literature regarding the protonation state of Glu181 residue,[14−20] a recent study by Hall et al.[21] has shown that changing the protonation state of Glu181 has a rather minimal effect on properties of PSB11 in rhodopsin. The average equilibrium structure of the rhodopsin models is generated via geometry optimization by relaxing the chromophore, Lys296 residue, and the two TIP3P-type water molecules, while the rest of the protein is kept frozen in its X-ray position during optimization procedure. Such a fixed structure is taken as representative of the average protein environment. With the exception of Lys296, the residue charges are described by the standard Amber force field.[22]

Recently we have shown that CASPT2//CASSCF/MM calculations provide a quantitative evaluation of structural and spectroscopic parameters for rhodopsin,[11−13] GFP,[23] and retinal-based molecular switches.[24,25] Also, previous CASSCF/Amber studies on the RR spectrum of *Rh-1HZX*[13] showed a relatively good agreement with the experimental spectrum.[8] However, a modest basis set (3-21g*) used in these studies resulted in significant blueshift of the most intense band in the calculated spectrum with respect to the measured one.[8] Therefore, in our present CASSCF simulations of the *Rh-1HZX* RR spectrum we have employed a more extensive basis set (6-31g*) than before.[13] Additionally, it should be pointed out that the RR spectrum of *Rh-1U19* has been simulated for the first time. The effect of isotopic substitution and normal mode composition analysis was done to aid in the assignment of experimental bands. The wavenumber shifts were calculated upon C_{10}-D, C_{14}-D, 10,11-^{13}C, 14,15-^{13}C, and N-D substitution and compared with those measured previously[7] in RR experiments. Potential energy distribution (PED) contribution to each of the calculated vibrational frequency gives insight into the normal mode composition which in turn aids in the assignment of the measured resonance Raman bands. Veda4[26] software was used to perform PED analysis.

We have calculated Raman intensities under resonant conditions applying a sum-over-states formalism developed by Albrecht[27] where the transition polarizibility tensor is written as

$$\alpha_{fi}^{\rho\sigma}(\Omega) = \sum_{e}\sum_{v}\left[\frac{\langle f|\mu_{ge}^{\rho}|k\rangle\langle k|\mu_{eg}^{\sigma}|i\rangle}{E_{ek}-E_{gi}-\Omega+i\Gamma_{ek}} + \frac{\langle f|\mu_{ge}^{\sigma}|k\rangle\langle k|\mu_{eg}^{\rho}|i\rangle}{E_{ek}-E_{gf}+\Omega+i\Gamma_{ek}}\right] \tag{1}$$

In eq 1 the sum runs over all electronic $|e\rangle$ and vibrational $|v\rangle$ states, $|i\rangle$ and $|f\rangle$ are initial and final vibrational states, respectively, of the electronic ground state, while $|k\rangle$ is an intermediate vibrational state of the electronic excited state, Ω is the frequency of the incident light, E_{gi}, E_{ek}, and E_{gf} are vibronic energies of initial, intermediate and final states, Γ_{ek} is a damping factor associated with the g→e electronic transition, and $\mu_{ge/eg}^{\rho/\sigma}$ is the electronic transition dipole moment.

Upon expanding the transition dipole moments in the Taylor series in terms of the molecular normal modes and ignoring the vibronic coupling effects, the Franck−Condon (FC) mechanism can be described by the following expression

$$\alpha_{fi}^{\rho\sigma}(\Omega) = \sum_{e}\mu_{ge}^{\rho 0}\mu_{eg}^{\sigma 0}\sum_{v}\left[\frac{\langle f|k\rangle\langle k|i\rangle}{E_{ek}-E_{gi}-\Omega+i\Gamma_{ek}} + \frac{\langle f|k\rangle\langle k|i\rangle}{E_{ek}-E_{gf}+\Omega+i\Gamma_{ek}}\right] \tag{2}$$

If only one electronic excited state contributes to the Raman scattering eq 2 simplifies to

$$\alpha_{fi}^{\rho\sigma}(\Omega) = \sum_{e}\mu_{ge}^{\rho 0}\mu_{eg}^{\sigma 0}\sum_{v}\left[\frac{\langle f|k\rangle\langle k|i\rangle}{E_{ek}-E_{gi}-\Omega+i\Gamma_{ek}}\right] \tag{3}$$

where $\mu_{ge/eg}^{\rho 0/\sigma 0}$ is a pure electronic transition dipole moment.

By adapting harmonic approximation and identical vibrational frequencies and normal coordinates in the ground and excited electronic states it is possible to calculate the FC overlap from recursion formulas given in ref 28. Subsequently, the square of the transition polarizibility is proportional to the dimensionless parameter B_k through the relation[29]

$$|(\alpha_{fi}^{\rho\sigma}(\Omega))_k|^2 \propto \frac{B_k^2}{2} \tag{4}$$

and this in turn is related to the RR intensity of the *k*th vibration

$$I_k \propto \frac{B_k^2}{2} \tag{5}$$

Dimensionless displacements B_k of the potential energy surface minima along the *k* totally symmetric vibrational modes are defined as[29−31]

$$B_k = S_k^T \Delta X\left(\frac{\mu_k\omega_k}{\hbar}\right)^{1/2} \tag{6}$$

where S_k is a 3N-dimensional vector containing the Cartesian nuclear displacements in Q_k normal mode with the associated frequency ω_k and reduced mass μ_k. ΔX is the 3N-dimensional vector containing the differences of the nuclear position vectors in the resonant and ground electronic states.[30,31]

There have been successful attempts to calculate RR spectra using Kramers−Kronig transform procedure which eliminates the need for explicit summation over intermediate vibrational levels.[32−36] An alternative to the sum-over-states formulation is the Heller's time-dependent approach.[37−39] In the "short-time" limit of the time-dependent approach[36,37] which applies to preresonance conditions or fast electronic relaxation the relative intensities are given by

$$I_k = \omega_k^2 B_k^2 \tag{7}$$

where ω_k is the frequency of the kth vibration and dimensionless parameters B_k are calculated from the excited-state gradients. Thus, within this approximation no explicit knowledge of the excited-state equilibrium structure is required.

Based on eqs 5 and 7 it is clear that to evaluate the resonance Raman intensities we need dimensionless parameters. These in turn can be calculated having the equilibrium geometries of the ground state and the excited state (or excited-state gradient at the ground state equilibrium geometry) in resonance with the excitation wavelength as well as the vibrational frequencies at the ground state equilibrium geometry.

The QM/MM employed in this study is fully described in ref 11. In short, the QM subsystem consists of retinal and the last bond of Lys296 side chain. We use a hydrogen link-atom scheme with the frontier placed at the C_ε-C_δ bond of the Lys296. The *ab initio* calculations are based on the CASSCF level of theory. In the optimization step the 6-31G* basis set was used, while the 3-21G* basis set was chosen to obtain second-derivatives. In the geometry optimization procedure the active space comprises the full π-system of PSB11 (12 electrons in 12 π-orbitals), which is reduced to 8 electrons in 8 orbitals during the frequency calculations. Accordingly, in the latter the 2 lowest occupied and 2 highest unoccupied retinal π-orbitals were excluded from the active space. CASSCF/MM geometry optimization of the ground state and optically allowed excited state rhodopsin structures as well as frequency calculations in the ground state were carried out with the programs Gaussian03[40] and Tinker.[41]

In calculations of resonance Raman intensities for *Rh-1U19* we used the sum-over-states approach described by eq 3. Since eq 5 is often employed in simple estimation of RR intensities of large molecules we compared a spectrum resulting from eq 5 with the more accurate one obtained from eq 3. Furthermore, the "short-time" approximation is also applied to model Raman spectrum of *Rh-1U19*. We examined some possible approximations originating from the sum-over-states as well as from the "short-time" approaches by comparing the resulting simulated RR spectra to each other and to the experimental spectrum. Notice that eq 3 provides the possibility of calculating RR intensities not only for fundamentals but also for overtones and combination bands; however, it significantly increases the computational effort. On the other hand, the two other methods described above are much more efficient but can only be used to obtain intensities of fundamentals.

The qualitative difference between simplified sum-over-states and "short-time" approaches is illustrated in Figure S1 (Supporting Information). Spectra A and B obtained with the use of sum-over-states relations (eqs 3 and 5, respectively) combined with B_k calculated from the shift between the excited state and ground state equilibrium positions reveal very similar intensity distribution. It is interesting to note that fundamentals and overtones do not manifest themselves in the 700−1750 cm^{-1} frequency region of spectrum A (Figure S1 (Supporting Information)). On the other hand, comparison of spectra A and B with the spectrum determined from the "short-time" approximation (spectrum C) based on the excited state gradient's B_k reveals subtle changes in the intensity pattern of the 900−1050 cm^{-1} frequency region, notably a band at around 940 cm^{-1} which is extremely weak in spectrum C, while in other theoretical and experimental spectra[8] it brings substantial intensity. Moreover, the intensity of the 1632 cm^{-1} band is exaggerated in comparison to its experimental counterpart. Overall, the simulated spectra originated from simplified approaches are amazingly similar to the spectrum obtained from more demanding the sum-over-states approach expressed by eq 3. In light of these findings we will use eq 5 to calculate RR spectra of *Rh-1U19* and *Rh-1HZX*.

To improve the agreement between calculated and experimental frequencies we used a scaling factor for CASSCF-based frequencies equal to 0.9 to account for errors due to incomplete treatment of dynamic electron correlation, basis set truncation, modest active space, and anharmonic effects. The spectra were obtained as superpositions of the Lorentzian curve with the line width of 10 cm^{-1}.

Results and Discussion

As discussed above, Strambi et al.[6] have analyzed the sensitivity of the absorption maxima of rhodopsin to the change in the crystallographic structure (mainly differing for the relocation of one of the internal water molecules). To do so, they have calculated the ground state equilibrium structures as well as the excitation energies for the *Rh-1HZX* and *Rh-1U19* models. Inspection of Figure 2 shows that the W1 position is hardly changed in the models. On the other hand, in *Rh-1HZX*, W2 forms a single hydrogen bond with the O1 carboxylate oxygen of Glu113 whereas, in *Rh-1U19*, W2 is hydrogen-bonded to both O1 and to the oxygen of the nearby peptide bond. It is interesting to note that a major relocation of W2 water molecule in *Rh-1U19* while leading to a large (0.7−0.8 Å) decrease in the -C=NH(+)----O1(-) salt-bridge distance—exposing the -C=NH(+) to a more negative electrostatic potential—does not dramatically affect the excitation energy.[6] This is explained with the relocation of the retinal chain shown in Figure 2 where we report a superimposed PSB11 structure in *Rh-1HZX* and *Rh-1U19*. Indeed the computed change in the cavity generated electrostatic potential[6] points to a compensation mechanism where the shifting of the -C=NH(+) chromophore position in *Rh-1U19* with respect to *Rh-1HZX* results in the exposure of such moiety to a more positive electrostatic potential that

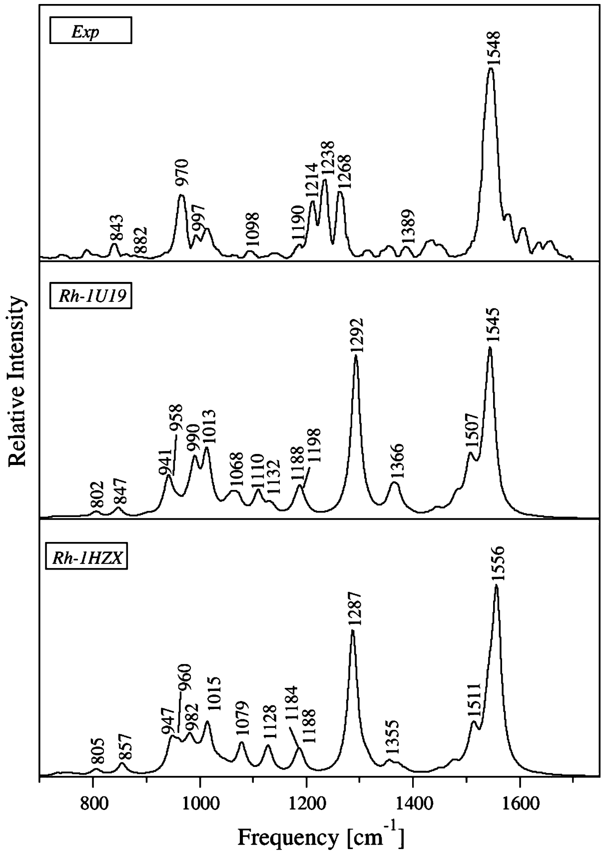

Figure 3. Simulated resonance Raman spectra for *Rh-1HZX* and *Rh-1U19* and their comparison with the experimental spectrum.[7]

overcompensates the effect of the closer O1 counterion negative charge. While such an effect is responsible for a ca. 4 kcal·mol^{-1} decrease in vertical excitation energy,[6] we want to determine if this effect is also accompanied by a change in the RR spectra of the corresponding models. In other words, a large change in hydrogen-bonding of the chromophore shall manifest itself in altered vibrational frequencies and/or intensities of specific vibrational modes and thus can be conveniently investigated by comparing the vibrational activity of RR spectra for both rhodopsin models.

The RR spectra of both models are reported in Figure 3 together with the observed spectrum. As it was shown by Mathies and co-workers the most characteristic parts of the resonance Raman spectrum of bovine rhodopsin are (1) the ethylenic band observed between 1500 and 1650 cm^{-1}, (2) the structurally sensitive fingerprint region observed in the 1100−1350 cm^{-1} frequency range, (3) the hydrogen out-of-plane (HOOP) region observed in the 900−1100 cm^{-1} frequency range, and (4) the low-frequency region comprising of torsional modes associated with the isomerization reaction.[8]

The high-frequency region of the *Rh-1HZX* model is qualitatively similar to that of *Rh-1U19* (Figure 3). There are two strong lines at 1556 and 1542 cm^{-1} in the former that correspond to peaks at 1545 and 1536 cm^{-1} in *Rh-1U19*. These intense lines are assigned to an in-phase stretching of the C11=C12 bond combined with the C9=C10 stretch. The ethylenic stretching frequency in *Rh-1U19* is shifted down by 11 cm^{-1} from the frequency in *Rh-1HZX*, and this is consistent with a red-shift of its absorption.[6] This frequency downshift also corresponds well to the increase in the C11=C12 and C9=C10 distances by 0.004 and 0.003 Å, respectively, going from *Rh-1HZX* to *Rh-1U19*. In the experiment[8] the lower-intense line was not detected, so it may be hidden under the fairly broad band at 1548 cm^{-1}. Consistently with *Rh-1HZX*, there is also a weaker line calculated on the left wing of the 1545 cm^{-1} band in *Rh-1U19*. This band is shifted by 6 cm^{-1} relative to the frequency in *Rh-1HZX* (1542 cm^{-1}) and is due to noticeable contribution from the C13=C14 stretch.

The frequency of the C=N stretching is considered to be a sensitive probe of the Schiff base-protein interactions in rhodopsin.[1] Strambi et al.[6] have demonstrated that relocation of one internal (W2) water molecule in *Rh-1U19* results in a strongly reduced C=NH(+)----O1(−) salt-bridge distance that must induce a decrease in double bond delocalization, an increase in vertical excitation energy, and a modified hydrogen-bond network. As explained above, such effects are more than counterbalanced by an effective PSB11 displacement to a region with a larger protein-generated positive potential that explains the calculated red-shift relative to the *Rh-1HZX* model. Indeed, the C=N stretching mode in *Rh-1HZX* was obtained at 1640 cm^{-1}, while in *Rh-1U19* at 1632 cm^{-1} and likely corresponds to the band at 1655 cm^{-1} in the measured spectrum.[8] However, it is interesting that the calculated frequency shift induced by N-deuteration, which is 42 cm^{-1} in *Rh-1U19*, drops to 24 cm^{-1} in *Rh-1HZX* (experimental shift is in a range of 31−35 cm^{-1})[7,49] implying much stronger coupling of the C=N stretch with the N−H bending vibration in *Rh-1U19*. The considerably lower frequency shift predicted for *Rh-1HZX* can be ascribed to the weakened Schiff base hydrogen bonding in the *Rh-1HZX* model, in accordance with recently calculated structural data.[6,12]

The frequencies of C−C stretches are sensitive to local geometry and thus provide valuable information on the conformation of retinal.[1,8] The fingerprint region is characterized by single-bond C−C stretching modes and spans 1100−1350 cm^{-1} spectral range. In the calculated resonance Raman spectra of both *Rh-1HZX* and *Rh-1U19* two modest bands are observed at 1188 and 1128 cm^{-1} in the former and 1198 and 1132 cm^{-1} in the latter (Figure 3 and Table 1). For *Rh-1HZX*, the 1188 cm^{-1} mode can be assigned to the C8−C9 stretch, while the 1184 cm^{-1} mode can be assigned to the C12−C13 stretch. The corresponding modes in *Rh-1U19* are upshifted by 10 and 4 cm^{-1}, respectively. A normal-mode analysis in this region is obscured by the fact that C−C stretches are strongly delocalized over the discussed fingerprint modes and thus difficult to assess in terms of local mode coordinates in agreement with previous DFT-based vibrational study.[43] However, the assignment was facilitated by calculating the positions of the fingerprint modes for the isotopically labeled analogues of *Rh-1HZX* and *Rh-1U19*. In fact, the C12−C13 stretch can be assigned with confidence at 1184 cm^{-1} in *Rh-1HZX* (1188 cm^{-1} in *Rh-1U19*) as only this line does exhibit the characteristic coupling with C14H bending, shifting up by 33 cm^{-1} in C14D derivative (38 cm^{-1} in *Rh-1U19*). Similarly, the 1188 cm^{-1} mode in *Rh-1HZX* (1198 cm^{-1} in *Rh-1U19*) can be characterized as the C8−C9 stretch based on the 33 cm^{-1} (32

Table 1. Selected Calculated Normal Mode Frequencies (cm^{-1}) and Relative Intensities of the PSB11 Chromophore of Rhodopsin *Rh-1HZX* and *Rh-1U19* Models[c]

	Rh-1HZX		*Rh-1U19*		experiment	
assignment	freq	I/I_{1556}[a]	freq	I/I_{1545}[a]	freq	I/I_{1548}
C=N stretch	1640	0.004	1632	0.002	1655	0.069
in-phase C=C stretch	1556	1.000	1545	1.000	1548	1.000
C8−C9 stretch	1188	0.096	1198	0.023	1214	0.210
C12−C13 stretch	1184	0.075	1188	0.179	1238	0.250
C14−C15 stretch	1128	0.173	1132	0.074	1190	0.029
C10−C11 stretch	1058	0.004	1055	<0.001	1098	0.026
C11=C12 A_2 HOOP - C11=C12 torsion	982	0.153	990	0.327	970	0.260
C7=C8 A_u HOOP + C7=C8 torsion	960	0.033	958	0.044	976	[b]
C10H wag - C7=C8 B_g HOOP	857	0.074	847	0.066	882	<0.01
C7=C8 B_g HOOP + C10H wag	805	0.036	802	0.020	843	0.040

[a] Resonance Raman intensity of a mode relative to the intensity of the ethylenic stretching mode (1556 cm^{-1} in *Rh-1HZX* and 1545 cm^{-1} in *Rh-1U19*). Intensities were calculated using eq 5. [b] No detectable scaterring intensity in the observed spectrum (ref 8). [c] Comparison with the experimental data from ref 8.

cm^{-1} in *Rh-1U19*) upshift upon C10D substitution. The C10−C11 stretch in *Rh-1HZX* is predominantly localized at the 1058 cm^{-1} mode on the basis of its 11 cm^{-1} downshift to 1047 cm^{-1} in 10,11-^{13}C derivative. Also, the same magnitude of the shift in the 10,11-^{13}C spectrum of *Rh-1U19* indicates that the 1055 cm^{-1} mode is of C10−C11 character. A very weak C10−C11 line seen in the experimental spectrum[8] at 1098 cm^{-1} does have a negligible intensity in the calculated spectra. In *Rh-1U19* contribution from the C14−C15 single bond can be found in numerous modes; however, the mode with the strongest intensity is located at 1132 cm^{-1}. This mode becomes even stronger in *Rh-1HZX*. The assignment of the C14−C15 stretch at 1128 cm^{-1} is strongly supported by the 24 cm^{-1} (22 cm^{-1} in *Rh-1U19*) isotopic shift in the 14,15-^{13}C derivative in good agreement with the 22 cm^{-1} experimental shift.[7] Nevertheless, the calculated C14−C15 stretching frequency in both *Rh-1HZX* and *Rh-1U19* is considerably lower than the measured value (ca. 60 cm^{-1})[8] reflecting the exaggerated contribution from C−C−H and C−N−H bending motions. A prominent band calculated at ca. 1290 cm^{-1} in both cavities can be attributed to the 1268 cm^{-1} 11H−12H rocking, totally symmetric motion. The intensity of this mode calculated for *Rh-1HZX* and *Rh-1U19* is too strong relative to the corresponding ethylenic band when compared to the experimental intensity pattern.[8]

The analysis of the vibrational activity applied to the 1100−1650 cm^{-1} region shows a dramatic intensity increase of the line assigned to the C14−C15 stretching mode as compared to the intensities of the C8−C9 and C12−C13 stretchings when going from *Rh-1U19* to *Rh-1HZX*. Although the calculated RR intensities of the bands ascribed to C8−C9, C12−C13, and C10−C11 stretchings are too weak in comparison to the measured values,[8] these data indicate that the intensity pattern of the fingerprint region in the RR spectrum of *Rh-1U19* reveals closer agreement with the observed spectrum. It is interesting to note that the frequencies of the corresponding C−C stretching modes decrease, while the frequency of the corresponding ethylenic mode increases in *Rh-1HZX* relative to *Rh-1U19*, thus reflecting more delocalized electronic structure of the red-absorbing *Rh-1U19* (Table 1).

In our studies we have selected a single scaling factor for all normal-mode frequencies; however, one may notice a rather interesting pattern—the frequencies of the C−C stretches are consistently 16−62 cm^{-1} downshifted relative to the experimental values. A rationale for the red-shifted C−C frequencies is the CASSCF tendency to lengthen the C−C single bonds in retinal backbone.[44] On the other hand, there is no anticipated blueshift of the in-phase C=C frequency in both rhodopsin models (3 cm^{-1} decrease in *Rh-1U19* and 8 cm^{-1} increase in *Rh-1HZX*) as compared to the observed value,[7] despite the fact that CASSCF-based C=C bonds are strongly strengthened in relation to experimental data.[5] However, the inclusion of a dynamic correlation energy through denisity functional theory (DFT) frequency calculations on the CASSCF-derived equilibrium structures of both rhodopsin models shifts the calculated frequency of the C11=C12 stretching mode above the measured value up to 1557 cm^{-1} in *Rh-1U19* and 1567 cm^{-1} in *Rh-1HZX*.[50] Moreover, reduced active space in the CASSCF calculations and consequently unbalanced electron correlation as well as modest basis set also have a large impact on the systematic deviation of the calculated frequencies and the measured ones. To refine C−C vibrational frequencies one would have to derive a set of scaling factors, but this is beyond the scope of the present work.

In contrast to the fingerprint modes, HOOP modes are highly localized, and their assignment becomes straightforward. Since the relative intensity of these modes is sensitive to structural perturbation it does provide information on protein-chromophore interactions in rhodopsin,[7,8] rhodopsin intermediates,[45−48] and other visual pigments.[42,49] The spectrum of *Rh-1HZX* is characterized by strong bands at 1015, 982, 960, and 947 cm^{-1} that have their counterparts in *Rh-1U19* spectrum at 1013, 990, 958, and 941 cm^{-1}. The bands at ca. 1130 cm^{-1} are assigned to methyl rocking vibrations. The calculations predict that the 990 cm^{-1} mode contains HOOP and torsional character of the C11=C12 bond. This mode was observed at 970 cm^{-1} in the experimental resonance Raman spectrum.[8] It shifts down by 8 cm^{-1} and decreases in intensity when going from *Rh-1U19* to *Rh-1HZX*. The normal mode calculated at ca. 960 cm^{-1} in both *Rh-1HZX* and *Rh-1U19* is a coupled vibration of the C7=C8 A_u HOOP and C7=C8 torsion. This HOOP mode was detected experimentally at 976 cm^{-1}.[8] It seems that *Rh-1HZX* provides slightly better correlation with the experimental data concerning C11=C12 and C7=C8 HOOP frequencies. On the other hand, a rather strong C11=C12 HOOP peak in *Rh-1U19* closely mirrors the observed intensity (Table 1). There is yet another intense band in this region located at essentially the same frequency (941 cm^{-1} in *Rh-1U19* and 947 cm^{-1} in *Rh-1HZX*) and having the same intensity in both models with large contributions from C14H and NH waggings. It has no detectable intensity in the experimental spectrum. Finally, two normal modes calculated at 847 and 802 cm^{-1} in *Rh-1U19* (857 and 805 cm^{-1} in *Rh-1HZX*) have been assigned to C10H wag in combination with the C7=C8 B_g HOOP mode. The former mode is characterized by stronger, while the latter one by weaker C10H wag relative amplitude (Table 1). Frequencies of C10H wag in both models are only slightly affected by 10,11-^{13}C substitution (ca. 3 cm^{-1}) but downshift dramatically upon C_{10}-D substitution (ca. 125 cm^{-1}) in line with experimental data.[51]

Conclusions

In this work we have investigated how the change in the reference X-ray crystallographic structure including the relocation of a protein pocket internal water molecule may affect the vibrational properties of rhodopsin. Accordingly, the resonance Raman spectra of *Rh-1U19* and *Rh-1HZX* have been simulated by performing CASSCF/Amber vibrational frequency calculations supported by normal mode and isotopic substitution analyses.

On the basis of high-level *ab initio* calculations we managed to describe subtle changes in the vibrational structure of rhodopsin chromophore. Specifically, a significantly shorter counterion-Schiff base distance in *Rh-1U19* relative to *Rh-1HZX* manifests itself in altered vibrational frequencies and/or intensities of ethylenic, C−C bond stretching, and HOOP modes as well as frequency shift induced by N-deuteration of C=ND. Additionally, the downshifted ethylenic frequency of *Rh-1U19* is consistent with a redshift of its absorption maximum in agreement with previous studies on the electronic absorption spectra.[6]

A comparison of the most characteristic parts of the resonance Raman spectra calculated for *Rh-1HZX* and *Rh-1U19* with their experimental counterparts[8] reveals the following:

(1) The RR intensity distribution of the ethylenic band in both rhodopsin models is very similar to each other and quite similar to the experimental one. Frequencies of the vibrational modes in the C=C ethylenic band of *Rh-1U19* are in better agreement with the experimental values, e.g. the most active C=C mode is calculated at 1545 cm^{-1} for the *Rh-1U19* model, which is only 3 cm^{-1} off the experimental value, while this difference equals 8 cm^{-1} for *Rh-1HZX*.

(2) The location of the C−C vibrational modes in the fingerprint region of *Rh-1U19* more closely resembles the pattern of the measured spectrum than does the simulated spectrum based on the *Rh-1HZX* model—the frequencies of the *Rh-1U19* modes lie 4−10 cm^{-1} closer to their experimental counterparts than *Rh-1HZX* modes with the exception of the C10−C11 mode which reveals 3 cm^{-1} smaller gap between theory and experiment in case of *Rh-1HZX* model. Also, the RR intensities of C−C vibrational modes of *Rh-1U19* reveal closer agreement with the corresponding experimental intensities.

(3) The C=NH mode and its deuterated form −C=ND are calculated at frequencies that become sligthly closer (by ca. 3 cm^{-1}) to the corresponding measured values[7] in case of *Rh-1HZX* than *Rh-1U19*; however, the significantly lower deuterium shift obtained for the former model (24 cm^{-1} in *Rh-1HZX* vs 42 cm^{-1} in *Rh-1U19*) reflects the weakened Schiff base hydrogen bonding in *Rh-1HZX* as compared to the one in *Rh-1U19*.

(4) In the HOOP region observed in the 900 to 1050 cm^{-1} frequency range the relative intensity pattern of the 9-Me rock and the most active C11=C12 HOOP mode is reversed with respect to the experimental spectrum. DFT-based simulation of this spectral region, which reveals correct intensity distribution, points out to the importance of dynamic correlation effects in quantitative reproduction of the HOOP region of RR spectra of rhodopsin.[50]

Minor discrepancies between observed and calculated intensities may originate from both shortcomings of the approximate sum-overstates model, e.g. the assumption that only FC-type scattering is important and/or the neglect of the normal coordinate rotation and anharmonic effects as well as from shortcomings of the QM/MM methodology, e.g. reduced active space, lack of dynamic correlation energy, truncated basis set, lack of force field polarizibility[52] or chosen ionization status of protein residues (e.g. for Glu181).

Overall, despite the limited level of theory employed to calculate the RR spectra, our calculations do a fairly good job in reproducing the major structural features of the rhodopsin spectrum. In particular, the *Rh-1U19* model of rhodopsin seems to offer a slightly better agreement with the experimental resonance Raman spectrum[8] than *Rh-1HZX* model does.

Acknowledgment. M.O. is grateful to the Center for Photochemical Sciences and the College of Arts and Sciences for start-up funding.

Supporting Information Available: Simulated resonance Raman spectra obtained from the sum-over-states formalism and "short-time" approximation of Heller's time dependent approach. This material is available free of charge via the Internet at http://pubs.acs.org.

References

(1) Mathies, R. A.; Lugtenburg, J. In *Handbook of Biological Physics*; Stavenga, D. G., De Grip, W. J., Pugh, N. A., Jr., Eds.; Elsevier: New Amsterdam, The Netherlands, 2000; Vol. 3, pp 55−90.

(2) Palczewski, K.; Kumasaka, T.; Hori, T.; Behnke, C. A.; Motoshima, H.; Fox, B. A.; Le Trong, I.; Teller, D. C.; Okada, T.; Stenkamp, R. E.; Yamamoto, M.; Miyano, M. *Science* **2000**, *289*, 739–745.

(3) Teller, D. C.; Okada, T.; Behnke, C. A.; Palczewski, K.; Stenkamp, R. E. *Biochemistry* **2001**, *40*, 7761–7772.

(4) Okada, T.; Fujiyoshi, Y.; Silow, M.; Navaro, J.; Landau, E. M.; Shichida, Y. *Proc. Natl. Acad. Sci. U.S.A.* **2002**, *99*, 5982–5987.

(5) Okada, T.; Sugihara, M.; Bondar, A. N.; Elstner, M.; Entel, P.; Buss, V. *J. Mol. Biol.* **2004**, *342*, 571–583.

(6) Strambi, A.; Coto, P. B.; Ferré, N.; Olivucci, M. *Theor. Chem. Acc.* **2007**, *118*, 185–191.

(7) Palings, I.; Pardoen, J. A.; Van der Berg, E.; Winkel, C.; Lugtenburg, J.; Mathies, R. A. *Biochemistry* **1987**, *26*, 2544–2556.

(8) Lin, S. W.; Groesbeek, M.; van der Hoef, I.; Verdegem, P.; Lugtenburg, J.; Mathies, R. A. *J. Phys. Chem. B* **1998**, *102*, 2787–2806.

(9) Kochendoerfer, G. G.; Lin, S. W.; Sakmar, T. P.; Mathies, R. A. *Trends. Biochem. Sci.* **1999**, *24*, 300–305.

(10) Kandori, H.; Schichida, Y.; Yoshisawa, T. *Biochemistry (Moscow)* **2001**, *66*, 1197–1209.

(11) Ferré, N.; Olivucci, M. *J. Am. Chem. Soc.* **2003**, *125*, 6868–6869.

(12) Andruniów, T.; Ferré, N.; Olivucci, M. *Proc. Natl. Acad. Sci. U.S.A.* **2004**, *101*, 17908–17913.

(13) Frutos, L. M.; Andruniów, T.; Ferré, N.; Olivucci, M. *Proc. Natl. Acad. Sci. U.S.A.* **2007**, *104*, 7764–7769.

(14) Birge, R. R.; Murray, L. P.; Pierce, B. M.; Akita, H.; Baloghnair, V.; Findsen, L. A.; Nakanishi, K. *Proc. Natl. Acad. Sci. U.S.A.* **1985**, *82*, 4117–4121.

(15) Yan, E. C. Y.; Kazmi, M. A.; Ganim, Z.; Hou, J. M.; Pan, D. H.; Chang, B. S. W.; Sakmar, T. P.; Mathies, R. A. *Proc. Natl. Acad. Sci. U.S.A.* **2003**, *100*, 9262–9267.

(16) Yan, E. C. Y.; Kazmi, M. A.; De, S.; Chang, B. S. W.; Seibert, C.; Marin, E. P.; Mathies, R. A.; Sakmar, T. P. *Biochemistry* **2002**, *41*, 3620–3627.

(17) Ludeke, S.; Beck, R.; Yan, E. C. Y.; Sakmar, T. P.; Siebert, F.; Vogel, R. *J. Mol. Biol.* **2005**, *353*, 345–356.

(18) Martinez-Mayorga, K.; Pitman, M. C.; Grossfield, A.; Feller, S. E.; Brown, M. F. *J. Am. Chem. Soc.* **2006**, *128*, 16502–16503.

(19) Rohrig, U. F.; Guidoni, L.; Rothlisberger, U. *Biochemistry* **2002**, *41*, 10799–10809.

(20) Han, M.; Dedecker, B. S.; Smith, S. O. *Biophys. J.* **1993**, *65*, 899–906.

(21) Hall, K. F.; Vreven, T.; Frisch, M. J.; Beapark, M. J. *J. Mol. Biol.* **2008**, *383*, 106–121. Fahmy, K.; Jager, F.; Beck, M.; Zvyaga, T. A.; Sakmar, T. P.; Siebert, F. *Proc. Natl. Acad. Sci. U.S.A.* **1993**, *90*, 10206–10210.

(22) Cornell, W. D.; Cieplak, P.; Bayly, C. I.; Gould, I. R.; Merz, K. M., Jr.; Ferguson, D. M.; Spellmeyer, D. C.; Fox, T.; Caldwell, J. W.; Kollman, P. A. *J. Am. Chem. Soc.* **1995**, *117*, 5179–5197.

(23) Sinicropi, A.; Andruniów, T.; Ferré, N.; Basosi, R.; Olivucci, M. *J. Am. Chem. Soc.* **2005**, *127*, 11534–11535.

(24) Andruniów, T.; Fantacci, S.; De Angelis, F.; Ferré, N.; Olivucci, M. *Angew. Chem., Int. Ed.* **2005**, *44*, 6077–6081.

(25) Lumento, F.; Zanirato, V.; Fusi, S.; Busi, E.; Latterini, L.; Elisei, F.; Sinicropi, A.; Andruniów, T.; Ferré, N.; Basosi, R.; Olivucci, M. *Angew. Chem., Int. Ed.* **2007**, *46*, 412–420.

(26) Jamroz, M. H. *Vibrational Energy Distribution Analysis VEDA 4*; Warszawa, 2004.

(27) Albrecht, A. C. *J. Chem. Phys.* **1961**, *34*, 1476–1484.

(28) Manneback, C. *Physica* **1951**, *XVII*, 1001–1010.

(29) Negri, F.; Orlandi, G. Electronic and vibronic spectra of molecular systems: models and simulations based on quantum chemically computed molecular parameters. In *Computational Photochemistry*; Olivucci, M., Ed.; Elsevier: New Amsterdam, The Netherlands, 2005; Vol. 16, pp 129−169.

(30) Andruniow, T.; Pawlikowski, M. *Acta Phys. Polon.* **1996**, *93*, 707–715.

(31) Andruniow, T.; Pawlikowski, M.; Zgierski, M. Z. *J. Phys. Chem. A* **2000**, *104*, 845–851.

(32) Tonks, D. L.; Page, J. B. *Chem. Phys. Lett.* **1979**, *66*, 449–453.

(33) Blazej, D. C.; Peticolas, W. L. *J. Chem. Phys.* **1980**, *72*, 3134–3142.

(34) Chinsky, L.; Laigle, A.; Peticolas, W. L.; Turpin, P.-Y. *J. Chem. Phys.* **1982**, *76*, 1–5.

(35) Peticolas, W. L.; Rush, T., III *J. Comput. Chem.* **1995**, *16*, 1261–1270.

(36) Neugebauer, J.; Hess, B. A. *J. Chem. Phys.* **2004**, *120*, 11564–11577.

(37) Lee, S.-Y.; Heller, E. *J. Chem. Phys.* **1979**, *71*, 4777–4788.

(38) Meyers, A. B.; Mathies, R. A.; Tannor, D. J.; Heller, E. J. *J. Chem. Phys.* **1982**, *77*, 3857–3866.

(39) Myers, A. B. *J. Raman Spectrosc.* **1997**, *28*, 389–401.

(40) Frisch, M. J.; Trucks, G. W.; Schlegel, H. B.; Scuseria, G. E.; Robb, M. A.; Cheesman, J. R.; Montgomery, J. A., Jr.; Vreven, T.; Kudin, K. N.; Burant, J. C.; Millam, J. M.; Iyengar, S. S.; Tomasi, J.; Barone, V.; Mennucci, B.; Cossi, M.; Scalmani, G.; Rega, N.; Petersson, G. A.; Nakatsuji, H.; Hada, M.; Ehara, M.; Toyota, K.; Fukuda, R.; Hasegawa, J.; Ishida, M.; Nakajima, T.; Honda, Y.; Kitao, O.; Nakai, H.; Klene, M.; Li, X.; Knox, J.; Hratchian, H. P.; Cross, J. B.; Bakken, V.; Adamo, C.; Jaramillo, J.; Gomperts, R.; Stratmann, R. E.; Yazyev, O.; Austin, A. J.; Cammi, R.; Pomelli, C.; Ochterski, J. W.; Ayala, P. Y.; Morokuma, K.; Voth, G. A.; Salvador, P.; Dannenberg, J. J.; Zakrzewski, V. G.; Dapprich, S.; Daniels, A. D.; Strain, M. C.; Farkas, O.; Malick, D. K.; Rabuck, A. D.; Raghavachari, K.; Foresman, J. B.; Ortiz, J. V. Cui, Q.; Baboul, A. G.; Clifford, S.; Cioslowski, J.; Stefanov, B. B.; Liu, G.; Liashenko, A.; Piskorz, P.; Komaromi, I.; Martin, R. L.; Fox, D. J. Keith, T.; Al-Laham, M. A.; Peng, C. Y.; Nanayakkara, A.; Challacombe, M.; Gill, P. M. W.; Johnson, B.; Chen, W.; Wong, M. W.; Gonzalez, C.; People, J. A. *Gaussian03, revision C02*; Gaussian Inc.: Wallingford, CT, 2004.

(41) Ponder, J. W.; Richards, F. M. *J. Comput. Chem.* **1987**, *8*, 1016–1024.

(42) Pan, D.; Ganim, Z.; Kim, J. E.; Verhoeven, M. A.; Lugtenberg, J.; Mathies, R. A. *J. Am. Chem. Soc.* **2002**, *124*, 4857–4864.

(43) Touw, S. I. E.; De Groot, H. J. M.; Buda, F. *J. Phys. Chem. B* **2004**, *108*, 13560–13572.

(44) Aquino, A. J. A.; Barbatti, M.; Lischka, H. *ChemPhysChem* **2006**, *7*, 2089–2096.

(45) Palings, I.; Van der Berg, E. M. M.; Lugtenburg, J.; Mathies, R. A. *Biochemistry* **1989**, *28*, 1498–1507.

(46) Yan, E. C. Y.; Ganim, Z.; Kazmi, M. A.; Chang, B. S. W.; Sakmar, T. P.; Mathies, R. A. *Biochemistry* **2004**, *43*, 10867–10876.

(47) Kim, J. E.; Mc Camant, D. W.; Zhu, L.; Mathies, R. A. *J. Phys. Chem. B* **2001**, *105*, 1240–1249.

(48) Kukura, P.; Mc Camant, D. W.; Yoon, S.; Wandschneider, D. B.; Mathies, R. A. *Science* **2005**, *310*, 1006–1009.

(49) Pan, D.; Mathies, R. A. *Biochemistry* **2001**, *40*, 8557–8562.

(50) B3LYP/6-31g* Hessian calculations on the CASSCF/Amber optimized ground-state equilibrium structure. For DFT vibrational frequencies 0.97 scaling factor was employed.

(51) Eyring, G.; Curry, B.; Broek, A.; Lugtenburg, J.; Mathies, R. *Biochemistry* **1982**, *21*, 384–393.

(52) Söderhjelm, P.; Husberg, C.; Strambi, A.; Olivucci, M.; Ryde, U. *J. Chem. Theory Comput.* **2009**, *5*, 649–658.

CT900071C

J. Chem. Theory Comput. **2009,** *5,* 3105–3113

JCTC Journal of Chemical Theory and Computation

An Improved Reaction Coordinate for Nucleic Acid Base Flipping Studies

Kun Song,[†] Arthur J. Campbell,[†] Christina Bergonzo,[†] Carlos de los Santos,[‡]
Arthur P. Grollman,[‡] and Carlos Simmerling*,[†,§]

Department of Chemistry, Department of Pharmacological Sciences, and Center for Structural Biology, Stony Brook University, Stony Brook, New York 11794-3400

Received April 2, 2009

Abstract: Base flipping is a common strategy utilized by many enzymes to gain access to the functional groups of nucleic acid bases in duplex DNA which are otherwise protected by the DNA backbone and hydrogen bonding with their partner bases. Several X-ray crystallography studies have revealed flipped conformations of nucleotides bound to enzymes. However, little is known about the base-flipping process itself, even less about the role of the enzymes. Computational studies have used umbrella sampling to elicit the free energy profile of the base-flipping process using a pseudodihedral angle to represent the reaction coordinate. In this study, we have used an unrestrained trajectory in which a flipped base spontaneously reinserted into the helix in order to evaluate and improve the previously defined pseudodihedral angle. Our modified pseudodihedral angles use a new atom selection to improve the numerical stability of the restraints and also provide better correlation to the extent of flipping observed in simulations. Furthermore, on the basis of the comparison of potential of mean force (PMF) generated using different reaction coordinates, we observed that the shape of a flipping PMF profile is strongly dependent on the definition of the reaction coordinate, even for the same data set.

1. Introduction

Base flipping (also known as base eversion) is a type of local DNA motion in which a base group loses the hydrogen bonds with its base pair partner and is everted from the intra-helical to extra-helical position.[1] Base flipping was first observed in the DNA/methyltransferase complex X-ray crystal structure.[2,3] Studies have shown that base flipping is a common strategy for enzymes to read and chemically modify base groups which are otherwise protected by their base pair partner, or their own sugar and phosphate groups.[1] A variety of these enzymes exist, such as methyltransferases, glycosylases, and endonucleases. A number of crystal structures with everted DNA base groups inside the active site of the enzyme have been published.[4−8] These structures reveal the conformations of the everted base groups, but they provide little insight into the conformational changes that occur during the flipping process and, more importantly, the possible transient role of enzyme functional groups in the facilitation of base flipping. The rate of base flipping can be measured experimentally by methods such as proton exchange.[9,10] However, studies have shown that this method may overestimate the flipping rate since proton exchange may occur in structures with limited solvent accessibility and thus not require complete base flipping.[11]

Several computational approaches have been applied to this subject.[11−19] It is currently necessary to force eversion using restraints in order to model the process during computationally tractable simulations since uncatalyzed base flipping occurs on the millisecond time scale.[9] In one of the earliest studies, Keepers et al. used a distance restraint between the N1(pyrimidine) and N3(purine) to force the base pair to break.[20,21] However, the distance restraint cannot specify which of the two bases to flip, or distinguish between major or minor groove flipping pathways. Inspired by the correlation between the base opening angle and the ζ dihedral

---

* Corresponding author e-mail: carlos.simmerling@stonybrook.edu.

[†] Department of Chemistry.

[‡] Department of Pharmacological Sciences.

[§] Center for Structural Biology.

10.1021/ct9001575 CCC: $40.75

Table 1. Sequence of the Duplex DNA Used in Our Simulations[a]

	1	2	3	4	5	6	7	8	9	**10**	11	12	13	14	15	16		
		G	G	T	A	G	A	T	C	**C**	G	G	A	C	G	C		
5′	A	C	C	A	T	C	T	A	G	**G**	C	C	T	G	C	G	T	5′
		32	31	30	29	28	27	26	25	**24**	23	22	21	20	19	18	17	

[a] The base pair C10:G24 is the targeted central base pair, and G24 is the target base for flipping.

angle seen in the crystal structure, Chen et al. applied restraint forces on the ζ angle and glycosidic angles of the target nucleotide to force base pair opening.[22] This procedure assumes that only two backbone dihedral angles of the targeted nucleotide are responsible for base flipping, which may not be generally true. It has been shown that using this method can generate artificial conformations.[12] More promising approaches have employed more sophisticated reaction coordinates; these have been applied by Lavery and coworkers using internal coordinates[13−16] and MacKerell and co-workers using a center of mass pseudodihedral angle[11,17−19] (the latter is hereafter referred to as the CPD angle). The results from these two approaches are in reasonable agreement. Due to the nature of its definition using a standard dihedral angle with points defined by center of mass groups, MacKerell's pseudodihedral angle method is relatively easier to implement in current molecular dynamics simulation algorithms. An excellent recent application of this method to cytosine 5-methyltransferase from HhaI suggests that the enzyme shifts the equilibrium to the flipped state by destabilizing the DNA duplex and stabilizing the everted conformation.[17]

In the present study, we first tested the CPD definition to study base flipping using the Amber simulation package and then improved the CPD definition.[23] Our results show that MacKerell's highly valuable CPD definition can have several potential disadvantages in spite of its multiple strengths. Using the traditional CPD definition, we find that there are large energy fluctuations and occasional simulation instability when the base is everted. Another disadvantage is that there is not a unique mapping between the CPD angle and the extent of eversion; we observed that significantly different structures can have comparable CPD angles when using the previous definition. On the basis of our molecular dynamics (MD) simulations of spontaneous base pair formation in unrestrained simulation, we identified several reasons for the weaknesses described above. We thus modified the CPD definition to employ two separate definitions of different groups of atoms to define the pseudodihedral angle (hereafter referred to as CPDa and CPDb); we find that these better represent base flipping. Simulations using the CPDa/b reaction coordinates were able to give a more reliable representation of the base-flipping pathway with improved correlation between the reaction coordinate and the extent of eversion, along with improved simulation stability. The two new CPDa/b angles were applied to calculate the free energy profile of base flipping for guanine in a DNA duplex. The free energy barrier of the base flipping is comparable with that of previous studies. The relationship between the specific definition of the reaction coordinate and the overall shape of the resulting free energy profile is discussed.

2. Methods

2.1. System Preparation. The initial structure was standard B-form duplex DNA built using the NUCGEN program in the Amber simulation package.[23] The DNA sequence used is shown in Table 1 below. The targeted central base pair for flipping was C10:G24, and G24 was the base group (hereafter referred to as the target base group) for base flipping.

The initial coordinate and parameter files were created using the LEAP module of Amber on the basis of the structure generated by NUCGEN, solvated in truncated octahedron boxes with a minimum 8 Å buffer between the box edge and the nearest solute atom. The TIP3P water model[24] was used to explicitly represent water molecules. The DNA parameters employed ff99,[25,26] with the parmBSC0 modified α/γ torsional terms.[27] These coordinates were used for all simulations.

2.2. Molecular Dynamics Simulations. All molecular dynamics simulations were carried out with the SANDER module in Amber.[23] Following the procedure used in previous studies,[28,29] the solvated systems were minimized and equilibrated in three steps: (i) 50 ps MD simulation[30] with DNA atoms constrained and movement allowed only for water; (ii) five 1000-step cycles of minimization, in which the positional restraints on the DNA were gradually decreased; (iii) four cycles of 5000-step MD simulation with decreasing restraints on the DNA. A final 500 ps of MD was performed without restraints. The resulting structures were used in umbrella sampling simulations.

SHAKE[31] was used to constrain bonds involving hydrogen atoms. The nonbonded cutoff was 8 Å. The particle mesh Ewald method[32,33] was used to calculate long-range electrostatics. Constant pressure (1 atm) and temperature (330 K, slightly elevated to improve sampling) were maintained by the weak coupling algorithm with a coupling constant of 1 ps.[34] A 0.002 ps time step was used.

2.3. Structural Analysis. To obtain unbiased structural analyses on the three types of reaction coordinates presented in this work, we generated an unrestrained MD simulation starting from a structure containing an everted target base, which then spontaneously reinserted into the duplex during the simulation. In this simulation, the same sequence of DNA duplex and the simulation conditions described in the previous sections were used. The root-mean-square deviation (rmsd) of all heavy atoms in the central three base pairs was calculated, with the reference structure of a standard B-form duplex DNA. The glycosidic angle of the G24 nucleotide was also measured, using the dihedral angle O4′−C1′−N9−C4. The distance between the central base pair units is represented by the distance between N1 of G24 and N3 of C10.

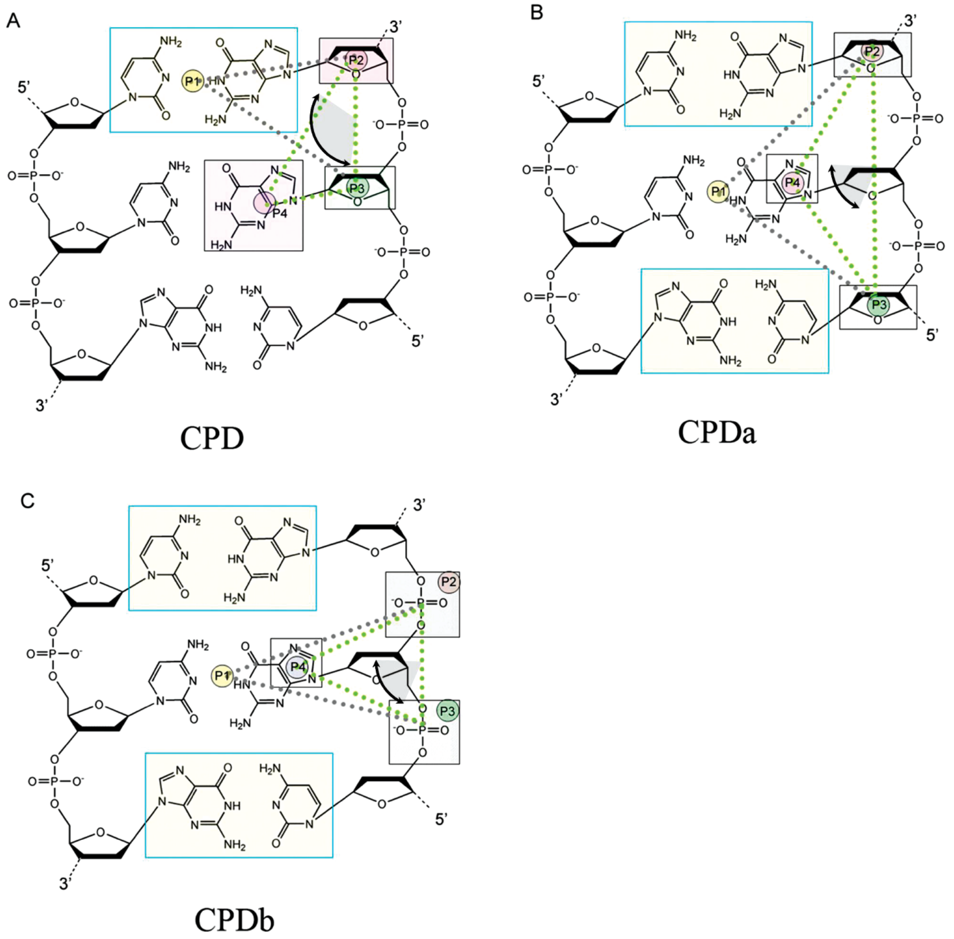

Figure 1. Definitions of various reaction coordinates for base eversion. (A) CPD: MacKerell et al.'s original COM pseudodihedral angle definition. (B) CPDa: the modified COM pseudodihedral (CPD) angle definition, in which p1 is defined by the mass center of the two flanking base pairs, p2 and p3 are defined by the flanking sugar groups, and p4 is defined by the five-member ring of the flipping purine (or the entire six-membered ring for a flipping pyrimidine). (C) CPDb: a similar definition to that of CDPa, but using the phosphate groups for p2 and p3. The dotted lines show the two planes which define the pseudodihedral angles.

2.4. The Definition of the Base-Opening Dihedral Angle. Umbrella sampling[35−38] was used to calculate the potential of mean force (PMF) as a function of our new center of mass pseudodihedral angles CPDa/b. The definitions of two proposed variations on this new flipping metric, CPDa and CPDb, are shown in Figure 1. The Sander module of Amber9 was modified to support these restraints. The four points for each dihedral form two triangular planes which share one side defined between P2 and P3. The base opening angle is defined by the angle between these two planes. Changes from the definition of MacKerell at al. involve the use of both flanking base pairs for the P1 center of mass (as opposed to only one flanking pair) and using either the sugars or phosphates flanking the flipping base as points P2 and P3. Point P4 was defined using only the five-member ring of the purine in order to remove the influence of glycosidic rotation on the flipping angle, which occurs if the entire purine base is included in COM point P4 (data not shown).

2.5. Umbrella Sampling and Potential of Mean Force Calculations. The procedure for umbrella sampling was adapted from previous studies.[11] Starting from the standard B-form conformation, the initial structure of each window was generated by a 0.5 ps simulation with a restraint force constant of 10 000 kcal/(mol × radian^2) in a serial fashion, which used the previous window's last structure as the starting structure of the current window. Each window was separated by 5° from the flanking windows. After the initial structures were generated, 500 ps simulations using the same definition of restraint and a 1000 kcal/(mol × radian^2) restraint constant were carried out for the sampling. The eversion angle and energy data were recorded at each time step. The other parameters of these simulations were the same as those of the standard MD simulations. The resulting PMF was obtained by a WHAM analysis[36−38] of the data using a program provided by Alan Grossfield (freely available at http://dasher.wustl.edu/alan).

3. Results and Discussion

3.1. Simulation of Spontaneous Base Pair Formation. Umbrella sampling simulations provide the PMF along the chosen reaction coordinates for a system. To generate an accurate free energy profile along a conformational change of interest, the reaction coordinate should be able to represent conformational change faithfully. To evaluate the extent to which various reaction coordinates can represent the process

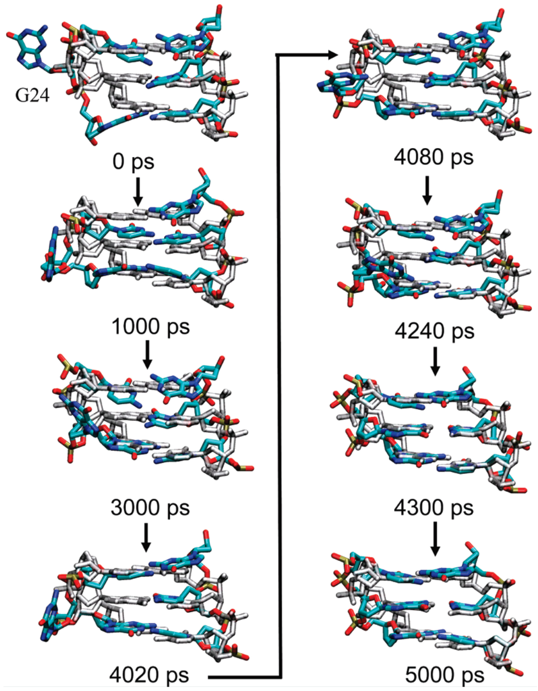

Figure 2. Snapshots taken from the base pair reforming trajectory viewed from the major groove. For clarity, water, hydrogen atoms, and DNA outside the central three base pairs are not shown. The simulated structures are colored by atom type. The structure in gray indicates the same duplex in a standard B-form conformation for reference. The time sequence is described in the text.

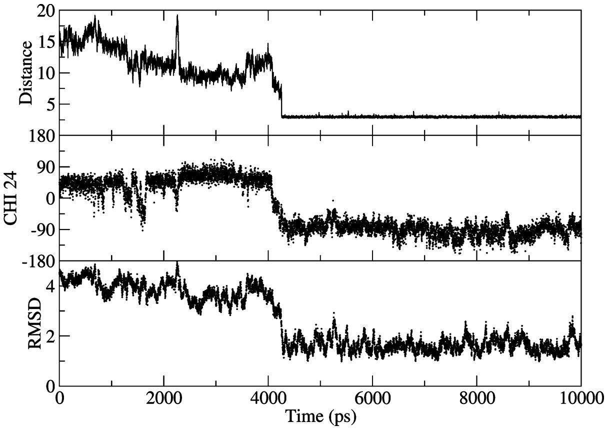

Figure 3. Data from the unrestrained trajectory with spontaneous base pair formation. The upper panel shows the heavy-atom-to-heavy-atom hydrogen-bonding distance between atom N1 of residue G24 and atom N3 of residue C10 between the bases in the new base pair. The middle panel shows the glycosidic angle of the flipped G24 nucleotide. The lower panel shows the rmsd of all atoms in the central three base pairs as compared to standard B-form DNA.

of a base-flipping event, we generated an unrestrained trajectory for a duplex in explicit water where a base pair spontaneously formed from the everted position, since it is a faster event than base opening. The starting structure was obtained from an umbrella sampling simulation using the CPD definition at −140°. A 10-ns unrestrained MD simulation was carried out. From the original everted position, the guanine spontaneously returned to the duplex and reformed the Watson−Crick base pair with the cytosine in less than 5 ns. Several snapshots taken from the trajectory are shown in Figure 2. In the starting structure (0 ps), the everted base (G24) is completely outside of the duplex. At ∼1 ns, it moved closer to the major groove, and the purine ring adopted a conformation nearly perpendicular to the other, stacked base groups. This conformation was stable until ∼3 ns, during which the purine ring attempted to reinsert into the duplex but was unsuccessful since the G24 was still in the syn conformation. It returned back to its previous everted position at ∼4 ns, adopted an anti conformation at ∼4.2 ns, and then successfully reinserted into the duplex at ∼4.3 ns. The newly formed base pair was stable for the remainder of the 10 ns simulation (only 5 ns is shown in Figure 2).

The observation of spontaneous base pair formation provides an excellent data set for evaluation of the various parameters in the base eversion restraints that will be used for umbrella sampling. In particular, any measure of base flipping should reproduce the observation that the first attempt at reinsertion by the base was unsuccessful, after which it moved back out of the major groove and then successfully inserted. We calculated several properties of the DNA duplex along this trajectory, such as the distance between the forming base pair (represented by the distance between N1 of G24 and N3 of C10), the glycosidic angle of the flipped G24 base, and the rmsd value of the central three base pairs relative to the standard B-form DNA. The results are shown in Figure 3.

At the beginning of the simulation, the distance between the central two bases was ∼15 Å. The flipped base G24 was in a syn conformation, with the glycosidic angle at ∼55°. The rmsd value of the central three base pairs was ∼5 Å compared to standard B-form DNA. The distance decreased to about 3 Å at ∼4.3 ns ps; further analysis confirmed that this was accompanied by the formation of all three Watson−Crick hydrogen bonds. The reformed hydrogen bonds were stable for the rest of the simulation. Also at 4.3 ns, the glycosidic angle changed to ∼ −90°, falling within the anti range, and the rmsd value decreased to ∼1.5 Å, indicating that the structure was highly similar to canonical B-form DNA.

3.2. Evaluation of Alternate Base Flipping Reaction Coordinates. The unrestrained MD trajectory exhibited a pathway of spontaneous base pair reforming, which provides an excellent data set for evaluation of the CPD reaction coordinate using COM groups as defined by MacKerell et al. and comparison to the modified approach with different selections for the COM groups (Figure 1). CPD denotes the base opening angle calculated using MacKerell's et al.'s center of mass pseudodihedral angle (Figure 1A). CPDa and CPDb are the new center of mass pseudodihedral angles (Figure 1B,C). During the analysis, we have found that, in the original CPD definition, the center of mass of the flipped base and the next two centers of mass can become collinear (Figure 4, structure image shown in Figure S1, Supporting Information). Therefore, we have also measured angles defined by these three neighboring COM positions for each CPD definition using the angle defined by points 2−3−4

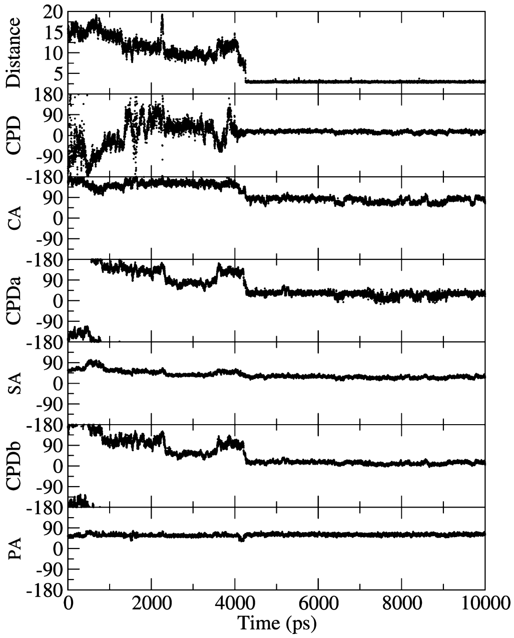

Figure 4. The evaluation of the reaction coordinates defined by MacKerell et al. and the new definitions. The first panel is the distance between the two bases in the base pair being formed, which is the heavy-atom-to-heavy-atom hydrogen-bonding distance between residue G24 atom N1 and residue C10 atom N3. The pseudodihedral angles are defined as the angles between two planes (see Figure 1). CPD is the original dihedral reaction coordinate. CPDa is the pseudodihedral angle using sugar groups. CPDb is the angle using phosphate groups. Angles between points 2, 3, and 4 for CPD, CPDa, and CPDb are shown as CA, SA (sugar angle), and PA (phosphate angle), respectively. Instability in the dihedral results when these angles adopt values very near 0° or 180°.

shown in Figure 1a. Instability in the dihedral calculation should be expected if this angle approaches 0° or 180°.

From Figure 4, we can see that there are several potential disadvantages using the COM groups as originally defined by the original CPD angle. The first disadvantage is that the reaction coordinate does not have a one-to-one correlation between the measured and actual extent of eversion. For example, CPD-dihedral angle values sampled for everted conformations (between 2100 and 3100 ps) are comparable to those sampled after the base pair has formed at 4300 ps. This means two different points on the base everting pathway will have the same value of the reaction coordinate. This is caused by the definition of the CPD angle; the last three points in the CPD definition (P2, P3, and P4, see Figure 1a) can become collinear in everted conformations, resulting in numerical instability. According to the original CPD definition, negative values denote flipping along a major groove pathway, and positive values indicate the minor groove pathway. While the sign of a particular flipping direction (major/minor) is arbitrary and depends on whether the CPD is defined from the 3′ or 5′ side of the flipping base, the data should be consistent once a definition of CPD is chosen. However, although the trajectory was visually confirmed to sample only the major groove pathway, the CPD during the simulation adopted both negative and positive values, suggesting that the sign is not a reliable indicator of the flipping directions.

By using the new definitions (CPDa and CPDb in Figure 4), the reaction coordinate values and the position of the base group have an improved correlation. The CPDa and CPDb angles gradually reduced from ~180° (extrahelical) at the beginning of the simulation to 50° at 2300 ps. The flipped base was close to its intrahelical position at 2300 ps, except that the base was in its syn conformation, not in the anti conformation required for proper Watson−Crick pairing (see the chi24 in Figure 3). Steric hindrance with the phosphodiester backbone prevents rotation about the glycosidic bond in this position; thus, the base once again moved out of the major groove, with the CPDa and CPDb correctly reflecting this change, with values increasing between 3600 and 4200 ps. The extra-helical base then rotated to an anti conformation and subsequently reinserted, restoring the Watson−Crick pair. This is represented with the low (~0) and steady values of the CPDa and CPDb flipping angles in Figure 4; we note that with the CPDa and CPDb definitions the intrahelical values (near 0) were not seen for any of the everted conformations. This is in contrast to the "intrahelical" CPD values observed at multiple points prior to the actual reinsertion event.

The second disadvantage of the original pseudodihedral definition is that one of the two angles (CA in Figure 4) connecting the four centers of mass can adopt values close to 0° or 180° when the base is extrahelical. From Figure 4, we can see that angle CA is very close to 180° before the base pair is reformed at about 4000 ps (the distance in panel 1 of Figure 4 can be used as an indicator of the base pair reforming). After the base pair formed (the distance becomes a steady line at about 3 Å), the CA angle adopted values near 90°. The dihedral angles are defined by four points, where each set of three consecutive points defines a plane. The dihedral angle is the angle between these two planes. When the last three consecutive points are close to being linear (0° or 180°), a slight change of the position of the fourth point can greatly change the definition of the second plane, which results in large fluctuations in the dihedral angle (the second panel in Figure 4) and resulting forces. This caused unpredictable instabilities in simulations with everted bases (data not shown); CPD dihedral angle differences of ~40° were observed for nearly identical structures sampled during short time spans (Figure S1, Supporting Information). In the new definitions, both angles (PA and SA in Figure 4) had values well away from 0° and 180° during the entire profile, resulting in improved numerical stability of the dihedral angle.

The third disadvantage of the old definition is less explicit. The definition of CPD is not symmetric (Figure 1), and the choice of P1 and P2 dihedral points as being either the 3′ or 5′ side of the flipping base is arbitrary. Due to the asymmetric structure of the DNA duplex, a free energy profile calculated using the two points from the 3′ side differs from that obtained with restraints for the dihedral points defined on the 5′ side. By using the new definition, the 5′ and 3′ sides

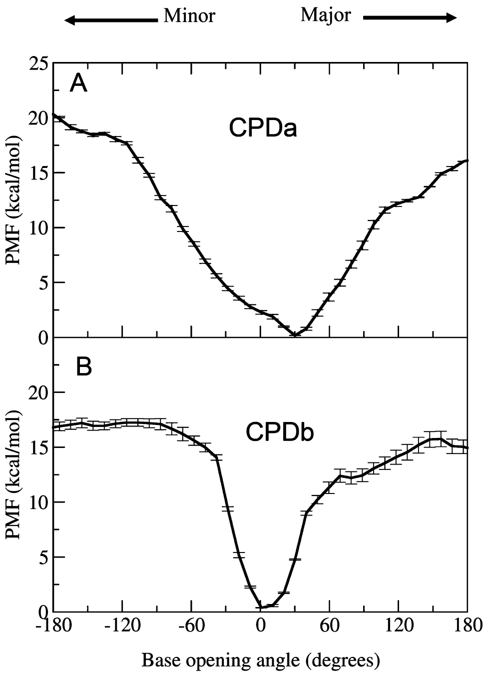

Figure 5. Free energy profiles using the two new pseudodihedral eversion definitions. The *x* axis is the pseudodihedral angle. Panel A shows the result using the center of mass of the sugar rings as points P2 and P3 (CPDa). Panel B shows the result using the center of mass of the phosphates as dihedral points P2 and P3 (CPDb). Positive/negative values reflect flipping into major/minor grooves, respectively. The solid line shows the free energy profile calculated using the last 400 ps of a total 500 ps per window. The error bar shows the difference of the results calculated using the last 400 ps data and the last 200 ps data.

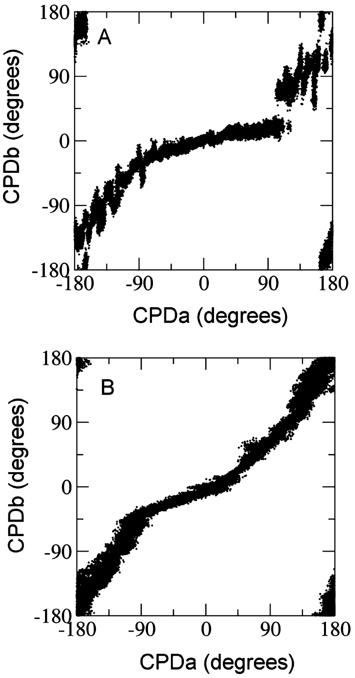

Figure 6. The correlation of the two CPDa/b definitions. Panel A shows the structures sampled using the CPDa restraint. Panel B shows the structures sampled using the CPDb restraint. The *x* axis shows the postprocessing results using CPDa, while data for CPDb are are on the *y* axis. Regardless of the restraint used to generate the structures, CPDa is more sensitive than CPDb to changes in the region near 0°.

are both included in a single calculation, with the resulting PMF being less ambiguous.

3.3. The Free Energy Profiles Calculated Using the New Definitions. The free energy profiles for base eversion using our two new CPDa/b dihedral angle definitions in umbrella sampling have been calculated (Figure 5). The upper panel shows the PMF profile using the centers of mass of the deoxyribose rings groups as dihedral points P2 and P3 (CPDa, Figure 1b). The lower panel shows the results using the phosphates as P2 and P3 (CPDb, Figure 1c). To estimate the convergence of the calculation, we also calculated the free energy profile using the second half of the data and generated error bars using the difference between the two results.

From Figure 5, we can see that there are certain similarities and differences between the two energy profiles. Both profiles can be divided into two regions: the "basin" and the "plateau" regions. The basin region is near the energy minimum and has a lower free energy and steeper slope. The plateau region reflects everted bases and is further from the minimum with a high free energy value and less energetic dependence on the angle. The basin region for the profile using the phosphate groups (CPDb) was between −45° and +45°. The basin using the sugar group for the PMF reaction coordinate (CPDa) is significantly broader, ranging from −120° to +120°. In both cases, the barriers of the PMFs (after the basin region ends) at the major groove pathway were lower than those at the minor groove pathway. The values for using the sugar rings were about 13 kcal/mol for the major groove and 18 kcal/mol for the minor groove. The values for using phosphate groups were about 12 kcal/mol for the major groove and 15 kcal/mol for the minor groove. These results agree reasonably with calculations by Banavali and MacKerell, showing that the energy barriers for G flipping are 18.7 and 21.3 kcal/mol for the major and minor groove, respectively.[11] The positions of the minima and height of the energy barriers of Benavali and MacKerell's and our studies are similar but do not exactly match. One possible reason is that the sequence contexts are different between these two studies. However, both experimental and theoretical studies have suggested that base opening rates have little dependence on sequence context.[9,39] The differences may also be due to the influence of the reaction coordinate definition on the PMF details, or the enforcement of periodicity in the free energy calculation, or the difference between CHARMm and Amber force fields. The present results are also comparable to the Amber results of Priyakumar and MacKerell,[12] though that study used an older version of the Amber DNA force field than used here.

Although the free energy barriers were similar in the two free energy profiles in Figure 5, the widths of the basin regions were significantly different. The basin is much wider for the CPDa definition. To understand why the free energy profiles are different, we calculated the correlations between CPDa and CPDb definitions for structures sampled in the two umbrella sampling runs, which are shown in Figure 6. Data from both simulations have a high correlation between

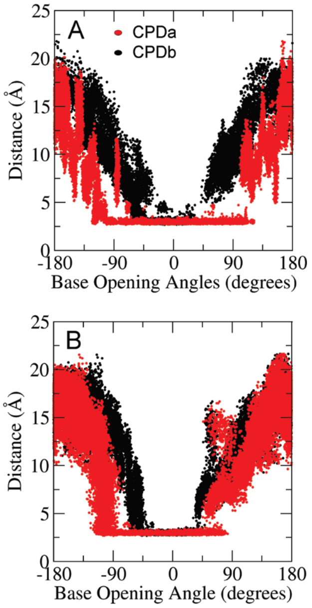

Figure 7. The correlation between the distance of the two bases (distance between atom N1 of residue G24 and atom N3 of residue C10) and the CPDa/b base opening angles. The upper figure shows the structures sampled in the umbrella sampling using CPDa as the reaction coordinate. The lower figure shows the structures sampled in the umbrella sampling using CPDb as the reaction coordinate. For each simulation, the data shown in red are the postprocessing results using the CPDa definition, and those in black are the results using CPDb. Both plots indicate that the CPDa definition has a broader range of values for base-paired structures as compared to CPDb, independent of which restraint was used to generate the flipping trajectory.

CPDa and CPDb values. However, both correlation figures are not straight lines. There is a flat phase near 0°, which corresponds to the intrahelical conformation of the base. In other words, the intrahelical space is wider using CPDa as reaction coordinates than using CPDb, even for the same structure sets. This is due to the difference in the geometry of the two definitions in the intrahelical region. In Figure 4, we can see that CPDa is has obtuse angle SA, and the PA of CPDb is ~60° when the base is in its intrahelical conformation. Since it corresponds to the intrahelical conformation, the basin region is wider in CPDa space.

We further analyzed the correlation between flipping angle and base pair distance to investigate the properties of these two reaction coordinate definitions (Figure 7). Figure 7a shows the structures sampled in the umbrella sampling simulation using the CPDa restraints. Figure 7b shows the structure sampled in the umbrella sampling simulation using CPDb restraints. For all structures in each simulation, we calculated the distance between the flipping base and its partner, as well as flipping angles measured using both dihedral definitions. As we observed with the comparison of the two dihedral angles in Figure 6, data from simulations performed with either definition as the restraint are consistent. In both cases, the base pair distance was about 3 Å and stable for the region around a base opening angle of 0°. In both simulations, the region of close contact between the bases covers a significantly larger range when using CPDa as a reaction coordinate than when using CPDb as a reaction coordinate, even when they were applied to the same set of structures. This confirms that CPDb is more sensitive to the true extent of base opening. We can also see that the structures sampled using CPDb (Figure 7b) are more similar among windows than the ones sampled using CPDa (Figure 7A). The structures sampled using CPDa (Figure 7a) seem more poorly converged. The reason CPDa and CPDb behave differently may be due to the number of internal coordinates encompassed in the two definitions. CPDb includes two phosphate groups and one sugar ring between P2 and P3, while CPDa includes two phosphate groups and three sugar rings (see Figure 1). Since the CPDa definition has a more complex conformation space, it is more sensitive to structural fluctuations in the backbone.

4. Conclusion

Base flipping is an important event, and computational tools have been shown to be essential in studying processes such as an enzymatic role in flipping. Starting from a flipped conformation, we have generated a fully unrestrained MD trajectory in which an everted guanine base spontaneously returned to its intrahelical conformation and reformed its Watson−Crick pair with the cytosine partner. This trajectory was used to evaluate a previously proposed pseudodihedral angle and how well it describes the extent of eversion. We found several disadvantages in the definition, including the potential for numerical instability, and used the data to propose two modified pseudodihedral definitions which can successfully avoid the observed disadvantages. The free energy profiles of the base flipping using the new definitions have been calculated, and the results reasonably agree with previously published results. We also compared the two modified definitions. The one using the center of mass of the phosphate groups has a tighter correlation with the base opening angle; therefore, it is a better representation for base flipping. The reaction coordinate using the center of mass of the sugar groups has a larger conformation space and appeared to be more difficult to use in generating well-converged data. In closing, we remind the reader that using any restraint to impose a reaction coordinate may introduce artifacts in the data as compared to fully unrestrained systems.

Supporting Information Available: Figures of structures with everted base and sample input file listing atoms in COM restraint groups for CPD definitions. This material is available free of charge via the Internet at http://pubs.acs.org.

Acknowledgment. Support for this project was provided by NIH GM6167803 (C.S.), CA17395 (A.P.G. & C.S.), NSF 0549370 (C.B. and A.J.C.), and supercomputer resources through the National Computational Science Alliance grant MCA02N028 (C.S.).

References

(1) Roberts, R. J.; Cheng, X. D. Base flipping. *Annu. Rev. Biochem.* **1998**, *67*, 181.

(2) Klimasauskas, S.; Kumar, S.; Roberts, R. J.; Cheng, X. D. HhaI Methyltransferase Flips Its Target Base out of the DNA Helix. *Cell* **1994**, *76*, 357–369.

(3) Reinisch, K. M.; Chen, L.; Verdine, G. L.; Lipscomb, W. N. The Crystal-Structure of Haeiii Methyltransferase Covalently Complexed to DNA - an Extrahelical Cytosine and Rearranged Base-Pairing. *Cell* **1995**, *82*, 143–153.

(4) Sugahara, M.; Mikawa, T.; Kumasaka, T.; Yamamoto, M.; Kato, R.; Fukuyama, K.; Inoue, Y.; Kuramitsu, S. Crystal structure of a repair enzyme of oxidatively damaged DNA, MutM (Fpg), from an extreme thermophile, Thermus thermophilus HB8. *Embo J.* **2000**, *19*, 3857–69.

(5) Fromme, J. C.; Verdine, G. L. Structural insights into lesion recognition and repair by the bacterial 8-oxoguanine DNA glycosylase MutM. *Nat. Struct. Biol.* **2002**, *9*, 544–52.

(6) Fromme, J. C.; Verdine, G. L. DNA lesion recognition by the bacterial repair enzyme MutM. *J. Biol. Chem.* **2003**, *278*, 51543–8.

(7) Gilboa, R.; Zharkov, D. O.; Golan, G.; Fernandes, A. S.; Gerchman, S. E.; Matz, E.; Kycia, J. H.; Grollman, A. P.; Shoham, G. Structure of formamidopyrimidine-DNA glycosylase covalently complexed to DNA. *J. Biol. Chem.* **2002**, *277*, 19811–6.

(8) Serre, L.; Pereira de Jesus, K.; Boiteux, S.; Zelwer, C.; Castaing, B. Crystal structure of the Lactococcus lactis formamidopyrimidine-DNA glycosylase bound to an abasic site analogue-containing DNA. *Embo J.* **2002**, *21*, 2854–65.

(9) Leroy, J. L.; Kochoyan, M.; Huynhdinh, T.; Gueron, M. Characterization of Base-Pair Opening in Deoxynucleotide Duplexes Using Catalyzed Exchange of the Imino Proton. *J. Mol. Biol.* **1988**, *200*, 223–238.

(10) Coman, D.; Russu, I. M. A nuclear magnetic resonance investigation of the energetics of basepair opening pathways in DNA. *Biophys. J.* **2005**, *89*, 3285–3292.

(11) Banavali, N. K.; MacKerell, A. D. Free energy and structural pathways of base flipping in a DNA GCGC containing sequence. *J. Mol. Biol.* **2002**, *319*, 141–160.

(12) Priyakumar, U. D.; MacKerell, A. D. Computational approaches for investigating base flipping in oligonucleotides. *Chem. Rev.* **2006**, *106*, 489–505.

(13) Giudice, E.; Varnai, P.; Lavery, R. Base pair opening within B-DNA: free energy pathways for GC and AT pairs from umbrella sampling simulations (vol 31, pg 1434, 2003). *Nucleic Acids Res.* **2003**, *31*, 2703–2703.

(14) Giudice, E.; Varnai, P.; Lavery, R. Energetic and conformational aspects of A:T base-pair opening within the DNA double helix. *ChemPhysChem.* **2001**, *2*, 673.

(15) Giudice, E.; Lavery, R. Nucleic acid base pair dynamics: The impact of sequence and structure using free-energy calculations. *J. Am. Chem. Soc.* **2003**, *125*, 4998–4999.

(16) Varnai, P.; Lavery, R. Base flipping in DNA: Pathways and energetics studied with molecular dynamic simulations. *J. Am. Chem. Soc.* **2002**, *124*, 7272–7273.

(17) Huang, N.; Banavali, N. K.; MacKerell, A. D. Protein-facilitated base flipping in DNA by cytosine-5-methyltransferase. *Proc. Natl. Acad. Sci. U. S. A.* **2003**, *100*, 68–73.

(18) Huang, N.; MacKerell, A. D. Specificity in protein-DNA interactions: Energetic recognition by the (cytosine-C5)-methyltransferase from HhaI. *J. Mol. Biol.* **2005**, *345*, 265–274.

(19) Priyakumar, U. D.; MacKerell, A. D. Base flipping in a GCGC containing DNA dodecamer: A comparative study of the performance of the nucleic acid force fields, CHARMM, AMBER, and BMS. *J. Chem. Theory Comput.* **2006**, *2*, 187–200.

(20) Keepers, J.; Kollman, P. A.; James, T. L. Molecular mechanical studies of base-pair opening in d(CGCGC):d(GCGCG), dG5.dC5, d(TATAT):d(ATATA), and dA5.dT5 in the B and Z forms of DNA. *Biopolymers* **1984**, *23*, 2499–511.

(21) Keepers, J. W.; Kollman, P. A.; Weiner, P. K.; James, T. L. Molecular mechanical studies of DNA flexibility: coupled backbone torsion angles and base-pair openings. *Proc. Natl. Acad. Sci. U. S. A.* **1982**, *79*, 5537–41.

(22) Chen, Y. Z.; Mohan, V.; Griffey, R. H. The opening of a single base without perturbations of neighboring nucleotides: a study on crystal B-DNA duplex d(CGCGAATTCGCG)2. *J. Biomol. Struct. Dyn.* **1998**, *15*, 765–77.

(23) Case, D. A.; Cheatham, T. E.; Darden, T.; Gohlke, H.; Luo, R.; Merz, K. M.; Onufriev, A.; Simmerling, C.; Wang, B.; Woods, R. J. The Amber biomolecular simulation programs. *J. Comput. Chem.* **2005**, *26*, 1668–1688.

(24) Jorgensen, W. L.; Chandrasekhar, J.; Madura, J. D.; Impey, R. W.; Klein, M. L. Comparison of Simple Potential Functions for Simulating Liquid Water. *J. Chem. Phys.* **1983**, *79*, 926–935.

(25) Cornell, W. D.; Cieplak, P.; Bayly, C. I.; Gould, I. R.; Merz, K. M.; Ferguson, D. M.; Spellmeyer, D. C.; Fox, T.; Caldwell, J. W.; Kollman, P. A. A 2Nd Generation Force-Field for the Simulation of Proteins, Nucleic-Acids, and Organic-Molecules. *J. Am. Chem. Soc.* **1995**, *117*, 5179–5197.

(26) Wang, J. M.; Cieplak, P.; Kollman, P. A. How well does a restrained electrostatic potential (RESP) model perform in calculating conformational energies of organic and biological molecules. *J. Comput. Chem.* **2000**, *21*, 1049–1074.

(27) Perez, A.; Marchan, I.; Svozil, D.; Sponer, J.; Cheatham, T. E., III.; Laughton, C. A.; Orozco, M. Refinement of the AMBER force field for nucleic acids: improving the description of alpha/gamma conformers. *Biophys. J.* **2007**, *92*, 3817–29.

(28) Song, K.; Hornak, V.; de Los Santos, C.; Grollman, A. P.; Simmerling, C. Computational analysis of the mode of binding of 8-oxoguanine to formamidopyrimidine-DNA glycosylase. *Biochemistry* **2006**, *45*, 10886–94.

(29) Song, K.; Hornak, V.; De Los Santos, C.; Grollman, A. P.; Simmerling, C. Molecular mechanics parameters for the FapydG DNA lesion. *J. Comput. Chem.* **2007**.

(30) Beveridge, D. L.; Barreiro, G.; Byun, K. S.; Case, D. A.; Cheatham, T. E., III.; Dixit, S. B.; Giudice, E.; Lankas, F.; Lavery, R.; Maddocks, J. H.; Osman, R.; Seibert, E.; Sklenar, H.; Stoll, G.; Thayer, K. M.; Varnai, P.; Young, M. A. Molecular dynamics simulations of the 136 unique tetranucleotide sequences of DNA oligonucleotides. I. Research design and results on d(CpG) steps. *Biophys. J.* **2004**, *87*, 3799–813.

(31) Ryckaert, J. P.; Ciccotti, G.; Berendsen, H. J. C. Numerical-Integration of Cartesian Equations of Motion of a System with Constraints - Molecular-Dynamics of N-Alkanes. *J. Comput. Phys.* **1977**, *23*, 327–341.

(32) Darden, T.; York, D.; Pedersen, L. Particle Mesh Ewald - an N.Log(N) Method for Ewald Sums in Large Systems. *J. Chem. Phys.* **1993**, *98*, 10089–10092.

(33) Cheatham, T. E.; Miller, J. L.; Fox, T.; Darden, T. A.; Kollman, P. A. Molecular-Dynamics Simulations on Solvated Biomolecular Systems - the Particle Mesh Ewald Method Leads to Stable Trajectories of DNA, Rna, and Proteins. *J. Am. Chem. Soc.* **1995**, *117*, 4193–4194.

(34) Berendsen, H. J. C.; Postma, J. P. M.; Vangunsteren, W. F.; Dinola, A.; Haak, J. R. Molecular-Dynamics with Coupling to an External Bath. *J. Chem. Phys.* **1984**, *81*, 3684–3690.

(35) Kottalam, J.; Case, D. A. Dynamics of Ligand Escape from the Heme Pocket of Myoglobin. *J. Am. Chem. Soc.* **1988**, *110*, 7690–7697.

(36) Kumar, S.; Bouzida, D.; Swendsen, R. H.; Kollman, P. A.; Rosenberg, J. M. The Weighted Histogram Analysis Method for Free-Energy Calculations on Biomolecules. 1. The Method. *J. Comput. Chem.* **1992**, *13*, 1011–1021.

(37) Kumar, S.; Rosenberg, J. M.; Bouzida, D.; Swendsen, R. H.; Kollman, P. A. Multidimensional Free-Energy Calculations Using the Weighted Histogram Analysis Method. *J. Comput. Chem.* **1995**, *16*, 1339–1350.

(38) Roux, B. The Calculation of the Potential of Mean Force Using Computer-Simulations. *Comput. Phys. Commun.* **1995**, *91*, 275–282.

(39) Krueger, A.; Protozanova, E.; Frank-Kamenetskii, M. D. Sequence-dependent base pair opening in DNA double helix. *Biophys. J.* **2006**, *90*, 3091–9.

CT9001575

JCTC Journal of Chemical Theory and Computation

A General Boundary Potential for Hybrid QM/MM Simulations of Solvated Biomolecular Systems

Tobias Benighaus and Walter Thiel*

Max-Planck-Institut für Kohlenforschung, Kaiser-Wilhelm-Platz 1 45470, Mülheim an der Ruhr, Germany

Received August 17, 2009

Abstract: We present a general boundary potential for the efficient and accurate evaluation of electrostatic interactions in hybrid quantum mechanical/molecular mechanical (QM/MM) approaches called solvated macromolecule boundary potential (SMBP), which is designed for QM/MM calculations with any kind of QM method. The SMBP targets QM/MM single-point energy calculations and geometry optimizations. In the SMBP scheme, the outer solvent and macromolecule region is described by a boundary potential obtained with the use of Poisson−Boltzmann calculations (treating the bulk solvent as a dielectric continuum). In the QM calculations, the SMBP is represented by virtual point charges on a surface enclosing the explicitly treated inner region. These charges and their interactions with the QM density are determined through a self-consistent reaction field procedure. The accuracy of the SMBP is evaluated on three diverse test systems: the intramolecular proton transfer of glycine in water, the hydroxylation reaction in *p*-hydroxybenzoate hydroxylase, and the spin state energy splittings in the pentacoordinated ferric complex of cytochrome P450cam. In the case of solvated glycine, application of the SMBP turns out to be problematic since analogous QM/MM/SMBP and full QM/MM geometry optimizations lead to different close-lying local minima. In both enzymes, the SMBP performs very well and closely reproduces the results from full QM/MM optimizations of these more rigid test systems. Starting from optimized QM/MM/SMBP structures along a reaction path, one can apply the previously implemented generalized solvent boundary potential (GSBP) to sample over MM phase space in QM/MM free energy calculations within the framework of free energy perturbation theory. This reduces the overall computational costs of sampling by 1 order of magnitude while maintaining good accuracy. The combined use of SMBP and GSBP thus allows for efficient QM/MM free energy studies of enzymes.

1. Introduction

Hybrid quantum mechanical/molecular mechanical (QM/MM) methods have become established tools for studying large biomolecules, with an increasing number of applications being devoted to the computation of free energy differences.[1−12] In these systems, long-range electrostatic interactions can have a significant influence on the stability of transition states or the relative energies of different configurations. Therefore, an accurate description of these interactions is indispensable for meaningful computations of properties that require extensive configurational sampling, for example, free activation or reaction energies.[13−16] While the development of efficient and accurate methods to describe electrostatic interactions improved the reliability of classical molecular dynamics (MD) simulations significantly,[14] these methods have only recently been adapted to the QM/MM framework.[17−21]

In the context of biomolecular simulations, one is frequently interested in localized processes in small active regions. The surrounding outer region often only serves to exclude solvent molecules, to constrain the active site geometries, and to provide a suitable electrostatic potential that supports a catalytic reaction, for example, by stabilization

---

* Corresponding author e-mail: thiel@mpi-muelheim.mpg.de.

10.1021/ct900437b CCC: $40.75

of the transition state. For this class of systems, boundary potentials are suitable for treating long-range electrostatic interactions.[22−33] In this approach, the biomolecular system is subdivided into an inner region, comprising the active site and the adjacent part of the enzyme, and an outer region, comprising the rest of the enzyme and the outer solvent molecules. A perfect boundary potential describes the entire effect of the outer region such that the statistical properties of the inner region interacting with the boundary potential are identical to those of the full solvated biomolecule. Consequently, the boundary potential may be constructed rigorously by integration over all degrees of freedom of the outer region.[33] An efficient implementation, however, necessitates the introduction of further approximations.

The generalized solvent boundary potential (GSBP) developed by Im et al. in 2001 is a notably attractive and successful boundary potential.[34] In this approach, the outer region solvent molecules are represented by a polarizable dielectric continuum (PDC) and the outer region charge distribution by fixed point charges. Electrostatic interactions with the outer region are separated into a static solvent-shielded field induced by the outer region point charges interacting with the dielectric, and a dynamic reaction field that is induced by interaction of the inner region charge distribution with the dielectric. A great advantage of the GSBP is the possibility to handle irregularly shaped dielectric boundaries. The GSBP was first applied successfully in classical simulations.[34,35] It was later adapted for use in combination with a hybrid QM/MM Hamiltonian,[20] with the self-consistent-charge density-functional tight-binding (SCC-DFTB) method[36] as the QM component. The resulting SCC-DFTB/MM/GSBP approach proved to be efficient and accurate and was applied in several studies of biological systems.[37−40] It was only found to be problematic in one case where the macromolecule underwent major conformational changes.[41] Since the fixation of the outer region is the fundamental assumption that allows for a closed-form expression for the electrostatics, the GSBP is not adequate to study nonlocal processes. Recently, the GSBP was implemented for NDDO-based semiempirical QM/MM Hamiltonians, and an evaluation showed that the GSBP allows accurate semiempirical QM/MM MD simulations at significantly reduced computational costs compared to standard QM/MM methods.[21]

Although semiempirical QM/MM MD simulations enable sufficient sampling of phase space, they suffer from the inaccuracies of the semiempirical QM Hamiltonian. As QM/MM MD simulations with accurate density functional or ab initio methods are prohibitively expensive, several schemes have been devised to approximate free energy differences on the basis of first-principles quantum mechanics.[1,8,42−50] The QM/MM free energy perturbation (FEP) method[51] is one of these approaches. It is based on three assumptions: (1) the dynamics of the QM and MM subsystems are independent; (2) the entropy change in the QM region can be estimated from the harmonic approximation, and (3) commonly, the electrostatic QM/MM interactions are approximated by interactions between QM and MM point charges, with the QM charges fitted to the electrostatic potential (ESP).[2] These approximations reduce the computational costs significantly such that computation of free energy differences is possible with accurate QM/MM methods. The validity of this approach is supported by successful applications[3,52−54] and comparisons to nonapproximated free energy methods.[7,10]

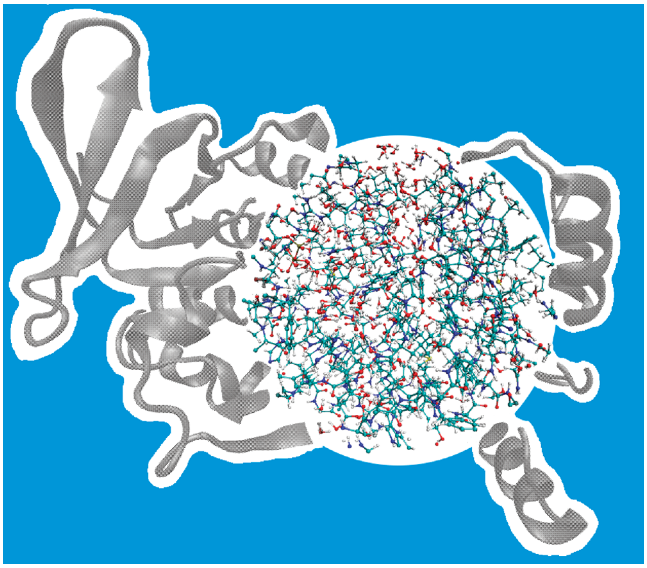

Figure 1. Illustration of the boundary potential approach. The explicit inner region is represented atomistically. The implicit outer macromolecule region is depicted by gray ribbons, and the implicit solvent region is represented by the blue area.

In this article, we present a general boundary potential for QM/MM calculations that offers two new possibilities. First, it extends the QM/MM method to a general three-layer approach that describes the outer solvent and macromolecule region by a boundary potential and thus allows for an accurate description of long-range electrostatic interactions and bulk solvent effects. Second, within the FEP framework, it allows application of the GSBP to sample the MM phase space more efficiently. Both options are available in combination with every QM/MM potential. Since this boundary potential mimics the electrostatic potential of the outer region of macromolecules in solution, we denote it the solvated macromolecule boundary potential (SMBP).

2. Methods

This section begins with a definition of the different regions into which the full system is separated using a boundary potential approach. Then, the theory of the GSBP is briefly reviewed, and the new SMBP for QM/MM calculations is introduced. Finally, we show how the combined use of the SMBP and GSBP allows efficient ab initio QM/MM free energy calculations within the FEP framework.

2.1. Separation of Regions. The foundation of any boundary potential approach is the separation of the full system into an inner and outer region. This partitioning is illustrated in Figure 1. All atoms in the inner region (colored atomistic representation) are simulated explicitly, while the influence of the outer region (shown in gray ribbons) on the inner region is mimicked by the boundary potential.

The atoms in both regions interact with the dielectric continuum that represents the bulk solvent (blue area).

Considering a macromolecule R surrounded by N solvent molecules in a boundary potential approach, the inner region comprises the inner part of the macromolecule (R_i) and the n inner solvent molecules, while the outer $N - n$ solvent molecules and the outer part of the macromolecule (R_o) belong to the outer region. Statistical expectation values depending only on the degrees of freedom of the inner region can be computed on the surface of the potential of mean force (PMF) $W(R_\mathrm{i}, 1, ..., n)$.

$$e^{-\beta W(R_\mathrm{i},1,...,n)} = \frac{1}{C}\int' \mathrm{d}R_\mathrm{o}\, \mathrm{d}(n+1)\cdots \mathrm{d}N e^{-\beta U(R,1,...,N)} \tag{1}$$

The PMF is obtained by integrating out the degrees of freedom of the outer region, including only those configurations with all outer region atoms outside the inner region (as indicated by the primed integral). Beglov and Roux demonstrated that the PMF is related to the reversible thermodynamic work necessary to assemble the inner region if the integration constant C is chosen accordingly.[33] This allows separation of the PMF into contributions that arise from configurational restrictions (ΔW_cr), nonpolar interactions (ΔW_np), electrostatic interactions (ΔW_elec), and the potential energy of the isolated inner region (U).

$$\begin{aligned} W(R_i, 1, ..., n) = {} & U(R_i, 1, ..., n) + \Delta W_\mathrm{cr} + \\ & \Delta W_\mathrm{np}(R_i, 1, ..., n) + \Delta W_\mathrm{elec}(R_i, 1, ..., n) \end{aligned} \tag{2}$$

Although the accuracy of the GSBP and the SMBP decreases in the immediate vicinity of the boundary, it is important to ensure that the inner region preserves its shape. Therefore, it is necessary to fix the outer layer of the inner region.[21] As a consequence, the inner region is further subdivided into an active explicit and a frozen explicit region.

2.2. Generalized Solvent Boundary Potential. The objective of the GSBP is to provide an efficient and accurate approximation of the electrostatic contribution to the PMF. Hence, the outer solvent molecules are described by a PDC and the outer macromolecule region by fixed point charges. In this case, the electrostatic contributions to the PMF consist of direct Coulombic interactions of the inner and outer regions ($U_\mathrm{elec}^\mathrm{io}$), and the solvation free energy resulting from interaction with the PDC ($\Delta W_\mathrm{elec}^\mathrm{solv}$). This term stems from the interaction of the charge distribution of the entire macromolecule, represented by point charges q_A, with the reaction field potential $\phi_\mathrm{rf}(\mathbf{r})$.

$$\Delta W_\mathrm{elec}^\mathrm{solv} = \frac{1}{2}\sum_A q_A\, \phi_\mathrm{rf}(\mathbf{r}_A) \tag{3}$$

The reaction field potential is the difference of the electrostatic potentials in solution and in vacuum that are computed by solving the linearized PB equation.[55]

$$\nabla[\varepsilon(\mathbf{r})\, \nabla\phi(\mathbf{r})] - \bar{\kappa}^2(\mathbf{r})\, \phi(\mathbf{r}) = -4\pi\rho(\mathbf{r}) \tag{4}$$

Here, $\rho(\mathbf{r})$ is the charge density, $\varepsilon(\mathbf{r})$ is the space-dependent dielectric constant, and $\bar{\kappa}(\mathbf{r})$ is the modified Debye–Hückel screening factor. Direct computation of this term during sampling is prohibitively expensive since it would require solving the PB equation for each configuration. To isolate the dynamic contributions, the charge distribution is separated into an inner and outer part, and as a consequence $\Delta W_\mathrm{elec}^\mathrm{solv}$ splits up into outer–outer, inner–outer, and inner–inner contributions.

$$\Delta W_\mathrm{elec}^\mathrm{solv} = \Delta W_\mathrm{elec}^\mathrm{oo} + \Delta W_\mathrm{elec}^\mathrm{io} + \Delta W_\mathrm{elec}^\mathrm{ii} \tag{5}$$

The interaction of the outer region charge distribution with the self-induced reaction field ($\Delta W_\mathrm{elec}^\mathrm{oo}$) is constant throughout sampling and can therefore be neglected. Calculation of the direct Coulombic interactions of the inner and outer regions and the inner–outer contribution to the solvation free energy can be combined efficiently.

$$\begin{aligned} \Delta W_\mathrm{elec}^\mathrm{io} + U_\mathrm{elec}^\mathrm{io} &= \sum_{A\in \mathrm{inner}} q_A\, \phi_\mathrm{rf}^\mathrm{o}(\mathbf{r}_A) + U_\mathrm{elec}^\mathrm{io} \\ &= \sum_{A\in \mathrm{inner}} q_A \phi_\mathrm{s}^\mathrm{o}(\mathbf{r}_A) \end{aligned} \tag{6}$$

Since the outer region is constant, the electrostatic potential of the outer region in solution, $\phi_\mathrm{s}^\mathrm{o}$, is constant for all inner region configurations, and therefore, this ansatz offers a massive reduction of computational cost. The inner–inner contributions, however, remain problematic since the inner reaction field potential depends on the inner region configuration. To find an analytical expression for this term, a Green's function approach is used to express the inner reaction field potential.

$$\phi_\mathrm{rf}^\mathrm{i}(\mathbf{r}) = \int \mathrm{d}\mathbf{r}'\, \rho_i(\mathbf{r}')\, G_\mathrm{rf}(\mathbf{r}, \mathbf{r}') \tag{7}$$

Now, the inner charge distribution and the reaction field Green's function are projected onto the same set of basis functions $\{b_n\}$, and the solvation energy of the inner region can be expressed as a matrix product of the reaction field matrix, M_rf, and the generalized multipole moments of the inner charge distribution, Q_n. This leads to the final expression for the electrostatic contribution to the PMF.

$$\Delta W_\mathrm{elec}^\mathrm{GSBP} = \sum_{A\in \mathrm{inner}} q_A \phi_\mathrm{s}^\mathrm{o}(\mathbf{r}_A) + \frac{1}{2}\sum_{mn} Q_m M_{mn} Q_n \tag{8}$$

Although this ansatz circumvents repeated solution of the PB equation during sampling, it is important to point out that computation of the reaction field matrix necessitates solving the PB equation a few hundred times before the simulation. Therefore, use of the GSBP is connected with a significant overhead.[21]

In the QM/MM approach, the inner region is subdivided into a QM and a MM region, and concomitantly, the inner region charge distribution splits up into QM and MM charge distributions that interact separately with the static outer region potential, $\phi_\mathrm{s}^\mathrm{o}$, and the reaction field Green's function, G_rf.

$$\Delta W_{\text{elec}}^{\text{GSBP}} = \sum_{A\in \text{MM}} q_A \phi_s^o(\mathbf{r}_A) + \int d\mathbf{r}\, \rho^{\text{QM}}(\mathbf{r})\, \phi_s^o(\mathbf{r}) + \frac{1}{2}\sum_{mn} Q_m^{\text{QM}} M_{mn} Q_n^{\text{QM}} + \sum_{mn} Q_m^{\text{QM}} M_{mn} Q_n^{\text{MM,cs}} + \frac{1}{2}\sum_{mn} Q_m^{\text{MM}} M_{mn} Q_n^{\text{MM}} \tag{9}$$

The charge-shift scheme is employed to avoid overpolarization of the QM electron density, by distributing the charges of MM atoms at the QM/MM boundary over the neighboring MM atoms and correcting for the resulting change in the dipole moment.[56] Therefore, the QM multipole moments (Q_m^{QM}) interact with the multipole moments of the charge-shifted MM charge distribution ($Q_n^{\text{MM, cs}}$) via the reaction field matrix (M_{mn}).

The main issue of any QM/MM implementation of the GSBP is the representation of the continuous QM charge density, $\rho^{\text{QM}}(\mathbf{r})$. In previous implementations,[20,21] the QM density was represented by Mulliken charges.[57]

$$\rho^{\text{QM}}(\mathbf{r}) = \sum_A q_A^{\text{Mulliken}}(\mathbf{r}_A)\, \delta(\mathbf{r} - \mathbf{r}_A) \tag{10}$$

This choice has the two advantages that the working equations of the GSBP for MM methods can be easily extended to the QM/MM case and that the interaction of the QM density with the boundary potential during the self-consistent field (SCF) procedure can be expressed in simple terms that have to be added to the Fock matrix. However, there are also two disadvantages. First, the GSBP has to be implemented for each QM program and method individually. Second, to compute accurate analytical gradients, it is necessary to calculate the derivative of the Mulliken charges, which involves solution of the coupled-perturbed SCF (CPSCF) equations. While the computational costs of this step are acceptable for semiempirical methods, they will increase significantly for higher-level QM methods with larger atomic orbital basis sets.[21]

2.3. Solvated Macromolecule Boundary Potential. The design of the SMBP was guided by the requirements that it should be conceptually similar to the GSBP, efficient in geometry optimizations, and applicable in QM/MM calculations with any kind of QM method.

We first consider the definition of the dielectric boundary: The core of the GSBP is the analytical expression for the electrostatic interaction with the outer region charge distribution that is shielded in a nontrivial way by the PDC. To find a closed-form expression for this potential, it is necessary to assume that the dielectric interface is fixed during the simulation.[34] Usually, in solutions of the PB equation, the interface is defined by the superposition of the van der Waals (vdW) envelope of the atoms. In the GSBP, a constant and smooth dielectric interface throughout dynamics simulations is ensured by extending the dielectric cavity region that encloses the inner region. For the sake of consistency, the same approach is used in the SMBP. The inner region is restricted to have a spherical shape with radius R_{inner} that comprises all inner region atoms. Since all atoms inside the sphere are modeled explicitly, the dielectric constant inside the inner region is set to 1. In the bulk solvent and the macromolecule region, the dielectric constant is set to ε_s and ε_m, respectively. To secure that the shape of the interface is independent of the position of the active atoms, the radius of the inner region cavity is extended by ΔR. This value has to be chosen to be sufficiently large to avoid the vdW radius of any active atom touching the interface. The resulting shape of the dielectric interface in the SMBP is illustrated in Figure 2. A previous evaluation of the GSBP showed that its accuracy deteriorates close to the boundary of the inner region.[21,35] Therefore, it was found necessary to freeze the outer layer of the inner region, providing an "insulation" region with a thickness of 2−3 Å.[21] In Figure 2, this is the area between the red and black line. Here, the atoms are described explicitly, but their positions are fixed.

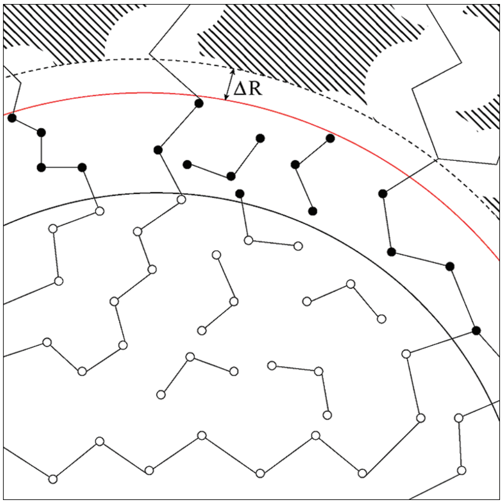

Figure 2. Definition of the constant dielectric interface in the SMBP and the GSBP. The extended cavity region is encircled by the dashed black line, and the implicit solvent region is indicated by the hatched area. An "insulation" region of frozen explicit atoms (black circles) ensures (see text) that the dielectric interface is not touched by the van der Waals radius of any active explicit atom (white circles). The inner region and the active region are encircled by red and black lines, respectively.

The construction of the SMBP is based on the same approximations as in the case of the GSBP. Outer macromolecule and bulk solvent regions are represented by fixed point charges and a PDC, respectively, so that the electrostatic contributions to the PMF consist of direct Coulombic interactions ($U_{\text{elec}}^{\text{io}}$) and the solvation free energy ($\Delta W_{\text{elec}}^{\text{solv}}$). Again, the outer−outer contribution to the solvation free energy is constant and therefore neglected, so that the SMBP takes the following form:

$$\Delta W_{\text{elec}}^{\text{SMBP}} = U_{\text{elec}}^{\text{io}} + \Delta W_{\text{elec}}^{\text{io}} + \Delta W_{\text{elec}}^{\text{ii}} \tag{11}$$

As in the GSBP, the electrostatic interactions of the inner region with the outer region charges ($U_{\text{elec}}^{\text{io}}$) and with the response of the PDC to the outer region charges ($\Delta W_{\text{elec}}^{\text{io}}$) are combined for efficient computation (eq 6).

$$\Delta W_{\text{elec}}^{\text{SMBP}} = \int d\mathbf{r}\, \rho_i(\mathbf{r})\, \phi_s^o(\mathbf{r}) + \Delta W_{\text{elec}}^{\text{ii}} \tag{12}$$

In the GSBP, $\Delta W_{\text{elec}}^{\text{ii}}$ is approximated by a closed-form expression that is based on a basis set representation of the inner region charge distribution and the reaction field Green's function (see eqs 7 and 8). This approach is designed for MD simulations but is computationally not efficient for geometry optimizations or single-point calculations. Using a standard-sized basis set to represent the charge density, computation of the reaction field matrix corresponds to solving the PB equation about 800 times. Even with a large active region, geometry optimizations rarely take more than than 800 steps to converge, and therefore solving the PB equation after each step is more efficient. Since geometry optimizations are the field of application of the SMBP, we use a different ansatz and update the individual contributions to the PMF by solving the PB equation whenever needed. This is the main conceptual difference between SMBP and GSBP.

In the QM/MM/SMBP approach, the inner region charge distribution splits up into QM and MM charge densities, leading to a more complicated expression.

$$\begin{aligned}\Delta W_{\text{elec}}^{\text{SMBP}} = \frac{1}{2}\int d\mathbf{r}\, d\mathbf{r}'[\rho_{\text{QM}}(\mathbf{r}) + \rho_{\text{MM}}(\mathbf{r})] \times \\ G_{\text{rf}}(\mathbf{r},\mathbf{r}')[\rho_{\text{QM}}(\mathbf{r}') + \rho_{\text{MM}}(\mathbf{r}')] + \\ \int d\mathbf{r}[\rho_{\text{QM}}(\mathbf{r}) + \rho_{\text{MM}}(\mathbf{r})]\,\phi_{\text{s}}^{\text{o}}(\mathbf{r})\end{aligned} \tag{13}$$

This can also be formulated as the interaction with the individual potentials $\phi_{\text{tot}}^{\text{QM}}$ and $\phi_{\text{tot}}^{\text{MM}}$ that are experienced by the QM and MM charge densities, respectively:

$$\Delta W_{\text{elec}}^{\text{SMBP}} = \int d\mathbf{r}\, \rho_{\text{QM}}(\mathbf{r})\, \phi_{\text{tot}}^{\text{QM}}(\mathbf{r}) + \int d\mathbf{r}\, \rho_{\text{MM}}\, \phi_{\text{tot}}^{\text{MM}}(\mathbf{r}) \tag{14}$$

with

$$\phi_{\text{tot}}^{\text{QM}}(\mathbf{r}) = \phi_{\text{s}}^{\text{o}}(\mathbf{r}) + \phi_{\text{rf}}^{\text{MM}}(\mathbf{r}) + \frac{1}{2}\phi_{\text{rf}}^{\text{QM}}(\mathbf{r}) \tag{15}$$

$$\phi_{\text{tot}}^{\text{MM}}(\mathbf{r}) = \phi_{\text{s}}^{\text{o}}(\mathbf{r}) + \frac{1}{2}\phi_{\text{rf}}^{\text{MM}}(\mathbf{r}) \tag{16}$$

Both inner region reaction field potentials, $\phi_{\text{rf}}^{\text{QM}}$ and $\phi_{\text{rf}}^{\text{MM}}$, are computed by solving the PB equation in solution and in a vacuum with all charges set to zero except the explicit QM and MM charges, respectively (see eq 4). Since $\phi_{\text{rf}}^{\text{QM}}$ and $\phi_{\text{rf}}^{\text{MM}}$ depend on the inner region charge distributions, they have to be calculated for each inner region configuration, that is, after each step in a geometry optimization.

Moreover, computation of the QM reaction field potential is exacerbated by the mutual dependence of the QM wave function and the QM reaction field potential via the QM charge density. To find a self-consistent solution to the SCF and the PB equation at the same time, a doubly iterative self-consistent reaction field (SCRF) scheme is employed.

In previous implementations of the GSBP for QM/MM methods, the interaction of the QM charge density was modeled by QM Mulliken charges interacting with the boundary potential. Although this leads to simple additional terms that have to be added to the Fock matrix, it also necessitates modifications to the QM programs.[20,21] In accordance with the modular philosophy of ChemShell, a different approach is used in the SMBP to describe the interaction of the QM charge density with the boundary potential. The boundary potential is projected onto a set of N virtual surface charges $\{q_i\}$, which are distributed uniformly on a sphere with radius $R_{\text{inner}} + \Delta R$ that defines the extended dielectric cavity (see Figure 3).

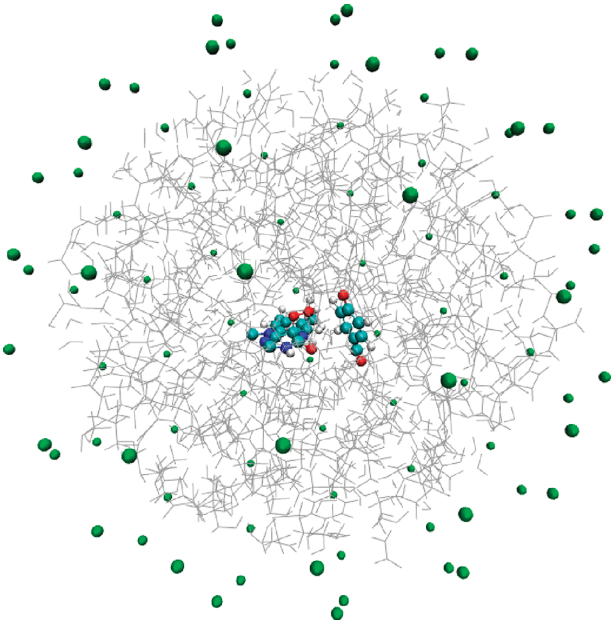

Figure 3. Distribution of virtual surface charges used to represent the SMBP (green balls) in the case of *p*-hydroxybenzoate hydroxylase (see section 4.2). The QM region and the explicit MM region are shown as a ball-and-stick model and as gray lines, respectively.

$$\phi_{\text{tot}}^{\text{QM}}(\mathbf{r}) \approx \sum_{i}^{N} \frac{q_i}{|\mathbf{r} - \mathbf{r}_i|} \tag{17}$$

The values of the surface charges are optimized to reproduce $\phi_{\text{tot}}^{\text{QM}}$ at the position of the QM atoms by minimization of the penalty function $\tilde{F}$.

$$\tilde{F} = \sum_{j}^{\text{QM}} \left[\phi_{\text{tot}}^{\text{QM}}(\mathbf{r}_j) - \sum_{i}^{N} \frac{q_i}{|r_{ij}|}\right]^2 \tag{18}$$

The minimization of $\tilde{F}$ starts with all virtual surface charges set to zero. The charges are optimized with a conjugate gradient algorithm until $\phi_{\text{tot}}^{\text{QM}}$ is reproduced with a maximum absolute deviation of 2×10^{-5} au at the position of every QM atom. The QM wave function is optimized in the presence of the atomic charges of the inner MM region and the virtual surface charges. The surface charge projection approach has the advantage of allowing the application of the SMBP in combination with every QM program that can handle external point charges.

For each new geometry, the MM reaction field potential $\phi_{\text{rf}}^{\text{MM}}$ is computed by neglecting all charges in the outer region and the QM region. Since the MM charges are not polarizable and the potential is independent of the QM charge distribution, the MM reaction field does not have to be updated due to changes in the QM density. Subsequently, a SCRF calculation proceeds as follows: (1) Initially, the QM reaction field potential $\phi_{\mathrm{rf}}^{\mathrm{QM}}$ is computed on the basis of a guess for the atomic QM charges. (2) Then, the total potential experienced by the QM atoms, $\phi_{\mathrm{tot}}^{\mathrm{QM}}$, is assembled and projected onto a set of virtual surface charges $\{q_i\}$. (3) Next, the QM wave function is computed in the field of the inner MM region point charges and the surface charges. After convergence, the QM ESP charges based on the new wave function are calculated. (4) With these new QM charges, the PB equation is solved again to update the QM reaction field potential. (5) Finally, the potential is checked for convergence. If the deviations in the QM reaction field potential are too large, the algorithm returns to step 2 and updates the wave function and the QM reaction field potential. (6) Upon convergence, the force contributions from the total potential are computed and added to the gradient.

These force contributions are the derivative of the electrostatic contribution to the PMF with respect to the atomic coordinates. For a QM atom, this yields

$$\begin{aligned}\frac{\partial}{\partial x_A}\Delta W_{\mathrm{elec}}^{\mathrm{SMBP}} = {} & \frac{\partial}{\partial x_A}\frac{1}{2}\int \mathrm{d}\mathbf{r}\,\mathrm{d}\mathbf{r}'\,\rho_{\mathrm{QM}}(\mathbf{r})\,G_{\mathrm{rf}}(\mathbf{r},\mathbf{r}')\,\rho_{\mathrm{QM}}(\mathbf{r}') + \\ & \frac{\partial}{\partial x_A}\int \mathrm{d}\mathbf{r}\,\mathrm{d}\mathbf{r}'\,\rho_{\mathrm{QM}}(\mathbf{r})\,G_{\mathrm{rf}}(\mathbf{r},\mathbf{r}'\,\rho_{\mathrm{MM}}(\mathbf{r}') + \\ & \frac{\partial}{\partial x_A}\int \mathrm{d}\mathbf{r}\,\rho_{\mathrm{QM}}(\mathbf{r})\,\phi_{\mathrm{s}}^{\mathrm{o}}(\mathbf{r}) \\ = {} & \int \mathrm{d}\mathbf{r}\left[\frac{\partial}{\partial x_A}\rho_{\mathrm{QM}}(\mathbf{r})\right]\phi_{\mathrm{tot}}^{\mathrm{grad}}(\mathbf{r})\end{aligned} \tag{19}$$

with

$$\phi_{\mathrm{tot}}^{\mathrm{grad}}(\mathbf{r}) = \phi_{\mathrm{s}}^{\mathrm{o}}(\mathbf{r}) + \phi_{\mathrm{rf}}^{\mathrm{MM}}(\mathbf{r}) + \phi_{\mathrm{rf}}^{\mathrm{QM}}(\mathbf{r}) \tag{20}$$

Projection of the total gradient potential $\phi_{\mathrm{tot}}^{\mathrm{grad}}$ onto a set of K gradient surface charges $\{q_p\}$ leads to the following approximation:

$$\frac{\partial}{\partial x_A}\Delta W_{\mathrm{elec}}^{\mathrm{SMBP}} \approx \int \mathrm{d}\mathbf{r}\left[\frac{\partial}{\partial x_A}\rho_{\mathrm{QM}}(\mathbf{r})\right]\left[\sum_{p}^{K}\frac{q_p}{|\mathbf{r}_p - \mathbf{r}|}\right] \tag{21}$$

These terms are computed and added to the QM gradient automatically by every standard quantum chemistry code if the QM gradient calculation is performed in the presence of a set of point charges that encompasses the point charges of the inner MM atoms and the gradient surface charges. For SCF wave functions, solution of the CPSCF equations is not necessary for gradient computations, since all terms involving derivatives of variationally optimized orbital coefficients are zero. In the QM/MM/SMBP approach, however, the Fock matrix in the gradient calculation is not strictly diagonal because the virtual surface charges are different in the energy and the gradient calculations (see eqs 15 and 20). Thus, the QM wave function is not converged in the field of the gradient surface charges. However, the QM contribution to the total gradient potential is very small, and the differences between virtual surface charges for energy and gradient calculations are therefore almost zero. By comparison to finite-difference gradient calculations, we found that all terms involving orbital coefficient derivatives can be neglected in geometry optimizations with standard convergence criteria (see Table S1 in the Supporting Information). If the dielectric constant of the solvent region is 1, that is, in case of a calculation in vacuo, all reaction field contributions are zero, and the analytical gradient is exact within the QM/MM/SMBP approximation. In summary, the potential projection approach offers a two-fold advantage: First, the SMBP can be used in combination with every quantum chemistry code, and second, solution of the CPSCF equation can be avoided for all practical purposes. Conceptually similar SCRF procedures have been used previously to combine pure QM[58] and hybrid QM/MM approaches[59] with implicit solvation models. The method presented in this work extends upon these approaches and employs a combination of the SCRF procedure and virtual surface charges to compute and represent a boundary potential that mimics not only the implicit solvent but also the outer macromolecule region.

For an MM atom, the derivative takes a similar form:

$$\frac{\partial}{\partial x_A}\Delta W_{\mathrm{elec}}^{\mathrm{SMBP}} = \int \mathrm{d}\mathbf{r}\left[\frac{\partial}{\partial x_A}\rho_{\mathrm{MM}}(\mathbf{r})\right]\phi_{\mathrm{tot}}^{\mathrm{grad}}(\mathbf{r}) \tag{22}$$

As the MM charges are constant, the derivative of the MM charge distribution is just the derivative of the function that is used to distribute the MM charges onto the grid employed for solving the PB equation.[60]

2.4. QM/MM/GSBP-FEP Approach.

Since the QM/MM-FEP approach has been presented in detail previously,[2,10] we discuss it only briefly to explain how the SMBP makes it possible to use the QM/MM/GSBP method for all QM/MM Hamiltonians.

In the FEP approach, the free energy difference is divided into three contributions that are computed individually:

$$\Delta A = \Delta E_{\mathrm{QM}} + \Delta A_{\mathrm{QM/MM}} + (\Delta A_{\mathrm{QM}} - \Delta E_{\mathrm{QM}}) \tag{23}$$

At first, the potential energy profile is calculated by means of constrained optimizations. A reaction coordinate ξ describing the reaction is defined and used to split the reaction into discrete windows characterized by a corresponding value of ξ_i. For each window i, the reaction coordinate is constrained to some ξ_i, and all other QM and MM degrees of freedom are optimized. This yields the potential energy profile of the reaction and a set of geometries along the reaction coordinate.

Next, the difference of the free QM/MM interaction energy, $\Delta A_{\mathrm{QM/MM}}^{i\to i+1}$, between every two adjacent windows i and $i + 1$ is calculated. The difference is computed as a "perturbation" of the structure of window i with the QM structure of window $i + 1$.

$$\Delta E_{\mathrm{pert}}^{i\to i+1} = E_{\mathrm{QM/MM}}(\mathbf{r}_{\mathrm{QM}}^{i+1}, \mathbf{r}_{\mathrm{MM}}^{i}) - E_{\mathrm{QM/MM}}(\mathbf{r}_{\mathrm{QM}}^{i}, \mathbf{r}_{\mathrm{MM}}^{i}) \tag{24}$$

The change in the free energy that corresponds to the perturbation of the QM structure is obtained by sampling over the MM phase space at window i. This means that the MM forces refer to the interaction with the QM structure of window i, which is frozen during sampling.

$$\Delta A^{i\rightarrow i+1}_{\mathrm{QM/MM}} = -\frac{1}{\beta}\ln\langle \exp(-\beta \Delta E^{i\rightarrow i+1}_{\mathrm{pert}})\rangle_{\mathrm{MM},i} \tag{25}$$

Here, β is $1/(k_{\mathrm{B}}T)$, with k_{B} being the Boltzmann constant. Using the electronic embedding scheme,[61] an exact calculation of the electrostatic QM/MM interactions necessitates solving the SCF equations for each MM configuration during sampling. In the QM/MM-FEP approach, computation of these interactions is drastically simplified by two assumptions: the QM density is frozen and approximated by atomic ESP charges. Therefore, all QM calculations are avoided during sampling.

Finally, the energy of the QM part is corrected for entropic effects. At the stationary points, the correction ($\Delta A_{\mathrm{QM}} - \Delta E_{\mathrm{QM}}$) is evaluated from harmonic frequency calculations of the QM atoms and standard methods from statistical thermodynamics.[2,62]

The SMBP allows computation of the potential energy profile and the molecular and electronic structures of the discrete windows with the same approximations as in the GSBP. The outer region solvent molecules are represented by a PDC and the outer macromolecule charges by fixed point charges. The explicit atoms do not interact directly with all outer region charges but only with the potential that is induced by these charges in interaction with the PDC. This potential is computed as the finite-difference solution to the PB equation and is saved on a grid, which allows massive computational savings. Therefore, the geometries, QM densities, and ESP charges that result from (constrained) geometry optimizations with the QM/MM/SMBP method can be used for sampling the free energy difference over the MM phase space with the GSBP. At this point, it seems adequate to highlight the complementary nature of the approximations in QM/MM-FEP and in the GSBP. The QM/MM-FEP ansatz reduces the problem of configurational sampling with a QM/MM Hamiltonian to a sampling over MM phase space with a classical MM method. The GSBP enhances the efficiency of classical MM simulations by representing the outer part of the system by a boundary potential. Hence, these two approaches complement each other and may be combined without a loss of efficiency. Also in the GSBP, the QM density is represented by the ESP charges, leading to simple expressions for the QM multipole moments and the interaction with the static outer region potential.

$$Q_n^{\mathrm{QM}} = \sum_{A\in \mathrm{QM}} q_A^{\mathrm{ESP}} b_n(\mathbf{r}_A) \tag{26}$$

$$\int \mathrm{d}\mathbf{r}\, \rho^{\mathrm{QM}}(\mathbf{r})\, \phi_{\mathrm{s}}^{\mathrm{o}}(\mathbf{r}) = \sum_{A\in \mathrm{QM}} q_A^{\mathrm{ESP}} \phi_{\mathrm{s}}^{\mathrm{o}}(\mathbf{r}_A) \tag{27}$$

Since values and positions of the ESP charges are different for windows i and $i + 1$, the GSBP will contribute to the QM/MM energy difference that is sampled in eq 25. As the QM atoms are fixed, computation of the QM gradient in interaction with the GSBP is not necessary. The MM gradient is calculated in analogy to other QM/MM/GSBP implementations.[20,34]

3. Computational Details

The SMBP was implemented in a developmental version of the modular program package ChemShell.[56,63] The energy and gradient evaluations for the QM part were performed with the MNDO[64] and Turbomole 5.7.1 programs.[65] For the MM part, the DL_POLY[66] code was employed to run the CHARMM22 force field in all calculations.[67] Hydrogen link atoms in combination with the charge-shift scheme[56] were applied to saturate the QM system. Stationary points were optimized in hybrid delocalized internal coordinates using the HDLCOpt optimizer.[68] The PB equation was solved with the ChemShell PB module that uses the optimal successive over-relaxation method in combination with Gauss-Seidel relaxation to compute the electrostatic potential.[69,70] A maximum absolute change in every grid point of 2×10^{-5} au was employed as a convergence criterion. Third-order B splines were used to interpolate between the grid points.[71] The definition of the dielectric boundary was based on vdW radii from the CHARMM22 force field. All MD simulations were performed unter NVT conditions at a temperature of 300 K, which was controlled by a Nosé-Hoover chain thermostat.[72−75] The mass of deuterium was assigned to all hydrogen atoms, and free water molecules were kept rigid with SHAKE constraints.[76] A time step of 1 fs was used. The QM reaction field potential was considered converged when the root-mean-squared deviation dropped below 2×10^{-5} au. In the first iteration of the SCRF procedure, all QM atoms were assumed to be neutral.

4. Results

In this section, we evaluate the performance of the SMBP using three test cases: the proton transfer reaction in solvated glycine, the hydroxylation reaction in *p*-hydroxybenzoate hydroxylase (PHBH), and the spin state energy gaps in cytochrome P450cam. Glycine surrounded by explicit water molecules is a highly flexible and polar system, which makes it a challenging test case: the reaction energy of the intramolecular proton transfer is sensitive to the description of the solvent, and many solvation models incorrectly predict the neutral form to be more stable than the zwitterionic form.[77−80] The hydroxylation reaction in the catalytic cycle of PHBH has been much studied theoretically[9,81−85] and has become a prototypical test system for benchmarking theoretical treatments of enzymatic reactions.[12] The relative spin state energies of cytochrome P450cam[86,87] provide another, rather different test case: here, we address the pentacoordinated ferric complex whose spin state energies are strongly affected by the protein environment.[88] Taken together, we thus have three diverse systems to evaluate the accuracy and range of applicability of the SMBP.

Previous studies indicate that it may sometimes be important to allow fluctuations in the number of solvent molecules in approaches based on inner regions of fixed size.[89,90] This should not be problematic in the present test calculations, which address localized events at the center of the inner region (using a fixed number of solvent molecules).

4.1. Glycine in Water. The glycine/water model system was set up using a commonly applied protocol of solvation and equilibration steps by means of classical MD simulations with the CHARMM program.[91] The glycine molecule was solvated in a TIP3P water ball with 30 Å radius. All water molecules with an oxygen atom within 2.8 Å of any glycine atom were deleted, and the system was equilibrated. These steps were repeated until the number of water molecules was stable, leading to a total system size of 12 769 atoms with 4253 TIP3P water molecules. Finally, the system was equilibrated by means of a 500 ps classical MD simulation, and five configurations were selected after 340, 380, 420, 460, and 500 ps. For each configuration, the inner region was centered on the C_α carbon of the glycine and defined to encompass all water molecules with any atom within 18 Å of the center. In all subsequent QM/MM geometry optimizations, the glycine molecule and all water molecules with any atom within 14 Å of the center were allowed to move, while all other water molecules were frozen. The radius of the extended dielectric cavity was set to 21 Å, and a set of 90 virtual surface charges was used to represent the boundary potential in the QM calculations. The glycine molecule was described quantum mechanically with the AM1 Hamiltonian,[92] and the water molecules were treated by the force field or the SMBP. The details of this setup are summarized in Table S2 (Supporting Information).

In a vacuum environment, that is, with a dielectric constant of 1 anywhere in space, the electrostatic potential of the SMBP has to be identical to the exact potential from Coulombic electrostatics. Therefore, the accuracy of the QM/MM/SMBP approach can be evaluated in vacuo by direct comparison to standard QM/MM calculations. To allow the use of finely spaced grids in the finite-difference solution of the PB equation also for large biomolecules, we employed a focusing approach.[93] The PB equation is first solved with a coarse outer grid that covers the full biomolecule. Then, the PB equation is solved again with a fine inner grid that focuses onto the inner region. The boundary values of the inner grid are set by interpolation from the outer grid. The spacings of the two grids are the most important parameters of the SMBP. Hence, the accuracy of the SMBP was evaluated for all mesh size combinations of 0.15, 0.25, 0.4, 0.6, and 0.8 Å for the inner grid and 0.80, 1.25, 1.50, 1.75, and 2.50 Å for the outer grid.

Tables 1 and 2 show the mean absolute (MAD) and maximum absolute deviations (MAX) of the components of the electrostatic gradient for configuration 1. Similar deviations were observed for the other configurations (see Tables S3 and S4 in the Supporting Information). Although only 90 virtual surface charges are used to represent the static potential that is induced by almost 10 000 atoms in the outer region, the electrostatic gradient at the position of the QM atoms is reproduced with high accuracy. For all mesh size combinations, the MAD and MAX values are on the order of 0.3×10^{-4} au and 1.6×10^{-4} au, respectively. Moreover, the accuracy seems to be independent of the grid spacing within the chosen limits. Both findings suggest that the static outer region potential varies only slowly and has no detailed structure in the QM region.

Considering all atoms within 16 Å of the center, the SMBP reproduces the gradient of the electrostatic potential with high accuracy if the spacing of the inner grid is ≤0.4 Å. Under these conditions, the MAX values are below 4×10^{-4} au. The spacing of the outer grid does not influence the accuracy unless very fine inner grids are used. As one approaches the boundary separating inner and outer regions, the static outer region potential naturally becomes stronger and more complex. Nevertheless, its details are captured with sufficient accuracy also at the position of all inner region atoms which have a distance of up to 20 Å to the center due to the residue-based selection criterion that was employed to define the inner region. With an inner grid spacing of ≤0.25 Å, the MAD values do not exceed 0.4×10^{-4} au, and maximum deviations are around 5.5×10^{-4} au.

Table 1. Mean Absolute Deviations (MAD) [10^{-4} au] of the Electrostatic Forces Computed with the SMBP for Configuration 1 of the Glycine/Water System[a]

	inner grid size [Å]				
outer grid size [Å]	0.15	0.25	0.40	0.60	0.80
	MAD - QM atoms				
0.80	0.31	0.31	0.31	0.32	0.31
1.25	0.31	0.31	0.31	0.31	0.31
1.50	0.35	0.32	0.33	0.33	0.33
1.75	0.33	0.32	0.32	0.32	0.32
2.50	0.33	0.34	0.34	0.34	0.33
	MAD - atoms within 16 Å				
0.80	0.18	0.10	0.15	0.20	0.26
1.25	0.21	0.15	0.19	0.23	0.28
1.50	0.28	0.21	0.26	0.29	0.34
1.75	0.26	0.19	0.24	0.27	0.32
2.50	0.29	0.23	0.28	0.30	0.35
	MAD - atoms within 20 Å				
0.80	0.23	0.27	0.57	1.02	1.42
1.25	0.28	0.32	0.61	1.04	1.44
1.50	0.37	0.38	0.67	1.09	1.48
1.75	0.34	0.36	0.65	1.08	1.46
2.50	0.38	0.39	0.68	1.10	1.48

[a] Different mesh size combinations were used.

Table 2. Average Maximum Absolute Deviations (MAX) [10^{-4} au] of the Electrostatic Forces Computed with the SMBP for Configuration 1 of the Glycine/Water System[a]

	inner grid size [Å]				
outer grid size [Å]	0.15	0.25	0.40	0.60	0.80
	MAX - QM atoms				
0.80	1.53	1.64	1.57	1.55	1.60
1.25	1.62	1.69	1.65	1.65	1.67
1.50	1.62	1.66	1.64	1.64	1.66
1.75	1.59	1.65	1.61	1.61	1.64
2.50	1.57	1.63	1.60	1.60	1.62
	MAX - atoms within 16 Å				
0.80	1.53	1.64	3.72	7.16	9.08
1.25	1.67	1.90	3.68	7.08	8.89
1.50	3.22	2.90	3.91	7.30	9.45
1.75	2.32	2.44	3.73	7.14	9.02
2.50	3.15	3.06	3.88	7.19	9.51
	MAX - atoms within 20 Å				
0.80	2.41	5.43	14.79	35.67	35.35
1.25	2.91	5.57	14.59	35.46	35.27
1.50	4.93	5.79	14.53	35.42	34.71
1.75	3.60	5.64	14.52	35.39	35.03
2.50	4.67	5.51	14.25	35.11	34.81

[a] Different mesh size combinations were used.

The accuracy of the SMBP depends strongly on the radial position of the atoms since the electrostatic potential is more complex at the boundary. Figure 4 illustrates this point and shows that the increase of the MAD and MAX values in proximity to the boundary is strongly affected by the mesh

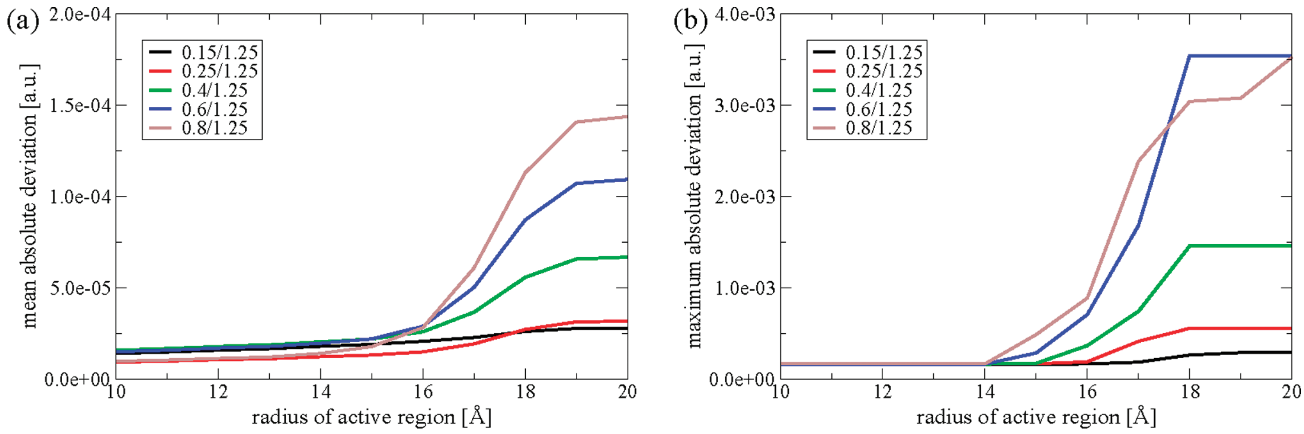

Figure 4. Mean absolute deviations (a) and maximum absolute deviations (b) of the electrostatic forces of all atoms inside the active region relative to the exact QM/MM values. Results are shown for different mesh sizes of the inner grid and plotted as a function of the radius of the active region. An outer grid size of 1.25 Å is used, and all calculations were performed on configuration 1 of the glycine/H_2O test system. The radius of the inner region was 18 Å (see text).

size of the inner grid. The deviations increase only slowly with grid spacings of 0.15 or 0.25 Å, and much more rapidly for coarser inner grids.

Overall, the accuracy provided by the SMBP is sufficient for QM/MM geometry optimizations where the default convergence criterion is a maximum gradient component of 4.5×10^{-4} au.[68] Therefore, an inner grid spacing of 0.25 Å excels as the best choice, providing high accuracy at tolerable computational costs. Using a finer grid spacing of 0.15 Å seems to yield only marginal improvements but raises computational demands significantly. The mesh size of the outer grid has no observable influence on the accuracy. Since computational costs are only slightly affected by the outer grid spacing, we opt for a rather fine outer grid with a mesh size of 1.25 Å in combination with an inner grid spacing of 0.25 Å in all calculations.

Representation of the boundary potential by a small set of point charges in the QM calculations is one of the main approximations connected with the SMBP. The accuracy converges rapidly with respect to the number of point charges, as illustrated in Figure 5. The MAD and MAX deviations of the gradient components are around 0.3×10^{-4} and 1.7×10^{-4} au, respectively, if the number of point charges is greater than 20. The residual error is not caused by the point charge representation but results from the limited accuracy of the boundary potential, which is computed from a finite-difference solution of the PB equation. Similar deviations are encountered for the MM atoms within 16 Å of the center that interact directly with the boundary potential without a charge representation (see Tables 1 and 2). Hence, higher accuracies can only be achieved with finer mesh sizes and not with a higher number of virtual surface charges. A set of 90 point charges was employed for all calculations reported in this article.

Using electronic embedding, computation of QM/MM energies and gradients necessitates evaluation of numerous one-electron integrals and their derivatives with respect to the position of the MM atoms. Therefore, computation of these terms constitutes a significant share of the total computational costs of the QM calculation. The SMBP allows us to replace the numerous outer MM atoms by a small set of point charges that reproduces the electrostatic potential in the QM region. In a vacuum environment, the analytical QM/MM/SMBP gradient is exact, and the additional costs of the SCRF procedure can be avoided. Hence, application of SMBP in vacuo offers a reduction of computational costs for QM/MM geometry optimizations. As in standard QM/MM calculations, the bulk solvent is then modeled by fixed water molecules which contribute to the static outer region potential (ϕ_s^o in eq 12). Table 3 shows the computation times for the QM part of single-point QM/MM and QM/MM/SMBP energy and gradient evaluations. Timings were performed for three QM methods: the semiempirical AM1 method, the pure density functional BLYP,[94,95] and the hybrid density functional B3LYP.[96] Two different basis sets were employed in the density functional theory calculations: the small SVP[97] and the larger TZVPP[98] basis sets. If the QM calculation is not dominated by the two-electron part, that is, if semiempirical methods, pure functionals, or small basis sets are employed, application of the SMBP can reduce computational costs by up to 60%. Even

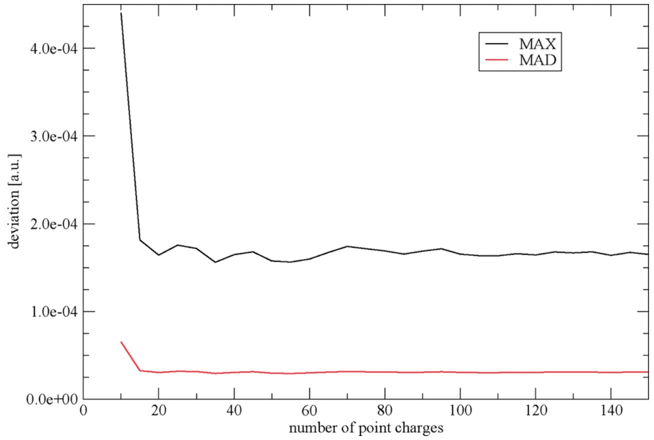

Figure 5. Mean absolute (MAD) and maximum absolute deviations (MAX) of the QM gradient components relative to the exact values from full QM/MM calculations. The results are plotted as a function of the number of point charges that are used to represent the boundary potential in the QM calculations. All calculations were performed on configuration 1 of the glycine/H_2O test system.

Table 3. Computation Time for a Single QM Energy and Gradient Evaluation for the Glycine/Water System[a]

		computation time [s]		
QM method	basis	QM/MM	QM/MM/SMBP	savings [%]
AM1		0.5	0.2	−57
BLYP	SVP	76.8	30.5	−60
B3LYP		87.0	39.5	−54
BLYP	TZVPP	303.1	126.1	−58
B3LYP		542.5	370.5	−31

[a] All timings were computed serially on 2.6 GHz AMD Opteron machines with 16 GB of memory.

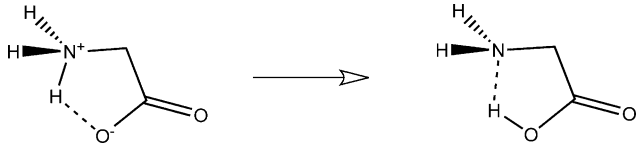

Figure 6. Intramolecular proton transfer reaction in glycine.

for the hybrid B3LYP functional with a larger basis set, computation time is reduced by about 30%. Computational savings strongly depend on the size of the QM region, the inner region and the outer region, and on the QM method employed and can vary significantly for different systems.

The reaction and activation energies for the intramolecular proton transfer process in glycine (Figure 6) were computed using the standard QM/MM and the new QM/MM/SMBP Hamiltonian for the five different configurations. The results in Table 4 show little agreement of QM/MM and QM/MM/SMBP results for the individual configurations. For configurations 3 and 5, deviations of the QM/MM/SMBP results from the QM/MM values are on the order of 1 kcal/mol. Higher deviations of reaction and activation energies up to 6 kcal/mol are encountered for the other configurations. These strong discrepancies can be attributed to the high flexibility and polarity of the system. A closer inspection of the reactant structures revealed that a small number of water molecules at the boundary of the active region adopt a different orientation in the QM/MM/SMBP optimized structures. Due to the hydrogen-bonding network, some of these modifications get relayed to the center of the water sphere and modify the hydrogen-bonding situation in close proximity to the QM region. For this reason, geometry optimizations of the starting structures with the QM/MM and QM/MM/SMBP approach lead to different local minima. Since the relative energies depend on the solvation of the polar groups of the reactant and product state, the reaction energies vary significantly when starting from different local minima. However, when computations of the reaction profiles are initiated from the same local minimum, that is, by using QM/MM optimized geometries as input structures for QM/MM/SMBP geometry optimizations, both methods provide virtually identical results (see Table 4). This is not practical in applications where QM/MM/SMBP should be used for geometry optimizations but shows that QM/MM/SMBP can reproduce QM/MM results accurately. In summary, for systems with a large number of close-lying local minima that have significantly different characteristics, geometry optimizations using QM/MM and QM/MM/SMBP can yield deviating results because of convergence to different local minima.

The mean values of the reaction and activation energies for the five configurations considered differ by less than 1 kcal/mol between QM/MM and QM/MM/SMBP (Table 4). Moreover, the mean values from QM/MM/SMBP calculations lie within the error bars of the QM/MM mean values (corresponding to a confidence level of 68%), while the standard deviations within the individual data sets range from 3−6 kcal/mol. One may expect in general that the mean values of interest from QM/MM and QM/MM/SMBP optimizations will tend to approach each other for a sufficiently large number of configurations.

4.2. *p*-Hydroxybenzoate Hydroxylase. The setup for PHBH was based on a system that has been used in previous QM/MM studies of PHBH.[9,81,82] It was generated by solvating the enzyme (394 amino acids) containing the flavin-adenine hydroperoxide cofactor (FADHOOH), the dianionic *p*-hydroxybenzoate substrate (pOHB), and 294 crystallographic water molecules in a 90 Å water box. The system was equilibrated with gradually decreasing harmonic restraints on the non-water atoms, followed by a MD run with harmonic restraints acting only on the FADHOOH and pOHB. In the resulting structure that served as a starting point for our setup, all water molecules outside 11 Å from any protein atom were discarded.[9,81,82]

Due to a change of force field from GROMOS (previously) to CHARMM (this study), the system was re-equilibrated for 500 ps with constraints on the cofactor, substrate, and all water molecules outside 2.9 Å from any protein atom. Two configurations were selected from this MD run after 460 and 500 ps that were used as starting structures to locate the stationary points of the hydroxylation reaction. The QM

Table 4. Reaction and Activation Energies for the Proton Transfer Reaction in Solvated Glycine

	reaction energies [kcal/mol]			activation energies [kcal/mol]		
configuration	QM/MM	QM/MM/SMBP	QM/MM/SMBP(opt)[a]	QM/MM	QM/MM/SMBP	QM/MM/SMBP(opt)[a]
1	6.84	8.42	6.88	30.01	30.09	30.01
2	9.54	15.61	9.61	32.28	36.43	32.31
3	6.51	7.68	6.61	26.82	27.10	26.84
4	7.27	1.39	7.28	31.18	27.92	31.14
5	13.57	14.58	13.53	32.66	33.35	32.62
mean value	8.75	9.54	8.78	30.73	31.20	30.58
standard deviation of data[b]	2.94	5.77	2.91	2.69	4.46	2.34
standard deviation of mean[c]	1.32	2.58	1.31	1.20	1.99	1.04

[a] Starting from QM/MM optimized structures. [b] Standard deviation of individual energy values. [c] Standard deviation of the mean value (68% confidence limit).

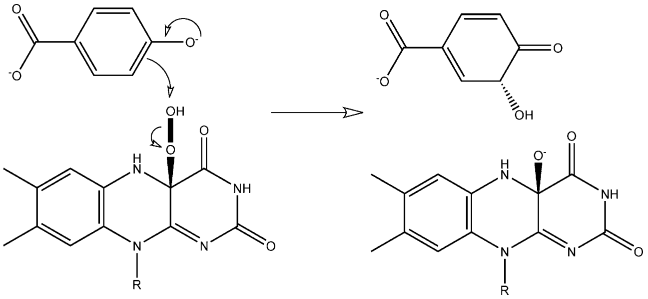

Figure 7. Hydroxylation reaction catalyzed by PHBH. R denotes the ribityl side chain of the flavin cofactor.

Table 5. Potential and Free Energies of Activation and Reaction of the Hydroxylation Reaction in PHBH [in kcal/mol]

configuration	Hamiltonian	ΔE	$\Delta E^‡$	ΔA	$\Delta A^‡$
1	QM/MM	−47.44	22.42	−50.38	21.27
	QM/MM/BP[a]	−48.65	21.56	−50.47	20.40
2	QM/MM	−48.90	22.00	−51.28	19.49
	QM/MM/BP[a]	−49.33	21.95	−52.84	19.17

[a] Outer macromolecule region is represented by SMBP in geometry optimizations and by GSBP in FEP calculations.

region consisted of pOHB and the isoalloxazine part of FADHOOH up to the first methylene unit of the ribityl side chain that was saturated with a hydrogen link atom. The semiempirical AM1 Hamiltonian was employed to describe the QM part. The inner region was centered on the initial position of the distal oxygen atom of the hydroperoxo group of FADHOOH. All charge groups with any atom within 18.5 Å of the center belonged to the inner region and were modeled explicitly. All charge groups with any atom within 16 Å of the center belonged to the active region and were allowed to move.

In the hydroxylation step of the PHBH catalytic cycle, the OH unit of the hydroperoxo group of FADHOOH is transferred to the meta carbon atom of pOHB (see Figure 7). To compute the potential energy profile and split the reaction into discrete windows for the FEP calculations, a reaction coordinate was defined:

$$\zeta = d(\mathrm{O_d{-}O_p}) - d(\mathrm{C_m{-}O_d}) \qquad (28)$$

Here, O_d and O_p designate the distal and proximal oxygen atoms of the hydroperoxo unit of FADHOOH, respectively. C_m is the meta carbon atom of pOHB. Starting from the two initial structures, the stationary points of this reaction were located using the QM/MM and the QM/MM/SMBP Hamiltonian. Both methods yield similar results (Table 5). For configuration 1, QM/MM and QM/MM/SMBP geometry optimizations lead to slightly different local minima, as indicated by a root-mean-square (rms) deviation (of the active atoms) of 5.4 pm. However, the reaction and activation energies deviate by only 1.2 and 0.9 kcal/mol, respectively. These differences are in the same range as the differences between the two configurations on the pure QM/MM level. For configuration 2, both Hamiltonians lead to the same local minimum with a rms deviation of 0.8 pm. Hence, the reaction and activation energies differ by only 0.4 and 0.1 kcal/mol, respectively. The plot of the potential energy profile in Figure 8 illustrates this impressive agreement.

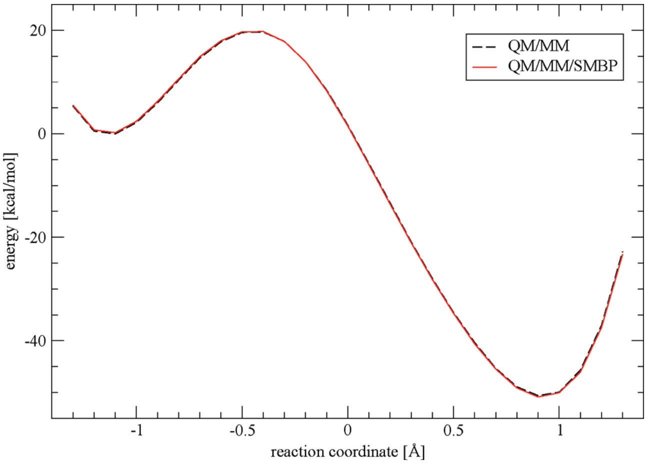

Figure 8. Potential energy profile of the OH transfer reaction in PHBH computed with QM/MM and QM/MM/SMBP independently (configuration 2). The QM atoms are described by the AM1 method and the MM atoms by the CHARMM force field.

The optimized geometries of the discrete windows along the reaction coordinate were used as input structures to sample over the MM phase space in the framework of FEP. For each window, the QM atoms were fixed, and the QM charge density was approximated by constant ESP charges. For the structures that were optimized with the QM/MM/SMBP Hamiltonian, the GSBP could be applied to accelerate the MD steps. To avoid mobile water molecules or flexible residues approaching the boundary separating the inner and outer regions, the size of the active region was reduced in the QM/MM/GSBP calculations. Here, all atoms within 15 Å of the center were allowed to move. Moreover, a spherical restraint with a radius of 17 Å and a force constant of 0.004 au was applied to all active atoms to avoid any mobile residue leaving the inner region. For both Hamiltonians, the molecular structure in each window was equilibrated for 10 ps followed by a FEP production run of 10 ps. The resulting MD data was coarse-grained and subjected to a standard set of statistical tests to ensure a lack of trend and correlation.[10] If necessary, data points at the beginning of the production run were discarded (at most 4 ps so that production runs lasted at least 6 ps for each window).

For configuration 1, the free energies of activation and reaction deviate by 0.9 and 0.1 kcal/mol, respectively (Table 5). The results for configuration 2 are similar with deviations of 0.3 and 1.6 kcal/mol, respectively. Figure 9 illustrates that the free energy profiles computed with and without GSBP agree well for all stages of the reaction. In view of the other approximations that are necessary for QM/MM-FEP simulations, the deviations caused by the GSBP seem small and tolerable. Application of the GSBP offers massive computational savings. In the PHBH system, the computational time for a single MD step of the FEP calculation is reduced by 95% from 116.2 s to only 4.9 s (Table 6). Even when taking the GSBP overhead into account, the computational costs of QM/MM/GSBP-FEP calculations are roughly 1 order of magnitude smaller than those of standard QM/MM-FEP

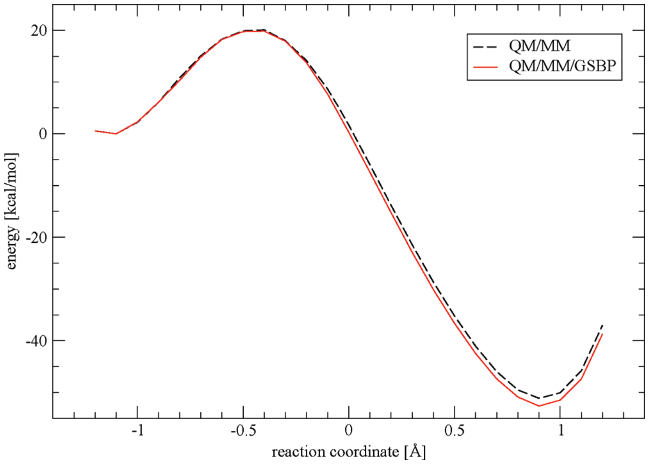

Figure 9. Free energy profile of the OH transfer reaction in PHBH computed with QM/MM and QM/MM/GSBP independently (configuration 2, excluding entropic QM contributions). The QM atoms are described by the AM1 method and the MM atoms by the CHARMM force field.

Table 6. Computation Time per MD Step [s] in FEP Simulations of the PHBH Model System[a]

module	QM/MM	QM/MM/GSBP
MM energy+gradient	69.2	2.6
QM energy+gradient	0.4	0.0
FEP	46.6	2.2
GSBP		0.1
total	116.2	4.9

[a] All values are averaged over 200 MD steps and were computed serially on 2.6 GHz AMD Opteron machines with 16 GB of memory.

calculations. In modeling enzymatic reactions, the combination of SMBP and GSBP for geometry optimizations and FEP calculations thus offers good accuracy combined with high efficiency.

4.3. Cytochrome P450cam. A recent QM/MM study addressed the steric and electrostatic factors that affect the geometrical and electronic structure of the pentacoordinated cytochrome P450cam complexes.[88] Among other properties, the energies of the doublet and quartet states relative to the sextet state were found to be strongly influenced by the protein environment. Therefore, we have chosen the spin state energy gaps of the ferric complex as a challenging protein test system to see if the SMBP is able to reproduce such subtle energy differences.

The system setup was based on the X-ray structure of the ferric complex (PDB code 1DZ4)[99] that was subjected to a standard solvation and relaxation protocol, followed by a protonation procedure that led to a final system with a total charge of $-9e$. Our calculations started from the two structures selected previously from a classical MD simulation after 31 and 93 ps.[88] For the QM calculations, three different density functionals were used that combine Becke's B88 exchange functional[94] with a varying fraction of Hartree−Fock (HF) exchange and the Lee−Yang−Parr (LYP) correlation functional:[95] BLYP, B3LYP,[96] and BHLYP.[100] We used the 6-31+G* basis for all atoms coordinated to the iron and the 6-31G basis set for the remaining ligand atoms. The iron atom was described by a Wachters all-electron basis set with additional sets of diffuse d and polarizing f functions.[101−103]

The QM region included the iron−porphyrin system of the heme unit and the sulfur atom of the coordinating Cys357 (with a hydrogen link atom attached to sulfur). The atoms of all residues with any atom within 4 Å of the heme−Cys357 complex or the camphor substrate were allowed to move; all other atoms were frozen. In the QM/MM/SMBP calculations, the inner region was centered on the initial position of the iron atom with an extended dielectric cavity radius of 29 Å. All residues with any atom within 20 Å of the iron atom belonged to the inner region and were described explicitly. The influence of all other residues was mimicked by the boundary potential.

The initial structures were first optimized in the sextet state with the QM/MM and the QM/MM/SMBP Hamiltonian, respectively. The two resulting geometries were subsequently reoptimized in the quartet and doublet state.

In the original study,[88] the B3LYP functional was found to provide the most realistic description of the spin state splittings with the correct sextet ground state, although the doublet−sextet gap is overestimated. Here, we are not interested in the absolute quality of the QM/MM results but want to know how well the QM/MM/SMBP approach can reproduce the QM/MM results. The values for the spin state energy gaps are given in Table 7. For eight out of 12 energy gaps, the QM/MM/SMBP results are within 0.1 kcal/mol of the full QM/MM results. The maximum absolute deviation is 0.21 kcal/mol, and the absolute deviations of the individual QM and MM components rarely exceed 0.4 kcal/mol. Moreover, subtle effects are reproduced very well: When the B3LYP functional is used, the QM calculation (in the field of the protein point charges) favors the quartet state over the sextet state by 0.71 kcal/mol in configuration 31. This preference is overcompensated by the MM contribution that favors the sextet state by 1.54 kcal/mol, leading to a QM/MM energy difference of 0.83 kcal/mol. In the QM/MM/SMBP calculations both components are reproduced almost exactly and sum up to an energy gap of 0.82 kcal/mol in favor of the sextet state. The results for configuration 93 are similar. These data show that the SMBP reproduces the electrostatic effects of the protein environment onto the QM and MM regions accurately, implying that geometry optimizations with the QM/MM/SMBP approach lead to highly similar local minima on the potential energy surface compared to standard QM/MM optimizations. This is corroborated by a direct comparison of the QM/MM and QM/MM/SMBP optimized geometries in Table S5 (Supporting Information): The rms deviations (of the active atoms) are usually around 1 pm or less. Only for the B3LYP optimized structures of configuration 31 are there larger rms deviations of about 6 pm. These can be traced back to a 30° rotation of a methyl group attached to the porphine ring in a hydrophobic environment. However, the corresponding spin state gaps are not affected by this peripheral conformational change and match almost perfectly.

In summary, optimizations with the QM/MM/SMBP Hamiltonian lead to biomolecular structures that either are almost identical to those from full QM/MM optimizations or they represent nearby local minima which are as representative for the molecular and electronic structure of the

Table 7. Sextet−Quartet and Sextet−Doublet Energy Gaps in Cytochrome P450cam [in kcal/mol] Computed with the Standard QM/MM and the Approximated QM/MM/SMBP Hamiltonian for Two Configurations and Three Different Density Functionals (BLYP, B3LYP, BHLYP)

			BLYP			B3LYP			BHLYP		
snapshot	Hamiltonian	gap	QM/MM	QM	MM	QM/MM	QM	MM	QM/MM	QM	MM
31	QM/MM	$E(^4A)-E(^6A)$	−9.50	−11.31	1.81	0.83	−0.71	1.54	16.49	14.40	2.09
		$E(^2A)-E(^6A)$	−9.98	−9.74	−0.24	6.94	7.11	−0.18	28.80	28.92	−0.12
	QM/MM/SMBP	$E(^4A)-E(^6A)$	−9.63	−10.89	1.26	0.82	−0.74	1.56	16.50	14.42	2.08
		$E(^2A)-E(^6A)$	−10.19	−9.80	−0.39	7.10	7.00	0.10	28.70	28.34	0.36
93	QM/MM	$E(^4A)-E(^6A)$	−9.52	−11.00	1.48	0.73	−0.98	1.72	16.40	13.69	2.72
		$E(^2A)-E(^6A)$	−10.66	−10.49	−0.17	6.33	6.75	−0.43	28.74	28.96	−0.22
	QM/MM/SMBP	$E(^4A)-E(^6A)$	−9.54	−10.62	1.08	0.83	−0.83	1.67	16.34	13.69	2.65
		$E(^2A)-E(^6A)$	−10.70	−10.32	−0.39	6.44	6.36	0.08	28.66	29.00	−0.35

biomolecule as those resulting from standard QM/MM optimizations.

5. Conclusion

In this article, we have introduced a general boundary potential (SMBP) for hybrid QM/MM calculations that complements the previously implemented boundary potential (GSBP). Both the SMBP and the GSBP extend the QM/MM approach to a three-layer model in which the outer solvent molecules and outer macromolecule region are represented by a boundary potential. Therefore, both account for the effect of bulk solvent and treat long-range electrostatic interactions accurately and efficiently. In both cases, the reaction field potential in the inner region needs to be computed by a finite-difference solution of the Poisson−Boltzmann equation (describing the bulk solvent as a dielectric continuum). In the GSBP scheme, this inner reaction field potential is expressed by its Green's function and is represented by a reaction field matrix that is determined once and for all at the beginning of a simulation and is then used to calculate the corresponding electrostatic interactions with the inner region charge density. In the SMBP scheme, the inner reaction field potential is computed on-the-fly as needed, and the interactions with the QM density are handled by a self-consistent reaction field procedure and a set of virtual surface charges that represent the SMBP in the QM calculations.

The GSBP performs best in MD simulations where the initial overhead for constructing the reaction field matrix (typically about 800 Poisson−Boltzmann calculations) is quickly overcompensated by the gains in each of the many steps during the MD simulation. The SMBP targets single-point calculations and geometry optimizations with a limited number of steps where the on-the-fly approach is most efficient. Since the approximations in the GSBP and SMBP treatments are very similar by design, and compatible with each other, the electronic and molecular structures resulting from QM/MM/SMBP geometry optimizations can be used as starting points for sampling over MM phase space using the QM/MM/GSBP Hamiltonian in the FEP framework. Free energy calculations on the PHBH enzyme show that this reduces the computational costs of the FEP calculations by 1 order of magnitude. The combined use of the SMBP and GSBP for computing potential energy profiles and subsequent sampling, respectively, thus provides an attractive and efficient strategy to perform free energy QM/MM calculations.

The GSBP implementation at the QM/MM level requires modifications of the underlying QM code, and corresponding work has been reported up to now only for semiempirical QM methods.[20,21] By contrast, because of its representation in terms of virtual surface charges, the SMBP can be used with any standard QM code that can handle external point charges, thus allowing for ab initio QM/MM/SMBP and DFT/MM/SMBP geometry optimizations in the context of three-layer QM/MM/continuum models. Another practical advantage of the SMBP is that it also offers significant speedups for standard two-layer QM/MM calculations: thousands of MM charges are replaced by a small set of virtual surface charges (with little overhead since no SCRF procedure is required in this case) whose electrostatic interactions with the inner region are easily computed (with overall savings typically by a factor of 2).

The accuracy of the SMBP has been evaluated by comparing the results from QM/MM/SMBP calculations to those from standard QM/MM calculations for three diverse test systems: Glycine in water turned out to be problematic for the SMBP. Due to the high flexibility of the polar solvent, many close-lying minima with different hydrogen-bond patterns and different relative energies exist, and as a consequence, geometry optimizations by QM/MM and QM/MM/SMBP normally follow a different course and yield different local minima (unless starting from a given QM/MM minimum which is retained by QM/MM/SMBP). The individual reaction and activation energies for proton transfer in solvated glycine thus differ appreciably between QM/MM and QM/MM/SMBP, while the mean values for a small sample of five configurations are much closer to each other (within 1 kcal/mol). The two enzymatic test systems are more rigid. They are treated by the SMBP with impressive accuracy. Geometry optimizations by QM/MM and QM/MM/SMBP normally follow the same course and lead to essentially identical structures, and relative energies differ on average by less than 1 kcal/mol. The magnitude of these deviations is comparable to the spread of results that naturally occurs for different initial configurations. Finally, in the case of PHBH, the combined use of the SMBP and GSBP leads to free energy profiles and barriers that are essentially the same as those from full QM/MM calculations. We conclude that these boundary potentials enable us to treat enzymes at the QM/MM level efficiently and with good accuracy.

Acknowledgment. This work was supported by the Max Planck Initiative on Multiscale Materials Modeling. T.B. gratefully acknowledges a Kekulé scholarship from the Fonds der Chemischen Industrie and helpful discussions with Dr. M. Waller. T.B. thanks Dr. A. Altun and Dr. S. Thiel for providing the molecular structures of cytochrome P450cam and *p*-hydroxybenzoate hydroxylase.

Note Added after ASAP Publication. This article was published ASAP on October 14, 2009. Table 3 has been modified. The correct version was published on October 22, 2009.

Supporting Information Available: Details of the glycine/water test system; evaluation of the accuracy of the electrostatic forces for the glycine/water system in bulk solvent and in vacuum; rms deviations of the QM/MM and QM/MM/SMBP optimized structures of cytochrome P450cam. This information is available free of charge via the Internet at http://pubs.acs.org.

References

(1) Hu, H.; Yang, W. *Annu. Rev. Phys. Chem.* **2008**, *59*, 573–601.

(2) Zhang, Y.; Liu, H.; Yang, W. *J. Chem. Phys.* **2000**, *112*, 3483–3492.

(3) Cisneros, G. A.; Liu, H.; Zhang, Y.; Yang, W. *J. Am. Chem. Soc.* **2003**, *125*, 10384–10393.

(4) Ridder, L.; Rietjens, I. M. C. M.; Vervoort, J.; Mulholland, A. J. *J. Am. Chem. Soc.* **2002**, *124*, 9926–9936.

(5) Kaminski, G. A.; Jorgensen, W. L. *J. Phys. Chem. B* **1998**, *102*, 1787–1796.

(6) Acevedo, O.; Jorgensen, W. L.; Evanseck, J. D. *J. Chem. Theory Comput.* **2007**, *3*, 132–138.

(7) Rod, T. H.; Ryde, U. *J. Chem. Theory Comput.* **2005**, *1*, 1240–1251.

(8) Strajbl, M.; Hong, G.; Warshel, A. *J. Phys. Chem. B* **2002**, *106*, 13333–13343.

(9) Senn, H. M.; Thiel, S.; Thiel, W. *J. Chem. Theory Comput.* **2005**, *1*, 494–505.

(10) Kästner, J.; Senn, H. M.; Thiel, S.; Otte, N.; Thiel, W. *J. Chem. Theory Comput.* **2006**, *2*, 452–461.

(11) Senn, H. M.; Thiel, W. *Top. Curr. Chem.* **2007**, *268*, 173–290.

(12) Senn, H. M.; Thiel, W. *Angew. Chem., Int. Ed.* **2009**, *48*, 1198–1229.

(13) Warshel, A.; Papazyan, A. *Curr. Opin. Struct. Biol.* **1998**, *2*, 211–217.

(14) Sagui, C.; Darden, T. A. *Annu. Rev. Biophys. Struct.* **1999**, *28*, 155–179.

(15) Davis, M. E.; McCammon, J. A. *Chem. Rev.* **1990**, *90*, 509–521.

(16) Garcia-Viloca, M.; Gao, J.; Karplus, M.; Truhlar, D. G. *Science* **2004**, *303*, 186–195.

(17) Nam, K.; Gao, J.; York, D. M. *J. Chem. Theory Comput.* **2005**, *1*, 2–13.

(18) Gao, J.; Alhambra, C. *J. Chem. Phys.* **1997**, *107*, 1212–1217.

(19) Walker, R. C.; Crowley, M. F.; Case, D. A. *J. Comput. Chem.* **2008**, *29*, 1019–1031.

(20) Schaefer, P.; Riccardi, D.; Cui, Q. *J. Chem. Phys.* **2005**, *123*, 014905/1−14.

(21) Benighaus, T.; Thiel, W. *J. Chem. Theory Comp.* **2008**, *4*, 1600–1609.

(22) Friedman, H. L. *Mol. Phys.* **1975**, *29*, 1533–1543.

(23) Wang, L.; Hermans, J. *J. Phys. Chem.* **1995**, *99*, 12001–12007.

(24) Berkowitz, M.; McCammon, J. A. *Chem. Phys. Lett.* **1982**, *90*, 215–217.

(25) Brooks, III, C. L.; Karplus, M. *J. Chem. Phys.* **1983**, *79*, 6312–6325.

(26) Brunger, A.; Brooks, III, C. L.; Karplus, M. *Chem. Phys. Lett.* **1984**, *105*, 495–500.

(27) Brunger, A.; Brooks, III, C. L.; Karplus, M. *Proc. Natl. Acad. Sci. U.S.A.* **1985**, *82*, 8458–8462.

(28) Lee, F. S.; Warshel, A. *J. Chem. Phys.* **1992**, *97*, 3100–3107.

(29) Alper, H.; Levy, R. M. *J. Chem. Phys.* **1993**, *99*, 9847–9852.

(30) Essex, J. W.; Jorgensen, W. L. *J. Comput. Chem.* **1995**, *16*, 951–972.

(31) Warshel, A.; King, G. *Chem. Phys. Lett.* **1985**, *121*, 124–129.

(32) Tironi, I. G.; Sperb, R.; Smith, P. E.; van Gunsteren, W. F. *J. Chem. Phys.* **1995**, *102*, 5451–5459.

(33) Beglov, D.; Roux, B. *J. Chem. Phys.* **1994**, *100*, 9050–9063.

(34) Im, W.; Bernèche, S.; Roux, B. *J. Chem. Phys.* **2001**, *114*, 2924–2937.

(35) Banavali, N. K.; Im, W.; Roux, B. *J. Chem. Phys.* **2002**, *117*, 7381–7388.

(36) Elstner, M.; Porezag, D.; Jungnickel, G.; Elstner, J.; Haugk, M.; Frauenheim, T.; Suhai, T.; Seifert, G. *Phys. Rev. B* **1998**, *58*, 7260–7268.

(37) König, P. H.; Ghosh, N.; Hoffmann, M.; Elstner, M.; Tajkhorshid, E.; Frauenheim, T.; Cui, Q. *J. Phys. Chem. A* **2006**, *110*, 548–563.

(38) Ma, L.; Cui, Q. *J. Am. Chem. Soc.* **2007**, *129*, 10261–10268.

(39) Zhu, X.; Jethiray, A.; Cui, Q. *J. Chem. Theory Comput.* **2007**, *3*, 1538–1549.

(40) Riccardi, D.; König, P.; Prat-Resina, X.; Yu, H.; Elstner, M.; Frauenheim, T.; Cui, Q. *J. Am. Chem. Soc.* **2006**, *128*, 16302–16311.

(41) Riccardi, D.; Schaefer, P.; Cui, Q. *J. Phys. Chem. B* **2005**, *109*, 17715–17733.

(42) Chandrasekhar, J.; Smith, S. F.; Jorgensen, W. L. *J. Am. Chem. Soc.* **1984**, *106*, 3049–3059.

(43) Chandrasekhar, J.; Jorgensen, W. L. *J. Am. Chem. Soc.* **1985**, *107*, 2974–2975.

(44) Jorgensen, W. L. *Acc. Chem. Res.* **1989**, *22*, 184–189.

(45) Chandrasekhar, J.; Smith, S. F.; Jorgensen, W. L. *J. Am. Chem. Soc.* **1985**, *107*, 154–163.

(46) Kuhn, B.; Kollmann, P. A. *J. Am. Chem. Soc.* **2000**, *122*, 2586–2596.

(47) Kollmann, P. A.; Kuhn, B.; Donini, O.; Perakyla, M.; Stanton, R.; Bakowies, D. *Acc. Chem. Res.* **2001**, *34*, 72–79.

(48) Bentzien, J.; Mueller, R. P.; Floriá, J.; Warshel, A. *J. Phys. Chem. B* **1998**, *102*, 2293–2301.

(49) Olsson, M. H. M.; Hong, G.; Warshel, A. *J. Am. Chem. Soc.* **2003**, *125*, 5025–5039.

(50) Warshel, A. *Annu. Rev. Biophys. Biomol. Struct.* **2003**, *32*, 425–443.

(51) Zwanzig, R. W. *J. Chem. Phys.* **1954**, *22*, 1420–1426.

(52) Cisneros, G. A.; Wang, M.; Silinski, P.; Fitzgerald, M. C.; Yang, W. *Biochemistry* **2004**, *43*, 6885–6892.

(53) Wang, M.; Lu, Z.; Yang, W. *J. Chem. Phys.* **2004**, *121*, 101–107.

(54) Donini, O.; Darden, T.; Kollman, P. A. *J. Am. Chem. Soc.* **2000**, *122*, 12270–12280.

(55) Klapper, I.; Hagstrom, R.; Fine, R.; Sharp, K.; Honig, B. *Proteins* **1986**, *1*, 47–59.

(56) Sherwood, P.; et al. *J. Mol. Struct. (THEOCHEM)* **2003**, *632*, 1–28.

(57) Mulliken, R. S. *J. Chem. Phys.* **1962**, *36*, 3428–3439.

(58) Tannor, D. J.; Marten, B.; Murphy, R.; Friesner, R. A.; Sitkoff, D.; Nicholls, A.; Honig, B.; Ringnalda, M.; Goddard, W. A. *J. Am. Chem. Soc.* **1994**, *116*, 11875–11882.

(59) Hayik, S. A.; Liao, N.; Merz, K. M. *J. Chem. Theory Comput.* **2008**, *4*, 1200–1207.

(60) Im, W.; Beglov, D.; Roux, B. *Comput. Phys. Commun.* **1998**, *111*, 59–75.

(61) Bakowies, D.; Thiel, W. *J. Phys. Chem.* **1996**, *100*, 10580–10594.

(62) Jensen, F. Transition State Theory and Statistical Mechanics. In *Introduction to Computational Chemistry;* John Wiley & Sons: Chichester; England, **1999**; pp 301–304.

(63) ChemShell. http://www.chemshell.org (accessed August 14, 2009).

(64) Thiel, W. MNDO2004; Max-Planck-Institut für Kohlenforschung: Mülheim an der Ruhr, Germany, 2004.

(65) Ahlrichs, R.; Bär, M.; Häser, M.; Horn, H.; Kölmel, C. *Chem. Phys. Lett.* **1989**, *162*, 165–169.

(66) Smith, W.; Forester, T. *J. Mol. Graph.* **1996**, *14*, 136–141.

(67) MacKerell, A. D.; et al. *J. Phys. Chem. B* **1998**, *102*, 3586–3616.

(68) Billeter, S. R.; Turner, A. J.; Thiel, W. *Phys. Chem. Chem. Phys.* **2000**, *2*, 2177–2186.

(69) Press, W. H.; Flannery, B. P.; Teukolsky, S. A.; Vetterlig, W. T. Partial Differential Equations. In *Numerical Recipes in C*; Cambridge University Press: Cambridge, England, 1988; pp 673−680.

(70) Nicholls, A.; Honig, B. *J. Comput. Chem.* **1991**, *12*, 435–445.

(71) Im, W.; Seefeld, S.; Roux, B. *Biophys. J.* **2000**, *79*, 788–801.

(72) Nosé, S. *J. Chem. Phys.* **1984**, *81*, 511–519.

(73) Nosé, S. *Mol. Phys.* **1984**, *52*, 255–268.

(74) Hoover, W. G. *Phys. Rev. A* **1985**, *31*, 1695–1697.

(75) Martyna, G. J.; Klein, M. L.; Tuckerman, M. *J. Chem. Phys.* **1992**, *97*, 2635–2643.

(76) Ryckaert, J.-P.; Ciccotti, G.; Berendsen, H. J. C. *J. Comput. Phys.* **1977**, *23*, 327–341.

(77) Bandyopadhyay, P.; Gordon, M. S. *J. Chem. Phys.* **2000**, *113*, 1104–1109.

(78) Bandyopadhyay, P.; Gordon, M. S.; Mennucci, B.; Tomasi, J. *J. Chem. Phys.* **2002**, *116*, 5023–5032.

(79) Gontrani, L.; Mennucci, B.; Tomasi, J. *J. Mol. Struct. (THEOCHEM)* **2000**, *500*, 113–127.

(80) Cui, Q. *J. Chem. Phys.* **2002**, *117*, 4720–4728.

(81) Claeyssens, F.; Harvey, J. N.; Manby, F. R.; Mata, R. A.; Mulholland, A. J.; Ranaghan, K. E.; Schütz, M.; Thiel, S.; Thiel, W.; Werner, H.-J. *Angew. Chem., Int. Ed.* **2006**, *45*, 6856–6859.

(82) Mata, R. A.; Werner, H.-J.; Thiel, S.; Thiel, W. *J. Chem. Phys.* **2008**, *128*, 025104/1−8.

(83) Ridder, L.; Mulholland, A. J.; Vervoort, J.; Rietjens, I. M. C. M. *J. Am. Chem. Soc.* **1998**, *120*, 7641–7642.

(84) Ridder, L.; Harvey, J. N.; Rietjens, I. M. C. M.; Vervoort, J.; Mulholland, A. J. *J. Phys. Chem. B* **2003**, *107*, 2118–2126.

(85) Billeter, S. R.; Hanser, C. F. W.; Mordasini, T. Z.; Scholten, M.; Thiel, W.; van Gunsteren, W. F. *Phys. Chem. Chem. Phys.* **2001**, *3*, 688–695.

(86) Shaik, S.; Kumar, D.; de Visser, S. P.; Altun, A.; Thiel, W. *Chem. Rev.* **2005**, *105*, 2279–2328.

(87) Shaik, S.; Cohen, S.; Wang, Y.; Chen, H.; Kumar, D.; Thiel, W. *Chem. Rev.* ASAP article, DOI: 10.1021/cr900121s.

(88) Altun, A.; Thiel, W. *J. Phys. Chem. B* **2005**, *109*, 1268–1280.

(89) Woo, H.-J.; Dinner, A. R.; Roux, B. *J. Chem. Phys.* **2004**, *121*, 6392–6400.

(90) Deng, Y.; Roux, B. *J. Chem. Phys.* **2008**, *128,* 115103/1−8.

(91) Brooks, B. R.; Bruccoleri, R. E.; Olafson, B. D.; States, D. J.; Swaminathan, S.; Karplus, M. *J. Comput. Chem.* **1983**, *4*, 187–217.

(92) Dewar, M. J. S.; Zoebisch, E. G.; Healy, E. F.; Stewart, J. J. P. *J. Am. Chem. Soc.* **1985**, *107*, 3902–3909.

(93) Gilson, M. K.; Sharp, K. A.; Honig, B. H. *J. Comput. Chem.* **1987**, *9*, 327–335.

(94) Becke, A. D. *Phys. Rev. A* **1988**, *38*, 3098–3100.

(95) Lee, C.; Yang, W.; Parr, R. G. *Phys. Rev. B* **1988**, *37*, 785–789.

(96) Becke, A. D. *J. Chem. Phys.* **1993**, *98*, 5648–5652.

(97) Schäfer, A.; Horn, H.; Ahlrichs, R. *J. Chem. Phys.* **1992**, *97*, 2571–2577.

(98) Schäfer, A.; Huber, C.; Ahlrichs, R. *J. Chem. Phys.* **1994**, *100*, 5829–5835.

(99) Schlichting, I.; Berendzen, J.; Chu, K.; Stock, A. M.; Maves, S. A.; Benson, D. E.; Sweet, R. M.; Ringe, D.; Petsko, G. A.; Sligar, S. G. *Science* **2000**, *287*, 1615–1622.

(100) Becke, A. D. *J. Chem. Phys.* **1993**, *98*, 1372–1377.

(101) Wachters, A. J. H. *J. Chem. Phys.* **1970**, *52*, 1033–1036.

(102) Hay, P. J. *J. Chem. Phys.* **1977**, *66*, 4377–4384.

(103) Bauschlicher, C. W., Jr.; Langhoff, S. R.; Partridge, H.; Barnes, L. A. *J. Chem. Phys.* **1989**, *91*, 2399–2411.

CT900437B

JCTC Journal of Chemical Theory and Computation

On the Use of low-resolution Data to Improve Structure Prediction of Proteins and Protein Complexes

Marco D'Abramo,[†] Tim Meyer,[†] Pau Bernadó,[‡] Carles Pons,[§,⊥]
Juan Fernández Recio,[§] and Modesto Orozco*,[†,||,⊥]

Molecular Modeling and Bioinformatics Unit, IRB-BSC Joint Research Program in Computational Biology, Institute for Research in Biomedicine Josep Samitier 1-5, Barcelona 08028, Spain and Barcelona Supercomputing Center, Jordi Girona 29, Barcelona 08034, Spain, Structural and Computational Biology Program, Institute for Research in Biomedicine Josep Samitier 1-5, Barcelona 08028, Spain, Life Sciences Department, Barcelona Supercomputing Center, Jordi Girona 29, Barcelona 08034, Spain, Departament de Bioquímica i Biología Molecular, Facultat de Biología, Universitat de Barcelona, Avgda Diagonal 645, Barcelona 08028, Spain, and National Institute of Bioinformatics, Parc Científic de Barcelona, Josep Samitier 1-5, Barcelona 08028, Spain

Received June 16, 2009

Abstract: We present a systematic study of the ability of low-resolution experimental data, when combined with physical/statistical scoring functions, to improve the quality of theoretical structural models of proteins and protein complexes. Particularly, we have analyzed in detail the "extra value" added to the theoretical models by: electrospray mass spectrometry (ESI-MS), small-angle X-ray scattering (SAXS), and hydrodynamic measurements. We found that any low-resolution structural data, even when (as in the case of mass spectrometry) obtained in conditions far from the physiological ones, help to improve the quality of theoretical models, but not all the coarse-grained experimental results are equally rich in information. The best results are always obtained when using SAXS data as experimental constraints, but either hydrodynamics or gas phase CCS data contribute to improving model prediction. The combination of suitable scoring functions and broadly available low-resolution structural data (technically easier to obtain) yields structural models that are notably close to the real structures.

Introduction

The prediction of the three-dimensional structures of proteins based only on the knowledge of their sequences has been the "Holy Grail" of computational biology for many years. Proteins with very close homologues of known structure can now be safely modeled with a quite good global quality,[1,2] but there are still many proteins for which homologues cannot be found in structural databases, and they have to be modeled based on more risky threading or ab initio methods.[2] Recent versions of these programs, combined with suitable scoring functions, are able to provide ensembles of reasonable solutions among which the real one is hidden. Unfortunately, as CASP experiments have demonstrated,[3] it is not always easy to detect the best solution among many reasonable ones. The situation is even more challenging in the prediction of protein−protein complexes, especially in those cases where an important degree of structural distortion in the monomers is required for the assembly. Although recent CAPRI (http://www.ebi.ac.uk/msd-srv/capri) experiments have demonstrated that, at least in some cases, it is possible to produce

---

* Corresponding author. E-mail: modesto@mmb.pcb.ub.es.

[†] Molecular Modeling and Bioinformatics Unit, Institute for Research in Biomedicine and Barcelona Supercomputing Center.

[‡] Structural and Computational Biology Program, Institute for Research in Biomedicine.

[§] Life Sciences Department, Barcelona Supercomputing Center.

[||] Universitat de Barcelona.

[⊥] National Institute of Bioinformatics.

10.1021/ct900305m CCC: $40.75

theoretical models of sufficient quality for accurate biological and functional annotation, there are still too many cases for which even the best protein−protein docking codes suggest structural models that are very far from the reality.[4] Errors in the prediction of the structure of proteins or protein complexes might lead to the design of irrelevant experiments and to the formulation of erroneous functional hypothesis.

Due to the complexity of predicting the structure of proteins and protein complexes based only on theoretical methods, several authors have supported the use of experimental data to restrain the accessible space to be sampled by the theoretical algorithms. In this field, the combination of physical methods like molecular dynamics (MD) with high-resolution techniques, such as X-ray or NMR spectroscopy, has been very fruitful for many years and is considered the gold standard for protein structure determination.[5] Unfortunately, high-resolution methods are not always easy to apply in a high-throughput mode for proteins of moderate or large size, and MD is not the best technique to predict the novo protein structures due to CPU requirements and to force-field uncertainties. Thus, alternative methods need to be designed to combine methods for the prediction of the structure of proteins and protein complexes with easy-to-obtain low-resolution structural data.

Evolutionary analysis, through the detection of correlated mutations,[6] the evolutionary trace method,[7] or the use of environment-specific substitution tables,[8] is a source of low-resolution data that can be easily incorporated into structure prediction to discard unlikely models.[9−11] Site-directed mutagenesis has been another source of data on the location of individual residues in different protein regions or on the relative positioning of pairs of residues in the three-dimensional structure.[12,13] A similar type of information can be obtained by using covalent cross-linkers coupled, for example, to mass spectroscopic measures.[14] However, all these techniques have obvious caveats: (i) evolutionary analysis from multiple sequence/structure alignments is prone to error, and it requires a massive amount of data that is not always available, and (ii) site-directed mutagenesis and cross-linking experiments are technically complex and (as correlated mutations) provide only local information of a few selected residues, not on global three-dimensional structure. Cryo-electron tomography is a very promising technique able to provide detailed structural information of the sample but not fast and cheap enough, yet, to be easily used in a high-throughput context. We believe that more general structural information on proteins and complexes can be gained from other low-resolution biophysical methods, such as the small-angle X-ray scattering (SAXS) hydrodynamic radius (R_h) estimations derived from hydrodynamic measurements or the apparent charge or collision cross-sections (CCS) determined in mass spectroscopy experiments. All these methods are simple and fast and can be performed at a high-throughput regime, making them ideal for proteome-scale or cell-scale determination of proteins or protein−protein complexes. Unfortunately, none of them is able to provide by themselves unambiguous three-dimensional structural models of proteins. In this paper, we provide a systematic analysis on the robustness of these low-resolution data and on their ability to enrich structural predictions of theoretical models of protein and protein−protein complexes.

Methods

Calculation of Synthetic Low-Resolution Structural Data. We have explored three experimental observables providing low-resolution structural information on proteins: (i) the collision cross-section (CCS), (ii) the small-angle X-ray scattering spectra (SAXS), and (iii) the hydrodynamic radius (R_h). CCS is experimentally derived from the time-of-flight of protein ions in a spectrometer drift tube in the presence of inert gases under electrospray vaporization conditions and provides information on the effective area of collision of the inert molecules with a protein under vacuum conditions.[15] SAXS profiles are experimentally obtained from the analysis of the elastically scattered X-rays by particles in solution and provide low-resolution (>15 Å) structural information of them, essentially referring to their size and shape.[16−18] Finally, the hydrodynamics radii also provide information on the overall size of the proteins determined by its self-diffusion coefficients via the Stokes−Einstein relationship.[19] For benchmark purposes, low-resolution structural data were simulated here from known experimental structures or from MD trajectories to probe the robustness of the data to dynamics and/or environmental effects (see below).

A subset of CCS values were evaluated using: (i) the most accurate (but computationally demanding) trajectory method (TM),[23] where the colliding ions are treated as a collection of atoms, each one represented by a 12−6−4 potential (i.e., including a realistic treatment of long-range interactions between the ion and the buffer gas, which have been found to significantly affect the CCS), and the orientationally averaged collision integral is determined by averaging over all possible collision geometries and (ii) the faster but less accurate projection approximation (PA), as implemented in the sigma software,[31] which essentially finds the average "shadow" as a trial conformer is rotated through all possible orientations, disregarding the details of the scattering process. The good correlation between PA and TM values ($r = 0.99$, data not shown) allowed to extrapolate accurate TM-CCS values by applying an empirical correction factor of 1.3 to the PA-CCS estimates. The SAXS curves were simulated by means of the CRYSOL program[22] using default parameters, and the HydroNMR[20] software package was used to calculate R_h using a value of 3.3 Å as the atomic element radius.[21] The calculation of low-resolution parameters from known experimental data raises some concerns that need to be considered before evaluating the information load contained in these data: (i) in the case of CCS, experimental measures are recorded in the gas phase, and it is not clear how well gas-phase structures represent solution ensembles,[24,25] (ii) Dynamics effects are expected to introduce non-negligible changes of different magnitude, and (iii) low-resolution experimental measures are always prone to errors and to uncertainties that cannot be neglected. Thus, as a first step in our study, we checked the goodness of gas-phase electrospray mass spectrometric (MS-ESI) experiments as sources of structural information on the solution structure.

This was done by performing extended (0.1 μs long) MD simulations in gas-phase conditions for different proteins: bovine pancreatic trypsin inhibitor (1BPI), Cytochrome c6 (1LS9), egg-white lysozyme (1LYS), and ubiquitin (1UBQ) as well as protein−protein complexes: (1ACB, 1CBW, 1CSE, and 3TGI). Protein charges were determined from their empirical relationship to the solvent accessible surface area (SASA),[26] charges were placed at most favorable positions using an iterative titration algorithm[27] which yields a quite symmetric charge distribution (less careful titration procedures, leading to local charge concentration, are likely to produce artifactual unfoldings of protein structure even during short MD simulations). Previous calculations on a large set of protein folds[27] demonstrated that the trajectories are not very sensitive to alternative (if reasonable) choices of titrable site, which means that the ensemble of conformations sampled for the most stable charge configuration (for a given charge state) is a good representative of the ensemble of conformations found experimentally (where different distributions of charge might coexist). In order to check the importance of the total charge in the structure, we performed additional simulations using slightly different charge states for three proteins for which CCS was experimentally determined for different charge states (1UBQ, 1LS9 and 1LYS; see data on http://www.indiana.edu/~clemmer/Research). For one of the proteins (1UBQ), calculations were repeated using a large charge density to check whether or not the protein structure will be stable when very heavily charged.

MD simulation protocols described elsewhere[27] were used to obtain vacuum trajectories for the different protein systems. In order to guarantee that results were not contaminated from force-field uncertainties, protein simulations were repeated using three of the most popular force fields (AMBER-parm03,[28] OPLSAA,[29] and CHARM22[30]). These calculations did not reveal any force-field dependent artifacts, and accordingly, more costly simulations for protein complexes were performed considering only the parm03 force field. Snapshots from the 0.1 μs trajectories were collected every 2 ps and used for structural analysis and for the computation of the CCS. All gas-phase simulations were carefully checked to verify the lack of structural distortions in the gas phase, which could create doubts on the validity of the CCS measures as descriptors of protein structure in solution.

The robustness of low-resolution measures to protein flexibility was analyzed by running MD simulations for the different proteins and protein complexes (see Table 1) in aqueous solution using the TIP3P water model[32] with periodic boundary conditions and with particle mesh corrections[33] in the isothermal ($T = 300$ K) isobaric ($P = 1$ atm) ensemble. Trajectories were collected using AMBER parm03 for 100 ns (10 for complexes) after 1 ns of equilibration, following the procedure noted elsewhere.[27] MD ensembles were collected and used to predict the R_h, CCS, and SAXS profiles, which were then compared to those obtained by a single structure (experimental or the MD-averaged one). Experimental data, when used to determine a single structure, have an associated error related to the technique itself and to the fluctuations in the structure. To estimate an upper limit for this magnitude, we used the standard deviations (σ) in the parameters, as provided by MD simulations, which undoubtedly represent an overestimation of the experimental uncertainty, i.e., values outside the $\pm 3\sigma$ interval for CCS ($\pm 2\sigma$ for $<\chi>_\mathrm{SAXS}$ and R_h), with respect to those corresponding to the experimental structures were disregarded. This choice means that the test of enrichment below represents then a lower limit of accuracy for the proposed methodology.

Empirical Scoring Functions. We have complemented the use of low-resolution structural data by introducing the empirical scoring functions developed to detect local errors in the structures of protein monomers and protein complexes, which are probably not detected in low-resolution structural data, as those used in this paper. For this purpose, ProSA-II[34] was used to study monomeric proteins, and pyDock[35] was used to analyze protein complexes. ProSA-II is a diagnostic tool that is based on the use of residue−residue potentials of mean force derived from the statistical analysis of all available protein structures. The scoring function in pyDock is composed of "soft-truncate" van der Waals (with 0.1 weighting factor; AMBER parameters; with maximum values of +1.0 kcal/mol), Coulombic electrostatics (with distance-dependent dielectric constant, AMBER charges with the Coulombic term truncated to ± 1.0 kcal/mol), and accessible surface-area-based desolvation energy with atomic solvation parameters (ASP) previously optimized for rigid-body docking. This scoring scheme has shown top performance in the scorer experiment at the most recent CAPRI competition. Before pyDock scoring, incomplete side chains have been automatically rebuilt with SCWRL 3.0.[36]

Set of Predicted Structures. The ability of low-resolution data (supplemented by empirical scoring functions) to improve model prediction was first tested using all the model sets submitted to the CASP7 competition. For each model, CCS, SAXS curve, R_h, and PROSA-II, Z-scores[34] were computed. Models showing one or more of the four observables (CCS, $<\chi>_\mathrm{SAXS}$, R_h, and $Z_\mathrm{score}^\mathrm{PROSA}$) in severe disagreement (see above) with the corresponding experimental structure were discarded, and a new prediction set was calculated. In order to generate the prediction curves of the protein complexes, all the available models for predictors found in the CAPRI experiment web site (http://www.ebi.ac.uk/msd-srv/capri) were used. The general protocol for structure observable prediction was as above, with the only difference that we used the energy-based scoring function provided by pyDock instead of that in PROSA-II. In all cases, refined predictions were compared to a background model obtained by repeating the procedure but setting to infinite level of noise.

Results and Discussion

Effect of Structural Flexibility on Low-Resolution Data. MD simulations were used to generate ensembles of conformations for different proteins and protein complexes and to check the robustness of the different low-resolution data to structural fluctuations. Average results in Table 1

Table 1. MD Simulations for the Different Proteins and Protein Complexes[a]

simulation[b]	RMSd Å	std dev	TmScore (Å)	std dev	R_g (Å)	std dev	R_h (Å)	std dev	CCS (Å^2)
1UBQ P03	4.2	0.3	1.4	0.1	11.8	0.1	17.0	0.1	1 054
1UBQ C22	4.4	0.2	1.9	0.1	11.7	0.1	17.0	0.2	1 043
1UBQ ON2	4.5	0.2	1.9	0.1	11.8	0.1	17.0	0.1	1 051
1UBQ P99 T3P	1.5	0.4	1.2	0.1	11.8	0.1	17.3	0.2	1 084
1UBQ X-ray					11.6		17.1		972
1UBQ expt									1 050[c]
1BPI P03	2.4	0.2	1.4	0.1	11.7	0.1	16.1	0.2	919
1BPI C22	2.6	0.2	2.0	0.2	11.5	0.1	16.1	0.3	912
1BPI ON2	2.8	0.2	2.0	0.1	11.4	0.1	15.9	0.3	916
1BPI P99 T3P	1.2	0.2	1.4	0.1	11.0	0.1	15.9	0.2	977
1BPI X-ray					11.3		16.2		797
1BPI expt									900[c]
1LYS P03	2.8	0.1	1.9	0.1	13.7	0.1	19.3	0.1	974
1LYS C22	3.5	0.2	2.1	0.1	13.8	0.1	19.6	0.1	988
1LYS ON2	4.4	0.2	2.3	0.1	13.7	0.1	19.6	0.1	996
1LYS P99 T3P	1.0	0.2	1.1	0.1	14.2	0.1	20.2	0.1	1 088
1LYS X-ray					13.9		19.8		1 031
1LS9 P03	2.4	0.1	1.7	0.1	12.0	0.1	17.4	0.2	761
1LS9 C22	3.6	0.3	2.1	0.1	12.2	0.1	17.5	0.2	777
1LS9 ON2	2.9	0.2	2.0	0.1	12.2	0.1	17.6	0.2	778
1LS9 P99 T3P	1.3	0.3	1.5	0.2	12.4	0.1	18.1	0.2	820
1LS9 X-ray					12.0		17.7		716[c]

complexes	RMSd (Å)	std dev	TmScore (Å)	std dev	R_g (Å)	std dev	R_h (Å)	std dev	CCS (Å^2)
1ACB X-ray					19.1		27.2		1 842
1ACB T3P	1.6	0.2	1.3	0.3	19.4	0.1	26.8	0.2	1 916
1ACB vac	3.0	0.1	2.5	0.3	17.4	0.1	25.6	0.2	1 772
1CBW X-ray					18.8		27.4		1 797
1CBW T3P	1.8	0.5	1.5	0.8	19.2	0.1	27.0	0.3	1 917
1CBW vac	4.7	0.2	2.1	0.1	17.1	0.0	26.0	0.2	1 799
1CSE X-ray					19.1		27.2		1 858
1CSE T3P	1.2	0.2	0.8	0.1	19.4	0.1	26.8	0.2	1 906
1CSE vac	2.9	0.3	1.8	0.2	18.5	0.1	25.6	0.2	1 782
3TGI X-ray					17.2		25.8		1 749
3TGI T3P	1.3	0.2	1.1	0.1	18.8	0.1	26.4	0.3	1 809
3TGI vac	5.8	0.4	3.2	0.2	18.1	0.1	25.2	0.3	1 770

[a] The code after the PDB name indicates the force field used in the protein MD simulations (P03 = AMBER-parm03, C22 = CHARM22, and ON2 = OPLSAA). T3P and vac denotes simulations in water using the TIP3P water model and in vacuum conditions, respectively. [b] Charge states used in the MD simulations were +6 for 1UBQ, +6 for 1BPI, +8 for 1LYS, and +7 for 1LS9. Where available, the corresponding experimental CCS values for the same charge state used in the simulation are reported. [c] Experimental CCS values were taken from ref 41a for 1UBQ, from ref 41b for 1BPI, and from ref 41d41d for 1LS9.

and specific examples in Figure 1 demonstrate that flexibility introduced by MD simulation does not disrupt the native conformation but leads to a non-negligible oscillation in structure. Differences in the oscillation of RMSd and Tm-Scores indicate that most of the structural variation found along the trajectories is localized in loops, which is expected to be very mobile in aqueous solution, but the remaining regions of proteins are quite stable after 0.1 μs (see Figure 1). Very interestingly, the total number of residue−residue contacts is also very stable along the trajectory (Figure 2), but individual residue−residue contacts are much more labile. In fact, less than 50% of the "native" contacts appearing in the MD-averaged structure are present during the entire trajectory, while the rest are in fast interchange (Figure 2). Interestingly, while MD and experimental structures are very close (see Supporting Information, Figure S1), only 70−80% of the experimental native contacts are conserved more than 10% of the time in our trajectories. All these results suggest that some caution is necessary in the interpretation of the concept of native contact, since large portions of proteins behave like liquids or melted solids,[37] with many residues being quite promiscuous. On the contrary, the global structure seems quite insensitive to flexibility effects, suggesting that the overall structure descriptors, which can be easily obtained from low-resolution experiments, might be also quite robust to structural oscillation in water at room temperature. This is confirmed by inspection of Figures 3 and 4, which illustrate that all the low-resolution structural descriptors considered here — CCS, R_h, and SAXS curves — are very stable and show only moderate variations along the trajectory. All of these findings strongly suggest that these structural descriptors can be safely used as structural restraints to derive an average protein (or protein complex) structure.

Reliability of Structural Data Obtained in the Gas Phase. As noted above, a second topic of concern is whether or not structural data in the gas phase (like CCS) reflect the structural properties in solution. In order to analyze this point, we performed extended MD simulations of isolated proteins and of protein complexes in the gas phase, using simulation conditions similar to those of electrospray mass spectroscopy.[27] As previously found for other proteins,[27,38−40] vaporization preserves surprisingly well (at least in the submicrosecond time scale) the structure of proteins, at both the local

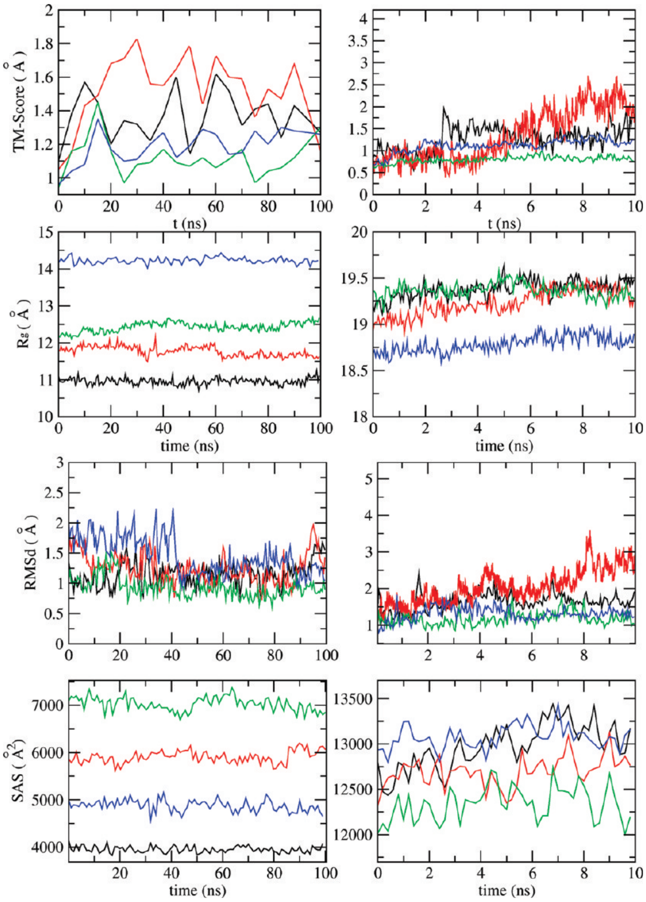

Figure 1. Variation of different structural descriptors along MD trajectories of some proteins and protein complexes. Top to bottom: TmScore, radii of gyration, root-mean-square derivation, and solvent accessible surface. Left: monomeric proteins (green: 1LYS, red: 1LS9, blue: 1UBQ, and black: 1BPI). Right: protein complexes (green: 1CSE, red: 1CBW, blue: 3TGI, and black: 1ACB).

and global levels (see Figures 5 and 6 and Supporting Information, Figure S1). Particularly, global structural descriptors are always well maintained irrespective of the force field used for the simulations (Figure 6), suggesting that gas-phase data derived from electrospray experiments contain structural information that could be used to understand the structure of proteins in solution. This is confirmed when analyzing the CCS obtained from MD trajectories in the gas phase, which are only slightly smaller than those derived from trajectories in solution (in average 6%, see Figure 7). The agreement between the MD gas phase CCS and the CCS derived from the X-ray structure is good (6% overestimation), in fact better than obtained between X-ray CCS and MD-solution CCS (aqueous simulations overestimate by 12% the CCS expected for the protein in X-ray structure), suggesting that the crystal lattice is compressing slightly the protein with respect to the dilute aqueous conditions and confirming that in vacuo structural information can be used to obtain structural insights for the protein in solution. Two additional points are worth noting here: (i) the excellent agreement found between the available experimental (gas phase) and MD-computed values (Figure 7), which reinforces the confidence in our simulations and (ii) the smaller standard deviation in the structural descriptors associated to gas phase simulations, which confirms the idea that in the gas phase the structure of the protein is rigidified, reducing the impact of flexibility (Figure 7).

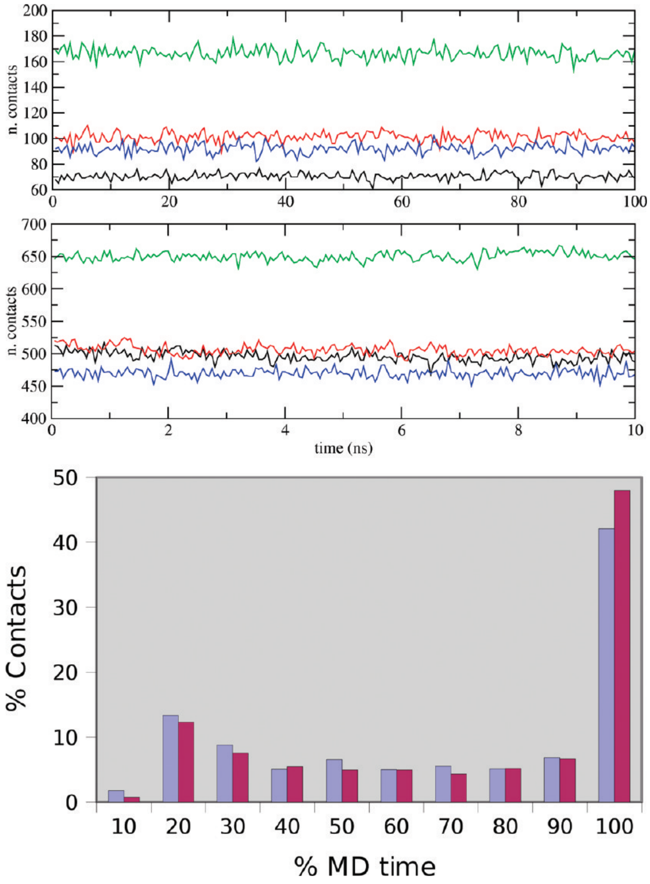

Figure 2. Oscillation in the total number of residue−residue contacts along the trajectories of proteins (top panel; color code in Figure 1) and protein complexes (bottom panel; color code in Figure 1). The histogram in the bottom corresponds to the distribution of residue contacts (blue protein monomers and red protein complexes) according to their persistence in trajectory (from 10 to 100%). In all cases, a residue is considered in contact when the Cα-Cα distance is lower than 7 Å in MD trajectories of proteins and protein complexes.

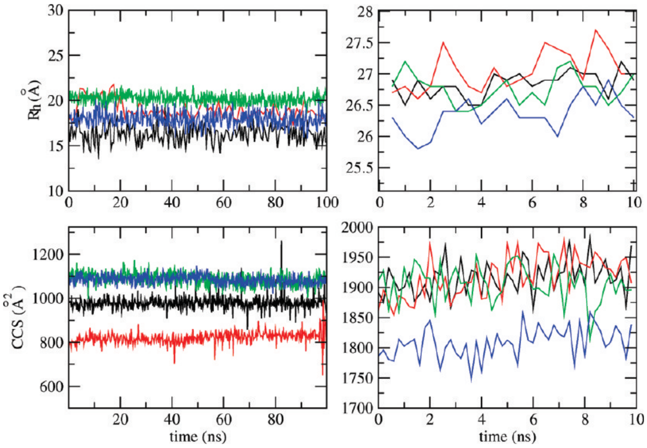

Figure 3. Oscillation of R_h (top plots) and CCS (bottom plots) versus time for some protein monomers (left) and protein-complexes (right). Color code as in Figure 1.

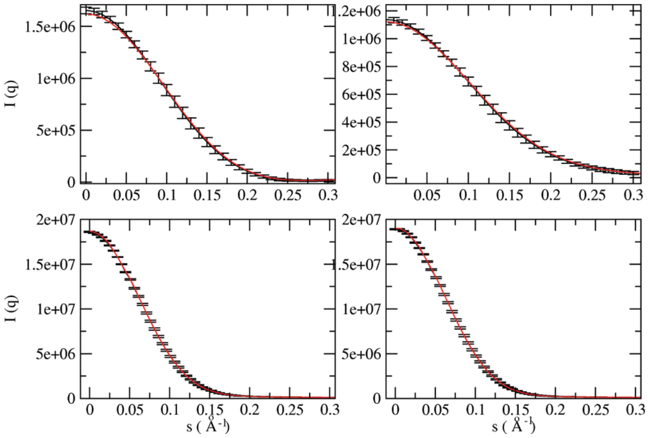

Figure 4. Superposition of SAXS curves obtained for protein structures sampled during MD trajectories of two proteins (left) and two protein complexes (right). The line in red corresponds to the curve simulated for a single average structure, while the line in black (with standard deviations) corresponds to the averaged spectra. Note that in the region richer in information (*s* around 0.1), the black and red lines are equivalent.

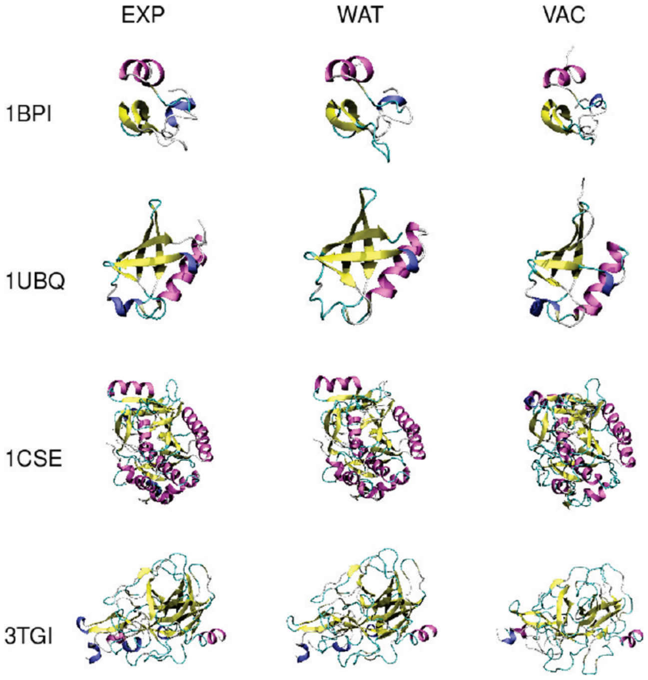

Figure 5. Representation of the experimental and MD-averaged structures of selected monomeric proteins (1BPI and 1UBQ) and protein complexes (1CSE and 3TGI). In all cases, the experimental structure, the MD-averaged one in aqueous solution, and the MD-averaged structure obtained after extended simulation in the gas phase are displayed.

In order to check whether or not results were too dependent on the total charge assigned to the protein, we collected additional trajectories for ubiqutin, cytochrome C and lysozime using a range of charge states around the expected optimum one (see above). Results, reported in the Supporting Information, Figure S2, strongly suggest that within the region of interest (i.e., close to the expected charge state), the protein structure is quite insensitive to changes in total charge, in good agreement with the experimental data[41] (see Supporting Information, Figure S2). For one of the proteins (ubiquitin), for which a very large positive charge was considered, protein unfolding was observed (see Supporting Information, Figure S2), in agreement with results reported by other groups.[41d] The fact that, in these extreme conditions, the MD-simulated CCS was smaller than that of the experimentally found[41a] is not unexpected, and simply reflects that the trajectory was too short to reproduce a complete unfolding, which, according to experimental measures, is expected to happen in the millisecond time scale.[41d,25b] In any case, it seems that, unless extreme charge conditions are considered, the gas phase CCS remains close to those expected for solution structures.

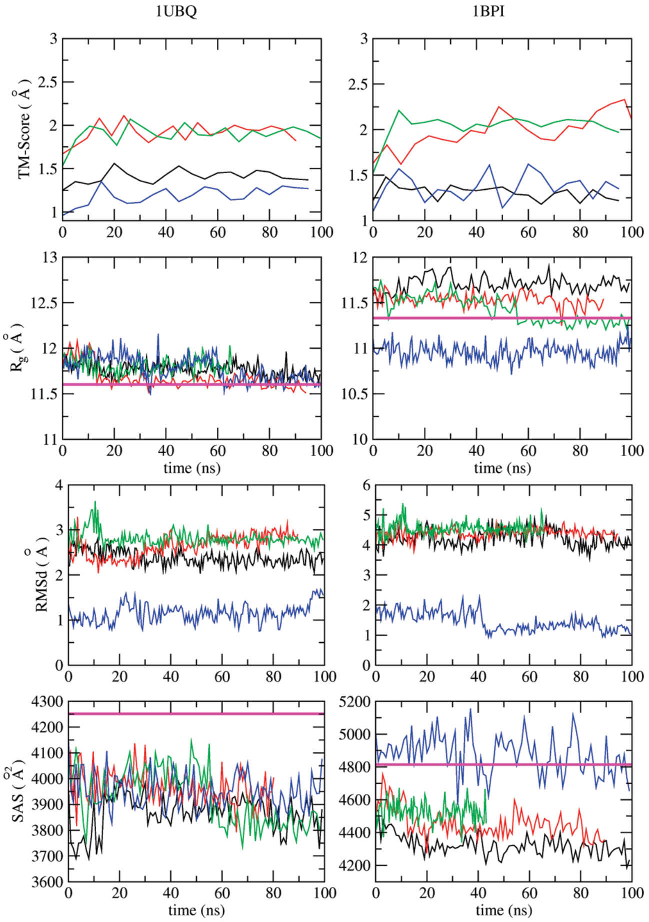

Figure 6. Global structural descriptors (TmScore, gyration radii, RMSd, and SAS) for proteins in the gas phase for 1BPI and 1UBQ obtained from MD simulations in the gas phase with CHARM22 (green), OPLSAA (red), and AMBER-parm03 (black) force fields. The reference results for the simulation in solution are displayed in blue, and the values derived from the experimental structure (crystal) are shown as straight lines in magenta.

MD simulations suggest that protein complexes are stable in the gas phase for long periods of time, and that the sampled gas-phase structures are not far away from the standard sampled structures in aqueous solution (see Figure 5). This is clearly shown in different metrics displayed in Figure 8, which demonstrate that the conclusions derived for proteins are also valid for noncovalent protein complexes and that despite non-negligible local distortions the overall shapes of the protein complexes are well preserved in the gas phase, at least in the submicrosecond time scale. Not

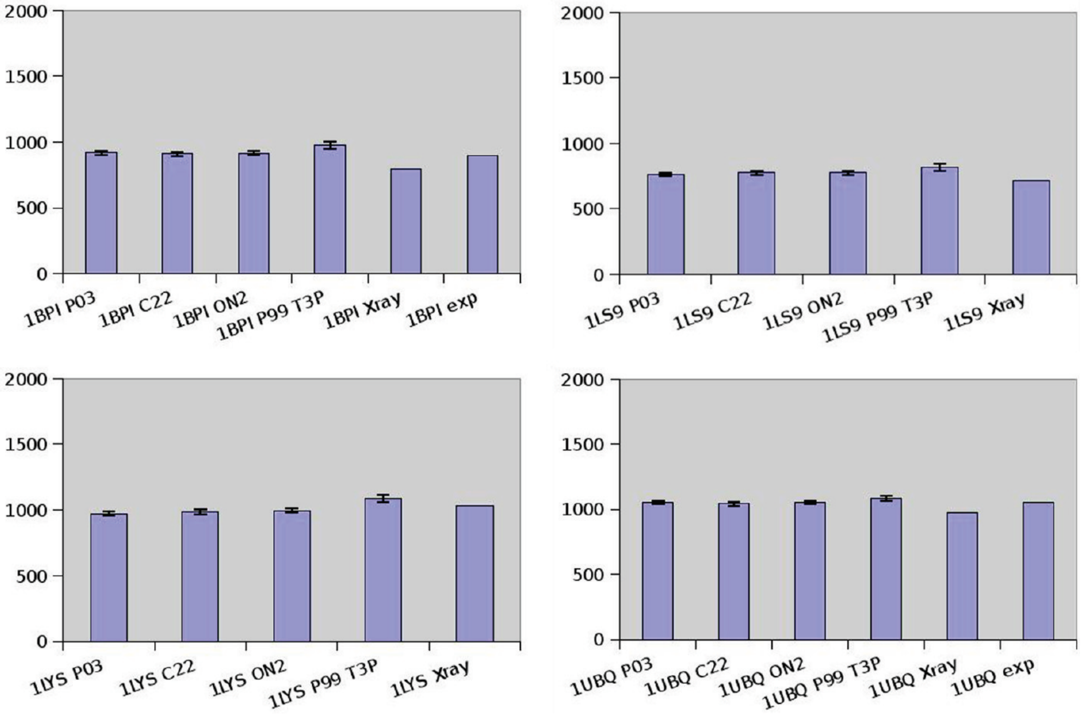

Figure 7. CCS (in Å^2) for four small proteins, as determined from MD simulations in the gas phase considering different force-fields. Results, obtained from MD simulations in solution, of crystal structure and, when available, experimental ESI measures are displayed for comparisons. Standard deviations associated to the different MD averages are shown.

surprisingly then, there is a close correspondence between the CCS obtained from MD simulations in the gas phase and those obtained in aqueous trajectories (Figure 9). In fact, the agreement with X-ray values is better for gas-phase simulations (3% underestimation) than for solution trajectories (5% overestimation), mimicking the results found for isolated proteins and showing that, while proteins in pure water expand with respect to crystal conditions, they compress when moving to the gas phase. In summary, MD simulations strongly suggest that gas phase experiments like MS-ESI produce valuable data on the structure of protein and protein complexes in solution.

Information Load in Low-Resolution Structural Data. It is clear that the amount of information in the low-resolution data considered here is modest, and that these techniques alone are unable to unambiguously determine the three-dimensional structure of proteins or protein complexes. Thus, the R_h gives only information on the shape of a molecule perpendicular to an external field, is quite ambiguous in terms of structure definition, and is prone to artifacts for proteins with tails. The CCS is a magnitude related to the molecular surface in conditions far from the physiological ones, and the information derived is then unable to differentiate between different conformations displaying similar molecular surface. Finally, the SAXS spectrum contains, in principle, all possible structural information on the protein, but interpretation of the SAXS spectrum is difficult, and ambiguous assignments are often derived. However, despite all their limitations, these methods are quite powerful to discard erroneous solutions that can be obtained from modeling techniques. This is shown when scanning the CASP7 deposited model for monomeric proteins. Thus, if we randomly select five models (for each target) from those deposited in the CASP7 database, we have a random probability around 50% of choosing one of the good solutions (we considered good solutions those with a (GDT $-5) > \mathrm{GDT}_{\text{best solution}}$; GDT being a score function defined by CASP7 evaluators).[42] This probability sharply increases to 70% (CCS and R_h) and 80% (SAXS) when low-resolution structural data are used to clean up unrealistic models, see Figure 10. However, the largest enrichment is obtained when low-resolution structural data, which provide global information on the protein structure, are combined with statistical potentials like ProSA, which detect local errors undetectable in low-resolution data. Thus, when combining ProSA with CCS and R_h restrains, the chances of finding the good model among five randomly chosen increases to 86% and to more than 98%, if ProSA is combined with SAXS spectra (see Figure 10). In summary, low-resolution data, especially SAXS spectra, combined with standard statistical potentials dramatically increases the possibilities to find good structural models when using standard protein-modeling tools.

The same analysis performed for protein complexes, using now the CAPRI database, provides qualitatively similar results. Thus, we have a random probability around 30% of finding an acceptable prediction (as defined by CAPRI evaluators),[43] when only five random models are selected. The chances increase to 45 (R_h), 55 (CCS), and 75% (SAXS) when low-resolution structural data are used as restrains (Figure 11). Again the chances increase when an empirical potential, such as pyDock, is used to detect local errors and an experimental low-resolution data are used to detect global structural errors. Thus, when pyDock is combined with CCS, the chances of finding an acceptable structure in five

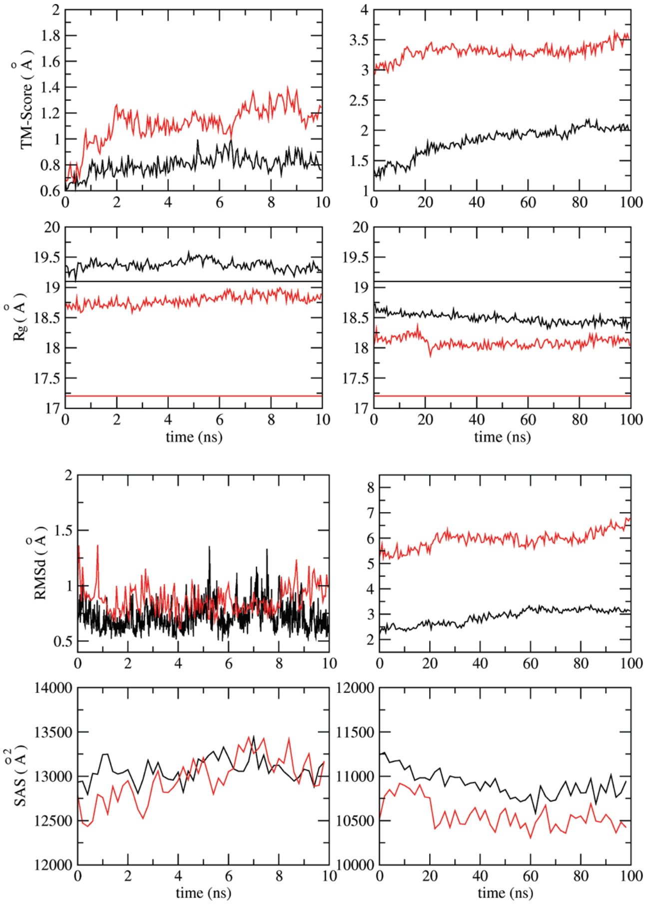

Figure 8. Global structural descriptors (TmScore, gyration radii, RMSd, and SAS) for protein complexes (1CSE and 3TGI) obtained from MD simulations in the gas phase (right panels). The reference results for the simulation in solution are displayed on the left panels, and the values derived from the experimental structure (crystal) are shown as straight lines.

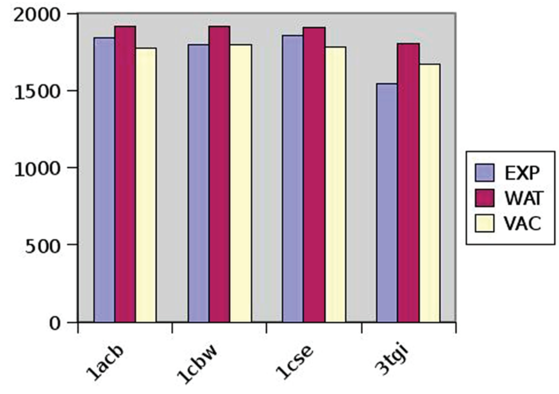

Figure 9. CCS (in Å^2) of different protein complexes as determined from MD simulations in the gas phase, MD simulations in solution, and crystal structures.

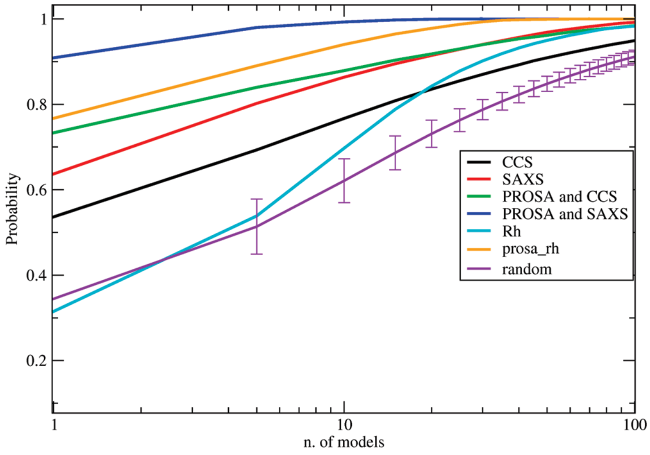

Figure 10. Enrichment curves for the prediction of the best structural model of monomeric proteins obtained using data from the CASP7 experiment.

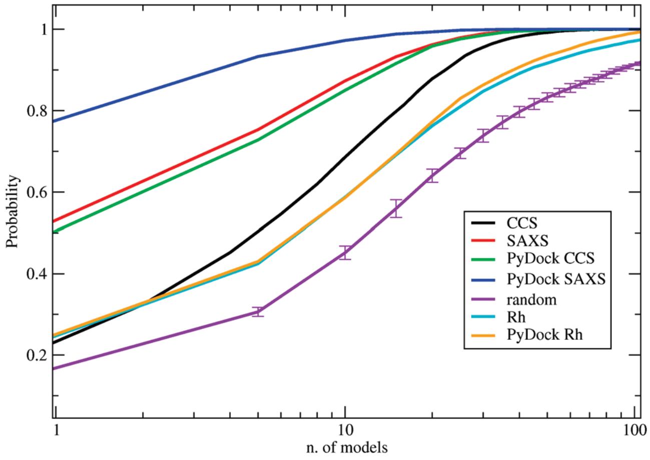

Figure 11. Enrichment curves for the prediction of the best structural model of protein complexes obtained by using data from the CAPRI experiment.

randomly selected ones increase to more than 70%, the chances increasing to 94% if PyDock is combined with SAXS spectra. In summary, even for the very difficult case of protein complex prediction, low-resolution structural data, especially when combined with statistical potentials, dramatically increases the chances of selecting good structural models from the ensemble of solutions provided by standard modeling techniques (see Figure 11).

Conclusions

Low-resolution structural data are very robust and quite insensitive to oscillations due to the intrinsic flexibility of proteins. Global descriptors of proteins, like the collision cross-section, are quite robust to dramatic changes in the environment, allowing then the use of structural information derived from very hostile conditions, such as the gas phase, to gain insight into the structure of the proteins (and protein complexes) in aqueous solutions. Importantly, despite the reduced information content existing in hydrodynamic radii, collision cross sections, or SAXS curves, these magnitudes can be used to detect errors in theoretical structural models that were accepted by scoring procedures in leading modeling tools. The global result is an overall improvement in the quality of the final suggested models of proteins and of protein−protein complexes. The improvement is especially important when the low-resolution data are combined with empirical potentials, such as ProSA or pyDock. Finally, the analysis of CASP7 and CAPRI experiments demonstrates that SAXS is the richest source of structural information of the three considered here, while the hydrodynamic radius (even useful) provides a more reduced amount of information. Overall, our results demonstrate that low-resolution structural data, in general, is easy to obtain and can be efficiently used to increase the chances of success in the prediction of the three-dimensional structure of proteins and protein complexes, even when obtained in conditions quite far from the physiological ones.

Acknowledgment. This work has been supported by the Spanish Ministry of Education and Science (BIO2006-01602, CONSOLIDER Project in Escience, and BIO2008-02882), the Spanish Ministry of Health (COMBIOMED network), the Fundación Marcelino Botín, and the National Institute of Bioinformatics. All calculations were performed in the MareNostrum supercomputer at the Barcelona Supercomputing Center.

Supporting Information Available: Figures show the stability of secondary structures and the comparison between experimental and simulated CCS values. This material is available free of charge via the Internet at http://pubs.acs.org.

References

(1) Marti-Renom, M. A.; Stuart, A. C.; Fiser, A.; Sanchez, R.; Melo, F.; Sali, A. *Annu. Rev. Biophys. Bio.* **2000**, *29*, 291.

(2) Simons, K. T.; Strauss, C.; Baker, D. *J. Mol. Biol.* **2001**, *306*, 1191.

(3) Kryshtafovych, A.; Fidelis, K.; Moult, J. *Proteins* **2007**, *69*, 194.

(4) Lensink, M. F.; Mendez, R.; Wodak, S. J. *Proteins* **2007**, *69*, 704.

(5) Karplus, M.; Kuriyan, J. *Proc. Natl. Acad. Sci. U.S.A.* **2005**, *102*, 6679.

(6) Pazos, F.; Helmer-Citterich, M.; Ausiello, G.; Valencia, A. *J. Mol. Biol.* **1997**, *271*, 511.

(7) Lichtarge, O.; Yamamoto, K. R.; Cohen, F. E. *J. Mol. Biol.* **1997**, *274*, 325.

(8) Chelliah, V.; Chen, L.; Blundell, T. L.; Lovell, S. C. *J. Mol. Biol.* **2004**, *342*, 1487.

(9) Aloy, P.; Querol, E.; Aviles, F. X.; Sternberg, M. J. *J. Mol. Biol.* **2001**, *311*, 395.

(10) Chelliah, V.; Blundell, T. L.; Fernandez-Recio, J. *J. Mol. Biol.* **2006**, *357*, 1669.

(11) Juan, D.; Pazos, F.; Valencia, A. *Proc. Natl. Acad. Sci. U.S.A.* **2008**, *105*, 934.

(12) Matsumoto, R.; Sali, A.; Ghildyal, N.; Karplus, M.; Stevens, R. L. *J. Biol. Chem.* **1995**, *270*, 19524.

(13) Xu, L. Z.; Sanchez, R.; Sali, A.; Heintz, N. *J. Biol. Chem.* **1996**, *271*, 24711.

(14) Andrea, S. *J. Mass. Spectrom.* **2003**, *38*, 1225.

(15) Covey, T.; Douglas, D. J. *J. Am. Soc. Mass Spectrom.* **1993**, *4*, 616.

(16) Petoukhov, M. V.; Svergun, D. I. *Curr. Opin. Struct. Biol.* **2007**, *17*, 562.

(17) Putnam, C. D.; Hammel, M.; Hura, G. L.; Tainer, J. A. *Q. Rev. Biophys.* **2007**, *40*, 191.

(18) Koch, M. H.; Vachette, P.; Svergun, D. I. *Q. Rev. Biophys.* **2003**, *36*, 147.

(19) Tanford, C. In *Physical Chemistry of Macromolecules*; J. Wiley and Sons: New York, 1961.

(20) Garcia de la Torre, J.; Huertas, M. L.; Carrasco, B. *J. Magn. Reson.* **2000**, *147*, 138.

(21) Bernado, P.; Garcia de la Torre, J.; Pons, M. *J. Biomol. NMR* **2002**, *23*, 139.

(22) Svergun, D.; Barberato, C.; Koch, M. H. J. *J. Appl. Crystallogr.* **1995**, *28*, 768.

(23) Mesleh, M. F.; Hunter, J. M.; Shvartsburg, A. A.; Schatz, G. C.; Jarrold, M. F. *J. Phys. Chem.* **1996**, *100*, 16082.

(24) Shelimov, K. B.; Clemmer, D. E.; Hudgins, R. R.; Jarrold, M. F. *J. Am. Chem. Soc.* **1997**, *119*, 2240.

(25) (a) Jarrold, M. F. *Annu. Rev. Phys. Chem.* **2000**, *51*, 179. (b) Breuker, K.; McLafferty, F. W. *Proc. Natl. Acad. Sci. U.S.A.* **2008**, *105*, 18145.

(26) Kaltashov, I. A.; Mohimen, A. *Anal. Chem.* **2005**, *77*, 5370.

(27) Meyer, T.; de la Cruz, X.; Orozco, M. *Structure* **2009**, *17*, 88.

(28) Duan, Y.; Wu, C.; Chowdhury, S.; Lee, M. C.; Xiong, G.; Zhang, W.; Yang, R.; Cieplak, P.; Luo, R.; Lee, T.; Caldwell, T.; Wang, J.; Kollman, P. *J. Comput. Chem.* **2003**, *24*, 1999.

(29) Kaminski, G. A.; Friesner, R. A.; Tirado-Rives, J.; Jorgensen, W. L. *J. Phys. Chem. B* **2001**, *105*, 6474.

(30) MacKerell, A. D.; Bashford, D.; Bellott; Dunbrack, R. L.; Evanseck, J. D.; Field, M. J.; Fischer, S.; Gao, J.; Guo, H.; Ha, S.; Joseph-McCarthy, D.; Kuchnir, L.; Kuczera, K.; Lau, F. T. K.; Mattos, C.; Michnick, S.; Ngo, T.; Nguyen, D. T.; Prodhom, B.; Reiher, W. E.; Roux, B.; Schlenkrich, M.; Smith, J. C.; Stote, R.; Straub, J.; Watanabe, M.; Wiorkiewicz-Kuczera, J.; Yin, D.; Karplus, M. *J. Phys. Chem. B* **1998**, *102*, 3586.

(31) Scarff, C. A.; Thalassinos, K.; Hilton, G. R.; Scrivens, J. H. *Rapid Commun. Mass. Spectrom.* **2008**, *22*, 3297.

(32) William, L. J.; Jayaraman, C.; Jeffry, D. M.; Roger, W. I.; Michael, L. K. *J. Chem. Phys.* **1983**, *79*, 926.

(33) Darden, T.; York, D.; Pederson, L. *J. Chem. Phys.* **1993**, *98*, 10089.

(34) Sippl, M. J. *Proteins* **1993**, *17*, 355.

(35) Cheng, T. M.; Blundell, T. L.; Fernandez-Recio, J. *Proteins* **2007**, *68*, 503.

(36) Canutescu, A. A.; Shelenkov, A. A.; Dunbrack, R. L., Jr. *Protein Sci.* **2003**, *12*, 2001.

(37) Rueda, M.; Ferrer-Costa, C.; Meyer, T.; Perez, A.; Camps, J.; Hospital, A.; Gelpi, J. L.; Orozco, M. *Proc. Natl. Acad. Sci. U.S.A.* **2007**, *104*, 796.

(38) Bothner, B.; Siuzdak, G. *ChemBioChem* **2004**, *5*, 258.

(39) Jarrold, M. F. *Annu. Rev. Phys. Chem.* **2000**, *51*, 179.

(40) Patriksson, A.; Marklund, E.; van der Spoel, D. *Biochemistry* **2007**, *46*, 933.

(41) (a) Valentine, S. J.; Counterman, A. E.; Clemmer, D. E. *J. Am. Soc. Mass Spectrom.* **1997**, *8*, 954. (b) Shelimov, K. B.; Clemmer, D. E.; Hudgins, R. R.; Jarrold, M. F. *J. Am. Chem. Soc.* **1997**, *119*, 2240. (c) Valentine, S. J.; Anderson, S. J.; Ellington, A. E.; Clemmer, D. E. *J. Phys. Chem. B* **1997**, *101*, 3891. (d) Segev, E.; Wyttenbach, T.; Bowers, M. T.; Gerber, R. B. *Phys. Chem. Chem. Phys.* **2008**, *10*, 3077.

(42) CASP7; http://predictioncenter.org/casp7. Accessed Sept 4, 2009.

(43) CAPRI; http://www.ebi.ac.uk/msd-srv/capri. Accessed Sept 8, 2009.

CT900305M

Quantum Chemistry on Graphical Processing Units. 2. Direct Self-Consistent-Field (SCF) Implementation. [*J. Chem. Theory Comput. 5,* 1004–1015 (2009)]. By Ivan S. Ufimtsev and Todd J. Martinez*.

In our recent manuscript,[1] we compared timings for Coulomb matrix formation on graphical processing units (GPUs) with a previous implementation reported by Yasuda.[2] Our intention was to compare the performance that could be obtained from porting CPU code to the GPU as compared to completely redesigning the algorithms for stream processors. It has come to our attention that Yasuda's implementation was in fact not ported from CPU code but rather from code developed for the GRAPE-DR (a custom accelerator that has many features in common with stream processors). Had this been clear to us from ref 2, there would have been no reason to compare timings of the two implementations. A further issue is that the timings presented in Table 4 of ref 2 were misinterpreted. Although the caption states "Computational Time in Seconds of the Coulomb Potential Evaluation During *the* SCF Iteration" (emphasis added), these timings in fact refer to the entire SCF procedure, that is, *all* SCF iterations. Prof. Yasuda has kindly informed us how many iterations were required in each case. Thus, we present a revised table that is a fair comparison and should replace Table 2 in ref 1. The timings for the "present work" correspond to Coulomb matrix formation in the first 13/11 iterations for taxol/valinomycin, respectively. The difference in timings observed reflects different compilers and CPU hardware as well as coding strategies and algorithms. For example, accumulation of the two-electron integrals in ref 1 was performed with single precision accuracy (in the code version designed for the G80 architecture), while emulation of double precision accuracy was used in ref 2. Nevertheless, one can conclude that both implementations perform similarly. This is not surprising since both reflect redesign of the fundamental algorithms for the stream processor.

Table 2. *J*-Matrix Formation Time (in Seconds) for Taxol and Valinomycin Molecules Using 3-21G and 6-31G Basis Sets[a]

	J-matrix formation time (seconds)			
	Gaussian on GPU[7]		present work	
molecule	3-21G	6-31G	3-21G	6-31G
Taxol (13 iterations)	16.8	31.9	5.1	13.4
Valinomycin (11 iterations)	23.8	57.4	8.3	22.6

[a] Previously reported GPU-accelerated timings are compared to timings from our code. Timings for the present work include construction and sorting of pair quantities, data transfer to/from the GPU, construction of *J* on the GPU, and post-processing of the intermediate *J*-matrix on the CPU. All timings were obtained on one GeForce 8800GTX card. The GPU code was compiled with Nvidia CUDA Compiler ver. 2.0.

References

(1) Ufimtsev, I. S.; Martinez, T. J. *J. Chem. Theory Comput.* **2009**, *5*, 1004.
(2) Yasuda, K. *J. Comput. Chem.* **2008**, *29*, 334.

CT900433G

10.1021/ct900433g